ADVERTIMENT. La consulta d'aquesta tesi queda condicionada a l'acceptació de les següents condicions d'ús: La difusió d'aquesta tesi per mitjà del servei TDX (www.tesisenxarxa.net) ha estat autoritzada pels titulars dels drets de propietat intel·lectual únicament per a usos privats emmarcats en activitats d'investigació i docència. No s'autoritza la seva reproducció amb finalitats de lucre ni la seva difusió i posada a disposició des d'un lloc aliè al servei TDX. No s'autoritza la presentació del seu contingut en una finestra o marc aliè a TDX (framing). Aquesta reserva de drets afecta tant al resum de presentació de la tesi com als seus continguts. En la utilització o cita de parts de la tesi és obligat indicar el nom de la persona autora.

ADVERTENCIA. La consulta de esta tesis queda condicionada a la aceptación de las siguientes condiciones de uso: La difusión de esta tesis por medio del servicio TDR (www.tesisenred.net) ha sido autorizada por los titulares de los derechos de propiedad intelectual únicamente para usos privados enmarcados en actividades de investigación y docencia. No se autoriza su reproducción con finalidades de lucro ni su difusión y puesta a disposición desde un sitio ajeno al servicio TDR. No se autoriza la presentación de su contenido en una ventana o marco ajeno a TDR (framing). Esta reserva de derechos afecta tanto al resumen de presentación de la tesis como a sus contenidos. En la utilización o cita de partes de la tesis es obligado indicar el nombre de la persona autora.

WARNING. On having consulted this thesis you're accepting the following use conditions: Spreading this thesis by the TDX (www.tesisenxarxa.net) service has been authorized by the titular of the intellectual property rights only for private uses placed in investigation and teaching activities. Reproduction with lucrative aims is not authorized neither its spreading and availability from a site foreign to the TDX service. Introducing its content in a window or frame foreign to the TDX service is not authorized (framing). This rights affect to the presentation summary of the thesis as well as to its contents. In the using or citation of parts of the thesis it's obliged to indicate the name of the author

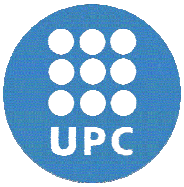

UNIVERSITAT POLITÈCNICA DE CATALUNYA

DEPARTAMENT D'ENGINYERIA QUÍMICA

"Design, synthesis, characterization and development of novel organic conducting polymers with technological applications"

David Aradilla Zapata

Advisors: Dr. Francesc Estrany Coda and Dr. José Ignacio Iribarren Laco

Barcelona, December 2012

I dedicate this work to my parents and my brother

Agradecimientos

El transcurso de esta tesis ha sido un viaje lleno de aventuras donde he tenido el placer de conocer a muchas personas que han contribuido de forma muy especial a la consecución de este trabajo.

En primer lugar querría expresar mi más sincera gratitud al Prof. Carlos Alemán por haberme brindado la oportunidad de realizar la tesis en su grupo de investigación IMEM. Para mí ha sido un verdadero placer haber llevado a cabo esta tesis en su grupo. Gracias por toda tu atención, ayuda, disponibilidad, inspiración y consejos. Querría expresarle también mi gratitud por haber contribuido de forma muy especial en la consecución de una tesis multidisciplinar. En segundo lugar un agradecimiento muy especial a mis directores, Dr. Francesc Estrany y Dr. José Ignacio Iribarren por toda su atención, supervisión, ayuda, dirección y discusiones científicas que me ayudaron mucho en la consecución de esta tesis. Un agradecimiento especial a la Dra. Elaine Armelin por su inestimable ayuda, amabilidad y asistencia a nivel experimental cuando la he necesitado. No querría olvidarme del Prof. Ramón Oliver a quién le agradezco enormemente su particular forma de ver, entender y comprender la vida, pero sobre todo por sus valores.

Durante el devenir de esta tesis numerosas personas han compartido sus conocimientos y experiencia conmigo para que pudiera formarme y aprender, de forma que merecen mi más profundo agradecimiento. Primeramente, en el lado experimental quiero expresar mi gratitud a la Dra. Maria Teresa Casas y al Prof. Jordi Puiggalí por las imágenes TEM proporcionadas en este trabajo y por sus disquisiciones e interpretaciones en este campo tan difícil. En esta línea no querría olvidarme tampoco de dar las gracias a la Dra. Lourdes Franco y el Dr. Abdelilah Alla por sus ensayos termogravimétricos y al Dr. Bruno Teixeira por haberme enseñado el funcionamiento del equipo UV-Visible. Gracias de nuevo también a la Dra. Elaine Armelin y a la Dra. Lourdes Franco por sus explicaciones y conocimiento en el equipo de infrarrojos. Un emotivo agradecimiento al Dr. Nestor Veglio por sus ensayos de DRX y muchas gracias por haber compartido su sabiduría en este campo conmigo y que desafortunadamente nos dejó hace algún tiempo. Descansa en paz. Por otro lado, quiero expresar mi profundo agradecimiento a los técnicos del CRnE por toda su inestimable ayuda, atención y disponibilidad que siempre me han prestado. En este sentido mis más sinceras gracias al Dr. Trifón Trifonov y a la Dra. Montserrat Dominguez. Gracias Trifón por haberme enseñado y formado en el arte de la microscopía, el perfilómetro, el

UV-Visible y por los ensayos de DRX. A la Dra. Montserrat quiero agradecerle los ensayos de XPS y su formación en el equipo de interferometría. Una mención especial merecen también el Dr. Gerard Oncins y el Dr. Jordi Díaz por haberme enseñado el interesante mundo de la microscopía de fuerzas atómicas (AFM). Gracias por vuestro conocimiento, paciencia y por todo lo que me enseñasteis que sin duda alguna me ha servido de gran ayuda en mi formación en este apasionante mundo. Al hablar del AFM hay una persona que también merece unas líneas de agradecimiento por haberme formado y complementado en el uso de este equipo. Mis más emotivas gracias a mi director, el Dr. Francesc Estrany. No querría acabar este apartado sin olvidarme de mis compañeros de laboratorio y despacho a quienes agradezco su atención, ayuda y amabilidad prestada durante estos cuatros años. Por otro lado quiero también agradecer a los compañeros de la planta de arriba por su ayuda y amabilidad cuando he necesitado alguna cosa. Gracias.

En el ámbito teórico quiero agradecer al Dr. David Zanuy, al Dr. Guillem Revilla, al Dr. Francisco Rodriguez-Ropero, al Dr. David Curcó y a Esther por su atención, disponibilidad, ayuda, conocimiento y resolución de consultas en el ámbito de la simulación. En este sentido quiero también agradecer también al Prof. Carlos Alemán la oportunidad que me dio para poder realizar algunos trabajos en el campo de la química computacional, por su ayuda, conocimiento y atención prestada en la realización de algunos trabajos teóricos.

En el transcurso de esta tesis tuve la oportunidad de realizar dos estancias en el extranjero. En este aspecto me gustaría expresar mi más sincero agradecimiento a l'École Nationale Supérieure de chimie de Paris y al grupo "*Équipe de modélisation des systèmes complexes*" dirigido por el Prof. Carlo Adamo. Gracias a todo el grupo por su acogida y amabilidad prestada durante mi estancia allí. Un especial agradecimiento al Prof. Carlo Adamo y a la Prof. Ilaria Ciofini por haberme enseñado la metodología TD-DFT. En segundo lugar, quiero expresar también mi gratitud al departamento de física-química de la Universidade Federal do Rio Grande do Sul por su acogida y muy especialmente al grupo de la Prof. Denise Azambuja por su cooperación, amabilidad y atención durante mi estancia con ellos. Quiero de forma especial agradecer a la Prof. Denise y a Viviane el haberme enseñado los secretos de la técnica de impedancia EIS que tanto me han servido en mis resultados. Durante mis estancias quiero agradecer que me sintiera uno más y realmente me sentí como en casa. Muchas gracias a todos.

No querría olvidarme en este apartado de agradecimientos a las personas que han aportado su granito de arena de forma diferente. En este aspecto, quiero expresar un agradecimiento especial al Sr. José Luis, técnico informático del departamento que en más de una ocasión me ha sacado de apuros, gracias por tu paciencia, disponibilidad y atención. Siguiendo esta línea, gracias también a las personas que conforman el equipo administrativo del departamento por su gestión en los procesos burocráticos, especialmente a la Sra. Irene y la Sra. Francina por haberme ayudarme en estos asuntos, de nuevo muchísimas gracias por la amabilidad, eficacia, información y atención que siempre me habéis prestado durante este tiempo.

Antes de finalizar la parte de agradecimientos querría expresar mi gratitud a la UPC por haberme concedido la beca a partir de la cual he podido desarrollar mi tesis.

No querría olvidarme de todas aquellas personas que me han apoyado en los momentos buenos pero también en los complicados y difíciles de esta tesis. En este sentido mi más personal agradecimiento a mis amigos, familiares y a mi novia.

Para acabar, una vez más quiero expresar mi agradecimiento a todas las personas que han contribuido a que esta tesis vea la luz ya que sin ellos no hubiera sido posible. Gracias a todos por todo.

Abstract

The development and innovation of new materials has awakened a great interest in the society since Antiquity. The most important progresses occurred in our history have been always involved in the discovery of materials (*e.g.* fire, bronze or iron). Within this context, the technology and processing of materials have triggered important advances in our society. In the last decades, a novel family of polymer known as conducting polymers has revolutionized the field of polymers due to its high conductivity and electrochemical activity, which behave and exhibit properties similar to metals or semiconductors. Their unusual and promising features have culminated in a great impact in the growth of new and recent technologies such as nanotechnology, nanobiotechnology, nanophysics or nanoelectronics, respectively. Precisely, innovative technological applications made from conducting polymers have been widely reported in these fields. Thus, new electronic and electronical devices such as biosensors, supercapacitors, organic light emitting diodes, electrochromic devices, photovoltaic cells, or actuators have been carried out. However, conducting polymers present some drawbacks and limitations according to their chemical nature and synthesis process. Among the most important, solubility, processing, mechanical properties, cost and stability limit their practical industrial applications. Over the past decade, a great number of investigations and tremendous efforts have been carried out to understand the mechanisms and optical, chemical, structural, electrochemical and topological properties of conducting polymers with the aim of solving the aforementioned problems.

In this thesis, a series of novel organic conducting polymers have been synthesized using alternative methods based on electrochemical techniques, which have allowed to broaden the knowledge in the field of characterization by means of topological, spectroscopic, electrochemical and structural techniques. Among the variety of synthesis techniques of conducting polymers, layer-by-layer (LbL) has been one of the most important to build multilayered systems. Thus, in this thesis the LbL has shown to be an excellent procedure to explore new applications in the field of energy storage by using conducting polymers. On the other hand, recently, the influence of new sustituents on functionalized conducting polymers has been proved to modify the structural, optical and physical properties of conducting polymers. Within this context, synthesis of novel functionalized conducting polymers bearing strong electron-withdrawing sustituents such as cyano group or halide atoms have been widely studied and characterized

throughout this thesis. These substituents have emerged as promising candidates in the field of chemical sensors and electrochromic devices. Although the functionality of polymers or the development of new techniques are excellent procedures to synthesize and to develop new properties in the field of conducting polymers, it is worth mentioning that the substrate plays a crucial role on the electrochemical field. Accordingly, the substrates can also modify and change the properties of conducting polymers during the electropolymerization process. In this way, different and modified substrates were employed in this work with the aim of achieving new applications in the field of corrosion inhibitors or as supercapacitors. Supercapacitor as energy storage device has been an outstanding application during this thesis. On the other hand, the field of nanotechnology has taken an important part in this thesis through development and design of promising hybrid nanocomposites based on conducting polymers and clay with technological applications and interesting optoelectronic properties.

In this thesis, the contribution of theoretical techniques based on quantum mechanical calculations has allowed to predict some electronic and structural properties of conjugated polymers, which could be corroborated experimentally. The quantum mechanics is an useful tool to check experimental results and to understand mechanisms not fully understood at experimental level. Therefore, theoretical calculations have provided promising information to obtain new insights in the field of conducting polymers.

Objectives

The objective of this thesis is focused on the understanding of structural mechanisms and knowledge of novel organic conducting polymers for technological applications. The achievement of this objective has been developed using the following structure:

a) To synthesize and to characterize novel conducting polymers based on pyrrole and thiophene derivatives through electrochemical methods to determine their physical, structural, electrochemical and topological properties. To understand and to compare the experimental assays with theoretical methods to predict electronic and structural properties.

b) To develop a new procedure of the layer-by-layer technique (LbL) based on electrochemical methods to synthesize multilayered systems. To analyze, to understand and to correlate the effect among layers of conducting polymers with their chemical nature by using microscopic, spectroscopic and electrochemical techniques.

c) To study the influence of strong electron-withdrawing sustituents such as cyano group and halide atoms on the electronic, optical, electrochemical, morphological and structural properties of thiophene and pyrrole derivatives. To analyze and to evaluate their influences on applications such as chemical sensors or electrochromic devices.

d) To synthesize and to characterize new hybrid nanocomposites from inorganic (mineral clays) and organic materials (conducting polymers) through electrochemical methods to be employed as corrosion inhibitors and supercapacitors. To determine the optimal concentration of clay to obtain the best properties.

e) To analyze the influence of self-assembled monolayers of octanethiol and dodecanethiol on steel substrates to evaluate the growth of conducting polymers and their performances as corrosion inhibitors and supercapacitors.

f) To study the substrate effect on the growing of conducting polymers during the first stages of polymerization (nucleation) by using substrates of different chemical nature. To analyze their morphology and capacitive properties to be employed as supercapacitors.

g) To investigate the influence of the I^-/I_3^- redox pair on the capacitive properties of conducting polymer films.

h) To explore applications in the field of energy storage in order to develop a new all-conducting polymer rechargeable battery. To study the optoelectronic properties of conducting polymers in hybrid nanocomposites.

Synopsis

This thesis is focused on the design, synthesis, characterization and development of novel organic conducting polymers with technological applications in the fields of electronic and electric devices, corrosion inhibitors and chemical sensors. The structure of this work has been divided into different chapters as follows:

Chapter I

The first chapter is devoted to provide a general introduction of the background of conducting polymers. Besides, a description of the structure and mechanism of conducting polymers is described. In this chapter a deep background of the research topics based on this work are detailed as follows:

- Multilayered systems based on conducting polymers
- Influence of the substrate on the polymerization of conducting polymers
- Functionality of conducting polymers
- Nanotechnology in conducting polymers

Chapter II

A description of the methodology employed in this thesis is summarized in this chapter. The methodology of this thesis has been divided into two different structures. The first one is devoted to the experimental techniques, which are focused on electrochemical, spectroscopic, morphological and structural techniques. The second part represents the theoretical methodology, which is mainly based on quantum mechanics fundamentals.

Chapter III

This third chapter is focused on studying a new procedure of synthesis of polymers based on the layer-by-layer (LbL) technique. In this chapter, a new methodology of the LbL technique based on potentiostatic electrochemical methods in order to synthesize multilayered systems is described. The characterization of these systems was carried out using microscopic and electrochemical techniques. The synergistic effect produced among conducting polymers layers constituted excellent improvements in terms of electrochemical properties compared with the pure homopolymers, which allowed to develop symmetric multilayered supercapacitors.

Chapter IV

The influence of the substrate on the properties of conducting polymers was studied in this chapter. Different substrates such as indium tin oxide and steel were used to study the growing mechanism (nucleation, and growth) of poly(3,4-ethylenedioxythiophene) and its electrochemical properties. The results showed important differences on its morphology by using ITO or steel substrates, respectively. This effect being particularly interesting in supercapacitive properties. Moreover, the substrate effect was also studied from thiol modified-steel to evaluate its influence on the structure of conducting polymers and applications as corrosion inhibitors.

Chapter V

In this chapter a new strategy to synthesize nanocomposite materials using conducting polymer matrix and inorganic materials (mineral clays) has been reported. The polymeric matrix is made of PEDOT and the inorganic material is montmorillonite (MMT). The first part of the chapter is devoted to characterize and optimize nanocomposites using electrochemical techniques with the goal of obtaining exfoliated structures. The second part is related with the optimization of the content of reinforcement to determine the best ratio properties / structure. Finally, new multilayered electrochemical nanocomposites were studied and characterized.

Chapter VI

The sixth chapter is focused on the synthesis of a new pyrrole derivative (poly[N-(2-cyanoethylpyrrole)). An exhaustive chemical, physical, topological and electrochemical characterization of this polymer was carried out. The influence of the cyano group on the structural conformation and electronic properties of this polymer was studied at theoretical level and compared with experimental assays. The strong electron-withdrawing effect of cyano group showed relevant importance on its use as chemical sensor.

Chapter VII

The seventh chapter presents the results of the study of a new conducting polymer family, known as poly(3-halidethiophene)s. The chapter is focused on the study of the influence of halide atoms on the electronic and structural properties of thiophene.

Chapter VIII

The last chapter of results of this thesis is devoted to study the applications of conducting polymers in the field of energy storage through development of new electronic devices based on batteries. Moreover, the influence of some elements on photovoltaic cells such as the I^-/I_3^- redox pair were studied in the application as organic ultracapacitors. Finally, a study about the optoelectronic properties of hybrid nanocomposites based on conducting polymers and clay was carried out.

Chapter IX and X

The last chapters of this thesis are devoted to the summary, discussion and conclusions of the results obtained throughout this thesis.

LIST OF SYMBOLS AND ABBREVIATIONS

A	Absorbance or electrode area
ABSA	Aminobenzensulfonic acid
ADP	Average Degree of Polymerization
AFM	Atomic Force Microscopy
AISI	American Iron Steel Industry
AOM	Atomic Overlap Matrices
a.u.	Atomic Units
BFEE	Boron Trifluoride Diethyl Etherate
[BMIM]PF_6	1-butyl-3-methylimidazolium hexafluorophosphate
BSSE	Basis Set Superposition Error
[$(Bu)_4NBF_4$]	Tetrabutylammonium tetrafluoroborate
B3LYP	Beckes's three parameter hybrid functional with the Lee, Yang and Parr expression
B3P86	B3 functional with the Perdew expression
B3PW91	B3 functional with the Perdew and Wang's expression
C	Couloumb
c	Concentration of the electroactive species
CA	Chronoamperometry
C-AFM	Conductive Atomic Force Microscopy
CC	Chronocoulometry
C_{DL}	Double Layer Capacitance
cm^2	Centimeter square
CNT	Carbon Nanotube
CP	Chronopotentiometry; Conducting Polymer or Counterpoise
C_{PS}	Faradaic Pseudo-capacitance
CV	Cyclic Voltammetry
CPE	Constant Phase Element
D	Diffusion Coefficient
DFT	Density Functional Theory
dl	Doping level
DNA	Deoxyribonucleic Acid
DSSC	Dye-Sensitized Solar Cell

DRX	X-Ray Diffraction
E	Potential
EA	Electron Affinity
EC	Equivalent Circuit
ECD	Electrochromic Device
E_d	Energy Density
EDX	Energy Dispersive X-ray
EIS	Electrochemical Impedance Spectroscopy
ESPR	Electrochemical Surface Plasmon Resonance
E_{max}	Maximum specific energy
E_p^a	Oxidation Potential Peak
E_p^c	Cathodic Potential Peak
eV	Electron-volts
ε_g	π-π^* lowest electron transition energy or band gap energy
ε^{ox}	Onset potential for oxidation
F	Faraday or Faraday's constant (96500 C)
f	Frequency
f	Doping level
FLU	Fluctuation Index of Aromaticity
FTIR	Fourier-Transform Infrared
GGA	Generalised Gradient Approximation
GIAO	Gauge Including Atomic Orbitals
GRP	Galvanostatic Recurrent Pulse
h	Planck's constant
HF	Hartree-Fock
HOMA	Harmonic oscillator model of aromaticity
HOMO	Highest Occupied Molecular Orbital
Hz	Hertz
I	Current
IP	Ionization Potential
ITO	Indium-Tin-Oxide
j	Current density
K_p	Electron transfer rate constant
KT	Koopman's theory

l	Thickness or number of bonds
LB	Langmuir-Blodgett
LbL	Layer-by-Layer
LDA	Local Density Approximation
LED	Light Emitting Diode
LES	Loss of Electroactivity or Electrostability
LUMO	Lowest Unoccupied Molecular Orbital
M	Molar mass of the monomer
MCI	Electronic-based Multicenter Index
MEH-PPV	Poly(2-methoxy-5-(20-ethylhexyloxy)-1,4-phenylenevinylene)
MeOHPy	Hydroxymethylpyrrole
ml	Multilayer
MMT	Montmorillonite
MP	Moller Plesset
M/Q	Current Productivity
m_{dop}	Mass of dopant per polymer unit of mass
m_{pol}	Mass of polymer
n	Number of repeat units
n_{av}	Average number of electrons per monomer
NCMPy	N-(2-cyanomethyl)pyrrole
NMR	Nuclear Magnetic Resonance
NICS	Magnetic-based Nucleus Independent Chemical Shifts
NRSM	Non-Volative Resistive Switching Memory
n_{ox}	Number of electrons consumed to incorporate a monomer into a polymer
OCP	Open Circuit Potential
OLED	Organic Light Emitting Diode
P	Power density
PAA	Polyacrylic Acid
PAH	Poly(allylamine hydrochloride)
PANBS	Poly(aniline-N-butylsulfonate)
PAni	Polyaniline
PB	Prussian Blue
PBrTh	Poly(3-bromothiophene)

PClTh	Poly(3-chlorothiophene)
PCM	Polarizable Continuum Model
P_d	Power Density
PDDA	Poly(diallyldimethylammonium chloride)
PE	Polyelectrolyte
PEDOT	Poly(3,4-ethylenedioxythiophene)
PEI	Poly(ethylenimine)
PFTh	Poly(3-fluorothiophene)
PMMA	Poly(metacrylic acid)
PNCPy	Poly[N-(2-cyanoethyl)pyrrole]
PNMPy	Poly(N-methylpyrrole)
PPV	Poly(p-phenylene vinylene)
PPy	Polypyrrole
PSS	Poly(styrenesulfonic) acid
PTh	Polythiophene
PVP	Poly(4-vinylpyridine)
PVPON	Poly(vinylpyrrolidone)
PVS	Poly(vinylsulfate)
Q	Voltammetric Charge
Q	Frequency independent constant
Q_D	Total charge used for the polymer deposition
Q_o	Total charge of oxidized species
Q_{pol}	Polymerization Charge
Q_{II}	Voltammetric Charge corresponding to the second cycle
R	Gas constant (8.314 $J \cdot K^{-1} \cdot mol^{-1}$)
r	Roughness
R_{CT}	Charge Transfer Resistance
RE	Reference Electrode
RGP	Recurrent Galvanostatic Pulse
RMS	Root-Mean-Square
R_i	Bond length
R_{opt}	Optimal bond length
R_S	Ohmic Resistance
SAMs	Self-Assembled Monolayers

SC	Specific Capacitance
SCF	Self Consistent Field
SCRF	Self Consistent Reaction Field
SEM	Scanning Electron Microscopy
SI	Self-interaction
SPFELS	Surface Plasmon Field-Enhanced Light Scattering
S_{pol}	Surface of polymerization
STM	Scanning Tunneling Microscope
STQN	Synchronous Transit-Guided Quasi-Newton
T	Thermodynamic Temperature
TD	Time Dependent
TEM	Transmission Electron Microscopy
TGA	Thermogravimetric Analysis
t_c	Charge Time
t_d	Discharge Time
t_{pol}	Polymerization Time
UV-vis	Ultraviolet-Visible
V	Volt
V_{max}	Potential at the beginning of the discharge test
V_{pol}	Volume of polymer
VRH	Variable Range Hopping
W	Warburg
WE	Working electrode
w	Angular frecuency
w/w	Dry weight
W_{ox}	Weight of the oxidized polymer
XPS	X-ray Photoelectron Spectroscopy
XRD	X-ray Diffraction
Z'	Real Impedance
Z''	Imaginary Impedance
ZPVE	Zero-Point Vibrational Energies
σ_o	Conductivity
β	Charge transfer coefficient
δ	Thickness of fibers

ρ	Density
η	Current efficiency of polymerization; or Coulombic efficiency
Ω	Ohms
λ^{max}	Maximal Wavelength (Absorption)
κ	Electrical conductivity
θ and χ	Dihedral angles
τ	Incubation Time or Polymerization Time
υ	Frequency or scan rate
Δ	Length of fibers or porosity
ΔE	Relative Energy
ΔE^{int}	Interaction Energy
ΔE^{sol}	Interaction Energy in Solution
ΔG^{sol}	Free Energy of Solvation
Δp	Reduction of porosity
ΔQ	Difference of voltammetric charges
δQ	Redox efficiency
ΔV	Potential window

Table of contents

Chapter 1. Introduction

1.1. Conducting polymers

It is well known that polymers are used mainly as insulator materials in electrical and electronical applications, although they exhibit other properties such as low density, lightness, stability and ease of fabrication. However, since the discovery of a new class of organic materials named as conducting polymers (CPs) in 1977 by Alan McDiarmid, Alan Heeger, and Hideki Shirakawa,[1] our concept and perspective of polymers changed forever. They achieved that iodine doped trans-polyacetylene exhibited a conductivity value of 10^3 $S \cdot cm^{-1}$. This conductivity value being similar to metals such as copper. Thus, a new class of organic materials with electrical and optical properties similar to metals and inorganic semiconductors had been discovered. A new era in the field of polymers had born. Thanks to this discovery they were awarded by the Nobel Prize in 2000. Nowadays, the field of conducting polymers has grown exponentially since the conducting polymers are promising materials in the field of chemistry and physics.

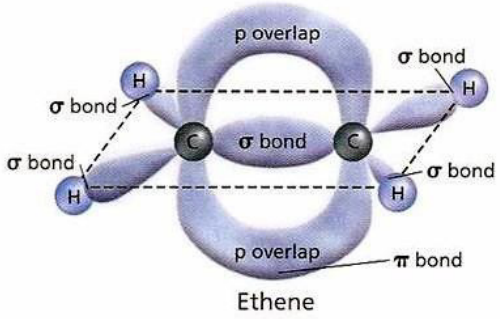

Figure 1. *Overlapping of orbitals forms σ and π-bonds in the chemical structure of conducting polymers (www.megamolecules.com)*

The main characteristic of conducting polymers is based on extended conjugated π system, where the π-electron delocalization along their backbone provides interesting optical and electrical properties (*e.g.* electrical conductivity, low energy optical transitions, low ionization potential and high electron affinity). This feature is denoted as alternating single and double bonds according to the chemical and electronic nature of these compounds. Conducting polymers show a particular characteristic since the carbon atoms located at the centers of the polymer backbone present sp^2 hybridization. Consequently, the valence electrons can move freely in a p_z orbital. The delocalized electrons have high mobility when the polymer is oxidized (doped state) and it justifies the high conductivity values as can be seen in Figure 1. The conductivity of conjugated polymers can be ranged from 10^{-8} up to 10^5 $S \cdot cm^{-1}$ depending on the synthesis

conditions. Nowadays, since the conductivity is originated from the chemical nature of the polymers, conducting polymers are also known as intrinsically conducting polymers.

The structure of CPs can be classified in linear or polyheterocycles. Nowadays, polyheterocycles are the most studied since their aromaticity provides good thermal properties and stability. Next, some of the most important aromatic conducting polymers studied in this work are represented.

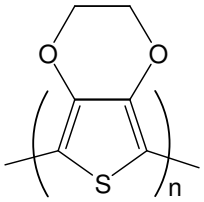

PEDOT

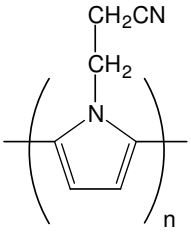

Poly[N-(2-cyanoethylpyrrole)]

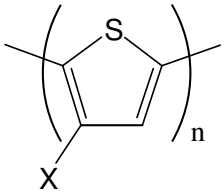

X= F	poly(3-fluorothiophene)	PFTh
X= Cl	poly(3-chlorothiophene)	PClTh
X= Br	poly(3-bromothiophene)	PBrTh

Halide thiophenes

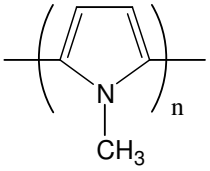

Poly(N-methylpyrrole)

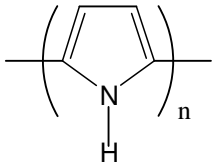

Polypyrrole

Figure 2. *Representative examples of conjugated polymers*

Conducting polymers have attracted a great attention due to their excellent properties in different technological applications such as chemical sensors (*e.g.* biosensor),[2-4] molecular electronic devices (*e.g.* diodes and field effect transistors),[5,6] batteries,[7] biomedical engineering,[8-10] corrosion inhibitors,[11-13] electrochromic devices,[14,15] supercapacitors,[16,17] electroluminescence,[18] photovoltaic cells,[19,20] dye-sensitized solar cells (DSSCs),[21] biofuel cells[22] or as drug delivery.[23,24]

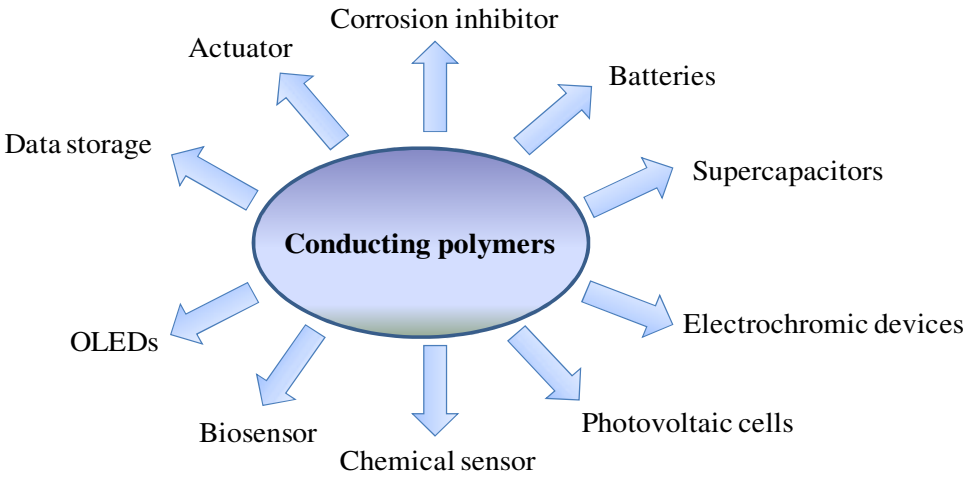

Figure 3. *Technological applications of conducting polymers*

Poly(thiophene), poly(aniline), poly(pyrrole), poly(phenylene) and their derivatives are considered the most important conducting polymers. During the last decades, these conducting polymers have been widely studied and characterized.[25-27]

1.1.1. Polypyrrole

Polypyrrole (PPy) is one of the most important conducting polymers, which presents a heterocyclic structure as can be seen in Scheme 1. Since its first discovery in 1916,[28] polypyrrole has been widely studied and investigated due to its ionic exchange properties, high conductivity, biocompatibility, electroactivity, ease of preparation or high yield redox process.[29,30] Moreover, these interesting properties have been used in technological applications such as supercapacitors,[31,32] batteries,[33] bioactive platforms,[34] corrosion inhibitors[35] and biomedicine.[36,37]

About its process of synthesis, polypyrrole can be synthesized by using several polymerization techniques such as plasma,[38,39] vapor phase,[40,41] and electrochemical[42] and chemical methods.[43]

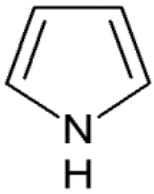

Scheme 1. *Structure of poly(pyrrole)*

Although the electrochemical polymerization mechanism of CPs has not been yet fully known and understood, it is widely accepted that the process is based on the radical-radical mechanism.[44] This mechanism is mainly formed by four steps as can be observed in Figure 4. The first step consists of the oxidation of the corresponding monomer to form a radical cation. Secondly, the cation radicals form dimmers by radical-radical coupling. Next, the polymeric chain grows forming oligomeric species. Finally, when the chain length increases a film of polymer is deposited on the electrode.

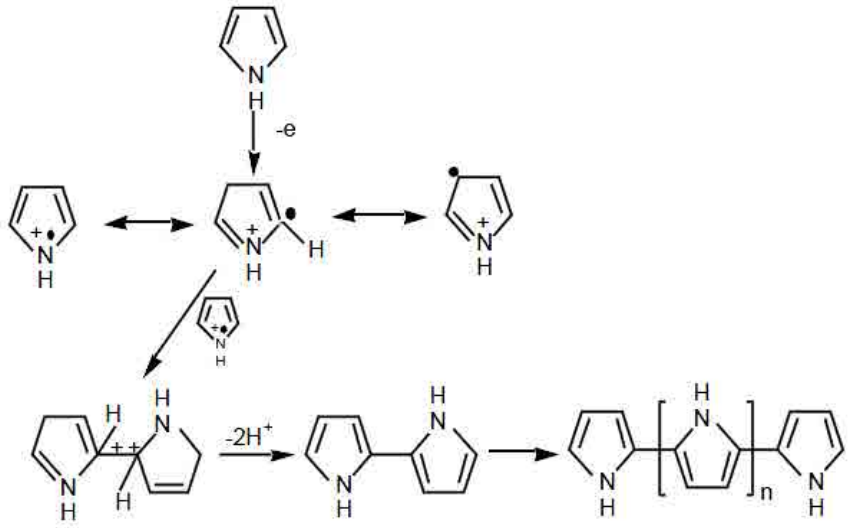

Figure 4. *Electropolymerization mechanism of polypyrrole*

A particular characteristic of pyrroles, and in general for conducting polymers synthesized by means of electrochemical methods is their insolubility in organic solvents. This feature can be explained according to their relatively nature rigid.[45] Particularly, pyrrole according to its chemical structure is polymerized through α-α linkages. This structure is the most desirable since it favors a high degree of conjugation along the backbone. Nevertheless, it is not the only possible structure, pyrrole and derivative pyrrole can polymerize through α – β linkages as it is shown in Figure 5. Consequently, pyrrole can form cross-linked structures, which reduce the planarity and rigidification of the polymer. Within this context, the processing of conducting polymers is practically intractable.

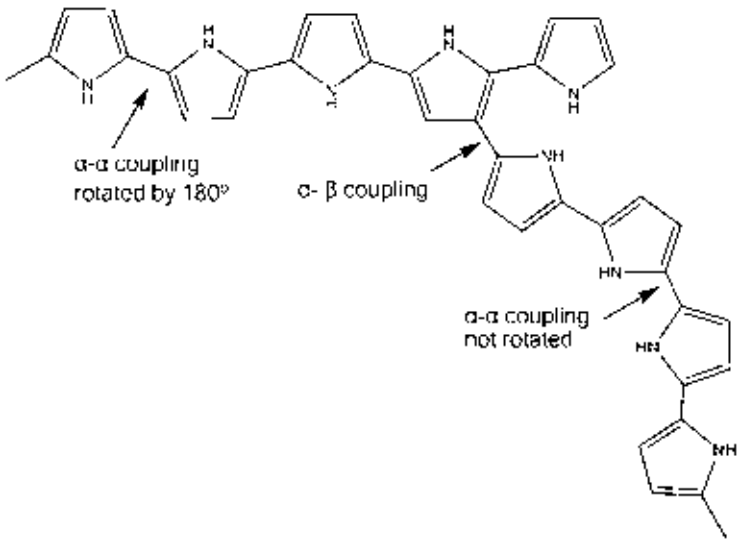

Figure 5. *Possible chemical structure for polypyrrole chains*

Another important drawback of polypyrroles is their over-oxidation because of the presence strong aqueous nucleophiles (*e.g.* OH^-, Br^- or H_2O). The nucleophilic attact produced by these chemical groups provokes the formation of carbonyl groups (C=O), which decrease the conjugative effect on the π-conjugated system, and consequently the conductivity is affected as well.[46]

Its particular structure allows to synthesize functionalized polymers. The functionality of polymers through different processes such as copolymerization or incorportation of sustituents have been very successful strategies to modify the electrical, physical, structural and topological properties of conducting polymers. Two pyrrole derivatives have been studied in this work, the poly(N-methylpyrrole) and the poly(N-[2-cyanoethylpyrrole]).

1.1.2. Polythiophene

Particularly, among CPs, thiophene has exhibited excellent environmental and thermal stabilities in both, the neutral and oxidized state and low band gap (2 eV).[47] Apart from its aforementioned properties, thiophene presents a characteristic chemical structure, which allows to be functionalized at the terminal α or side β positions.[48,49] This feature is being widely used in the field of opto-electronic devices and nonlinear optic since it affects directly the gap energy (ε_g).[50]

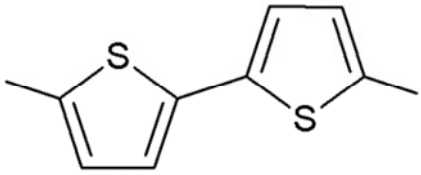

Scheme 2. *Structure of polythiophene*

Thiophene can be polymerized by means of electrochemical and chemical. Chemical polymerization of thiophene can be carried out through an organic solution containing the monomer and $FeCl_3$ as dopant agent. By substituting at the β position important improvement in terms of processability and solubility can be obtained in thiophene, subsequently, this process will be explained with more details. The electropolymerization mechanism of thiophene is displayed in Figure 6. The principle of polymerization is similar to the process described for PPy films.

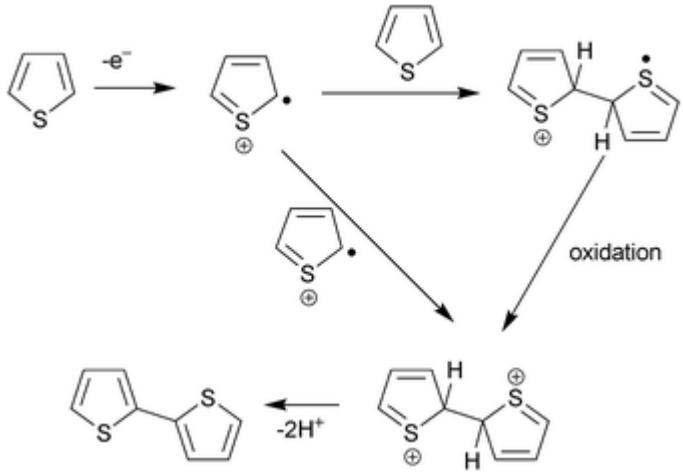

Figure 6. *Electropolymerization mechanism of polythiophene*

1.1.2.1. Poly(3,4-ethylenedioxythiophene)

In this thesis, PEDOT has received a special attention due to its unique properties, thus, a brief description is detailed in this section.

Poly(3,4-ethylenedioxythiophene) (abbreviated as PEDOT) was synthesized in the late 80's at the Bayer AG research laboratories in Germany.[51,52] The structure of this polymer is shown in Scheme 3. According to its chemical structure, PEDOT prevents the formation of irregular bonds such as α – β or β – β bonds because the β – β bonds of the ring are blocked by an ethylenedioxy group.[53]

Among thiophene derivatives, poly(3,4-ethylenedioxythiophene) has received a great deal of attention due to its interesting properties such as low band gap, high

conductivity (up to 550 $S \cdot cm^{-1}$) and good environmental stability.[54,52,55] Precisely, one of its interesting properties is focused on the electronic band gap (*e.g.* the π-π^* lowest transition) due to its low band gap (1.6 – 1.7 eV), which provides a bluish tonality.[56] This value is lower than thiophene band-gap energy (~2.0 eV). According to its properties, PEDOT has been employed in electrochromic devices,[57] fuel cells,[58] as biomaterial,[59,60] field emitter,[61] DSSCs,[62] and biosensor.[63] However, one of the most important drawbacks is its poor solubility in organic solvents and water. Recently, important investigations on the use of surfactants, polyelectrolytes or ionomers have been carried out to solve the insolubility problem. One of the most used surfactants is poly(styrene sulfonic acid), which has been proved to be a good candidate to obtain PEDOT films in presence of aqueous media.

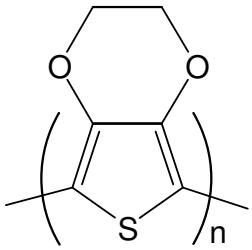

Scheme 3. *Structure of poly(3,4-ethylenedioxythiophene)*

During the last years, *in situ* polymerization has been widely used in the synthesis of conducting polymers. Among different techniques derived from this process, it is worth noting liquid-phase polymerization, electrochemical polymerization, or vapor-phase polymerization, respectively. In this thesis, the electrochemical polymerization has been the most employed technique according to its multiple advantages, which will be explained in the next section.

1.2. Theory and structure of conducting polymers

Conducting polymers known also in the literature as "organic semi-conductor" or "synthetic metals" are mainly characterized by their high conductivity and low band-gap energy, which have been employed in electrical and optical applications. In this work, we have been interested in studying heterocyclic polymers since they present narrow band-gap energy and good stability according to the resonance of the aromatic rings. These aforementioned optical characteristics are due to the mobility of charge carriers along the π-conjugated system formed by overlapped delocalized p-orbitals.

Within this context, aromatic conducting polymers present two different non-degenerate states corresponding to benzenoid and quinoid forms, as follows:

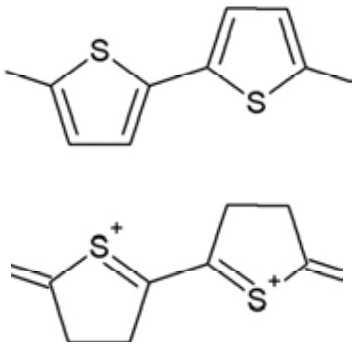

Figure 7. *Polythiophene in aromatic (up) and quinoidal (down) resonance forms*

It is worth noting that the high conductivity values are only achieved when the polymer adopts a quinoid form (doped state), whereas the benzenoid structure exhibit very low conductivity.

Previously, we cited that one of the most important characteristics of π-organic systems is the conductivity. Conductivity is related with a physicochemical phenomenon called doping process. In general, doping process consists of removing an electron from the valence band or adding an electron to the conduction band. Both cases are shown to increase the conductivity according to the creation of mobile charges,[64] although its value depends on the doping level. Particularly, the doping process can be achieved through two different routes as follows:

- *Oxidation (p – doping):* This process consists of removing an electron of the polymer backbone, which results in the formation of a radical cation called polaron. The polaron has the ability to move along the polymer backone increasing his capacity of charge carriers (holes or electrons), as a consequence an important increase of conductivity can be achieved. The p-doping process is the most employed in conducting polymers due to the easiness of the procedure.

Oxidation (p-doping)

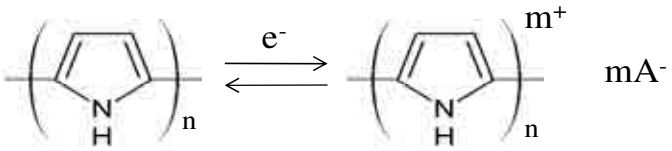

Reduction (undoping)

- *Reduction (n – doping):* In reductive doping the conducting polymers form polymeric anions that are balanced by cationic species.

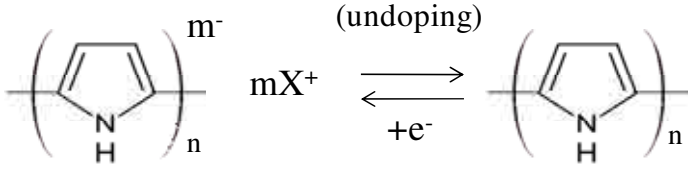

(n-doping)

It is worth noting that the doping process can be obtained through several techniques such as chemical, electrochemical, ion implantation or photochemical doping, respectively.

a) *Chemical doping.* The doping process is accomplished in the vapor phase by exposing the polymer to the vapor of the dopant or in the liquid phase by immersing the polymer films in the dopant solution.
b) *Electrochemical doping.* Conjugated polymers can be doped and undoped by immersing the material as an electrode in an organic electrolyte solution with the application of a current through the electrochemical system.
c) *Ion implantation.* When the proper ion beams are used, conjugated polymers can become conducting by implanting ions in the polymer's lattice, forming covalent bonds with the material.
d) *Photochemical doping.* This is accomplished by treating the polymer with the dopant species, which are initially inert towards the materials, followed by ultraviolet radiation.

In this thesis, the electrochemical doping will be an important part to accomplish the synthesis of conducting polymers.

During the process of oxidation of conducting polymers, the systems require the incorporation of counter anions, denoted as dopant agents, to compensate the charge into the polymeric backbone, therefore, an electroneutrality equilibrium is reached.

Normally, the doping level ranged from 0.20 to 0.50 for conducting polymers depending on the synthesis conditions.

It should be noted that the doping effect presents a relevant importance on the energy diagrams since it allows to understand better the conductivity process in the field of materials. The theory employed to explain the electronic structure of a material is known as band theory (Figure 8), which was employed to determine the conductivity classification of conducting polymers.[65] According to the band theory, the materials can be classified as conductors, semiconductors or insulators. For conductor materials (*e.g.* metals) the valence band (VB) and conduction band (CB) are overlapped, which defines a gap energy value of zero. In semiconductors materials, the gap energy is estimated to be 2-3 e.V. Finally, for the insulator materials their value is higher than 3.0 eV.

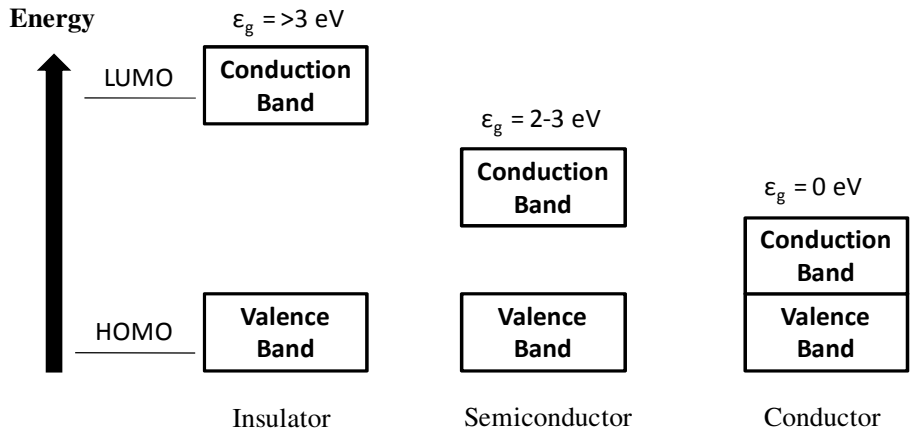

Figure 8. *Energy level diagrams of insulators, semiconductors, and metals*

A representation of the different materials, which belong to the insulator, semiconductor and metals family is displayed as follows:

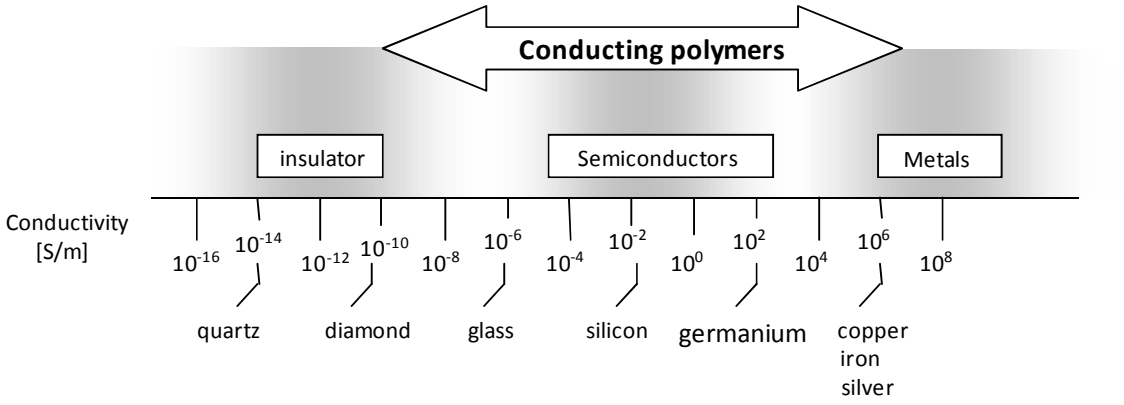

Figure 9. *Comparison of conductivities of various materials.*

As can be seen in Figure 10, gap energy (ε_g, expressed in eV) of a material can be defined as the difference energy between the Highest Occupied Molecular Orbital (HOMO), which can be ascribed to the valence band and the Lowest Occupied Molecular Orbital (LUMO), which represents the conduction band. LUMO orbital can be expressed as the electron affinity of the material, whereas HOMO orbital corresponds to the ionization potential. This magnitude presents a direct correlation with optical and electrical properties, such as conductivity. However, this model is not enough to explain all mechanism associated in the electronic properties of conducting polymers, since multiple factors can affect them.

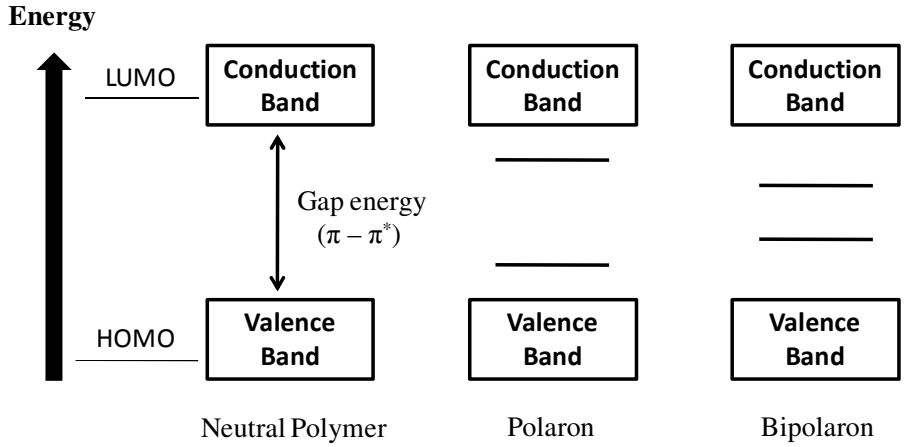

Figure 10. *Electronic transitions for neutral, polaron and bipolaron structures of conducting polymers*

According to the aforementioned characteristic, band gap energy is also related with the degree of π orbital overlap along the chain. Precisely, conducting polymers exhibit a low gap energy value (1.5 – 2.2 eV), which represents a light absorption with wavelengths higher than 500 nm. Within context, there are several factors that can affect the gap energy property (*e.g.* effect of substituents, π-conjugation length, or doping level). Thus, for example, when the conjugation length increases, the energy required for the transition HOMO – LUMO decreases, and consequently the gap energy (ε_g) is lower. The doping level of the material also plays a key factor on the electrical and optical properties of CPs. Moreover, rigid and planar structures are excellent candidates due to their ability to increase the mobility of electrons. Among its applications, the low band-gap energy values exhibited by some conducting polymers (*e.g.* PEDOT) are being employed as organic light emitting diodes (OLEDs) or in photovoltaic devices.

Gap energy values can be measured by using different procedures based on optical (UV-Vis) and electrochemical (CV) methods, which will be explained in the later section.

As it has been mentioned previously, doping process is a crucial parameter to understand the conductivity in organic semi-conductor polymers. According to Figure 10 polarons and bipolarons play an important role on the electronic structure and conductivity of conducting polymers.[65,66]

Doping process presents a great importance on the morphological characteristics of conducting polymers. Thus, in an oxidative doping process the incorporation of counterions (A^-) is necessary to balance the total charge of the system. Therefore, an expansion occurs. However, the dedoping process is ascribed to the expulsion of the ions, as a consequence, a contraction process is favored. This property has been recently employed in biomimetic muscles.

1.3. A new approach to multilayered systems based on conducting polymers from the layer-by-layer (LbL) technique: Design, development, tendencies and applications[a]

1.3.1. Introduction

Nowadays, diverse procedures have been employed to build multilayered systems based on Langmuir-Blodgett (LB), self-assembling (SAM),[1,2] vapor deposition, and spin-coating,[3,4] techniques. Among them, the layer-by-layer deposition was pioneered by Iler in 1966 through charged colloids, which was a great advance in the field of multilayered systems.[5] In the beginning of 1990s, Decher and coworkers[6] demonstrated the deposition of multilayered films made from conventional polyectrolytes (*e.g.* polyanions and polycations).[7-9] Since its discovery the Layer-by-Layer (LbL) technique is one of the most important procedures to develop new nanostructured materials, which has awakened a great interest.[10,11] Precisely, the development of this technique has triggered great advances in the field of nanotechnology.[12,13] The control and organization of nanometric structures based on the self-assembly technique has devoted tremendous efforts in several applications such as biosensors.[14]

[a] All references and images listed in section 1.3 were ordered according to the review in preparation.

The LbL assembly exhibits numerous advantages, which are detailed as follows:

- Versatility
- Simplicity
- Ease of preparation
- Environmentally friendly
- Independence of the shape of the substrate
- Construction of films made of different chemical species.
- Inexpensiveness
- Good reproducibility
- Controlling of composition, properties and structure at nanometric level
- Maximal interaction among layers

During the last decade, important advances have been focused on the development of new polyelectrolytes such as proteins, dyes, dendrimers, viologens, mineral clays, nanoparticles, polysaccharides, or phtalocyanines. These novel polyelectrolytes have allowed to design new nanomaterials with interesting applications, which will be discussed in later sections.

1.3.2. LbL Multilayer film of polyelectrolytes

Initially, LbL technique was developed by Décher and coworkers in the early of 1990.[7-9] This technique was demonstrated to be an excellent tool to build multilayered ultrathin systems. The working principle of this technique is based on the process of consecutive immersion of the substrate into oppositely charged polyelectrolyte (PE) solutions. A great number of substrates have been employed in the LbL deposition (e.g. glass, silicon wafers, mica, quartz and metallic surfaces).

A depiction of the LbL method is shown in Figure 1.

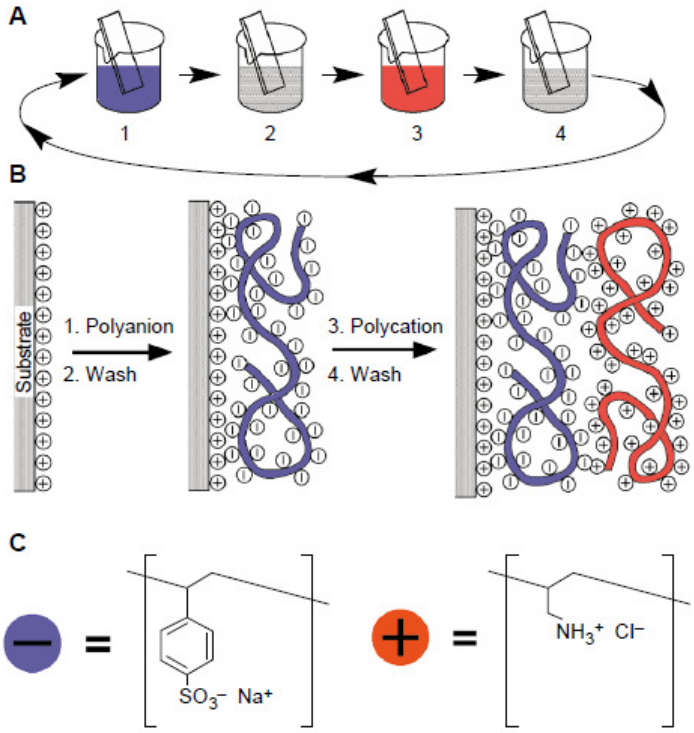

Figure 1. *(**A**) Schematic of the film deposition process using slides and beakers. Steps 1 and 3 represent the adsorption of a polyanion and polycation, respectively, and steps 2 and 4 are washing steps. The four steps are the basic buildup sequence for the simplest film architecture, (A/B)n. The construction of more complex film architectures requires only additional beakers and a different deposition sequence. (**B**) Simplified molecular picture of the first two adsorption steps, depicting film deposition starting with a positively charged substrate. Counterions are omitted for clarity. The polyion conformation and layer interpenetration are an idealization of the surface charge reversal with each adsorption step. (**C**) Chemical structures of two typical polyions, the sodium salt of poly(styrene sulfonate) and poly(allylamine hydrochloride).*[7]

The process is divided into different steps. Firstly, a substrate with a charged surface is immersed into a solution containing the corresponding polyelectrolyte with opposite charge to the surface. Next, the previous system (monolayer) is immersed again into a solution containing a new polyelectrolyte with opposite charge. The process can be repeated until the number of layers is achieved. It is worth noting that between each step a rinsing process is occurred since it is important to remove the excess of PE. During the building of multilayered systems based on polyelectrolytes, the first step plays an important role due to the charge overcompensation process produced during the adsorption of polyelectrolyte on the surface.[15,16] This effect leads to the reversal of surface charge, which has been found to be fundamental to constitute the formation of

multilayer films.[17,18] Although the general process is described using two different polyelectrolytes (polyanion and polycation), some studies have been devoted to study the influence of more than two polyelectrolytes, thus, polyacrylic acid (PAA), poly(allylamine hydrochloride) PAH, and poly(sodium styrene sulfonate) PSS polyelectrolytes were fabricated for multilayered films.[19]

Within this context, the global process has been classified in three zones.[20]

1. *Precursor zone.* This zone represents the first step where the layer is adsorbed onto the substrate surface. This first step is highly controlled by the chemical nature of the substrate, thus, the charge overcompensation process plays a crucial role on the adsorption process.
2. *Core zone.* The second zone is where the growth of layers is occurred.
3. *Outer zone.* The last zone is influenced by the film/solution and film/air interfaces.

The growth of layers using the LbL technique can be carried out through a linear or exponential behavior.[21] A linear growth (*l-LbL*) represents a linear relation between the mass and thickness when the number of depositions is increased. On the other hand, the film mass and thickness can also grow exponentially when the number of adsorptions is increased *(e-LbL).* An example of e-LbL behavior are some biological polyelectrolytes (e.g. polypeptides or polysaccharides), whereas l-LbL behavior are commonly focused on linear polyelectrolytes (*e.g.* PSS/PAH-PAA).[21] Figure 2 shows the morphological characterization based on atomic force microscopy (AFM) and scanning electron microscopy of the PSS/PAH-PAA multilayered polyelectrolytes.

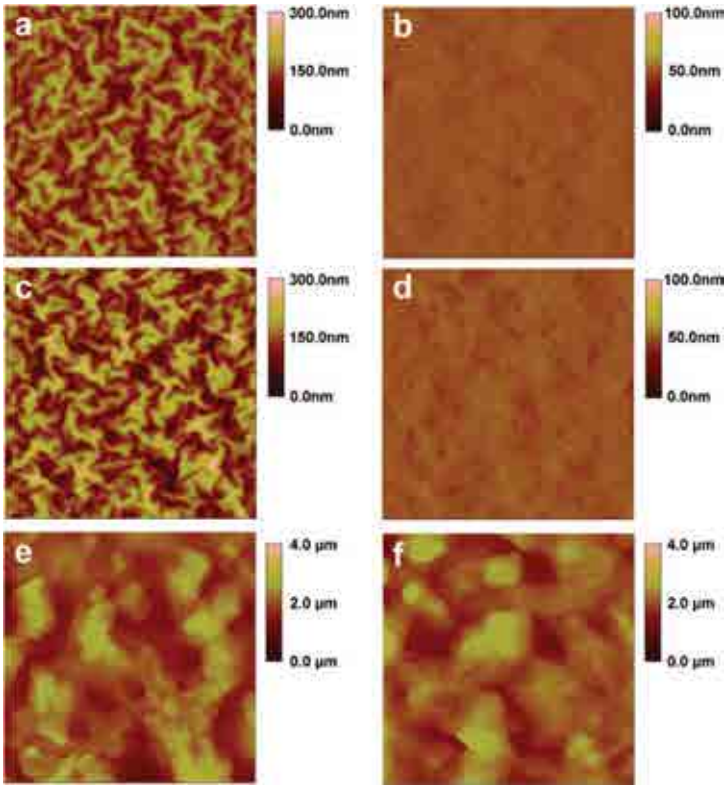

Figure 2. *AFM images of the PSS/PAH-PAA films: (a) (PSS/ PAH-PAA0.25)*19.5, (b) (PSS/PAH-PAA0.25)*20, (c) (PSS/PAH-PAA0.5)*19.5, (d) (PSS/PAH-PAA0.5)*20, (e) (PSS/ PAH-PAA0.75)*19.5, and (f) (PSS/PAH-PAA0.75)*20 films. Size: (a-d) 5 × 5 µm and (e, f) 10 × 10 µm.*[19]

PEs are made of polymers containing an electrolyte group on the chain. Among conventional PEs, two main categories are represented as function of their electrical charges, polycations (positive charge) and polyanions (negative charge). Poly(vinylsulfate) (PVS), poly(sodium styrenesulfonate) (PSS) are employed as polyanions, whereas poly(allylamine hydrochloride) (PAH), poly(ethylenimine) (PEI), poly(acrylic acid) (PAA) and poly(diallyldimethylammonium chloride) (PDDA) are polycations. Another important and common division is based on their degree of ionization. Thus, a strong polyelectrolyte is considered when its degree of ionization is independent of solution pH, and weak if the degree of ionization is pH dependent. PDDA, PVS and PSS are strong polyelectrolytes whereas PAH and PAA are weak polyelectrolytes.

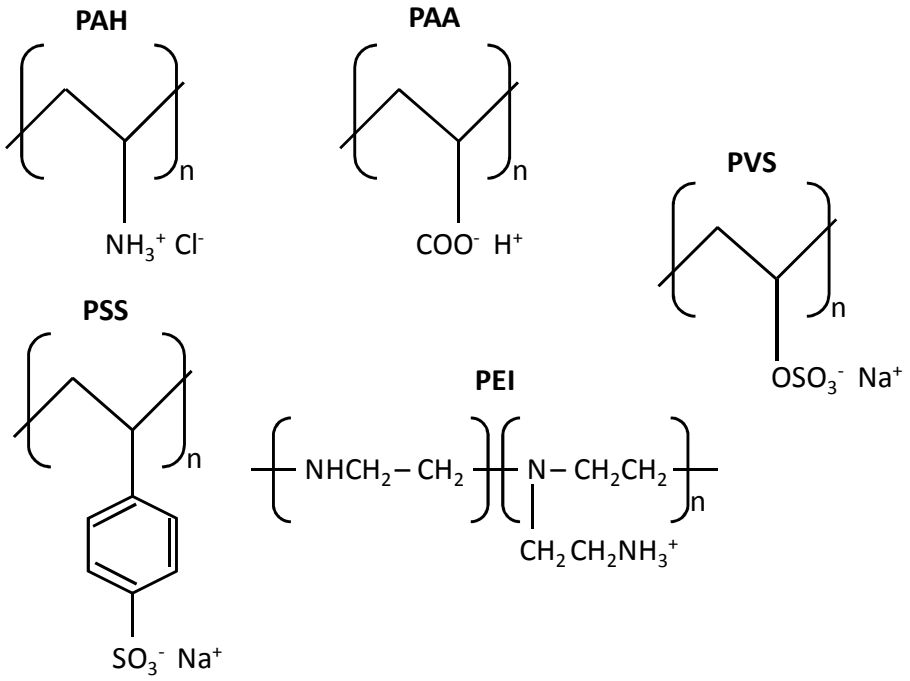

Scheme 1. *Chemical structures of conventional polyelectrolytes used in the LbL technique.*

The process of self-assembled polyelectrolyte is influenced by several factors, which have been widely investigated.[21,22] Among the most critical parameters are the pH,[23-29] ionic strength,[30-32] solvent,[33] temperature,[34] salt,[35-37] electrochemical effects[38,39] and dipping time.[40] Recently, new strategies have been reported to minimize the dipping time using dynamic sequential LbL deposition[41] and dipping spray.[42,43]

The driving forces of self-assembled polyelectrolytes are based on electrostatic interactions.[44] However, non-electrostatic interactions based on hydrogen bondings,[45] charge-transfer interactions,[46,47] and hydrophobic interactions[48] have also been evidenced. Thus, hydrogen bondings between PAA and polyacrylamide (PAA),[49] PAA with poly(4-vinylpyridine) (PVP) layers[50] or poly(methacrylic acid) (PMMA) with poly(vinylpyrrolidone) (PVPON) layers[51] were evidenced. The structures of multilayered polyelectrolytes using the LbL technique have been demonstrated using several techniques such as X-ray reflectivity,[52,53] neutron reflectrometry,[54] Förster energy transfer,[55,56] dynamic contact angle,[57] small angle scattering[58] and nuclear magnetic resonance (NMR).[59a)] Recently, advanced techniques based on plasmon spectroscopy have allowed to identify self-assembled multilayered systems.[59b)]

Conventional polyelectrolytes have been widely used in different technological fields, such as chemical sensors (*e.g* biosensors),[60-63] electrochromic devices,[64] photovoltaic cells,[65] corrosion inhibitors,[66,67] fuel cells,[68,69] textile industry (*e.g.*

cotton),[70,71] membrane technology,[72,73] electrochemistry,[74] enzymatic catalysis,[75] biomedicine,[76,77] hydrophobic coatings[78] or in nanotechnology.[79-82]

Precisely, the nanotechnology has awakened a great interest in the field of conventional polyelectrolytes, recently a strategy for fabricating graphene sheets from PAA and PSS has been carried out. The Figure 3 shows the success of the LbL methodology to fabricate graphene nanosheets from conventional polyelectrolytes.[83]

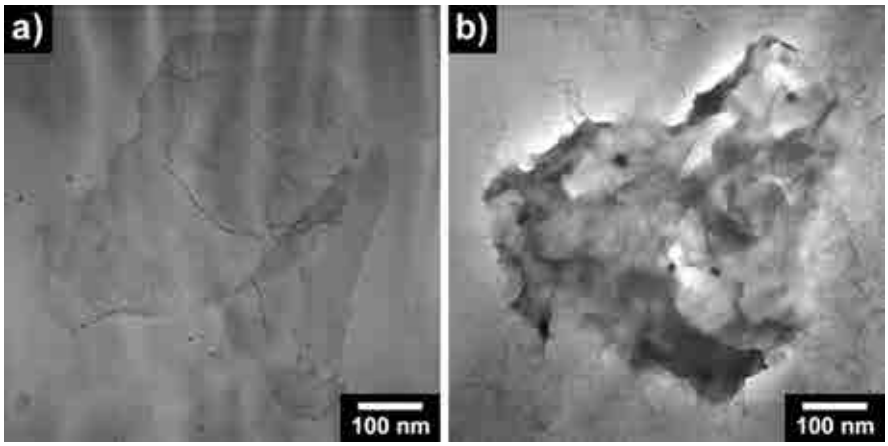

Figure 3. *TEM image of graphene nanosheets prepared by LbL selfassembly approach: (a) with a metallic dopant, (b) without a metallic dopant.*[83]

Another interesting research field of the self-assembled polyelectrolytes is focused on biomedical applications.[84] Studies of polyelectrolytes (LPEI, PSS, PAA or HA) have been applied in drug delivery (*e.g.* antibiotics).[85]

In addition, the presence of novel polyelectrolytes based on biological natural entities such as proteins, chitosans or biopolymers (polylactide) has triggered important advances in the field of medicine,[86] in this way, works devoted on biomimetic coating,[87] scaffolds,[88] cell immobilization,[89] or drug delivery[90] have been reported.

Alternated layers of polyanions and polycations (polyelectrolytes) have shown to be a successful procedure to build nanometric thin films with interesting properties, which have allowed to design and develop new devices as cited previously. However, polyelectrolytes can be constituted by other species. Over the last decade, numerous species have been combined with polyelectrolytes using the LbL technique. Regarding to this topic, the exploration of new species able to form novel multilayered systems with polyelectrolytes is a great challenge. Next, a list of the species combined with polyelectrolytes through self-assembling LbL technique is displayed:

a) *Phtalocyanines.* Phtalocyanines have demonstrated to be promising species in the field of LbL.[91] *Li et al* studied some phtalocyanine derivatives,[92,93] specifically, nickel phtalocyanines have been studied in presence of PDDA providing improvements on the electronic and opto-electronic properties of ITO substrates.[94,95] Moreover, alternated layers of phtalocyanines with polyelectrolytes (PSS and PDDA) were proved successfully on the development of organic transistors.[96]

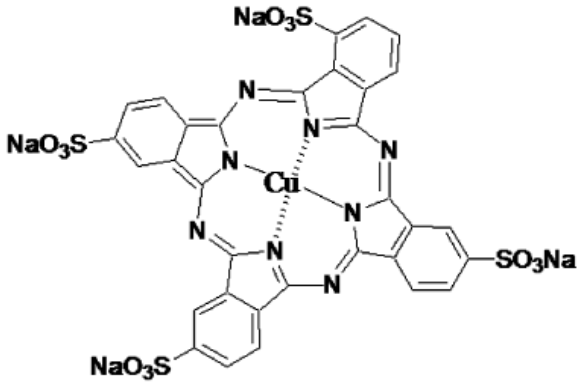

Scheme 1. *Structure of one of the most employed phtalocyanine.*

b) *Viologens*. In this field, viologens were self-assembled with PSS and PAH to build multilayered systems with high redox activity.[97] The LbL technique showed that viologens assembled with PSS exhibited much higher stability than conventional methods of multilayered systems (*e.g.* LB).[98]

c) *Proteins and enzymes*. Biological polyelectrolytes such as proteins and enzymes in presence of conventional polyelectrolytes exhibited interesting applications through the LbL assembly technique. Within this context, elastin-like polypeptide was successfully performed as cellular platform in presence of PEI and PAA.[99] The results showed an increase of cell proliferation and cytoskeletal organization in presence of PEI and PAA electrolytes, which is shown in Figure 4

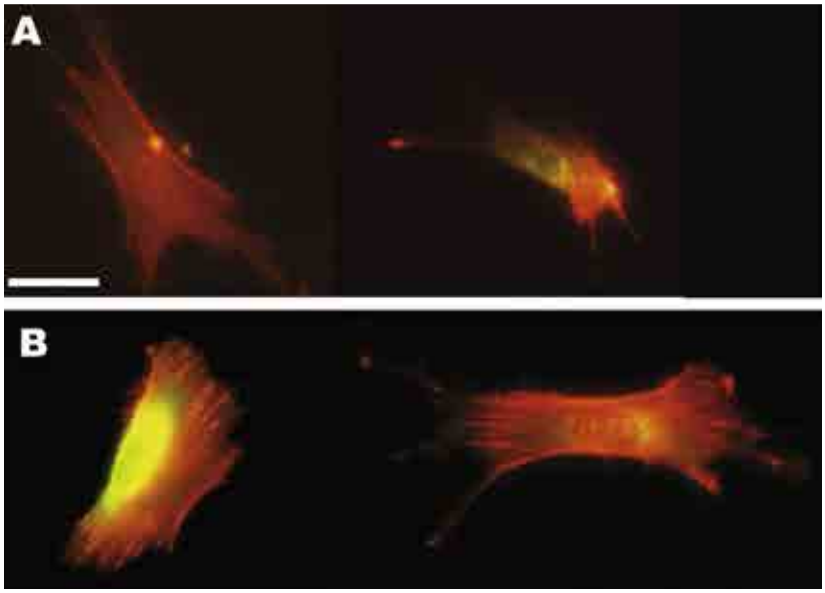

Figure 4. *Cytoskeletal organization and focal adhesions for fibroblasts adhered on (A) glass and (B) (ELP–PEI/ELP–PAA)10 at 0.01% (w/v). Scale bar = 50 μm.*[99]

Furthermore, proteins such as bacteriorhodopsin were studied by electrostatic layer-by-layer assembly with PDDA to improve photoelectric properties.[100] Multilayers made of polyaminoacid has awakened a great interest in biomedical applications, thus poly-lysine, alginate and PEI films were grown on biological surfaces, exhibiting interesting applications in biomedicine.[101] Precisely, poly-alginate was studied in presence of PAH/PSS on the development of microcapsules with biotechnological applications.[102] *Lvov et al* studied the self-assembling via layer-by-layer of water-soluble proteins such as cytochrome, myoglobin, lysozyme, histone, hemoglobin, glucoamylase and glucose oxidade with conventional polyelectrolytes.[103-105]

In the field of enzymes, multilayer assembly of bienzymes with conventional polyelectrolytes (PDDA) through layer-by-layer deposition was reported for the fabrication of biomicropatterns.[106]

d) *Mineral clays*. Clay minerals have shown to be a class of inorganic materials with a great versatility since they have been employed using different deposition techniques, which are represented in Figure 5.

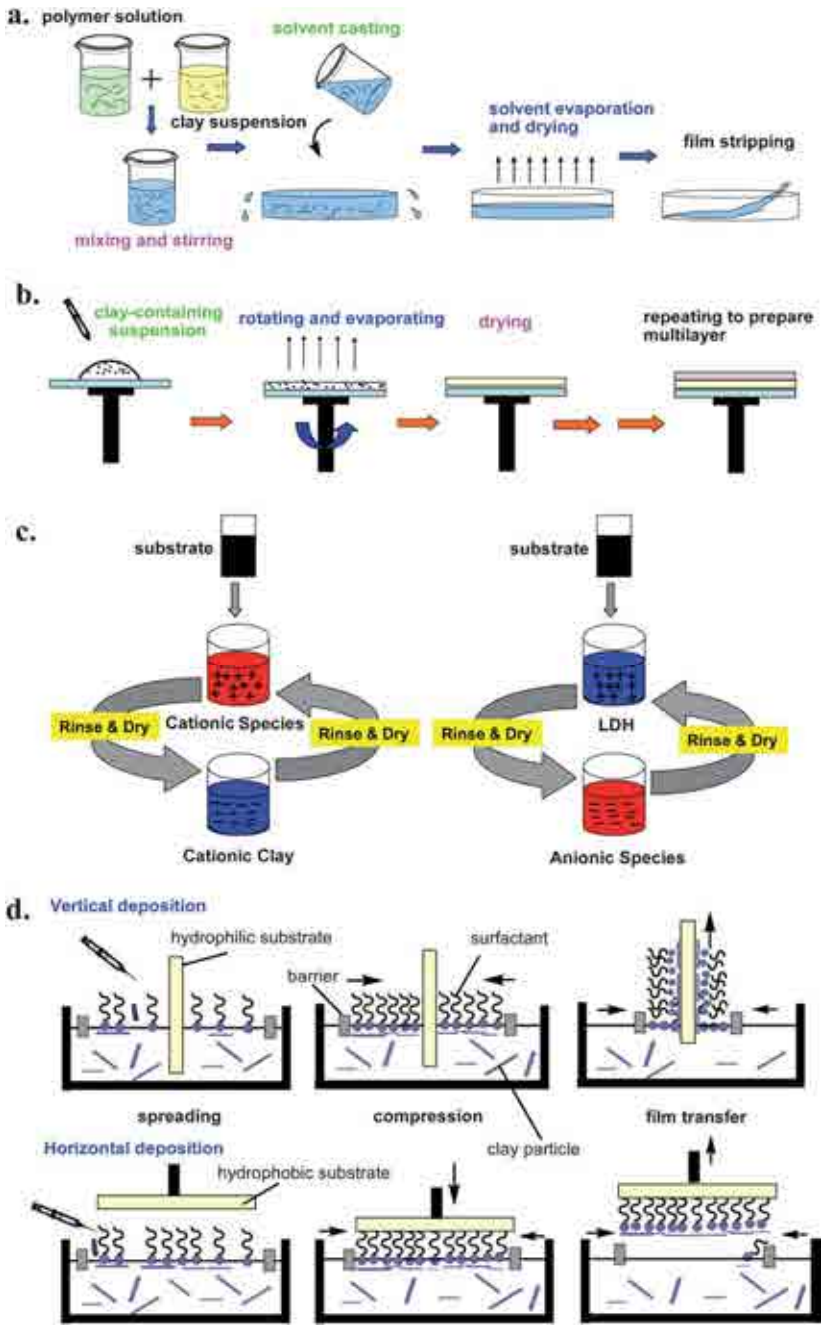

Figure 5. *The preparation methods of clay-containing films. a. solvent casting; b. spin-coating; c. layer-by-layer (LbL) assembly; d. Langmuir–Blodgett (LB) technique.*[107]

Clay minerals have been widely used in the LbL self-assembly deposition with conventional PEs showing excellent barrier, mechanical and thermal properties, among others.[107] Among mineral clays, smectite group is one of the most important mineral clays, specifically MMT is the most representative within this group. MMT has been employed in presence of polyelectrolytes due to its improvement in mechanical properties in terms of high mechanical strength and resilience to crack proliferation.[108] However, other mineral clays such as

hectorite,[109] laponite,[110,111] have also been self-assembled with conventional polyelectrolytes. An example of multilayered sytems based on mineral clays (laponite) and conventional polyelectrolytes (PEI) is displayed in Figure 6 .

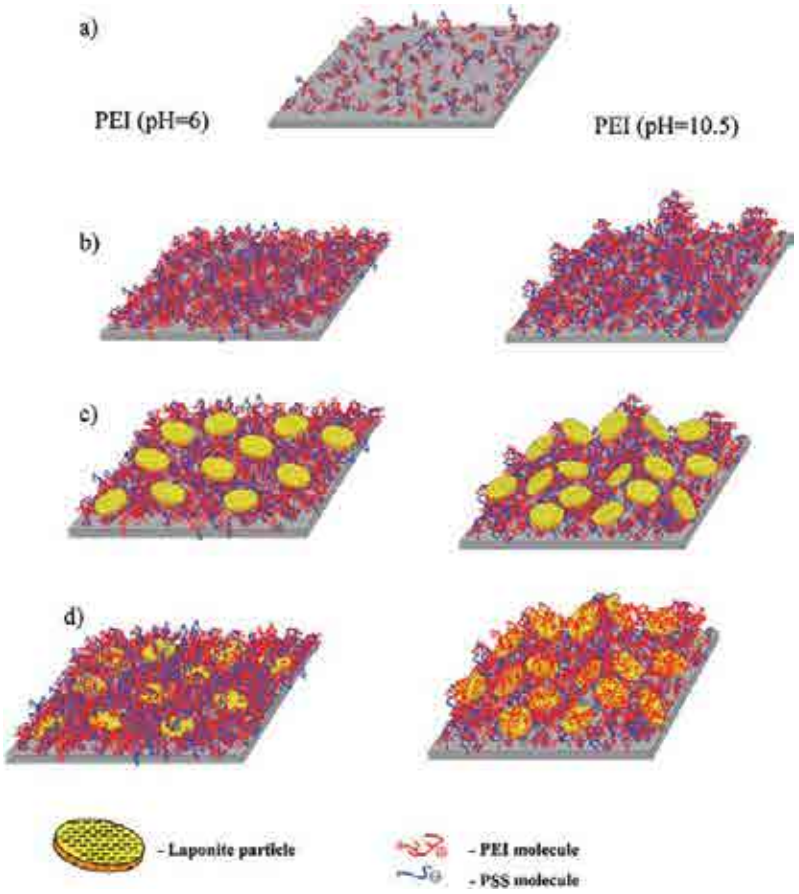

Figure 6. *Scheme of formation of PEI/PSS multilayer films with laponite: (a) one adsorbed bilayer,(b) polyelectrolyte multilayerfilms, (c, d) multilayer films with laponite.*[107]

e) *Inorganic particles.* Inorganic particles have been studied in presence of polyelectrolytes. The most common inorganic particles are divided into important two groups, which can be defined as based on metallic oxides and metallic particles. Among metallic oxides combined with conventional polyelectrolytes are found as follows:

- *PEI/SiO_2:* The presence of SiO_2 nanoparticles in polyelectrolytes such as PEI provokes a different growth, thus, a e-LbL growth was observed for this system.[112] Moreover, studies with other polyelectrolytes were reported.[113,114]

- *PDDA-PSS/SnO_2:* The effect of SnO_2 nanoparticles in PDDA-PSS electrolytes evidenced a time dependent conducting behavior, which could be explained by a self-heating mechanism.[115]
- *PAH-PAA and PSS-PDDA/TiO_2:* Dye-Sensitized Solar Cell fabricated by electrostatic layer-by-layer assembly of conventional polyelectrolytes and TiO_2 nanoparticles.[116,117]
- *PSS-PAH/Iron Oxide:* Magnetic particles have experimented an important evolution on the LbL assembly with polyelectrolytes.[118] Thus, systems containing magnetic particles have allowed to improve and tune the magnetic properties of multilayered systems based on PSS-PAH/Iron oxide. [119] The configuration of these systems is represented in Figure 7.

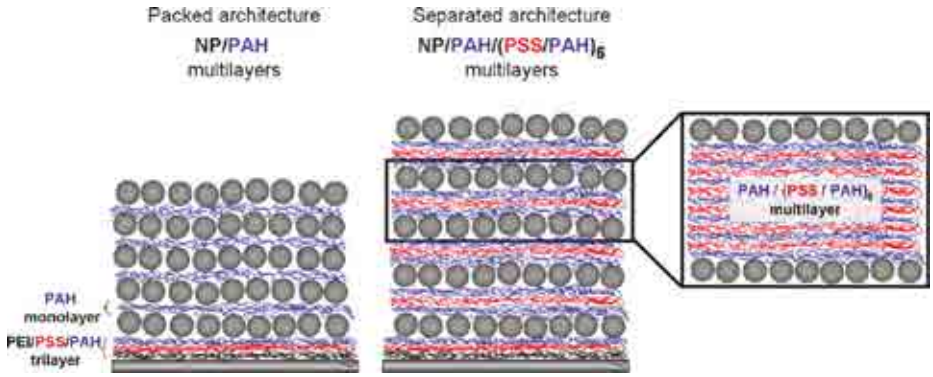

Figure 7. *Idealized Representations of Packed Architecture (NP/PAH)5 and Well-Separated Architecture (NP/PAH(PSS/ PAH)6)5 Each Comprised of Five Layers of Iron Oxide NPs.*[119]

- *PAH-PDDA/MnO_x:* An electrochemical method to perform multilayered systems based on manganese oxides and polyelectrolytes was successfully carried out.[120]

The second group based on metallic particles is mainly devoted to Au particles. According to the data some studies have been investigated using Au and polyelectrolytes. Within this context, PEI/Au[121] and PDDA/Au particles[122] systems were investigated.

Another important class of inorganic particles are the polyoxometalates, which are schematized in Figure 8. These materials have highlighted their performance on the LbL technique in presence of conventional polyelectrolytes.[123,124] Some specific cases were devoted to

Polyoxometalates/PDDA[125,126] or Polyoxometalates/PAH[127] have been reported.

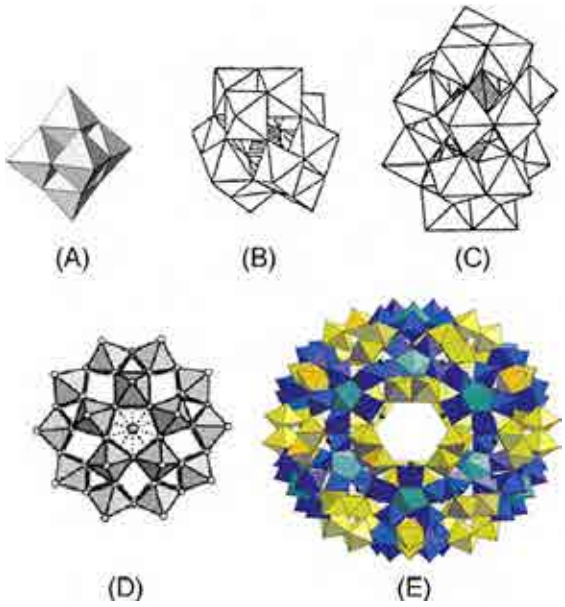

Figure 8. *Structures of some typical POMs. Isopolyanions: (A) $[Mo_6O_{19}]^{n-}$. Heterpolyanions: (B) Keggin-type $[XM_{12}O_{40}]^{3-/4}$; (C) Wells-Dawson type $[X_2M_{18}O_{62}]^{n-}$; (D) Preyssler-type $[MP_5W_{30}O_{110}]^{14/12-}$. Giant nanosized polymolybdate clusters: (E) Keplerate $[Mo_{132}O_{372}(CH_3COO)_{30}(H_2O)_{72}]^{42-}$.*[124]

f) *Dendrimers.* Multilayers dendrimers structures have been obtained by the LbL assembly of oppositely charged species with great interest in the field of biosensors.[128] One of the most common dendrimers employed in this technique is the poly(amido amine) (PAMAM) dendrimer,[128-131] which is represented in Figure 9.

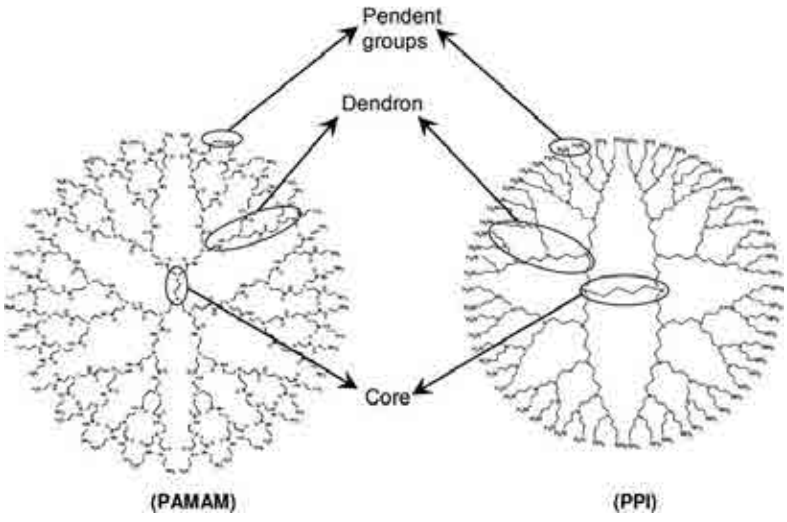

Figure 9. *The typical structure of poly(amido amine) (PAMAM) and poly(propylene imine) (PPI) dendrimer with three distinct domains: core, dendron and pendent groups.*[128]

Finally, other compounds employed in the LbL technique in presence of polyelectrolytes are dyes. PDDA and PAH polyelectrolytes have emerged as a promising polyelectrolytes in the field of dyes (cyanine dye/PDDA),[132] (Congo red dye/PDDA),[133] or (amaranth dye/PAH) respectively.[134] Polysaccharides focused on chitosans are the most important.[135]

1.3.3. Self-assembling of polyconjugated polyelectrolytes

Among polyelectrolytes, the conjugated polymers electrolytes have shown a great interest among researchers.[136-138] Excellent optical and electrochemical properties due to their capacities to act as electron donors and acceptors have been reported.[139] In the last years, thiophene derivative polyelectrolytes have received special attention,[140,141] specifically, *Lukkari et al* reported multilayered polyelectrolytes based on poly(alkoxythiophene).[142-144] Besides, *Zotti et al* studied other thiophene derivatives since they are more easily self-assembled than polyaniline or polypyrrole, consequently, layers of α,ω-bis(carboxyhexyl)sexithiophene were deposited with non electroactive layers of polyallylamine and polystyrenesulfonate.[145,146] Within this context, *Advincula et al* studied sexithiophene and thiophene with polycarbazole through the layer-by-layer self-assembly deposition technique[147,148] by Electrochemical-Surface Plasmon Resonance (ESPR). [149]

Another important family of polyconjugated electrolytes are pyrrole derivatives, which were employed as molecular junctions,[150] or biosensors.[151]

1.3.4. Self-assembling of polyelectrolytes with conducting polymers

Self-assembled conducting polymers with polyelectrolytes have emerged as promising materials due to their interesting electrochemical properties.[152] In this section, a new insight of the self-assembling between polyelectrolytes and conducting polymers is discussed. Initially PEs and CPs were studied through their interactions.[153,154] Some examples are discussed as follows:

Initially, PPV was reported using the LbL technique[155] exhibiting excellent photovoltaic [156] and electroluminescence properties.[157] These properties were studied in contact with a PAni derivative.[158]

PPy is one of the most important conducting polymers due to its high conductivity, and biocompatibility. Initially, PPy multilayered films were initially reported by Nicolau using different substrates. The XPS and SEM techniques showed the success of

the LbL technique using a solution containing Py and $FeCl_3$.[159] Since then, PPy has been employed using different polyelectrolytes such as PSS for microelectromechanical systems (MEMs),[160] and to prepare hollow capsules.[161] Due to its biocompatibility, PPy and electrolytes based on enzymes have been studied as biosensors of glucose and cholesterol.[162]

Another important conjugated polymer family is polyaniline (PAni). PAni has been widely studied due to its interesting properties in terms of environmental stability. Therefore, PAni is one of the most promising conducting polymers in the field of the LbL technique.[163] PAni has been employed in presence of some conventional polyelectrolytes such as PSS, PAH, PVSS, PDDA or PAA.[164] Precisely, PAni/PAH systems have been performed as humidity sensors.[165] In the last years, multilayered systems based on PAni/PSS have also been reported as humidity sensors,[166] electrochromic devices,[167] and to fabricate hollow-shell particles,[168] and porous materials.[169] Moreover, the PAni/PVSS system performed by the layer-by-layer technique showed excellent anti-corrosive properties,[170] and some applications as electronic device,[171] and pH sensors[172] have been reported. PAni/ PDDA multilayered systems were employed as biosensor of glucose.[173] Another important conventional polyelectrolyte (PAA) has been studied in presence of PAni through the LbL with interesting properties in ionic engineering,[174] charge transport[175] or as pH sensor.[176] The success of these polyelectrolytes with PAni using the self-assembling LbL technique allowed to build multilayered systems using the aforementioned polyelectrolytes as biosensors.[177]

However, PAni has been studied in presence of other electrolytes, based on biological polyelctrolytes such as polysaccharides in biosensors,[178] oligonucleotides[179] and specifically, nanocapacitors built from LbL using PAni and poly(γ-glutamic acid) were reported.[180] Nanometric polyelectrolytes such as metal oxides has been employed with PAni. Prussian Blue (PB), a polyoxometalate derivative was built by LbL with interesting properties in terms of electrochromic properties.[181] More recently, dendrimers have been considered as promising materials in the field of polyelectrolytes, thus, the high physical and electrochemical stability showed by poly(amido amine) dendrimer in presence of PAni allowed to design biosensors or electrocatalyst.[182] These dendrimers were studied in presence of magnetic particles (Fe_3O_4) to be used as nonvolatile resistive switching memory (NRSM) devices[183] and biosensor.[184]

Other PAni derivatives employed as anionic polymers such as poly(aniline-N-butylsulfonate)s (PANBS) combined with polyaniline through electrostatic layer-by-layer self-assembly were reported with promising properties in the field of electrochromic devices.[185-187] In this context, poly(o-methoxyaniline) is another important polyaniline derivative, which was built by using layer-by-layer films with conventional polyelectrolytes.[188-190] Biological polyelectrolytes such as RNA have been also employed with PAni derivatives, which have allowed to develop biomedical applications.[191]

Recently, the concept of fibers has emerged as a promising field in the LbL technique since important advances in the construction of scaffolds have been reported.[192] In the field of conducting polymers due to its interesting applications, precisely, PAni nanofibers were widely studied, and applications as sensors, memory devices, catalyst, have been reported.[193,194] According to its interesting applications the concept of conductivity remains not fully understood, however, *Jiang et al* proposed currently several conduction mechanism in polyaniline nanofibers.[195] The synthesis of PAni nanofibers has aroused a special attention on the LbL assembly technique. Within context, PAni nanofibers were reported by using the LbL assembly with applications in the field of fuel cells.[196] Different polyelectrolytes such as PAA or PSS has been combined with PAni fibers through LbL assembly for electrochemical sensors,[197] optical devices,[198] or biosensors.[199]

In the previous section we discussed about the importance of polyconjugated polyelectrolytes, specifically, thiophene derivatives. Precisely, poly(3,4-ethylenedioxythiophene) is an important derivative thiophene, which exhibit excellent properties and whose applications have been extensively studied. The most common electrolyte used in multilayered systems based on PEDOT and PEDOT derivatives is PSS.[200-203] Although PEDOT/PSS has been combined with PAH for the fabrication of cellulose fibers,[204] and PHA/PSS for transistors.[205] PEDOT/PSS systems have been studied in the field of the LbL through different polyelectrolytes such as viologens and due to their high electrochromic efficiency.[206] Nevertheless, PEDOT/PAH systems combined with polyoxometalates exhibited also an enhancement of the electrochromic properties.[207] Particularly, some PEDOT derivatives in presence of PAH were reported by *Reynolds* and coworkers as promising electrochromic materials.[208,209]

The success of the LbL technique has been demonstrated by using several techniques based on plasmon methods. Thus, surface plasmon resonance spectroscopy

(SPS) and surface plasmon field-enhanced light scattering (SPFELS) were proved to be excellent techniques in the construction of multilayered systems based on conducting polymers and electrolytes.[210,211]

1.3.5. Self-assembling of polyelectrolytes with conducting polymers through nanotechnology

As we discussed previously, LbL technique is an excellent procedure to control the thickness at nanometric level. This feature has been focused on different aspects of nanotechnology. Within context, polyelectrolytes have emerged as a challenge in this field.[212-214] One of the aims of nanotechnology is the control of the molecular organization, which can be regulated through templates. Within this context, polyelectrolytes have been designed by using nanotemplates such as nanotubes (Fig. 10) or nanopores with promising technological applications.[215] Recent advances have been carried out by using alternative templates focused on colloidal nanotemplates, which offers the opportunity to fabricate novel nanomaterials based on rods, spheres, or fibers.[216] The applications of the nanotechnology by using the LbL technique from polyelectrolytes are widely focused on a great variety of biomedical applications (*e.g.* delivery drugs).[217]

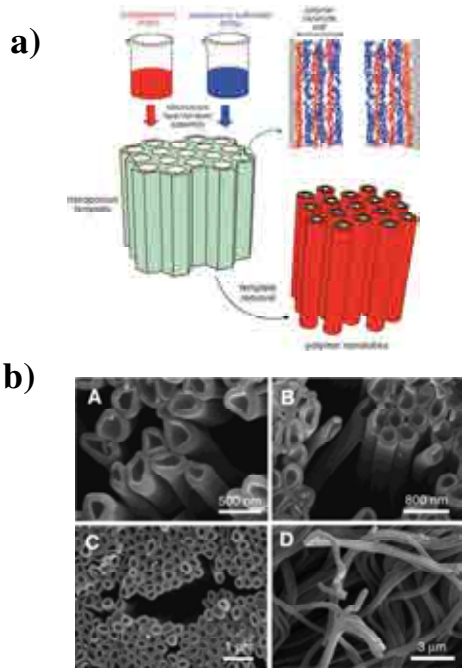

Figure 10. *a) Simplified representation of the formation of polyelectrolytes nanotubes through sequential assembly of polycations and polyanions inside the nanoporous template and the subsequent removal of the nanotemplate. b) Scanning electron micrographs at different magnifications (A-D) of polyelectrolyte nanotubes obtained via nanotemplated LbL assembly.*[215]

The nanotechnology according to the size, geometry, shape can be divided into different categories, 0D, 1D and 2D structures, respectively. Among 1D structures, carbon nanotubes (CNT) have been employed in the LbL assembly technique in presence of polyelectrolytes (conventional).[218-225] Important advances have been reported to improve the properties obtained from the LbL.[226] This new nanomaterials have been used as capacitors, batteries or electrochemical sensors.[227,225] An example is displayed in Figure 11.

Moreover, optoelectronic and electrical properties has been enhanced in presence of nanotubes with polyelectrolytes (PSS).[228,229] Precisely, these systems, NCT-PSS were combined with PANI fibers to study its electrochemical properties.[230] The presence of some polyelectrolytes such as PAA, PEI and PSS have improved the mechanical properties of carbon nanotubes using the LbL assembly technique.[231-233] The applications of these systems have been focused on electrocatalytic properties,[234] neuroprosthetic implants[235] or as flame-retardants.[236]

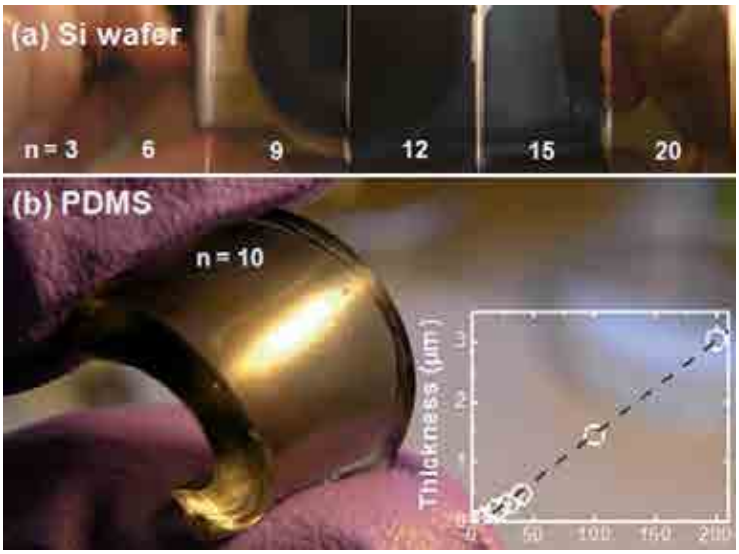

Figure. 11. *Images of LbL-MWNT electrodes on (a) Si wafers and (b) polydimethylsiloxane (PDMS) substrates. Number on image indicates the number of bilayer (n) in* $(MWNT\text{-}NH_3^+/MWNT\text{-}COO^-)_n$. *Thickness of the LbL-MWNT electrodes as a function of the number of bilayers is shown in the inset, showing a linear relationship for LbL-MWNT electrodes with thicknesses from 20 nm to 3 nm.* [227]

CNT has been employed with conducting polymers through the LbL technique, thus CNT have been combined with PEDOT,[237] PAni,[238,239] PPy,[240-244] and PPV[245,246] with promising applications as biosensors.[238,239,242,244] Other polyelectrolytes based on dendrimers have been reported as potentiometric sensors in presence of CNT.[247]

Conducting polymers has been combined with nanometric materials through the LbL, specifically, PPV has been combined with CdSe particles with photovoltaic and electroluminiscence properties.[248-250] PPV derivatives were self-assembled with fullerenes to be used as photovoltaic cells.[251] CdSe nanoparticles has been also employed with thiophene derivatives (*e.g.* 3-methylthiophene) in the construction of Zener diodes,[252] or with water-soluble polythiophene derivatives exhibiting photoresponsive properties.[253,98] Precisely, these polymers were studied in mechanism sof charge carriers under oxidation.[254]

Again, PAni has shown to be an excellent candidate in the self-assembling with nanoparticles. Recently, systems based on PAni and V_2O_5 nanoparticles were studied due to their electrochromogenic and electrochemical properties.[255-257] Metalic particles such as Au have emerged a great interest in polymers.[258] Metallic nanoparticles, such Au or Pt have been studied in PAni and PTh through the LbL assembly.[259-262] *Knoll et al* studied PAni/Au multilayered films as biological sensors.[263] Magnetic particles were studied with PAni,[264] PPy[265] and PAni derivatives.[266] *Kulesza et al* PAni and polyoxometalates showed excellent electrocatalytic and electrochemical properties.[267-271]

One of the most important metallic nanoparticles is TiO_2. This nanoparticle has awakened a great interest in the field of LbL and conducting polymers, respectively. The combination of both TiO_2 and thiophene derivatives have shown excellent results to develop new organic-based optoelectronic devices, among the most important are PEDOT,[272] poly(3-hexylthiophene),[273] poly(thiophene-3 acetic acid),[274] and PAni.[275] Other metallic nanoparticles such as SnO_2 or platinum were employed in conducting polymers[276-279.]

Recently, in the field of nanotechnology the presence of a new material known as fullerene has emerged as a promising candidate in the LbL technique. Thus, combination of fullerene with PEDOT/PPV,[280] P3TH,[281-283] or PPV[284] has been reported.

1.3.6. Self-assembling of conducting polymers using the electrochemical LbL

The electrochemical deposition of multilayered systems have been performed in different polyelectrolytes,[285] specifically, biological macromolecules as DNA were electrochemically deposited onto poly(p-aminobenzensulfonic acid) (Pp-ABSA) as biological sensors of dopamine and uric acid.[286]

Electrochemically deposited conducting polymer films have been recently studied due to its interesting applications. Multilayered systems based on conducting polymers have been synthesized using electrochemical methods. Multilayered structure of PPy was carried out by potentiostatic methods (*e.g.* chronoamperometry) to evaluate its electrochemical properties and ion transport.[287] Furthermore, PPy and PPy derivatives were built through a potentiostatic pulse regime as amperometric sensor.[288] Multilayered systems based on PPy and PAni were galvanostatically deposited on steel to evaluate their performance as corrosion inhibitors.[289] Within this context, PAni/Poly(N-methylaniline) systems were employed as corrosion inhibitors.[290] The construction of multilayered system made of PPy and PTh based from electrochemical methods was evaluated as electrochemical actuator.[291] PPy and PEDOT were built from alternated layers to be performed as actuators.[292] Among derivatives PTh, PEDOT has been also employed as chemical sensor in presence of PAni. In this way, PEDOT/PAni multilayered systems were constructed to be used as gas sensors.[293]

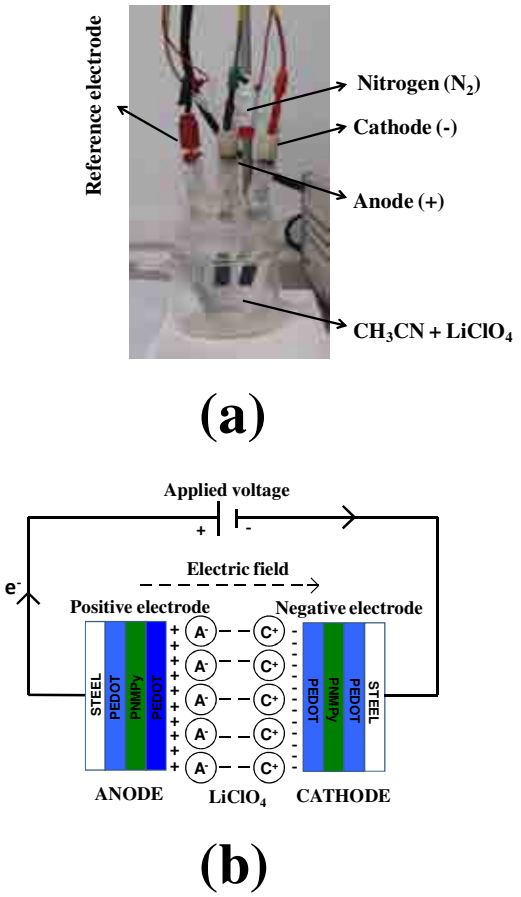

Figure 12. *Fabrication set-up (a) and scheme (b) of the supercapacitor constructed using two identical electrodes of 3-layered ml-PEDOT/PNMPy (θ= 300 s).*[298]

Recently, our group developed multilayered systems based on PEDOT/PNMPy[294-296] with applications as corrosion inhibitors,[297] and supercapacitors.[298] The combination of more than two conducting polymers (PEDOT, PPy and PNCNPy) was also studied and characterized.[299] The LbL based on electrochemical allowed us to build multilayered systems based on CPs. The results showed that the synergistic effects at the interfaces between consecutive layers increased the porosity compared with those of individual conducting polymer under the same conditions. The porosity was evidenced play a key role on the performance of supercapacitors, thus, supercapacitors in the type I configuration were fabricated according to Figure 12.

1.3.7. Summary and Outlook

Recently, new strategies have been carried out to design multilayered systems, one of the most important is based on the layer-by-layer deposition. Precisely, this technique has emerged a great influence in the field of nanotechnology since it allows to improve the orientation and growth of molecular organizations at nanometric level. The advance of this technique has awakened interest in the design of new nanostructured materials due to its versatility and simplicity, thus, multilayered systems made of different chemical nature have been carried out. As it was discussed previously, a great variety of materials can be employed by using the LbL technique. However, in the last years, conducting polymers have emerged as promising materials in the different technological and academic areas. Within this context, this study has provided an overview of the properties and applications of organic conjugated polymers. The fabrication of multilayered systems based on these systems has exhibited interesting applications in electronic and electronical devices, biomedicine or in the field of photovoltaic cells.

In this work, a new perspective of the LbL technique in the field of conducting polymers by using electrochemical methods has been discussed. The works reported in the literature show that this methodology has provided significant developments in specific applications, such as supercapacitors or corrosion inhibitors. This methodology represents one of the most interesting and useful procedures to build multilayered systems.

1.3.8. References

[1]. Schreiber, F. *Prog. Surf. Sci.* **2000**, *65*, 151.

[2]. Ulman, A. *An Introduction to Ultrathin Organic Films: From Langmuir–Blodgett to Self- Assembly* **1991**, Academic Press, Boston.

[3]. Lee, S. S.; Hong, J.-D.; Kim, C. H.; Kim, K.; Koo, J. P.; Lee, K. B. *Macromolecules* **2001**, *34*, 5358.

[4]. Chiarelli, P. A.; Johal, M. S.; Casson, J. L.; Roberts, J. B.; Robinson, J. M.; Wang, H.-L. *Adv. Mater.* **2001**, *13*, 1167.

[5]. Iler, R. K. *J. Colloid Interface Sci.* **1966**, *21*, 569.

[6]. Decher, G., Hong, J.-D. *Makromol. Chem., Macromol. Symp.* **1991**, *46*, 321.

[7]. Decher, G. *Science* **1997,** *277*, 1232.

[8]. Decher, G.; Schmitt, J. *Prog. Colloid Polym. Sci.* **1992**, *89*, 160.

[9]. Decher, G.; Hong, J. D.; Schmitt, J. *Thin Solid Films* **1992**, *210*, 831.

[10]. Bertrand, P.; Jonas, A.; Laschewsky, A.; Legras, R. *Macromol. Rapid. Commun.* **2000**, *21*, 319.

[11]. Hammond, P. T. *Curr. Opin. Colloid. In.* **2000**, *4*, 430.

[12]. Hammond, P. T. *Adv. Mater.* **2004**, *16*, 1271.

[13]. Holder, E.; Tessler, N.; Rogach, A. L. *J. Mater. Chem.* **2008**, *18*, 1064.

[14]. Qin, X.; Wang, H.; Wang, X.; Li, S.; Miao, Z.; Huang, N.; Chen, Q. *Mater. Sci. Eng. C* **2009**, *29*, 1453.

[15]. Joanny, J. F. *Eur. Phys. J.* **1999**, *9*, 117.

[16]. Schlenoff, J. B.; Dubas, S. T. *Macromolecules* **2001**, *34*, 592.

[17]. Steitz, R.; Jaeger, W.; Klitzing, R. *Langmuir* **2001**, *17*, 4471.

[18]. Blomberg, E.; Poptoshev, E.; Claesson, P. M.; Caruso, F. *Langmuir* **2004**, *20*, 5432.

[19]. Guo, Y.; Geng, W.; Sun, J. *Langmuir* **2009**, *25*, 1004.

[20]. Ladam, G.; Schaad, P.; Voegel, J. C.; Schaaf, P.; Decher, G.; Cuisinier, F. *Langmuir* **2000**, *16*, 1249.

[21]. Klitzing, R. *Phys. Chem. Chem. Phys.* **2006**, *8*, 5012.

[22]. Dubas, S. T.; Schlenoff, J. B. *Macromolecules* **1999**, *32*, 8153.

[23]. Kolasinska, M.; Warszynski, P. *Appl. Surf. Sci.* **2005**, *252*, 759.

[24]. Elzbieciak, M.; Zapotoczny, S.; Nowak, P.; Krastev, R.; Nowakowska, M.; Warszynski, P. *Langmuir* **2009**, *25*, 3255.

[25]. Elzbieciak, M.; Kolasinska, M.; Warszynski, P. *Colloids Surf. A* **2008**, *321*, 258.

[26]. Yang, S.; Zhang, Y.; Zhang, X.; Xu, J. *Soft Matter* **2007**, *3*, 463.

[27]. Burke, S. E.; Barrett, C. J. *Pure. Appl. Chem.* **2004**, *76*, 1387.

[28].Kolasinska, M.; Krastev, R.; Warszynski, P. *J. Colloid Interface Sci.* **2007**, *305*, 46.

[29]. Yoo, D.; Shiratori, S. S.; Rubner, M. F. *Macromolecules* **1998**, *31*, 4309.

[30]. Lowack, K.; Helm, C. A. *Macromolecules* **1998**, *31*, 823.

[31]. Trybala, A.; Szyk-Warszynska, L.; Warszynski, P. *Colloids Surf. A* **2009**, *343*, 127.

[32]. Schoeler, B.; Kumaraswamy, G.; Caruso, F. *Macromolecules* **2002**, *35*, 889.

[33]. Poptoshev, E.; Schoeler, B.; Caruso, F. *Langmuir* **2004**, *20*, 829.

[34]. Büscher, K.; Graf, K.; Ahrens, H.; Helm, C. A. *Langmuir* **2002**, *18*, 3585.

[35]. Schlenoff, J. B.; Ly, H.; Li, M. *J. Am. Chem. Soc.* **1998**, *120*, 7626.

[36]. Clark, S. L.; Montague, M. F.; Hammond, P. T. *Macromolecules* **1997**, *30*, 7237.

[37]. McAloney, R. A.; Sinyor, M.; Dudnik, V.; Goh, M. C. *Langmuir* **2001**, *17*, 6655.

[38]. Guillaume-Gentil. O.; Graf, N.; Boulmedais, F.; Schaaf, P.; Vörös, J.; Zambelli, T. *Soft Matter* **2010**, *6*, 4246.

[39]. Ko, Y. H.; Kim, Y. H.; Park, J.; Nam, K. T.; Park, J. H.; Yoo, P. J. *Macromolecules* **2011**, *44*, 2866.

[40]. Mermut, O.; Barrett, C. J. *J. Phys. Chem. B* **2003**, *107*, 2525. *Langmuir* **2004**, *20*, 829.

[41]. Kim, H.-J.; Lee, K.; Kumar, S.; Kim, J. *Langmuir* **2005**, *21*, 8532.

[42]. Izquierdo, A.; Ono, S. S.; Voegel, J. C.; Schaaf, P.; Decher, G. *Langmuir* **2005**, *21*, 7558.

[43]. Schlenoff, J. B.; Dubas, S. T.; Farhat, T. *Langmuir* **2000**, *16*, 9968.

[44]. Hoogeveen, N. G.; Cohen Stuart, M. A. C.; Fleer, G. J.; Böhmer, M. R. *Langmuir* **1996**, *12*, 3675.

[45]. Quinn, J. F.; Johnston, A. P. R.; Such, G. K.; Zelikin, A. N.; Caruso, F. *Chem. Soc. Rev.* **2007**, *36*, 707.

[46]. Shimazaki, Y.; Mitsuishi, M.; Ito, S.; Yamamoto, M. *Langmuir* **1997**, *13*, 1385.

[47]. Shimazaki, Y.; Mitsuishi, M.; Ito, S.; Yamamoto, M. *Langmuir* **1998**, *14*, 2768.

[48]. Kotov, N. A. *Nanostruct. Mater.* **1999**, *12*, 789.

[49]. Yang, S. Y.; Rubner, M. F. *J. Am. Chem. Soc.* **2002**, *124*, 2100.

[50]. Wang, L.; Wang, Z.; Zhang, X.; Shen, J.; Chi, L.; Fuchs, H. *Macromol. Rapid Commun.* **1997**, *18*, 509.

[51]. Sukhishvili, S.; Granick, S. *J. Am. Chem. Soc.* **2000**, *122*, 9550.

[52]. Schmitt, J.; Griinewald, T.; Decher, G.; Pershan, P. S.; Kjaer, K.; Lösche, M. *Macromolecules* **1993**, *26*, 7058.

[53]. Kellogg, G. J.; Mayes, A. M.; Stockton, W. B.; Ferreira, M.; Rubner, M. F.; Satija, S. K. *Langmuir* **1996**, *12*, 5109.

[54]. Lösche, M.; Schmitt, J.; Decher, G.; Bouwman, W. G.; Kjaer, K. *Macromolecules* **1998**, *31*, 8893.

[55]. Baur, J. W.; Rubner, M. F.; Reynolds, J. R.; Kim, S. *Langmuir* **1999**, *15*, 6460.

[56]. Caruso, F.; Donath, E.; Möhwald, H. *J. Phys. Chem. B* **1998**, *102*, 2011.

[57]. Chen, J.; Luo, G.; Cao, W. *J. Colloid Interface Sci.* **2001**, *238*, 62.

[58]. Estrela-Lopis, I.; Leporatti, S.; Moya, S.; Brandt, A.; Donath, E.; Möhwald, H. *Langmuir* **2002**, *18*, 7861.

[59]. a) Schönhoff, M.; Schwartz, B.; Larsson, A.; Kuckling, D. *Prog. Colloid. Polym. Sci.* **2002**, *121*, 80. b) Sankaran, B.; Reynolds, J. R. *Macromolecules* **1997**, *30*, 2582.

[60]. Ram, M. K.; Bertoncello, P.; Ding, H.; Paddeu, S.; Nicolini, C. *Biosens. Bioelectron.* **2001,** *16*, 849.

[61]. Hoshi, T.; Saiki, H.; Kuwazawa, S.; Tsuchiya, C.; Chen, Q.; Anzai, J.-I. *Anal. Chem.* **2001**, *73*, 5310.

[62]. Zhao, W.; Xu, J.-J.; Chen, H.-Y. *Electroanal.* **2006**, *18*, 1737.

[63]. Yang, X.; Johnson, S.; Shi, J.; Holesinger, T.; Swanson, B. *Sens. Actuators B* **1997**, *45*, 87.

[64]. Nguyen, C. A.; Argun, A. A.; Hammond, P. T.; Lu, X.; Lee, P. S. *Chem. Mater.* **2011**, *23*, 2142.

[65]. Tokuhisa, H.; Hammond, P. T. *Adv. Funct. Mater.* **2003**, *13*, 831.

[66]. Dai, J.; Sullivan, D. M.; Bruening, M. L. *Ind. Eng. Chem. Res.* **2000**, *39*, 3528.

[67]. Grigoriev, D. O.; Köhler, K.; Skorb, E.; Shchukin, D. G.; Möhwald, H. *Soft Matter* **2009**, *5*, 1426.

[68]. Argun, A. A.; Ashcraft, J. N.; Hammond, P. T. *Adv. Mater.* **2008**, *20*, 1539.

[69]. Aschcraft, J. N.; Argun, A. A.; Hammond, P. T. *J. Mater. Chem.* **2010**, *20*, 6250.

[70]. Wang, Q.; Hauser, P. J. *Cellulose* **2009**, *16*, 1123.

[71]. Hyde, K.; Dong, H.; Hinestroza, J. P. *Cellulose* **2007**, *14*, 615.

[72]. Yilmaztürk. S.; Deligöz, H.; Yilmazoglu, M.; Damyan, H.; Öksuzömer, F.; Koç, S. N.; Durmus, A.; Gürkaynak, W. A. *J. Membr. Sci.* **2009**, *343*, 137.

[73]. Ono, S. S.; Decher, G. *Nano Lett.* **2006**, *6*, 592.

[74]. DeLongchamp, D. M.; Hammond, P. T. *Chem. Mater.* **2003**, *15*, 1165.

[75]. Datta, S.; Cecil, C.; Bhattacharyya, D. *Ind. Eng. Chem. Res.* **2008**, *47*, 4586.

[76]. Boudou, T.; Crouzier, T.; Ren, K.; Blin, G.; Picart, C. *Adv. Mater.* **2009**, *21*, 1

[77]. Lichter, J. A.; Van Vliet, K. J.; Rubner, M. F. *Macromolecules* **2009**, *42*, 8573.

[78]. Zhai, L.; Cebeci, F. C.; Cohen, R. E.; Rubner, M. F. *Nano Lett.* **2004**, *4*, 1349.

[79].Shi, X.; Shen, M.; Möhwald, H. *Prog. Polym. Sci.* **2004**, *29*, 987.

[80]. Rhodes, C. P.; Long, J. W.; Doescher, M. S.; Fontanella, J. J.; Rolison, D. R. *J. Phys. Chem. B* **2004**, *108*, 13079.

[81]. Tang, Q.; Wu, J.; Li, Q.; Lin, J. *Polymer* **2008**, *49*, 5329.

[82]. Kong, H.; Luo, P.; Gao, C.; Yan, D. *Polymer* **2005**, *45*, 2472.

[83]. Hong, J.-Y.; Shin, K.-Y.; Kwon, O. S.; Kang, H.; Jang, J. *Chem. Commun.* **2011**, *47*, 7182.

[84]. De Geest, B. G.; De Koker, S.; Sukhorukov, G. B.; Kreft, O.; Parak, W. J.; Skitarch, A. G.; Demeester, J.; De Smedt, S. C.; Hennink, W. E. *Soft Matter* **2009**, *5*, 282.

[85]. Moskowitz, J. S.; Blaisse, M. R.; Samuel, R. E.; Hu, H.-P.; Harris, M. B.; Martin, S. D.; Lee, J. C.; Spector, M.; Hammond, P. T. *Biomaterials* **2010**, *31*, 6019.

[86]. Sato, K.; Yoshida, K.; Takahashi, S.; Anzai, J.-i. *Adv. Drug Deliver Rev.* **2011**, *63*, 809.

[87]. Costa, R. R.; Custódio, C. A.; Arias, F. J.; Rodríguez-Cabello, J. C.; Mano, J. F. *Small* **2011,** *7*, 2640.

[88]. Carletti, E.; Endogan, T.; Hasirci, N.; Hasirci, V.; Maniglio, D.; Motta, A.; Migliaresi, C. *J. Tissue Eng. Regen. Med.* **2011**, *5*, 569.

[89]. Costa, N. L.; Sher, P.; Mano, J. F. *Adv. Eng. Mater.* **2011**, *13*, B218.

[90]. Manna, U.; Patil, S. *Langmuir* **2009**, *25*, 10515.

[91]. Woojung, C.; Naito, M.; Fujii, R.; Morisue, M.; Fujiki, M. *Thin Solid Films* **2009**, *518*, 625.

[92]. Lütt, M.; Fitzsimmons, M. R.; Li, D. *J. Phys. Chem. B* **1998**, *102*, 400

[93]. Li, D.; Lütt, M.; Fitzsimmons, M. R.; Synowicki, R.; Hawley, M. E.; Brown, G. W. *J. Am. Chem. Soc.* **1998,** *120,* 8797.

[94]. Li, L. S.; Wang, R.; Fitzsimmons, M.; Li, D. *J. Phys. Chem. B* **2000,** *104,* 11195.

[95]. Li, L. S.; Jia, Q. X.; Li, A. D. Q. *Chem. Mater.* **2002**, *14*, 1159.

[96]. Locklin, J.; Shinbo, K.; Onishi, K.; Kaneko, F.; Bao, Z.; Advincula, R. C. *Chem. Mater.* **2003**, *15*, 1404.

[97]. Laurent, D.; Schlenoff, J. B. *Langmuir* **1997**, *13*, 1552.

[98]. Huang, H.-X.; Qian, D.-J.; Nakamura, N.; Nakamura, C.; Wakayama, T.; Miyake, J. *Electrochim. Acta* **2004**, *49*, 1491.

[99]. Swierczewska, M.; Hajicharalambous, C. S.; Janorkar, A. V.; Megeed, Z.; Yarmush, M. L.; Rajagopalan, P. *Acta Biomater.* **2008**, *4*, 827.

[100]. He, J.-A.; Samuelson, L.; Li, L.; Kumar, J.; Tripathy, S. K. *J. Phys. Chem. B.* **1998**, *102*, 7067.

[101]. Elbert, D. L.; Herbert, C. B.; Hubbell, J. A. *Langmuir* **1999**, *15*, 5355.

[102]. Zhu, H.; Srivastava, R.; McShane, M. J. *Biomacromolecules* **2005**, *6*, 2221.

[103]. Lvov, Y.; Ariga, K.; Kunitake, T. *Chem. Lett.* **1994**, *23*, 2323.

[104]. Lvov, Y.; Ariga, K.; Ichinose, I.; Kunitake, T. *J. Am. Chem. Soc.* **1995**, *117*, 6117.

[105]. Lvov, Y.; Ariga, K.; Ichinose, I.; Kumitake, T. *Thin Solid Films* **1996**, *284*, 797.

[106]. Shi, L.; Lu, Y.; Sun, J.; Zhang, J.; Sun, C.; Liu, J.; Shen, J. *Biomacromolecules* **2003**, *4*, 1161.

[107]. Zhou, C.-H.; Shen, Z.-F.; Liu, L.-H.; Liu, S.-M. *J. Mater. Chem.* **2011**, *21*, 15132.

[108]. Kotov, N. A.; Magonov, S.; Tropsha, E. *Chem. Mater.* **1998**, *10*, 886.

[109]. Kleinfeld, E. R.; Ferguson, G. S. *Science* **1994**, *265*, 370.

[110]. Lutkenhaus, J. L.; Olivetti, E. A.; Verploegen, E. A.; Cord, B. M.; Sadoway, D. R.; Hammond, P. T. *Langmuir* **2007**, *23*, 8515.

[111]. Elzbieciak, M.; Wodka, D.; Zapotoczny, S.; Nowak, P.; Warszynski, P. *Langmuir* **2010**, *26*, 277.

[112]. Peng, C.; Thio, Y. S.; Gerhardt, R. A.; Ambaye, H.; Lauter, V. *Chem. Mater.* **2011**, *23*, 4548.

[113]. Lvov, Y.; Ariga, K.; Onda, M.; Ichinose, I.; Kunitake, T. *Langmuir* **1997**, *13*, 6195.

[114]. Ariga, K.; Lvov, Y.; Ichinose, I.; Kunitake, T. *App. Clay Sci.* **1999**, *15*, 137.

[115]. Shin, Y. J.; Zhang, Q.; Hua, F. *Thin Solid Films* **2008**, *516*, 3167.

[116]. He, J.-A.; Mosurkal, R.; Samuelson, L. A.; Li, L.; Kumar, J. *Langmuir* **2003**, *19*, 2169.

[117]. Kotov, N. A.; Dékány, I.; Fendler, J. H. *J. Phys. Chem.* **1995**, *99*, 13065.

[118]. Singamaneni, S.; Bliznyuk, V. N.; Binek, C.; Tsymbal, E. Y. *J. Mater. Chem.* **2011**, *21*, 16819.

[119]. Pichon, B. P.; Louet, P.; Felix, O.; Drillon, M.; Begin-Colin, S.; Decher, G. *Chem. Mater.* **2011**, *23*, 3668.

[120]. Nakayama, M.; Tagashira, H. *Langmuir* **2006**, *22*, 3864.

[121]. Yuan, W.; Li, C. M. *Langmuir* **2009**, *25*, 7578.

[122]. Cant, N. E.; Zhang, H.-L.; Critchley, K.; Mykhalyk, T. A.; Davies, G. R.; Evans, S. D. *J. Phys. Chem. B* **2003**, *107*, 13557.

[123]. Long, D.-L.; Tsunashima, R.; Cronin, L. *Angew. Chem. Int. Ed.* **2010**, *49*, 1736.

[124]. Liu, S.; Tang, Z. *Nano Today* **2010**, *5*, 267.

[125]. Wang, B.; Vyas, R. N.; Shaik, S. *Langmuir* **2007**, *23*, 11120.

[126]. Anwar, N.; McCormac, T.; Compain, J. D.; Mialane, P.; Dolbecq, A.; Laffir, F. *Electrochim. Acta* **2012**, *59*, 1.

[127]. Caruso, F.; Kurth, D. G.; Volkmer, D.; Koop, M. J.; Müller, A. *Langmuir* **1998**, *14*, 3462.

[128]. Satija, J.; Sai, V. V. R.; Mukherji, S. *J. Mater. Chem.* **2011**, *21*, 14367.

[129]. Bliznyuk, V. N.; Rinderspacher, F.; Tsukruk, V. V. *Polymer* **1998**, *39*, 5249.

[130]. Tsukruk, V. V.; Rinderspacher, F.; Bliznyuk, V. N. *Langmuir* **1997**, *13*, 2171.

[131]. Watanabe, S.; Regen, S. L. *J. Am. Chem. Soc.* **1994**, *116*, 8855.

[132]. Fukumoto, H.; Yonezawa, Y. *Thin Solid Films* **1998**, *327*, 748.

[133]. Ariga, K.; Lvov, Y.; Kunitake, T. *J. Am. Chem. Soc.* **1997**, *119*, 2224.

[134]. Dey, D.; Hussain, S. A.; Nath, R. K.; Bhattacharjee, D. *Spectrochim. Acta A* **2008**, *70*, 307.

[135]. Cai, K.; Rechtenbach, A.; Hao, J.; Bossert, J.; Jandt, K. D. *Biomaterials* **2005**, *26*, 5960.

[136]. Jiang, H.; Taranekar, P.; Reynolds, J. R.; Schanze, K. S. *Angew. Chem. Int.* **2009**, *48*, 4300.

[137]. Hoven, C. V.; Garcia, A.; Bazan, G. C.; Nguyen, T.-Q. *Adv. Mater.* **2008**, *20*, 3793.

[138]. Berlin, A.; Zotti, G. *Macromol. Rapid Commun.* **2000**, *21*, 301.

[139]. Choi, K.; Zentel, R. *Macromol. Chem. Phys.* **2006**, *207*, 1870.

[140]. Takeoka, Y.; Iguchi, Y.; Rikukawa, M.; Sanui, K. *Synth. Met.* **2005**, *154*, 109.

[141]. Zotti, G.; Vercelli, B.; Berlin, A. *Acc. Chem. Res.* **2008**, *41*, 1098.

[142]. Lukkari, J.; Salomäki, M.; Viinikanoja, A.; Ääritalo, T.; Paukkunen, J.; Kocharova, N.; Kankare, J. *J. Am. Chem. Soc.* **2001,** *123*, 6083.

[143]. Viinikanoja, A.; Areva, S.; Kocharova, N.; Ääritalo, T.; Vuorinene, M.; Savunen, A.; Kankare, J.; Lukkari, J. *Langmuir* **2006**, *22*, 6078.

[144]. Lukkari, J.; Salomäki, M.; Ääritalo, T.; Loikas, K.; Laiho, T.; Kankare, J. *Langmuir* **2002,** *18*, 8496.

[145]. Zotti, G.; Zecchin, S.; Berlin, A.; Schiavon, G.; Giro, G. *Chem. Mater.* **2001**, *13*, 43.

[146]. Zotti, G.; Vercelli, B.; Berlin, A.; Pasini, M.; Nelson, T. L.; McCullough, R. D.; Virgili, T. *Chem. Mater.* **2010**, *22*, 1521.

[147]. Sriwichai, S.; Baba, A.; Deng, S.; Huang, C.; Phanichpant, S.; Advincula, R. C. *Langmuir* **2008**, *24*, 9017.

[148]. Waenkaew, P.; Taranekar, P.; Phanichphant, S.; Advincula, R. C. *Macromol. Rapid Comun.* **2007**, *28*, 1522.

[149]. Sriwichai, S.; Baba, A.; Deng, S.; Huang, C.; Phanichpant, S.; Advincula, R. C. *Langmuir* **2008**, *24*, 9017.

[150]. Vercelli, B.; Zotti, G.; Berlin, A.; Grimoldi, S. *Chem. Mater.* **2006**, *18*, 3754.

[151]. Baba, A.; Taranekar, P.; Ponnapati, R. R.; Knoll, W.; Advincula, R. C. *ACS Appl. Mater. Interfaces* **2010**, *2*, 2347.

[152]. Vyas, R. N.; Wang, B. *Int. J. Mol. Sci.* **2010**, *11*, 1956.

[153]. Stockton, W. B.; Rubner, M. F. *Macromolecules* **1997**, *30*, 2717.

[154]. Fou, A. C.; Rubner, M. F. *Macromolecules* **1995**, *28*, 7115.

[155]. Lehr, B.; Seufert, M.; Wenz, G.; Decher, G. *Supramol. Sci.* **1995**, *2*, 199.

[156]. Ogawa, M.; Tamanoi, M.; Ohkita, H.; Benten, H.; Ito, S. *Sol. Energ. Mat. Sol. C* **2009**, *93*, 369.

[157]. Eckle, M.; Decher, G. *Nano Lett.* **2001**, *1*, 45.

[158]. Marletta, A.; Piovesan, E.; Dantas, N. O.; de Souza, N. C.; Olivati, C. A.; Balogh, D. T.; Faria, R. M.; Oliveira, O. N. Jr. *J. Appl. Phys.* **2003**, *94*, 5592.

[159]. Pigois-Landureau, E.; Nicolau, Y. F.; Delamar, M. *Synth. Met.* **1995**, *72*, 111.

[160]. Bush, B.; Xu, G.; Carraro, C.; Maboudian, R. *Sens. Actuators A* **2006**, *126*, 194.

[161]. Yang, X.; Dai, T.; Wei, M.; Lu, Y. *Polymer* **2006**, *47*, 4596.

[162]. Vidal, J. C.; García, E.; Castillo, J. R. *Sens. Actuators B* **1999**, *57*, 219.

[163]. Cheung, J. H.; Stockton, W. B.; Rubner, M. F. *Macromolecules* **1997**, *30*, 2712.

[164]. Li, D.; Ding, W.; Wang, X.; Lu, L.; Yang, X. *J. Mater. Sci. Lett.* **2001**, *20*, 1925.

[165]. Nohria, R.; Khillan, R. K.; Su, Y.; Dikshit, R.; Lvov, Y.; Varahramyan, K. *Sens. Actuators B* **2006**, *114*, 218.

[166]. Li, D.; Jiang, Y.; Li, Y.; Yang, X.; Lu, L.; Wang, X. *Mater. Sci. Eng. C* **2000**, *11*, 117.

[167]. Ram, M. K.; Salermo, M.; Adami, M.; Faraci, P.; Nicolini, C. *Langmuir* **1999**, *15*, 1252.

[168]. Park, M.-K.; Onishi, K.; Locklin, J.; Caruso, F.; Advincula, R. C. *Langmuir* **2003**, *19*, 8550.

[169]. Ravati, S.; Favis, B. D. *Polymer* **2011**, *52*, 718.

[170]. Gomes, E. C.; Oliveira, M. A. S. *Surf. Coat. Tech.* **2011**, *205*, 2857.

[171]. Santos, M. C.; Munford, M. L.; Bianchi, R. F. *Mater. Sci. Eng. B* **2012**, *177*, 359.

[172]. Vieira, N. C. S.; Fernades, E. G. R.; Faceto, A. D.; Zucolotto, V.; Guimaraes, F. E. G. *Sens. Actuators B* **2011**, *160*, 312.

[173]. Shin, Y. J.; Kim, S. H.; Yang, D. H.; Kwon, H.; Shin, J. S. J. *J. Ind. Eng. Chem.* **2010**, *16*, 380.

[174]. Farhat, T. R.; Hammond, P. T. *Chem. Mater.* **2006**, *18*, 41.

[175]. Ge, C.; Armstrong, N. R.; Saavedra, S. S. *Anal. Chem.* **2007**, *79*, 1401.

[176]. Ge, C.; Doherty, W. J.; Mendes, S. B.; Armstrong, N. R.; Saavedra, S. S. *Talanta* **2005**, *65*, 1126.

[177]. Tian, S.; Baba, A.; Liu, J.; Wang, Z.; Knoll, W.; Park, M.-Y.; Advincula, R. *Adv. Funct. Mater.* **2003**, *13*, 473.

[178]. Lakard, B.; Magnin, D.; Deschaume, O.; Vanlancker, G.; Glinel, K.; Demoustier-Champagne, S.; Nysten, B.; Jonas, A. M.; Bertrand, P.; Yunus, S. *Biosens. Bioelectron.* **2011**, *26*, 4139.

[179]. Travas-Sejdic, J.; Soman, R.; Peng, H. *Thin Solid Films* **2006**, *497*, 96.

[180]. Barrientos, H.; Moggio, I.; Arias-Marin, E.; Ledezma, A.; Romero, J. *Eur. Polym. J.* **2007**, *43*, 1672.

[181]. DeLongchamp, D. M.; Hammond, P. T. *Chem. Mater.* **2004**, *16*, 4799.

[182]. Li, C.; Mitamura, K.; Imae, T. *Macromolecules* **2003**, *36*, 9957.

[183]. Kim, Y.; Lee, C.; Shim, I.; Wang, D.; Cho, J. *Adv. Mater.* **2010**, *22*, 5140.

[184]. Yoon, H. C.; Hong, M.-Y.; Kim, H.-S. *Anal. Chem.* **2000**, *72*, 4420.

[185]. Kim, E.; Jung, S. *Chem. Mater.* **2005**, *17*, 6381.

[186]. Kim, Y.; Kim, E. *Curr. Appl. Phys.* **2006**, *6S1*, e202.

[187]. Jung, S.; Kim, H.; Han, M.; Kang, Y.; Kim, E. *Mater. Sci. Eng. C* **2004**, *24*, 57.

[188]. Raposo, M.; Oliveira, O. N. Jr. *Langmuir* **2002**, *18*, 6866.

[189]. Ragupathy, D.; Gopalan, A. I.; Lee, K.-P.; Manesh, K. M. *Electrochem. Commun.* **2008**, *10*, 527.

[190]. Gheith, M. K.; Sinani, V. A.; Wicksted, J. P.; Matts, R. L.; Kotov, N. A. *Adv. Mater.* **2005**, *17*, 2663.

[191]. Recksiedler, C. L.; Deore, B. A.; Freund, M. S. *Langmuir* **2006**, *22*, 2811.

[192]. Woodfield, T. B. F.; Malda, J.; de Wijn, J.; Péters, F.; Riesle, J.; van Blitterswijk, C. A. *Biomaterials* **2004**, *25*, 4149.

[193]. Li, D.; Huang, J.; Kaner, R. B. *Acc. Chem. Res.* **2009**, *42*, 135.

[194]. Zeng, F.-W.; Liu, X.-X.; Diamond, D.; Lau, K. T. *Sens. Actuators B* **2010**, *143*, 530.

[195]. Lin, Y.-F.; Chen, C.-H.; Xie, W.-J.; Yang, S.-H.; Hsu, C.-S.; Lin, M.-T.; Jian, W.-B. *ACS Nano* **2011**, *5*, 1541.

[196]. Michel, M.; Ettingshausen, F.; Scheiba, F.; Wolz, A.; Roth, C. *Phys. Chem. Chem. Phys.* **2008**, *10*, 3796.

[197]. Hu, Z.; Xu, J.; Tian, Y.; Peng, R.; Xian, Y.; Ran, Q.; Jin, L. *Electrochim. Acta* **2009**, *54*, 4056.

[198]. Tang, Q.; Wu, J.; Sun, X.; Li, Q.; Lin, J. *J. Colloid Interf. Sci.* **2009**, *337*, 155.

[199]. Shin, Y. J.; Kameoka, J. *J. Ind. Eng. Chem.* **2012**, *18*, 193.

[200]. Wakizaka, D.; Fushimi, T.; Ohkita, H.; Ito, S. *Polymer* **2004**, *45*, 8561.

[201]. Zotti, G.; Zecchin, S.; Schiavon, G.; Vercelli, B.; Groenendaal, L. B. *Chem. Mater.* **2003**, *15*, 2222.

[202]. Jiang, G.; Baba, A.; Advincula, R. *Langmuir* **2007**, *23*, 817.

[203]. Smith, R. R.; Smith, A. P.; Stricker, J. T.; Taylor, B. E.; Durstock, M. F. *Macromolecules* **2006**, *39*, 6071.

[204]. Wistrand, I.; Lingström, R.; Wagberg, L. *Eur. Polym. J.* **2007**, *43*, 4075.

[205]. Stricker, J. T.; Gudmundsdóttir, A. D.; Smith, A. P.; Taylor, B. E.; Durstock, M. F. *J. Phys. Chem. B* **2007,** *111,* 10397

[206]. DeLongchamp, D. M.; Kastantin, M.; Hammond, P. T. *Chem. Mater.* **2003**, *15*, 1575.

[207]. Liu, S.; Xu, L.; Li, F.; Xu, B.; Sun, Z. *J. Mater. Chem.* **2011**, *21*, 1946.

[208]. Cutler, C. A.; Bouguettaya, M.; Reynolds, J. R. *Adv. Mater.* **2002**, *14*, 684.

[209]. Cutler, C. A.; Bouguettaya, M.; Kang, T.-S.; Reynolds, J. R. *Macromolecules* **2005**, *38*, 3068.

[210]. Baba, A.; Park, M.-K.; Advincula, R. C.; Knoll, W. *Langmuir* **2002**, *18*, 4648.

[211]. Zhang, N.; Schweiss, R.; Knoll, W. *J. Solid State Electrochem.* **2007**, *11*, 451.

[212]. Shrivastava, S.; Kotov, N. A. *Acc. Chem. Res.* **2008**, *41*, 1831.

[213]. Hammond, P. T. *Adv. Mater.* **2004**, *16*, 1271.

[214]. Ariga, K.; Hill, J. P.; Ji, Q. *Phys. Chem. Chem. Phys.* **2007**, *9*, 2319.

[215]. Azzaroni, O.; Lau, K. H. A. *Soft Matter* **2011**, *7*, 8709.

[216]. Wang, Y.; Angelatos, A. S.; Caruso, F. *Chem. Mater.* **2008**, *20*, 848.

[217]. de Villiers, M. M.; Otto, D. P.; Strydom, S. J.; Lvov, Y. M. *Adv. Drug Deliver Rev.* **2011**, *63*, 701.

[218]. Rouse, J. H.; Lillehei, P. *Nano Lett.* **2003**, *3*, 59.

[219]. Kim, B.; Sigmund, W. M. *Langmuir* **2003**, *19*, 4848.

[220]. Shen, J.; Hu, Y.; Qin, C.; Ye, M. *Langmuir* **2008**, *24*, 3993.

[221]. Park, H. J.; Kim, J.; Chang, J. Y.; Theato, P. *Langmuir* **2008**, *24*, 10467.

[222]. Xu, Z.; Gao, N.; Dong, S. *Talanta* **2006**, *68*, 753.

[223]. Srivastava, S.; Podsiadlo, P.; Critchley, K.; Zhu, J.; Qin, M.; Shim, B. S.; Kotov, N. A. *Chem. Mater.* **2009**, *21*, 4397.

[224]. Deng, C.; Chen, J.; Nie, Z.; Si, S. *Biosens. Bioelectron.* **2010**, *26*, 213.

[225]. Munge, B.; Liu, G.; Collins, G.; Wang, J. *Anal. Chem.* **2005**, *77*, 4662.

[226]. Gittleson, F. S.; Kohn, D. J.; Li, X.; Taylor, A. D. *ACS Nano* **2012**, *6*, 3703.

[227]. Lee, S. W.; Gallant, B. M.; Byon, H. R.; Hammond, P. T.; Horn, Y. S. *Energy Environ. Sci.* **2011**, *4*, 1972.

[228]. Shim, B. S.; Tang, Z.; Morabito, M. P.; Agarwal, A.; Hong, H.; Kotov, N. A. *Chem. Mater.* **2007**, *19*, 5467.

[229]. Park, H. J.; Oh, K. A.; Park, M.; Lee, H. *J. Phys. Chem. C* **2009**, *113*, 13070.

[230]. Hu, Z.; Xu, J.; Tian, Y.; Peng, R.; Xian, Y.; Ran, Q.; Jin, L. *Carbon* **2010**, *48*, 3729.

[231]. Mamedov, A. A.; Kotov, N. A.; Prato, M.; Guldi, D. M.; Wicksted, J. P.; Hirsch, A. *Nat. Mater.* **2002**, *1*, 190.

[232]. Olek, M.; Ostrander, J.; Jurga, S.; Möhwald, H.; Kotov, N.; Kempa, K.; Giersig, M. *Nano Lett.* **2004**, *4*, 1889.

[233]. Shim, B. S.; Zhu, J.; Jan, E.; Critchley, K.; Kotov, N. A. *ACS Nano* **2010**, *4*, 3725.

[234]. Zhang, M.; Yan, Y.; Gong, K.; Mao, L.; Guo, Z.; Chen, Y. *Langmuir* **2004**, *20*, 8781.

[235]. Gheith, M. K.; Sinani, V. A.; Wicksted, J. P.; Matts, R. L.; Kotov, N. A. *Adv. Mater.* **2005**, *17*, 2663.

[236]. Kim, Y. S.; Davis, R.; Cain, A. A.; Grunlan, J. C. *Polymer* **2011**, *52*, 2847.

[237]. Jan, E.; Hendricks, J. L.; Husaini, V.; Richardson-Burns, S. M.; Sereno, A.; Martin, D. C.; Kotov, N. A. *Nano Lett.* **2009**, *9*, 4012.

[238]. Liu, J.; Tian, S.; Knoll, W. *Langmuir* **2005**, *21*, 5596.

[239]. Qu, F.; Yang, M.; Jiang, J.; Shen, G.; Yu, R. *Anal. Biochem.* **2005**, *344*, 108.

[240]. Chen, H.; Guo, L.; Ferhan, A. R.; Kim, D.-H. *J. Phys. Chem. C* **2011**, *115*, 5492.

[241]. Shirsat, M. D.; Too, C. O.; Wallace, G. G. *Electroanal.* **2008**, *20*, 150.

[242]. Shahrokhian, S.; Kamalzadeh, Z.; Saberi, R.-S. *Electroanal.* **2011**, *23*, 2925.

[243]. Shahrokhian, S.; Kamalzadeh, Z.; Saberi, R.-S. *Electrochim. Acta* **2011**, *56*, 10032.

[244]. Shahrokhian, S.; Asadian, E. *J. Electroanal. Chem.* **2009**, *636*, 40.

[245]. Almeida, L. C. P.; Zucolotto, V.; Domingues, R. A.; Atvars, T. D. Z.; Nogueira, A. F. *Photochem. Photobiol. Sci.* **2011**, *10*, 1766.

[246]. Li, J.; Liu, Y.; Wei, W.; Luo, S. *Anal. Lett.* **2011**, *44*, 1226.

[247]. Siqueira, J. R. Jr.; Werner, C. F.; Bäcker, M.; Poghossian, A.; Zucolotto, V.; Oliveira, O. N. Jr.; Schöning, M. J. *J. Phys. Chem. C* **2009**, *113*, 14765.

[248]. Liang, Z.; Dzienis, K. L.; Xu, J.; Wang, Q. *Adv. Funct. Mater.* **2006**, *16*, 542.

[249]. Gao, M.; Richter, B.; Kirstein, S.; Möhwald, H. *J. Phys. Chem. B* **1998**, *102*, 4096.

[250]. Gao, M.; Richter, B.; Kirstein, S. *Adv. Mater.* **1997**, *9*, 802.

[251]. Mwaura, J. K.; Pinto, M. R.; Witker, D.; Ananthakrishnan, N.; Schanze, K. S.; Reynolds, J. R. *Langmuir* **2005**, *21*, 10119.

[252]. Cassagneau, T.; Mallouk, T. E.; Fendler, J. H. *J. Am. Chem. Soc.* **1998**, *120*, 7848.

[253]. Wang, S.; Li, C.; Shi, G. *Sol. Energ. Mat. Sol. C* **2008**, *92*, 543.

[254]. Rapta, P.; Lukkari, J.; Tarábek, J.; Salomäki, M.; Jussila, M.; Yohannes, G.; Riekkola, M.-L.; Kankare, J.; Dunsch, L. *Phys. Chem. Chem. Phys.* **2004**, *6*, 434.

[255]. Huguenin, F.; Ferreira, M.; Zucolotto, V.; Nart, F. C.; Torresi, R. M.; Oliveira, O. N. Jr. *Chem. Mater.* **2004**, *16*, 2293.

[256]. Ferreira, M.; Huguenin, F.; Zucolotto, V.; da Silva, J. E. P.; Córdoba de Torresi, S. I.; Temperini, M. L. A.; Torresi, R. M.; Oliveira, O. N. Jr. *J. Phys. Chem. B* **2003**, *107*, 8351.

[257]. Schweiss, R.; Zhang, N.; Knoll, W. *J. Sol-Gel Sci. Technol.* **2007**, *44*, 1.

[258]. Shan, J.; Tenhu, H. *Chem. Commun.* **2007**, 4580.

[259]. Lange, U.; Ivanov, S.; Lyutov, V.; Tsakova, V.; Mirsky, V. M. *J. Solid State Electrochem.* **2010**, 14, 1261.

[260]. Zanfrognini, B.; Zanardi, C.; Terzi, F.; Ääritalo, T.; Viinikanoja, A.; Lukkari, J.; Seeber, R. *J. Solid State Electrochem.* **2011**, *15*, 2395.

[261]. Ivanov, S.; Lange, U.; Tsakova, V.; Mirsky, V. M. *Sens. Actuators B* **2010**, *150*, 271.

[262]. Palmero, S.; Colina, A.; Muñoz, E.; Heras, A.; Ruiz, V.; López-Palacios, J. *Electrochem. Commun.* **2009**, *11*, 122.

[263]. Tian, S.; Liu, J.; Zhu, T.; Knoll, W. *Chem. Mater.* **2004**, *16*, 4103.

[264]. Paterno, L. G.; Soler, M. A. G.; Fonseca, F. J.; Sinnecker, J. P.; Sinnecker, E. H. C. P.; Lima, E. C. D.; Novak, M. A.; Morais, P. C. *J. Phys. Chem. C* **2009**, *113*, 5087.

[265]. Kim, H. S.; Sohn, B. H.; Lee, W.; Lee, J. K.; Choi, S. J.; Kwon, S. J. *Thin Solid Films* **2002**, *419*, 173.

[266]. Paterno, L. G.; Fonseca, F. J.; Alcantara, G. B.; Soler, M. A. G.; Morais, P. C.; Sinnecker, J. P.; Novak, M. A.; Lima, E. C. D.; Leite, F. L.; Mattoso, L. H. C. *Thin Solid Films* **2009**, *517*, 1753.

[267]. Karnicka, K.; Chojak, M.; Miecznikowski, K.; Skunik, M.; Baranowska, B.; Kolary, A.; Piranska, A.; Palys, B.; Adamczyk, L.; Kulesza, P. J. *Bioelectrochemistry* **2005**, *66*, 79.

[268]. Kulesza, P. J.; Chojak, M.; Karnicka, K.; Miecznikowski, K.; Palys, B.; Lewera, A. *Chem. Mater.* **2004**, *16*, 4128.

[269]. Kulesza, P. J.; Karnicka, K.; Miecznikowski, K.; Chojak, M.; Kolary, A.; Barczuk, P. J.; Tsirlina, G.; Czerwinski, W. *Electrochim. Acta* **2005**, *50*, 5155.

[270]. Kulesza, P. J.; Chojak, M.; Miecznikowski, K.; Lewera, A.; Malik, M. A.; Kuhn, A. *Electrochem. Commun.* **2002**, *4*, 510.

[271]. Wang, Y.; Guo, C.; Chen, Y.; Hu, C.; Yu, W. *J. Colloid Interf. Sci.* **2003**, *264*, 176.

[272]. Sakai, N.; Prasad, G. K.; Ebina, Y.; Takada, K.; Sasaki, T. *Chem. Mater.* **2006**, *18*, 3596.

[273]. Kang, H.; Lee, C.; Yoon, S. C.; Cho, C.-H.; Cho, J.; Kim, B. J. *Langmuir* **2010**, *26*, 17589.

[274]. Ding, H.; Ram, M. K.; Nicolini, C. *J. Mater. Chem.* **2002**, *12*, 3585.

[275]. Zhang, X.; Yan, G.; Ding, H.; Shan, Y. *Mater. Chem. Phys.* **2007**, *102*, 249.

[276]. Ram, M. K.; Yavuz, Ö.; Aldissi, M. *Synth. Met.* **2005**, *151*, 77.

[277]. Ram, M. K.; Yavuz, Ö.; Lahsangah, V.; Aldissi, M. *Sens. Actuators B* **2005**, *106*, 750.

[278]. Müller, K.; Park, M.-K.; Klapper, M.; Knoll, W.; Müllen, K. *Macromol. Chem. Phys.* **2007**, *208*, 1394.

[279]. Vercelli, B.; Zotti, G.; Berlin, A. *J. Phys. Chem. C* **2009**, *113*, 3525.

[280]. Masuda, K.; Ikeda, Y.; Ogawa, M.; Benten, H.; Ohkita, H.; Ito, S. *ACS Appl. Mater. Interfaces* **2010**, *2*, 236.

[281]. Masuda, K.; Ogawa, M.; Ohkita, H.; Benten, H.; Ito, S. *Sol. Energ. Mat. Sol. C* 2009, *93*, 762.

[282]. Hsu, C.-L.; Lin, C.-T.; Huang, J.-H.; Chu, C.-W.; Wei, K.-H.; Li, L.-J. *ACS Nano* **2012**, *6*, 5031.

[283]. Wang, Y.; Tong, S. W.; Xu, X. F.; Özyilmaz, B.; Loh, K. P. *Adv. Mater.* **2011**, *23*, 1514.

[284]. Mattoussi, H.; Rubner, M. F.; Zhou, F.; Kumar, J.; Tripathy, S. K.; Chiang, L. Y. *Appl. Phys. Lett.* **2000**, *77*, 1540.

[285]. Crespilho, F. N.; Zucolotto, V.; Oliveira, O. N. Jr.; Nart, F. C. *Int. J. Electrochem. Sci.* **2006**, *1*, 194.

[286]. Lin, X.; Kang, G.; Lu, L. *Bioelectrochemistry* **2007**, *70*, 235.

[287]. Kepas, A.; Grzeszczuk, M. *J. Electroanal. Chem.* **2005**, *582*, 209.

[288]. Kranz, C.; Wohlschläger, H.; Schmidt, H.-L.; Schuhmann, W. *Electroanal.* **1998**, *10*, 546.

[289]. Tan, C. K.; Blackwood, D. J. *Corros. Sci.* **2003**, *45*, 545.

[290]. Narayanasamy, B.; Rajendran, S. *Prog. Org. Coat.* **2010**, *67*, 246.

[291]. Han, G.; Shi, G. *Sens. Actuators B* **2004**, *99*, 525.

[292]. Zainudeen, U. L.; Careem, M. A.; Skaarup, S. *Sens. Actuators B* **2008**, *134*, 467.

[293]. Hao, Q.; Wang, X.; Lu, Lude.; Yang, X.; Mirsky, V. M. *Macromol. Rapid Commun.* **2005,** *26*, 1099.

[294]. Estrany, F.; Aradilla, D.; Oliver, R.; Alemán, C. *Eur. Polym. J.* **2007**, *43*, 1876.

[295]. Estrany, F.; Aradilla, D.; Oliver, R.; Armelin, E.; Alemán, C. *Eur. Polym. J.* **2008**, *44*, 1323.

[296]. Aradilla, D.; Estrany, F.; Armelin, E.; Alemán, C. *Thin Solid Films* **2010**, *518*, 4203.

[297]. Aradilla, D.; Ocampo, C.; Armelin, E.; Alemán, C.; Oliver, R.; Estrany, F. *Mater. Corros.* **2007**, *58*, 867.

[298]. Aradilla, D.; Estrany, F.; Alemán, C. *J. Phys. Chem. C* **2011**, *115*, 8430.

[299]. Aradilla, D.; Estrany, F.; Oliver, R.; Alemán, C. *Eur. Polym. J.* **2010**, *46*, 2222.

1.4. Functionality of conducting polymers

1.4.1. Effect of electron-withdrawing substituents on the properties of conducting polymers

As it was previously in the first part of the introduction, the optical properties of conducting polymers are mainly influenced by their nature chemical. On the basis of this data, some studies have been carried out to modify electronic properties from the presence of new functional groups. Thus, the functionality based on the incorporation of chemical groups in the polymer backbone has been gathering more and more attention among the researchers due to its interesting properties. The results have shown some benefits in terms of decreasing of band-gap energy, increasing of solubility or changes in solvatochromic and thermochromic properties. These changes, especially important in the optical properties (*e.g.* band-gap energy) can be ascribed to the rotation of neighboring atomic rings, which leads to a decrease of π conjugation, changing the electronic structure responsible of the electronic properties, and therefore the colour changes.[67] The introduction of electron donating substituents into a conjugated chain is a used method to decrease the oxidation potential by raising the energy of the valence band electrons (HOMO of the conjugated chain). At the same time, there is a small perturbation on the energy of the conduction band (LUMO of the conjugated chain), which leads to a decrease in the polymer's electronic band gap. Thus, functionalized thiophenes using substituents such as alkyl groups were synthesized succesfully to improve their stability, processability and solubility.[68] The substitution process in CPs affects the structural conformation and subsequently, the electronic, conductive and optical properties of conducting polymers. Therefore, substitution process is an effective and practical method to modify and modulate properties in the field of polymers.[69]

This strategy has not only been employed in the family of thiophene, thus, pyrrole is usually substituted at the nitrogen atom due to the ease of substitution. In contrast, thiophene is generally substituted at β position. Functionalized pyrroles have been widely studied through N-substituted alkyl pyrroles, which reduce the conductivity of the polymers due to the increase of the distance among chains.[70] However, other functionalized pyrroles based on carboxylic acid sustituents have been reported in the literature[71,72] due to their potential in biomedical applications.[73]

In this thesis, an important research topic has been focused on studying the influence of some electron-withdrawing sustituents, specifically halide atoms and cyano group (-

CN), on the structural, topological, physical and optical properties of some pyrrole and thiophene derivatives. Next, a brief description of state-of-the-art is detailed for both cyano and halide sustituents, respectively.

1.4.1.1. Halide atoms

Thiophene, and pyrrole derivatives have been one of the interest topics in this work.. The presence of strong electron-withdrawing substituents such as the cyano group or halide atoms has awakened a great interest due to their influences on the electronic and optical properties of CPs. Precisely, among 3-halidethiophenes the presence of the chlorine and bromine atoms has gained special attention among researchers. Recently, poly(3-chlorothiophene) (PClTh) has been synthesized using ionic liquids through electrochemical methods on different substrates (*e.g.* WO_3 and TiO_2).[74,75] However, other solvents such as boron trifluoride diethyl ether (BFEE) in combination with strong acids (sulfuric acid and trifluroacetic acid) were also employed to obtain PClTh.[76,77] The structural and conformational changes of PClTh were studied through the Raman spectroscopy.[78-80] As we discussed in previous sections, copolymerization is an useful procedure to improve and to modify properties in CPs compared with those referred to individual homopolymers, thus, copolymerizations of PClTh with furan,[81] and 3-methylthiophene[82,83] were reported showing improvements in some structural properties.

Poly(3-bromothiophene) (PBrTh) is another important conducting polymer in the 3-halidethiophene family. PBrTh has been also synthesized in different substrates (*e.g.* WO_3 and TiO_2) using ionic liquids.[84-86] In this context, PBrTh was synthesized in common organic solvents (*e.g.* nitrobenzene, acetonitrile, dichloromethane and 1,2-dichloroethane),[87-89] however, high oxidation potentials were required to polymerize the monomer (~2.0 V). Consequently, PBrTh films were found exhibit poor mechanical properties and high instability. The presence of strong Lewis acid such as BFEE provided the possibility to reduce the oxidation potential of the corresponding monomer (BrTh), thus, electrogenerated films were more stable in BFEE than in common organic solvents.[90,91] Within context, the copolymerization made of PBrTh and 3-butylthiophene was reported to improve the mechanical and electrochemical properties of PBrTh.[92] At characterization level, studies devoted to analyze the morphological and topological properties of PBrTh films by using scanning tunneling microscopy (STM) have been reported.[93,94] Among its main applications PBrTh has been employed in electrochromic devices.[90,85]

The synthesis of fluorothiophene was carried out by using chemical routes.[95,96] However, there are scarce works devoted to characterize the electrochemical and electronic properties of PFTh due to its polymerization is quite difficult.[97]

1.4.1.2. Cyano group (-CN)

Cyano group is a strong electron-withdrawing substituent, which has been incorporated to modify some properties on conducting polymers such as the increase in the oxidation potential or improvement of the electron transport along the polymer backbone.[98] This group provides interesting applications in conducting polymers such as electrocatalyst,[99] immunosensor,[100] or supercapacitor.[101] Within this context, the cyano group has been also employed in photovoltaic cells[102] and light-emitting diodes (LEDs).[103] The presence of this substituent has influenced in the electronic properties of conducting polymers.[104-106] In this thesis, we have been focused on a conducting polymer bearing the cyano group, specifically, poly[N-(2-cyanoethylpyrrole)].This polymer has been employed in different applications as detector of biological units (*e.g.* dopamine),[107-109] gas-solvent sensor,[110-112] inmunosensor,[100] and recently in nanotechnology to fabricate nanowires.[113]

1.5. Nanotechnology in the field of conducting polymers

Over the last decade, nanotechnology has awakened a great curiosity among researchers due to its promising and remarkable applications in different technological areas. The concept of nanotechnology deals with the precise control of materials at nanoscale, which at least one of the dimensions is smaller than 100 nm. Within this context, one of the main goals of nanotechnology is focused on developing new nanocomposites, which consist in inorganic fillers (*e.g.* nanotubes, graphene, metal oxides or mineral clays) dispersed into a matrix constituted by polymer. Precisely, the dispersion of the filler plays a key factor on the success of the nanocomposite. Nanotechnology plays an important role on the structure/property ratio according to the properties of the nanometric scale (*e.g.* high active surface). The synthesis of new hybrid nanocomposites consist in obtaining and improving structural properties based on the synergistic effects of the compounds. This effect provides improvements on the electrical and chemical properties, which can be exploited in charge storage devices or in chemical sensors. One of the main challenges of nanotechnology consists of controlling the structure of materials, through the size, architecture, composition, self-

assembly, and hybridization, respectively. This aim has been developed through wet-chemical and electrochemical methods, which have allowed to design sensors or fuel cells.[114] This effect has been highly attractive in the field of conducting polymers.[115] Recently, important investigations have been carried out to evaluate the performance of nanocomposites based on conducting polymers as sensors.[116]

Undoubteadly, nanotechnology has emerged as a promising field in conducting polymers according to its interesting properties in terms of thermal and electrical stability, mechanical strength and charge storage.[117,118] As we cited previously, the key role on nanotechnology corresponds to the size of the compounds, however, the conformation of the nanostructures is relatively important. There are four types of nanostructures: zero, one, two, and three dimension structures, specifically, zero and one-dimensional conducting polymer nanocomposites have attracted a great deal of attention in the fields of nanotechnology and nanoscience.[119-121] Within 1-D nanostructures (nanowires, nanotubes, nanorods and nanofibers) have been employed in metals[122] and conducting polymers.[123] Precisely, polyaniline (PAni) has awakened a considerable interest due to its capability to form 1-D nanometric morphologies.[124,125] The aim of building 1-D nanostructures made of conducting polymers focuses on the ability to possess superior properties due to their high surface area-to-volume ratio. According to the excellent properties exhibited by 1-D nanostructures based on conducting polymers, numerous applications in nanophotonics, nanoelectronics and biosensors have been carried out.[126-128]

During the last decade, inorganic nanostructured materials such as metallic oxides and nitrides have been employed for advanced energy conversion and storage devices (*e.g.* lithium batteries, fuel cells and supercapacitors),[129,130] hydrogen storage[131] and also in the construction industry.[132] Hybrid organic-inorganic nanocomposites have allowed to design, and to synthesize new nanocomposites with interesting technological applications.[133]

Among 2-D nanostructures, nanolayers are the most common. Mineral clays belong to the general family of layered aluminosilicates. Clays are a class of inorganic materials divided in seven main groups: kaolin-serpentine, pyrophyllite-talc, smecticte, vermiculite, mica, chlorite and interstratified clay minerals.[134] Mineral clays have been employed as reinforcement in conventional polymers exhibiting interesting results in terms of mechanical properties (*e.g.* impact strength and tensile elongation at break),[135] sensors,[136] and in aerospace applications.[137] Among mineral clays, montmorillonite

(MMT) [$M_x(Al_{x-2}Mg_x)Si_4O_{10}(OH)_2.nH_2O$] is an important clay in the smectite's group and due to its abundance and low-cost is one of the most commonly used clays in the field of nanocomposites. Moreover, they present high strength, stiffness and high aspect ratio of each platelet. However, the main characteristics of the montmorillonite are its particle size, cationic exchange and adsorption properties.

The structure of MMT is described in Figure 12. Its cristaline structure is clearly defined, which is formed by fusing two silica tetrahedral sheets with an edge-shared octahedral sheet of alumina or magnesium. The space generated between the layers is denominated as gallery. These galleries are occupied by cations (*e.g.* Na^+ or Al^{+3}) which balance the charge deficiency generated by isomorphous substitution within the layers (*e.g.* Al^{+3} replaced by Mg^{+2} or Mg^{+2} replaced by Li^+). Due to the weak forces generated (van der Waals) among layers and low negative charge per unit cell these mineral clays can be successfully employed as reinforcement in nanocomposites.

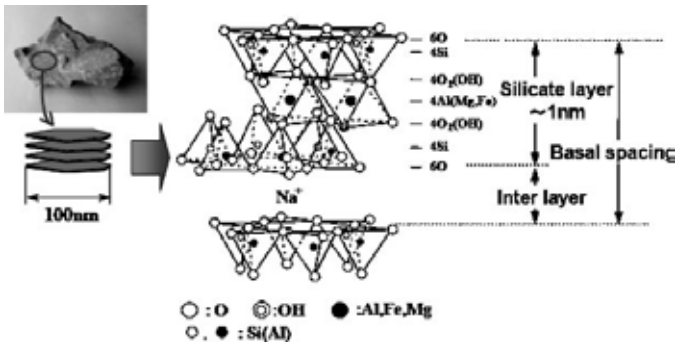

Figure 12. *Crystaline structure of montmorillonite*[134]

These features attracted a great attention in the conducting polymers field. Thus, several studies have been reported employing PANI/MMT with anti-corrosive properties.[138,139] Recently, PEDOT/MMT nanocomposites have been synthesized by using chemical and electrochemical techniques.[140-142] Modification of MMT improves the compatibility of the clay with the conducting polymer and eases exfoliated nanocomposites. In this thesis, synthesis, characterization and development of novel hybrid nanocomposites with technological applications in the field of charge storage have been carried out.

1.6. Influence of the substrate on the properties of conducting polymers

In general terms, currently, many technological applications require substrates, which have specific properties to develop and to improve novel materials. Within this context, coatings play a key role on the plastic industry, thus, important investigations on adhesives and friction and wear coatings have been carried out. During the last years, important advances in the modification of substrates have been reported, which has converted this research topic in one of the most important in the field of polymers. Among the most innovative techniques are the surface grafting, and plasma treatment. The main goal is to modify and to improve the physical and structural properties of materials.

The synthesis of conducting polymers can be carried out using either chemical or electrochemical methods. However, the field of electrochemistry in the synthesis of conducting polymers has evolved considerably in the last years.[143] This thesis is mainly focused on the electrochemical synthesis where the supporting electrolyte (saline specie), solvent and substrate play an important role during the polymerization. Within this context, the size of the anions has been proved to have a great influence on the redox properties and porosity of conducting polymers.[144] Thus, small anions (*e.g.* Cl^-, Br^-, ClO_4^-, NO_3^- or BF_4^-) has shown to improve the anionic exchange properties and higher porosity when they are incorporated in conducting polymer, in contrast, large anions (dodecylsulfonate or polyvinylsulfonate) are excellent candidate to be employed in cationic exchange properties.[145] On the other hand, the characteristics of the solvent are a high dielectric constant to ensure a good ionic conductivity, and good resistance to avoid non-desirable secondary reactions, such as decomposition of the polymer.

Another important parameter is the substrate, the choice of substrates is a critical parameter on the morphology of thin films. Thus, surface treatments before or after electrochemical deposition of conducting polymer films affect directly the growth of polymer thin films and therefore their properties. Nowadays, stainless steel and indium tin oxide substrates are the most used according to their properties.

The substrate influences the growing of CPs, specially, during the nucleation and growing processes. Furthermore, substrates play a key role on the adhesion properties, consequently, organic substrates made of polyolefins have been reported to improve the adherence and growth of CPs.[146] ITO substrate is a special substrate due to its

transparency and conductivity. According to its properties, this substrate is widely used in photovoltaic devices employing PEDOT:PSS conducting polymer. However, scarce works have been devoted to study the influence of ITO substrate in the growth of PEDOT.[147] Some conducting polymers such as PANI has been reported in terms of growth using ITO,[148] gold,[149] and graphite[150,151] substrates. Poly(3-methylthiophene) growth was studied by STM microscope on ITO substrate.[152] Poly(o-anisidine) growth was evaluated on steel substrates by using electrochemical methods.[153] Nevertheless, PEDOT growth was studied in platinum substrate reflecting significant differences with ITO substrate.[154] Within this context, PEDOT films in presence of poly(styrene sulfonate) were grown electrochemically onto ITO substrate in BFEE media for photovoltaic applications.[159] Finally, growth mechanisms of others conducting polymers such as PPy were studied at different substrates (*e.g.* graphite,[155,156] titanium,[157] ITO[158]).

For this purpose, morphological studies using different and modified substrates have been carried out in this thesis to study the effect of substrate on the morphology and properties of conducting polymers.

1.7. References

[1]. Shirakawa, H.; Louis, E. J.; MacDiarmid, A. G.; Chiang, C. K.; Heeger, A. J. *Chem. Soc. Chem. Commun.* **1977**, 578.

[2]. Gerard, M.; Chaubey, A.; Malhotra, B. D. *Biosens. Bioelectr.* **2002**, *17*, 345.

[3]. Lange, U.; Roznyatovskaya, N. V.; Mirsky, V. M. *Anal. Chim. Acta* **2008**, *614*, 1.

[4]. Peng, H.; Zhang, L.; Soeller, C.; Travas-Sejdic, J. *Biomaterials* **2009**, *30*, 2132.

[5]. Saxena, V.; Malhotra, B. D. *Curr. Appl. Phys.* **2003**, *3*, 293.

[6]. Horowitz, G. *Adv. Mater.* **1998**, *10*, 365.

[7]. Cai, Z.; Geng, M.; Tang, Z. *J. Mater. Sci.* **2004**, *39*, 4001.

[8]. Guimard, N. K.; Gomez, N.; Schmidt, C. E. *Prog. Polym. Sci.* **2007**, *32*, 876.

[9]. Smela, E. *Adv. Mater.* **2003**, *15*, 481.

[10]. Zelikin, A. N.; Lynn, D. M.; Farhadi, J.; Martin, I.; Shastri, V.; Langer, R. *Angew. Chem.* **2002**, *114*, 149.

[11]. Tallman, D. E.; Spinks, G.; Dominis, A.; Wallace, G. G. *J. Solid State Electrochem.* **2002**, *6*, 73.

[12]. Rohwerder, M.; Michalik, A. *Electrochim. Acta* **2007**, *53*, 1300.

[13]. Rammelt, U.; Nguyen, P. T.; Plieth, W. *Electrochim. Acta* **2003**, *48*, 1257.

[14]. Sonmez, G.; Sonmez, H. B.; Shen, C. K. F.; Wudl, F. *Adv. Mater.* **2004**, *16*, 1905.

[15]. Carpi, F.; De Rossi, D. *Opt. Laser Technol.* **2006**, *38*, 292.

[16]. Arbizzani, C.; Mastragostino, M.; Meneghello, L.; Paraventi, R. *Adv. Mater.* **1996**, *8*, 331.

[17]. Soudan, P.; Lucas, P.; Ho, H. A.; Jobin, D.; Breau, L.; Bélanger, D. *J. Mater. Chem.* **2001**, *11*, 773.

[18]. Friend, R. H.; Gymer, R. W.; Holmes, A. B.; Burroughes, J. H.; Marks, R. N.; Taliani, C.; Bradley, D. D. C.; Dos Santos, D. A.; Brédas, J. L.; Lögdlund, M.; Salaneck, W. R. *Nature* **1999**, *397*, 121.

[19]. Zhang, F.; Johansson, M.; Andersson, M. R.; Hummelen, J. C.; Ingänas, O. *Adv. Mater.* **2002**, *14*, 662.

[20]. Facchetti, A. *Chem. Mater.* **2011**, *23*, 733.

[21]. Nogueira, A. F.; Longo, C.; De Paoli, M. A. *Coord. Chem. Rev.* **2004**, *248*, 1455.

[22]. Inamuddin, Shin, K. M.; Kim, S. I.; So, I.; Kim, S. J. *Electrochim. Acta* **2009**, *54*, 3979.

[23]. Pernaut, J.-M.; Reynolds, J. R. *J. Phys. Chem. B* **2000**, *104*, 4080.

[24]. Svirskis, D.; Travas-Sejdic, J.; Rodgers, A.; Garg, S. *J. Controlled Release* **2010**, *146*, 6.

[25]. Gurunathan, K.; Murugan, A. V.; Marimuthu, R.; Mulik, U. P.; Amalnerkar, D. P. *Mater. Chem. Phys.* **1999**, *61*, 173.

[26]. Feast, W. J.; Tsibouklis, J.; Pouwer, K. L.; Groenendaal, L.; Weijer, E. W. *Polymer* **1996**, *37*, 5017.

[27]. Pron, A.; Rannou, P. *Prog. Polym. Sci.* **2002**, *27*, 135.

[28]. Nalwa, H. S. *Advanced Functional Molecules and Polymers: Volume 3: Electronic and Photonic Properties*; Taylor & Francis, 2001.

[29]. Wang, L. X.; Li, X. G.; Yang, Y. L. *React. Funct. Polym.* **2001**, *47*, 125.

[30]. Ateh, D. D.; Navsaria, H. A.; Vadgama, P. *J. R. Soc. Interface* **2006**, *3*, 741.

[31]. Zhang, J.; Kong, L. B.; Li, H.; Luo, Y.; Kang, L. *J. Mater. Sci.* **2010**, *45*, 1947.

[32]. Zang, J.; Li, X. *J. Mater. Chem.* **2011**, *21*, 10965.

[33]. Guo, Z. P.; Wang, J. Z., Liu, H. K.; Dou, S. X. *J. Power Sources* **2005**, *146*, 448.

[34]. Lee, J. W.; Serna, F.; Nickels, J.; Schmidt, C. E. *Biomacromolecules* **2006**, *7*, 1962.

[35]. Fenelon, A. M.; Breslin, C. B. *Electrochim. Acta* **2002**, *47*, 4467.

[36]. Lee, J. Y.; Bashur, C. A.; Goldstein, A. S.; Schmidt, C. E. *Biomaterials* **2009**, *30*, 4325.

[37]. Wuang, S. C.; Neoh, K. G.; Kang, E. T.; Pack, D. W.; Leckband, D. E. *J. Mater. Chem.* **2007**, *17*, 3354.

[38]. Hosono, K.; Matsubara, I.; Murayama, N.; Shin, W.; Izu, N.; Kanzaki, S. *Thin Solid Films* **2003**, *441*, 72.

[39]. Cruz, G. J.; Morales, J.; Olayo, R. *Thin Solid Films* **1999**, *342*, 119.

[40]. Kim, J.; Sohn, D.; Sung, Y.; Kim, E.-R. *Synth. Met.* **2003**, *132*, 309.

[41]. Tan, S. N.; Ge, H. *Polymer* **1996**, *37*, 965.

[42]. Pringle, J. M.; Efthimiadis, J.; Howlett, P. C.; Efthimiadis, J.; MacFarlane, D. R.; Chaplin, A. B.; Hall, S. B.; Officer, D. L.; Wallace, G. G.; Forsyth, M. *Polymer* **2004**, *45*, 1447.

[43]. Sak-Bosnar, M.; Budimir, M. V.; Kovac, S.; Kukulj, D.; Duic, L. *Polym. Sci. A, Polym. Chem.* **1992**, *30*, 1609.

[44]. Skotheim, T. A.; Reynolds J. R. *Handbook of Conducting Polymers: Conjugated polymers*; CRC Press, 2007.

[45]. Butterworth, M. D.; Corradi, R.; Johal, J.; Lascelles, S. F.; Maeda, S.; Armes, S. P. *J. Colloid Interface Sci.* **1995**, *174*, 510.

[46]. Ge, H. L.; Qi, G. J.; Kang, E. T.; Neoh, K. G. *Polymer* **1994**, *35*, 504.

[47]. Patil, A. O.; Heeger, A. J.; Wudl, F. *Chem. Rev.* **1988**, *88*, 183.

[48]. Chan, H. S. O.; Ng, S. C. *Prog. Polym. Sci.* **1998**, *23*, 1167.

[49]. Sonmez, G.; Sonmez, H. B.; Shen, C. K. F.; Wudl, F. *Adv. Mater.* **2004**, *16*, 1905.

[50]. Fichou, D. *J. Mater. Chem.* **2000**, *10*, 571.

[51]. Heywang, G.; Jonas, F. *Adv. Mater.* **1992**, *4*, 116.

[52]. Groenendaal, L. B.; Jonas, F.; Freitag, D.; Pielartzik, H.; Reynolds, J. R. *Adv. Mater.* **2000**, *12*, 481.

[53]. Kudoh, Y.; Akami, K.; Kusayanagi, H.; Matsuya, Y. *Synth. Met.* **2001**, *123*, 541.

[54]. Kirchmeyer, S.; Reuter, K. *J. Mater. Chem.* **2005**, *15*, 2077.

[55]. Pettersson, L.; Johansson, T.; Carlsson, F.; Arwin, H.; Inganas, O. *Synth. Met.* **1999**, *101*, 198.

[56]. Dietrich, M.; Heinze, J.; Heywang, G.; Jonas, F. *J. Electroanal. Chem.* **1994**, *369*, 87.

[57]. Kumar, A.; Welsh, D. M.; Morvant, M. C.; Piroux, F.; Abboud, K. A.; Reynolds, J. R. *Chem. Mater.* **1998**, *10*, 896.

[58]. Winther-Jensen, B.; Winther-Jensen, O.; Forsyth, M.; MacFarlane, D. R. *Science* **2008**, *321*, 671.

[59]. Richardson-Burns, S. M.; Hendricks, J. L.; Foster, B.; Povlich, L. K.; Kim, D-H.; Martin, D. C. *Biomaterials* **2007**, *28*, 1539.

[60]. Collazos-Castro, J. E.; Polo, J. L.; Hernández-Labrado, G. R.; Padial-Cañete, V.; García-Rama, C. *Biomaterials* **2010**, *31*, 9244.

[61]. Joo, J.; Park, S.-H.; Seo, D.-S.; Lee, S.-J.; Kim, H.-S.; Ryu, K.-W.; Lee, T.-J.; Seo, S.-H.; Lee, C.-L. *Adv. Funct. Mater.* **2005**, *15*, 1465.

[62]. Koh, J. K.; Kim, J.; Kim, B.; Kim, J. H.; Kim, E. *Adv. Mater.* **2011**, *23*, 1641.

[63]. Santhosh, P.; Manesh, K. M.; Uthayakumar, S.; Komathi, S.; Gopalan, A. I.; Pee, K.-P. *Bioelectrochemistry* **2009**, *75*, 61.

[64]. Chandrasekhar, P. *Conducting Polymers, Fundamental and Applications*; Kluwer Academic Publishers, 1999.

[65]. Bredas, J. L.; Street, G. B. *Acc. Chem. Res.* **1985**, *18*, 309.

[66]. Wise, D. L. *Electrical and optical polymer systems*; CRC Press, 1998.

[67]. Belletête, M.; Mazerolle, L.; Desrosiers, N.; Leclerc, M.; Durocher, G. *Macromolecules* **1995**, *28*, 8587.

[68]. Hsu, W.; Levon, K.; Ho, K.; Myerson, A.; Kwei, T. K. *Macromolecules* **1993**, *26*, 1318.

[69]. Pan, J.; Chua, S.; Huang, W. *Chem. Phys. Lett.* **2002**, *363*, 18.

[70]. Garnier, F.; Tourillon, G.; Gazard, M.; Dubris, J. C. *J. Electroanal. Chem.* **1983**, *148*, 299.

[71]. McCarthy, G. P.; Armes, S. P.; Greaves, S. J.; Watts, J. F. *Langmuir* **2007**, *13*, 3686.

[72]. Maeda, S.; Corradi, R.; Armes, S. P. *Macromolecules* **1995**, *28*, 2905.

[73]. Lee, J.-W.; Serna, F.; Nickels, J.; Schmidt, C. E. *Biomacromolecules* **2006**, *7*, 1692.

[74]. Song, X. C.; Zheng, Y. F.; Ma, R.; Yin, H. Y. *J. Macromol. Sci. B* **2012**, *51*, 1080.

[75]. Pang, Y.; Li, X.; Shi, G.; Wang, F.; Jin, L. *Thin Solid Films* **2008**, *516*, 6512.

[76]. Xu, J.; Shi, G.; Chen, F.; Wang, F.; Zhang, J.; Hong, X. *J. Appl. Polym. Sci.* **2003**, *87*, 502.

[77]. Xu, J. K.; Shi, G. Q.; Xu, Z. J.; Chen, F. G.; Hong, X. Y. *J. Electroanal. Chem.* **2001**, *514*, 16.

[78]. Shen, Y.; Wu, P. *Polymer* **2006**, *47*, 7111.

[79]. Chen, F.; Shi, G.; Zhang, J.; Fu, M. *Thin Solid Films* **2003**, *424*, 283.

[80]. Shi, G.; Xu, J.; Fu, M. *J. Phys. Chem. B* **2002**, *106*, 288.

[81]. Alakhras, F.; Holze, R. *J. Solid State Electrochem.* **2008**, *12*, 81.

[82]. Pang, Y.; Xu, H.; Li, X.; Ding, H.; Cheng, Y.; Shi, G.; Jin, L. *Electrochem. Commun.* **2006**, *8*, 1757.

[83]. Shi, G. Q.; Zhang, J. X.; Chen, F. E.; Xu, J. K.; Hong, X. Y. *Acta Chim. Sinica* **2001**, *59*, 1818.

[84]. Song, X. C.; Zheng, Y. F.; Ma, R.; Yin, H. Y. *Micro Nano Lett.* **2012**, *6*, 273.

[85]. Xu, H.; Pang, Y. H.; Li, X. Y.; Ding, H. L.; Cheng, Y. X.; Shi, G. Y.; Jin, L. T. *Acta Chim. Sinica* **2006**, *64*, 2254.

[86]. He, X.; Li-Ping, Z.; Su-Jie, X.; Yue-Zhong, X.; Guo-Yue, S.; Li-Tong, J. *Chines J. Chem.* **2008**, *26*, 1991.

[87]. El-Maghraby, A. A.; Abou-Elenien, G. M.; El-Abdallah, G. M. *Synth. Met.* **2010**, *160*, 1335.

[88]. Shi, L. H.; Roncali, J.; Garnier, F. *J. Electroanal. Chem.* **1989**, *263*, 155.

[89]. Waltman, R. J.; Bargon, J.; Diaz, A. F. *J. Phys. Chem.* **1983**, *87*, 1459.

[90]. Alkan, S.; Cutler, C. A.; Reynolds, J. R. *Adv. Funct. Mater.* **2003**, *13*, 331.

[91]. Zhou, L.; Xue, G. *Synth. Met.* **1997**, *87*, 193.

[92]. Zhou, L.; Li, Y.; Xue, G. *Thin Solid Films* **1998**, *335*, 112.

[93]. Caple, G.; Wheeler, B. L.; Swift, R.; Porter, T. L.; Jeffers, S. *J. Phys. Chem.* **1990**, *94*, 5639.

[94]. Porter, T. L.; Jeffers, S.; Caple, G.; Wheeler, B. L.; Swift, R. *Surf. Sci.* **1990**, *238*, L433.

[95]. Pomerantz, M.; Turkman, N. *Synthesis – Stuttgart* **2008**, *15*, 2333.

[96]. Elkassmi, A.; Fache, F.; Lemaire, M. *Synth. Commun.* **1994**, *24*, 95.

[97]. Elkassmi, A.; Fache, F.; Lemaire, M. *J. Electroanal. Chem.* **1994**, *373*, 241.

[98]. Gambhir, S.; Wagner, K.; Officer, D. L. *Synth. Met.* **2005**, *154*, 117.

[99]. Philips, M. F.; Gopalan, A. I.; Lee, K.-P. *Catal. Commun.* **2011**, *12*, 1084.

[100]. Ouerghi, O.; Senillou, A.; Jaffrezic-Renault, N.; Martelet, C.; Ben Ouada, H.; Cosnier, S. *J. Electroanal. Chem.* **2001**, *501*, 62.

[101]. Fusalba, F.; Ho, H. A.; Breau, L.; Bélanger, D. *Chem. Mater.* **2000**, *12*, 2581.

[102]. Sahu, D.; Padhy, H.; Patra, D.; Huang, J.-H.; Chu, C.-W.; Lin, H.-G. *J. Polym. Sci. A Polym. Chem.* **2010**, *48*, 5812.

[103]. Cirpan, A.; Rathnayake, H. P.; Gunbas, G.; Lahti, P. M.; Karasz, F. E. *Synth. Met.* **2006**, *156*, 282.

[104]. Ferdous, S.; Lagowski, J. B. *J. Polym. Sci. B Polym. Phys.* **2007**, *45*, 1983.

[105]. Hapiot, P.; Demanze, F.; Yassar, A.; Garnier, F. *J. Phys. Chem.* **1996**, *100*, 8397.

[106]. Meeto, W.; Suramitr, S.; Lukes, V.; Wolschann, P.; Hannongbua, S. *J. Mol. Struct.* **2010**, *939*, 75.

[107]. Fabregat, G.; Córdova-Mateo, E.; Armelin, E.; Bertrán, O.; Alemán, C. *J. Phys. Chem. C* **2011**, *115*, 14933.

[108]. Martí, M.; Fabregat, G.; Estrany, F.; Alemán, C.; Armelin, E. *J. Mater. Chem.* **2010**, *20*, 10652.

[109]. Arrigan, D. W. M. *Anal. Commun.* **1997**, *34*, 241.

[110]. Deng, Z.; Stone, D. C.; Thompson, M. *Analyst* **1997**, *122*, 1129.

[111]. Deng, Z.; Stone, D. C.; Thompson, M. *Can. J. Chem.* **1995**, *73*, 1427.

[112]. Deng, Z.; Stone, D. C.; Thompson, M. *Analyst* **1996**, *121*, 1341.

[113]. McCarthy, C. P.; McGuinness, N. B.; Alcock-Earley, B. E.; Breslin, C. B.; Rooney, A. D. *Electrochem. Commun.* **2012**, *20*, 79.

[114]. Guo, S.; Wang, E. *Acc. Chem. Res.* **2011**, *44*, 491.

[115]. Winokur, M. J.; Chunwachirasiri, W. *J. Polym. Sci., Part B: Polym. Phys.* **2003**, *41*, 2630.

[116]. Rajesh, Ahuja, T.; Kumar, D. *Sens. Actuators B* **2009**, *136*, 275.

[117]. Gangopadhyay, R.; De A. *Chem. Mater.* **2000**, *12*, 608.

[118]. Grimsdale, A. C.; Müllen, K. *Angew. Chem. Int.* **2005**, *44*, 5592.

[119]. Lu, X.; Zhang, W.; Wang, C.; Wen, T.-C.; Wei, Y. *Prog. Polym. Sci.* **2011**, *36*, 671.

[120]. Pecher, J.; Mecking, S. *Chem. Rev.* **2010**, *110*, 6260.

[121]. Zhao, Y. S.; Fu, H.; Peng, A.; Ma, Y.; Xiao, D.; Yao, J. *Adv. Mater.* **2008**, *20*, 2859.

[122]. Chen, J.; Wiley, B. J.; Xia, Y. *Langmuir* **2007**, *23*, 4120.

[123]. Chen, N.; Huang, C.; Yang, W.; Chen, S.; Liu, H.; Li, Y.; Li, Y. *J. Phys. Chem. C* **2010**, *114*, 12982.

[124]. Wang, Y.; Tran, H. D.; Kaner, R. B. *Macromol. Rapid Commun.* **2011**, *32*, 35.

[125]. Li, D.; Huang, J.; Kaner, R. B. *Acc. Chem. Res.* **2009**, *42*, 135.

[126]. Kim, F. S.; Ren, G.; Jenekhe, S. A. *Chem. Mater.* **2011**, *23*, 682.

[127]. Lin, K.-C.; Tsai, T.-H.; Chen, S.-M. *Biosens. Bioelectron.* **2010**, *26*, 608.

[128]. Tran, H. D.; Li, D.; Kaner, R. B. *Adv. Mater.* **2009**, *21*, 1487.

[129]. Arico, A. S.; Bruce, P.; Scrosati, B.; Tarascon, J.-M.; Van Schalkwijk, W. *Nature Mat.* **2005**, *4*, 366.

[130]. Simon, P.; Gogotsi, Y. *Nature Mat.* **2008**, *7*, 845.

[131]. Niemann, M. U.; Srinivasan, S. S.; Phani, A. R.; Kumar, A.; Goswami, D. Y.; Stefanakos, E. K. *J. Nanomaterials* **2008**, 1.

[132]. Lee, J.; Mahendra, S.; Alvarez, P. J. J. *ACS Nano* **2010**, *4*, 3580.

[133]. Sanchez, C.; Julian, B.; Belleville, P.; Popall, M. *J. Mater. Chem.* **2005**, *15*, 3559.

[134]. Zhang, D.; Zhou, C-H.; Lin, C-X.; Tong, D-S.; Yu, W-H. *App. Clay Sci.* **2010**, *50*, 1.

[135]. Chen, B.; Evans, J. R. G. *Soft Matter* **2009**, *5*, 3572.

[136]. Mousty, C. *App. Clay Sci.* **2004**, *27*, 159.

[137]. Njuguna, J.; Pielichowski, K. *Adv. Eng. Mater.* **2004**, *6*, 193.

[138]. Kim, B. H.; Jung, J. H.; Kim, J. W.; Choi, H. J.; Joo, J. *Synth. Met.* **2001**, *117*, 115.

[139]. Olad, A.; Rashidzadeh, A. *Prog. Org. Coat.* **2008**, *62*, 293.

[140]. Letaïef, S.; Aranda, P.; Fernández-Saavedra, R.; Margeson, J. C.; Detelliera, C.; Ruiz-Hitzky, E. *J. Mater. Chem.* **2008**, *18*, 2227.

[141]. Rajapakse, R. G. M.; Higgins, S.; Velauthamurty, K.; Bandara, H. M. N.; Wijeratne, S.; Rajapakse, R. M. M. Y. *J. Compos. Mater.* **2010**, *45*, 597.

[142]. Sarioglan, S. *Particul. Sci. Technol.* **2012**, *30*, 68.

[143]. Inzelt, G. *Conducting polymers, a new era in electrochemistry*; Springer, 2008.

[144]. Sadki, S.; Schottland, P.; Brodie, N.; Sabouraud, G. *Chem. Soc. Rev.* **2000**, *29*, 283.

[145]. Bidan, G.; Ehui, B.; Lapkowski, M. *J. Phys. D.* **1988**, *21*, 1043.

[146]. Neoh, K. G.; Teo, H. W.; Kang, E. T.; Tan, K. L. *Langmuir* **1998**, *14*, 2820.

[147]. Zhou, C.; Liu, Z.; Du, X.; Ringer, S. P. *Synth. Met.* **2010**, *160*, 1636.

[148]. Venancio, E. C.; Costa, C. A. R.; Machado, S. A. S.; Motheo, A. J. *Electrochem. Commun.* **2001**, *3*, 229.

[149]. Jeon, D.; Kim, J.; Gallagher, M. C.; Willis, R. F.; Kim, Y. T. *J. Vac. Sci. Technol. B* **1991**, *9*, 1154.

[150]. Hwang, B.-J.; Santhanam, R.; Wu, C.-R.; Tsai, Y.-W. *J. Solid State Electrochem* **2001**, *5*, 280.

[151]. Hwang, B.-J.; Santhanam, R.; Wu, C.-R.; Tsai, Y.-W. *Electroanal.* **2001**, *13*, 37.

[152]. Lukkari, J.; Heikkila, L.; Alanko, M.; Kankare, J. *Synth. Met.* **1993**, *55*, 1311.

[153]. Pawar, P.; Wankhede, M. G.; Patil. P. P.; Sainkar, S. R. *Mater. Sci. Eng. A* **2003**, *A347*, 365.

[154]. Randriamahazaka, H.; Noël, V.; Chevrot, C. *J. Electroanal. Chem.* **1999**, *472*, 103.

[155]. Hwang, B. J.; Santhanam, R.; Lin, Y. L. *Electrochim. Acta* **2001**, *46*, 2843.

[156]. Hwang, B. J.; Santhanam, R.; Lin, Y. L. *Electroanal.* **2003**, *15*, 115.

[157]. De Giglio, E.; Guascito, M. R.; Sabbatini, L.; Zambonin, G. *Biomaterials* **2001**, *22*, 2609.

[158]. Sutton, S. J.; Vaughan, A. S. *Polymer* **1995**, *36*, 1849.

[159]. Yan, J.; Sun, C.; Tan, F.; Hu, X.; Chen, P.; Qu, S.; Zhou, S.; Xu, J. *Sol. Energ. Mat. Sol. C* **2010**, *94*, 390.

.

Chapter 2. Methodology

2.1. Experimental methods

2.1.1. Electrochemical techniques

The synthesis of conducting polymers can be obtained using different methods such as chemical oxidation, electrochemical polymerization, vapor phase polymerization or plasma polymerization, respectively. However, electrochemical and chemical methods are the most used. In this thesis we are focused on the electrochemical methods since it allows several advantages compared with chemical methods:

a) Control the film thickness through the polymerization parameters, specifically time and consumed charge.
b) Choice of a wide range of counterions in the electropolymerization process, which influence directly on the electronic, morphological and redox properties.
c) Control of the oxidation state of the polymer (oxidized or neutral).
d) High doping level.
e) Absence of catalyst.
f) Direct deposition of the polymer film in oxidized state (doped).

All electrochemical polymerizations were carried out by using an electrochemical cell, which is formed by three electrodes, a working electrode (WE), a counter-electrode (CE) and a reference electrode (RE). In the working electrode takes place the polymerization (oxidation of monomer), thus, it is considered one of the most important electrodes in the polymerization process. The WE (anode electrode) can be made of different materials, such as glassy carbon, stainless steel, indium-tin oxide (ITO) coated glass, gold or platinum. In this thesis, steel and ITO substrates were employed. On the other hand, the CE (cathode electrode) employed in this thesis was mainly platinum and steel, respectively. An Ag/AgCl reference electrode was employed in all experiments. This electrode has an $E^{\circ} = 0.222$ V vs hydrogen.

Figure 1. *Images of the electrodes employed in the electropolymerization process. Reference electrode, working electrode and counter electrode (From left to right)*

The electrochemical cell was connected through a galvanostat-potentiostat equipment according to Figure 2.

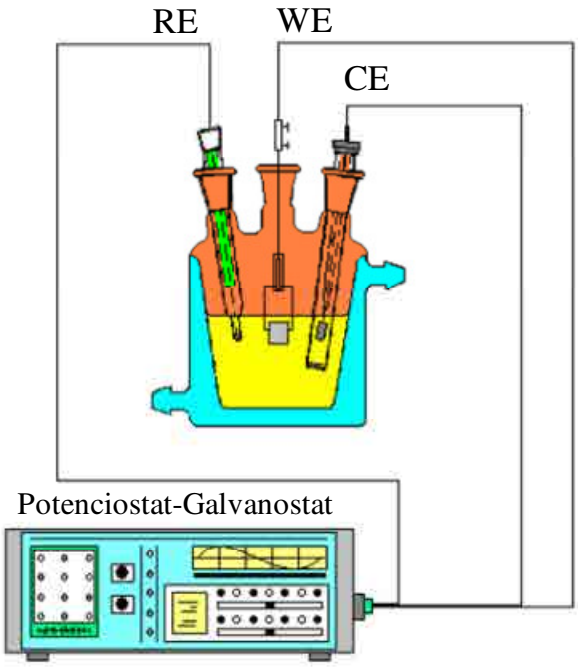

Figure 2. *General scheme of the electropolymerization process*

The electropolymerization process is carried out through a solution, which is formed as follows:

2. *Solvent:* The electrolyte is the ionic conduction medium between the electrodes. Two examples of the solvents used in this thesis are acetonitrile, water and boron trifluoride diethyl etherate. Water is polar and can easily dissolve common salts, but its stable potential window is quite narrow preventing accurate electrochemical measurements at higher potentials (*e.g.* water oxidation at 1.10 V). On the other hand, acetonitrile is mor estable and offers a much wider potential window for the

electrochemical measure due to its less polarity. In this way, salt with larger ions are chosen (*e.g.* perchlorate)

3. *Dopant agent:* $LiClO_4$ or $[(Bu)_4NBF_4]$
4. *Monomer:* Py, EDOT, NCMPy, NMPy, XTh (being X=Cl and Br)

The main techniques employed in this work to carry out the polymerization of conducting polymers are based on potentiodynamic (cyclic voltammetry), potentiostatic (chronoamperometry) and galvanostatic (constant current) methods.

All electrochemical polymerizations were carried out by using an AUTOLAB-PGSTAT 202 N or a Versastat II potentiostat/galvanostat.

2.1.1.1. Chronoamperometry (CA)

Among potentiostatic methods (constant voltage), choronoamperometry is the most successful method to synthesize conducting polymers. The principle of this technique is focused on applying a constant voltage (*e.g.* oxidation potential of the corresponding monomer) to deposit a film onto the substrate.

Figure 3. *Deposition of a conducting polymer film onto a steel substrate using the chronoamperometry technique*

The consumed charge during the electropolymerization process can be estimated as follows:

$$Q_{pol} = \int_0^t I \cdot dt \qquad (1)$$

where Q_{pol} is the polymerization electrical charge, I is the intensity and dt is the passed time during the electrochemical process. From this process and knowing the deposited mass onto the electrode after polymerization, it is possible to calculated the current productivity (expressed in $g \cdot C^{-1}$). This data is very useful to estimate the thickness (ℓ) of the electrodeposited films using the next equation:

$$l = Q_{pol} \cdot \frac{M}{Q} \cdot \rho^{-1} \qquad (2)$$

where Q_{pol} is the polymerization charge (in $C \cdot cm^{-2}$), M/Q is the current productivity (in $g \cdot C^{-1}$), and ρ is the density (in $g \cdot cm^{-3}$)

Subsequently, a characteristic plot of the chronoamperometry technique is represented in Figure 4.

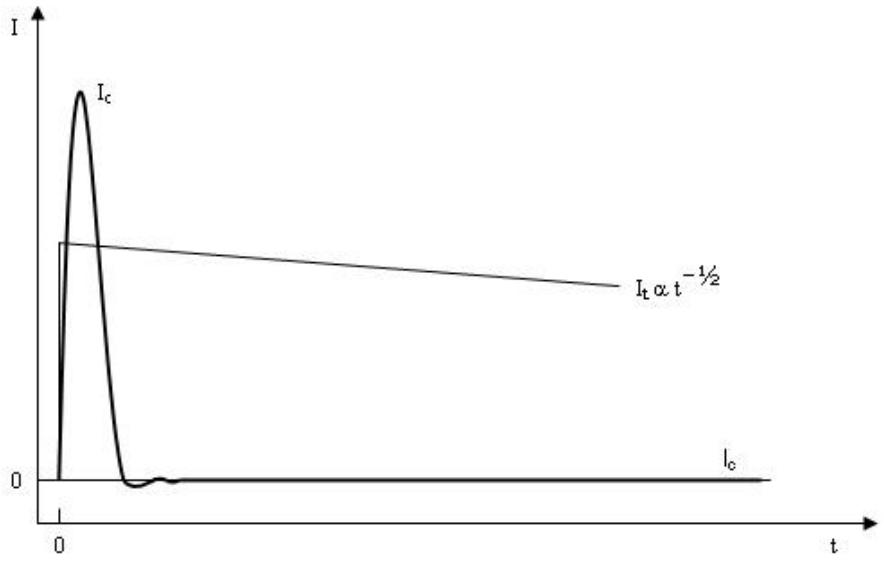

Figure 4. *Characteristic plot of the chronoamperometry technique*

The function of this plot is fitted by the Cotrell's equation, which is given as:

$$I = n_{av} FAC^* \left(\frac{D}{\pi t_{pol}} \right)^{\frac{1}{2}} \qquad (3)$$

where n is the average number of electrons transferred during the process, F is the Faraday's constant (~96500 $C \cdot mol^{-1}$), A is the electrode area (in cm^2), C is the concentration of the electroactive species (in $mol \cdot cm^{-3}$), D is the diffusion coefficient (in $cm^2 \cdot s^{-1}$).

2.1.1.2. Chronocoulometry (CC)

The CC technique is an electrochemical method employed to control and to fix the polymerization charge (Q_{pol}) in a period of time applying a potential step. The principle is similar to the CA technique.

2.1.1.3. Cyclic voltammetry (CV)

Cyclic voltammetry is one of the most common electrochemical techniques employed in the field of electrochemistry to determine information of the electrochemical processes occurred in redox reactions. This technique is widely employed to characterize conducting polymers. The technique is based on measurement of the current at the working electrode as a function of the applied potential. Thus, from CV it is possible to determine oxidation and reduction potential peaks of the electroactive species contained in a solution.

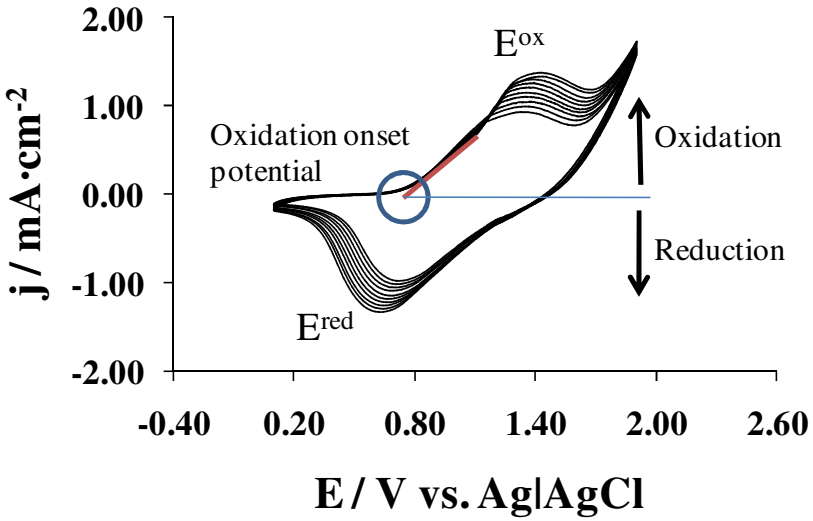

Figure 5. *Cyclic voltammetry obtained from potentiodynamic methods of a film of poly(3-chlorothiophene)*

A typical cyclic voltammetry is shown in Figure 5, where it is possible to observe the two peaks associated to a reversible redox process. The positive peak (E^{ox}) corresponds to the oxidation of the polymer, whereas the negative peak (E^{red}) represents the reduction of the polymer. From this curve we can obtain information about the different oxidation states of the species in solution.

CV technique is also employed in the field of conducting polymers to evaluate the charge storage (electroactivity) and the loss of electrostability. These properties are obtained in a solution containing the corresponding electrolyte and solvent, where successive oxidation-reduction cyles are applied to the polymer. Within this context, electronic properties of conducting polymers (*e.g.* ionization potential) have been estimated by using CV technique from the oxidation onset potential proposed by *Bredas et al*[1]:

$$IP = E^{onset(ox)} + 4.4\ V \qquad (4)$$

2.1.1.4. Chronopotentiometry (CP)

Chronopotentiometry is a useful technique based on galvanostatic methods where a current density is applied on the working electrode. The response consists of a potential as a function of time. This technique involves the possibility to control oxidation-reduction states of electroactive species. Moreover, CP has been shown to be an efficient electrochemical technique to synthesize conducting polymers. Under an applied current, monomers are oxidized at the anode and eventually form a polymer film. In this thesis, CP has been widely employed to obtain different redox states of conducting polymers using the access (doping) or exit (undoping) of anions from the total charge consumed.

A derived technique of the CP is the recurrent galvanostatic pulse (RGP). This technique is based on the same procedure, although successive charge – discharge cycles are obtained. The procedure has been used to characterize some conducting polymers in electronic applications such as batteries or supercapacitors devices. A representation of this technique is displayed in Figure 6.

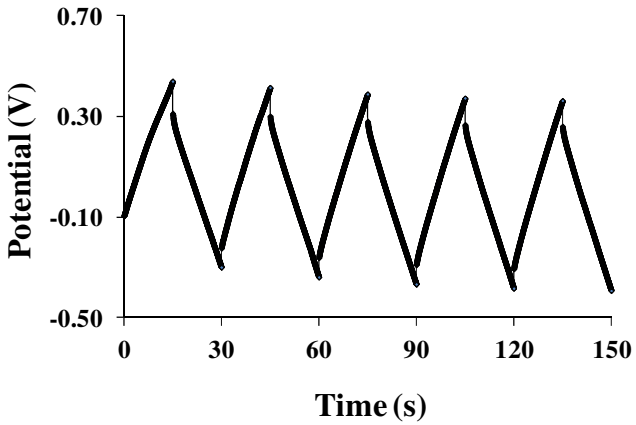

Figure 6. *Typical plot of the recurrent galvanostatic pulse (RGP)*

2.1.2. Morphological techniques

2.1.2.1. Scanning Electron Microscopy (SEM)

Scanning electron microscopy (SEM) is a powerful morphological technique, which allows to observe the surface, topography and relief of a material from images using

electrons. The working of a scanning electron microscope is based on the use of electrons rather than light to form an image of objects. The shorter wavelength of electrons permits image magnifications higher than conventional light microscopy. The detector equipment is very sensitive being able to reveal detail up to 1-5 nm in size and thus must operate within an ultra-high vacuum for accurate measurement. The electrons that are emitted to interact with the sample can be captured by various detectors and can yield different results for each: secondary electrons (inelastic collisions), back-scattered electrons (elastic collisions), characteristic X-rays, transmitted electrons. Each of these emissions occurs because of different energy levels of the incident electron. For example, low energies will promote secondary electron emission while higher energies will promote X-ray emission.

In this technique, the microscope is equipped with an energy dispersive X-rays (EDX) spectroscopy system, which provides information on the elemental composition of the polymers. In this thesis, all samples were examined from a Zeiss Neon 40 microscope. Samples were mounted on aluminum studs using adhesive graphite tape. In insulator samples was necessary to sputter-coated them with graphite before analysis.

2.1.2.2. Atomic Force Microscopy (AFM)

The atomic force microscope (AFM) is one of the most commonly used and powerful tools for determining the surface morphology, roughness, thickness and topography of materials. The film thickness measurement is performed carefully scratching the film in the representative area.

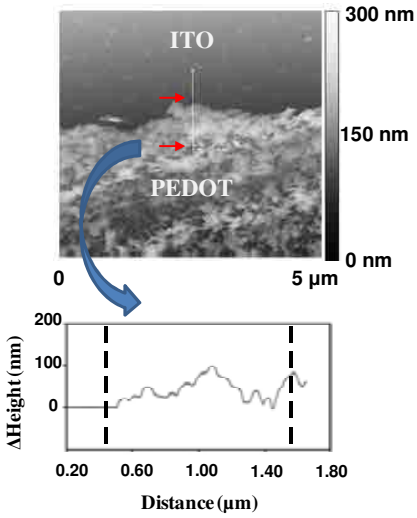

Figure 7. *Example of PEDOT film thickness measurement using AFM cross section analysis*

The physical operation of AFM involves a cantilever with a sharp tip which is extremely sensitive to small forces, and which makes contact with the sample surface. The surface topography is monitored by the deflection of a laser beam focused on the back of the tip. As the sample is scanned, the tip and cantilever move up and down over the surface in response to the extremely small repulsive force (10^{-9} to $l0^{-8}$ N) between the atoms of the sharp tip and the surface atoms. Thus, the laser deflections are recorded by the photodiode array which translates these results into topographic features. The force is held constant by means of a feed-back loop in the so-called 'constant force mode'. As variations on this theme, *contact mode* operation involves direct contact of the tip with the surface. The tip is in perpetual contact with the sample and the detected net force is the sum of the attractive and repulsive force between the tip and the sample. in *non-contact mode* the tip is vibrated above the surface, and the detection is made via van de Waals, magnetic or electrostatic forces, enabling rougher surfaces to be imaged from a distance, while in *tapping mode* the cantilever is vibrated with a larger amplitude and the vibrating tip contacts the sample surface many times per data point. The technology for AFM has taken many features directly from STM, including techniques for vibration isolation, sample approach and scanning, optical beam deflection of laser light to measure cantilever deflection (other approaches being possible), feedback control and image processing

The tapping mode is the procedure employed in this work. The most important characteristics of this mode are described as follows:

- The elimination of a large part of permanent shearing forces and the causing of less damage to the sample surface.
- High lateral resolution
- Lower forces and less damage to soft samples in air

The AFM instrument used in this study was a Molecular Imaging PicoSPM using a NanoScope IV controller in ambient conditions. The tapping mode AFM was operated at constant deflections (*i.e.* vertical constant force with triangular shaped gold-coated silicon nitride). The row scanning frequenct was set to 1 Hz Each image was generally taken using a scan window size 5 x 5 μm^2, a total of 65.536 topographic data.

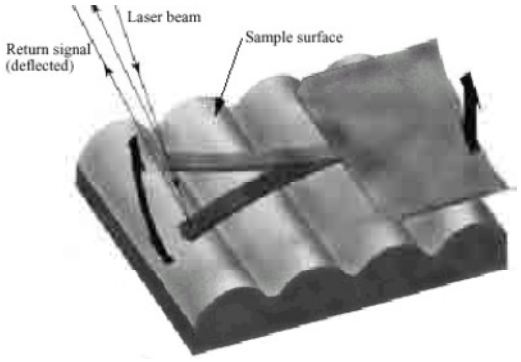

Figure 8. *Principle setup of an AFM: A laser beam is deflected from the cantilever. The deflection is detected by a quad photo detector arrangement.*[2]

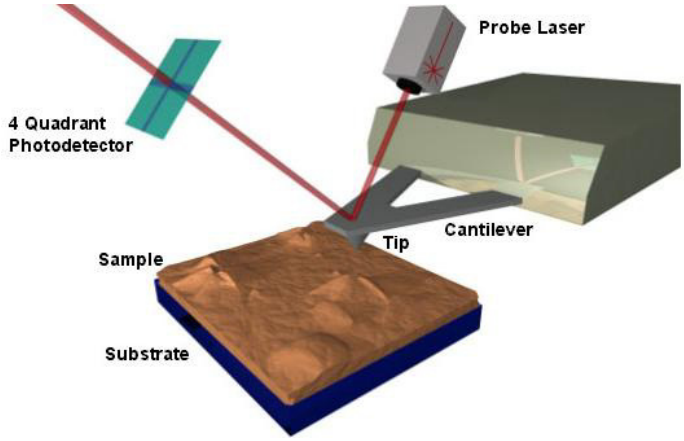

Figure 9. *Schematic illustration of an atomic force microscope (AFM) (www.barrett-group.mcgill.ca)*

2.1.2.3. Transmission Electron Microscopy (TEM)

The working principle of this technique consists of an electron beam, which passes through a very thin section (nanometric scale) of the sample and an image is obtained due to the differences in electron density of the materials. Electrons are generated by the microscope through a process known as termionic emission from a tungsten filament. The TEM microscope has been employed in this thesis to observe the presence of clays in nanocomposites.

Transmission electron microscopy (TEM) was carried out with a Philips TECNAI 10 microscope at an accelerating voltage of 100 kV. The specimens were prepared by embedding in a low viscosity modified Spurr epoxy resin and curing them at 40ºC for a few days and then at 60ºC for some hours. Ultrathin sections (less than 100 nm) were cut at room temperature using Sorvall Porter-Blum microtome equipped with a diamond

knife. Finally, the sections were collected in a though filled with water and lifted onto carbon coated copper grids. To prevent diffusion of the epoxy resin into the polymer film, a thin layer of carbon was evaporated over the film surface.

2.1.3. Spectroscopic techniques

2.1.3.1. Electrochemical Impedance Spectroscopy (EIS)

In the field of electrochemistry the interface generated between the working electrode (solid) and the environment (electrolyte solution) represents a great interest since its importance on the final properties of the materials. EIS technique presents relevant information about the interface process occurred at the surface among different materials, which provides information about physical-chemical properties (*e.g.* Charge-transfer phenomena, or diffusion). In this technique, a small perturbation (normally a sinusoidal potential wave) is applied to an electrochemical cell, where the system gives a response due to a shift in the phase and amplitude of this sinusoidal voltage. A frequency analyser measures this difference in amplitude in a range of frequencies. The result is expressed in terms of impedance (Z), which defines as the resistance to the flow of an alternating electrical current. Thus, the impedance Z can be expressed as:

$$Z(w) = -\frac{E_0 \exp(jwt)}{I_0 \exp(jwt - \Phi)} = [Z]\exp(j\Phi) = Z' + jZ' \qquad (5)$$

This equation defines the impedance Z at a frequency w as a vector in the complex plane of magnitude |Z| with an angle f between the Z and the real (Z') axis. These vectors can be plotted in complex plane plots known as Nyquist plots. In the case of Nyquist plots, the graph represents the real component (Z′) on the x-axis and the imaginary component (-Z″) on the y-axis. From Nyquists diagrams it is possible to obtain information of the capacitive properties of conducting polymers using the following equation:

$$SC = -\frac{1}{2\pi \cdot f \cdot Z_{im} \cdot m} \qquad (6)$$

where f is the frequency, Z_{im} is the imaginary component and m is the mass of polymer.

Another important graph in the EIS techniques is the Bode plot, which represents the total impedance (Z) as a function of the phase angle (θ) and the frequency (f). The Bode plots provides information about how the impedance depends on the frequency. Thus,

the plot uses the logarithm of frequency to allow a very wide frequency range to be plotted. The Bode plot shows also the magnitude of impedance (Z) on a log axis axis so that it is easy to plot wide impedance ranges on the same set of axes.

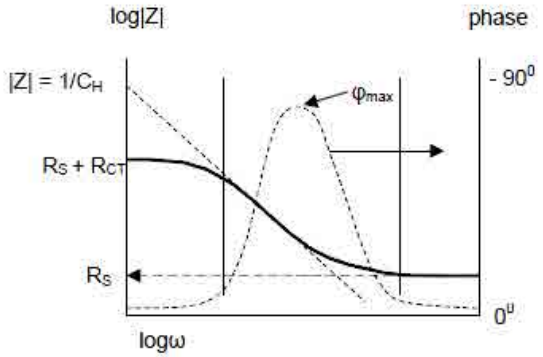

Figure 10. *Bode plot for a simple electrochemical system*

The log |Z| *vs.* log ω curve can be used to determined values of R_S and R_{CT}. At the highest frequencies, the ohmic resistance dominates the impedance and log R_S can be read from the high frequency horizontal plateau. At the lowest frequencies, R_{CT} also contributes, and log(R_{CT} + R_S) can be read from the low frequency horizontal plateau. At intermediate frequencies, this curve should be a straight line with a slope of -1. Extrapolating this line to the log |Z| axis at ω = 1 (log ω = 0) yields the value of Helmotz capacitance (C_H). C_H is a capacitance ascribed to the double layer formed in the electrode/electrolyte interface. The charge accumulated on the surface of the electrode generates an opposite charge appeared in the electrolytic solution for compensation. This capacitance of the interface is normally expressed in $\mu F \cdot cm^{-2}$.

The Body plot shows also the phase angle (φ). At the high and low frequency limits, the phase angle is nearly zero. At the intermediate frequencies, the phase angle increases as the imaginary component of the impedance increases.

In this thesis, the systems evaluated from EIS technique were represented using the Nyquist's diagrams and fitted through an equivalent circuit according to the experimental data. The elements used in the circuits correspond to resistors (*e.g.* solution, charge-transfer and Warburg resistance), capacitors (*e.g.* pseudo-capacitance), inductors and constant phase elements (CPE). These elements provide information about the physical-chemical process and transport phenomena where a good accuracy and understanding can be obtained. Although the response of the system is different for each case, some specific trends are specified such as the electron-transfer kinetic dominates at high frequencies, whereas diffusion dominates at lower frequencies.

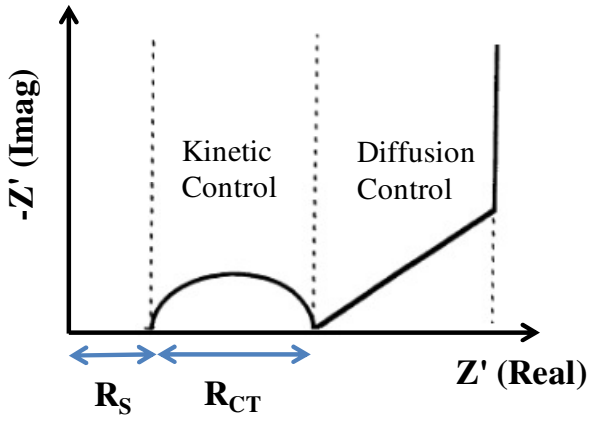

Figure 11. *Nyquist plot*

The aim of this technique in this thesis consists of describing the physical-chemical processes occurred between the interfaces polymer-metal and polymer-electrolyte solution, respectively.

2.1.3.2. Visible and Ultraviolet Spectroscopy (UV-Vis)

UV-Vis technique can be considered one of the most important techniques to study, to characterize and to determine conformational structures and electronic properties in conducting polymers, such as the gap-energy (ε_g) property. CPs present an extended system of alternating simple and double bonds whereby they can absorb light in the UV and visible region. From UV-Vis technique we can evaluate the different electronic transitions, which are associated to characteristic wavelengths (λ). Depending on the range of wavelength, specific transitions can take place (σ, n or π). Thus, when a molecule absorbs energy an electron is excited from an occupied orbital (σ, n or π) to an unoccupied orbital of greater energy (σ^* or π^*). The peaks in an UV-Vis spectrum are commonly due to $n - \pi^*$ or $\pi - \pi^*$ transitions.

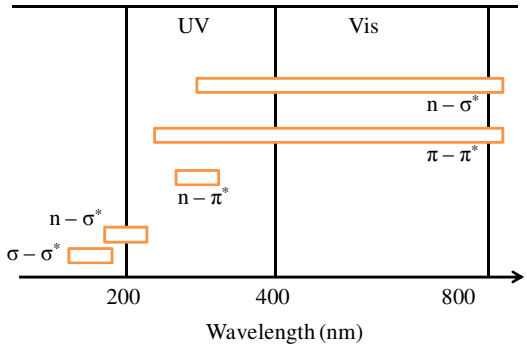

Figure 12. *Electronic transitions in the absorption spectra corresponding to UV-Visible region*

Specifically, π-π^* transitions are one of the most important to determine the gap energy. There are mainly two different methods to evaluate it using the UV-Vis technique.

The wavelength (λ) employed in this work ranged from 300 to 900 nm. The absorption spectra were obtained from polymeric films deposited on ITO and steel electrodes using a UV-visible-NIR Spectrometer (Shimadzu 3600). In this work, UV-Vis technique has been employed to determine electronic transitions and doping-undoping states in CPs.

Methods to evaluate the gap energy (ε_g) from UV-Vis technique

a) *Intersection:* Using this method, it should be noted the next equations. First it is important to take into account the Planck's equation as follows:

$$E = h\,\upsilon \qquad (7)$$

where *h* is the Planck's constant ($6.62 \cdot 10^{-34}$ J·s) and υ is the frequency (Hz).

Secondly, the relation between the frequency and speed of light (c) can be expressed as:

$$\lambda = \frac{c}{f} \qquad (8)$$

where λ is the wavelength.

Finally, combining Eqn (5) and (6) we obtained the following relation:

$$\lambda = \frac{hc}{\varepsilon_g} \qquad (9)$$

Thus, the electronic property in eV can be estimated from UV-Vis using:

$$\varepsilon_g = \frac{1240}{\lambda^{onset}} \qquad (10)$$

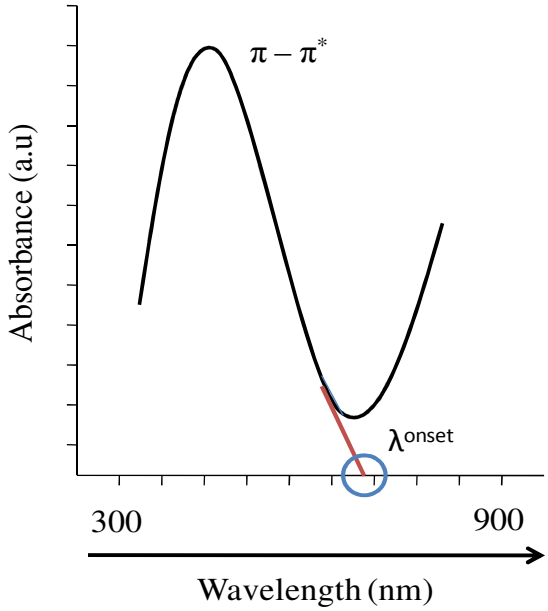

Figure 13. *Gap energy (ε_g) calculated from the equation 10*

b) Tauc's relation: The optical ε_g was calculated with the help of the $(h\nu \times \alpha)^2$ versus $h\nu$ plot (where α is the absorption coefficient, h is Planck's constant, and ν is the frequency).

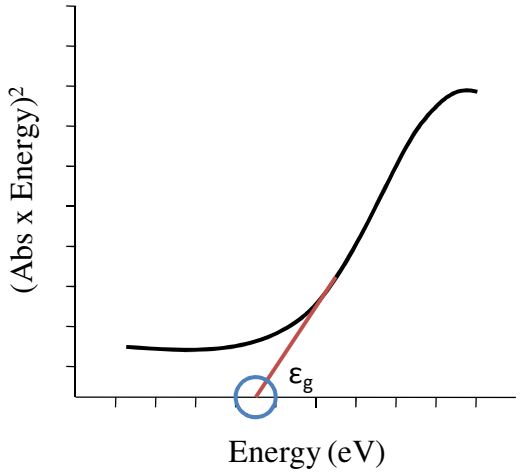

Figure 14. *Absorption edge analysis to extract the band gap according to Tauc's relation.*

2.1.3.3. Fourier Transform Infrared Spectroscopy (FTIR)

Fourier Transform Infrared Spectroscopy is a useful tool to evaluate and to determine chemical compounds in liquids, gases, powders and films through of their structural groups. This technique is widely used in conducting polymers due to its sensitivity, simplicity and fast response. In this thesis, the use of this technique has been employed to characterize chemically the corresponding conducting polymer, from a

structural point of view, and to evaluate the induced changes in the polymeric structure according to the oxidation (doping) – reduction (undoping) processes. This evaluation can be carried out through the detection of the dopant agent (*e.g.* ClO_4^- at approximately 1100 cm^{-1} or BF_4^- at 1060 cm^{-1}). In this thesis, the spectra were obtained from powder using a FTIR 4100 Jasco spectrophotometer taking 32 scans at a resolution of 4 cm^{-1}.

2.1.3.4. X-Ray Photoelectron Spectroscopy (XPS)

XPS spectroscopy (or also known as Electron Spectroscopy for Chemical Analysis) is a spectroscopic surface technique that analyzes the elemental composition, and electronic and chemical state of the elements present in the surface of the material. A schematic illustration of the XPS technique is displayed as follows:

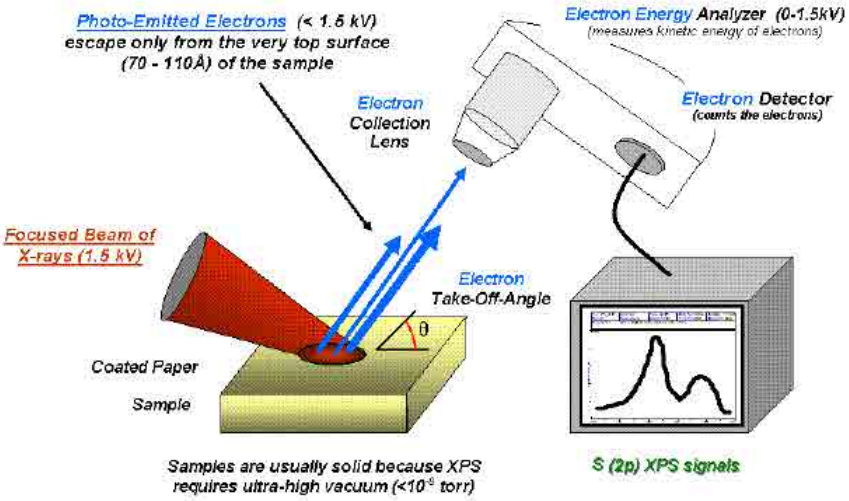

Figure 15. *Schematic illustration of the X-Ray Photoelectron Spectroscopy (XPS) technique* [3]

Each atom in the surface has core electron with the characteristic binding energy that is equal to the ionization energy of that electron. When an X-ray beam impacts on the sample surface, the energy of the X-ray photon is adsorbed completely by the core electron of an atom. If the photon energy, *hv*, is large enough, the core electron will then escape from the atom and is emitted out of the surface. The binding energy of the core electron is given by the following equation:

$$E_{binding} = E_{photon} - E_{kinetic} - \phi \qquad (11)$$

where $E_{binding}$ is the energy of the electron emitted from one electron configuration within the atom, E_{photon} is the energy of the X-ray photons being used, $E_{kinetic}$ is the kinetic energy of the emitted electron as measured by the instrument and Φ is the work function of the spectrometer. XPS spectra are obtanined by irradiating the material with

a beam of X-rays where measuring the $E_{kinetic}$ and number of electrons that escape from the surface the data can be analyzed.

XPS measurements were performed using a SPECS system equipped with an Al anode XR50 source operating at 150 W and a Phoibos 150 MCD-9 detector XP. The partial pressure of the argon flood gun was below $1.5 \cdot 10^{-9}$ mbar.

2.1.4. Physical, structural and thermal techniques

2.1.4.1. Thermogravimetric analysis (TGA)

Thermogravimetric analysis (TGA) measures the loss of weight of a material as a function of temperature. The instrument typically comprises of a sample holder which continually measures the mass of the sample, and a combustion chamber, which heats/cools the sample to the desired temperature. This technique is widely used to evaluate the thermal degradation of a polymer. TGA can provide information about the decomposition temperatures of materials, thermal stability, absorbed moisture content, and the content of inorganic material in a sample or reaction kinetics.

Thermogravimetric analysis were performed using a PerkinElmer TGA-6 thermobalance at a heating rate of 10ºC/min under a nitrogen atmosphere.

2.1.4.2. X-Ray Diffraction (XRD)

This technique is usually employed to study structural properties of materials such as the crystalline state. The principle is based on the Bragg's equation, which is showed as follows:

$$2dsen\theta = n\lambda \qquad (12)$$

where λ is the wavelength of the beam, d is the spacing between diffracting planes, θ is the incident angle and n corresponds to the diffraction order.

In this thesis, this technique has been used to determine the structure of nanocomposites containing mineral clays. XRD technique provides information about the positions, shape and intensity of the signals corresponding to the diffraction planes. The peak positions, intensities, widths and shapes in the resultant X-ray pattern provide important information about the structure of the material. According to the position of these peaks, it is possible evaluate the different possibilities of the structure of

nanocomposites, which can be classified as intercalated, aggregated or exfoliated structures.

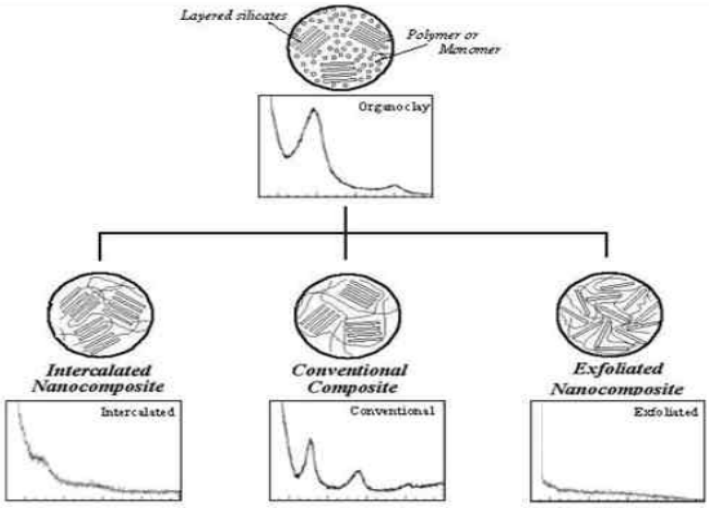

Figure 16. *XRD patterns of nanocomposites.*

X-ray diffraction (XRD) spectra of samples were carried out using an automated diffractometer, Bruker D8 Advance, using Cu-K α radiations (λ=1.5406 Å). The instrument was operated at 40 kV and 40 mA and diffraction patterns were taken at ambient laboratory temperature using 10s/angular step (1 angular step = 0.02º).

2.1.4.3. Density

Density of polymers was evaluated from flotation's method.

2.1.4.4. Adherence

Adherence measurements were carried out by using the sellotape test. This methods is represented as follows:

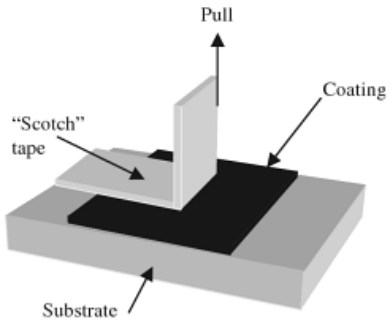

Figure 17. *Scheme of the sellotape test (ASTM D3359-87. Standard test method for measuring adhesion by tape test. American Society for Testing and Materials, 1987)*

2.1.4.5. Conductivity

Conductivity (σ) was measured from the 2-probe technique, which consists of measuring the resistance among the two silver terminals of a film. According to the law of conductivity combined with the geometric and physical properties of the material, the conductivity can be measured as follows:

$$\sigma = \frac{l^2 \cdot \rho_{pol}}{R \cdot m_{pol}} \qquad (13)$$

where l is the length among the two silver terminals of a film, ρ is the density of the polymer, R is the resistance and m_{pol} is the mass of polymer.

Figure 18. *Schematic representation of surface resistance measurement between two electrodes*

2.2. Theoretical methods

2.2.1. Quantum mechanics (QM)

Quantum mechanics explains that electrons have both particle and wave characteristics according to the Schrödinger's equation, which defines and describes the wavefunction of a particle as follows:

$$\hat{H}\,\psi(\vec{r},t) = E\,\psi(\vec{r},t) \qquad (14)$$

where $\hat{H}$ is the Hamiltonian operator which contains a combination of operators, such as kinetic energy of nuclei, kinetic energy of electrons, potential energy of nuclei-electrons, potential energy of nuclei-nuclei and potential energy of electron-electron, E

is the energy of the system and ψ is the wave function that describes the molecular orbitals.

2.2.2. Born-Oppenheimer Approximation

One of the most important parameters in the Schrodinger's equation corresponds to the Hamiltonian operator ($\widehat{H}$). As it was explained in the previous section, the Hamiltonian operator results of the combination of different operators. Within this context, the Born-Oppenheimer approximation[4] consists in that the mass of nuclei are much heavier than electrons, thus, the nuclei moves much more slowly than electrons. According to this statement, the Born-Oppenheimer approximation removes the nuclear kinetic energy. Consequently, the Hamiltonian operator can be expressed as the sum of the electronic energy and the nuclear repulsion energy:

The electronic energy is $\widehat{H} = -\frac{1}{2}\sum_{i=1}^{n} \nabla^2 - \sum_{\mu=1}^{N}\sum_{i=1}^{n} \frac{Z_\mu}{r_{\mu i}} + \sum_{i=1}^{n-1}\sum_{j=i+1}^{n} \frac{1}{r_{ij}}$

and the nuclear repulsion energy is $V = \sum_{\mu=1}^{N-1}\sum_{\nu=\mu+1}^{N} \frac{Z_\mu Z_\nu}{r_{\mu\nu}}$ (15)

Solving a QM problem implies solving the Schrödinger equation, which is only affordable by using some approximations. In this sense *Ab initio* calculations, semi-empirical calculations and calculations based in the Density Functional Theory (DFT) are extensively widespread to solve QM problems. In thesis, *Ab initio* and DFT calculations have been employed.

2.2.3. Ab initio methods

Ab initio calculations are grounded on solving the Schrödinger equation (Eqn 12) without using any empirical adjustment, *i.e.* first principles. Thus *ab initio* calculations are based only on basic physical theory. The simplest *ab initio* method is the Hartree-Fock (HF) method or Self Consistent Field (SCF) procedure.[5] The HF wave function is approximated to a single Slater determinant of spin orbitals. Schrödinger equation is solved through an iterative process applying the variational principle, *i.e.* the energy of any approximate wave function is always larger than the exact energy. Since one electron wave functions are used, electron-electron interactions are neglected and each electron interacts only with the mean field arising from all the remaining electrons, which is described by the Fock operator.

The major weakness of HF method is the fact that it does not describes electron correlation properly since each electron is considered to move in an electrostatic field whereas in reality electrons repeal each other. Instead of calculating repulsions between electrons explicitly, repulsions are calculated between one electron and the average field of all of the other electrons. Consequently, that electrons avoid each other cannot be treated. Thus, Hartree-Fock energies are too high, since electrons can get too close to each other, so high interactions *e.g.*, coulomb repulsions, are overestimated.[6,7] This deficiency makes HF method not reliable to get accurate estimates of systems where electron correlation plays an important role such as π-stacking interactions or chemical reactions.

As we cited previously, any wave function obtained by solving the Hartree-Fock equation is called a *Self Consistent Field* (SCF) wave function (meaning that the field experienced by and atom depends on the global distribution of atoms). The basic idea of the SCF method consists of making an initial guess for the spin orbitals, thus it is possible to calculate the average field for a new set of spin orbitals. By using these new spin orbital one can obtain a new field and repeat the procedure until self-consistency is reached.

Post-HF methods correct the aforementioned deficiency (electron correlation). In this thesis one post-HF methods has been used: the Møller Plesset (MP) procedure.[8] Møller Plesset is based on perturbation theory. The philosophy behind MP methods is that a correction term handles electron correlation by promoting electrons from occupied to virtual molecular orbitals giving electrons more room to move and thus making it easier for them to avoid one another. The Hamiltonian operator is defined as the addition of a perturbation operator ($\hat{V}$) to the unperturbed HF Hamiltonian ($\hat{H}^0$):

$$\hat{H} = \hat{H}^0 + \lambda \cdot \hat{V} \qquad (16)$$

where λ is a dimensionless parameter taking values compressed between 0 and 1. Thus both wavefunction and energy are described by this perturbed Hamiltonian operator.

$$\Psi = \psi^{(0)} + \lambda \cdot \psi^{(1)} + \lambda^2 \cdot \psi^{(2)} + \ldots + \lambda^n \cdot \psi^{(n)} \qquad (17)$$

$$E = E^{(0)} + \lambda \cdot E^{(1)} + \lambda^2 \cdot E^{(2)} + \ldots + \lambda^n \cdot E^{(n)} \qquad (18)$$

where $\psi^{(n)}$ is the n^{th} correction of the wave function related to the number of virtual spin orbitals and $E^{(n)}$ is the n^{th} correction energy term. Since HF energy is the sum of terms $E^{(0)}$ and $E^{(1)}$ electronic correlation corrections are taken into account from the second term (MP2).

2.2.4. Density Functional Theory calculations (DFT)

The DFT methods are based in the theory developed by Kohn and Sham[9]: the electronic density of a system can be represented as the sum of N monoelectric orbital densities, which ensures the DFT calculations to be easily applicable and provide the energy of the fundamental state. Using these ideas, the electronic energy, which includes electron correlation, is calculated as the sum of several terms that depend on the electronic density. In this context the electronic energy can be calculated using the following equation:

$$E = E^T + E^V + E^J + E^{XC} \qquad (19)$$

where E^T is the kinetic energy, E^v contains the terms of the potential energy nucleus-electron and the repulsive term between nuclei, E^J represents the Coulombic repulsion energy between electrons and, finally, E^{XC} is interchange-correlation energy. All of these energetic terms, with exception of the nucleus-nucleus repulsion, depend on the electronic density ρ.

The term E^{XC} is not determined directly in this approximation, due to its unknown mathematical formulation. Usually this term is described as a sum of an exchange term E^X and another of electronic correlation.

$$E^{XC} = E^X(\rho) + E^C(\rho) \qquad (20)$$

The exchange term can be calculated by using approximations that applies a homogeneous electron density, such as the Local Density Approximation (LDA)[10] and by using gradient corrected functionals such as the so called Generalised Gradient Approximation (GGA) methods. LDA methods consists of considering the functional density at local level. Thus, the exchange term is a function, which depends on the functional density at that point in space. On the other hand, GGA methods are based on

the functional density and their gradient, respectively. Some examples of exchange terms categorized in GGA methods are displayed as follows:

- Functional BP86 (Becke exchange)[11]
- Local correlation functional of Perdew[12]
- PBE (Perdew, Burke, Ernzherhof)[13,14]

2.2.4.1. Hybrid Functionals

In order to calculate more efficiently the term E^X, it is possible to use a mixture of the HF exchange with the DFT exchange-correlation, what is known as *hybrid functional.*

The B3LYP functional is one of the most common in the literature. This function has three parameters, which are associated to Becke exchange[11] and correlation of Lee, Yang and Parr.[15]

$$E_{xc}^{B3LYP} = E_{xc}^{LDA} + a_o\left(E_x^{HF} - E_x^{LDA}\right) + a_x\left(E_x^{GGA} - E_x^{LDA}\right) + a_c\left(E_c^{GGA} - E_c^{LDA}\right) \qquad (21)$$

where the parameters a_o, a_x, and a_c are 0.20, 0.72 and 0.81, respectively.[16]

In this thesis, the B3LYP functional has been widely used due to its ability to provide a very satisfactory description of the molecular geometry and relative energy for the minimum energy conformations of heterocyclic oligomers.[17]

2.2.5. Gaussian Function as Basis Set

In quantum mechanics, the calculations are performed using a set of basis functions. A basis set is a linear combination of the basis functions, which are composed of atomic functions with specific coefficients. Thus, in molecular calculations it is necessary use a number of atomic orbitals for each basis set. Initially, Slater orbitals were the first types of atomic orbitals (STO), which were used as basis functions because of their similarity with the solutions of the hydrogen atom. Nevertheless, the calculation of the three- and four-center two-electron integrals with Slater orbitals resulted extremely slow and without analytical form. Within this context, Gaussian functions provided an advance since the important computational savings. The Gaussian function type orbital (GTO) is composed of the minimum number of basis functions, denoted as GTO-nG, where n refers to the number of Gaussian primitive functions that comprise a single basis function. However, for large systems it is necessary add more functions, which

are denoted as polarization and diffuse function. As follows, a brief notation about their specific characteristics is detailed:

- *Polarization functions*

  Polarization functions are indicated by an asterisk (*). A single asterisk denotes a basis set with polarization on the heavy atoms, which allows that molecular orbitals to be more asymmetric about the nucleus. On the other hand, two asterisks (**) indicate that polarization functions are added to hydrogen and helium atoms.

- *Diffuse functions*

  Diffuse functions are indicated by a plus sign (+) when they added only to heavy atoms and with two plus signs (++) when they are also added to helium and hydrgogen atoms.

2.2.6. Time Dependent Density Functional Theory (TD-DFT)

In this thesis excited states on conducting polymer systems were calculated by using two different methodologies, DFT and TD-DFT. DFT methodologies are concerned with systems subject to a static external potential, which are described by the Schrödinger equation. Excited-state properties in terms of the corresponding densities are difficult to calculate by using DFT. The simplest DFT scheme for the computation of excitation energies is the evaluation of the total energy difference between the initial and the final sates. This method can be applied when both the initial and the final state are within the reach of DFT. However, in general, excited states cannot always be identified with a DFT solution. In this context, TD-DFT methodology provides an accurate description in order to evaluate excited states.[18,19] Thus, TD-DFT is an extension of DFT with time dependent external potential according to Runge – Gross theorem.[20] This theorem states that there exists an one-to-one correspondence between the time-dependent external potential, $\upsilon(\vec{r},t)$ and the time-dependent electron density, $\rho(\vec{r},t)$ for a systems evolving from a fixed initial many-body state. Thus, the densities $\rho(\vec{r},t)$ and $\rho'(\vec{r},t)$ evolving from the same intial sate Ψ_o under the influence of two potentials $\upsilon(\vec{r},t)$ and $\upsilon'(\vec{r},t)$ are always different provided that the potentials differ by more than a purely time dependet function.

This technique is widely employed in chemistry to get properties about:

- Calculation of frequency-dependent polarizability.
- Electronic circular dichroism spectra.
- Description of the first singlet excited state surface.

2.2.7. Solvent effects

The effect of the solvent on QM calculations was estimated following the polarizable continuum model (PCM) developed by Tomasi and co-workers.[21,22] This self-consistent reaction field (SCRF) method involves the generation of a solvent cavity from spheres centered at each atom in the molecules and the calculation of virtual point charges on the cavity surface representing the polarization of the solvent. The magnitude of these charges is proportional to the derivative of the solute electrostatic potential at each point calculated from the molecular wavefunction. Then, the point charges are included in the one-electron Hamiltonian inducing polarization of the solute. An iterative calculation is carried out until the wavefunction and the surface charges are self-consistent.

Within PCM method the transfer of a given solute from the gas phase into solution can be portioned into three steps:

- Creation of the solute cavity inside bulk solvent.
- Generation of the van der Waals particle inside the cavity.
- Generation of the solute charge distribution in solution.

The net molecular free energy of a system in solution (ΔG_{solv}) is the sum of these three terms:

$$\Delta G_{solv} = \Delta G_{cav} + \Delta G_{vdw} + \Delta G_{elec} \qquad (22)$$

where ΔG_{cav} is the work involved to increase the cavity, ΔG_{vdw} is the contribution due to the van der Waals interactions and ΔG_{elec} is the electrostatic component of the ΔG_{solv} and it corresponds to the work required in the polarization process. Interaction potential between solvent and solute is introduced in the solute electronic Hamiltonian as a perturbation operator ($\hat{V}_r$). Thus the Schrödinger equation, being $\hat{H}^0$ the solute's Hamiltonian operator, is expressed as follows:

$$\left(\hat{H}^0 + \hat{V}_R\right)\psi = E\,\psi \qquad (23)$$

2.2.8. Electronic properties

- *Ionization Potential (IP) and Electron Affinity (EA)*

The IP values were determined using two different methodologies. The first one is the Koopman's theorem (KT),[23] according to which the IPs were taken as the negative of the highest occupied molecular orbital (HOMO) energy (*e.g.* $IP^{KT} = -\varepsilon_{HOMO}$). According to the Janak's theorem can be applied to density functional theory (DFT) calculations.[24] The second methodology is calculated as the energy difference between the optimized structures of the cation radical and neutral complexes (first adiabatic ionization potential; IP^{1a}). To evaluate the influence of the solvent media in IP^{1a}, calculations in solvent solutions are performed for the oxidized and neutral states of complexes.

On the other hand, the EAs were calculated using the Koopman's theorem: $EA = -\varepsilon_{LUMO}$, where ε_{LUMO} refers to the energy of the lowest unoccupied molecular orbital (LUMO).

- *Gap energy (ε_g)*

The π-π^* lowest electron transition energies (ε_g) is estimated using two different strategies. In the first, ε_g is approximated as the difference between the HOMO and the lowest unoccupied molecular orbital (LUMO), ($\varepsilon_g = \varepsilon_{HOMO} - \varepsilon_{LUMO}$). Thus, Levy and Nagy evidenced that ε_g can be rightly estimated by this procedure using DFT calculations.[25] The second estimation of ε_g is derived from the excitation energies calculated with time-dependent density functional theory (TD-DFT). This methodology provides an accurate description of the experimental ε_g values.

2.2.9. Basis Set Superposition Error (BSEE)

In the previous section a explanation bout Gaussian functions was discussed. However, an important concept was not analyzed, which concerns Gaussian functions, the basis set superposition error (BSSE).[26] Two different species (A and B) with their corresponding basis functions can experiment a variation of the basis set when both A and B are in contact, thus, A specie presents a larger basis set than its corresponding

isolated state. Consequently, this modification of the basis set is called as *basis set superposition error*. This error can be processed by using the counterpoise method (CP).[27] This method is explained from the interaction energy, which is expressed as follows:

$$\Delta E^{int} = E(AB)_{ab} - E(A)_a - E(B)_b \qquad (24)$$

where $E(AB)_{ab}$, E(A) and E(B) are the energy of AB complex, monomer A and monomer B, respectively. The subscript indicates the corresponding basis set for AB, A and B. Thus, due to the incompleteness of the basis set for A and B species, the BSSE is presented in the interaction energy. Consequently, using the counterpoise method, the BSSE in the interaction energy is described as following:

$$\Delta E^{BSSE} = E(A,AB)_{ab} + E(B,AB)_{ab} - E(A,AB)_a - E(B,AB)_b \qquad (25)$$

where $E(A,AB)_{ab}$ represents the energy of specie A in the structure of the complex with the full basis set of the complex. $E(B, AB)_{ab}$ represents the energy of specie B in the structure of the complex with the full basis set of the complex. $E(A, AB)_a$ and $E(B, AB)_b$ are the energies of A and B with their own basis functions in the structure of the complex.

Finally, the corrected binding energy ($\Delta E^{int(c)}$) results as:

$$\Delta E^{int\,(c)} = \Delta E^{int} - \Delta E^{BSSE} \qquad (26)$$

2.3. References

[1]. Brédas, J. L.; Silbey, R.; Boudreaux, D. S.; Chance, R. R. *J. Am. Chem. Soc.* **1983**, *105*, 6555.

[2]. MultiMode™ SPM Instruction Manual, digital instruments.

[3]. Thesis "*Preparation of electroconductive paper by deposition of conducting polymer*" Montibon, E. **2007**.

[4]. Born, M.; Oppenheimer, R. *Ann. Phys. (Leipzig)* **1927**, *84*, 457.

[5]. a) Hartree D.R. *Proc. Cambridge Phil. Soc.* **1928**, *24*, 89 b) Slater J.C. *Phys. Rev.* **1930**, *35*, 210 c) Fock V. *Z. Physik* **1930**, *61*, 126.

[6]. Levine, I. N. *Quantum Chemistry*, 5th edition, Prentice Hall **2000**

[7]. Cramer, C. J. *Essentials of Computational Chemistry: theories and models*, Jon Wiley & Sons Ltd. **2002**

[8]. Slater, J. C. *Int. J. Quantum Chem. Symp.* **1975**, *9*, 7.

[9]. Hohenberg, P. Kohn, W. *Phys. Rev. B* **1964**, *136*, B864.

[10]. a) Møller C., Plesset M.S. *Phys. Rev.* **1934**, *46*, 618 b) Binkley J.S., Pople J.A. *Int. J. Quantum Chem.*, **1975**, *9*, 229.

[11]. Becke, A. D. *Phys. Rev. A.* **1988**, *38*, 3098.

[12]. Perdew, J. P. *Phys. Rev. B.* **1986**, *33*, 8822.

[13]. Perdew, J. P.; Burke, K.; Ernzerhof, M. *Phys. Rev. Lett.* **1996**, *77*, 3865.

[14]. Perdew, J. P.; Burke, K.; Ernzerhof, M. *Phys. Rev. Lett.* **1997**, *78*, 1396.

[15]. Lee, C.; Yang, W.; Parr, G. R. *Phys. Rev. B* **1998**, *37*, 785.

[16]. Becke, A. D. *J. Chem. Phys.* **1993**, *98*, 5648.

[17]. Torras, J.; Bertrán, O.; Alemán. C. *J. Phys. Chem. B* **2009**, *113*, 15196.

[18]. Chong, D. P. "*Recent advances in the density functional methods*" Vol. 1, 2 (1996).

[19]. Marques, M. A. L.; Ullrich, C.; Nogueira, F.; Rubio, A.; Burke, K.; Gross, E. K. U. "*Time-Dependent Density Functional Theory*" (2006).

[20]. Runge, E.; Gross, E. K. U. *Phys. Rev. Lett.* **1984**, *52*, 997.

[21]. Miertuš S.; Scrocco E.; Tomasi J. *Chem. Phys.* **1981**, *55*, 117.

[22]. Miertuš S.; Scrocco E.; Tomasi J. *Chem. Phys.* **1982**, *65*, 239.

[23]. Koopmans, T. *Physica* **1934**, *1*, 104.

[24]. Janak, J. F. *Phys. Rev. B* **1978**, *18*, 7165.

[25]. Levy, M.; Nagy, A. *Phys. Rev. A* **1999**, *59*, 1687.

[26]. van Duijneveldt, F. B.; van Duijneveldt-van de Rijdt, J. G. C. M.; van Lenthe, J. H. *Chem. Rev.* **1994**, *94*, 1873.
[27]. Boys, S. F.; Bernardi, F. *Mol. Phys.* **1970**, *19*, 553.

Chapter 3. Multilayered systems based on thiophene and pyrrole derivatives

3.1. Morphology and growing of nanometric multilayered films formed by alternated layers of poly(3,4-ethylenedioxythiophene) and poly(N-methylpyrrole).[a]

3.1.1. Introduction

3.1.2. Methods

3.1.3. Results and discussion

3.1.4. Conclusions

3.1.5. References

[a]Results presented in this chapter were published in *Thin Solid Films* **2010**, *518*, 4203.

3.2. Properties of nanometric and micrometric multilayered films made of three conducting polymers.[b]

3.2.1. Introduction

3.2.2. Methods

3.2.3. Results and discussion

3.2.4. Conclusions

3.2.5. References

[b]Results presented in this chapter were published in *Eur. Polym. J.* **2010**, *46*, 2222.

3.3. Symmetric supercapacitors based on multilayers of conducting polymers.[c]

3.3.1. Introduction

3.3.2. Methods

3.3.3. Results and discussion

3.3.4. Conclusions

3.3.5. References

[c]Results presented in this chapter were published in *J. Phys. Chem. C* **2011**, *115*, 8430.

3.1. Morphology and growing of nanometric multilayered films formed by alternated layers of poly(3,4-ethylenedioxythiophene) and poly(N-methylpyrrole).

3.1.1. Introduction

The layer-by-layer technique based on electrostatic or other molecular forces creates an advantageous approach to construct different types of self-assembled materials. Since the technique was first developed by Decher and others[1-4] it has been extensively applied in preparing various materials.[1-10] Within the field of conducting polyconjugated polymers, ultrathin films of multilayered systems fabricated by electrostatic self-assembly have been studied,[11-22] those prepared using poly(3,4-ethylenedioxythiophene):poly(styrenesulfonate) (PEDOT:PSS) and a polyelectrolyte, *i.e.* typically poly(allylamine hydrochloride), being the most studied.[17-22] Furthermore, conducting multilayered ultrathin films involving polyaniline,[11-12] polypyrrole[13,14] and some polythiophene derivatives[14-22] have been also characterized and reported.

Multilayered systems formed by two or more conducting polymers can be also prepared using a layer-by-layer electrodeposition technique.[23,24] In this case, individual anodic polymerization processes, which are developed using two or more electrochemical cells containing solutions of different monomers, provide films formed by layers of different polymers. The thickness of each layer depends on the polymerization time (θ) employed for the corresponding electropolymerization process. In a recent study it was showed that the electrochemical stability and the ability to store charge of multilayered systems formed by PEDOT and poly(N-methylpyrrole) (PNMPy),[23] hereafter abbreviated ml-PEDOT/PNMPy, were significantly higher than those of the copolymers derived from mixtures of 3,4-ethylenedioxythiophene (EDOT) and N-methylpyrrole (NMPy), poly(EDOT-*co*-NMPy), with different concentration ratios[25,26] and the individual homopolymers.[27] Furthermore, analyses of ml-PEDOT/PNMPy films containing 3, 5, 7 and 9 layers revealed that the properties of these multilayered systems enhance significantly with the number of layers, while the properties of the homopolymers does not depend on the thickness of the films after a threshold value of ($l \approx 4$ μm).[24] These results clearly led us to conclude that, although

polyheterocyclic conducting copolymers usually do not present practical advantages, multilayered systems of conducting homopolymers are very promising materials for different technological applications.

The excellent electroactivity and electrostability of ml-PEDOT/PNMPy systems were attributed to the interface between the PEDOT and PNMPy layers. Thus, the coupling between the layers of the two conducting polymers is, in terms of enhancement of the properties, significantly more positive for the multilayered films than the interaction of EDOT and NMPy monomers in copolymers. This feature led to design a strategy to optimize the properties of multilayered systems, which was based on increase the dimensional ratio between the interface and bulk regions by reducing the thickness of the layers.[23] Thus, the dimensions of the interface between consecutive layers are very small with respect to the bulk of the layers when the thickness of the films is within the micrometric scale., *i.e.* the dimensional ratio interface:bulk is extremely low. However, when the polymerization time used for the electrogeneration of the layers is reduced to decrease the thickness of the films to the nanometric scale, the interface:bulk dimensional ratio increases significantly. Interestingly, ml-PEDOT/PNMPy nanometric films containing 3, 5 and 7 layers confirmed that the ability to store charge of multilayered films increase with the interface:bulk dimensional ratio.[23] Furthermore, the reduction of the thickness of the layers improved the definition of the control voltammograms and decreased the potential required for both the oxidation of polarons in polymer chains and for the formation of bipolarons by oxidation of polarons. These results supported the importance attributed to the interactions in the coupling interface between consecutive layers of PEDOT and PNMPy.

The aim of this work is to investigate the coupling between consecutive layers in nanometric films of ml-PEDOT/PNMPy systems. For this purpose, the morphology (2-dimensions) and topography (3-dimensions) at the surface of the layers, as well as the average roughness (r), have been determined layer-by-layer for systems of up 5 layers using atomic force microscopy (AFM). In order to compare with the corresponding homopolymers, a initial study has been developed for individual PEDOT and PNMPy films obtained using identical polymerization times, *i.e.* similar thickness. In some stages, quantum mechanical calculations on reduced systems have been used to support the models proposed for the coupling and growing of the layers. In addition, different number of layers (ml-PEDOT/PNMPy) or different polymerization times (individual

PEDOT and PNMPy) were considered to examine the influence of the thickness in both the electroactivity and electrostability of the films. Furthermore, conductive-AFM (C-AFM) has been used to measure the conductivity at local regions. Findings provide conclusive evidences about the mechanisms of formation and growth of the multilayered and single component nanofilms, as well as about the interactions in the coupling interfaces of the ml-PEDOT/PNMPy.

3.1.2. Methods

Anodic electropolymerization. Solvent and monomers of analytical reagent grade were purchased from Aldrich and used as received without further purification. Anhydrous $LiClO_4$, analytical reagent grade, from Aldrich was stored in an oven at 80ºC before use in the electrochemical trials.

PEDOT, PNMPy and ml-PEDOT/PNMPy films were prepared by chronoamperometry (CA) under a constant potential of 1.40 V. Electrochemical experiments were performed on a PAR 273A potenciostat-galvanostat using a three-electrode two-compartment cell under nitrogen atmosphere (99.995% in purity) at 25 ºC. The working compartment was filled with 40 mL of a 10 mM monomer solution in acetonitrile with 0.1 M $LiClO_4$, while the cathodic compartment was filled with 10 mL of the same electrolyte solution. Steel AISI 316 sheets of 4 cm^2 area were employed as working and counter electrodes. It should be noted that, although there are chemically inert materials (Au, graphite carbon, etc.) with smaller roughness, electrodeposition on steel surfaces by in situ electropolymerization is highly desirable because the conducting polymers under study are used to prevent corrosion.[28,29] The reference electrode was a Ag|AgCl electrode containing a KCl saturated aqueous solution (E^o = 0.222 V *vs.* standard hydrogen electrode at 25 ºC), all the potentials (E) given in this work being referred to this electrode.

Nanometric multilayered films were prepared using a layer-by-layer electrodeposition procedure, which has been previously detailed.[23,24] In order to provide environmental stability, PEDOT was used for the first layer.[30] This was generated by immersing the working electrode for a polymerization time θ = 10 s in an EDOT solution. Next, the electrode coated with the PEDOT monolayer was immersed in a new cell filled with a NMPy solution. A layer of PNMPy, which was also generated using θ = 10 s, was deposited on the top of the previously generated PEDOT forming a bilayer.

After this, the electrode coated with the bilayer was immersed in a new cell filled with an EDOT solution, a 3-layered PEDOT/PNMPy/PEDOT film being obtained after applying a constant potential of 1.40 V and θ = 10 s. The same procedure was used to electrogenerate the 4-layered and 5-layered systems. On the other hand, in order to compare with the multilayered systems, films of PEDOT and PNMPy homopolymers were produced using θ = 10, 20, 30, 40 and 50 s.

Electrochemically derived properties. The thickness of the films (ℓ) was estimated by layer from the mass of polymer deposited in the electrode, m_{pol}, which was obtained using the following relation:

$$m_{pol} = Q_{pol}\left(\frac{m}{Q}\right) \quad (1)$$

where Q_{pol} is the polymerization charge(in millicoulombs per square centimeter) consumed in the generation of each layer and $\left(\frac{m}{Q}\right)$ the current productivity, the latter being previously determined for PEDOT[27] (0.875 mg·C^{-1}) and PNMPy[25] (0.619 mg·C^{-1}). The volume of polymer deposited in the electrode (V_{pol}) was obtained using the values of $m_{pol}$and the densities previously reported for PEDOT[26] (1.665 g·cm^{-3}) and PNMPy[25] (1.595 g·cm^{-3}). Accordingly, the thickness of each layer was calculated considering the surface of polymerization (S_{pol}), which is the surface of the electrode (4 cm^2), and V_{pol}.

The electroactivity and electrostability of the multilayered and single component films were determined by cyclic voltammetry (CV). Specifically, the electroactivity increases with the similarity between the anodic and cathodic areas of the first control voltammogram, while the electrostability decreases with the oxidation and reduction areas of successive control voltammograms. A scan rate of 100 mV·s^{-1} was used in all cases.

Morphology, topography and local conductivity. Topographic AFM images of multilayered single component films generated using θ = 10, 20, 30, 40 and 50 s were obtained with a Molecular Imaging PicoSPM using a NanoScope IV controller in ambient conditions. Local conductivities were determined using a Multimode Atomic Force Microscope attached to a Nanoscope IV controller (Digital Instruments, Santa Barbara, CA). Measurements were performed with the Conductive-AFM (C-AFM)

Electronic Application Module (Digital Instruments, Santa Barbara, CA) using conductive doped diamond coated tips (DDESP, Veeco, Santa Barbara, CA) in contact mode having a force constant of 42 N/m. C-AFM is suitable for imaging samples spanning a wide range of conductivity. This accessory is based on the application of a selected bias voltage between the conductive tip and the sample. While scanning in Contact Mode, a linear amplifier with a range of 1pA to 1μA senses the current passing through the sample. By maintaining a constant force between tip and sample, simultaneous topographic and current images were generated, enabling the direct correlation of local topography with electrical properties.

Nanometric measurements were conducted under ambient conditions at ~50% relative humidity and 20-22 ºC. The system was placed on an active vibration isolation table for minimum acoustic disturbance (20 series, TMC, Peabody, MA, USA).

Quantum mechanical calculations. Density Functional Theory (DFT) calculations were performed using the following combination: the Becke's three-parameter hybrid functional (B3)[31] with the Lee, Yang and Parr (LYP) expression[32] for the non-local correlation (B3LYP). Calculations were carried out considering an oxidized species (radical cation state), the unrestricted formalism of the B3LYP functional (UB3LYP) being used in all cases. The UB3LYP method was combined with the 6-31+G(d,p) basis set, *i.e.* UB3LYP/6-31+G(d,p), a double-zeta basis set with polarization and diffuse functions that was developed by Pople and co-workers.[33] The Gaussian 03 computer program[34] was used for all the calculations, geometry optimizations being performed using redundant coordinates.

Calculations were carried out on oligomers containing four heterocyclic rings, linear (those exclusively formed by inter-ring α,α-linkages) and branched structures (those derived from inter-ring couplings in the available β- and β'-positions of the NMPy units) being considered. All these oligomers, which were subjected to complete geometry optimizations at the UB3LYP/6-31+G(d) level, were considered in the oxidized state (charge= +1).

3.1.3. Results and discussion

Poly(N-methylpyrrole). 2D and 3D AFM images of PNMPy films obtained using θ = 10, 20, 30, 40 and 50 s are displayed in Figure 1, the values determined for the thickness (ℓ) and the roughness (r) being listed in Table 1. As can be seen, the surface of

the film shows well-defined sharp peaks after the first 10 s of electropolymerization (Figure 1a), which is consistent with the initial formation of independent PNMPy molecules that grow perpendicularly to the surface of the steel electrode. The value of *r*, which was determined for the region displayed in Figure 1a, indicates that molecular chains differ in about 55 chemical repeating units, *i.e* .*r* = 16.1 nm and the estimated length per chemical repeating unit is ~0.3 nm. Furthermore, these results suggest that polymer chains tend to grow linearly, which is consistent with the formation of films through the nucleation of independent chains (nucleation centres). Thus, the formation of chemical crosslinks seems relatively infrequent during the first step of the polymerization process. It is worth noting that chemical crosslinks are responsible of important chemical and thermal characteristics of electrogenerated PNMPy, *i.e.* these polymers are completely unsoluble in both organic and polar solvents and show thermal decomposition without previous melt at high temperatures.[25,26]

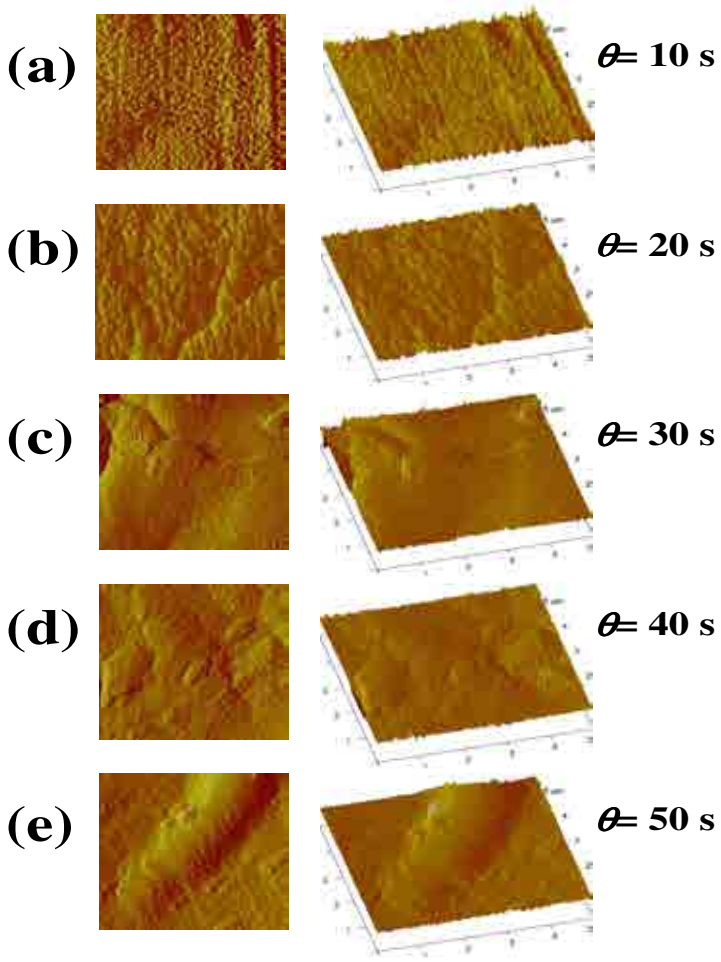

Figure 1. *2D AFM images of PNMPy films prepared using a total polymerization time of 10, 20, 30, 40 and 50 s. Scale bar: 1 μm.*

Significant changes are detected in the surface of the film yielded using θ = 20 s (Figure 1b). The peaks are broad and densely distributed, while the roughness is approximately twice the value determined for the films generated using θ = 10 s. The latter feature is clearly consistent with the linear growing of the molecular chains. Furthermore, the broadness of the peaks is explained by the formation of aggregates, *i.e.* packing of the molecular chains that grow perpendicular to the steel surface, that are probably stabilized by the perchlorate dopant anions. It is worth noting that the perpendicular growing of the chains is strongly supported by the identification of nucleation centres, which are clearly identified in Figures 1a and 1b, and variation of the roughness against θ, *i.e.* the value of r determined for θ = 20 s is almost twice that obtained for θ = 10 s (Table 1).

Table 1. *Average thickness (ℓ; in nm) and RMS roughness (r; in nm) of the PEDOT, PNMPy and ml-PEDOT/PNMPy nanometric films[a] electrogenerated on a steel substrate[b] by chronoamperometry using different polymerization times (θ).*

		θ = 10 s	θ = 20 s	θ = 30 s	θ = 40 s	θ = 50 s
PNMPy	ℓ(nm)	171	340	519	710	848
	r (nm)	16	31	56	40	66
PEDOT	ℓ (nm)	125	284	345	488	609
	r (nm)	60	71	40	117	136
ml-PEDOT/PNMPy	ℓ (nm)	125	304	419	607	713
	r (nm)	60	76	48	39	111

[a]*Scan size: 5μm x 5μm.*
[b]*The roughness determined for the steel substrate is 6 nm.*

The morphologic and topographic images of the films obtained using $\theta \geq$ 30 s are completely different to those found for θ = 10 and 20 s. Figures 1c-1e evidence the disappearance of nucleation centres found in the first steps of the electropolymerization process (Figure 1a). Thus, the peaks densely distributed are replaced by compact plateau regions located at different levels. This feature indicates that for $\theta \geq$ 30 s the electropolymerization process is clearly dominated by the formation of chemical crosslinks, even although the presence of some sparse narrow peaks suggests a small contribution of linear growing. Accordingly, it is concluded that the degree of crosslinking clearly increases with θ, which is consistent with the intrinsic

characteristics recently found for PNMPy using both theoretical calculations and CV experiments.[35] Thus, quantum mechanical calculations on small model oligomers formed by four NMPy units indicated that the branched architecture, *i.e.* that involving chemical couplings in the β and β' position of the NMPy, are more stable than the linear one, *i.e.* that exclusively formed by α,α'-linkages. On the other hand, the roughness determined for the films produced using θ = 30, 40 and 50 s ranges from 55.8 to 66.2 nm indicating that the topographical gap between the compact and well-defined plateaus is higher than that obtained for the peaks. Moreover, the fact that the roughness is smaller for θ = 40 s (r = 39.6 nm) than for θ = 30 and 50 s suggests that for this time interval the behaviour depends on the scanned region rather than on the polymerization time. Comparison among the roughness determined for the films obtained using θ = 30, 40 and 50 s indicates that, after 30 s, there is a growing process in which polymer chains form multidirectional branches. Thus, directional preference is detected in the growing of the PNMPy molecules, *i.e.* compact films are produced through a non-regular growing process.

Figure 2 compares the control voltammograms for 30 consecutive oxidation-reduction cycles of the PNMPy films prepared using θ = 10 s (l= 171 nm) and 50 s (l= 848 nm). As can be seen, the former film is very stable from an electrochemical point of view, the overlapping between the control voltammograms of the first (c_1) and last (c_{30}) oxidation-reduction cycles being almost perfect. The submicrometric PNMPy film obtained using θ = 50 s presents a completely different behaviour: the oxidation and reductions areas are about 90% smaller for c_{30} than for c_1. This difference is fully consistent with the 2D and 3D AFM images (Figure 1) discussed above. The characteristics of the nanometric film obtained in 10 s are the nucleation centres originated during the first steps of electrogeneration process and the absence of chemical crosslinks. Consequently, the structure of this material is suitable to allow the access and escape of dopant ions along the oxidation and reduction processes, respectively, ensuring its electrochemical stability. In contrast, the material generated using $\theta \geq$ 30 s shows a significant tendency to form a dense network of chemical crosslinks, which precludes the diffusion of the dopant ions. Thus, the formation of such crosslinks is evidenced by the low electroactivity and electrostability of this material. This enhances the compactness of the material with the number of oxidation-reduction process, which in turn also contributes to reduce the mobility of the dopant ions.

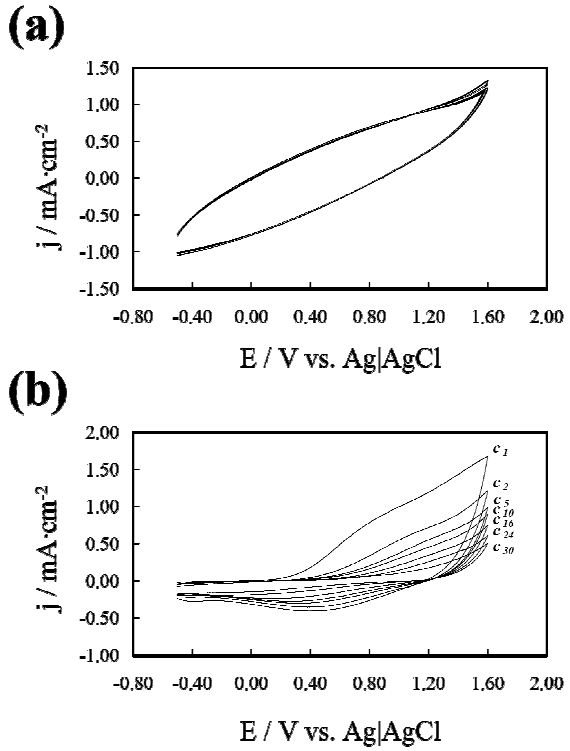

Figure 2. *Control voltammograms of 30 consecutive oxidation-reduction cycles of PNMPy films prepared using a total polymerization time of θ = 10 and 50 s (top and bottom, respectively). In order to clarify the presentation only selected voltammograms are displayed. The labels c_1 and c_{30} correspond to the voltammograms recorded in the first and thirtieth cycles, respectively.*

Poly(3,4-ethylenedioxythiophene). AFM images and electrochemical results obtained for PEDOT films are displayed in Figures 3 and 4, while the averaged values of the thickness and roughness are included in Table 1.

As can be seen in Figures 3a and 3b, films electrogenerated using θ = 10 and 20 s show similar surface topology. This consists on relatively dense distributions of sharp peaks that are grouped forming small and well-defined clusters that resemble *mountain ranges*. PEDOT molecules are exclusively formed by α,α-linkages since the dioxane ring fused onto the thiophene ring occupies the β-positions of the latter. Thus, these clusters should be identified as compact molecular aggregates of linear chains, which are probably stabilized by the incorporated perchlorate anions.[35] On the other hand, the roughness determined for these PEDOT films (r = 60 and 71 nm for θ = 10 and 20 s, respectively) reflect greater topographical slopes than in PNMPy generated using identical experimental conditions. This difference is because PEDOT chains grow linearly, whereas PNMPy molecules can form chemical crosslinks that reduce the

roughness of the surface. Thus, the aggregation of linear PEDOT molecules produce deep *ravines* that separate the *mountain ranges* mentioned above. These aggregates are stabilized by strong electrostatic interactions between the positive charges of the polymer chains, which were found to present a very high doping level,[27] and perchlorate anions. Furthermore, a previous X-ray study evidenced that electrochemically generated PEDOT adopts an amorphous organization.[27] Considering that the length of each EDOT unit within the polymer molecule, which was determined by quantum mechanical calculations, is 3.20 Å, the values of r reveal that PEDOT chains generated using $\theta = 10$ and 20 s differ in approximately 35 chemical repeating units.

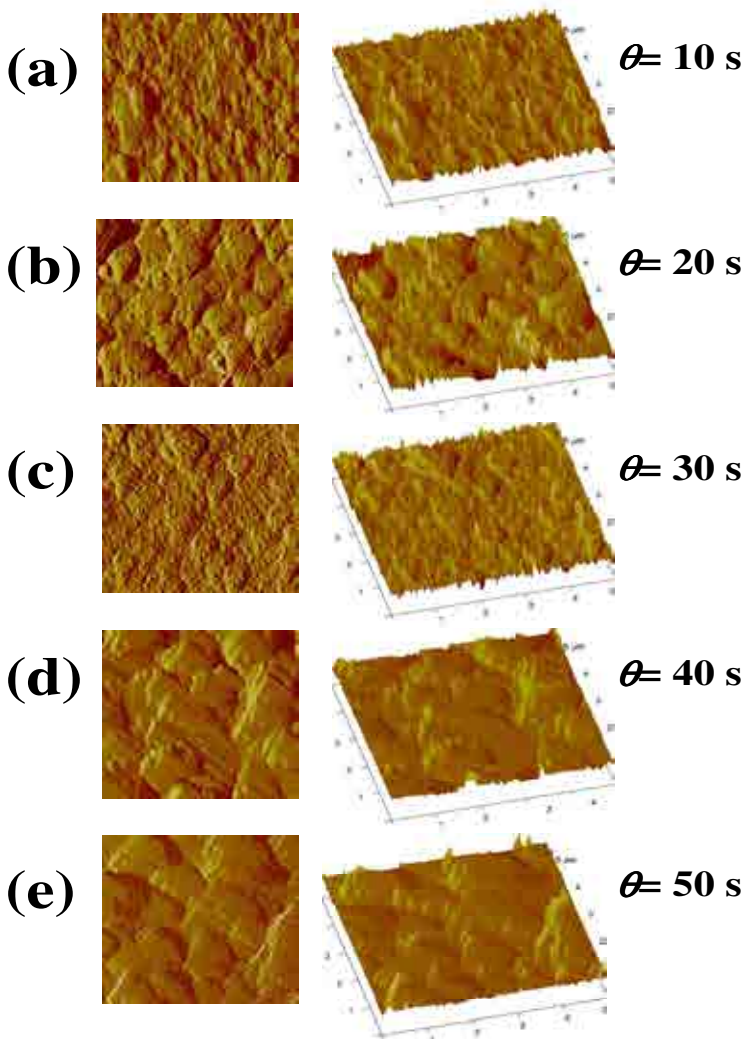

Figure 3. *2D (left) AFM images of PEDOT films prepared using a total polymerization time of 10, 20, 30, 40 and 50 s. Scale bar: 5 μm.*

An interesting phenomenon is detected in the surface of the films generated using θ = 30 s (Figure 3c): although there is a dense distribution of sharp peaks, the surface is much more levelled than those of θ = 10 and 20 s. Thus, the deep of the *ravines* that separate the *mountain ranges* is ~ 20-30 nm smaller suggesting that the molecular chains that grow in the interval of time ranging from 20 to 30 s mainly correspond to those located in the *ravines*. The filling of these areas produced an increase in the uniformity of the surface, which was reflected by a drastic reduction in the roughness (r = 40 nm).

The AFM images of the films obtained using θ = 40 and 50 s (Figures 3d and 3e) show compact blocks of aggregated molecules that form plateau regions located at different levels. Furthermore, it can be also detected a small number of narrow and sharp peaks grouped in small clusters that grow over the plateau regions. Accordingly, the growing of PEDOT chains is accompanied by rapid aggregation phenomena. This topography produces significant increases in the roughness that, due to the absence of crosslinking, is about twice that determined for PNMPy.

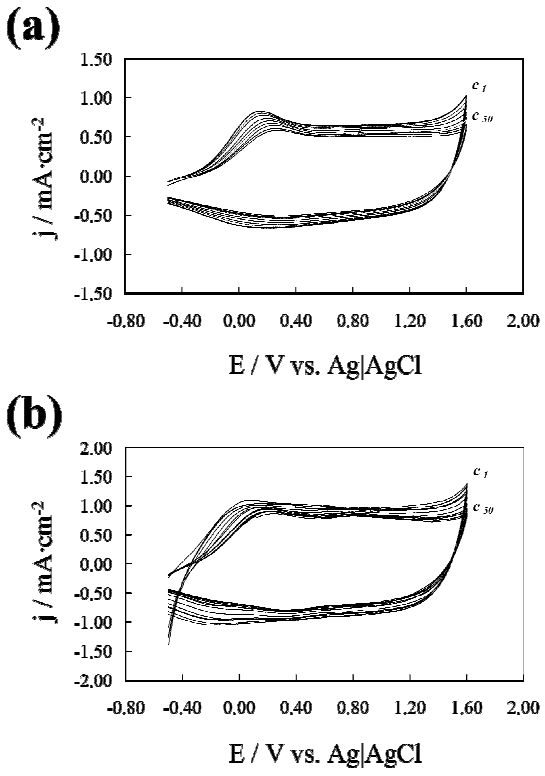

Figure 4. *Control voltammograms of 50 consecutive oxidation-reduction cycles of PEDOT films prepared using a total polymerization time of θ = 30 and 50 s (top and bottom, respectively). In order to clarify the presentation only selected voltammograms are displayed. The labels c_1 and c_{50} correspond to the voltammograms recorded in the first and fiftieth cycles, respectively.*

Inspection to the control voltammograms recorded for PEDOT indicates that the nanometric films generated in this work retain the remarkable electroactivity and electrochemical stability of the films previously studied,[24,27] which were produced using polymerization times ranging from300 to 1500 s, *i.e.* ℓ ranged from 2.35 to 11.15 μm. This feature, which is illustrated in Figure 4 showing the control voltammograms for 50 consecutive oxidation-reduction cycles of the films obtained using θ= 30 and 50 s, must be attributed to the lack of chemical crosslinks. Thus, the small reduction observed in the cathodic and anodic areas with the number of oxidation-reduction cycles should be exclusively attributed to the formation of compact aggregates, which make difficult the mobility of the dopant ions in this material.

Multilayered systems formed by poly(3,4-ethylenedioxythiophene) and poly(N-methylpyrrole). In order to provide environmental stability, PEDOT was used for the outside layers of the ml-PEDOT/PNMPy systems. Accordingly, the first PEDOT layer was generated using θ = 10 s, results being identical to those described above for the individual homopolymer (Figure 3a). After this, a bilayer was generated by electrodepositing PNMPy on the top of the PEDOT monolayer. The 2D and 3D AFM images of the resulting PNMPy surface, which are showed in Figure 5a, reveal a dense and uniform distribution of sharp peaks. This topography recalls that previously obtained for the PNMPy film directly deposited on the steel electrode (Figure 1a), being consistent with the generation of independent PNMPy molecules (nucleation centres) that grow perpendicular to the surface. Moreover, the roughness of the bilayer (r = 76 nm) corresponds to the sum of the values determined for the initial PEDOT layer (r = 60 nm) and the PNMPy film obtained using θ = 10 s (r = 16 nm). This feature indicates that, after tether to the emerging peaks of the PEDOT monolayer, PNMPy chains tend to grow linearly, *i.e.* the size of the branches is not enough to fill the *ravines* defined by neighboring peaks.

In order to support this experimental evidence, quantum mechanical calculations on positively charged tetramers formed by one EDOT and three NMPy repeating units were performed at the UB3LYP/6-31+G(d) level. Specifically, we compared the relative stability between the branched and linear architectures of the molecular chains. The unique molecule with linear architecture was constructed by attaching one EDOT unit and three NMPy rings consecutively through α,α'-linkages (EDOT-NMPy-NMPy-NMPy), while four different molecular systems with a branched architecture were

generated by considering a linear trimer with sequence EDOT-NMPy-NMPy and attaching a NMPy ring to the last two units of the linear trimer EDOT-NMPy-NMPy through β,α- and β',α-linkages. Interestingly, the linear molecule was more stable than the branched molecule of lowest energy by 1.5 kcal/mol. It is worth noting that, although the molecular scales of the molecular systems used for calculations and AFM images differ in two orders of magnitude (1-2 and 100 nm, respectively), quantum mechanical methods allow define the growing mechanism of polymer chains by predicting the relative stability of the different chemical bonds involved in them. These quantum mechanical results obtained in this work are consistent with the linear growth of the PNMPy chains that join to the PEDOT surface, even though some degree of branching is also suggested by the small energy difference between the linear and branched molecules.

The AFM images of the 3-layered film obtained by the electrodeposition of PEDOT (θ = 10 s) on the top of the PNMPy layer of the PEDOT/PNMPy bilayer are displayed in Figure 5b. As can be seen, the height of the peaks is lower than that obtained for the bilayer (Figure 5a), the topography of the surface being more uniform for the 3-layered film than for the 2-layered one. This feature is also reflected by the averaged roughness, r = 48 nm. Thus, the shape of the surface showed in Figure 5b could be described as small groups of peaks that stand out and alternate with localized depressions. These results indicate that, after bonding to the PNMPy surface, PEDOT chains grow in multiple directions and not only perpendicular to the surface. Thus, the attachment of the EDOT units to the reactive ends of both the linear and branched segments of the PNMPy chains explains the reduction of the roughness. Moreover, this multidirectional growing model is fully consistent with the topographical differences found with respect to the PEDOT homopolymer generated using θ = 30 s (Figure 3c). Accordingly, rigid PEDOT chains growing in different directions are not able to form compact aggregates, as those found in single component PEDOT films, due to the unfavourable spatial orientation.

Quantum mechanical calculations at the UB3LYP/6-31+G(d) level on a hexamer formed by two NMPy and four EDOT repeating units indicated that the linear structure NMPy-NMPy-EDOT-EDOT-EDOT-EDOT, which is exclusively formed by inter-ring α,α'-linkages, is significantly unfavored (8.3 kcal/mol) with respect to the branched structure constructed by attaching the EDOT-EDOT dimer to the second NMPy unit of

the linear tetramer NMPy-NMPy-EDOT-EDOT through a β,α-linkage. These calculations predict that the most stable chemical linkage in the interface region, which is not the α,α', will induce a variation in the shape of the polymer chains. Obviously, this change will affect to the morphology of the material, this effect increasing with the molecular size. It is worth noting that this theoretical prediction is fully consistent with the multidirectional growing proposed for the PEDOT chains of the third layer on the basis of the AFM images.

Figure 5c shows the 2D and 3D AFM images recorded for the 4-layered film, which was prepared by electrodepositing another PNMPy layer (θ = 10 s) on the top of the PEDOT/PNMPy/PEDOT 3-layered system. It is worth noting that the roughness of the surface (r = 39 nm), which is formed by a uniform dispersion of small peaks, is lower than in Figure 5b. This feature evidences that PNMPy chains are attached to the α-position of PEDOT molecules following the multidirectional growing described above for the 3-layered system. In this case, the proximity of reactive PNMPy chains strongly favours the formation of chemical crosslinks, which was not possible for PEDOT in the 3-layered system. In the resulting PNMPy crosslinked network, the linear segments that grow perpendicularly to the film surface are relatively short explaining the reduction in the roughness of the film.

Finally, Figure 5d displays the AFM images recorded for the 5-layered PEDOT/PNMPy/PEDOT/PNMPy/PEDOT system. The topography of the surface can be described as relatively short *mountain ranges* that stand out above the rest of the peaks and are separated by well-defined *valleys*. In some cases, the *mountain ranges* are wide enough to define compact blocks. This irregular topography produces an averaged roughness (r = 111 nm) that is significantly higher than that determined for the other ml-PEDOT/PNMPy systems. These features suggest that PEDOT molecules grow on the PNMPy surface by forming α,α-linkages with the reactive ends of PNMPy chains. Thus, the existence of other type of linkages is highly improbable due to the steric hindering associated to the dense crosslinked network of the fourth layer. Accordingly, the positions able to allow the perpendicular grow of PEDOT chains within such PNMPy network will be relatively scarce explaining both the irregular topography (Figure 5d) and the enhancement of the roughness. On the other hand, the small compact regions mentioned above (Figure 5d) should be exclusively attributed to the aggregation of PEDOT chains that are relatively close.

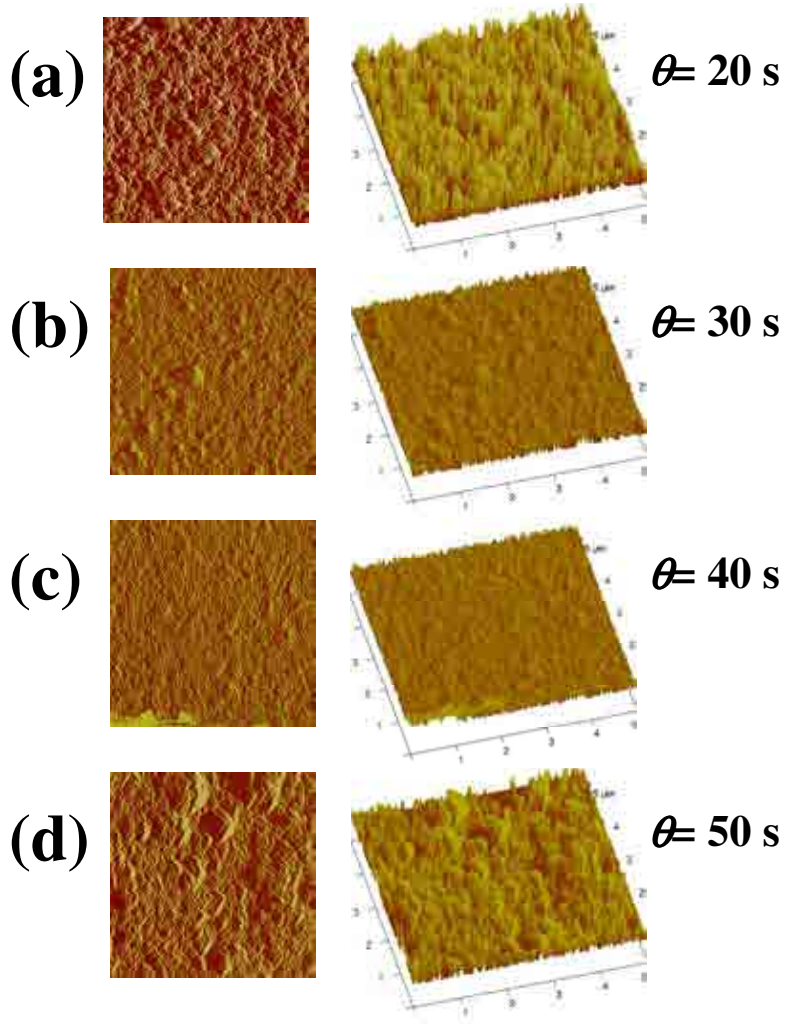

Figure 5. *2D AFM images of ml-PEDOT/PNMPy films prepared using a polymerization time of θ = 10 s for each layer. The images correspond to the PEDOT/PNMPy 2-layered system (θ = 20 s), PEDOT/PNMPy/PEDOT 3-layered system (θ = 30s) PEDOT/PNMPy/PEDOT/PNMPy 4-layered system (θ = 40 s) and PEDOT/PNMPy/PEDOT/PNMPy/PEDOT 5-layered system (θ = 50 s). Scale bar: 1 μm.*

In order to evaluate the electrochemical stability of the multilayered films, cyclic voltammetries were performed from -0.5 to 1.6 V at 100 $mV \cdot s^{-1}$. Figure 6 shows selected control voltammograms for 30 consecutive oxidation-reduction cycles of the nanometric films formed by the 3- and 5-layered systems. As can be seen, the cathodic and anodic areas of the first cycle (c_1) are significantly higher than those obtained for PEDOT films generated using θ = 30 and 50 s (Figure 4). Moreover, the electroactivity of the ml-PEDOT/PNMPy increases significantly with *n*, this increment being significantly higher than that obtained for PEDOT films. This is a very remarkable result since the variation in the thickness of the film is similar in both cases, *i.e.* $\Delta\ell_{ml\text{-}}$

$_{PEDOT/PNMPy}$ = 106 nm when the number of layers increases from 3 to 5 and $\Delta\ell_{PEDOT}$ = 121 nm when θ changes from 30 to 50 s (Table 1). However, the cathodic and anodic areas decreases significantly with the number of oxidation-reduction cycles indicating that, in spite of their remarkable electroactivity, the electrochemical stability of ml-PEDOT/PNMPy films is low. This electrochemical behavior is fully consistent with the AFM images and the mechanisms proposed for the growing of the multi-layered films. Specifically, the multidirectional growing proposed for the third layer and the dense crosslinked network of the fourth layer explains the low mobility of the dopant ions in these systems upon consecutive oxidation-reduction cycles, as well as the consequent enhancement of their compactness.

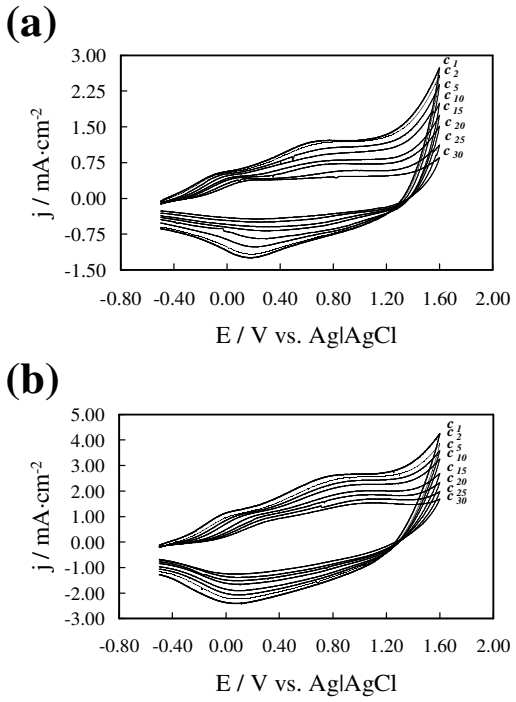

Figure 6. *Control voltammograms of 30 consecutive oxidation-reduction cycles of 3l-PEDOT/PNMPy and 5l-PEDOT/PNMPy films (top and bottom, respectively). In order to clarify the presentation only selected voltammograms are displayed. The labels c_1 and c_{30} correspond to the voltammograms recorded in the first and thirtieth cycles, respectively.*

Conductivity measurements in local regions. The electrical conductivity of ml-PEDOT/PNMPy films with 3-layered system was recently determined[24] using the sheet resistance procedure, which was previously described.[36] As this method requires specimens with reasonably good mechanical properties, measurements were performed on films prepared using polymerization times of 700 s for the first and last PEDOT layers (external sides of the films) and 200 s for the central PNMPy layer. The thickness

of the resulting 3-layered films, *i.e.* ℓ = 14 μm, was large enough to manipulate them without breaking, the measured electrical conductivity being 79 $S \cdot cm^{-1}$. Although this value is one order of magnitude smaller than that determined for PEDOT (210 $S \cdot cm^{-1}$),[26] it is significantly higher than that found for PNMPy ($5.5 \cdot 10^{-3}$ $S \cdot cm^{-1}$).[24] However, the most remarkable feature is that the conductivity of the 3-layered system was considerably higher than that of poly(EDOT-*co*-NMPy), which ranges from $6.9 \cdot 10^{-3}$ to $7.3 \cdot 10^{-1}$ $S \cdot cm^{-1}$ depending on the EDOT:NMPy molar ratios.

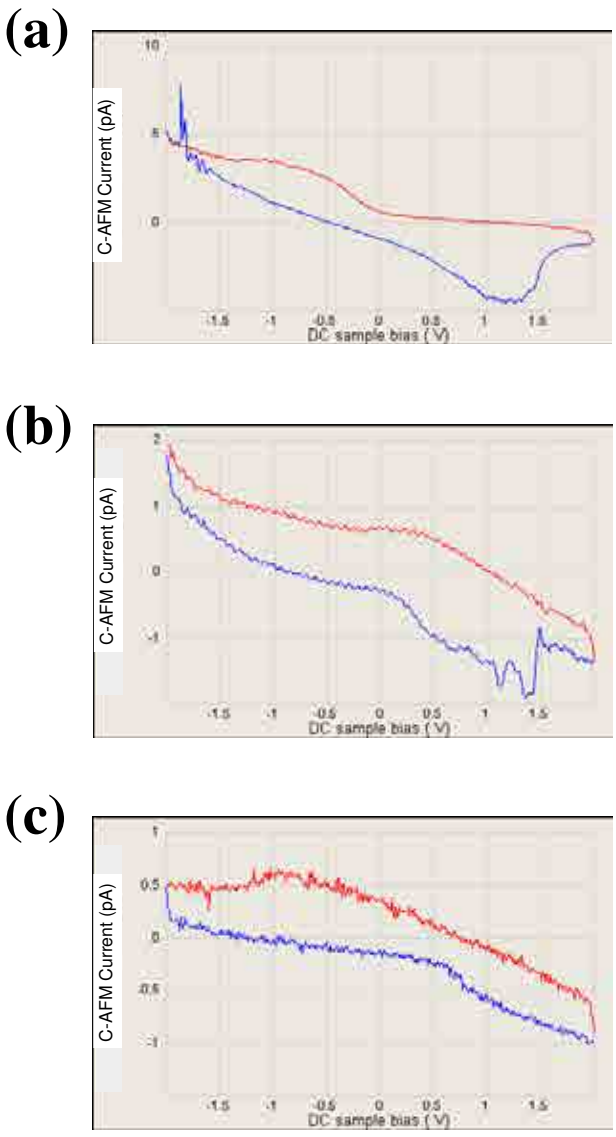

***Figure 7**. Current-voltage curve used to calculate the conductivity of PEDOT, PNMPy and 3l-PEDOT/PNMPy nanometric films (top, middle and bottom, respectively).*

In this work C-AFM has been used to investigate the local conductivity of PEDOT, PNMPy and ml-PEDOT/PNMPy nanometric films by measuring the current flow. Specifically, measurements were performed on PEDOT and PNMPy films prepared using θ = 30 s (ℓ = 345 and 519 nm, respectively) and the three layered system generated using θ = 10 s per layer (ℓ = 419 nm). The substrate-tip contact surface radius was determined using the Herz normal contact theory,[38] which takes into account the local contact surface deflection, and considering that the averaged Young's modulus for the conducting polymers and the tips diameter are 1400 kPa and 5.5 nm, respectively.

Five independent measurements of the conductivity perpendicular to the surface of the films, *i.e.* along their nanometric thickness, were obtained for PEDOT, PNMPy and the 3-layered system, the resulting average being $8.7 \cdot 10^{-5}$, $8 \cdot 10^{-6}$ and $1.0 \cdot 10^{-5}$ $S \cdot cm^{-1}$, respectively. Figure 7 shows the current-voltage curve (one of such five independent measurements) used to calculate the conductivity of the three materials. The resulting conductivities are several orders of magnitude smaller than those obtained using the sheet resistance method, *i.e.* along the macroscopic length of the films. Moreover, the nanometric conductivities of pure PEDOT and PNMPy differ by one order of magnitude only, while those measured using the sheet resistance method are different by five orders or magnitude. The difference between the electrical conductivities using the sheet resistance and C-AFM procedures was attributed to the large number local microscopic factors that alter the current flow along the thickness of the films: molecular branching and other types of molecular defects, contamination at the molecular level, charge polarization due to the dopant ions, etc. In other words, the current flow determined by C-AFM undergoes interferences induced by these microscopic phenomena,[38,39] while their effect in the macroscopic scale used by sheet resistance method is practically negligible.

3.1.4. Conclusions

The formation and growth mechanisms of single component and multilayed nanometric films of PNMPy and PEDOT have been determined using AFM. The morphological changes found for these systems are different from those reported for films obtained using other layer-by-layer deposition processes and different materials.[39,40] For PNMPy films, it was found that the first stages of the electropolymerization consist on the linear growth of molecular chains that nucleate the film, while after $\theta \geq 30$ s the process is dominated by formation of chemical crosslinks and branches. This interpretation is fully consistent with the high and low electrochemical stability of the PNMPy films prepared using $\theta < 30$ s and $\theta > 30$ s, respectively. In contrast, the large and well-defined plateau regions identified in the AFM images for single component PEDOT films electrogenerated using $\theta \geq 40$ s indicate that molecular chains tend to pack and form compact aggregates, which are probably stabilized by the perchlorate dopant anions. The linearity of the polymer molecules and the lack of chemical crosslinks explain the significant electroactivity and electrochemical stability of this material. On the other hand, the topographies recorded for ml-PEDOT/PNMPy nanometric films are consistent with a multidirectional growing model, which is induced by the PNMPy layer electrodeposited on the top of first PEDOT layer. Moreover, the results also indicate that the fourth PNMPy layer form a dense network of crosslinked chains. These features explain that, in spite of their remarkable electroactivity, *i.e.* it is significantly higher than those of single component PEDOT and PNMPy films, multilayered systems present a low electrochemical stability. From a qualitative point of view, electrical conductivities determined by C-AFM are consistent with those obtained using the sheet resistance method, evidencing that the electrical properties of multilayered films are similar to those of PEDOT homopolymer. The excellent electroactivities and good electrical conductivity of multilayered systems indicate that these materials are very promising from a technological point of view.

3.1.5. References

[1]. Decher, G. *Science* **1997**, *277*, 1232.

[2]. Decher, G.; Hong, J. *Makromol. Chem. Macromol. Symp.* **1991**, *46*, 321.

[3]. Decher, G.; Hong, J. D.; Schmitt, J. *Thin Solid Films* **1992**, *210*, 831.

[4]. Decher, G.; Schmitt, J. *Prog. Colloid Polym. Sci.* **1992**, *89*, 160.

[5]. Shi, X.; Caruso, F. *Langmuir* **2001**, *17*, 2036.

[6]. Calvo, E. J.; Forzani, E. S.; Otero, M. *Anal. Chem.* **2002**, *74*, 3281.

[7]. Dai, Z.; Voigt, A.; Leporatti, S.; Donath, E.; Dähne, L.; Möhwald, H. *Adv. Mater.* **2001**, *13*, 1339.

[8]. Caruso, F.; Shi, X.; Caruso, R. A.; Susha, A. *Adv. Mater.* **2001**, *13*, 740.

[9]. Ge, L.; Möhwald, H.; Li, J. *Chem. Eur. J.* **2003**, *9*, 2589.

[10]. Sukhorukov, G. B.; Brumen, M.; Donath, E.; Möhwald, H. *J. Phys. Chem. B* **1999**, *103*, 6434.

[11]. Cheung, J. H.; Stockton, W. B.; Rubner, M. F. *Macromolecules* **1997**, *30*, 2712.

[12]. Fou, A. C.; Rubner, M. F. *Macromolecules* **1995**, *28*, 7115.

[13]. Zheng, S.; Tao, C.; He, Q.; Zhu, H.; Li, J. *Chem. Mater.* **2004**, *16*, 3766.

[14]. Zotti, G.; Vercelli, B.; Berlin, A. *Acc. Chem. Res.* **2008**, *41*, 1098.

[15]. Zotti, G.; Zecchin, S.; Berlin, A.; Schiavon, G.; Giro, G. *Chem. Mater.* **2001**, *13*, 43.

[16]. Zotti, G.; Zecchin, S.; Schiavon, G.; Vercelli, B.; Berlin, A.; Porcio, W. *Chem. Mater.* **2004**, *16,* 2091.

[17]. Smith, R. R.; Smith, A.; Stricker, J. T.; Taylor, B. E.; Durstock M. F. *Macromolecules* **2006**, *39*, 6071.

[18]. Stricker, J. T.; Gudmundsdóttir, A. D.; Smith, A. P.; Taylor, B. E.; Durstock, M. F. *J. Phys. Chem. B* **2007**, *111*, 10397.

[19]. Wakizada, D.; Fushimi, T.; Ohkita, H.; Ito, S. *Polymer* **2004**, *45*, 8561.

[20]. DeLongchamp, D. M.; Kastantin, M.; Hammond, P. T. *Chem. Mater.* **2003**, *15*, 1575.

[21]. DeLongchamp, D. M.; Hammond, P. T. *Adv. Mater.* **2001**, *13*, 1455.

[22]. Jiang, G.; Baba, A.; Advincula, R. *Langmuir* **2007**, *23*, 817.

[23]. Estrany, F.; Aradilla, D.; Oliver, R.; Armelin, E.; Alemán, C. *Eur. Polym. J.* **2008**, *44*, 1323.

[24]. Estrany, F.; Aradilla, D.; Oliver, R.; Alemán, C. *Eur. Polym. J.* **2007**, *43*, 1876.

[25]. Oliver, R.; Muñoz, A.; Ocampo, C.; Alemán, C.; Estrany, F. *Chem. Phys.* **2006**, *328*, 299.

[26]. Ocampo, C.; Alemán, C.; Oliver, R.; Arnedillo, M. L.; Ruíz, O.; Estrany, F. *Polym. Int.* **2007**, *56*, 803.

[27]. Ocampo, C.; Oliver, R.; Armelin, E.; Alemán, C.; Estrany, F. *J. Polym. Res.* **2006**, *13*, 193.

[28]. Liesa, F.; Ocampo, C.; Alemán, C.; Armelin, E.; Oliver, R.; Estrany, F. *J. Appl. Polym. Sci.* **2006**, *102*, 1592.

[29]. Aradilla, D.; Ocampo, C.; Armelin, E.; Alemán, C.; Oliver, R.; Estrany, F. *Mater. Corr.* **2007**, *58*, 867.

[30]. Becke, A. D. *J. Chem. Phys.* **1993**, *98*, 1372.

[31]. Lee, C.; Yang, W.; Parr, R. G. *Phys. Rev. B* **1993**, *37*, 785.

[32]. Hariharan, P. C.; Pople, J. A. *Theor. Chim. Acta* **1973**, *28*, 213.

[33]. Gaussian 03, Revision B.02, M. J. Frisch, et al. Gaussian, Inc., Pittsburgh PA, 2003.

[34]. Alemán, C.; Casanovas, J.; Torras, J.; Bertran, O.; Armelin, E.; Oliver, R.; Estrany, F. *Polymer* **2008**, *49*, 1066.

[35]. Alemán, C.; Oliver, R.; Brillas, E.; Casanovas, J.; Estrany, F. *Chem. Phys.* **2005**, *314*, 1.

[36]. Brillas, E.; Carrasco, J.; Oliver, R.; Estrany, F.; Vilar, J.; Morlans, J. M. *Electrochim. Acta* **2000**, *45*, 4049.

[37]. Dintwa, E.; Tisjskens, E.; Ramon, H. *Granular Matter.* **2008**, *10*, 209.

[38]. Trionfi, A.; Scrymgeour, D. A.; Hsu, J. W. P.; Arlen, M. J.; Tomlin, D.; Jacobs, J. D.; Wang, D. H.; Tan, L. –S.; Vaia, R. A. *J. Appl. Phys.* **2008**, *104*, 083708.

[39]. Alexeev, A.; Loos, J. *Org. Electr.* **2008**, *9*, 149.

[40]. Lvov, Y.; Decher, G.; Möehwald, H. *Langmuir***1993**, *9*, 481.

[41]. Decher, G.; Lvov, Y.; Schmitt, J. *Thin Solid Films* **1994**, *244*, 772.

[42]. Ariga, K.; Onda, M.; Lvov, Y.; Kunitake, T. *Chem. Lett.* **1997**, *1*, 25.

3.2. Properties of nanometric and micrometric multilayered films made of three conducting polymers.

3.2.1. Introduction

The layer-by-layer (LbL) technique based on electrostatic or other molecular forces creates an advantageous approach to construct different types of self-assembled materials. Since the technique was first developed by Decher and others,[1-4] it has been successfully applied to fabricate ultrathin multilayered films of polyconjugated polymers.[5-15] Within this context, films fabricated by electrostatic self-assembly of poly(3,4-ethylenedioxythiophene):poly(styrenesulfonate) (PEDOT:PSS) and a polyelectrolyte, *i.e.* typically poly(allylamine hydrochloride), are the most studied.[11-15] Furthermore, conducting multilayered ultrathin films involving polypyrrole (PPy)[7,8] and some polythiophene derivatives[8-15] have been also reported.

On the other hand, the electrochemical use of LbL technique was used to prepare bilayers made of two conducting polymers (CPs) through their electrodeposition. In this methodology, individual anodic polymerization processes are used to prepare films formed by different layers. Among the studied systems, those with the more relevant properties were the bilayers made of PPy (inner layer)-poly(N-methylpyrrole) (outer layer),[16,17] and PPy – PPy[18,19] (abbreviated PPy/PNMPy and PPy/PPy, respectively), even though in the latter the composition of the two layers was identical.

Recently, multilayered systems formed by 3, 5, 7, and 9 alternated layers of two different CPs were prepared.[20,21] The thickness of each layer (ℓ) was controlled through the polymerization time used to generate it (θ_l), extending from a few nanometers ($\theta_l \leq$ 25 s) to some micrometers ($\theta_l \geq$ 1500 s). The stability and the ability to store charge of the multilayered systems formed by PEDOT and PNMPy,[16] hereafter abbreviated ml-PEDOT/PNMPy (where PEDOT refers to both the inner and outer layers and PNMPy indicate the central layer), were significantly higher than those of the copolymers derived from mixtures of the corresponding monomers with different concentration ratios[22,23] and the individual homopolymers.[24] Furthermore, the properties of these multilayered systems enhance significantly with the number of layers, while those of the homopolymers do not depend on the thickness of the films after a threshold value of a few micrometers.[20] The excellent properties of ml-PEDOT/PNMPy systems were

attrituted to the interface between the layers of the two CPs, their coupling being significantly more positive than the interaction of the different monomers in copolymers.[21]

The aim of this work is to extend the electrochemical LbL methodology to ultrathin multi-layered films prepared by the electrodeposition of the three different CPs. Preliminary experiments (described below) considering PEDOT, polypyrrole (PPy), poly[N-(2-cyanoethyl)pyrrole] (PNCPy) and PNMPy (Scheme 1) allowed to select the former three CPs for the preparation of the 4- and 7-layered films, the resulting systems being abbreviated ml-PEDOT/PPy/PNCPy. The properties of the latter systems have been examined, their advantages and limitations being discussed with respect to the multi-layered systems formed by two CPs, *i.e* ml-PEDOT/PPy, ml-PEDOT/PNCPy, and ml-PPy/PNCPy. Specifically, a great interest is devoted to the electroactivity and electrostability, which refer to the ability to store charge and electrochemical stability, respectively, the electrical conductivity, and the morphology of the new multilayered systems. It should be noted that the improvement of the electrochemical and electrical properties of systems based on CPs is essential for applications related with electronics, batteries, and anticorrosive coatings. Additionally, as ml-PEDOT/PPy, ml-PEDOT/PNCPy, and ml-PPy/PNCPy systems were not studied before, the influence of the substituent at the nitrogen atom of the pyrrole ring on the properties of these systems has been briefly discussed.

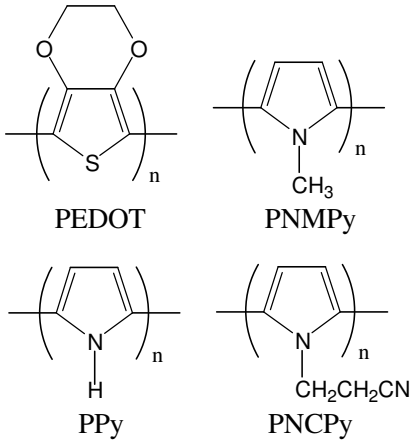

Scheme 1

3.2.2. Methods

Preparation of the multilayered films. 3,4-ethylenedioxythiophene (EDOT), pyrrole (Py), *N*-(2-cyanoethyl)pyrrole (NCPy), N-methylpyrrole (NMPy) and acetonitrile of analytical reagent grade were purchased from Aldrich. Anhydrous $LiClO_4$, analytical reagent grade, from Aldrich was stored in an oven at 80ºC before use in the electrochemical trials.

Multilayered films were prepared by chronoamperometry (CA) under a constant potential of 1.40 V.[22] Electrochemical experiments were conducted on a VersaStat II potenciostat-galvanostat connected to a computer controlled through a Power Suite Princenton Applied Research program using a three-electrode two-compartment cell under nitrogen atmosphere at 25 ºC. The working compartment was filled with 40 mL of a 10 mM monomer solution in acetonitrile with 0.1 M $LiClO_4$, while the cathodic compartment was filled with 10 mL of the same electrolyte solution. Steel AISI 316 sheets with an area of 4 cm^2 were employed as working and counter electrodes.Before each trial, electrodes were cleaned with acetone and dried in a nitrogen-flow. No polishing of the sheets was necessary because of the low roughness of steel AISI 316.[25] The reference electrode was an Ag|AgCl electrode containing a KCl saturated aqueous solution (E^o = 0.222 V *vs.* standard hydrogen electrode at 25 ºC), which was connected to the working compartment through a salt bridge containing the electrolyte solution.

The electrochemical LbL technique was used to prepare the multilayered films. For the generation of each layer the working electrode was immersed for a period of time θ_l in cells filled with 10 mM acetonitrile solution of the corresponding monomer with 0.1 M $LiClO_4$. The thickness of each layer, ℓ, was controlled through θ_l. After generate the first layer, the film was cleaned with acetonitrile and dried in a nitrogen flow before to generate each of the next layers.

Thickness of the films,electrochemical and electrical properties. The thickness of the films was estimated from the mass of polymer deposited in the electrode, m_{pol}, using the procedure reported by Schirmeisen and Beck.[26] Accordingly, m_{pol} was determined using the following relation:

$$m_{pol} = Q_{pol}\left(\frac{m}{Q}\right) \qquad (1)$$

where Q_{pol} is the polymerization charge in (millicoulombs per square centimetre) consumed in the generation of each layer and $\left(\frac{m}{Q}\right)$ is the current productivity. The volume of polymer deposited in the electrode, V_{pol}, was obtained using the values of m_{pol} and the density. The densities of PEDOT (1.66 $g \cdot cm^{-3}$) and PNMPy (1.52 $g \cdot cm^{-3}$) were reported in a previous works,[22,24] whereas those of the PPy (1.59 $g \cdot cm^{-3}$) and PNCPy (1.42 $g \cdot cm^{-3}$) have been determined by the flotation method using CCl_4/C_2H_5I and $CHCl_3/CH_2Cl_2$ mixtures, respectively, in which they are insoluble. The total thickness of each multilayered film (ℓ_{ml}) was obtained by summing the thickness determined for the individual layers, *i.e.* ($\ell_{ml} = \sum_{i=1}^{n} \ell_i$, where n is the total number of layers).

The ability to store charge (electroactivity) and electrochemical stability upon consecutive oxidation-reduction cycles (electrostability) of the multilayered films studied in this work were determined by cyclic voltammetry (CV) using an acetonitrile solution with 0.1M $LiClO_4$. The initial and final potentials were -0.50 V, while the reversal potential was 1.60 V.The electroactivity increases with the similarity between the anodic and cathodic areas of the first control voltammogram, whereas the electrostability decreases with the oxidation and reduction areas of consecutive control voltammograms. Accordingly, electroactivity and electrostability were determined through direct measure of the anodic and cathodic areas in the control voltammograms using the Power Suite Princeton Applied Research software. A scan rate of 100 $mV \cdot s^{-1}$ was used in all cases. The electrical conductivity (σ_0) of the multilayered systems was determined using the sheet-resistance method with a previously described procedure.[27]

Morphology. AFM images were obtained with a Molecular Imaging PicoSPM using a NanoScope IV controller in ambient conditions. The averaged RMS roughness (*r*) was determined using the statistical application of the Nanoscope software, which calculates the average considering all the values recorded in the topographic image with exception of the maximum and the minimum. Nanometric measurements were conducted under ambient conditions at ~50% relative humidity and 20-22 ºC. The system was placed on an active vibration isolation table for minimum acoustic disturbance (20 series, TMC, Peabody, MA, USA).

3.2.3. Results and discussion

Preparation and thickness of the films. Initially, six different 4-layered films made of three CPs by combining layers of PEDOT, PPy, PNCPy and PNMPy were electrogenerated. The chemical composition of these films, which were prepared using θ_l = 75 s, was PEDOT/A/B/PEDOT, where the first and last PEDOT indicate the inner and outer layers respectively and A/B is PNCPy/PNMPy, PNMPy/PNCPy, PPy/PNCPy, PNCPy/PPy, PPy/PNMPy or PNMPy/PPy, respectively. The two end layers of the films were made of PEDOT because it is a very stable material from both electrochemical and environmental points of view.[28-32] Differences in the measured electroactivities, which were obtained by determining the cathodic and anodic areas, reflect the influence of the chemical nature of the CPs on the electrochemical properties of these 4-layered films. Thus, the PEDOT/PPy/PNCPy/PEDOT and PEDOT/PNCPy/PNMPy/PEDOT films showed the highest and lowest electroactivity, respectively, the difference between them being of about 20%. The reduction in the ability to store charge of the remaining 4-layered films with respect to that of the PEDOT/PPy/PNCPy/PEDOT one ranged from 16% to 5%. According to these results, the rest of this work has been focused on ml-PEDOT/PPy/PNCPy systems.

Ml-PEDOT/PPy/PNCPy, ml-PEDOT/PPy and ml-PEDOT/PNCPy films were generated applying a constant potential of 1.40 V and θ_l = 10, 20, 30, 50, 75 and 100 s. The total thickness of *n*-layered films, ℓ_{ml}, was controlled through the total polymerization time, θ_{ml}, which is defined as: $\theta_{ml} = n \cdot \theta_l$. All the multilayered films produced in this work were adherent, uniform, insoluble and homogeneous, independently of θ_{ml}. Figure 1a represents ℓ_{ml} against θ_{ml} for the PEDOT/PPy/PNCPy/PEDOT films prepared in this work. The linear behaviour provides a growing rate of 11.5 nm·s^{-1} during the electropolymerization process, the ℓ_{ml} values experimentally determined for 40 and 400 s being 520 nm and 4.60 μm, respectively. However, the contribution of each polymer to such ℓ_{ml} values is different as it is reflected in Figure 1b, which depicts the values of ℓ determined for layers of PEDOT, PPy and PNCPy against θ_l. PEDOT layers are slightly thicker than PPy layers, the latter being in turn significantly thicker than the PNCPy ones. Thus, the growing rates of PEDOT, PPy and PCNPy layers during the corresponding anodic polymerization processes are 12.4, 11.8 and 9.7 nm·s^{-1}, respectively.

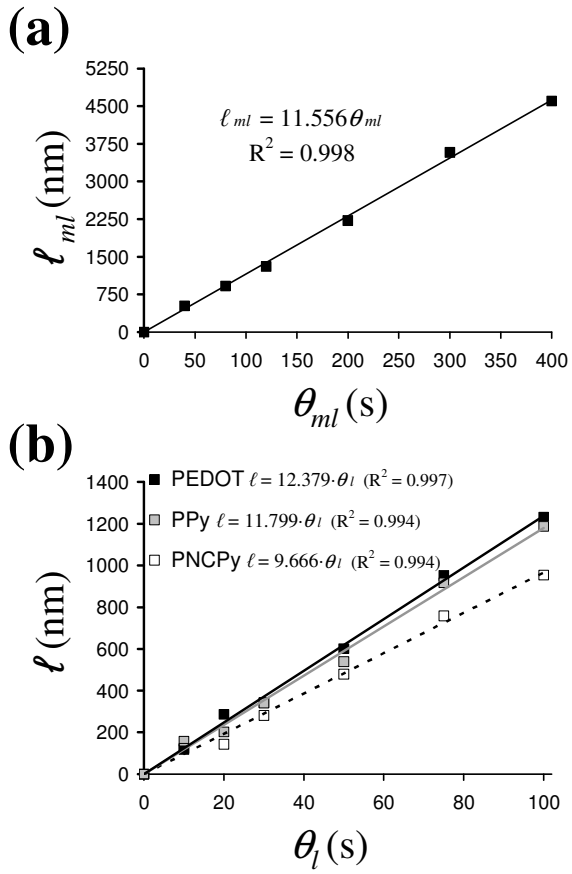

Figure 1. *Variation of: (a) the thickness of the PEDOT/PPy/PNCPy/PEDOT films (ℓ_{ml}) against the total polymerization time (θ_{ml}); and (b) the thickness of the PEDOT, PPy and PNCPy layers (ℓ) in PEDOT/PPy/PNCPy/PEDOT films against the polymerization time used to produce the layer (θ_l). The fittings used to obtain the growing rates are displayed in all cases.*

Influence of the number of components in the ability to store charge. Table 1 lists the relative electroactivities of the different systems discussed in this section, the 4-layered PEDOT/PPy/PNCPy/PEDOT film prepared using θ_l = 75 s (ℓ_{ml} = 3.58μm) being taken as reference. The control voltammogram of the latter system is compared in Figure 2a with those of the 3-layered PEDOT/PPy/PEDOT and PEDOT/PNCPy/PEDOT films, which were prepared using θ_l = 100 s (ℓ_{ml} = 3.61 and 3.37 μm, respectively), *i.e.* θ_{ml} = 300 s in the three cases. Determination of the cathodic and anodic areas indicates that the electroactivity of the 4-layered system made of 3-components is higher than that of the 3-layered PEDOT/PNCPy/PEDOT film, but almost identical to that measured for the PEDOT/PPy/PEDOT one (Table 1). These differences may be significantly influenced by the fact that the number of interfaces separating consecutive layers is higher in the 4-layered ml-PEDOT/PPy/PNCPy film than in the 3-layered ml-PEDOT/PPy and ml-PEDOT/PNCPy films. Thus, previous

studies indicated that the electroactivity of multilayered films increases considerably with the number of layers.[20]

Table 1. *Variation of the electroactivity (in %) relative to the 4-layered PEDOT/PPy/PNCPy/PEDOT film prepared using θ_l= 75 s and the electrostability[a] (in %) of the systems investigated in this work.*

Components	*Number of layers*	θ_l *(s)*	*Electroactivity*	*Electrostability*
PEDOT/PPy	3	10	-72	46
		20	-29	61
		75	-9	39
		100	-1	11
	7	100	+28	2
PEDOT/PNCPy	3	10	-85	58
		20	-39	58
		75	-20	44
		100	-14	12
	7	100	+14	5
PEDOT/Ppy/PNCPy	4	10	-42	68
		20	-29	51
		30	-12	53
		50	-4	50
		75	0	12
		100	+2	3
	7	100	+7	2

[a] *The electrostability was determined as the reduction in the electroactivity after 25 consecutive oxidation-reduction cycles (i.e. the reduction in % between the electroactivity measured in the 1st and the 25th control voltammograms).*

The effect of the number of interfaces is eliminated in Figure 2b, which compares the control voltammograms recorded for three 7-layered films produced using θ_l = 100 s (θ_{ml} = 700 s in all cases): one involving three components, PEDOT/PPy/PNCPy/PEDOT/PPy/PNCPy/PEDOT (ℓ_{ml} = 8.31 μm), and two made of alternated layers of PEDOT/PPy (ℓ_{ml} = 8.35 μm) and PEDOT/PNCPy (ℓ_{ml} = 7.93 μm). As expected the electroactivity of the ml-PEDOT/PPy and ml-PEDOT/PNCPy films is significantly higher than that displayed in Figure 2a, which is consequence of the increase in the number of layers. In contrast, the ability to store charge of the 7-layered film formed by three CPs remains similar to that obtained for the 4-layered one (Table 1). Consequently, the ability to store charge of ml-PEDOT/PPy/PNCPy is smaller than that of ml-PEDOT/PPy and ml-PEDOT/PNCPy, respectively.

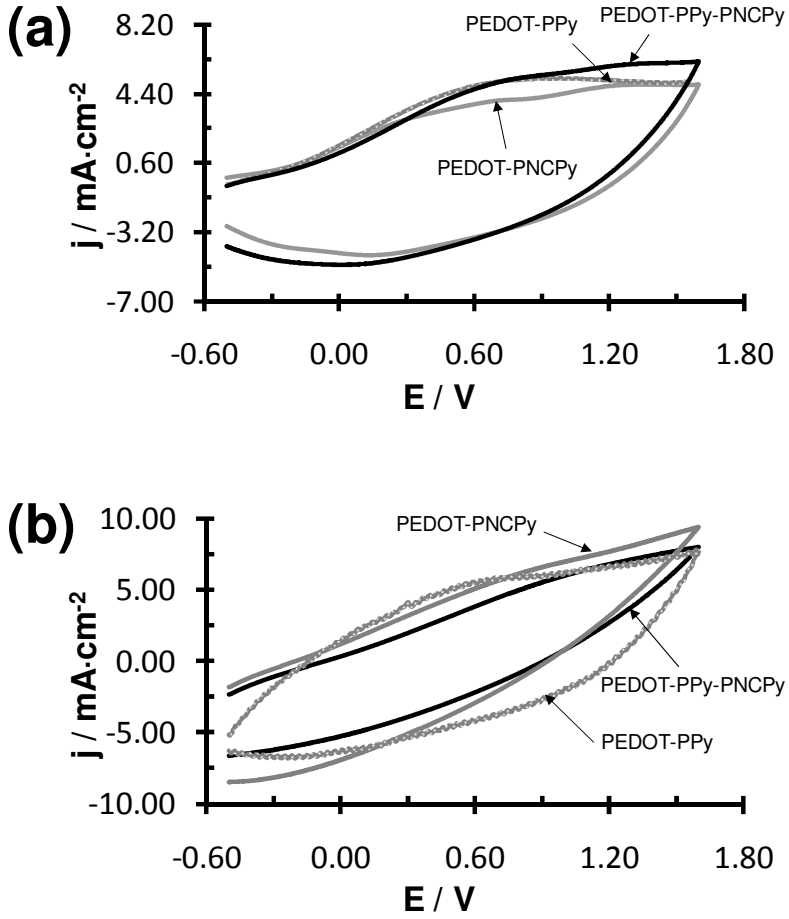

Figure 2. *Control voltammograms for the oxidation of: (a) the PEDOT/PPy/PNCPy/PEDOT (4-layered; θ_l = 75 s), PEDOT/PPy/PEDOT and PEDOT/PNCPy/PEDOT (3-layered; θ_l = 100 s) films produced using θ_{ml} = 300 s; and (b) the 7-layered ml-PEDOT/PPy/PNCPy, ml-PEDOT/PPy and ml-PEDOT/PNCPy films generated using θ_l = 100 s (θ_{ml} = 700 s in all cases).*

Considering that the thickness of the three films is similar, these results indicate that the third component reduces the ability to store charge, which should be attributed to the heterogeneity of the interfaces in the films made of three CPs, *i.e.* PEDOT···PPy, PPy···PNCPy and PNCPy···PEDOT.

In order to investigate the influence of θ_l in the electroactivity of ml-PEDOT/PPy/PNCPy systems, 4-layered films produced using θ_l values ranging 10 from 100 s were studied by CV. Figure 3 compares the voltammograms obtained for the films prepared using θ_l = 10 and 100 s. The electroactivity was found to increase very rapidly with θ_l until a threshold thickness was reached. After this, the enhancement of the ability to store charge was moderate of even negligible. Thus, results indicate that for the films prepared using $\theta_l \geq 50$ s the benefit produced by the interactions at the interfaces is dominated by the bulk at the different layers. Interestingly, the influence of θ_l on the 3-layered PEDOT/PPy/PEDOT and PEDOT/PNCPy/PEDOT films was significantly higher than that described for the 4-layered films (Table 1). These features are reflected in Figure 3, which also includes the voltammograms recorded for the 3-layered PEDOT/PPy/PEDOT and PEDOT/PNCPy/PEDOT films obtained using θ_l = 10 and 100 s. It should be noted that, although the relative variation of the electroactivity with θ_l is very similar for PEDOT/PPy/PEDOT and PEDOT/PNCPy/PEDOT films, the ability to store charge is larger for the former than for the latter for all the θ_l values.

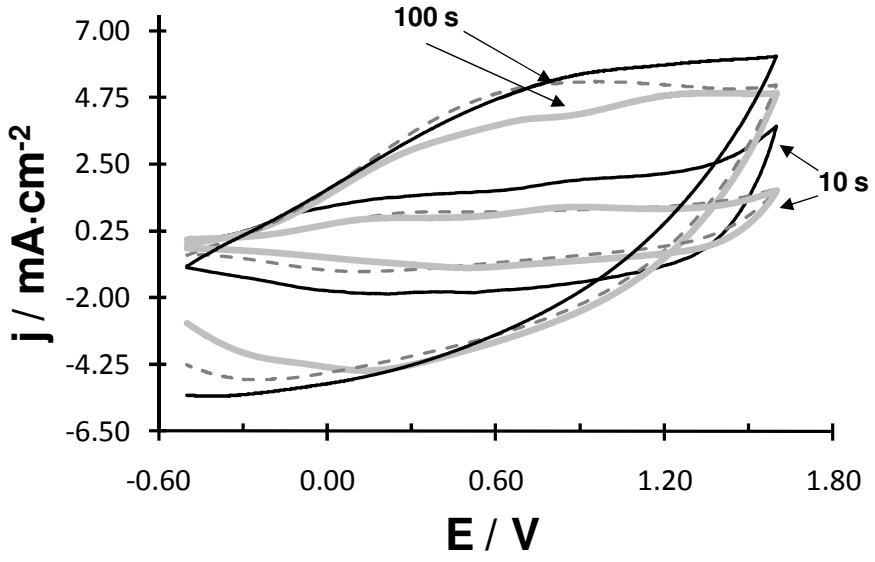

Figure 3. *Control voltammograms for the oxidation of the 4-layered PEDOT/PPy/PNCPy/PEDOT (solid and black line), 3-layered PEDOT/PPy/PEDOT (dashed and dark gray line) and 3-layered PEDOT/PNCPy/PEDOT (solid and light gray line) films generated using* θ_l *= 10 and 100 s.*

Influence of the number of components in the electrostability. Table 1 includes the electrostabilities of the multilayered systems investigated in this work. Figure 4a displays the first and the last control voltammograms from 25 consecutive oxidation-reduction cycles recorded for the 4-layered PEDOT/PPy/PNCPy/PEDOT films generated using θ_l = 10 and 75 s, *i.e.* nano- and micrometric layers, respectively. As it can be seen, the electrochemical stability strongly depends on the thickness of the film.

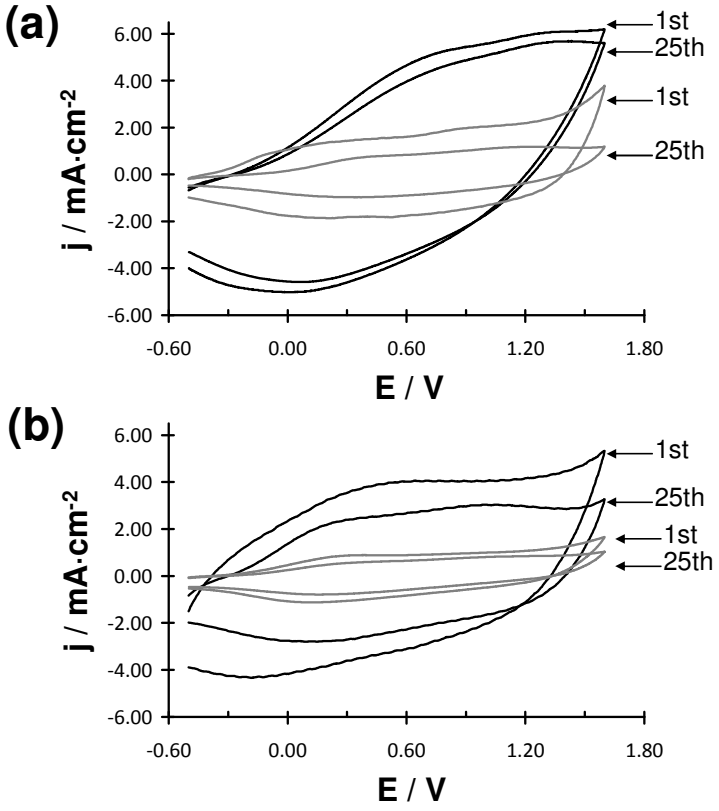

Figure 4. *First and last control voltammograms from 25 consecutive oxidation-reduction cycles of (a) 4-layered PEDOT/PPy/PNCPy/PEDOT and (b) 3-layered PEDOT/PPy/ PEDOT films prepared using θ_l = 75 s (black) and θ_l = 10 s (grey).*

Specifically, the reduction in the electroactivity after the 25th cycle with respect to the first cycle was significantly higher for the film made of nanometric layers than for the one with micrometric layers. The first and last control voltammograms from 25 consecutive oxidation-reduction cycles of the PEDOT/PPy/PEDOT films generated using the same experimental conditions are provided in Figure 4b. The reduction in the electroactivity of these films generated indicate that the electrostability of the ml-PEDOT/PPy films is higher than that of ml-PEDOT/PNCPy ones, even although the difference between the two systems decreases when the thickness of the films increases. In order to get a deeper insight into this feature, the electrostability of the 4-layered (ml-

PEDOT/PPy/PNCPy) and 3-layered (ml-PEDOT/PPy and ml-PEDOT/PNCPy) films prepared using θ_l = 10, 20, 30, 50, 75 and 100 s was investigated.

Figure 5 represents the loss of electroactivity against θ_l for the produced films. In all cases the electrostability increases with θ_l, the behavior showed by films made of two and three CPs being similar. The loss electroactivity is very significant when the thickness of film is below of a given threshold, which is reached when θ_l = 50 and 75 s for films made of three and two CPs, respectively, *i.e.* when the thickness of the films is close to 2 μm. After this, a pronounced increase of the electrostability is detected, the loss of electroactivity after the 25th cycle decreasing from ~50% to ~10%. The results obtained for the 7-layered ml-PEDO/PPy/PNCPy, ml-PEDOT/PPy and ml-PEDOT/PNCPy films produced using θ_l = 100 s were fully consistent with this behavior.

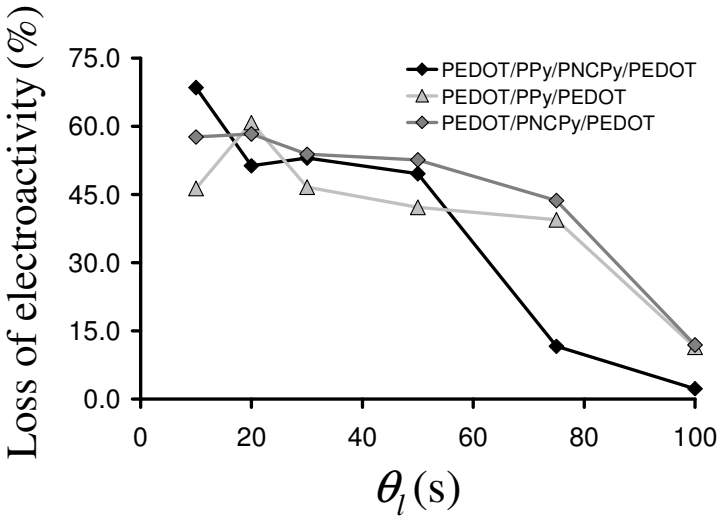

Figure 5. *Evolution of the loss of electroactivity upon 25 consecutive oxidation-reduction cycles against θ_l for the multilayered systems investigated in this work.*

Electrical Conductivity. The electrical conductivities (σ_0) measured for the ml-PEDOT/PPy/PNCPy, ml-PEDOT/PPy and ml-PEDOT/PNCPy films produced using θ_l = 75 and 100 s, *i.e.* films of micrometric thickness, are listed in Table 2. The σ_0 of the multilayered systems made of three CPs, which include 4- and 7-layered films, ranges from 3.7 to 8.9 S·cm^{-1}, evidencing that this property is practically independent of both the thickness of the films and the number of layers. These features are confirmed by the σ_0 determined for ml-PEDOT/PPy and ml-PEDOT/PNCPy films, which are one order of magnitude higher than those obtained for the ml-PEDOT/PPy/PNCPy ones. Thus, the σ_0 of the ml-PEDOT/PPy films ranges from 27 to 63 S·cm^{-1}, while that of ml-

PEDOT/PNCPy ones varies between 19 and 59 $S \cdot cm^{-1}$. On the other hand, the σ_0 values obtained for single layered films of PEDOT, PPy and PNCPy prepared using a polymerization time of 300 s are 160, 0.11 and $5 \cdot 10^{-3}$ $S \cdot cm^{-1}$, respectively. The σ_0 of PNCPy is very close to that reported for PNMPy ($5.5 \cdot 10^{-3}$ $S \cdot cm^{-1}$)[23] evidencing the negative influence of the N-substitution on the electric properties of PPy. Thus, substituents at the N-position produce severe steric clashes that disturb the molecular planarity and, therefore, reduce the π-conjugation.

Table 1. *Electrical conductivity (σ_0) of ml-PEDOT/PPy/PNCPy, ml-PEDOT/PPy and ml-PEDOT/PNCPy films.*

System (conditions)	**σ_0 ($S \cdot cm^{1}$)**
ml-PEDOT/PPy/PNCPy (4 layers; θ_l = 75 s)	6.8
ml- PEDOT/PPy/PNCPy (4 layers; θ_l = 100 s)	8.9
ml- PEDOT/PPy/PNCPy (7 layers; θ_l = 100 s)	5.2
ml-PEDOT/PPy (3 layers; θ_l = 75 s)	27
ml-PEDOT/PPy (3 layers; θ_l = 100 s)	63
ml-PEDOT/PPy (7 layers; θ_l = 100 s)	41
ml-PEDOT/PNCPy (3 layers; θ_l = 75 s)	19
ml-PEDOT/PNCPy (3 layers; θ_l = 100 s)	59
ml-PEDOT/PNCPy (3 layers; θ_l = 100 s)	32
PEDOT (1 layer; θ_l = 300 s)	137
PPy (1 layer; θ_l = 300 s)	0.11
PNCPy (1 layer; θ_l = 300 s)	$5 \cdot 10^{-3}$

The overall of these results reflects that multilayered systems are influenced by the σ_0 of each individual component and not only by the component of lowest σ_0, as is typically found in copolymers.[23] This represents a significant advantage from a technological point of view since the formation of multilayered films improves the ability to store charge with respect all the individual components, while the detriment in the conductivity with respect to the component with highest σ_0 is only moderate. However, it should be noted that in the case of films constituted by three CPs the influence of the material with lowest σ_0 is higher than in those made of two CPs.

Morphology of the layers. The morphologic and topographic analyses of the CP films are helpful to understand the electroactivity and electrostability of these materials. Figure 6 shows the 3D (height mode) AFM image of each layer for the PEDOT/PPy/PNCPy/PEDOT film produced using θ_l = 75 s. As it can be seen, the first PEDOT layer, which is directly electrodeposited on the steel electrode, presents an irregular and heterogeneous surface with an average roughness of r = 293 nm. In spite of this relatively low roughness, dense distributions of peaks grouped forming compact blocks located in plateau regions at high topological levels are clearly identified in Figure 6a. PEDOT molecules are exclusively formed by α-α linkages since the dioxane ring fused onto the thiophene ring occupies the β-positions of the latter. Thus, the absence of crosslinkings allows relate these clusters with compact molecular aggregates of linear chains, which are probably stabilized by the incorporated perchlorate anions.[33] Thus, the reduction in the cathodic and anodic areas with the number of oxidation-reduction cycles observed for PEDOT[24] should be attributed to such molecular aggregates, which make more difficult the mobility of the dopant ions in these compact regions. However, the mobility of the dopant anions upon oxidation and reduction processes in the remaining regions is not restricted by the formation of crosslinks explaining the excellent electrostability of this material.

On the other hand, PPy is known to present a significant tendency to form chemical crosslinks.[34] This is consistent with the 3D AFM image displayed in Figure 6b for the second layer of the ml-PEDOT/PPy/PNCPy film. Thus, PPy fills the spaces and voids detected in the first PEDOT layer providing a globular surface. As the electropolymerization of PPy is dominated by the crosslinks, which give place to a non-regular growing process, *i.e.* polymer chains form multidirectional branches, the average roughness decreases to r = 220 nm. The dense network of chemical crosslinks

precludes the diffusion of the dopant ions explaining the low electroactivity and electrostability of this material with respect to PEDOT. Regarding to the third layer, Figure 6c indicates that the globular morphology is even more pronounced for the PNCPy than for PPy, the roughness of the former material remaining relatively close (r = 253 nm) to that of the latter one. Again, this is fully consistent with electrochemical behaviour observed for PNCPy, *i.e.* low electroactivity and electrostability. Finally, the last PEDOT layer (Figure 6d) exhibits the expected irregular morphology and a significant increase of the roughness (r = 387 nm).

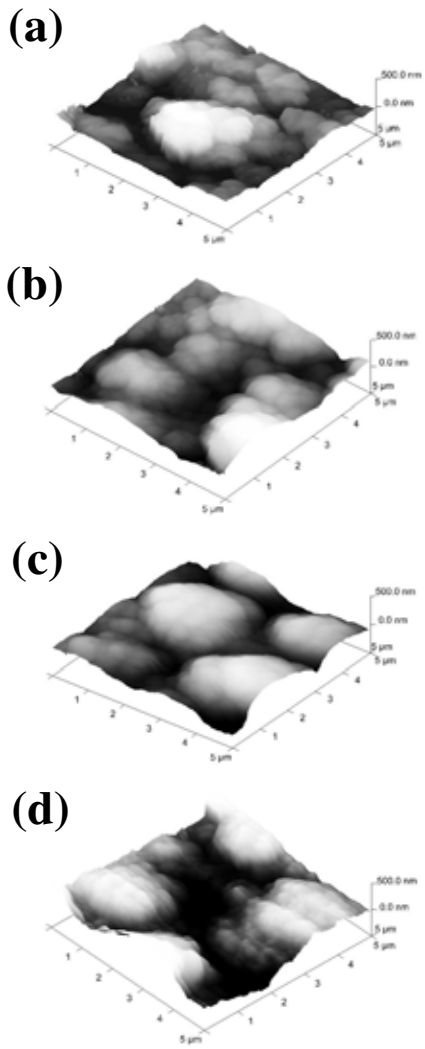

Figure 6. *3D AFM images the 4-layered ml-PEDOT/PPy/PNCPy film prepared using θ_l = (75s). The images correspond to the PEDOT layer directly electrodeposited on the steel electrodea), the PPy layer (b), the PNCPy layer (c) and the external PEDOT layer (d).*

3.2.4. Conclusions

Multilayered films constituted by three CPs (ml-PEDOT/PPy/PNCPy) have been prepared using the electrochemical LbL technique with different polymerization times, θ_l = 10, 20, 30, 50, 75 and 100 s, which allowed control the thickness of the layers. The electroactivity, electrostability and electrical conductivity of these films have been examined and compared with those of multilayered films made of two CPs (ml-PEDOT/PPy and ml-PEDOT/PNCPy). The electrochemical behavior of films formed by micrometric and nanometric layers has been found to be significantly different. More specifically, the ability to store charge of the ml-PEDOT/PPy/PNCPy films increases with θ_l until a threshold thickness (~ 2 μm) is reached, the increment of the electroactivity being very small or even negligible for thicker films. In opposition the loss of electroactivity upon consecutive oxidation-reduction cycles is relatively important for the ml-PEDOT/PPy/PNCPy films formed by nanometric layers, while the electrostability increases significantly for the films with $\ell_{ml} \geq 4$ μm. On the other hand, the heterogeneity introduced by the third CP seems to reduce the electroactivity and electrostability of the ml-PEDOT/PPy/PNCPy films with respect to those formed by two CPs only. Among the latter, the electrochemical properties of the ml-PEDOT/PPy films were better than those of the ml-PEDOT/PNCPy ones, *i.e.* the electroactivity and electrostability of the former were higher than those of the latter. Finally, the electrochemical properties of the ml-PEDOT/PPy/PNCPy films have been found to be fully consistent with the morphology and topography of the PEDOT, PPy and PNCPy layers, which were studied using AFM.

3.2.5. References

[1]. Decher, G. *Science* **1997**, *277*, 1232.

[2]. Decher, G.; Hong, J. *Makromol. Chem. Macromol. Symp.* **1991**, *46*, 321.

[3]. Decher, G.; Hong, J. D.; Schmitt, J. *Thin Solid Films* **1992**, *210*, 831.

[4]. Decher, G.; Schmitt, J. *Prog. Colloid Polym. Sci.* **1992**, *89*, 160.

[5]. Cheung, J. H.; Stockton, W. B.; Rubner, M. F. *Macromolecules* **1997**, *30*, 2712.

[6]. Fou, A. C.; Rubner, M. F. *Macromolecules* **1995**, *28*, 7115.

[7]. Zheng, S.; Tao, C.; He, Q.; Zhu, H.; Li, J. *Chem. Mater.* **2004**, *16*, 3766.

[8]. Zotti, G.; Vercelli, B.; Berlin, A. *Acc. Chem. Res.* **2008**, *41*, 1098.

[9]. Zotti, G.; Zecchin, S.; Berlin, A.; Schiavon, G.; Giro, G.; *Chem. Mater.* **2001**, *13*, 43.

[10]. Zotti, G.; Zecchin, S.; Schiavon, G.; Vercelli, B.; Berlin, A.; Porcio, W. *Chem. Mater.* **2004**, *16*, 2091.

[11]. Smith, R. R.; Smith, A.; Stricker, J. T.; Taylor, B. E.; Durstock M. F. *Macromolecules* **2006**, *39*, 6071.

[12]. Stricker, J. T.; Gudmundsdóttir, A. D.; Smith, A. P.; Taylor, B. E.; Durstock, M. F.*J. Phys. Chem. B* **2007**, *111*, 10397.

[13]. Wakizada, D.;Fushimi, T.; Ohkita, H.; Ito, S. *Polymer* **2004**, *45*, 8561

[14]. DeLongchamp, D. M.; Kastantin, M.; Hammond, P. T. *Chem. Mater.* **2003**, *15*, 1575.

[15]. Jiang, G.; Baba, A.; Advincula, R. *Langmuir* **2007**, *23*, 817.

[16]. Wodja, A.; Maksymiuk, K. *J. Electroanal. Chem.* **1997**, *424*, 93.

[17]. Dumanska, J.; Maksymiuk, K. *Corr. Sci.* **2002**, *44*, 1681.

[18]. Kepas, A.; Grzeszczuk, M. *J. Electroanal. Chem.* **2005**, *582*, 209.

[19]. Grzeszczuk, M.; Kalenik, J.; Kepas-Suwaran, A. *J. Electroanal. Chem.* **2009**, *626*, 47.

[20]. Estrany, F.; Aradilla, D.; Oliver, R.; Armelin, E.; Alemán, C. *Eur. Polym. J.* **2008**, *44*, 1323.

[21]. Estrany, F.; Aradilla, D.; Oliver, R.; Alemán, C. *Eur. Polym. J.* **2007**, *43*, 1876.

[22]. Oliver, R.; Muñoz, A.; Ocampo, C.; Alemán, C.; Estrany, F. *Chem. Phys.* **2006**, *328*, 299.

[23]. Ocampo, C.; Alemán, C.; Oliver, R.; Arnedillo, M. L.; Ruíz, O.; Estrany, F. *Polym. Int.* **2007**, *56*, 803.

[24]. Ocampo, C.; Oliver, R.; Armelin, E.; Alemán, C.; Estrany, F. *J. Polym. Res.* **2006**, *13*, 193.

[25]. Aradilla, D.; Estrany, F.; Armelin, E.; Alemán, C. *Thin Solid Films* **2010**, *518*, 4203.

[26]. Schirmesisen, M.; Beck, F. J. *J. Appl. Electrochem.* **1989**, *19*, 401.

[27]. Carrasco, J.; Brillas, E.; Fernández, V.; Cabot, P. L.; Garrido, J. A.; Centellas, F. *J. Electrochem. Soc.* **2001**, *148*, E19.

[28]. Groenendaal, B. L.; Jonas, F.; Freitag, D.; Pielartzik, H.; Reynolds, J. R. *Adv. Mater.* **2000**, *12*, 481.

[29]. Pei, Q.; Zuccarello, G.; Ahlskog, M.; Inganäs, O. *Polymer* **1994**, *35*, 1347.

[30]. Crispin, X.; Jakobsson, F. L. E.; Crispin, A.; Grim, P. C. M.; Andersson, P.; Volodin, A. *Chem. Mater.* **2006**, *18*, 4354.

[31]. Breiby, D. W.; Samuelsen, L. B.; Groenendaal, B.; Struth, B. *J. Polym. Sci: Part B: Polym Phys* **2003**, *41*, 945.

[32]. Jönsson, S. K. M.; Birgersson, J.; Crispin, X.; Grezynsky, G.; Osikowicz, A. W. D.; van der Gon, W. D. *Synth. Met.* **2003**, *139*, 1.

[33]. Alemán, C.; Oliver, R.; Brillas, E.; Casanovas, J.; Estrany, F. *Chem. Phys.* **2005**, *314*, 1.

[34]. Alemán, C.; Casanovas, J.; Torras, J.; Bertrán, O.; Armelin, E.; Oliver, R. *Polymer* **2008**, *49*, 1066.

3.3. Symmetric supercapacitors based on multilayers of conducting polymers.

3.3.1. Introduction

Among conducting polymers (CPs), polythiophene derivatives have emerged as promising materials in different fields, such as electronics, biotechnology and nanotechnology.[1-8] More specifically, poly(3,4-ethylenedioxythiophene), hereafter abbreviated PEDOT (Scheme 1), is one of the most important CPs due to its high conductivity (up to 500 S/cm), good thermal and chemical stability, fast doping-dedoping processes and excellent biocompatibility.[9-12] Moreover, PEDOT presents excellent electrochemical properties in terms of electroactivity and electrostability, explaining the high ability of this material to store charge (*i.e.* electrical energy).[13,14] Charge storage plays an important role in electronic devices, such as capacitors and supercapacitors.

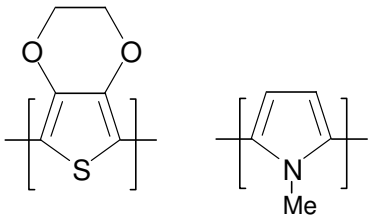

Scheme 1

Supercapacitors are electrochemical energy store devices that work like large version of common electrical capacitors. Unlike batteries, supercapacitors store their energy in an electrostatic field rather than in chemical form.[15-17] Batteries are charged when they undergo an internal chemical reaction, delivering the absorbed energy when they reverse the chemical reaction. In contrast, when a supercapacitor is charged, there is no chemical reaction, the energy being stored as a charge in the material. The exploration, improvement and discovery of new electrode materials to achieve supercapacitors with better electrochemical properties is a challenge. The principles of supercapacitors include an electric double layer and pseudo-capacitive charge-storage modes. The former, similar to a physical dielectric capacitor, is based on the separation of charges at the interface between a solid electrode and an electrolyte and the latter is a fast Faradaic process involving electrochemical redox reactions. Currently, the electrode

materials for supercapacitors mainly include carbon, transition metal oxides, and conducting polymers. The current state-of-the-art advanced materials for supercapacitors have been reviewed by different authors.[18-20] Among them, that reported by Snook *et al.*[20] is particularly interesting because they review supercapacitor electrodes that utilize CPs to bridge the gap between existing carbon-based supercapacitors and batteries to form units of intermediate specific energy. Specifically, these authors looked at the major CP materials, namely, polyaniline, polypyrrole, polythiophene and derivatives of polythiophene, as well as composites of these materials with carbon nanotubes and inorganic materials.

Although, PEDOT is considered a good candidate for capacitor electrodes because of its electrochemical properties,[21] its high molar mass and moderate specific capacitance compared with other CPs suggest the exploration of new alternatives.[22] In recent years significant efforts have been devoted to improve the capacitive properties of PEDOT.[10,23] Within this context, composites based on transition metal oxides (*e.g.* MnO_2, NiO, Fe_3O_4, and V_2O_5) embedded into a PEDOT polymeric matrix showed better capacitive properties than pure PEDOT.[24-26] Other approaches based on the preparation of PEDOT-containing nanocomposites and nanotubes have been used to improve the use of this CP for electrochemical capacitor electrodes.[27-29]

Supercapacitors based on CPs can be categorized into three different configurations.[30] Type I consists of symmetric systems, which use the same *p*-dopable CP for the two electrodes. Type II corresponds to asymmetric systems based on two different *p*-dopable CPs with very different electroactivities. Finally, type III supercapacitors are formed by symmetric systems that use the *p*-doped form of a CP as the positive electrode and the *n*-doped form of the same material as the negative electrode. Supercapacitor devices based on configurations of types I and II are the most common due to the fact that the preparation of *p*-doped CPs is easier than that of *n*-doped CPs.

Recently, some studies based on multilayered conducting systems that alternate PEDOT and poly(N-methylpyrrole) (PNMPy; Scheme 1) have been reported.[31,32] These multilayered materials, which were prepared using the layer-by-layer (LbL) electrodeposition technique, showed better electrochemical properties and higher ability to store charge than each of the two individual CPs. This improvement increased with the number of layers and was attributed to a synergistic effect produced by a favorable interaction between the PEDOT and PNMPy layers at the interfaces. Thus, the coupling

between PEDOT and PNMPy was found to be, in terms of enhancement of the electrochemical properties, significantly more positive for the multilayered films than the interaction of the corresponding monomers in copolymers.[33]

In this work the performance of multilayered systems made of PEDOT and PNMPy, hereafter denoted ml-PEDOT/PNMPy is examined to be used as supercapacitor electrodes of type I. For this purpose the capacitive properties of the multilayered systems have been investigated using cyclic voltammetry (CV) and electrochemical impedance spectroscopy (EIS) methods. Structural analyses based on scanning electron microscopy (SEM) and tapping-mode atomic force microscopy (AFM) have been used to rationalize the behavior of ml-PEDOT/PNMPy. Furthermore, in order to compare with the corresponding individual monolayered CPs, the whole study has been simultaneously developed for PEDOT and PNMPy considering experimental conditions identical to those used for ml-PEDOT/PNMPy.

3.3.2. Methods

Materials. 3,4-ethylenedioxythiophene (EDOT), N-methylpyrrole (NMPy) and acetonitrile of analytical reagent grade were purchased from Aldrich and used without further purification. Anhydrous lithium perchlorate ($LiClO_4$), analytical reagent grade, from Aldrich was stored in an oven at 80 ºC before use in the electrochemical trials.

Synthesis and electrochemical measurements. PEDOT and PNMPy were obtained by potentiostatic electropolymerization at 1.4 V[34] in an acetonitrile solution containing 0.01 M of the corresponding monomer and 0.1 M $LiClO_4$ using polymerization times (θ) ranging from 100 to 500 s. Polymerizations were carried out in a standard three-electrode cell consisting of steel AISI 316 sheets of 4 cm^2 area (or 1cm^2 for morphological studies; see below) serving as working and counter electrodes, and Ag|AgCl reference electrode containing a KCl saturated aqueous solution (E^o = 0.222 V at 25 ºC). In order to avoid interferences during the electrochemical analyses, the working and counter electrodes were cleaned with acetone and dried in an air-flow before each trial.

Chronoamperometric measurements during the anodic electrodeposition of monomers were controlled using a VersaStat II potenciostat-galvanostat connected to a computer controlled through a Power Suite Princenton Applied Research program. After electropolymerization, the coated electrodes were cleaned with acetonitrile

(generation medium) and dried with nitrogen. The LbL electrodeposition procedure used to prepare multilayered films of PEDOT and PNMPy (*i.e.* ml-PEDOT/PNMPy) was detailed in previous works.[31,32] A discussion about the effects of the order of the electrodeposited polymers and the number of layers on the main properties of these multilayered systems was recently reported.[31,32,35]

The specific capacitance (*SC*; in F/g) of the active materials in the electrode was calculated as:

$$SC = \frac{Q}{\Delta V m} \tag{1}$$

where Q is voltammetric charge, which is determined by integrating either the oxidative or the reductive parts of the cyclic voltammogram curve, ΔV is the potential window and m is the mass of polymer on the surface of the working electrode. The latter is derived from the productivity current and polymerization charge.[34] Additionally, the *SC* was determined using the galvanostatic charge/discharge curves by applying the following expression to the linear part of the profiles:

$$SC = \frac{i\Delta t}{\Delta V m} \tag{2}$$

where i is the current intensity and Δt is the time interval required for the change in voltage ΔV. The *SC* values measured for multilayered systems have been are referred in all cases to the mass of PEDOT exclusively.

The loss of electrostability (*LES*) was determined as:

$$LES = \frac{\Delta Q}{Q_i} 100 \tag{3}$$

where ΔQ is the difference of voltammetric charge between the second cycle and the last cycle and Q_i is the voltammetric charge corresponding to the second cycle. Finally, the coulomb efficiency (η) was defined as the ratio between the discharge and charge times (t_d and t_c, respectively):

$$\eta = \frac{t_d}{t_c} 100 \tag{4}$$

Electrochemical impedance spectra (EIS) were taken at open circuit (OCP) over the frequency range 10 kHz – 10 mHz with a potential amplitude of 0.05 V using an AUTOLAB-302N potentiostat/galvanostat. All the electrochemical assays were carried out in an acetonitrile solution containing 0.1 M $LiClO_4$.

Morphological characterization. Morphological studies were performed using SEM and tapping-mode AFM. Topographic AFM images were obtained with a Molecular Imaging PicoSPM using a NanoScope IV controller in ambient conditions. The root mean square (RMS) roughness (*r*) was determined using the statistical application of the Nanoscope software, which calculates the average considering all the values recorded in the topographic image with exception of the maximum and the minimum. AFM measurements were performed on various parts of the films, which produced reproducible images similar to those displayed in this work. SEM images were analyzed using a Focused Ion Beam Zeiss Neon40 scanning electron microscope at 3 kV.

3.3.3. Results and discussion

Electrochemical and capacitive behavior. The nearly rectangle shape of the CV curves recorded for PEDOT, PNMPy and ml-PEDOT/PNMPy films, which are displayed in the Figure 1, corresponds to that typically found for electrochemical capacitors.[21] PEDOT shows higher voltammetric charge than PNMPy prepared using identical experimental conditions, the *SC* (Eqn 1) measured for the former and the latter systems being 35 and 16 F/g, respectively. However, the best electrochemical performance for the development of capacitor electrodes was obtained for ml-PEDOT/PNMPy systems. Thus, *SC* values measured for the 3- and 5-layered films, and referred to the mass of PEDOT, were 50 and 62 F/g, reflecting that the synergistic effect between layers increases with the number of layers.

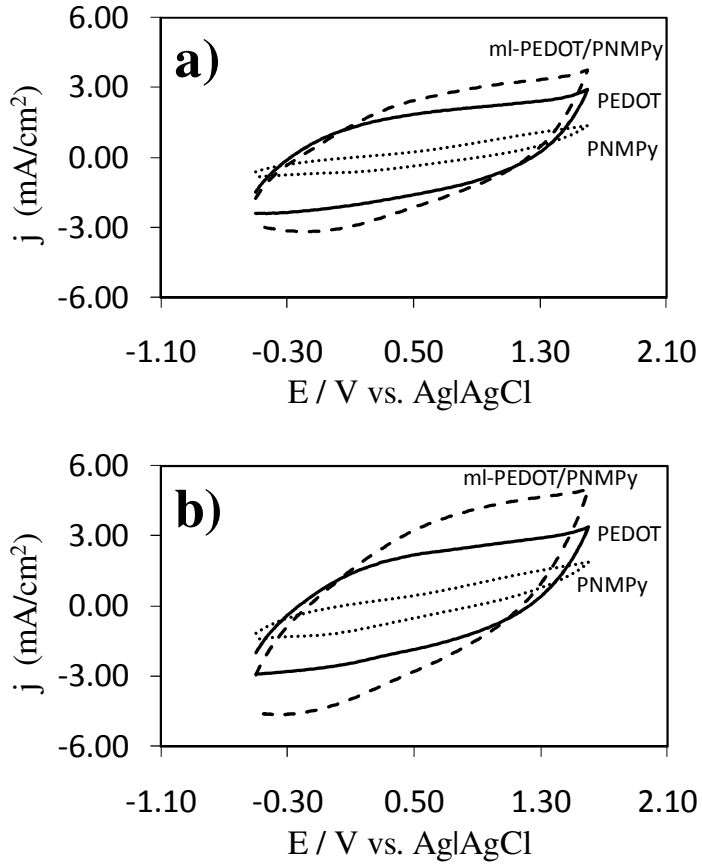

Figure 1. *Control voltammograms of PEDOT (solid line), PNMPy (dotted line) and ml-PEDOT/PNMPy (dashed line) films prepared using electropolymerization times (θ) of (a) 300 s and (b) 500 s. In the case of ml-PEDOT/PNMPy films voltammograms correspond to (a) 3-layered and (b) 5-layered systems, which were prepared considering a polymerization time of θ = 100 s per layer (i.e. the total electropolymerization time in multilayered films was 100·n s, where n refers to the number of layers). Scan rate: 100 mV/s. Initial and final potentials: -0.50 V; reversal potential: 1.60 V.*

Figure 2 compares the galvanostatic charge/discharge curves of PEDOT and ml-PEDOT/PNMPy. Charge and discharge profiles are linear and relatively symmetric, which indicate the capacitive behavior of the two systems. The *SC* determined according to Eqn 2 is 32 and 42 F/g for PEDOT and ml-PEDOT/PNMPy (3-layered), the latter value increasing to 53 F/g when the number of layers increases to 5. As it was expected, these galvanostatic values are in very good agreement with the values obtained by CV. The η (Eqn 4) follows the same behavior: 73%, 81% and 88% for PEDOT, 3- and 5-layered ml-PEDOT/PNMPy, respectively. The overall of these results indicate that ml-PEDOT/PNMPy is an appropriated material for applications based on capacitor electrodes.

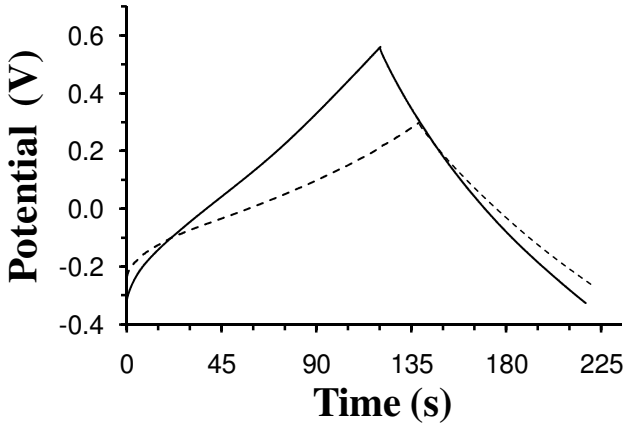

Figure 2. *Galvanostatic charge/discharge profiles of the PEDOT (solid line) and 3-layered ml-PEDOT/PNMPy (dashed line) capacitors. Current 1 mA.*

Figure 3 displays selected control voltammograms recorded at regular intervals from 200 consecutive oxidation-reduction cycles for the systems under study. According to the typical behavior of organic CPs, the cathodic and anodic areas decrease when the number of cycles increases in all cases. However, although multilayered films exhibit higher *SC* than PEDOT, the electrostability of the former is lower than that of the latter. This feature should be attributed to the poor electrochemical behavior of PNMPy. The electrostability of PEDOT increases with the electropolymerization time (*i.e.* ~4% when θ grows from 300 s to 500 s). Thus, the *LES* determined using Eqn 3 for the homopolymer films produced using θ = 300 and 500 s (Figures 3a and 3b) is 45% and 38%, respectively. This positive effect should be attributed to the thickness (ℓ) of the film, which increases with θ (*i.e.* ℓ = 2.35 and 4.05 μm for films prepared using θ = 300 and 500 s). The same behavior is observed for ml-PEDOT/PNMPy films. The *LES* values derived from Figures 3c and 3d are 62 % and 48 %, indicating that the electrostability improves with the number of layers (*i.e.* ℓ = 4.25 and 7.25 μm for the 3- and 5-layered films).

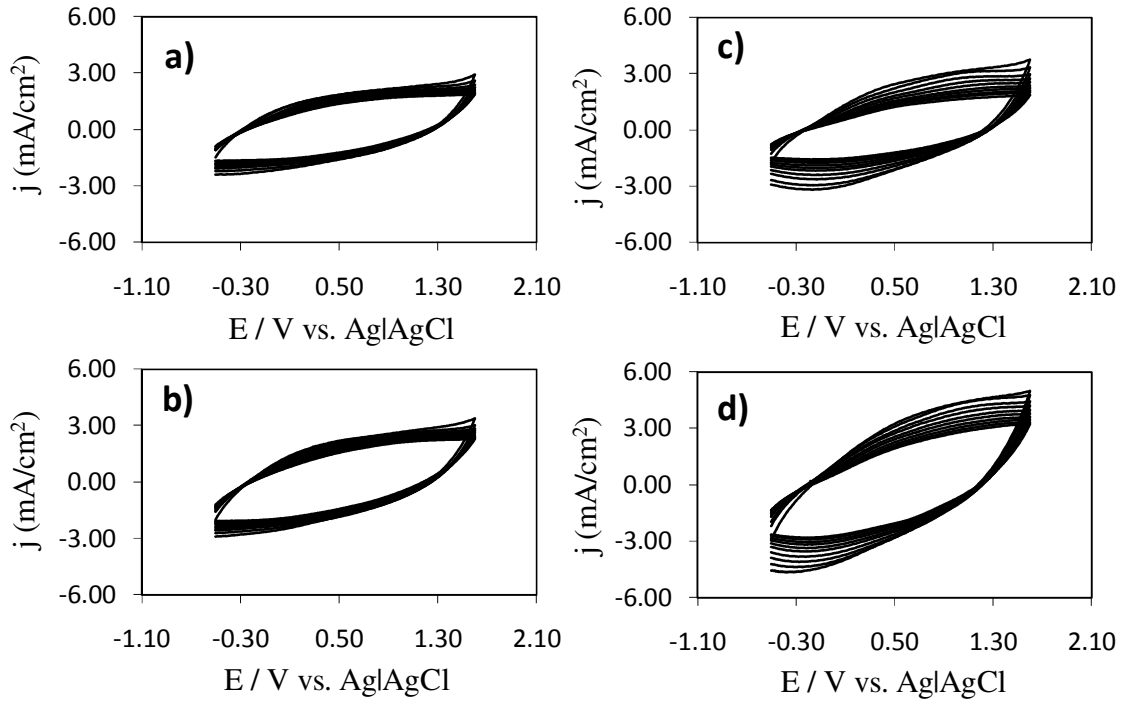

Figure 3. *Control voltammograms for 200 consecutive oxidation-reduction cycles for PEDOT films generated using (a) θ = 300 s and (b) θ = 500s, and ml-PEDOT/PNMPy films formed by (c) 3- and (d) 5-layers. Multilayered films were prepared considering θ = 100 s per layer (i.e. the total electropolymerization time in multilayered films was 100·n s, where n refers to the number of layers). In order to improve the clarity of the figures, only voltammograms corresponding to selected cycles (1, 10, 25, 40, 60, 80, 100, 125, 150, 175 and 200) are displayed. Voltammograms were recorded at 100 mV/s. Initial and final potentials: -0.50 V; reversal potential: 1.60 V.*

Investigation of the degradation of the capacitive properties undergone by organic materials is essential to ascertain their suitability as capacitor electrodes. Figure 4 shows the variation of the *SC* against the inverse of the number of consecutive oxidation-reducion cycles ($n_{ox\text{-}re}$). As it was expected from its poor electrochemical properties, PNMPy shows the worst performance as capacitor, independently of the thickness of the film. However, the most interesting result corresponds to the multilayered system, which shows better behavior than PEDOT. The values of *SC* extrapolated for an infinite number of $n_{ox\text{-}re}$ (denoted SC_∞) were obtained through a linear regression ($R^2 > 0.99$) of the *SC* values for $n_{ox\text{-}re} > 10$ (*i.e.* after the linear behavior is reached). The values obtained for the systems prepared using θ = 300 s are SC_∞ = 12.9, 7.0 and 15.8 F/g for PEDOT, PNMPy and ml-PEDOT/PNMPy (3-layers), while those produced for the films electrodeposited using θ = 500 s are SC_∞ = 19.8, 12.4 and 22.2 F/g for PEDOT, PNMPy and ml-PEDOT/PNMPy (5-layers), respectively. These results are fully consistent with

the observations previously discussed, the high SC_∞ values reached by the two ml-PEDOT/PNMPy systems being particularly remarkable.

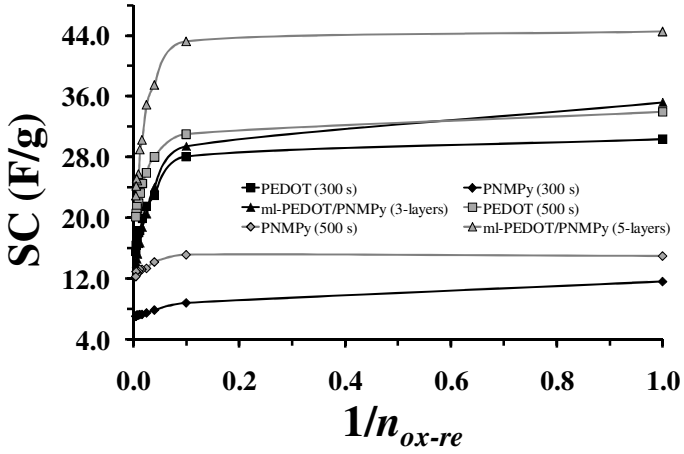

Figure 4. *Variation of the specific capacitante (SC) against the inverse of the number of consecutive oxidation-reduction cycles ($n_{ox\text{-}re}$) for PEDOT, PNMPy and ml-PEDOT/PNMPy systems. All the materials were obtained using θ = 300 and 500 s.*

Specific capacitance – structure relationships. The capacitive properties of PEDOT, PNMPy and ml-PEDOT/PNMPy can be explained by topology of the polymeric films at the surface, which was recently studied for nanometric films (*i.e.* films prepared using θ ≤ 40 s and with thickness ranging from ~100 to ~700 nm) using AFM.[36] In this work the topography and morphology of the micrometric films produced using $\theta \geq$ 100 s was examined. AFM and SEM images of micrometric PNMPy films (Figures 5 and Figure 6) reflect a globular compact structure that is consistent with a homogeneous distribution of the polymer chains. The surface becomes more compact and dense when θ increases, even though the increments of both the roughness and thickness are relatively low (*i.e.* r = 103 / 173 nm and ℓ = 1.06 / 2.61 μm for θ = 100 / 500 s). These features suggest the multidirectional growing of the crosslinked polymer chains, which is fully consistent with a previous theoretical study showing the intrinsic tendency of PNMPy to form chemical couplings in the β- and β'-positions of the repeating units.[37] Thus, the poor properties of PNMPy as capacitator are due to the compact structure produced by the lack of directional preferences in the electropolymerization, which makes difficult the access of the ions into the polymeric matrix during the faradaic processes.

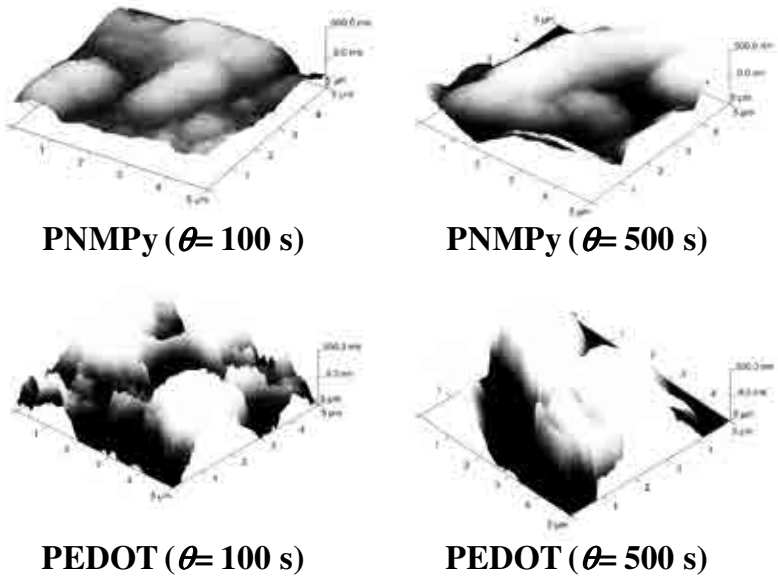

Figure 5. *3D AFM images of PNMPy and PEDOT films prepared using θ = 100 and 500 s.*

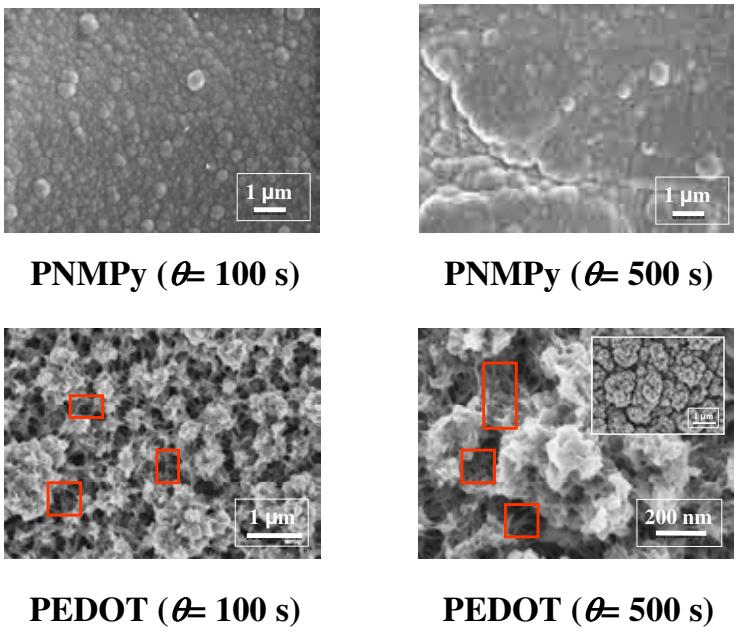

Figure 6. *SEM micrographs of PNMPy and PEDOT films prepared using θ = 100 and 500 s. Some networks of elements with a fiber-like morphology, which connect the clusters of aggregated PEDOT molecules, are pointed out using red boxes.*

AFM and SEM images of PEDOT films (Figure 5 and Figure 6) show small clusters of aggregated molecules that are located at very different levels. The roughness and the thickness of these films (*i.e.* r = 325 / 652 nm and ℓ = 1.34 / 5.41 µm for θ = 100 / 500 s) are higher than those determined for PNMPy films. The linear growing of PEDOT

molecules, which are exclusively formed by α-α linkages (*i.e.* the β-positions of the thiophene ring are occupied by the dioxane ring), allows the formation of a heterogeneous and porous morphology. Moreover, the micrographs displayed in Figure 6 evidence that the porosity of PEDOT is due to the existence of dense networks of thin fiber-like morphologies connecting the clusters of aggregated molecules. These characteristics explain the good capacitive properties of PEDOT since the transport of ions across the polymeric matrix is not precluded by the structure, as occurs for crosslinked PNMPy.

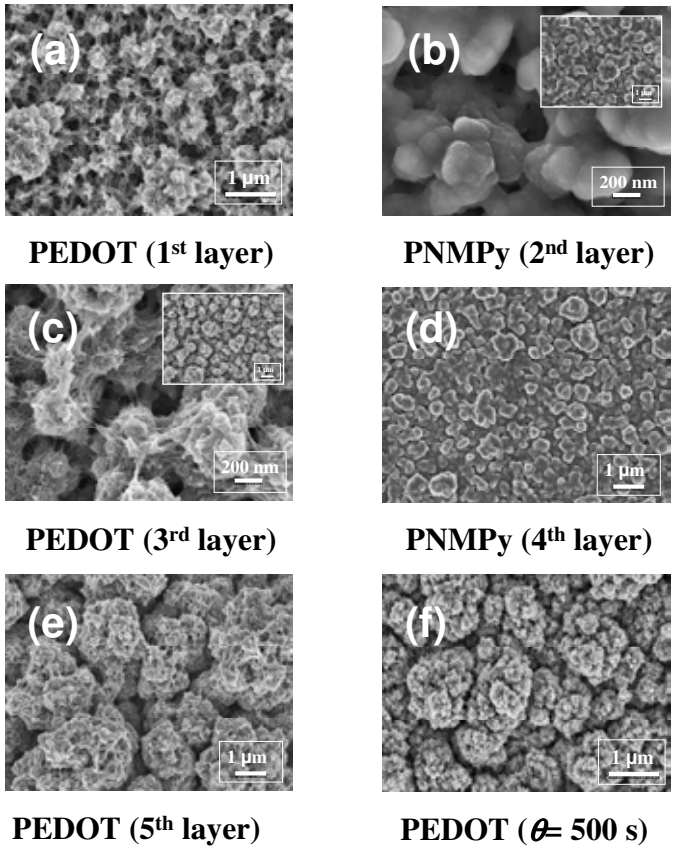

Figure 7. *SEM micrograph of each of layer in the 5-layered ml-PEDOT/PNMPy systems prepared using θ= 100 s per layer: (a) 1st layer – PEDOT; (b) 2nd layer – PNMPy; (c) 3rd layer – PEDOT; (d) 4th layer – PNMPy; and (e) 5th layer – PEDOT. A micrograph of the individual PEDOT film generated using θ = 500 s is displayed in (f). High resolution images (scale bar: 200 nm) are shown in (b) and (c), low resolution images (scale bar: 1 µm) being displayed in the inset.*

The different layers of ml-PEDOT/PNMPy show, in general, similar features to those discussed for individual PNMPy and PEDOT films. This is reflected in Figures 7a-7e, which display SEM micrographs for each of the five layers contained in a 5-layered film produced using θ = 100 s per layer. As it can be seen, alternated layers of

PEDOT and PNMPy retain the growing models proposed for the individual polymers during the electropolymerization process (*i.e.* formation of compact and porous structures for PNMPy and PEDOT layers, respectively). However, there is an important difference that is consistent with the highest *SC* values found of ml-PEDOT/PNMPy. This is that PEDOT layers grow on the PNMPy layers of the multilayered films are significantly more porous than PEDOT films directly electrodeposited on a steel substrate. This feature is evidenced in Figures 7e and 7f, which compare the morphology of the 5th layer of the ml-PEDOT/PNMPy film with that of a PEDOT film obtained using θ = 500 s. In spite of this, the roughness is considerably lower for the ml-PEDOT/PNMPy than for PEDOT (*i.e.* r = 362 and 652 nm for the 5-layered and the PEDOT films), the former presents not only more but also larger pores than the latter, explaining the different *SC* values determined for such two systems.

Influence of the number of oxidation-reduction cycles on the topography and morphology. Figures 8a shows the topographical changes undergone by PNMPy films after apply 10, 40 and 100 consecutive oxidation-reduction cycles ($n_{ox\text{-}r}$), while SEM micrographs of the morphology after $n_{ox\text{-}re}$ = 200 cycles are provided in Figure 9. The surface remains very compact in all cases, even though it becomes flatter when $n_{ox\text{-}re}$ increases (*i.e.* r = 85.7, 67.7 and 53.6 nm when $n_{ox\text{-}re}$ = 10, 40 and 100, respectively). This behavior allows one to explain the results displayed in Figure 4. Thus, the access and escape of the dopant anions, which is difficult since the first faradaic process, only reduces moderately when $n_{ox\text{-}re}$ increases (*i.e. SC* decreases about 15%-38% after 100 cycles, depending on the thickness) because of the small variation of the compactness.

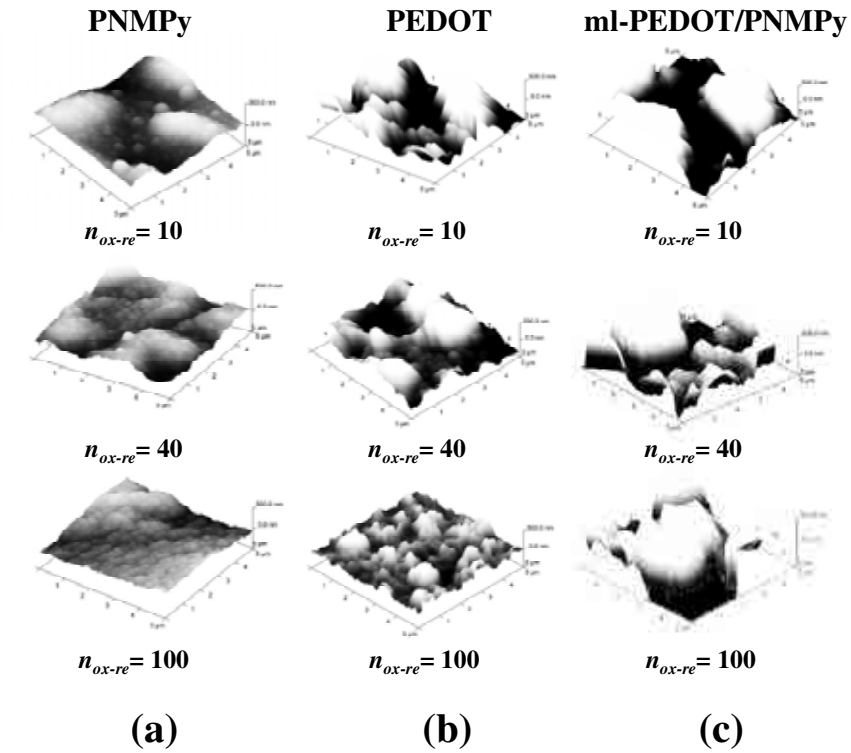

Figure 8. *3D AFM images showing the topographical changes induced by 10, 40 and 100 consecutive oxidation-reduction cycles (n_{ox-re}) in (a) PNMPy and (b) PEDOT generated using θ = 100 s, and in (c) ml-PEDOT/PNMPy (3-layered) film generated using θ = 100 s per layer.*

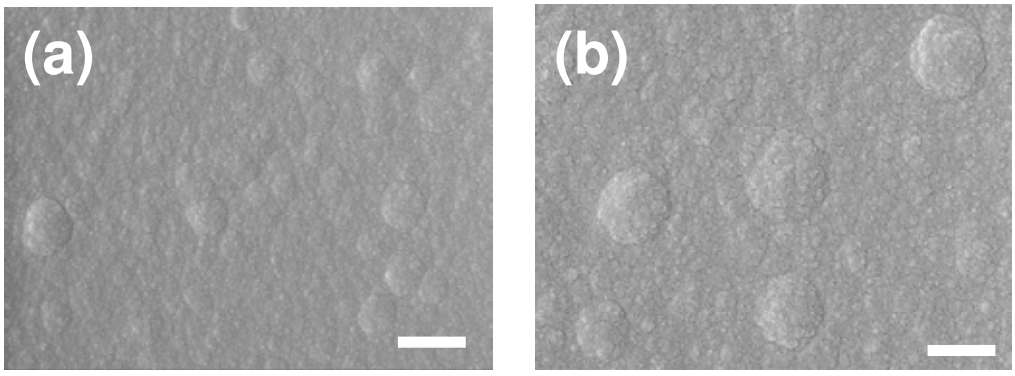

Figure 9. *SEM micrographs of the PNMPy films prepared using (a) θ = 300 s and (b) (a) θ = 500 s after electrochemical degradation through 200 consecutive oxidation-reduction cycles. Scale bar: 1 μm.*

3D AFM images of PEDOT films submitted to n_{ox-re} = 10, 40 and 100 cycles are displayed in Figure 8b. As it can be seen, the effects of the oxidation-reduction processes on PEDOT are very drastic: the CP undergoes not only a very significant reduction of the roughness, which decreases from 325 nm to 250, 182 and 91 nm after 10, 40 and 100 cycles, respectively, but also an enhancement of the compactness. Thus,

the sharp topographical irregularities associated to the linear growing of the polymer chains tend to disappear when $n_{ox\text{-}re}$ increases, the structure becoming more compact and less porous. As is reflected by the SEM micrographs displayed in Figure 10, which shows the morphological changes induced by 200 cycles on films generated using θ = 300 and 500 s, the variation of the porosity is consequence of the reduction of both the mean pore size and the number of pores. Thus, PEDOT undergoes significant structural changes, which affect not only to the clusters of aggregated molecules but also to the network of the elements with a fiber-like morphology that connect them. Thus, thin fiber-like elements tend to collapse forming thicker organizations that reduce the distance between neighboring clusters and, consequently, the porosity of the material.

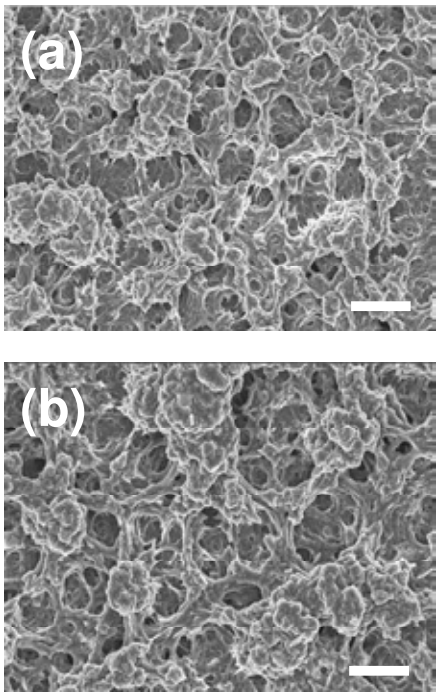

Figure 10. *SEM micrographs of the PEDOT films prepared using θ = (a) 300 and (b) 500 s after electrochemical degradation through 200 consecutive oxidation-reduction cycles. Scale bar: 1 μm.*

The reduction in the porosity has been quantified through the parameter Δ calculated as follows:[38]

$$\Delta = \frac{l_0 - l_{200}}{l_0} 100 \qquad (5)$$

where ℓ_0 and ℓ_{200} refers to the thickness before apply any redox cycles ($n_{ox\text{-}re}$ = 0) and after $n_{ox\text{-}re}$ = 200 (ℓ_{200} = 1.06 μm). The value of Δ obtained for PEDOT prepared using θ = 300 s, which showed the largest change, is 55%.

Interestingly, the effects are less dramatic in ml-PEDOT/PNMPy systems. This is reflected in Figure 8c, which shows the 3D AFM images of the 3-layered film after $n_{ox\text{-}re}$ = 10, 40 and 100 cycles. It is worth noting that the roughness remains relatively high, even when $n_{ox\text{-}re}$ = 100 (*i.e.* r = 631 nm before electrochemical degradation, decreasing to 512, 432 and 391 nm after 10, 40 and 100 cycles, respectively), and the topography retains the heterogeneous distribution of clustered molecules at different levels.

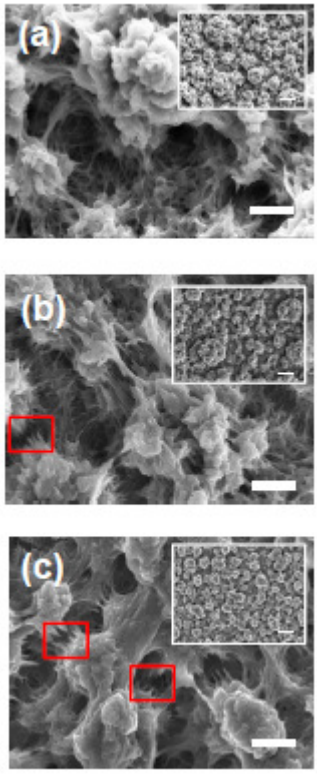

Figure 11. *SEM micrographs of the 3-layered ml-PEDOT/PNMPy systems prepared using θ = 100 s per layer after electrochemical degradation through (a) 10, (b) 100 and (c) 200 consecutive oxidation-reduction cycles. Low resolution images (scale bar: 1 μm) are shown as insets into the high resolution images (scale bar: 200 nm). Broken networks of elements with a fiber-like morphology are pointed out in (b) and (c) using red boxes.*

The influence of $n_{ox\text{-}re}$ on the morphology the 3-layered film is evidenced in the SEM images displayed in Figure 11. Low resolution images (insets) are fully consistent with AFM results, reflecting the reduction in the porosity undergone by the multilayered film upon increase $n_{ox\text{-}re}$. Moreover, the micrograph recorded after $n_{ox\text{-}re}$ = 200 cycles

indicates that clusters of aggregated molecules tend to collapse. The rapprochement among such aggregates is consequence of the rupture of the thin organizations with a fiber-like morphology that connect the neighboring clusters. As is illustrated in the high resolution images of Figure 11, the effect of the electrochemical degradation in the fibers-like elements is easily detectable when $n_{ox\text{-}re}$ = 100 cycles, even though it is more intense when $n_{ox\text{-}re}$ = 200 cycles. The value of Δ obtained for the 3-layered film is 58% (ℓ_{200} = 1.78 μm).

Impedance studies. Electrochemical impedance spectroscopy (EIS) was further employed to monitor the electrochemical behavior of the capacitive ml-PEDOT/PNMPy systems, which has been compared with that of PEDOT. Typical Nyquist diagrams for the 3-layered ml-PEDOT/PNMPy and PEDOT electrodes prepared using θ = 300 s are displayed in Figure 12.

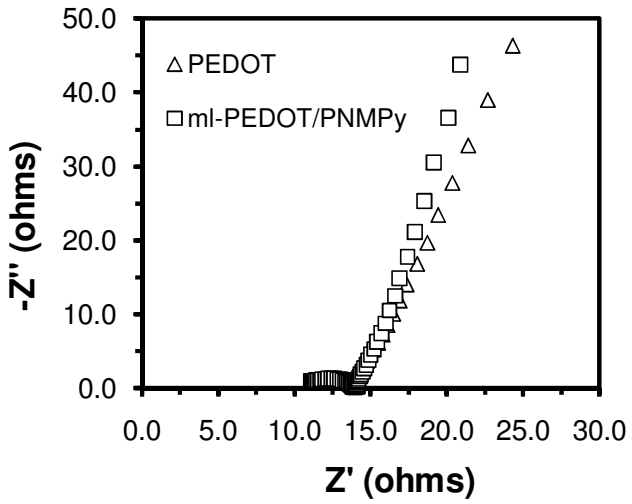

Figure 12. *EIS spectra (Nyquist impedance plots) over a frequency range of 100 kHz-10 mHz of PEDOT and 3-layered ml-PEDOT/PNMPy prepared using θ = 300 s.*

The two impedance curves show a single semi-circle in the high frequency region and a nearly vertical straight line in the low frequency region, indicating that the electrode process is dominated by charge transfer (*i.e.* electrochemical reaction) in the former region and by charge diffusion (*i.e.* mass transfer) in the latter one.[39] The intercept of the semi-circle with the real axis (Z') at high frequencies is the measure of the internal resistance (R_s), which can be used to evaluate the solution resistance. The origin of the semi-circle at the higher frequency range is due to the ionic charge transfer resistance (R_{ct}) at the electrode-solution interface, while is given by the diameter of the semi-circle along the real axis Z'. The R_{ct} determined for ml-PEDOT/PNMPy and

PEDOT is 2.8 and 3.0 Ω. These low values should be also attributed to the porous structure of the two materials, which increases the kinetic of electron transfer through redox processes.

It is worth noting that for both the PEDOT and, especially, the 3-layered systems the imaginary part of the impedance Z'' at low frequencies is almost perpendicular to the real part Z'. This feature proves the good capacitance behavior of the two systems, even though comparison of the profiles indicates that it is slightly better for the ml-PEDOT/PNMPy one.

Performance of multilayered ml-PEDOT/PNMPy systems as supercapacitor in type I configuration. A supercapacitor based on two identical electrodes of 3-layered ml-PEDOT/PNMPy (θ = 300 s) was constructed as is indicated in Figure 13, its performance being determined by measuring the *SC* (Eqn 1) and the η.

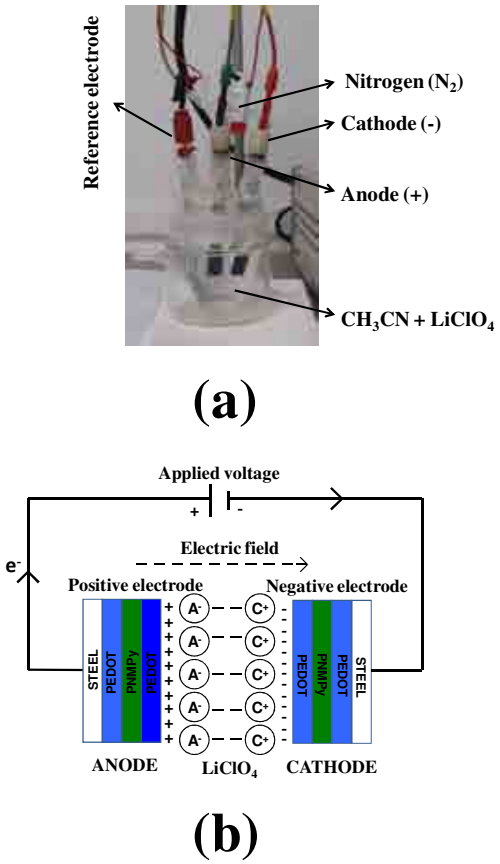

Figure 13. *Fabrication set-up (a) and scheme (b) of the supercapacitor constructed using two identical electrodes of 3-layered ml-PEDOT/PNMPy (θ = 300 s).*

Results are compared in Table 1 with those derived from a capacitor made of two PEDOT electrodes. It should be remarked that the *SC*s provided for the multilayered systems are referred to the mass of PEDOT exclusively, the mass of PNMPy being not

considered. Accordingly, the values obtained for ml-PEDOT/PNMPy and PEDOT are directly comparable. The *SC* determined for a symmetric assembly of two ml-PEDOT/PNMPy electrodes (90 F/g) is significantly higher (~ 119%) than that obtained for two PEDOT electrodes. It is worth noting that the *SC* obtained for ml-PEDOT/PNMPy is only ~9% lower than those measured for chemically modified graphene ultracapacitors (~99 F/g) using similar experimental conditions.[40] However, these values are lower than those reported for ultracapacitors fabricated using nanocomposites of PEDOT and inorganic materials (*e.g.* MoO_3, carbon nanotubes, MnO_2 and $NiFe_2O_4$), for which the specific capacitance ranged from 198 to 375 F/g.[41-44]

Table 1. *Performance of 3-layered ml-PEDOT/PNMPy and PEDOT electrodes (θ = 300 s in both cases) in capacitor configurations.*

	Symmetric assembly of two electrodes (Type I)		**Single electrode**	
	SC[a]	η[b]	*SC*[a]	η[b]
ml-PEDOT/PNMPy[c]	90	85	35	81
PEDOT	41	77	50	73

[a] Specific capacitance (in F/g) calculated according to Eqn (2). [b] Coulombic efficiency (in %) calculated according to Eqn (4). [c] In all cases the SCs provided for the multilayered systems are referred to the mass of PEDOT exclusively.

For the multilayered system the two electrodes configuration produces an enhancement of the *SC* with respect to a single electrode of 157%, whereas for PEDOT there is a reduction of 18%. Unfortunately, no significant increase was obtained in terms of η (Eqn 3) for the multilayered system, the values obtained for the single and two electrodes configurations differing in 5% only. In spite of this, it should be emphasized that η is 10% higher for ml-PEDOT/PNMPy than for PEDOT. The overall of these results indicate that ultracapacitors based on ml-PEDOT/PNMPy are promising candidates for the development of new electrical energy storage devices, which is consequence of the synergistic effect produced by the alternated layers of PEDOT and PNMPy.

3.3.4. Conclusions

Multilayered systems based on alternated layers of PEDOT and PNMPy have been prepared using the LbL technique by means of potentiostatic methods. Both CV experiments and charge/discharge curves indicate that the *SC* and η are higher for ml-PEDOT/PNMPy than for individual PEDOT and PNMPy, evidencing that the former systems are more appropriated for the preparation of capacitor electrodes than the latter CPs. This feature has been confirmed by analyzing the variation of *SC* against $n_{ox\text{-}re}$. Thus, the SC_∞ values grow in the following order: PNMPy << PEDOT < ml-PEDOT/PNMPy. The electrochemical and capacitive properties of the ml-PEDOT/PNMPy and two individual CPs are directly related with the structure of these materials. Specifically, both the porosity and its changes upon consecutive faradaic processes have been found to be directly related with the electrochemical and capacitive properties of the systems under study. Symmetric supercapacitors have been fabricated by assembling 3-layered ml-PEDOT/PEDOT and PEDOT electrodes. The *SC* determined for the ml-PEDOT/PNMPy supercapacitor is not only significantly higher than that of the PEDOT one but very similar to those reported in the literature for advanced ultracapacitors.

3.3.5. References

[1]. Meng, H.; Zheng, J.; Lovinger, A. J.; Wang, B.; Van Patten, P. G.; Bao, Z. *Chem. Mater.* **2003**, *15*, 1778.

[2]. Mazzeo, M.; Vitale, V.; Della Salla, F.; Anni, M.; Barbarella, G.; Favaretto, L.; Sotgiu, G.; Cingolani, R.; Gigli, G. *Adv. Mater.* **2005**, *17*, 34.

[3]. Huynh, W. U.; Dittmer, J. J.; Alivisatos, A. P. *Science* **2002**, *295*, 2425.

[4]. Bjork, P.; Thomsson, D.; Mirzov, O.; Wigenius, J.; Inganas, O.; Scheblykin, I. *Small* **2009**, *5*, 96.

[5]. Ho, H. A.; Leclerc, M. *J. Am. Chem. Soc.* **2004**, *126***,** 1384.

[6]. Hamedi, M.; Forchheimer, R.; Inganas, O. *Natur. Mat.* **2007**, *6*, 357.

[7]. Berridge, R.; Wright, S. P.; Skabara, P. J.; Dyer, A.; Steckler, T.; Argun, A. A.; Reynolds, J. R.; Ross, W. H.; Clegg, W. *J. Mat. Chem.* **2007**, *17***,** 225.

[8]. Marsh, R. A.; Hodgkiss, J. M.; Firend, R. H. *Adv. Mater.* **2010**, *22***,** 3672.

[9]. Lota, K.; Khomenko, V.; Frackowiak, E. *J. Phys. Chem. Solids.* **2004**, *65***,** 295.

[10]. Ryu, K. S.; Lee, Y. G.; Hong, Y. S.; Park, Y. J.; Wu, X. L.; Kim, K. M.; Kang, M.G.; Park, N. G.; Chang, S. H. *Electrochim. Acta* **2004**, *50*, 843.

[11]. Ghosh, S.; Inganas, O. *Electrochem. Solid State Lett.* **2000**, *3***,** 213.

[12]. del Valle, L. J.; Aradilla, D.; Oliver, R.; Sepulcre, F.; Gamez, A.; Armelin, E.; Alemán, C.; Estrany, F. *Eur. Polym. J.* **2007**, *43***,** 2342.

[13]. Tamburri, E.; Orlanducci, S.; Toschi, F.; Terranova, M. L.; Passeri, D. *Synth. Met.* **2009**, *159*, 406.

[14]. Ocampo, C.; Oliver, R.; Armelin, E.; Alemán, C.; Estrany, F. *J. Polym. Research.,* **2006**, *13***,** 193.

[15]. Kotz, R.; Carlen, M. *Electrochim. Acta* **2000**, *45*, 2483.

[16]. Frackowiak, E.; Beguin, F. *Carbon* **2002**, *40*, 1775.

[17]. Wang, Y. G.; Zhang, X. G. *Electrochim. Acta* **2004**, *49*, 1957.

[18]. Liu, C.; Li, F.; Ma, L.-P.; Cheng, H.-M. *Adv. Mater.* **2010**, *22*, E28.

[19]. Centi, G.; Perathoner, S. *Eur. J. Inorg. Chem.* **2009**, *26*, 3851.

[20]. Snook, G. A.; Kao, P.; Best, A. *J. Power Sources* **2011**, *196*, 1.

[21]. Xu, Y.; Wang, J.; Sun, W.; Wang, S. *J. Power Sources* **2006**, *159*, 370.

[22]. Han, G.; Yuan, J.; Shi, G.; Wei, F. *Thin Solid Films* **2005**, *474*, 64.

[23]. Stenger-Smith, D.; Webber, C. K.; Anderson, N.; Chafin, A. P.; Zong, K.; Reynolds, J. R. *J. Electrochem. Soc.* **2002**, *149*, A973.

[24]. Babakhani, B.; Ivey, D.G. *Electrochim. Acta* **2010**, *55*, 4014.

[25]. Sen, P.; De, A. *Electrochim. Acta* **2010**, *55*, 4677.

[26]. Fusalba, F.; Ho, H. A.; Breau, L.; Belanger, D. *Chem. Mater.* **2000**, *12*, 2581.

[27]. Chen, L.; Yuan, C.; Dou, H.; Gao, B.; Chen, S.; Zhang, X. *Electrochim. Acta* **2009**, *54*, 2335.

[28]. Peng, C.; Snook, G. A.; Fray, D. J.; Shaffer, M. P.; Chen, G. Z. *Chem. Commun.* **2006**, *44*, 4629.

[29]. Peng, C.; Jin, J.; Chen, G. Z. *Electrochim. Acta* **2007**, *53*, 525.

[30]. Rudge, A.; Davey, J.; Raistrick, I.; Gottesfeld, S.; Ferraris, J. P. *J. Power Sources* **1994**, *47*, 89.

[31]. Estrany, F.; Aradilla, D.; Oliver, R.; Alemán, C. *Eur. Polym. J.* **2007**, *43*, 1876.

[32]. Estrany, F.; Aradilla, D.; Oliver, R.; Alemán, C. *Eur. Polym. J.* **2008**, *44*, 1323.

[33]. Oliver, R.; Muñoz, A.; Ocampo, C.; Alemán, C.; Estrany, F. *Chem. Phys.* **2006**, *328*, 299.

[34]. Ocampo, C.; Oliver, R.; Armelin, E.; Alemán, C.; Estrany, F. *J. Polym. Res.* **2006**, *13*, 193.

[35]. Aradilla, D.; Estrany, F.; Oliver, R.; Alemán, C. *Eur. Polym. J.* **2010**, *46*, 2222.

[36]. Aradilla, D.; Estrany, F.; Armelin, E.; Alemán, C. *Thin Solid Films* **2010**, *518*, 4203.

[37]. Alemán, C.; Casanovas, J.; Torras, J.; Bertrán, O.; Armelin, E.; Oliver, R.; Estrany, F. *Polymer* **2008**, *49*, 1066.

[38]. Pal, E.; Hornok, V.; Sebo, D.; Majzik, A.; Dekany, I. *Colloid. Surf. B: Biointerf.* **2010**, *79*, 276.

[39]. Li, N.; Shan, D.; Xue, H. *Eur. Polym. J.* **2007**, *43*, 2532.

[40]. Stoller, M. D.; Park, S.; Zhu, Y.; Na, J.; Ruoff, R. S. *Nano Lett.* **2008**, *8*, 10.

[41]. Sen, P.; De, A. *Electrochim. Acta* **2010**, *55*, 4677.

[42]. Chen, L.; Yuan, C.; Dou, H.; Gao, B.; Chen, S.; Zhang, X. *Electrochim. Acta* **2009**, *54*, 2335.

[43]. Murugan, A.V.; Viswanath, A. K.; Gampet, G.; Gopinath, C. S.; Vijayamohanan, K. *Appl. Phys. Lett.* **2005**, *87*, 243511.

[44]. Sharma, R.; Zhai, L. *Electrochim. Acta* **2009**, *54*, 7148.

Chapter 4. Influence of the substrate on the properties of conducting polymers

4.1. Poly(3,4-ethylenedioxythiophene) on self-assembled alkanethiols monolayers for corrosion protection.[a]

[a]Results presented in this chapter were published in *Polym. Chem.* **2011**, *2*, 2548.

4.2. Ultraporous PEDOT for nanometric electrochemical supercapacitor.[b]

[b]Results presented in this chapter were published in *Thin Solid Films* **2012**, *520*, 4402.

4.3. Nanometric supercapacitor devices based on multilayered conducting polymers from self-assembled alkanethiols.[c]

4.2.3. Results and discussion

4.2.4. Conclusions

4.2.5. References

[c] Results presented in this chapter were submitted.

4.1. Effect of alkanethiols on the properties and protective abilities of poly(3,4-ethylenedioxythiophene)

4.1.1. Introduction

Many studies about the preparation and characterization of self-assembled monolayers (SAMs) at solid surfaces to fabricate interfaces with organized structures and well defined composition and thickness have been reported.[1] Self-assembly of molecular monolayers relies on spontaneous adsorption of a functional reagent from solution onto a surface, and microstructural organization of the adsorbates through the hydrophobic effect or van der Waals interactions. In particular, alkanethiols anchored to Au(111) surfaces have attracted considerable attention because of the strong interaction between the SH headgroup and the surface, providing a better understanding of the structural organization and properties of these layers.[2] The electron transfer behavior of SAMs[3] also led to the development of new strategies for modifying electrode surfaces aiming at control of their electrochemical processes.[4] Electrons can be transferred across an alkanethiol monolayer by a tunneling mechanism, which operates up to ~12 carbon atoms in the alkyl chain affording electroactive properties to such monolayers.[5]

A filed that has received attention in the last fifteen years is the anodic polymerization of conjugated conducting polymers (CPs) on electrodes modified with SAMs to control of surface properties and form stable surface modifications. Specifically, electrochemical oxidation of the corresponding monomers on polycrystalline platinum or gold electrodes coated with long-chain alkanethiols has been used to prepare, among others, polyaniline and some of its derivatives,[6-10] polypyrrole,[6,11,12] polybithiophene,[13,14] poly(3-methylthiophene)[15-17] and poly(3-octylthiophene).[18] In general, results indicated that the preadsorption of alkanethiol monolayers improves the electrochemical and optical properties of the conducting polymers.

Poly(3,4-ethylenedioxythiophene), hereafter abbreviated PEDOT (Scheme 1), is one of the most important CPs due to its high conductivity (up to 500 S/cm), good environmental and chemical stability, fast doping-dedoping processes and excellent biocompatibility.[19-22] Moreover, PEDOT presents excellent electrochemical properties in terms of electroactivity and electrostability, explaining the high ability of this material to store charge (*i.e.* electrical energy).[23-25] In spite of the impressive properties

of this CP, there is an unique study combining both PEDOT and SAMs, even though the latter was not used to modify the electrodes before electropolymerization but the films once generated.[26] Specifically, electrochemically grown films of PEDOT and other CPs were treated with alkane- and fluoroalkane-thiols for incubation periods ranging from 1 to 24 h.[26] Treatment of the investigated CPs resulted in covalent bonding of the thiol groups to the polymer backbone, even though this effect was lesser extent in PEDOT than in PPy and PAni. Furthermore, SAMs deposited onto the PEDOT and PPy films induced a reduction in the electroactivity, while coated PAni retained the electroactivity.

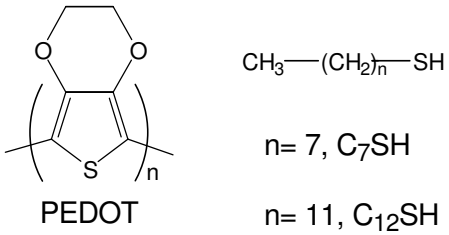

Scheme 1

The aim of this work is to examine the properties of PEDOT electrodeposited on alkanethiol-coated electrodes. Specifically, the surface of stainless steel substrates, which were successfully used to produce micrometric and nanometric PEDOT films with excellent electrical and electrochemical properties,[24,25,27] was treated with octanethiol (C_8SH) and dodecanethiol ($C_{12}SH$). The influence of the two alkanethiols on structural and electrochemical properties of PEDOT films has been examined in detail using X-ray photoelectron spectroscopy (XPS), atomic force microscopy (AFM), scanning electron microscopy (SEM) and cyclic voltammetry (CV). Furthermore, the impact of the SAMs on the corrosion resistance imparted by PEDOT films has been examined using electrochemical impedance spectroscopy (EIS) and SEM. For this purpose, PEDOT coatings electrodeposited on treated and untreated steel sheets were immersed in 3.5% NaCl aqueous solution, electrochemical and morphological changes at the surface of the barrier films being analyzed.

4.1.2. Methods

Chemicals. 3,4-ethylenedioxythiophene (EDOT) monomer, C_8SH, $C_{12}SH$ and acetonitrile (analytical reagent grade) were purchased from Aldrich and used as received. $LiClO_4$ analytical reagent grade from Aldrich was stored in an oven at 80 ºC before use in the electrochemical trials.

Monolayers formation. Thiol monolayers were prepared by immersing stainless steel electrodes, which were previously clear with acetonitrile, into 50 mL of alkanethiol as received from Aldrich for a time τ = 2, 10 or 24 h. Then, the C_8SH-steel and $C_{12}SH$-steel modified electrodes were removed from the solutions, rinsed with acetonitrile and dried with nitrogen.

Synthesis. PEDOT was obtained by potentiostatic electropolymerization (chronoamperometry, CA) at 1.40 V[24] in an acetonitrile solution containing 0.01 M of the corresponding monomer and 0.1 M $LiClO_4$ using polymerization times (θ) of 10 and 300 s. Polymerizations were carried out in a standard three-electrode two-compartment cell under nitrogen atmosphere (99.995% in purity) at 25ºC. Steel AISI 316 sheets of 4 cm^2 area (or 1 cm^2 for topographic and morphologic analyses; see below) were employed as working and counter electrodes, while the reference electrodes was an Ag|AgCl electrode containing a KCl saturated aqueous solution (Eº = 0.222 V at 25 ºC). In order to avoid interferences during the electrochemical analyses, the working and counter electrodes were cleaned with acetone and dried in an air-flow before each trial. The thickness of PEDOT films produced using θ = 10 and 300 s was determined to be ~150 nm[28] and 2.25-2.35 μm,[29] respectively.

Chronoamperometric measurements during the anodic polymerization process were controlled using a VersaStat II potenciostat-galvanostat connected to a computer controlled through a Power Suite Princenton Applied Research program. After electropolymerization, all coated electrodes were cleaned with acetonitrile (generation medium) and dried with nitrogen.

Electrochemical measures. The ability to store charge (electroactivity) and electrochemical stability upon consecutive oxidation-reduction cycles (electrostability) of PEDOT films grown in untreated-, C_8SH- and $C_{12}SH$-steel electrodes were determined by CV using an acetonitrile solution with 0.1 M $LiClO_4$. The initial and final potentials were -0.50 V, while the reversal potential was 1.60 V. The electroactivity increases with the similarity between the anodic and cathodic areas of the first control

voltammogram, whereas the electrostability decreases with the oxidation and reduction areas of consecutive control voltammograms. Accordingly, electroactivity and electrostability were determined through direct measure of the anodic and cathodic areas in the control voltammagrams using the Power Suite Princenton Applied Research software. The electrochemical thickness of both nanometric and micrometric PEDOT films was derived from the mass of the polymer deposited in the untreated-, C_8SH- and $C_{12}SH$-steel electrodes, using a previously described procedure.[29]

EIS measurements were performed using an AUTOLAB PGSTAT 30/FRA 2 system in potenciostatic mode at the open circuit potential (OCP). The amplitude of the EIS perturbation signal was 10 mV, and the studied frequency ranged from 10^5 to 10^{-2} Hz. Corrosion tests were performed using a 3.5% NaCl solution. All experiments were carried out at 25 ºC.

X-Ray Photoelectron Spectroscopy. Measures were performed using a SPECS system equipped with an Al anode XR50 source operating at 150 W and a Phoibos 150 MCD-9 detector XP. Samples of 1 cm^2 were fixed into the sample holder using double sided carbon tape. The pass energy was set at 25 eV using 0.1 eV steps. The partial pressure of the argaon flood gun was below $1.5 \cdot 10^{-9}$ mbar. Data acquisition and processing were achieved with the Advantage Software. Spectral calibration was determined by setting the main C1s component at 285 eV.

Atomic Force Microscopy. Topographic images were obtained with a Molecular Imaging PicoSPM using a NanoScope IV controller in ambient conditions. The tapping mode AFM was operated at constant deflections (*i.e.* vertical constant force with triangular shaped gold-coated silicon nitride. The row scanning frequency was set to 1 Hz and the physical tip-sample motion speed was 10 $\mu m \cdot s^{-1}$. The root-mean-square (RMS) roughness (*r*) was determined using the statistical application of the Nanoscope software, which calculates the average considering all the values recorded in the topographic image with exception of the maximum and the minimum. The scan window size was 5×5 μm^2 in all cases, a total of 65.536 topographic data being computed in each image. In all images acquired, which are 512×512 $pixel^2$ maps, differences in height are indicated by a color scale: dark is low, and white is high.

Scanning Electron Microscopy. SEM images were analyzed using a Focused Ion Beam Zeiss Neon40 scanning electron microscope at 3 kV.

Adherence. Measurements were based on the standard sellotape test (TESA-4204 BDF), which consists in cutting the film into small squares, sticking the tape and then stripping it. The ratio between the number of adherent film squares remaining and their total number gives the percentage adherence.

4.1.3. Results and discussion

Steel-modified electrodes. Figure 1 compares the height images and transversal section profiles determined by AFM for untreated-, C_8SH- and $C_{12}SH$-steel substrates, the latter two corresponding to an incubation of $\tau = 24$ h in the alkanethiol solution.

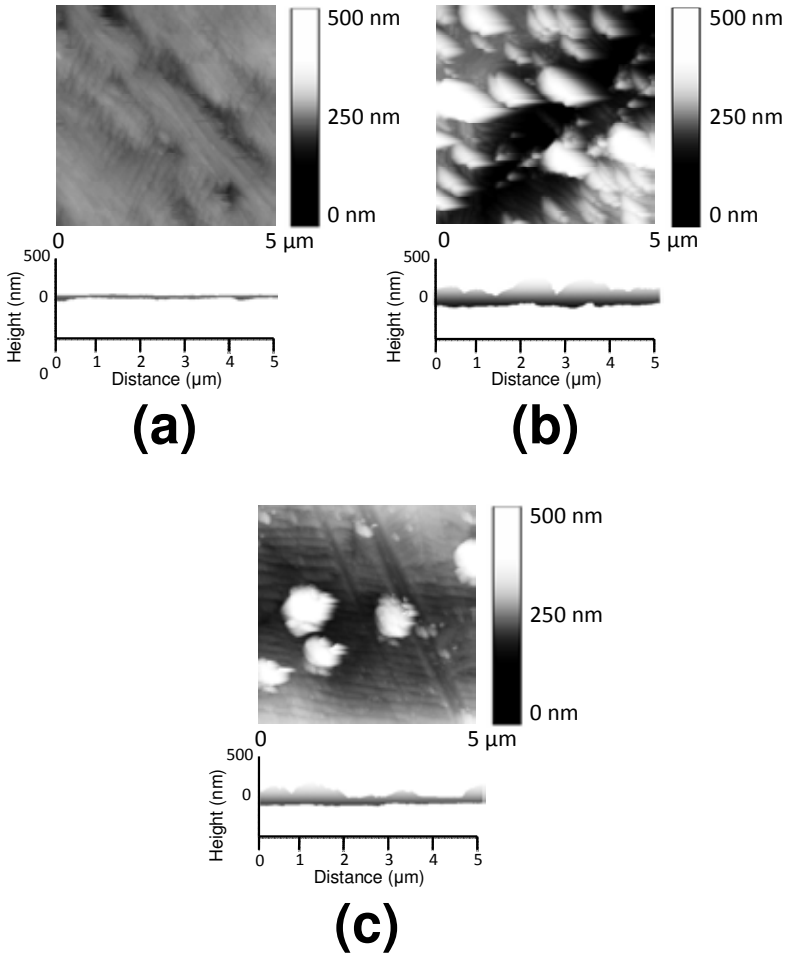

Figure 1. *AFM height image and transversal section profile of the substrates used in this work for electrochemical polymerization: (a) untreated-, (b) C_8SH- and (c) $C_{12}SH$-steel.*

As it can be seen, the untreated-steel surface is very flat showing a RMS roughness of only r = 11 nm. Deposition of alkanethiols produces significant variations in both the roughness, which is 57 and 27 nm for C_8SH- and $C_{12}SH$-steel, respectively, and topography of the surfaces. Regarding to the latter, irregularities are more frequent in C_8SH-steel than in $C_{12}SH$-steel. SAMs produced using the alkanethiol with the largest

hydrocarbon chain are more uniform and show less structural defects than those made with the shortest one, which should be attributed to the better packing of the former with respect to the latter. Thus, it is well known that long chain alkanethiols C_nSH with $n \geq 11$ form well-ordered monolayers on surfaces because of the close-packing of the molecules.[30,31]

To characterize the covalent attachment of the thiols to the surface of stainless steel, XPS analyses were performed. Figure 2a shows the high resolution spectra of the sulphur 2p region for $C_{12}SH$-steel prepared using $\tau = 2$ h. The S 2p binding energy ranges from 155 to 168 eV. The component at 162.87 eV (S $2p_{3/2}$) correspond to the steel-bound thiolate (S-Fe), whereas the component at 163.90 eV (S $2p_{1/2}$) can be assigned to unbound thiol (-SH) or disulfide bonds (S-S). [2a,32,33] The formation of SAMs on steel sheets is schematically depicted in Figure 3.

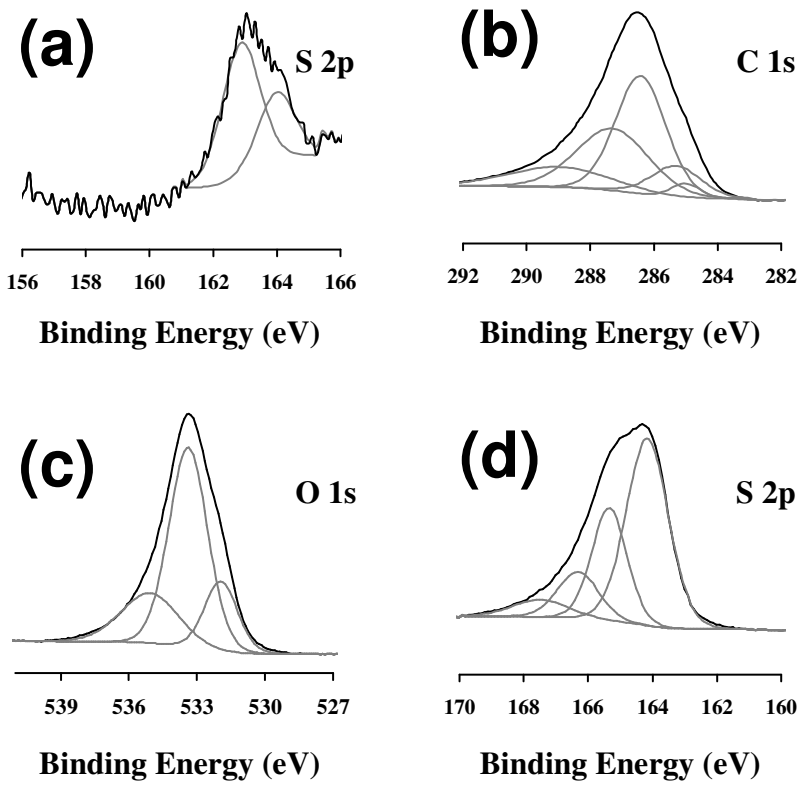

Figure 2. *High resolution XPS spectra of the: (a) sulphur 2p region for the $C_{12}SH$-steel (τ= 2 h) substrate; carbon 1s (b) oxygen 1s (c) and sulphur 2p (d) regions for the PEDOT film deposited on $C_{12}SH$-steel (τ = 2 h).*

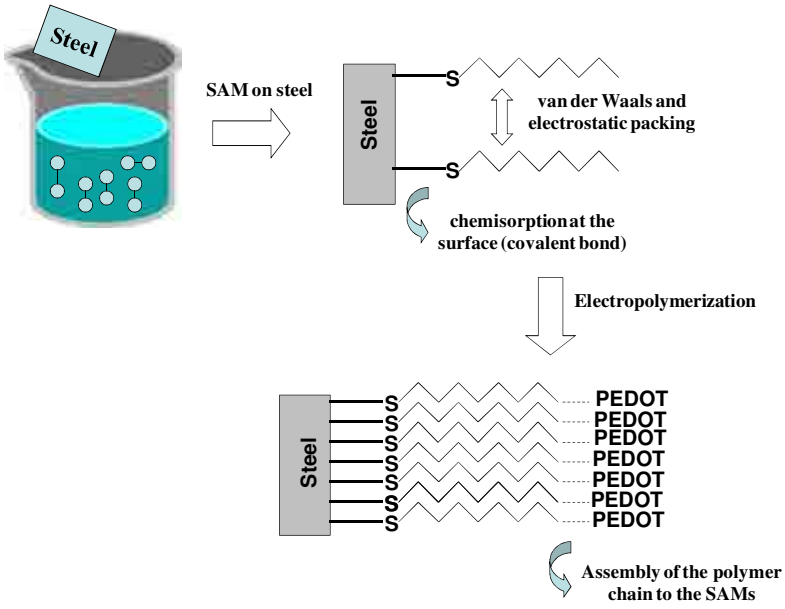

Figure 3. *Scheme illustrating the formation of SAMs of alkanethiols and the electropolymerization of PEDOT on modified electrodes.*

Micrometric PEDOT films. FTIR analyses indicate that the band centered at 756 cm^{-1}, which corresponds to the C^{α}-H out-of-plane bending mode, is detected in the spectrum recorded for pure EDOT monomer but not in the spectra of PEDOT films, independently of both the substrate and θ. This feature reflects that in all cases CA provides linear polymer molecules through the formation of α,α-linkages. Accordingly, electropolymerization of PEDOT using steel electrodes coated with alkanethiols was a success in all cases (Fig. 3).

AFM and SEM images of micrometric PEDOT films (θ = 300 s) deposited on untreated- and C_8SH-steel, where the SAMs of the latter substrate were prepared considering τ = 2 h, are displayed in Figure 4. The resemblance between the images obtained for the two systems, which in addition are very similar to those recorded form films deposited on C_{12}SH-steel and on modified substrates prepared using τ = 10 and 24 h, indicates that influence of the SAMs interface on the globular morphology is practically negligible when thickness of the film is within the micrometric scale. Similarly, electrochemical measures indicate that the influence of SAMs on the thickness is negligible, the values obtained for films deposited on C_8SH- and C_{12}SH-steel (Fig. 4c) being practically identical to those reported for films on untreated-steel (2.25 – 2.35 μm),[29] independent of τ. In spite of this, the roughness of the films obtained using C_8SH- and C_{12}SH-steel increases by ~22% and ~30%, respectively, with respect

to those generated using untreated steel [*e.g.* the average RMS roughness for films on untreated-, C_8SH- and $C_{12}SH$-steel (τ= 2 h) is 393, 488 and 524 nm, respectively].

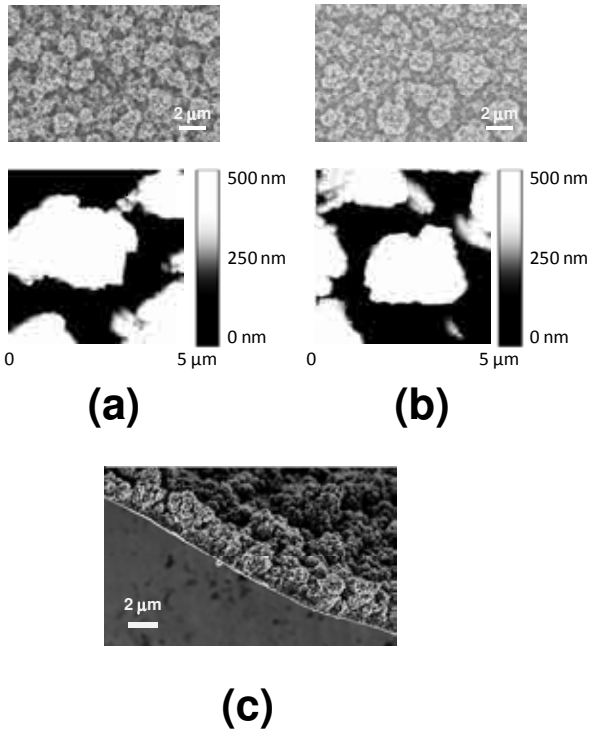

Figure 4. *SEM (top) and AFM height (bottom) images of micrometric PEDOT films deposited on (a) untreated- and (b) C_8SH-steel substrates. (c) SEM image showing the thickness of the micrometric PEDOT film deposited C_8SH-steel. Films were prepared considering a polymerization time of 300 s (thickness: 2.25-2.35 µm) and the modified substrate was obtained by immersing the steel electrode into 50 mL of octanethiol by τ= 24 h.*

XPS spectra of the C 1s (~288 eV), O 1s (~533 eV), S 2p (~165 eV) and Cl 2p (~206 eV) regions for PEDOT films obtained using untreated- and $C_{12}SH$-steel (τ= 2 h) electrodes were carried out to characterize the structure, counterion bonding and composition. The position of the peaks in the spectra was practically identical for both systems, the latter being the only displayed in Figure 2. Analysis of the C 1s region (Figure 2b) evidences four types of carbon, C-C/C-H (285.0 eV), C-S (285.3 eV) in the α position, C=C-O (286.3 eV) in the β position, and C-O-C (287.2 eV) in the ethylene bridge, which is in agreement with the values previously reported.[34,35] The carbon spectra also show an asymmetrical tail that resulted from a combination of π-π^* shake-up transition and possibly positively polarized or charged carbon.[34,36-38] The PEDOT characteristic C-O-C (533.3 eV) bonding is present in the O 1s region (Figure 2c) as well as a C-O (531.9 eV) contribution.[39] The PEDOT spin-split sulphur coupling, S $2p_{3/2}$ (164.1 eV) and S $2p_{1/2}$ (165.3 eV) with a separation of 1.18 eV[40] also present a

higher energy broad tail arising from positively charger sulphur within the thiophene ring (Figure 2d).[41-43] Another sulphur species observed at 166-167 eV has been attributed to oxidized S species, which may be due to fact that samples were repeatedly exposed to the atmosphere since their generation.[33]

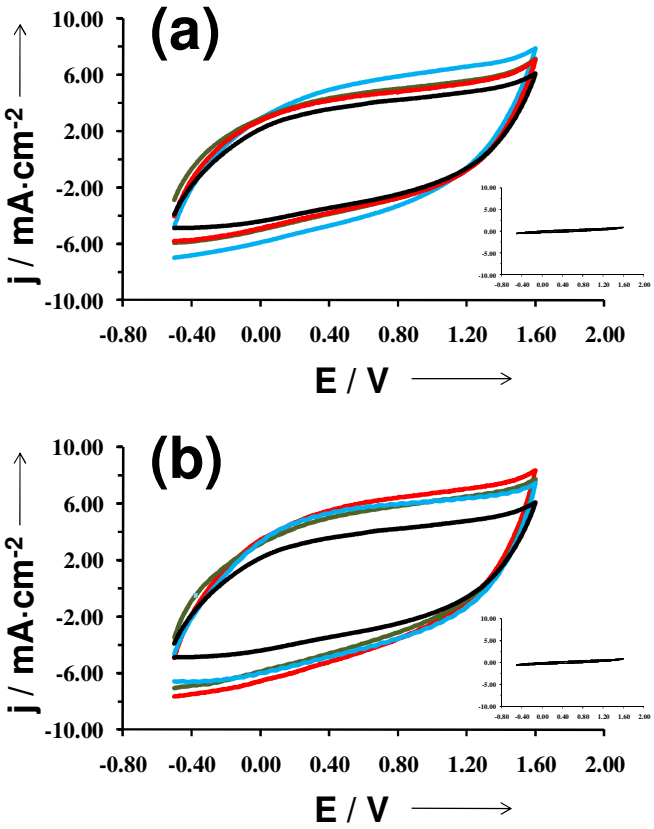

Figure 5. *Control voltammograms for the oxidation of micrometric PEDOT films deposited on untreated- (black line in both a and b), C_8SH- (a) and C_{12}SH-steel (b) substrates, the latter two being prepared considering τ = 2 h (blue line), 10 h (green line) and 24 h (red line). Voltammograms were recorded using a 4 cm^2 steel electrode in acetonitrile with 0.1M $LiClO_4$, at 100 $mV \cdot s^{-1}$ and 25ºC. Initial and final potentials: -0.50 V; reversal potential: 1.60 V. The absence of electrochemical activity of uncoated C_8SH- and C_{12}SH-steel substrates (blank samples) is evidenced in the insets of (a) and (b), respectively.*

Figure 5 compares the control voltammograms of micrometric PEDOT films deposited on untreated-, C_8SH- and C_{12}SH-steel, the latter two being prepared considering τ = 2, 10 and 24 h. As it can be seen, the electroactivity of films obtained using electrodes pre-treated with alkanethiols was significantly higher than that of PEDOT deposited on untreated-steel. Thus, the ability to store charge increases by ~ 22% and ~28% for C_8SH- and C_{12}SH-steel, respectively, even although such enhancement is practically independent of τ. On the other hand, the loss of electroactivity upon 30

consecutive oxidation-reduction cycles is of only 14% for PEDOT films deposited on untreated-steel, whereas the electrostability of films on C_8SH- and $C_{12}SH$-steel largely depends on τ.

This is reflected in Figure 6, which displays the variation of the loss of electroactivity against τ for the two types of pre-treated substrates. In both cases the loss of electroactivity increases with τ, even though films deposited on $C_{12}SH$-steel using τ = 2 and 10 h are more electrostable than those on untreated-steel.

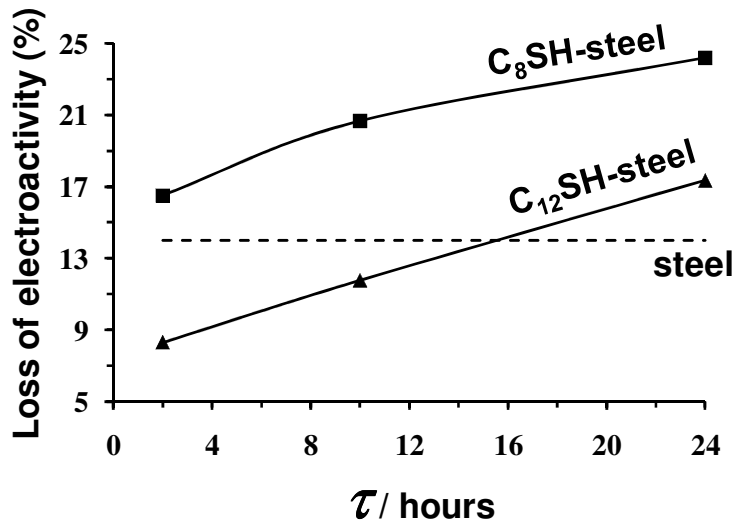

Figure 6. *Variation of the loss of electrostability of PEDOT films after 25 consecutive oxidation-reduction cycles against the period of time in which steel substrates were immersed in alkanethiol solutions (τ). The dashed line indicates the loss of electroactivity for PEDOT deposited on untreated-steel.*

The adherence was estimated using a normalized sellotape test, which gives a measure ranging from 0 to 100 %. Electrodes modified with SAMs improve the adherence of micrometric PEDOT films. Thus, adherence of PEDOT to the untreated-steel surface is 68% ± 1% while that of films deposited on C_8SH- and $C_{12}SH$-steel is 75% ± 1% and 83% ± 2%, respectively, independently of τ.

Nanometric PEDOT films. AFM images of nanometric PEDOT films (θ = 10 s) deposited on untreated, C_8SH- and $C_{12}SH$-steel (both τ = 2 and 24 h) are compared in Figure 7, while the roughness and the thickness of the films are listed in Table 1.

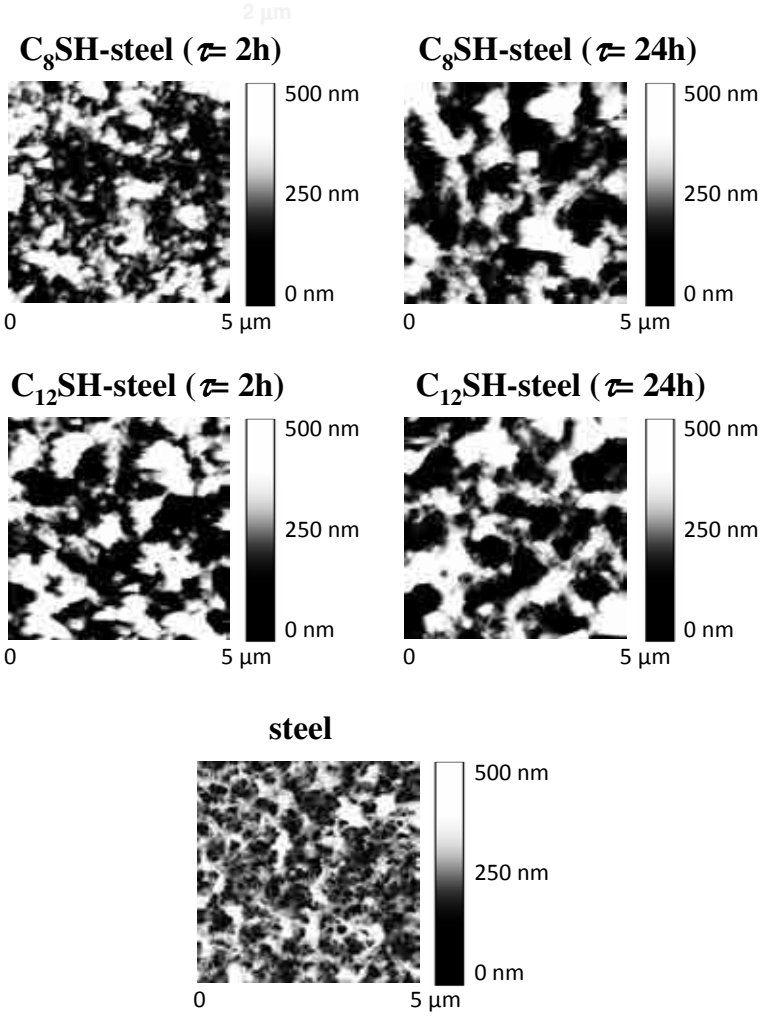

Figure 7. *AFM height images of nanometric PEDOT films deposited on untreated-, C_8SH-steel and C_{12}SH-steel substrates. Films were prepared considering a polymerization time of 10 s. Pre-treated substrates were obtained by immersing the steel electrodes into 50 mL of alkanethiol by τ = 2 and 24 h.*

As it can be seen, ultra-thin PEDOT films are significantly affected by the pre-treatment of the substrate, the thickness increasing with both the length of the alkyl chain in alkanehiol and τ. Specifically, comparison with the film deposited in untreated-steel indicates that the thickness increases from 16% to 54% and from 74% to 114% when the steel electrode is incubated in C_8SH and C_{12}SH solutions, respectively, for τ values ranging from 2 to 24 h.

Table 1. *Thickness (ℓ; in nm), roughness (r; in nm) and ℓ/r ratio of nanometric PEDOT films (θ= 10 s) deposited on untreated and pre-treated steel electrodes. C_8SH- and C_{12}SH-steel electrodes were prepared considering τ = 2, 10 and 24 h.*

Substrate	τ	ℓ	r	ℓ/r
Steel	-	153	67	2.3
Steel-C_8SH	2 h	178	78	2.3
	10 h	185	109	1.7
	24 h	236	87	2.7
Steel-C_{12}SH	2 h	267	100	2.7
	10 h	308	91	3.4
	24 h	343	93	3.7

The influence of the two alkanethiols on both the roughness and the topology is apparently different. Thus, although τ affects considerably both the roughness and topology of the films deposited on C_8SH-steel, this effect is less pronounced (topology) or almost inexistent (roughness) in films deposited on C_{12}SH-steel. The high density of small aggregates detected on porous films deposited on untreated-steel transforms into a distribution involving a few compact aggregates upon the pretreatment of the substrate. The dimensions (both height and diameter) and the density of such aggregates increases and decreases, respectively, with the size of the alkanethiol and, in the case of the C_8SH-steel electrode, with τ. This behavior should be attributed to the fact that SAMs of C_{12}SH are more regular and well-packed than those of C_8SH, the influence of the incubation time τ on the structure being much less relevant in the former than in the latter.

Similar features are evidences in Figure 8, which shows high- and low-resolution images of PEDOT films deposited on untreated-, C_8SH- and C_{12}SH-steel (τ = 2 h). Thus, the porosity of the films clearly grows in the following order: steel << C_8SH-steel << C_{12}SH-steel, evidencing that the pre-treatment of the substrates with alkanethiols affects significantly to the morphology of the surface.

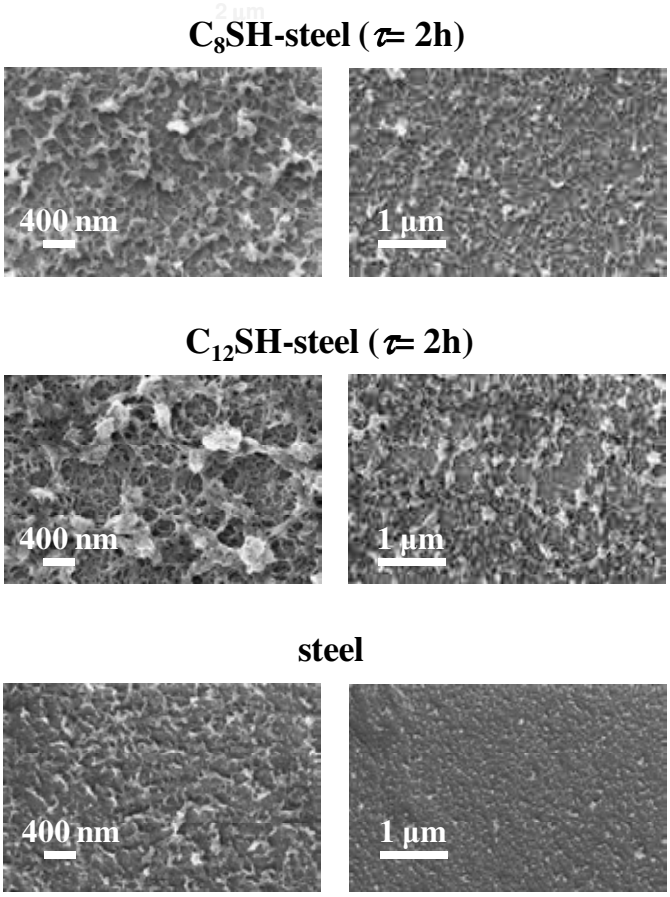

Figure 8. *High- and low-resolution SEM micrographs (left and right, respectively) of PEDOT films deposited untreated-, C_8SH- and C_{12}SH-steel substrates. Films were prepared considering a polymerization time of 10 s. Pre-treated substrates were obtained by immersing the steel electrodes into 50 mL of octanethiol by τ = 2 h.*

The electroactivity and electrostability of nanometric films deposited on C_8SH- and C_{12}SH-steel electrodes have been determined, results being expressed in Table 2 relative to those obtained for PEDOT generated on untreated-steel. As it can be seen, the electroactivity and electrostability of PEDOT films produced on the modified substrates are significantly higher than those of the material electropolymerized on untreated-steel. The electroactivity grows with the length of the alkanethiol, the maximum enhancement being achieved with the smallest incubation time in both cases. In contrast, the electrostability shows the opposite behavior: it increases with the incubation time and is higher for C_8SH-steel than for C_{12}SH-steel. On the other hand, it should be noted that adherence measurements on films produced using θ = 10 s are not representative due to their ultra-thin nature.

Table 2. *Electroactivity and electrostability (both in %) of nanometric PEDOT films (θ = 10 s) deposited on C_8SH- and C_{12}SH-steel electrodes with respect to films generated on untreated-steel. C_8SH- and C_{12}SH-steel electrodes were prepared considering τ = 2, 10 and 24 h.*

Substrate	Incubation time (τ)	Electroactivity	Electrostability
Steel-C_8SH	2 h	39	17
	10 h	36	21
	24 h	35	24
Steel-C_{12}SH	2 h	45	8
	10 h	43	12
	24 h	41	17

Corrosion protection. SAMs derived from alkanethiols were successfully applied to inhibit the corrosion of iron and other metallic substrates.[44,45] Thus, the formed stable hydrophobic films depressed significantly the metal dissolution of the underlying substrate. On the other hand, PEDOT has been found to impart protection against corrosion when it is used as anticorrosive additive in the formulation of conventional epoxy paints,[46,47] whereas the protective effect of PEDOT films directly deposited on the metal substrate was very slight.[48] In this section, we examine the benefits of the alkanethiols in the protective effects of PEDOT films.

The EIS plots obtained for PEDOT films (θ = 300 s) deposited on untreated- and C_8SH-steel (τ = 2 h) after 24, 168 and 480 h of immersion in a 3.5% NaCl solution are provided in Figure 8. The EIS diagrams obtained for the films deposited on C_8SH- and C_{12}SH-steel were very similar and, therefore, the latter are not reported here for the sake of simplicity. In all cases spectra show three well-characterized regions. At high frequencies (f > 25 Hz), a capacitive semi-circle related with the polymer-electrolyte interface is observed, its diameter determining the charge transfer resistance (R_{CT}) in parallel with the double layer capacitance (C_{DL}). At intermediate frequencies (25 Hz < f < 1.5 Hz), the spectra shows a linear line with a slope around 45º, which corresponds to a Warburg diffusion region and should be attributed to the semi-infinite diffusion of protons at the polymer-electrolyte interface. Finally, at the low frequency range (f < 1 Hz), a nearly vertical line is found due to the faradaic pseudocapacitance of the PEDOT film, as previously described.[49,50] Thus, at higher frequencies the process is charge-

transfer controlled while at lower frequencies the diffusion of charges in the CP film determines the impedance response. According to Hunter *et al.*,[51] the frequency range of the diffusion behavior is controlled by the diffusion coefficient and the film thickness. Thus, thick films show diffusion over a large frequency range while no diffusion region is detected in ultra-thin films.

EIS diagrams were analyzed using the equivalent circuit (EC) displayed in Figure 9c, which was previously proposed for CP coatings.[50,52] The proposed EC is given by $R_s[CPE_{DL}(R_{CT}\cdot W)]CPE_{PC}$, where: R_s is the ohmic resistance between the working and the reference electrodes; CPE_{DL} is the double layer capacitance; R_{CT} is the charge-transfer resistance in serial connection with a Warburg element, W, that accounts for diffusion; and CPE_{PC} is the pseudo-capacitance at lower frequencies. The capacitances were replaced by a constant phase element (CPE) that describes a non-ideal capacitor when phase angle is different from -90º. The CPE impedance is attributed to the distributed surface reactivity, surface heterogeneity, and roughness of the current and potential distribution, which is turn are related with the electrode geometry and the electrode porosity.[53] It should be noted that elements associated to the proposed EC, which was selected considering software limitations and the minimum number of circuit elements, are probably involved on both treated and untreated metal surface. The fitting with experimental data provided errors percentage smaller than 5% for each circuit component indicating a satisfactory behavior.

Table 3 shows the simulated values derived from the fitting of the EIS plots represented in Figures 9a and 9b to the EC displayed in Figure 9c. As it can be seen, the impedance is larger for samples deposited on the C_8SH-steel than for those generated on untreated steel. The observed increase of the R_{CT} values at the thiol modified samples was associated with the inhibition effect of thiol layer, decreasing the metal dissolution rate. Moreover the capacitance associated with this feature (CPE_{DL}) is lower than that of the sample deposited on untreated-steel, remaining practically unchanged during the immersion time, probably due to surface smoothing.[54] The Warburg impedance increases with the immersion time, assuming higher values at the samples deposited on C_8SH-steel. Additionally, the pores and/or defects of the CP coating can be blocked by corrosion products, making diffusion more difficult and hindering the access of the aggressive electrolyte to the metal surface, which led to an increase of the overall resistance.

Table 3. *Fitting parameters used to simulate the EIS data obtained for the systems studied in this work.*

Substrate	**Immersion time (h)**	**R_S ($\Omega \cdot cm^2$)**	**CPE_{DL} ($\mu F \cdot cm^{-2} \cdot s^{n-1}$)**	**n**	**R_{CT} ($\Omega \cdot cm^2$)**	**W ($\Omega \cdot cm^{-2}$)**	**CPE_{PC} ($mF \cdot cm^{-2} \cdot s^{n-1}$)**	**n**
Untreated-steel	24	7.02	15.40	0.94	33.6	12.04	20.60	0.85
	168	9.14	20.39	0.89	68.48	22.02	20.72	0.81
	480	10.41	21.73	0.86	104.4	20.53	21.05	0.95
C_8SH-steel	24	7.96	16.81	0.91	102.1	22.17	6.17	0.80
	168	8.16	14.70	0.88	172.9	33.26	6.79	0.79
	480	11.02	19.26	0.96	240.7	45.51	7.76	0.91

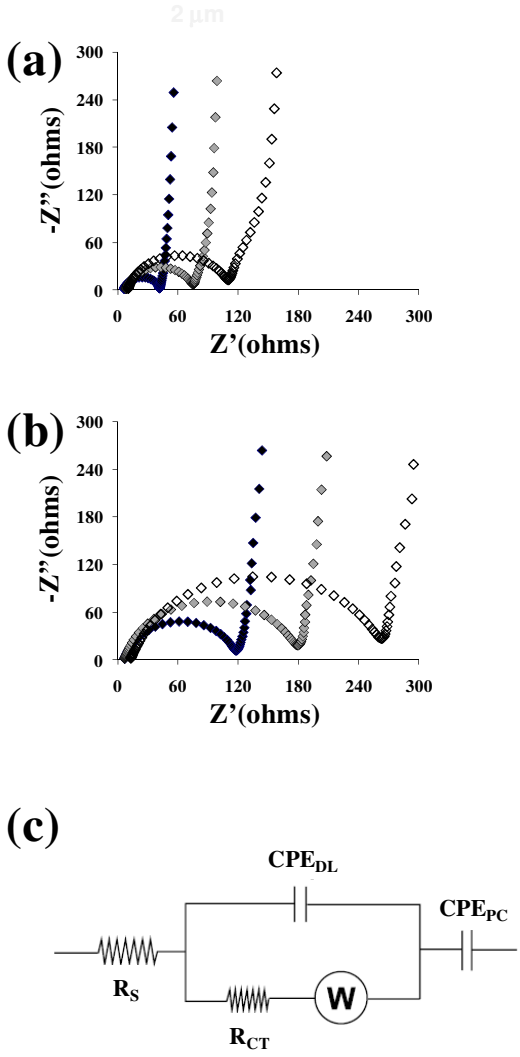

Figure 9. *Nyquist plots of PEDOT films deposited in (a) untreated- and (b) C_8SH-steel after immersion in a 3.5% NaCl solution during 24 (black symbols), 168 (grey symbols) and 480 h (empty symbols). Films were prepared considering a polymerization time of 300 s. Modified substrates were obtained by immersing the steel electrodes into 50 mL of alkanethiol by τ = 2 h. (c) Equivalent circuit used to simulate the experimental spectra displayed in (a) and (b).*

Figure 10a shows the surface of the PEDOT film deposited on C_8SH-steel after 168 h of immersion in a 3.5% NaCl solution. As it can be seen, salt aggregates tend to fill the pores at the surface of the CP, making difficult the access of the anions to the substrate. However, the same protection mechanism was also observed in PEDOT films generated on untreated-steel. Figure 10b shows the morphology of both the external and internal sides of the PEDOT film electropolymerized on the C_8SH-steel substrate after 480 h of exposure to the 3.5% NaCl solution. The film was washed with distilled water before to obtain the SEM micrographs. As it can be seen, the NaCl does not affect to the morphology of the CP, the aspect of the external side being very similar to that

displayed in Figure 4. However, detailed inspection of Figure 10b reveals that the morphology of the internal side is more compact than that of the external side. This observation is fully consistent with the results obtained for PEDOT films with nanometric thickness (Figures 7 and 8). Accordingly, the corrosion protection showed by EIS diagrams (Figure 9) should be attributed not only to the barrier effect produced by the SAMs of alkanethiol but also to their influence on morphology of the CP at the first stages of the electropolymerization process.

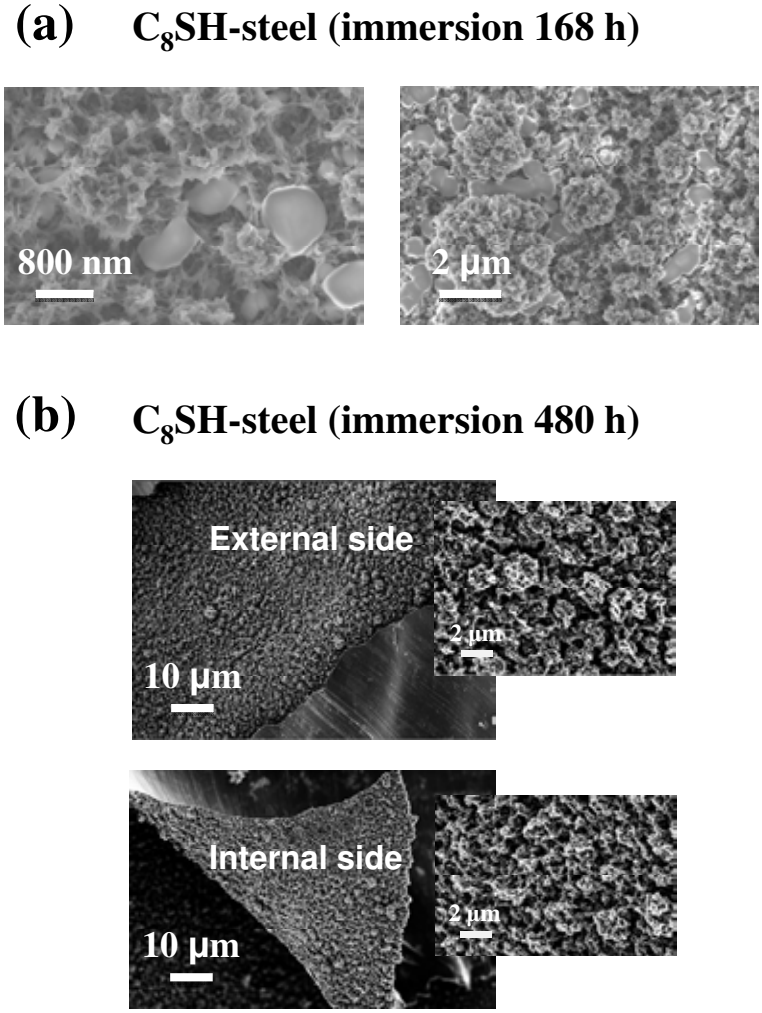

Figure 10. *SEM micrographs of PEDOT film deposited on C_8SH-steel: (a) high (right) and low (left) resolution images of surface after 7 days of exposure to a 3.5% NaCl solution; and (b) the internal and external sides washed with distilled water after 20 days of exposure to a 3.5% NaCl solution. Films were prepared considering a polymerization time of 300 s and the treated substrate was obtained by immersing the steel electrode into 50 mL of octanethiol by $\tau = 2$ h.*

4.1.4. Conclusions

SAMs of C_8SH and $C_{12}SH$ have been anchored to stainless steel substrates through C-S covalent bonds. Comparison of PEDOT films deposited on untreated-, C_8SH- and $C_{12}SH$-steel reveals that SAMs may affect the structural and electrochemical properties of the CP, even though the scale of such effects depends on the thickness of the films. Specifically, the topology and morphology at the surface of PEDOT films obtained using θ = 300 s, which present thickness larger than 2 μm, are not affected by alkanethiols. However, SAMs promote both the electroactivity and the adherence of micrometric films, such enhancements increasing with the length of alkyl chain of the alkanethiol. In contrast, the influence of SAMs in nanometric PEDOT films, produced using θ = 10 s, is more drastic, affecting the topology, morphology and electrochemical properties of the CP. The extension of such effects depends on the alkanethiol and, in some cases, also on the incubation period τ. Thus, although both C_8SH and $C_{12}SH$ increase the thickness, roughness, electroactivity and electrochemical stability of PEDOT, the range of variation of these properties against τ is considerably larger for the first alkanethiol than for the latter one. Furthermore, SAMs promote the formation of compact molecular aggregates reducing the porosity of nanometric films. The latter effect, which has been also evidenced in the first stages of the electropolymerization of micrometric PEDOT films, together with the intrinsic barrier properties of alkanethiol SAMs are responsible of the significant improvement of the abilities of this CP to inhibit corrosion. Thus, EIS experiments showed that PEDOT films deposited on C_8SH- and $C_{12}SH$-steel protect the metallic substrate against corrosion, whereas the protective effect of PEDOT deposited on untreated-steel is considerably lower.

4.1.5. References

[1]. Ulman, A. *An Introduction to Ultrathin Organic Films*; Academic: New York, 1991.

[2]. (a) Love, J. C.; Estroiff, L. A.; Kriebel, J. K.; Nuzzo, R. G.; Whitesides, G. M. *Chem. Rev.* **2005**, *105*, 1103. (b) Schreiber, F. *Prog. Surf. Sci.* **2000**, *65*, 151; (c) Smith, R. K.; Lewis, P. A.; Weiss, P. S. *Prog. Surf.Sci.* **2004**, *75*, 1. (d) Porter, M. D.; Bright, T. B.; Allara, D. L.; Chidsey, C. E. D. *J. Am. Chem. Soc.* **1987**, *109*, 3559. (e) Dubois, L. H.; Zegarski, B. R.; Nuzzo, R. G. *J. Am. Chem. Soc.* **1990**, *112*, 570.

[3]. Becka, A.; Miller, C. J. *J. Phys. Chem.* **1992**, *96*, 2657.

[4]. Allernan, S. K.; Weber, K.; Creager, S. E. *J. Phys. Chem.* **1996**, *100*, 17050.

[5]. Miller, C.; Cuendet, P.; Grätzel, M. *J. Phys. Chem.* **1991**, *95*, 877.

[6]. Sayre, C. N.; Collard, D. M. *Langmuir* **1997**, *13*, 714.

[7]. Sayre, C. N.; Collard, D. M. *Synth. Met.* **1995**, *69*, 459.

[8]. Mazur, M.; Predeep, P. *Polymer* **2005**, *46*, 1724.

[9]. Abaci, S.; Shannon, C. *Electrochim. Acta* **2005**, *50*, 2967.

[10]. Niu, L.; Latonen, R.-M.; Kvarnström, C.; Ivaska, A. *Electrochim. Acta* **2004**, *49*, 4455.

[11]. Meklhalif, Z.; Lang, P.; Gamier, F. *J. Electroanal. Chem.***1995**, *399*, 61.

[12]. Mazur, M.; Krusinski, P. *Langmuir* **2000**, *16*, 7962.

[13]. Li, X.; Zhang, X.; Sun, Q.; Lü, W.; Li, H. *J. Electroanal. Chem.* **2000**, *492*, 23.

[14]. Mekhalif, Z.; Delhalle, J.; Lang, P.; Gamier, F.; Pireaux, J.-J. *Synt.Met.* **1998**, *96*, 165.

[15]. Gonçalves, D.; Irene, E. A. *Electroanalysis* **2003**, *15*, 652.

[16]. Rozsnyai, L. F.; Wrighton, M. S. *Chem. Mat.* **1996**, *8*, 309.

[17]. Inaoka, S.; Collard, D. M. *Langmuir* **1999**, *15*, 3752.

[18]. Mazur, M.; Krysinski, P. *J. Phys. Chem. B* **2002**, *106*, 10349.

[19]. Lota, K.; Khomenko, V.; Frackowiak, E. *J. Phys. Chem. Solids.* **2004**, *65***,** 295.

[20]. Ryu, K. S.; Lee, Y. G.; Hong, Y. S.; Park, Y. J.; Wu, X. L.; Kim, K. M.; Kang, M.G.; Park, N. G.; Chang, S. H. *Electrochim. Acta* **2004**, *50*, 843.

[21]. Ghosh, S.; Inganas, O. *Electrochem. Solid State Lett.* **2000**, *3***,** 213.

[22]. del Valle, L. J.; Aradilla, D.; Oliver, R.; Sepulcre, F.; Gamez, A.; Armelin, E.; Alemán, C.; Estrany, F. *Eur. Polym. J.* **2007**, *43***,** 2342.

[23]. Tamburri, E.; Orlanducci, S.; Toschi, F.; Terranova, M. L.; Passeri, D. *Synth. Met.* **2009**, *159*, 406.

[24]. Ocampo, C.; Oliver, R.; Armelin, E.; Alemán, C.; Estrany, F. *J. Polym. Research.* **2006**, *13***,** 193.

[25]. Aradilla, D.; Estrany, F.; Alemán, C. *J. Phys. Chem. C.* **2011**, *115*, 8430.

[26]. Bergman, B.; Hanks, T. W. *Macromolecules* **2000**, *33*, 8035.

[27]. Estrany, F.; Aradilla, D.; Oliver, R.; Alemán, C. *Eur. Polym. J*. **2008**, *44***,** 1323

[28]. Aradilla, D.; Estrany, F.; Alemán, C. *J. Appl. Polym. Sci.* **2011**, *121*, 1982.

[29]. Aradilla, D.; Estrany, F.; Armelin, E.; Alemán, C. *Thin Solid Films* **2010**, *518*, 4203.

[30]. Bain, C. D.; Troughton, E. B.; Tao, Y.-T.; Evall, J.; Whitesides, G. M.; Nuzzo, R. G. *J. Am. Chem. Soc.* **1989**, *111*, 329.

[31]. Bain, C. D.; Whitesides, G. M. *Science* **1988**, *240*, 62.

[32]. Deng, W.; Yang, L.; Fujita, D.; Nejoh, H.; Bai, C. *Appl. Phys.* **2000**, *71*, 639.

[33]. Desikan, R.; Armel, S.; Meyer III, H. M.; Thundat, T. *Nanotechnology* **2007**, *18*, 424028.

[34]. Jönsson, S. K. M.; Birgerson, J.; Crispin, X.; Greczynski, G.; Osikowicz, W.; Denier Van Der. *Synth. Met.* **2003**, *139*, 1.

[35]. Jönsson, S. K. M.; de Jong, M. P.; Groenendaal, L.; Salaneck, W. R.; Fahlman, M. *J. of Phys. Chem. B* **2003**, *107*, 10793.

[36]. Khan,M. A.; Armes, S. P. *Langmuir* **2000**, *16*, 4171.

[37]. Riga, J.; Snauwaert, P.; De Pryck, A.; Lazzaroni, R.; Boutique, J. P.; Verbist, J. J.; Brédas, J. L.; André, J. M.; Taliani, C. *Synth. Met.* **1987**, *21*, 223.

[38]. Wu, C. R.; Nilsson, J. O.; Inganäs, O.; Salaneck,W. R.; Österholm, J. E.; Brédas, J. L. *Synth. Met.* **1987**, *21*, 197.

[39]. Jönssom, S. K. M.; Salaneck, W. R.; Fahlman, M. *J. Mater. Res.* **2003**, *18*, 1219.

[40]. Moulder, J. F.; Stickle, W. F.; Sobol, P. E.; Bomben, K. D. Handbook of X-ray Photoelectron Spectroscopy: A Reference Book of Standard Spectra for Identification and Interpretation o XPS Data. Eden Prairie, MN: Perkin-Elmer Corporation.

[41]. Greczynski, G.; Kugler, T.; Salaneck, W. R. *Thin Solid Films* **1999**, *354*, 129.

[42]. Kang, E. T.; Neoh, K. G.; Tan, K. L. *Physical Review B* **1991**, *44*, 10461.

[43]. Zotti, G.; Zecchin, S.; Schiavon, G. *Macromolecules* **2003**, *36*, 3337.

[44]. Grundmeier, G.; Reinartz, C.; Rohwerder, M.; Stratmann, M. *Electrochim. Acta* **1998**, *43*, 165.

[45]. Itoh, M.; Nishiharam H.; Aramaki, K. *J. Electrochem. Soc.* **1994**, *141*, 2018.

[46]. Armelin, E.; Meneguzzi, A.; Ferreira, C. A.; Alemán, C. *Surf. Coat. Technol.* **2009**, *203*, 3763.

[47]. Armelin, E.; Oliver, R.; Liesa, F.; Iribarren, J. I.; Estrany, F.; Alemán, C. *Prog. Org. Coat.* **2007**, *59*, 46.

[48]. Lallemand, F.; Plumier, F.; Delhalle, J.; Mekhalif, Z. *Appl. Surf. Sci.* **2008**, *254*, 3318.

[49]. Chen, W.-C.; When, T.-C.; Hu C.-C.; Golapan, A. *Electrochim. Acta* **2002**, *47*, 1305.

[50]. Sem, P.; De, A. *Electrochim. Acta* **2010**, *55*, 4677.

[51]. Hunter, B.; Tyler, P. S.; Smyrl, W. H.; White, H. S. *J. Electrochem.Soc.* **1987**, *134*, 2198.

[52]. Felhosi, I.; Telegdi, J.; Palinkas, G.; Kalman, E. *Electrochim. Acta* **2002**, *47*, 2335,

[53]. Jorcin, J.-B.; Orazem, M. E.; Pébère, N.; Tribollet, B. *Electrochim. Acta* **2006**, *51*, 1473.

[54]. Castagno, K. R. L.; Azambuja, D. S.; Dalmoro, V. *J. Appl. Electrochem.* **2008**, *39*, 93.

4.2. Ultraporous poly(3,4-ethylenedioxythiophene) for nanometric electrochemical supercapacitor

4.2.1. Introduction

The fabrication of thin and ultrathin (*i.e.* micrometric and nanometric thickness, respectively) films of conjugated organic conducting polymers (CPs) is a challenging task because these materials are usually insoluble, infusible and intractable. Within this context particular emphasis has been devoted to understand the fabrication mechanism of CPs by various techniques, as well as the influence of such techniques on their morphology and structure-properties relationships.[1-11] Thus, the ultimate goal is the control of the structure within the micro- and nanometric scales to build devices with well-defined properties.

Among the different techniques for the fabrication of thin films made of CPs, electrochemical deposition is relatively frequent. In the last years the structure and morphology of electrogenerated thin films made of CPs with important technological properties have been reported. Structure-properties relationships were examined for polypyrrole,[12,13] polyaniline,[14,15] and polythiophene[3,4,6-8,16-21] films grown on different surfaces, *e.g.* platinum, gold, steel and indium-tin oxide (ITO) electrodes. Within this field, films made of poly(3,4-ethylenedioxythiophene), abbreviated PEDOT, are particularly relevant because of its high electrical conductivity, transparency, environmental stability and fast doping-undoping mechanism.[22,23] Although the structure and morphology of PEDOT films with micrometric thickness have been studied in detail by different researchers,[8,19,20] studies on PEDOT ultrathin films are very scarce.[8,24] As a part of a wide study devoted to investigate multilayered (*i.e.* 3- and 5-layered) films made of two CPs, the surface topography of PEDOT films using atomic force microscopy (AFM) was recently examined. The thickness of such films, which were electrodeposited on steel AISI (American Iron Steel Industry) 316 L electrodes,[24] ranged from 125 to 600 nm. Results were correlated with the variation of the electrochemical activity at the nanometric scale.

The physical characteristics of the substrate are expected to have a very significant influence on both the properties and the structure of ultrathin electrodeposited films. Specifically, the roughness and chemical nature of the electrode surface plays a crucial role in the three dimensional organization of the CP chains, which may affect the access

and escape of the dopant ions along oxidation and reduction processes. The importance of this effect increases when the thickness of the film decreases, being significantly more pronounced in the nanometric scale than in the micrometric one.

Supercapacitors consist on electrochemical capacitors that can be used as charge storage devices to provide higher power density, energy density, and longer life cycle than batteries and conventional capacitors.[25-27] Therefore, the exploration, improvement and discovery of new electrode materials to achieve supercapacitors with better electrochemical properties is a challenge. Although, PEDOT is considered a good candidate for capacitor electrodes because of its electrochemical properties,[28] its high molar mass and moderate specific capacitance compared with other CPs suggest the exploration of new alternatives.[29] In recent years significant efforts have been devoted to improve the capacitive properties of PEDOT preparing composites based on transition metal oxides (*e.g.* MnO_2, MoO_3, $NiFe_2O_4$, and V_2O_5), which embedded into a PEDOT polymeric matrix, carbon nanotubes, etc.[30-33] The specific capacitance (SC) of these PEDOT-inorganic hybrid nanocomposites for ranged from 153 to 375 F/g.[34-40] In a very recent study, the behavior as supercapacitor of electrodes made of micrometric PEDOT films with those formed by alternated layers of PEDOT and poly(N-methylpyrrole) (ml-PEDOT/PNMPy) was compared.[41] The specific capacitance of ml-PEDOT/PNMPy (SC = 90 F/g) was found to be significantly higher than that of pure PEDOT (SC = 41 F/g), even though both were lower than those reported for PEDOT-inorganic hybrid nanocomposites.

Supercapacitors based on CPs can be categorized into three different configurations.[42] Type I consists on symmetric systems, which use the same *p*-dopable CP for the two electrodes. Type II corresponds to asymmetric systems based on two different *p*-dopable CPs with very different electroactivities. Finally, type III supercapacitors are formed by symmetric systems that use the *p*-doped form of a CP as the positive electrode and the *n*-doped form of the same material as the negative electrode. Supercapacitors devices based on configurations of types I and II are the most frequent due to the fact that the preparation of *p*-doped CPs is easier than that of *n*-doped CPs.

In this work a comprehensive study comparing ultrathin PEDOT films obtained by electropolymerization on ITO and steel substrates is discussed. For this purpose, the structure, surface morphology, topography, roughness and thickness of films prepared considering polymerization times ranging from 5 to 50 s have been examined using both

Scanning Electron Microscopy (SEM) and Atomic Force Microscopy (AFM). The electrochemical activity and stability of the produced films, which are ultraporous, have been correlated with the structural and morphological characteristics. In order to take advantage of their different electroactivities, ultraporous ultrathin PEDOT films deposited on ITO and steel have been used to fabricate asymmetric supercapacitors. The specific capacitance of these devices has been found to be higher than those reported in the literature for other advanced supercapacitors.

4.2.2. Methods

***Materials*.** 3,4-Ethylenedioxythiophene (EDOT) and acetonitrile of analytical reagent grade were purchased from Aldrich. Anhydrous $LiClO_4$, analytical reagent grade, from Aldrich was stored in an oven at 80ºC before use in the electrochemical trials.

Polymerization. PEDOT was polymerized by chronoamperometry (CA) under a constant potential of 1.40 V, which was reported to be the optimum oxidation potential for the experimental conditions used in this work.[43] All the anodic electropolymerizations and electrochemical experiments were performed using a VersaStat II potenciostat-galvanostat connected to a computer controlled through a Power Suite Princenton Applied Research program. Electrochemical experiments were conducted in a three-electrode two-compartment cell under nitrogen atmosphere (99.995% in purity) at 25ºC. The anodic compartment was filled with 40 ml of a 10 mM EDOT solution in acetonitrile containing 0.1 M $LiClO_4$ as supporting electrolyte, while the cathodic compartment was filled with 10 ml of the same electrolyte solution. Steel AISI 316 L and ITO sheets of 1×1 and 0.5×0.5 cm^2, respectively, were employed as working and counter electrodes for the generation in the different substrates. In order to avoid interferences during the electrochemical analyses, the working and counter electrodes were cleaned before each trial. Specifically, steel electrodes were cleaned with acetone while ITO electrodes were cleaned in an ultrasonic bath in different solvents: acetone, ethanol, de-ionized water, and isopropanol (5 min respectively), followed by an acetone washing. Finally, the ITO substrate was dried by a nitrogen flow. The reference electrode was an Ag|AgCl electrode containing a KCl saturated aqueous solution (E^o = 0.222 V at 25 ºC), which was connected to the working compartment through a salt bridge containing the electrolyte solution.

Atomic Force Microscopy. Topographic images of ultrathin and thin PEDOT films were obtained with a Molecular Imaging PicoSPM using a NanoScope IV controller in ambient conditions. The tapping mode AFM was operated at constant deflections (*i.e.* vertical constant force with triangular shaped gold-coated silicon nitride. The row scanning frequency was set to 1 Hz and the physical tip-sample motion speed was 10 $\mu m \cdot s^{-1}$. The root-mean-square (RMS) roughness (r) was determined using the statistical application of the Nanoscope software, which calculates the average considering all the values recorded in the topographic image with exception of the maximum and the minimum. The scan window size was 5×5 μm^2 in all cases, a total of 65.536 topographic data being computed in each image. In all images acquired, which are 512×512 $pixel^2$ maps, differences in height are indicated by a color scale: dark is low, and white is high.

Scanning Electron Microscopy. SEM micrographs were carried out with a Zeiss Neon 40 scanning electron microscope at 3.00 kV.

Thickness of the films and electrochemical measures. The electrochemical thickness of the films was estimated from the mass of polymer deposited in the electrode, m_{pol}, using the procedure reported by Schirmeisen and Beck[44] using a Sartorius ultra-microbalance. Accordingly, m_{pol} was determined using the following relation:

$$m_{pol} = Q_{pol}\left(\frac{m}{Q}\right) \qquad (1)$$

where Q_{pol} is the polymerization charge in (millicoulombs per square centimetre) consumed in the generation of each layer and $\left(\frac{m}{Q}\right)$ is the current productivity. The latter has been determined to be around 0.628 $mg \cdot C^{-1}$ for films grown on both steel AISI 316 L and ITO substrates. The volume of polymer deposited in the electrode (V_{pol}), which was obtained using the values of m_{pol} and the density, was used to determine the thickness considering that the surface of polymerization (S_{pol}) is identical to the surface of the electrode. The density of PEDOT (1.66 $g \cdot cm^{-3}$) was reported in a previous work.[43] The electroactivity and electrostability were determined by cyclic voltammetry determining the similarity between the anodic and cathodic areas of the control voltammogram. The electroactivity increases with the similarity between the anodic and

cathodic areas of the first control voltammogram, whereas the electrostability decreases with the oxidation and reduction areas of consecutive control voltammograms. A scan rate of 100 $mV \cdot s^{-1}$ was used in all cases. The initial and final potentials were -0.50 V, while the reversal potential was 1.60 V.

The doping level (*f*) of PEDOT electrodeposited on steel and ITO substrates has been determined electrochemically by using Eqn (2):[45]

$$f = \frac{2Q_o}{Q_d - Q_o}100 \qquad (2)$$

where Q_d is the total charge used for PEDOT deposition and Q_0 is total charge of oxidized species in the PEDOT films.

The specific capacitances (in F/g) of the active material in the electrodes were calculated as:

$$SC = \frac{Q}{\Delta V m} \qquad (3)$$

where Q is voltammetric charge, which is determined by integrating either the oxidative or the reductive parts of the cyclic voltammogram curve, ΔV is the potential window and m is the mass of polymer on the surface of the working electrode. The latter is derived from the productivity current and polymerization charge.[44] The Coulomb efficiency (η) was defined as the ration between the discharge and charge time (t_d and t_c, respectively):

$$\eta = \frac{t_d}{t_c}100 \qquad (4)$$

The loss of electrostability (*LES*) was determined as:

$$LES = \frac{\Delta Q}{Q_i}100 \qquad (5)$$

where ΔQ is the difference of voltammetric charge between the second cycle and the last cycle and Q_i is the voltammetric charge corresponding to the second cycle. The initial and final potentials used to measure the LES of the supercapacitors were -0.20 V, while the reversal potential was 1.20 V.

4.2.3. Results and discussion

In this work ultrathin PEDOT films have been electrochemically deposited on steel AISI 316 L and ITO substrates. Figure 1 shows AFM images of the two substrates evidencing that their surfaces are very flat, the values of RMS roughness being r = 11.4 and 4.2 nm for steel and ITO, respectively. On the other hand, the electrical properties of the two substrates have been extensively studied.[46-52]

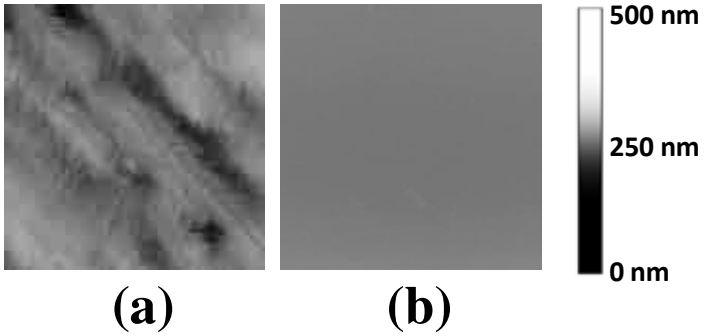

Figure 1. *2D AFM images of the steel (a) and ITO (b) surfaces before deposition.*

The electrical resistivity of the two materials are relatively similar (*i.e.* ~$10^{-4}\Omega\cdot$cm). Figure 2 compares the 2D height AFM images of PEDOT films obtained using polymerization times (θ) of 5, 10, 30, 50 and 300 s, while the averaged values of the roughness are listed in Table 1.

Table 1. *Thickness (ℓ, in nm) and roughness (r, in nm) of PEDOT films deposited in ITO and steel AISI 316 Lsubstrates using different polymerization times (θ, in s). Thickness of films produced on ITO has been determined using both AFM and electrochemical measures.*

θ (s)	ITO/PEDOT			Steel/PEDOT	
	ℓ (AFM)	ℓ (electroch.)	r	ℓ (electroch.)	r
5	51.7	50.4	46	31.4	63
10	125.4	122.9	51	89.6	73
30	212.4	195.2	77	147.6	87
50	391.2	382.2	97	311.1	136
300	-	3170	123	2350	325

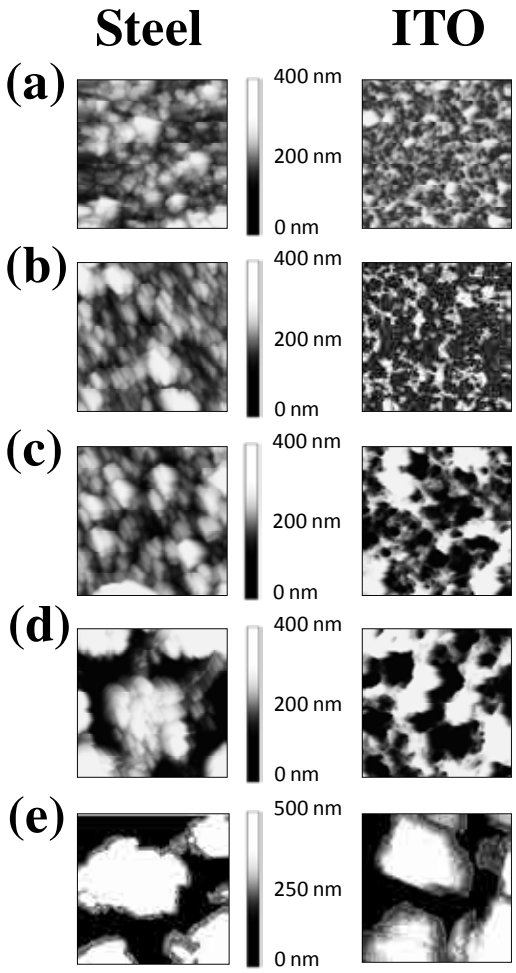

Figure 2. *2D height AFM images of PEDOT films deposited on steel (left) and ITO (right) electrodes using a polymerization time of θ = 5 (a), 10 (b), 30 (c), 50 (d) and 300 s (e).*

As it can be seen, the surface topology strongly depends on the nature of the substrate. At the lower polymerization times (θ = 5 and 10 s) polymer chains deposited on the steel surface tend to organize forming a dense distribution of sharp peaks grouped in clusters, *i.e.* independent *mountain ranges* separated by *valleys*. The size and number of these clusters increase and decrease, respectively, with the polymerization time. The image of the film obtained using θ = 5 s allows to identify a large number of clusters, each one occupying relatively a small area, which are separated by flat regions of very different sizes heterogeneously distributed. In contrast the image recorded for the film produced using θ = 50 s presents a reduced number of compact and, simultaneously, large blocks of aggregated polymers chains emerging over wide flat regions. Thus, enlargement of the polymerization time does not correspond to a homogeneous growing, in terms of high, of the clusters initially formed but an

aggregation of clusters, enhancing the difference with respect to the plateau regions, *i.e.* the surface is much less leveled. Consequently, the RMS average roughness increases with the polymerization time (Table 1). Moreover, analysis of the most suitable analytical model to describe the enhancement of the roughness r against the polymerization time indicates that the only expression with a regression coefficient $R^2 > 0.95$ is, with the obvious exception of a polynomial with several degrees of freedom, the linear one (Figure 3): $r = 0.9 \cdot \theta + 68.4$ ($R^2 = 0.984$).

The topography of the films electrodeposited in ITO electrodes is completely different from that discussed above for very short polymerization times, *i.e.* $\theta \leq 10$s. The surface of the films obtained using $\theta = 5$ s consists of a homogeneous and dense distribution of narrow peaks, which is preserved in the film produced using $\theta = 10$ s. The extremely low roughness of the ITO substratum allows the formation of multiple nucleation centers during the first steps of the electropolymerization process, which are randomly distributed over the electrode surface. The resemblance between the topology of the films deposited on ITO and steel increases with the polymerization time for $\theta > 30$ s (Figure 2), *i.e.* the tendency to form compact plateau regions located at different levels grows with the thickness of the films, even though the nanometric effect associated to the substrate is still present in the films obtained using $\theta = 50$ s. However, the images of the films produced using $\theta = 300$ s indicate that, in spite of the roughness of the films deposited on steel and ITO are very different (325 and 123 nm, respectively), the substratum does not affect to the topography at the micrometric scale. Figure 3 evidences that the roughness of the films deposited on ITO is smaller than those on steel in all cases. Moreover, the expression with the lowest number of degrees of freedom that describes the variation of the roughness against the polymerization time corresponds to $r = 20.1 \cdot \ln\theta + 10.8$ ($R^2 = 0.973$) reflecting that the substratum affects not only to the topography at the first stages of the anodic polymerization but also to the growing mechanism of the films.

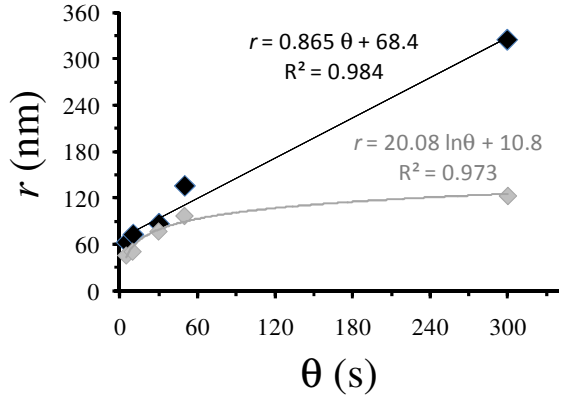

Figure 3. *Variation of the roughness (r) against the polymerization time (θ) for films of PEDOT deposited on steel (black) and ITO (gray).*

The thickness of the PEDOT films generated on the ITO electrodes has been determined using both AFM scratch and electrochemical techniques. The former method is based on the use of AFM topographic measurements to determine the height at the step defined by the ITO–PEDOT interface of films scratched without penetrate the substrate. This technique, which is schematized in Figure 4, is suitable for coatings with similar dimensions for the thickness and the surface roughness.

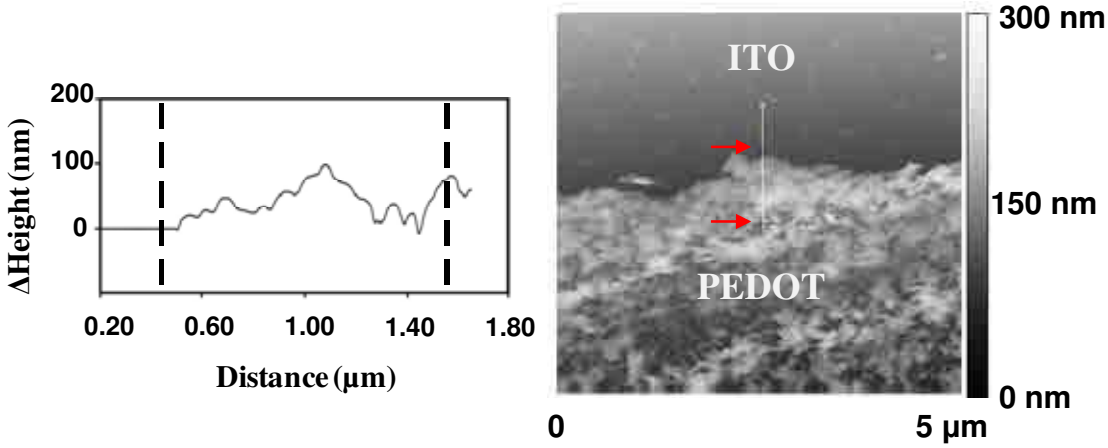

Figure 4. *Scheme showing the scratch AFM technique. Right: AFM image of a scratched PEDOT film electrodeposited on an ITO substrate using a polymerization time of θ = 5 s. Left: Dashed lines indicate the position of the step whose height is determined by AFM topography.*

On the other hand, the electrochemical values of the thickness were obtained from the mass of polymer deposited on the electrode and the current productivity.[8] Table 1 compares the AFM and electrochemical values of thickness for the films obtained using θ = 5, 10, 30 and 50 s. The excellent agreement between the two methods confirms that

the approximations intrinsic to the electrochemical method (*e.g.* homogeneous distribution of the mass on the electrode) are valid for ultrathin films. Interestingly, the thickness is smaller for the films deposited on steel (Table 1) that for those on ITO, even though the difference imposed by the substrates decreases when the polymerization time increases, *i.e.* it varies from 38% to 19% when the θ increases from 5 to 50 s.

Figure 5 represents the electrochemical thickness/roughness ratio (ℓ/*r*) against the polymerization time θ. It is worth noting that for both substrates the thickness increases faster than the roughness with θ, even though this effect is much more pronounced for ITO than for steel. Moreover, the largest difference in the ℓ/*r* ratio occurs for the micrometric films obtained using θ = 300 s, in which the linear behavior observed for the ultrathin films (θ ≤ 50 s) deviates towards a polynomial function. Accordingly, the ℓ/*r* profiles displayed in Figure 5 clearly indicate that the growing of the polymer chains is determined by the substrate.

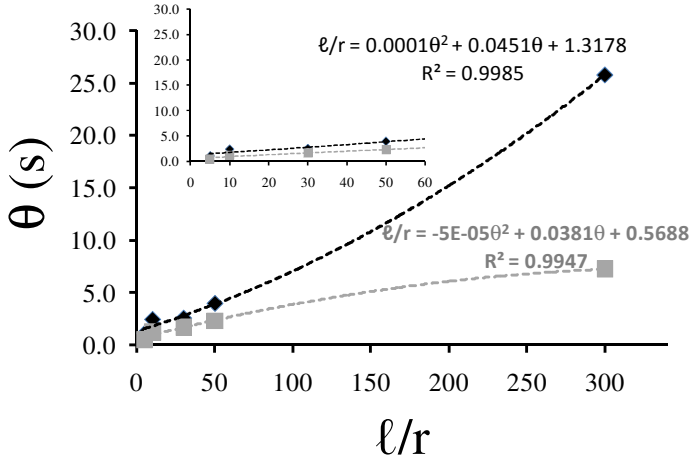

Figure 5. *Variation of the thickness/rougness ratio (ℓ/r) against the polymerization time θ for PEDOT films electrodeposited in steel (grey) and ITO (black) substrates. Profiles for θ ≤ 50 s are displayed in the inset. The thickness was determined electrochemically.*

Figure 6 shows SEM micrographs of the typical morphologies found at the surface of nanometric films electrodeposited on steel and ITO electrodes. The drastic effect of the substrate on the morphology of the ultrathin polymer films is consistent with AFM results. PEDOT films generated on steel present a relatively compact structure formed by the aggregation of sticks with a fiber-like morphology. This allows the formation of relatively narrow and tortuous pores, which are expected to play a crucial role in the excellent electrochemical properties of the material. In contrast the film obtained on

ITO presents an ultraporous morphology in which the polymer grows forming an interconnection of ultrathin sticks, which originates a network of relatively wide and deep channels.

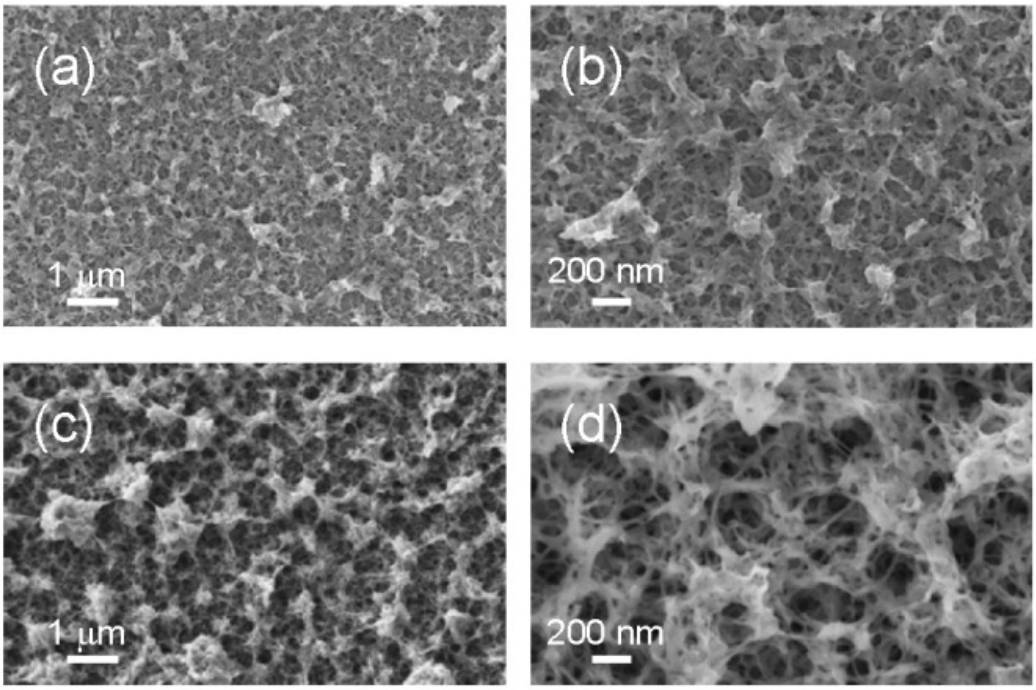

Figure 6. *Low-magnification (1 µm) and high magnification (200 nm) SEM images of PEDOT electrodeposited on steel (a and b) and ITO (c and d) substrates. Films displayed were obtained using a polymerization time of θ = 30 s.*

The particular morphology of PEDOT films deposited on ITO electrodes has been analyzed in more detail by performing SEM micrographs of the transversal section. ITO electrodes are made of a ~30 nm layer of indium-tin oxide spherical particles deposited on glass (Figure 7a), the porous network of ultrathin sticks of PEDOT growing homogeneously onto such layer (Figure 7b). This fiber-like structures has been characterized through two structural parameters: the thickness and the length (δ and Δ, respectively) of the sticks, which were determined from SEM micrographs.

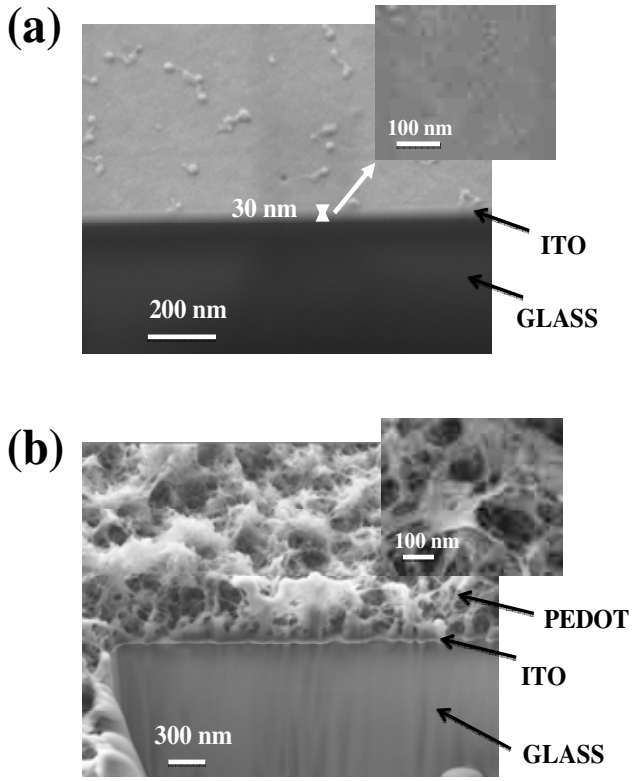

Figure 7. *SEM images of the transversal section of: (a) an ITO electrode; and (b) a PEDOT film (polymerization time of θ = 30 s) electrodeposited on ITO. The insets correspond to high magnification (100 nm) images.*

Interestingly, the average dimensions of the PEDOT ultrathin sticks, which are schematized in the micrograph displayed in Figure 8, do not depend on the polymerization time. Thus, δ and Δ range from 10 to 70 nm and from 40 to 400 nm, respectively, even though the average values are 24 and 162 nm. Accordingly, the Δ/δ ratio is ~7, which reflects that nanometric films deposited on ITO are formed by clusters of PEDOT chains growing through a longitudinal packing. PEDOT molecules are exclusively formed by α,α-linkages since the dioxane ring fused onto the thiophene ring occupies the β-positions of the latter. The absence of crosslinkings allows explain the longitudinal organization of the linear chains.

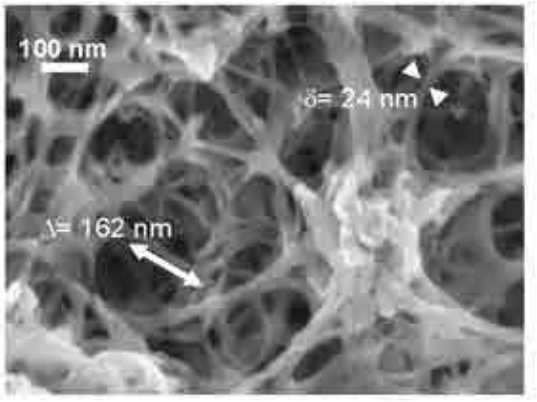

Figure 8. *SEM image of PEDOT electrodeposited on ITO (θ = 30 s). Average values for the thickness and length of the ultrathin sticks (δ and Δ, are indicated) electrodeposited on ITO. The insets correspond to high magnification (100 nm) images.*

These results are fully consistent with the enhancement of the electroactivity observed for PEDOT deposited on ITO with respect to that of the polymer generated using a steel substrate. This feature is illustrated in Figure 9a, which compares the control voltammograms recorded in the potential range of -0.50 to 1.60 V of films produced using θ = 10 s. The electroactivity reflects the ability to store charge, increasing with the similarity between the anodic and cathodic areas of the voltammogram. As it can be seen, the electroactivity is significantly higher for the ultrathin film deposited in ITO than for that in steel, indicating that the morphology obtained with the former substrate facilitates the access and escape of the dopant ions along the oxidation and reduction processes, respectively. The evolution of the different electroactivities with the polymerization time θ is displayed in Figure 9b, which represents the difference between the electroactivities of the PEDOT films deposited in the two substrates for θ = 5, 10, 30 and 50 s. In all cases the electroactivity of the films obtained using ITO electrodes is the highest, the relative gain increasing from 15% to 35 % when θ grows from 5 to 50 s.

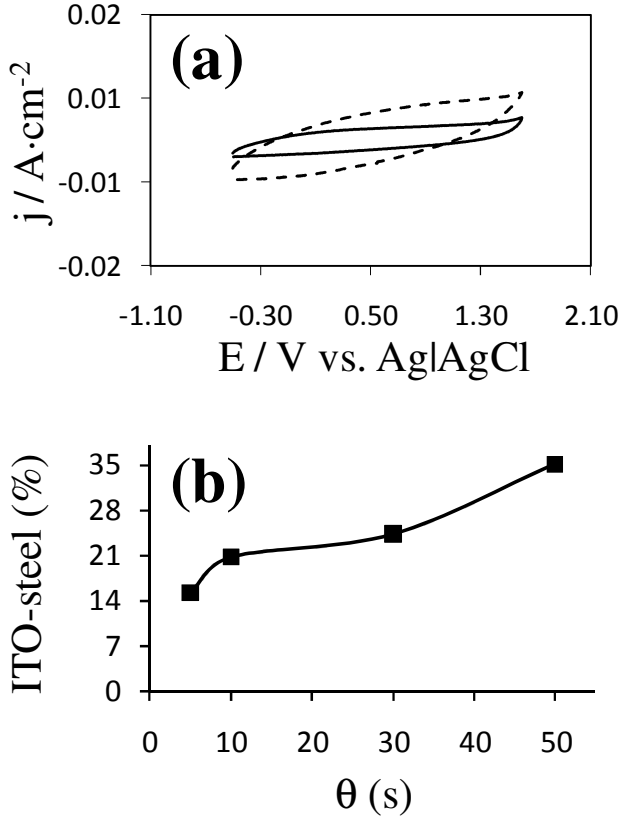

Figure 9. *(a) Control voltammogram for the oxidation of PEDOT films electrodeposited on ITO (dashed line) and steel (solid line), which were prepared using θ = 10 s. Initial and final potentials: -0.50 V; reversal potential: 1.60 V. (b) Evolution of the difference between the electroactivities (in %) measured for PEDOT films deposited in ITO and steel substrates against the polymerization time θ.*

As was mentioned in the Introduction section, type II supercapacitors correspond to asymmetric configurations based on two different CPs with very different electroactivities. In this work, asymmetric devices have been fabricated by combining PEDOT deposited on steel with PEDOT deposited on ITO electrodes in the same supercapacitor (*i.e.* steel/ITO and ITO/steel configurations). Thus, the electroactivities of such two electrodes are different enough to consider them as made of materials with different properties. Moreover, electrodes obtained using different polymerization times (*i.e.* θ = 5, 10, 30 and 50 s) were considered for the fabrication of asymmetric systems, even although for a given capacitor device θ was identical for the two electrodes. In addition, type I supercapacitors, which consists on symmetric systems that use the same p-dopable conducting polymer for the two electrodes, were fabricated using two identical electrodes of PEDOT deposited on steel or deposited on ITO (*i.e.* steel/steel

and ITO/ITO configurations). Again, the polymerization time θ was identical for the two electrodes of a given configuration.

Table 2. *Performance of asymmetric and symmetric supercapacitors prepared using ultrathin films of PEDOT. The specific capacitance (SC) and Coulomb efficiency (η) have been determined using Eqns 3 and 4, respectively.*

θ (s)	**SC (F/g)**	**η (%)**	**SC (F/g)**
	Asymmetric ITO/steel		**Asymmetric steel/ITO**
5	226	96	61
10	270	95	79
30	248	96	58
50	231	97	52
	Symmetric ITO/ITO		**Symmetric steel/steel**
5	258	83	52
10	288	82	67
30	267	82	48
50	261	84	45

The average specific capacitance (Eqn 3) obtained for all the possible configurations of symmetric and asymmetric supercapacitors are displayed in Table 2. As it can be seen, the specific capacitances of ITO/ITO and ITO/steel supercapacitors are one order of magnitude higher than those of steel/steel and steel/ITO. Moreover, in all cases the specific capacitances are similar for a given configuration. This feature indicates that, within the context of films with nanometric thickness obtained using $\theta \leq 50$ s, they are practically independent of θ. The largest specific capacitance for ITO/ITO and ITO/steel confirgurations, SC = 288 and 270 F/g, respectively, was obtained for the supercapacitor fabricated with films obtained using $\theta = 10$ s. These values were similar to that reported for supercapacitors fabricated using nanocomposites of PEDOT and inorganic materials (*e.g.* MnO_2, MoO_3, carbon nanotubes, V_2O_5 and $NiFe_2O_4$), for which the specific capacitance ranged from 153 to 375 F/g.[34-40] Moreover, it should be remarked that such large specific capacitances, which are frequent in PEDOT-inorganic hybrid nanocomposites, were never achieved before for PEDOT alone.[41]

On the other hand, the Coulombic efficiency (Eqn 4) has been measured for the symmetric and asymmetric configurations with largest specific capacitance (*i.e.* ITO/ITO and ITO/steel, respectively), results being included in Table 2. As it can be seen, Coulombic efficiencies were very high (*i.e.* close to 100%) for ITO/steel

supercapacitors, independently of the polymerization time. This excellent supercapacitor behavior is illustrated in Figure 10 for the ITO/steel assembly prepared using θ = 10 s, which shows the symmetrical and rectangular cyclic voltammetric curve characteristic of double layer capacitance. In opposition, the curve for the ITO/ITO configuration, which is also displayed in Figure 10, reveals a reduction of the electrochemical double layer capacitance. Thus, this voltammogram shows lower rectangularity and symmetry than that obtained for the ITO/steel configuration, this feature being consistent with low Coulombic efficiencies listed in Table 2 for this type of symmetric supercapacitors.

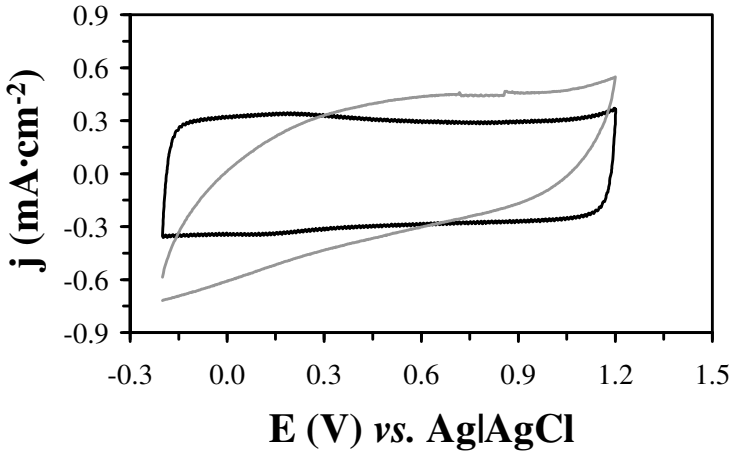

Figure 10. *Cyclic voltammograms of ITO/steel (black) and ITO/ITO (grey) assemblies prepared using θ = 10 s. Initial and final potentials: -0.20 V; reversal potential: 1.20 V.*

Figure 11 represents the variation of the *LES*, which was determined using Eqn 5, against the number of consecutive oxidation-reduction cycles ($n_{ox\text{-}red}$) for the asymmetric and symmetric supercapacitors fabricated with films deposited using θ = 10 s. For the asymmetric ITO/steel assembly the electrochemical stability decreases very slowly until $n_{ox\text{-}red}$ = 100 cycles. Then, the electrochemical stability remains constant at *LES* = 23% whereas the number of cycles grows until $n_{ox\text{-}red}$ = 200. This behavior differs from that observed for the symmetric steel/steel supercapacitor in which the *LES* increases progressively until reach a value of 46%. Although the loss of electrostability is very high in the first 100 cycles (*i.e.* *LES* = 41% for $n_{ox\text{-}red}$ = 100 cycles), a slow but progressive reduction is still detected when $n_{ox\text{-}red}$ grows from 100 to 200 cycles. An intermediate situation has been found for the steel/ITO and ITO/ITO supercapacitors, both showing a progressive reduction of the electrochemical stability till reach *LES* = 35% for $n_{ox\text{-}red}$ = 200 cycles. These results indicate that, although the specific capacitance of

ITO/ITO is slightly larger (*i.e.* 11 F/g) than that of ITO/steel, the electrochemical stability of the latter is higher than that of the latter.

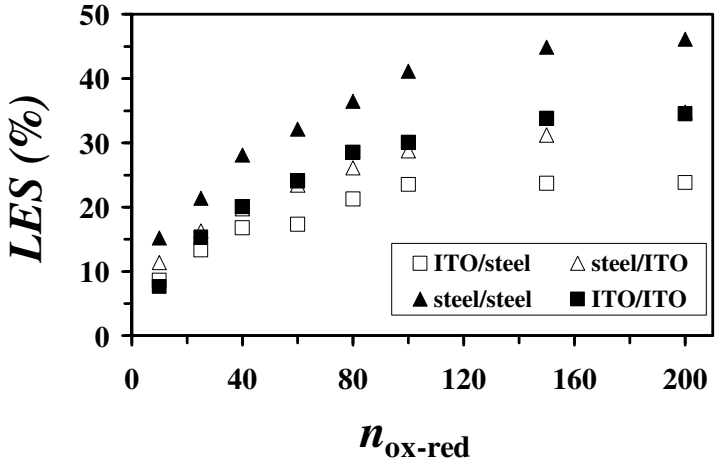

Figure 11. *Variation of the loss of electrostability (LES, in %) against the number of consecutive oxidation-reduction cycles ($n_{ox\text{-}red}$) for the ITO/steel (empty squares), steel/ITO (empty triangles), ITO/ITO (filled squares) steel/steel (filled triangles) supercapacitors. The polymerization time was θ = 10 s in all cases.*

The performance of the ITO/steel and ITO/ITO configurations, in terms of specific capacitance (Table 2), should be essentially attributed to the ultraporous network of ultrathin sticks induced by the ITO substrate when the electropolymerization time is very small. In order to quantify differences in the porosity of PEDOT deposited on ITO and steel, the reduction in the porosity (Δp) was evaluated as follows:

$$\Delta p = \frac{\ell_0 - \ell_{200}}{\ell_0} \cdot 100 \qquad (6)$$

where the ℓ_0 refers to the thickness of the film as generated, which shows the maximal porosity, and ℓ_{200} refers to the thickness of the film after 200 consecutive oxidation-reduction cycles. The value of Δp obtained for PEDOT deposited in steel and ITO using θ = 10 s is 39% and 48%, respectively, confirming that the porosity of the latter is remarkably higher. On the other hand, the very high efficiency ($\eta \geq 95\%$ in all cases) of the supercapacitors studied in this work is essentially due to the ultrathin nature of the films rather that the substrates used for their deposition. Thus, the Coulomb efficiency obtained for supercapacitors fabricated with micrometric films (θ = 300 s) was reported to be lower than 77%.[41]

Results obtained for the asymmetric ITO/steel supercapacitors not only show a very high specific capacitance but also a very remarkable electrochemical stability. The latter cannot be attributed to the doping level (Eqn 2), which was found to be similar for PEDOT deposited on ITO and steel substrates (f = 26% and 21%, respectively). However, the electrochemical stability, which is related with the access and escape of dopant ions along the oxidation and reduction processes, respectively, depends on the structure of the material. More specifically, the electrochemical stability is low in compact materials because of the low mobility of the ions. In contrast, porous materials facilitate the diffusion of the dopant ions, which results in high electrochemical stabilities. This behavior is consistent with the Δp values previously discussed. Moreover, the structural changes produced by the electrochemical degradation of the electrodes made of PEDOT deposited on ITO and steel was observed to be completely different. This feature is reflected in Figure 12, which compares the morphology of the electrodes before and after 200 consecutive oxidation-reduction cycles. Figure 12a evidences that, after 200 cycles, the electrode made of PEDOT deposited on ITO retains the ultraporous structure favoring the access and escape of the dopant ions during the electrochemical processes. In opposition, the electrode of PEDOT deposited on steel (Figure 12b) becomes compact after 200 consecutive redox cycles, which explains the low specific capacitance and electrochemical stability of the symmetric steel/steel supercapacitor.

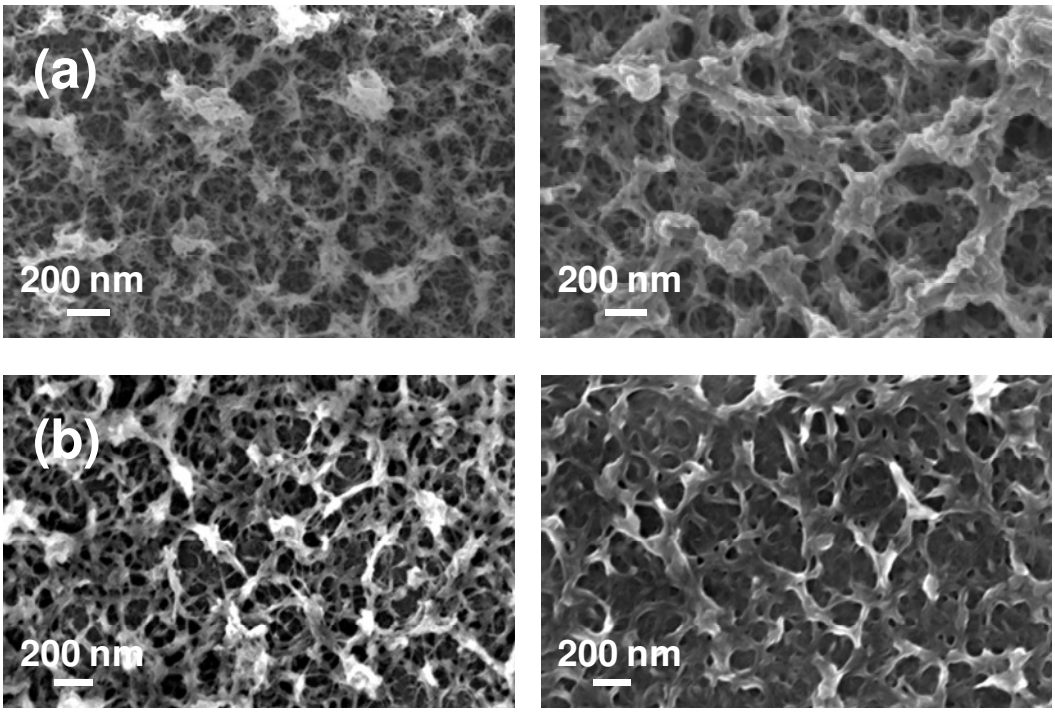

Figure 12. *High resolution SEM images of PEDOT of: (a) the steel coated electrode of the symmetric supercapacitor; and (b) the ITO coated electrode of the asymmetric supercapacitors. Micrographs at the right and the left correspond to material as prepared and after 200 consecutive oxidation-reduction cycles, respectively.*

In spite of ITO/steel, steel/ITO and ITO/ITO configurations contain ultraporous PEDOT deposited on ITO, the former asymmetric configuration shows the highest performance. These observations allow us to conclude that, in PEDOT-containing supercapacitors, the asymmetric assembly of electrodes with different electroactivities is favored with respect to the symmetric assembly of electrodes with identical electroactivities. Thus, although the specific capacitances of ITO/steel and ITO/ITO configurations are similar, the former arrangement presents better supercapacitor behavior, electrochemical stability and Coulombic effiency than the latter one. Moreover, comparison of ITO/steel and steel/ITO indicates that the most porous film largely prefers the anode while the most compact one should be located at the cathode. Thus, the performance ITO/steel assembly is remarkably higher than that of the steel/ITO one not only in terms of electrochemical stability and supercapacitor behavior but also in terms of specific capacitance.

4.2.4. Conclusions

Nanometric films of PEDOT have been prepared by anodic polymerization using both steel AISI 316 L and ITO substrates. The substrate has been found to have a dramatic influence on the roughness, the topography, the morphology and the thickness of the films, the latter being determined using both electrochemical measures and scratch AFM. In all cases the thickness was lower for films generated using steel electrodes than for those obtained using ITO surfaces, while the opposite behavior was found for the roughness. On the other hand, the morphology of films deposited on steel consists of compact and relatively dense packing of sticks, which originates porosity in the material. The porous allow the entrance and escape of dopant anions upon oxidation and reduction processes explaining the ability of PEDOT to store charge. The morphology of PEDOT deposited on ITO electrodes can be described as an ultraporous three-dimensional network of ultrathin sticks. This particular fiber-like morphology is fully consistent with the significant enhancement of electroactivity observed for the material deposited on ITO with respect to that obtained using steel electrodes. The influence of the substrate on the properties of the material decreases with the polymerization time, the effects significantly attenuated inexistent when the films became micrometric. Asymmetric supercapacitors made of electrodes consisting on PEDOT deposited on ITO and steel substrates were found to present very high specific capacitance (*i.e.* similar to those usually measured for PEDOT-inorganic hybrid nanocomposites), electrochemical stability, Coulombic efficiency and supercapacitor behavior. These exceptional properties must be attributed to the combination of three factors: ultrathin thickness of the PEDOT layer, the ultraporous structure induced by the ITO substrate, and the difference between the eletroactivity of the two electrodes. Moreover, these results allowed to conclude that the most porous and electroactive electrode prefers the anode while the least electroactive and more compact electrode is located at the cathode.

4.2.5. References

[1]. Armstrong, N. R.; Veneman, P. A.; Ratcliff, E.; Placencia, D.; Brumbach, M. *Acc. Chem. Res.* **2009**, *42*, 1748. .

[2]. Yang, F.; Forrest, S.R. *ACS Nano* **2008**, *2*, 1022.

[3]. Kim, Y.; Cook, S.; Tuladhar, S. M.; Choulis, S. A.; Nelson, J.; Durrant, J. R.; Bradley, D.D.C.; Giles, M.; McCulloch, I.; Ha, C.S.; Ree, M. *Natur. Mater.* **2006**, *5*197.

[4]. Barrière, F.; Fabre, B.; Hai, E.; Lejeune, Z.M.; Hwang, E.; Garno, J. C.; Nesterov, E. E.; Vicente, M. G. H. *Macromolecules* **2009**, *42*, 2981.

[5]. Conboy, J.C.; Olson, E. J. C.; Adams, D. M.; Kerimo, J.; Zaban, A.; Gregg, B. A.; Barbara, P. F. *J. Phys. Chem. B* **1998**, *102*, 4516.

[6]. Berlin, A.; Vercelli, B.; Zotti, G. *Polym. Rev.* **2008**, *48*, 493.

[7]. Marrikar, F. S.; Brumbach, M.;Evans, D. H.; Lebrón-Paler, A.; Pemberton, J. E.; Wysocki, R. J.; Armstrong, N.R. *Langmuir* **2007**, *23*, 1530.

[8]. Estrany, F.; Aradilla, D.; Oliver, R.; Armelin, E.; Alemán, C. *Eur. Polym. J.* **2008**, *44*, 1323.

[9]. Sarkar, N.; Ram, M. K.; Sarkar, A.; Narizzano, R.; Paddeu, S.; Nicolini, C. *Nanotechnology* **2000**, *11*, 30.

[10]. Song, J.; Han, D.; Guo, L.; Niu, L. *Nanotechnology* **2006**, *17*, 824.

[11]. Qu, L. T.; Shi, G. Q.; Yuan, J. Y.; Han, G. Y.; Chen, F. E.*J. Electroanal. Chem.* **2004**, *561*, 149.

[12]. Miles, M. J.; Smith, W. T.; Shapiro, J. S. *Polymer* **2000**, *41*, 3349.

[13]. Li, T.J.; Wang, E.; Green, M.; West, P. W. *Synth. Met.* **1995**, *74*, 127.

[14]. Mazur, M.; Blanchard, G. J. *Langmuir* **2004**, *20*, 3471.

[15]. Venancio, E. C.; Costa, C. A. R.; Machado, S. A. S.; Motheo, A. *Electrochem. Commun.* **2001**, *3*, 229.

[16]. Ocón, P.; Herrasti, P.; Rojas, S. *Polymer* **2001**, *42*, 2439.

[17]. Micaroni, L.; Dini, D.; Decker, F.; De Paoli, M. A. *J. Solid State Electrochem.* **1999**, *3*, 352.

[18]. Harris, C. J.; Belcher, W. J.; Dastoo, P.C. *Sol. Energy Mater. Sol. Cells* **2007**, *91,* 1127.

[19]. Yan, J.; Sun, C.; Tan, F.; Hu, X.; Chen, P.; Qu, S.; Zhou, S.; Xu, J. *Sol. Energy Mater. Sol. Cells* **2010**, *94*, 3390.

[20]. Zotti, G.; Zecchin, S.; Schiavon, G.; Vercelli, B.; Groenendaal, L. B. *Chem. Mater.* **2003**, *15*, 2222.

[21]. Estrany, F.; Aradilla, D.; Oliver, R.; Alemán, C. *Eur. Polym. J.* **2007**, *43*, 1876

[22]. Groenendaal, L.; Jonas, G.; Freitag, D.; Pielartzik, H.; Reynolds, J. R. *Adv. Mater.* **2000**, *12*, 481.

[23]. Pei, Q.; Zuccarello, G.; Ahiskog, M.; Inganas, O. *Polymer* **1994**, *35*, 1347.

[24]. Aradilla, D.; Estrany, F.; Armelin, E.; Alemán, C. *Thin Solid Films* **2010**, *518*, 4203.

[25]. Kotz, R.; Carlen, M. *Electrochim. Acta* **2000**, *45*, 2483.

[26]. Frackowiak, E.; Beguin, F. *Carbon* **2002**, *40*, 1775.

[27]. Wang, Y. G.; Zhang, X.G. *Electrochim. Acta* **2004**, *49*, 1957.

[28]. Xu, J.; Wang, J.; Sun, W.; Wang, S. *J. Power Sources* **2006**, *159*, 370.

[29]. Han, G.; Yuan, J.; Shi, G.; Wei, F. *Thin Solid Films* **2005**, *474*, 64.

[30]. Chen, L.; Yuan, C.; Dou, H.; Gao, B.; Chen, S.; Zhang, X. *Electrochim. Acta* **2009**, *54*, 2335.

[31]. Murugan, A. V.; Viswanath, A. K.; Gampet, G.; Gopinath, C. S.; Vijayamohanan, K. *Appl. Phys. Lett.* **2005**, *87*, 243511.

[32]. Sharma, R.; Zhai, L. *Electrochim. Acta* **2009**, *54*, 7148.

[33]. Sen, P. M.; De, M. *Electrochim. Acta* **2010**, *55*, 4677.

[34]. Banafsheh, B.; Ivey, D. G. *Electrochim. Acta* **2010**, *55*, 2014.

[35]. Chen, L.; Yuan, C.; Gao, B.; Chen, S.; Zhang, X. *J. Solid State Electrochem.* **2009**, *13*, 1925.

[36]. Murugan, A. V.; Viswanath, A. K.; Gopinath, C.S.; Vijayamohanan, K. *J. Appl. Phys.* **2006**, *100*, 074319.

[37]. Babakhani, B.; Ivey, D. G. *Electrochim. Acta* **2010**, *55*, 4014.

[38]. Fusalba, F.; Ho, H. A.; Breau, L.; Belanger, D. *Chem. Mater.* **2000**, *12*, 2581.

[39]. Peng, C.; Snook, G. A.; Fray, D. J.; Shaffer, M. P.; Chen, G. Z. *Chem. Commun.* **2006**, *44*, 4629.

[40]. Peng, C.; Jin, J.; Chen, G. Z. *Electrochim. Acta* **2007**, *53*, 525.

[41]. Aradilla, D.; Estrany, F.; Alemán, C. *J. Phys. Chem. C* **2011**, *115*, 8430.

[42]. Rudge, A.; Davey, J.; Raistrick, I.; Gottesfeld, S.; Ferraris, J. P. *J. Power Sources* **1994**, *47*, 89.

[43]. Ocampo, C.; Oliver, R.; Armelin, E.; Alemán, C.; Estrany, F. *J. Polym. Res.* **2006**, *13*, 193.

[44]. Schirmeisen, M.; Beck, F. J. *J. Appl. Electrochem.* **1989**, *19*, 401.

[45]. Kassmi, A. E.; Fache, F.; Lemaire, M. *J. Electroanal. Chem.***1994**, *373*, 241.

[46]. Stefanov, P.; Stoychev, D.; Stoycheva, M.; Gonzales-Elipe, A. R.; Marinova, T. S. *Surf. Unterface Anal.* **1999**, *28*, 106.

[47]. Benoy, M. D.; Mohammed, E. M.; Babu, S.; Binu, P. J.; Pradeep, B. *Brazil. J. Phys.* **2009**, *39*, 629.

[48]. Rottmannt, M.; Heckner, K.-H. *J. Phys. D: Appl. Phys.* **1995**, *28*, 1448.

[49]. Utsumi, K.; Matsunaga, O.; Takahata, T. *Thin Solid Films* **1998**, *334*, 30.

[50]. Senthilkumar, M.; Mathiyarasu, J.; Joseph, J.; Phani, K. L. N.; Yengaraman, V. *Macromol. Chem. Phys.* **2008**, *108*, 403.

[51]. Gettens, R. T. T.; Gilbert, J. L. *J. Biomed. Mater. Res.* **2009**, *90A*, 121.

[52]. Fattah-alhosseini, A.; Saatchi, A.; Golozar, M. A.; Raeissi, K. *J. Appl. Electrochem.* **2010**, *40*, 457.

4.3. Nanometric ultracapacitors fabricated using multilayers of conducting polymers on self-assembled octanethiol monolayers.

4.3.1. Introduction

During the last decades conducting polymers (CPs) have emerged as promising materials in different fields such as electronics, biotechnology and nanotechnology.[1-3] Among CPs, poly(3,4 ethylenedioxythiophene), hereafter, abbreviated PEDOT (Scheme 1), has received special attention due to its excellent electrochemical and thermal properties, high conductivity, good environmental stability in its doped state, mechanical flexibility, relative ease of preparation, and fast doping-undoping process.[4-6] According to these interesting properties, PEDOT has been applied as biomaterial,[7-9] solar cell,[10,11] electrochromic device,[12] hole injection layer in organic light-emitting diodes,[13] mechanical actuator,[14] electrochemical energy storage[15] and biosensor.[16] The applicability of PEDOT was initially limited by the serious problem of processability that typically affects thiophene-based CPs, its combination with poly(styrenesulfonic acid) (PSS) to form complexes in water emerging as an interesting alternative to overcome this drawback (*i.e.* PSS keeps PEDOT segments dispersed in the aqueous medium).[4-6] Thus, although PEDOT-PSS complexes are not truly water soluble, they form stable easy-to-process microdispersions.

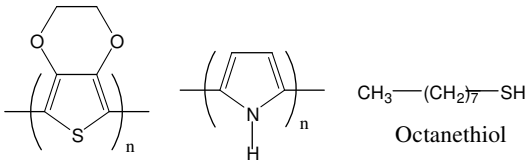

Scheme 1

The layer-by-layer (LbL) procedure, which was initially reported by Décher and coworkers,[17-19] is considered as a very powerful strategy for the fabrication of CPs that can be directly used for applications (*i.e.* without intermediate steps for their transformation). This methodology permits to build multilayered composites from solutions containing electrolytes of different charge, even though other strategies have

been developed to deposit multilayered systems (*e.g.* spin-coating, Langmuir-Blodgett and vapor techniques). The versatility, inexpensiveness and easiness of the LbL technique have allowed fabricate biosensors, solar cells, and electrochromic devices.[20-23] In particular, the LbL technique has been used to prepare multilayered systems formed by PEDOT and PSS, which have been widely studied and successfully applied in different technological fields.[24-27]

In recent studies, an alternative approach based on electrochemical techniques to produce multilayered systems formed by two, or even more, CPs has been developed.[28-31] This methodology, which is schematically described in Figure 1a, was used to construct multilayered systems based on PEDOT and different polypyrrole (PPy, Scheme 1) derivatives [*e.g.* poly(N-methylpyrrole) and poly(N-cyanoethylpyrrole)]. In this procedure a substrate is immersed into an initial solution containing the first monomer and the electrolyte (*e.g.* ethylenedioxythiophene, abbreviated EDOT, and lithium perchlorate, respectively). Application of potentiostatic methods leads to the formation of the first (internal) PEDOT layer. After this, such layer is rinsed with acetonitrile and, subsequently, immersed in a solution containing the second monomer (*e.g.* pyrrole, abbreviated Py) and the electrolyte, which can be identical or different from that used in the first step. Application of a voltage results in the formation of a PPy layer deposited onto the first one. Repetition of this procedure n times allows obtain n-layered systems. It should be mentioned that the polymerization time (θ) plays a fundamental role in the electrochemical LbL technique since it is intimately related with the thickness of the films.

On the other hand, in the last decade a number of studies devoted to investigate the surface properties of CPs deposited on electrodes modified with self-assembled monolayers or multilayers (abbreviated SAMs in both cases) of alkanethiols have been reported. Thus, SAMs of alkanethiols have been used to prepare PPy,[32-34] polyaniline (PAni),[34,35] and different polythiophene (PTh) derivatives,[36-39] including PEDOT.[39] SAMs of alkanetiols, which can be chemisorbed onto different metallic substrates (*e.g* steel, silver, platinum, gold or copper), significantly affects the growing mechanism of CPs. In particular, it is found that SAMs of different alkanethiols (octanethiol and dodecanethiol) adsorbed on steel electrodes have a drastic effect on the thickness, roughness, porosity, morphology and topology of PEDOT, even though such influences depend on the length of the alkyl chains, the incubation period used for the preparation of the SAMs and thickness of the CP film.[39] Regarding to the latter, the role of the

alkanethiols was found to be significantly more important in nanometric films than in micrometric one.[39] Furthermore, alkanethiols enhanced both the adherence and the corrosion protection imparted by PEDOT films to the steel substrate.

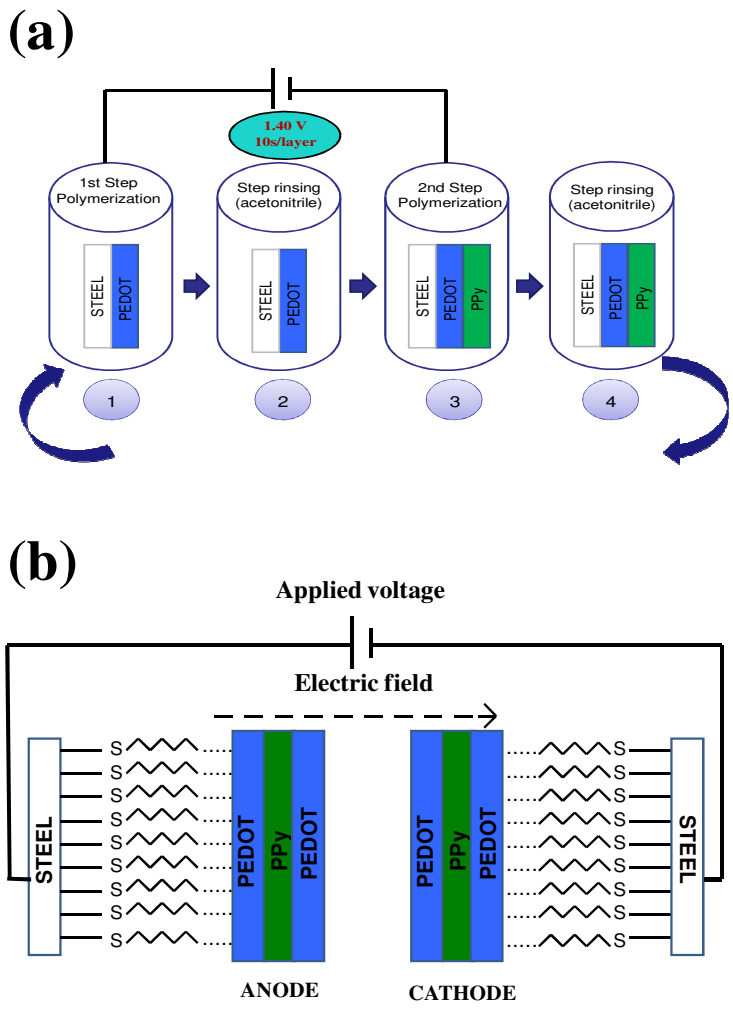

Figure 1. *(a) Scheme of the electrochemical layer-by-layer process used to prepare 3-layered films. (b) Scheme of the ultracapacitor constructed using two identical electrodes of PEDOT/PPy/PEDOT deposited steel treated with octanethiol (3-layered/C_8-SH ultracapacitor).*

In this study, a combination of both octanethiol-coated steel electrodes with the electrochemical LbL technique to fabricate 3-layered symmetric ultracapacitors made of alternated PEDOT and PPy films (*i.e.* PEDOT/PPy/PEDOT films in which the internal and external layers are of PEDOT while the intermediate layer is of PPy) with nanometric thickness (Figure 1b) is discussed. In order to compare the benefits induced by the octanethiol on the 3-layered system, nanometric symmetric ultracapacitors made of PEDOT/PPy/PEDOT and individual PEDOT using untreated steel electrodes were prepared. Properties of the fabricated ultracapacitors have been determined using cyclic

voltammetry (CV), galvanostatic recurrent pulse and electrochemical impedance spectroscopy (EIS) assays. This investigation has been completed with exhaustive morphological and structural studies based on using scanning electron microscopy (SEM) and atomic force microscopy (AFM), which have allowed to rationalize both the electrochemical and capacitance results.

4.3.2. Methods

Chemicals. EDOT, Py, octanethiol and acetonitrile of analytical reagent grade were purchased from Aldrich. Anhydrous $LiClO_4$, analytical reagent grade, from Aldrich was stored in an oven at 80ºC before use in the electrochemical trials.

Monolayers formation. Monolayers were prepared by immersing stainless steel AISI 316 electrodes, which were previously clean with acetone, into 50 mL of octanethiol as received from Aldrich for 2 hours. In a recent study this immersion period provides the best charge storage/electrostability ratio.[39] After this time, the steel modified electrodes were removed from the solutions, rinsed with acetonitrile and dried with nitrogen.

Synthesis of films. PEDOT and 3-layered films were prepared by chronoamperometry (CA) under a constant potential of 1.40 V.[28,40] Electrochemical experiments were conducted on a PGSTAT101 AUTOLAB potenciostat-galvanostat connected to a PC computer controlled through the NOVA 1.6 software, using a three-electrode two-compartment cell under nitrogen atmosphere at 25 ºC. The working compartment was filled with 40 mL of a 10 mM monomer solution in acetonitrile with 0.1 M $LiClO_4$, while the cathodic compartment was filled with 10 mL of the same electrolyte solution. The polymerization time (θ) used to produce individual PEDOT and PPy films was 30 s. Steel AISI 316 sheets with an area of 4 cm^2 were employed as working and counter electrodes. Before each trial, electrodes were cleaned with acetone and dried in a nitrogen-flow. The reference electrode was an Ag|AgCl electrode containing a KCl saturated aqueous solution (E^o = 0.222 V *vs.* standard hydrogen electrode at 25 ºC), which was connected to the working compartment through a salt bridge containing the electrolyte solution.

The electrochemical LbL technique was used to prepare the 3-layered PEDOT/PPy/PEDOT films. For the generation of each layer the working electrode was immersed for a period of 10 s in cells filled with 10 mM acetonitrile solution of the

corresponding monomer with 0.1 M $LiClO_4$. Accordingly, the total polymerization time, 3×10 s = 30 s, was identical to that of individual PEDOT films.

Fabrication of ultracapacitors. Symmetric (type I) ultracapacitors, which are based on two identical electrodes, were fabricated using 3-layered PEDOT/PPy/PEDOT films (θ = 10 s for each layer) deposited on untreated and octanethiol-steel, hereafter denoted 3-layered/steel and 3-layered/C_8-SH, respectively. A scheme of the 3-layered/C_8-SH ultracapacitor is displayed in Figure 1b. Furthermore, type I ultracapacitors fabricated using two identical PEDOT films (θ = 30 s) deposited on untreated steel, hereafter name PEDOT/steel, were fabricated for comparison. On the other hand, ultracapacitors based on individual PPy films have not been described because the electrochemical properties of this material, especially the ability to store charge, are significantly worse than those of PEDOT.[28]

Cyclic voltammetry. Cyclic voltammograms have been used to evaluate the specific capacitance (*SC*), the loss of electrostability (*LES*) and the doping level (dl). The *SC* of the fabricated ultracapacitors was calculated as:

$$SC = \frac{Q}{\Delta V m} \qquad (1)$$

where Q is voltammetric charge, which is determined by integrating either the oxidative or the reductive parts of the cyclic voltammogram curve, ΔV is the potential window and m is the mass of polymer on the surface of the working electrode. The electrochemical stability was evaluated through the loss of electrostability (*LES*), which was determined as:

$$LES = \frac{\Delta Q}{Q_i} 100 \qquad (2)$$

where ΔQ is the difference of voltammetric charge between the second cycle and the last cycle and Q_i is the voltammetric charge corresponding to the second cycle. In this work all values of *LES* were referred to 1000 consecutive oxidation-reduction cycles (n_{redox} = 1000).

Electrochemical estimation of the doping level (dl) was carried using the following Eqn:

$$dl = \frac{2Q_o}{Q_d - Q_o} 100 \quad (3)$$

where Q_D is the total charge used for the polymer deposition and Q_0 is total charge of oxidized species in the polymer films.

Galvanostatic recurrent pulse. Galvanostatic charge/discharge curves were used to evaluate the SC, the Coulomb efficiency (η), the energy density (E_d) and the power density (P_d). More specifically, the *SC* of supercapacitor films was obtained according to:

$$SC = \frac{I \cdot \Delta t}{\Delta V m} \quad (4)$$

where I is the applied current (1 mA), Δt is the time of discharge (in s), ΔV is the difference between the potential at the beginning and at the end of the discharge (in V).

The Coulomb efficiency (η), which is defined as the ratio between the discharge and charge times (t_d and t_c, respectively) corresponds to:

$$\eta = \frac{t_d}{t_c} \cdot 100 \quad (5)$$

The E_d and P_d at a constant current were determined using Eqns (6) and (7), respectively:

$$E_d = \frac{I \int \Delta V \cdot t}{m} \quad (6)$$

$$P_d = \Delta V \frac{I}{m} \quad (7)$$

Electrochemical Impedance Spectroscopy. EIS measurements were performed in potentiostatic mode at the open circuit potential (OCP) using an AUTOLAB PGSTAT 30/FRA 2 system. The amplitude of the EIS perturbation signal was 50 mV, and the studied frequency ranged from 10 kHz to 10 mHz.. EIS data were plotted in terms of real and imaginary parts of the impedance (Z' and -Z", respecively).

Scanning electron microscopy. SEM images were analyzed using a Focussed Ion Beam Zeiss Neon40-scanning electron microscope at 3 kV.

Atomic force microscopy. Topographic images were obtained with a Molecular Imaging PicoSPM using a NanoScope IV controller in ambient conditions. The tapping mode AFM was operated at constant deflections (*i.e.* vertical constant force with triangular shaped gold-coated silicon nitride). The row scanning frequency was set to 1 Hz and the physical tip–sample motion speed was 10 $\mu m \cdot s^{-1}$. The root-mean-square (RMS) roughness (r) was determined using the statistical application of the Nanoscope software, which calculates the average considering all the values recorded in the topographic image with exception of the maximum and the minimum. The scan window size was 5×5 μm^2 in all cases, a total of 65.536 topographic data being computed in each image. In all images acquired, which are 512×512 $pixel^2$ maps, differences in height are indicated by a color scale: dark is low and white is high.

Thickness and porosity. The thickness of the films (ℓ) was determined through electrochemical and structural measurements. Electrochemical estimations of the thickness were obtained by determining the current productivity through the mass-charge ratio and, subsequently, the mass of polymer deposited in the electrode at nanometric level.[41] Furthermore, the thickness was determined were determined in all cases by scratch AFM (*i.e.* measuring the cross-section of scratched films). The porosity was indirectly quantified through the parameter Δ:[42]

$$\Delta = \frac{\ell_0 - \ell_{1000}}{\ell_0} 100 \qquad (8)$$

where ℓ_0 and ℓ_{1000} refer to the thickness before applying any oxidation-reduction cycle ($n_{redox} = 0$) and after 1000 consecutive oxidation-reduction cycles ($n_{redox} = 1000$).

4.3.3. Results and Discussion

Table 1. *Electrochemical, structural, physical and morphological properties of the different ultracapacitors produced using a polymerization time of 30s.*

	3-layered/steel	**3-layered/C_8-SH**	**PEDOT/steel**
Charge per unit of mass ($C \cdot g^{-1}$)	211	314	135
Specific capacitance ($F \cdot g^{-1}$)[a]	101 / 121	150 / 164	64 / -
Coulombic efficiency (%)[b]	99	99	96
Doping level[c]	0.35	0.38	0.30
Energy density ($W \cdot h \cdot kg^{-1}$)[d]	12.9	15.7	-
Power density ($W \cdot kg^{-1}$)[e]	1944	2136	1128
Thickness (nm)[f]	289±32	337±38	208±26
Roughness (nm)[g]	96	150	82
		Stability	
Loss of electroactivity after 1000 oxidation-reduction cycles (%)[h]	91	86	90
Charge per unit of mass ($C \cdot g^{-1}$) after 1000 oxidation-reduction cycles	19	45	19
Specific Capacitance ($F \cdot g^{-1}$)[a] after 1000 oxidation-reduction cycles	9	21	9
Specific Capacitance ($F \cdot g^{-1}$)[a] after 2000 charge/discharge cycles	87	80	-

[a] Calculated using Eqn 1 (cyclic voltammograms) / Eqn 4 (galvanostatic charge/discharge curves). [b] Calculated using Eqn. 5. [c] Determined electrochemically using Eqn. 3. [d] Calculated using Eqn. 6. [e] Calculated using Eqn. 7. [f] Determined from the cross-section of the films by scratch AFM. [g] Determined by AFM. [h] Calculated using Eqn. 2.

Table 1 summarizes the electrochemical, capacitance and structural parameters determined for the three investigated ultracapacitors. Figure 2a compares the control voltammograms of 3-layered/steel and 3-layered/C_8-SH ultracapacitors. The ability to store charge of the latter configuration is significantly higher than of the ultracapacitor derived from 3-layered films deposited on untreated-steel. Thus, pre-treated electrodes enhance the electroactivity, the charge per unit area increasing from 211 $C \cdot g^{-1}$ (3-layered/steel) to 314 $C \cdot g^{-1}$ (3-layered/C_8-SH). The influence of the octanethiol on multilayered systems is similar to that previously reported for individual PEDOT films

(*i.e.* the electroactivity of films deposited on modified electrodes was found to be ~40% higher than that of the films generated using untreated-steel).[39]

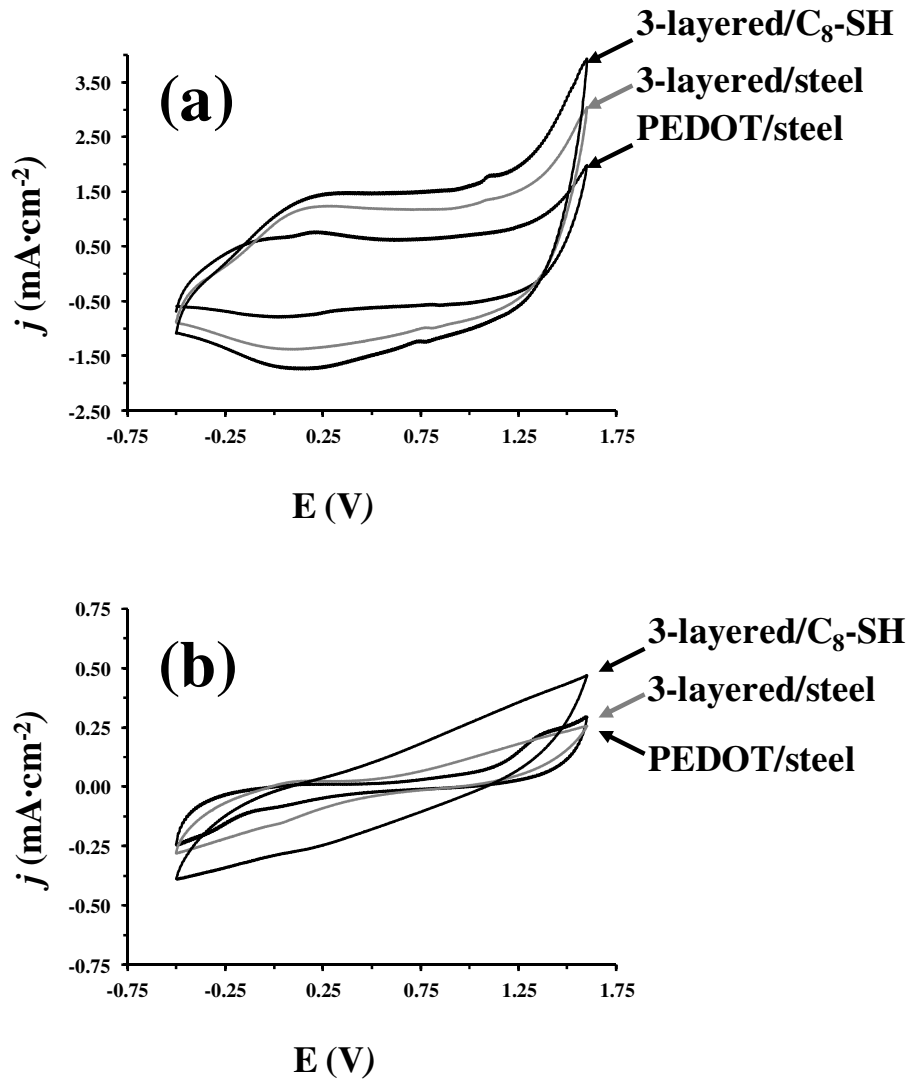

Figure 2. *Cyclic voltammograms for the fabricated nanometric ultracapacitors after (a) 2 and (b) 1000 consecutive oxidation reduction cycles. Scan rate: 100 mV/s. Initial and final potentials: -0.50 V; reversal potential: 1.60 V. All electrochemical assays were carried in an acetonitrile solution containing 0.1M* $LiClO_4$ *at room temperature.*

The control voltammogram collected for the PEDOT/steel ultracapacitor is included in Figure 2a. The favorable effects in the electrochemical properties produced by the alternation of layers of two different CPs, which were previously observed for single electrode configurations,[28-31] are retained in ultracapacitors formed by assemblies of two electrodes. Thus, the stored charge is 36% and 57% lower for 3-layered/steel and 3-layered/C_8-SH than for PEDOT/steel (135 $C \cdot g^{-1}$), respectively. The electrochemical

benefits found for multilayered systems involving two CPs with respect to those derived from an individual CP were explained by the favorable interactions in the interfaces.[28-31] These effects are enhanced in 3-layered/C_8-SH because of the presence of a new interface separating the octanethiol monolayer and the most internal PEDOT layer.

The *SC*s derived from cyclic voltammograms (Eqn 1) for 3-layered/C_8-SH, 3-layered/steel and PEDOT/steel ultracapacitors were 150, 101 and 64 $F \cdot g^{-1}$, respectively. These values are in excellent agreement with those obtained using galvasnostatic recurrent pulses (Eqn 4), which were 161 and 121 for 3-layered/C_8-SH and 3-layered/steel assemblies, respectively. These results clearly reflect the remarkable benefits induced by the above mentioned interfaces. Thus, the *SC* of the 3-layered/C_8-SH ultracapacitor is around 25-30 % higher than that of 3-layered/steel, which in turn is ~35 % higher than that of PEDOT/steel. On the other hand, the Coulomb efficiency (Eqn 5) is very high in all cases (Table 1).

Analysis of the doping level (Table 1) indicates that the salt structure of the 3-layered systems, especially the one deposited in pre-treated steel, is more marked than that of the PEDOT one. Thus, the doping level determined for 3-layered/C_8-SH, 3-layered/steel and PEDOT/steel films reflects that, in average, one perchlorate anion is used to balance the positive charge generated every ~2.5, ~3 and ~3.5 heterocyclic repeating units, respectively. The favorable effects produced by the interfaces are also evidenced in the power density of the ultracapacitors (Table 1): PEDOT/steel < 3-layered/steel < 3-layered/C_8-SH. However, in this case the effects associated to the multilayered nature of the film are significantly larger than those related with the pre-treatment of the substrate with octanethiol. Thus, the power density of PEDOT/steel is 42% smaller than that of 3-layered/steel while the difference between the power densities of the two 3-layered ultracapacitors is of 10% only. Similarly, the energy density is around 20% higher for 3-layered/C_8-SH than for 3-layered/steel (Table 1).

The electrochemical stability was similar for the three nanometric ultracapacitors. Figure 2b shows the control voltammograms of the three fabricated assemblies after 1000 consecutive oxidation-reduction cycles (n_{redox} = 1000). Despite the curves still show the nearly rectangular shape characteristic of capacitor devices after such huge amount of cycles, both the anodic and cathodic areas are considerably smaller than those collected for the first voltammogram (Figure 2a). This evidences a reduction of their electroactivities, which is reflected in the representation of the *LES* (Eqn. 2) against n_{redox} (Figure 3a). After n_{redox} = 100 cycles the *LES* of PEDOT/steel (62%) is

smaller than those of the 3-layered ultracapacitors (73% and 78% for films deposited in modified and unmodified steel, respectively), indicating that the electrochemical stability of the individual polymer is higher for this relatively low number of cycles. However, the *LES* of PEDOT/steel, 3-layered/C_8-SH and 3-layered/steel stabilizes at 89%, 86% and 91%, respectively, when n_{redox} = 800-850 cycles. Thus, when the number of cycles is large enough, the electrochemical stability of the 3-layered/C_8-SH assembly is the highest, even though the behavior of the three systems is very similar. Previous results on single electrodes indicated that the electrochemical stability of nanometric films is lower than that of the corresponding micrometric films, independently of their individual and multilayered nature.[29,31] Thus, the nanometric thickness of the films used to fabricate the assemblies explains the relatively low electrochemical stability of the ultracapacitors. The average thickness determined by AFM scratch for 3-layered/C_8-SH, 3-layered/steel and PEDOT/steel films was 337±38, 289±32 and 208±26 nm, respectively (Table 1).

Figure 3b represents the variation of the *SC* (Eqn. 1) against n_{redox}. The *SC* of both PEDOT/steel and 3-layered/steel ultracapacitors stabilizes at 9 $F \cdot g^{-1}$, which represents 14% and 9% of the initial value, respectively, in ~800 cycles. However, modification of the steel substrate with octanethiol improves the stability of the *SC*. Thus, the *SC* of 3-layered/C_8-SH stabilizes at 21 $F \cdot g^{-1}$ after ~800 cycles (14% of the initial value). Figure 3c represents the variation of the stored charge against n_{redox}. A similar behavior was observed for the stored charge, the values measured for fresh PEDOT/steel, 3-layered/steel and 3-layered/C_8-SH ultracapacitors (*i.e.* 135, 211 and 314 $C \cdot g^{-1}$, respectively) decreasing drastically after n_{redox} = 1000 cycles (*i.e.* 19, 19 and 45 $C \cdot g^{-1}$, respectively). However, despite of such drastic reduction, the charge storage of the 3-layered/C_8-SH assembly was the highest by at least two-folds.

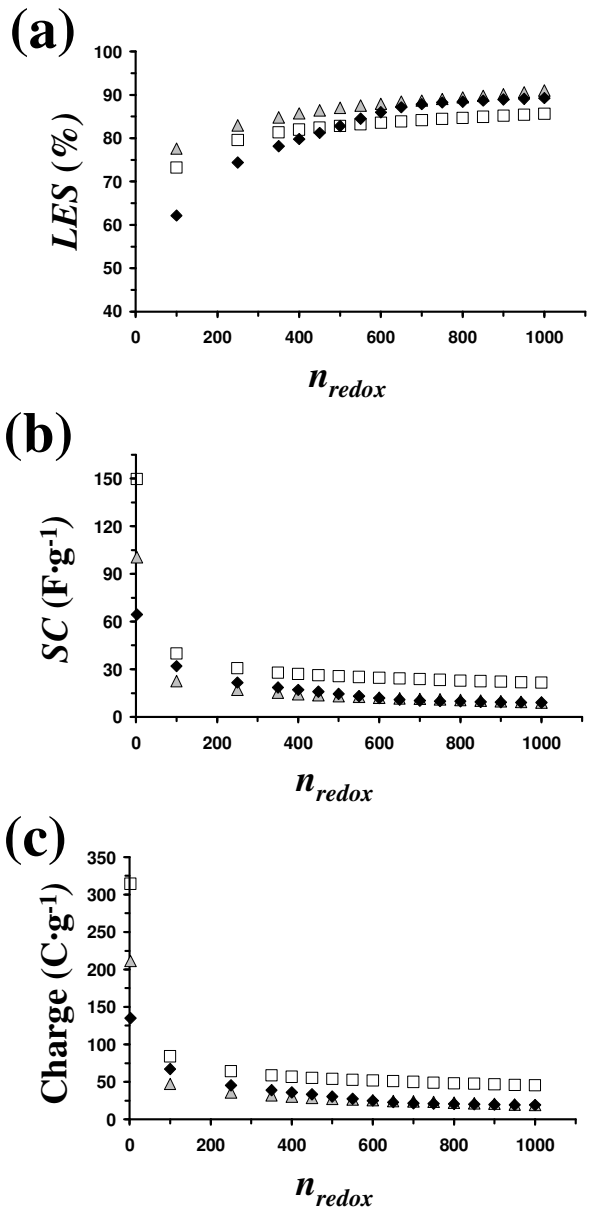

Figure 3. *Variation of the electrochemical properties of PEDOT/steel (black diamonds), 3-layered/steel (grey triangle) and 3-layered/C_8-SH (empty squares) ultracapacitors against the number of consecutive oxidation-reduction cycles (n_{redox}): (a) Loss of electrochemical stability (LES); (b) Specific capacitance (SC); and (c) Stored charge. Oxidation-reduction cycles were performed considering the potential interval comprised between -0.5 and 1.6 V. All properties were evaluated using an acetonitrile solution containing 0.1M $LiClO_4$ at room temperature.*

Results displayed in Figure 3 suggest that the stability of 3-layered nanometric ultracapacitors is low. However, it should be remarked that electrochemical degradation using oxidation-reduction cycles in a potential interval comprised between -0.5 and 1.6 V is an extremely aggressive assay. In order to illustrate that the stability of 3-layered/steel and 3-layered/C_8-SH ultracapacitors is relatively good, a less aggressive electrochemical method based on consecutive charge/discharge galvanostatic cycles has

been used. Charge and discharge profiles are linear and relatively symmetric in both cases (Figure 4a), which indicates the capacitive behavior of the two systems. Figures 4b and 4c represent the variation of the *LES* and *SC* (Eqn 4), respectively, against the number of charge/discharge cycles (n_{cd}).

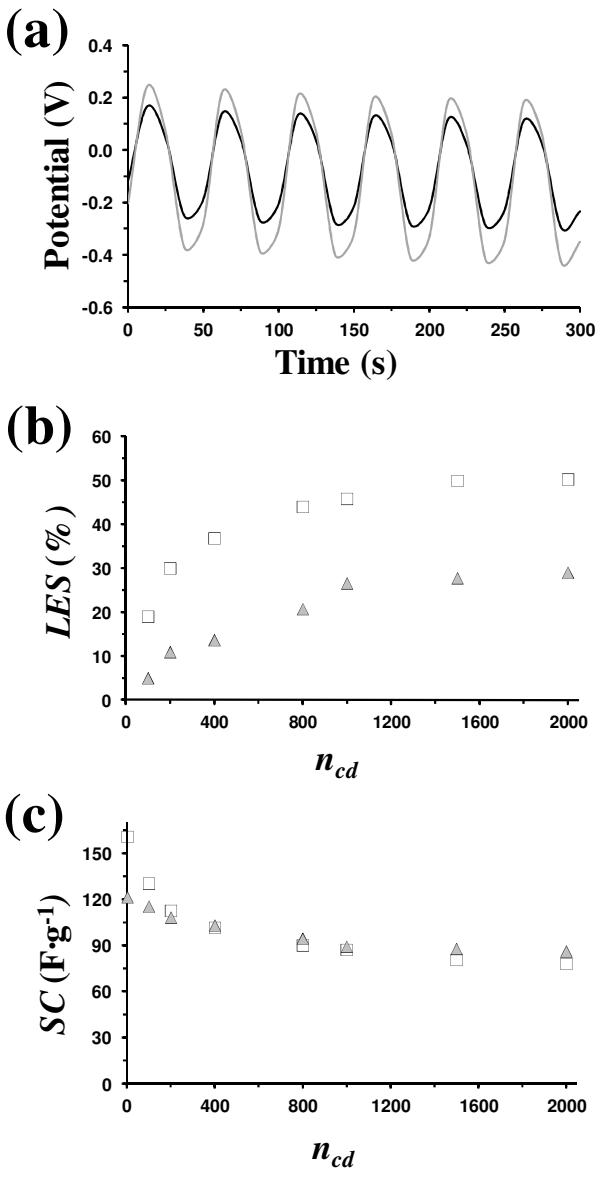

Figure 4. *(a) Galvanostatic charge/discharge curves for 3-layered/steel (grey line) and 3-layered/C_8-SH (black line) ultracapacitors. Variation of the electrochemical properties of 3-layered/steel (grey triangle) and 3-layered/C_8-SH (empty squares) ultracapacitors against the number of consecutive charge/discharge galvanostatic cycles (n_{redox}): (b) Loss of electrochemical stability (LES); and (c) Specific capacitance (SC). All properties were evaluated using an acetonitrile solution containing 0.1M $LiClO_4$ at room temperature.*

As it can be seen, the *LES* of 3-layered/steel and 3-layered/C_8-SH stabilizes at 30% and 50%, respectively, indicating that the electrochemical stability is higher for the former than for the latter (Figure 4b). In contrast, the stability of the *SC* is very similar for the two 3-layered ultracapacitors. Thus, the *SC* of 3-layered/steel and 3-layered/C_8-SH stabilizes at 87·and 80 $F \cdot g^{-1}$, respectively, after 2000 galvanostatic cycles (Figure 4c), which represent 30 hours of continuous working time. The overall of the results highlights the importance of the octanethiol SAM in the improvement of the electrochemical properties of 3-layered nanometric ultracapacitors but not on their stability, which is similar for assemblies with and without octanethiol.

Previous studies showed that the electrochemical and capacitive properties of CPs are intimately related with their surface morphology and topography.[31,41,42] The morphology of 3-layered/steel and 3-layered/C_8-SH has been investigated using SEM, illustrative micrographs being displayed in Figure 5. The morphology of the internal (first) PEDOT layer was identical to that recently described for individual nanometric PEDOT films generated using θ = 10 s.[39] PEDOT chains grow linearly forming small heterogeneous agglomerates (clusters) that are linked through sticks with fibre-like morphology. This growing mechanism is also valid for PEDOT films electrodeposited on pre-treated steel electrodes, even though octanethiol SAMs enhance the porosity of the layer (illustrative micrographs are reported in Figure 8 of reference 39).

The intermediate (second) PPy layer of 3-layered/steel films shows a compact and homogeneous globular morphology (Figure 5a). This morphology, which is similar to that reported for different N-substituted PPy derivatives [e.g. poly(N-methylpyrrole) and poly(N-(2-cyanoethyl)pyrrole)],[31,43] is due to the tendency of PPy to form cross-linked structures.[44] Thus, the formation of α-β linkages inhibits the presence of pores, favouring the formation of very compact clusters in the surface. High and low resolution micrographs of the intermediate PPy layer of 3-layered/C_8-SH films are provided in Figure 5b. The morphology obtained in this case is significantly less homogeneous and compact than that displayed in Figure 5a. Thus, the porous PEDOT layer electrodeposited on the modified steel electrode acts as a template altering some of characteristics typically found in PPy. Although the latter retains its typical globular morphology, the structure is heterogeneous and porous rather than homogeneous and compact.

The external (third) PEDOT layer of the 3-layered/steel (Figure 5c) shows the formation of clusters located at very different heights, which alternates with relatively

deep pores at the surface of the film. This morphology suggests that the roughness at the surface of the 3-layered/steel film is affected by the intermediate PPy layer. This feature was corroborated by AFM, the average roughness measured for 3-layered/steel and PEDOT/steel films being 96 and 82 nm, respectively. The morphology of the external PEDOT layer of the 3-layered/C_8-SH film is displayed in Figure 5d. In this case the intermediate PPy layer promotes the porosity of PEDOT deposited onto it. Thus, the presence of sticks with fibre-like morphology linking the clusters is minimized with respect to Figure 5c. Consequently, the pores typically found at the surface of nanometric PEDOT films become more clear and deep.

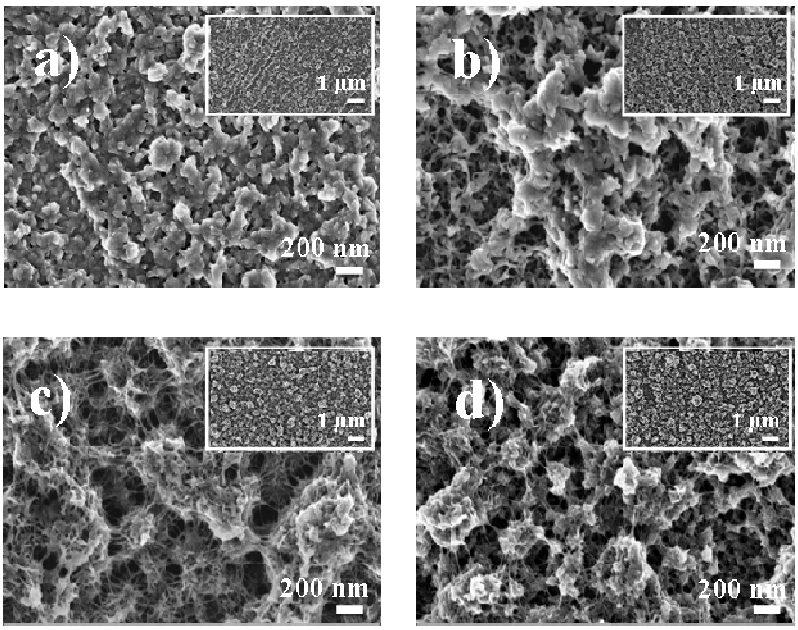

Figure 5. *High and low (inset) resolution (inset) SEM micrographs of the intermediate and external layers of 3-layered/steel and 3-layered/C_8-SH films: (a) PPy layer of 3-layered/steel; (b) PPy layer of 3-layered/C_8-SH; (c) PEDOT (external) of 3-layered/steel; and (d) PEDOT (external) of 3-layered/C_8-SH.*

Micrographs displayed in Figure 5 reflect the influence of the self-assembled octanethiol monolayer on the porosity of the 3-layered film. Thus, the octanethiol coating promotes a more regular electrodeposition in the first PEDOT layer, inducing some morphological changes related with the enhancement of the porosity. These changes are transmitted to the second layer and, subsequently, to the external layer, resulting in an overall increment of the porosity. It should be emphasized that this successful transmission process, in which each layer acts as a template for the next one, is only possible when the thickness of the layers is nanometric. Thus, the effect of the

octanethiol on the superficial morphology was found to disappear when the polymerization time increases to θ = 300 s (*i.e.* micrometric films).[39] On the other hand, Figure 6 shows high resolution micrographs of the cross-section of a 3-layered/C_8-SH film, allowing visual identification of the alternated layers of PEDOT and PPy. Elemental analyses by EDX corroborated the presence of unique elements in the different layers (*i.e.* sulfur in the internal and external layers, and nitrogen in the intermediate layer) verifying the success of the electrochemical LbL procedure.

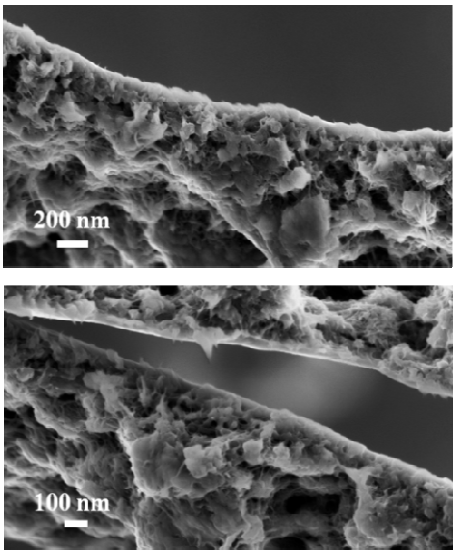

Figure 6. *Cross-section SEM micrographs of the 3-layered/C_8-SH film.*

Figure 7 compares AFM height images of the intermediate PPy and external PEDOT layers of 3-layered films deposited in untreated and octanethiol-treated steels (AFM images of the interal PEDOT layer directly deposited on the electrode were reported in Figure 7 of reference 39). As it can be seen, octanethiol affects not only to the topology, increasing the dimensions of the aggregates, but also de roughness, which is more pronounced in the 3-layered/C_8-SH than in the 3-layered/steel. The proposed growing mechanism is fully consistent with the thickness and roughness measured by AFM for 3-layered/steel, 3-layered/C_8-SH and PEDOT/steel films (Table 1). Specifically, the thickness of each layer in 3-layered films is ~100 nm, which facilitates the role played by the internal layers as templates of the intermediate and external ones. On the other hand, the roughness determined by AFM is 96, 150 and 82 nm for 3-layered/steel, 3-layered/C_8-SH and PEDOT/steel, respectively. These values corroborate that the intermediate PPy layer enhances the roughness of the external PEDOT layer, this effect

being especially remarkable for the 3-layered film electrodeposited onto the modified electrode.

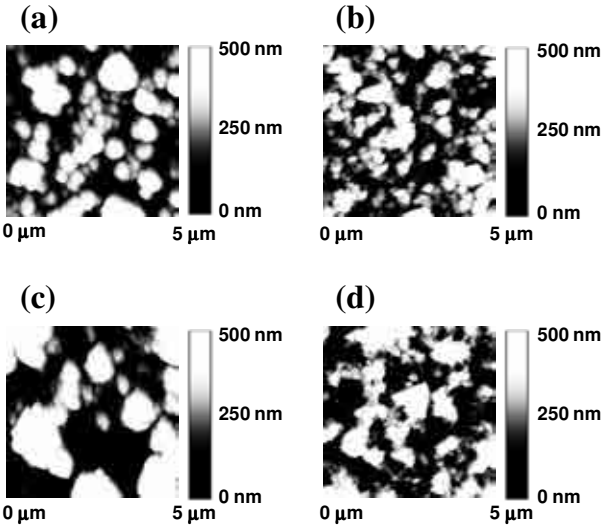

Figure 7. *Height AFM images of the intermediate and external layers of 3-layered films: (a) PPy layer of 3-layered/steel; (b) PPy layer of 3-layered/C_8-SH; (c) PEDOT (external) of 3-layered/steel; and (d) PEDOT (external) of 3-layered/C_8-SH.*

The values of Δ (Eqn. 8) indicate that the porosity increases as follows: PEDOT/steel (Δ = 37%) < 3-layered/steel (Δ = 43%) < 3-layered/C_8-SH (Δ = 57%), which is fully consistent with the existence of clear and deep pores in the latter (Figure 5d). The porosity is intimately related with the ability to store charge, which essentially depends on the mobility of perchlorate anions during the oxidation and reduction cycles (*i.e.* entrance into the polymeric matrix and escape from the polymeric matrix, respectively). Thus, the higher mobility of the counterions corresponds to the materials with better electrochemical and capacitive properties. Micrographs displayed in Figure 5 clearly indicate that such mobility is easier in 3-layered films than in PEDOT/steel, which is fully consistent with the electroactivity and *SC* discussed above for the three investigated ultracapacitors.

The morphological changes produced by the electrochemical degradation are illustrated in Figure 8, which shows the SEM micrographs collected for 3-layered/steel, 3-layered/C_8-SH and PEDOT/steel films after 1000 consecutive oxidation-reduction cycles. As it can be seen, the external morphology of the 3-layered/steel film becomes significantly more compact (Figure 8a), which is consistent with a drastic reduction in the thickness of the film (*i.e.* Δ= 43%). Thus, molecular aggregates and clusters tend to

collapse due of the rupture of the sticks with fiber-like morphology mentioned above (Figure 5c). The increment in the compactness with respect to the morphology displayed in Figure 5 (*i.e.* before anodic scans are applied) is still more drastic in the 3-layered/C_8-SH films (Figure 8b), as is reflected by Δ = 57%. This feature is fully consistent with the improvement in the electrochemical and capacitive properties of the 3-layered film induced by the octanethiol coating. Finally, the morphology of PEDOT/steels also becomes more (Figure 8c), even though in this case the relative change is smaller than that observed for the two 3-layered systems. This structure makes difficult the mobility of perchlorate anions with respect to the 3-layered ultracapacitors and, consequently, the capacitive properties of PEDOT/steel are the worst.

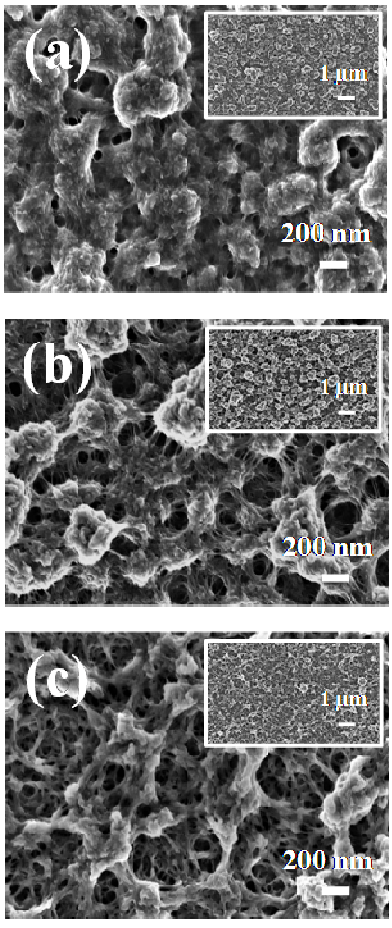

Figure 8. *High and low (inset) resolution SEM micrographs of the superficial morphology after 1000 consecutive oxidation-reduction cycles: (a) 3-layered/steel; (b) 3-layered/C_8-SH; and (c) PEDOT/steel.*

EIS was employed to obtain more information about the capacitive properties of the 3-layered ultracapacitors. Figure 9a shows the Nyquist plots recorded for 3-layered/steel

and 3-layered/C_8-SH ultracapacitors after 500 consecutive oxidation-reduction cycles in the potential range from -0.20 to 1.20 V at a scan rate of 20 $mV \cdot s^{-1}$.

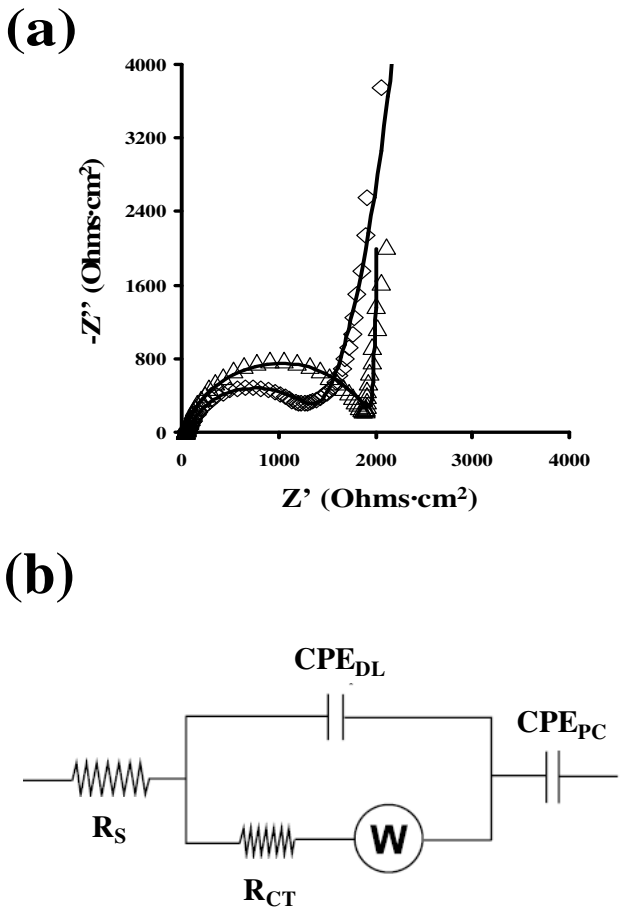

Figure 9. *(a) Nyquist diagrams of nanometric symmetric ultracapacitors after 500 consecutive oxidation-reduction cycles in the potential range between -0.20 and 1.20 V at a scan rate of 20 mV/s: 3-layered/steel (empty triangles) and 3-layered/C_8-SH (empty diamonds). Solid lines correspond to the fitting of the experimental data to the equivalent circuit displayed in (b).*

The experimental EIS diagrams were analyzed using the equivalent circuit (EC) displayed in Figure 9b, which was previously proposed for micrometric PEDOT films deposited onto modified steel electrodes.[39] The proposed EC is given by $R_s[CPE_{DL}(R_{CT}W)]CP_s$, where R_s represents the electrolyte resistance; CPE_{DL} is the double layer capacitance; R_{CT} is the charge-transfer resistance at the interface between the polymer film and the electrolyte, which is in serial connection with the Warburg element (W); and CP_s is to the pseudo-capacitance. R_s and R_{CT} correspond to the intercept of the semicircle with the real axis (Z') at high frequencies and the diameter of the semicircle along the real axis (Z'), respectively. The double layer capacitance was

replaced by a constant phase element (CPE) that describes a non-ideal capacitor when the phase angle is different from -90º. The CPE impedance is attributed to the distributed surface reactivity, surface heterogeneity, and roughness of the current and potential distribution, which are related with the electrode geometry and the electrode porosity.[45] The latter was expressed as $Z_{CPE} = [Q(j\omega)^n]^{-1}$, where Q is a frequency-independent constant, ω is the angular frequency and n values are the correlation coefficients for the CPE. The fitting with experimental data provided error percentage smaller than 5% for each circuit component, indicating a satisfactory behavior.

Nyquist plots show three well-defined regions, as can be observed in Figure 9a. EIS spectra show a depressed capacitive semi-circle at high frequencies related to the polymer–electrolyte interface. At intermediate frequencies a linear region with a slope around 45º is observed, reflecting a Warburg diffusion region. Finally, a nearly vertical line is found at low frequencies, which has been related to the faradaic pseudo-capacitance of the ultracapacitors. The simulated impedance parameters derived from the fitting of the experimental EIS plots with the EC displayed in Figure 9b are listed in Table 2. The R_{CT}, which indicates the facility to exchange anions between the polymer and the electrolyte, is lower for 3-layered/C_8-SH than for 3-layered/steel after 500 oxidation-reduction cycles, this feature being is in excellent agreement with the Δ values described above. It is worth noting that, after electrochemical degradation, a straight line is observed evidencing the excellent capacitive abilities of two 3-layered systems.

Table 2. *Data of EIS results obtained from the equivalent circuit for 3-layered/steel and 3-layered/C_8-SH ultracapacitors after 500 consecutive oxidation-reduction cyclcles in the potential interval from -0.20 to 1.20 V at a scan rate of 20 mV·s^{-1}.*

	R_s (Ω·cm^2) [a]	**CPE (μF·cm^{-2}·s^{n-1}) [b]**	**n**	**R_{CT} (Ω·cm^2) [c]**	**W (Ω·cm^{-2}) [d]**	**CP_s (mF·cm^{-2}·s^{n-1}) [e]**
3-layered/steel	35.36	24.63	0.83	1932.87	26.58	4.52
3-layered/C_8-SH	56.56	27.46	0.78	1304.28	21.44	3.74

[a] Electrolyte resistance. [b] Double layer capacitance. [c] Charge transfer resistance. [d] Warburg resistance. [e] Pseudo-capacitance.

4.3.4. Conclusions

The electrochemical characteristics of the investigated ultracapacitors depend on both the morphology and nanometric thickness of the assembled films. The highest performance in terms of ability to store charge and capacitance properties has been obtained for the 3-layered/C_8-SH symmetric ultracapacitor, the 3-layered/steel one being in turn better than the PEDOT/steel one. Thus, the 3-layered/C_8-SH shows the highest specific capacitance, capacity to store charge, Coulomb efficiency, energy density and power density. The effect of the octanethiol has been found to be particularly relevant in the specific capacitance, capacity to store charge and power density, even though it provides a benefit in all the investigated properties. The electrochemical stability of the ultracapacitors has been investigated using two different assays. The first one, which is very aggressive, is based on consecutive oxidation-reduction cycles in a relatively wide potential interval (*i.e.* from -0.50 to 1.60 V) while the second consists on conventional consecutive galvanostatic charge/discharge cycles. In both cases the stability of the 3-layered/C_8-SH ultracapacitor was the highest, the performance of this assembly being excepcionally good when it is evaluated using charge/discharge cycling (*i.e.* the *SC* after 2000 consecutive cycles is 80 $F \cdot g^{-1}$).

Octanethiol also affects the superficial morphology of the 3-layered film, enhancing both the roughness and porosity. These effects are transmitted layer-by-layer from the internal one to the external one. Thus, the internal and the intermediate layers act as nanometric templates of the intermediate and external layers, respectively, in the electrogeneration process. Measures of the thickness, roughness and porosity are fully consistent with this growing mechanism and the mobility of the perchlorate anions. The porosity, which was estimated by comparing the thickness of the films before and after electrochemical degradation, is ~50% higher for 3-layered/C_8-SH than for PEDOT/steel. Finally, EIS measures have been used to get additional information about the resistance and capacitance of the 3-layered devices, results being fully consistent with the electrochemical and structural observations. The overall of the results indicates that multilayered films of PEDOT and PPy deposited on steel coated with octanethiol are effective organic ultracapacitors.

4.3.5. References

[1]. Skotheim, T.A.; Reynolds, J. R. “Handbook of Conducting Polymers”, 3rd Edition. Conjugated Polymers. Vol. 1: Theory, synthesis, properties, and characterization. Vol. 2: Processing and Applications. CRC Press, Boca Raton 2007.

[2]. Wallace, G.G.; Spinks, G.M.; Kane-Maguire, L.A.P.; Teasdale, P.R. “Conductive Electroactive Polymers”, CRC Press, Boca Raton, 2009.

[3]. Freund, M.S.; Deore, B. “Self-Doped Conducting Polymers”, John Wiley & Sons Ltd, West Sussex, England, 2007.

[4]. Groenendaal, L.; Zotti, G.; Aubert, P.H.; Waybright, S.M.; Reynolds, J.R. *Adv. Mater.* **2003**, *15*, 855.

[5]. Groenendaal, B.L.; Jonas, F.; Freitag, D.; Pielartzik, H.; Reynolds J.R. *Adv. Mater.* **2000**, *12*, 481.

[6]. Kirchmeyer, S.; Reuter, K. *J. Mater. Chem.* **2005**, *15*, 2077.

[7]. Yang, J.; Kim, D.H.; Hendricks, J.L.; Leach, M.; Northey, R.; Martin, D.C. *Acta Biomaterialia* **2005**, *1*, 125.

[8]. Richardson-Burns, S.M.; Hendricks, J.L.; Foster, B.; Povlich, L.K.; Kim, D.H.; Martin, D.C. *Biomaterials* **2007**, *28,* 1539.

[9]. del Valle, L.J.; Aradilla, D.; Oliver, R.; Sepulcre, F.; Gamez, A.; Armelin, E.; Alemán, C.; Estrany, F. *Eur. Polym. J.* **2008**, *44*, 1323.

[10]. Williams, E.L.; Jabbour, G.E. *Appl. Phys. Lett.* **2005**, *87*, 223504.

[11]. Eom, S.H.; Senthilarasu, S.; Uthirakumar, P.; Yoon, S.C.; Lim, J.; Lee, C.; Jim, H. S.; Lee, J.; Lee, S.H. *Org. Electronics* **2009**, *10*, 536.

[12]. Sapp, S.A.; Sotzing, G.A.; Reddinger, J.L.; Reynolds, J.R. *Adv. Mater.* **1996**, *8*, 808.

[13]. Brown, T.M.; Kim, J.S.; Friend, R.H.; Cacialli, F.; Daik, R.; Feast, W.J. *Appl. Phys. Lett.* **1999**, *75*, 1679.

[14]. Khaldi, A.; Plesse, C.; Soyer C.; Cattan, E.; Vidal, F.; Legrand, C.; Teyssié, D. *Appl. Phys. Lett.* **2011**, *98*, 164101.

[15]. Liu, R.; Lee, S.B. *J. Am. Chem. Soc.* **2008**, *130*, 2942.

[16]. Park, J.; Kim, H.K.; Son Y. *Sens. Actuators B* **2008**, *133*, 244.

[17]. Decher, G.; Hong, J.D.; Schmitt, J. *Thin Solid Films* **1992**, *210*, 831.

[18]. Decher, G.; Schmitt, J. *Prog. Colloid Polym. Sci.* **1992**, *89*, 160.

[19]. Decher, G. *Science* **1997**, *277*, 1232.

[20]. Kim, Y.; Kim, E. *Curr. Appl. Phys.* **2006**, *6S1*, e202.

[21]. Ram, M.K.; Bertoncello, P.; Ding, H.; Paddeu, S.; Nicolini, C. *Biosens. Bioelectron.* **2001**, *16*, 849.

[22]. Recksiedler C.L.; Deore, B.A.; Freund, M.S. *Langmuir* **2006**, *22*, 2811.

[23]. Liang, Z.; Dzienis, K.L.; Xu, J.; Wang, Q. *Adv. Funct. Mater.* **2006**, *16*, 542.

[24]. Wakizaka, D.; Fushimi, T.; Ohkita, H.; Ito, S. *Polymer* **2004**, *45*, 8561.

[25]. Nah, Y. C.; Choi, W. S.; Kim, D. Y. *Solar Energy Materials & Solar Cells* **2008**, *92*, 1547.

[26]. Vacca, P.; Petrosino, M.; Miscioscia, R.; Nenna, G.; Minarini, C.; Sala, D.D.; Rubino, A. *Thin Solid Films* **2008**, *516*, 4232.

[27]. Sakai, N.; Prasad, G. K.; Ebina, Y.; Takada, K.; Sasaki, T. *Chem. Mater.* **2006**, *18*, 3596.

[28]. Aradilla, D.; Estrany, F.; Oliver, R.; Alemán, C. *Eur. Polym. J*. **2010**, *46*, 2222.

[29]. Estrany, F.; Aradilla, D.; Oliver, R.; Armelin, E.; Alemán, C. *Eur. Polym. J*. **2008**, *44*, 1323.

[30]. Estrany, F.; Aradilla, D.; Oliver, R.; Alemán, C. *Eur. Polym. J*. **2007**, *43*, 1876.

[31]. Aradilla, D.; Estrany, F.; Armelin, E.; Alemán, C. *Thin Solid Films* **2010**, *518*, 4203.

[32]. Mazur, M.; Krysinski, P. *Langmuir* **2000**, *16*, 7962.

[33]. Niu, L.; Latonen, R.-M.; Kvarnström, L.; Ivaska, A *Electrochim. Acta* **2004**, *49*, 4455.

[34]. Sayre, C. N.; Collard, D. M. *Langmuir* **1997**, *13*, 714.

[35]. Mazur, M.; Predeep, P. *Polymer* **2005**, *46*, 1724.

[36]. Rozsnyai, L. F.; Wrighton, M. S. *Chem. Mater.* **1996**, *8*, 309.

[37]. Inaoka, S.; Collard, D.M. *Langmuir* **1999**, *15*, 3752.

[38]. Mazur, M.; Krysinski, P. *J. Phys. Chem. B* **2002**, *106*, 10349.

[39]. Aradilla, D.; Azambuja, D.; Estrany, F.; Iribarren, J. I.; Ferreira, C.A.; Alemán, C. *Polym. Chem.* **2011**, *2*, 2548.

[40]. Ocampo, C.; Oliver, R.; Armelin, E.; Alemán, C.; Estrany, F. *J. Polym. Chem.* **2006**, *13*, 193.

[41]. Aradilla, D.; Estrany, F.; Aremlin, E.; Alemán, C. *Thin Solid Films* **2012**, *520*, 4402.

[42]. Aradilla, D.; Estrany, F.; Alemán, C. *J. Phys. Chem. C* **2011**, *115*, 8430.

[43]. Aradilla, D.; Estrany, F.; Armelin, E.; Oliver, R.; Iribarren, J.I.; Alemán, C. *Macromol. Chem. Phys.* **2010**, *211*, 1663.

[44]. Alemán, C.; Casanovas, J.; Torras, J.; Bertrán, O.; Armelin, E.; Oliver, R.; Estrany, F. *Polymer* **2008**, *49*, 1066.

[45]. Jorcin, J.-B.; Orazem, M. E.; Péberè, N.; Tribollet, B. *Electrochim. Acta,* **2006**, *51*, 1473.

Chapter 5. Hybrid nanocomposites

5.1. Conducting poly(3,4-ethylenedioxythiophene)-Montmorillonite exfoliated nanocomposites.[a]

5.1.1. Introduction

5.1.2. Methods

5.1.3. Results and discussion

5.1.4. Conclusions

5.1.5. References

[a]Results presented in this chapter were published in *Eur. Polym. J.* **2010**, *46*, 977.

5.2. Hybrid polythiophene-clay exfoliated nanocomposites for supercapacitor devices.[b]

5.2.1. Introduction

5.2.2. Methods

5.2.3. Results and discussion

5.2.4. Conclusions

5.2.5. References

[b]Results presented in this chapter were published in *J. Mat. Chem.* **2012**, *22*, 13110.

5.3. Supercapacitors made of multilayered electrochemical nanocomposites with anti-corrosive applications.

5.3.1. Introduction

5.3.2. Methods

5.3.3. Results and discussion

5.3.4. Conclusions

5.3.5. References

5.1. Conducting poly(3,4-ethylenedioxythiophene)-Montmorillonite exfoliated nanocomposites

5.1.1. Introduction

The development of polymer-clay nanocomposites is a field of increasing interest due to the important technological applications of these materials. Thus, composite systems formed by organic polymers and clay minerals structured at the nanoscale level, which usually present an unique layered structure, rich intercalation chemistry and availability at low cost, have been used to develop plastic materials with advanced mechanical properties, molecular barrier behavior, fire retardant abilities, enhanced thermal stability, etc., compared to the individual polymeric materials.[1-7]

On the other hand, electrically conducting polymers have also attracted much attention due to their many promising technological applications, as for example microelectronic devices, electroluminescence devices, corrosion inhibitors, electrochemomechanical devices and chemical sensors.[8] Among conducting polymers, polyaniline (PAni) and polypyrrole (PPy) are particularly attractive because of their simple synthesis, high conductivity and excellent environment stability. As a consequence, many PAni-clay[4,9-15] and PPy-clay[4,15-20] nanocomposites have been prepared and analyzed in the last years. Poly(3,4-ethylenedioxythiophene) (PEDOT), a polythiophene derivative with high electrical conductivity, transparency, structural stability, suitable morphology and fast doping-undoping mechanism,[21,22] has also attracted much attention. This material, which was originally described and is currently commercialized by the Bayer company, exhibits higher thermal and environmental stabilities, and easier processability than common conducting polymers, including PAni and PPy.[8,21,22] Consequently, it has been proposed for several technological applications, *e.g.* as sensor for specific DNA nucleotidic sequences,[23] molecular condenser[24,25] and anticorrosive additive of conventional organic coatings.[26]

Some hybrid nanocomposites formed by the combination of PEDOT and various inorganic materials have been reported in the last years, *e.g.* PEDOT-V_2O_5,[27] PEDOT-MoO_3,[28] PEDOT-graphite oxide[29] and PEDOT-clay.[30,31] PEDOT-clay nanocomposites were based on montmorillonite (MMT), an smectite group mineral clay that belongs to the general family of 2:1 layered silicates.[32] Unfortunately, PEDOT-MMT nanocomposites usually show an intercalative structure,[30] which is also frequently found

in PAni-MMT[32-35] and PPy-MMT,[19,36-38] rather than the more desirable exfoliated organization. Thus, complete exfoliation of MMT layers in conducting polymers is a challenging task that, sometimes, requires complex and expensive strategies, *e.g.* modifications of MMT with intercalative agents[39] and pre-synthesis of a graft copolymer.[40] In a very recent study, an exfoliated PEDOT-MMT nanocomposite was obtained by *in situ* polymerization in an aqueous suspension containing a MMT organically modified with octadecylammonium.[41] Unfortunately, the investigations devoted to fabricate conducting polymer-clay nanocomposites using simple anodic electropolymerization methods, which are frequently used for the preparation of individual conducting polymers, are very scarce.[42,43] Moreover, in spite of the excellent electrochemical and electrical properties of PEDOT,[21,22,44] such properties were never examined in its clay-containing nanocomposites.

In this work the preparation of exfoliated PEDOT-MMT nanocomposites by electropolymerization in aqueous solution was studied. Furthermore, the physical, electrochemical and electrical properties of the fabricated nanocomposites have been determined and compared with those obtained for PEDOT homopolymer prepared using identical experimental conditions.

5.1.2. Methods

Materials. 3,4-ethylenedioxythiophene (EDOT) monomer and MMT (bentonite) were purchased from Aldrich and used as received. $LiClO_4$ analytical reagent grade from Aldrich was stored in an oven at 80 ºC before use in the electrochemical trials.

Preparation. Both PEDOT and PEDOT-MMT nanocomposites were prepared by chronoamperometry (CA) under a constant potential of 1.10 V. Electrochemical experiments were performed on a Ecochimie model VersaStat II potenciostat-galvanostat using a three-electrode two-compartment cell under nitrogen atmosphere (99.995% in purity) at 25 ºC. The anodic compartment was filled with 40 mL of a 10 mM monomer solution in distilled water containing 0.1 M $LiClO_4$ as supporting electrolyte, while the cathodic compartment contained 10 mL of the same electrolyte solution without the monomer. Steel AISI 316 sheets of 4 cm^2 area were employed as working and counter electrodes. The reference electrode was an Ag|AgCl electrode containing a KCl saturated aqueous solution (E^o = 0.222 V *vs.* standard hydrogen electrode at 25 ºC), which was connected to the working compartment through a salt

bridge containing the electrolyte solution. All the potentials (E) given in this work refer to this electrode.

The amount of MMT in the monomer solution used to prepare PEDOT-MMT nanocomposites ranged from 1% to 10% w/w (dry weight), these concentration values being referred to that of the EDOT monomer. As a typical procedure, MMT was exfoliated in de-ionized water at neutral pH, being sonicated for 10 min with an ultrasonic generator. The resulting solution was stirred for 1 day using a magnetic stirrer. After this, a 10 mM EDOT solution in distilled water with 0.1 M $LiClO_4$ was added to the above exfoliated clay solution, and stirred for 20 h in a frozen environment (ice).

Electrochemical characterization. The electroactivity and electrostability of both the PEDOT homopolymer and the PEDOT-MMT nanocomposite were determined by cyclic voltammetry (CV). According to this procedure, electroactivity increases with the similarity between the anodic and cathodic areas of the first control voltammogram, while electrostability decreases with the oxidation and reduction areas of successive control voltammograms. A scan rate of 100 $mV \cdot s^{-1}$ was used in all cases.

The thickness of the films (ℓ) was estimated according to Schirmeisen and Beck[45] using the mass of polymer deposited in the electrode, m_{pol}, which was obtained using the following relation:

$$m_{pol} = Q_{pol}\left(\frac{m}{Q}\right) \qquad (1)$$

Where Q_{pol} is the polymerization charge (in millicoulombs per square centimeter) consumed in the generation of each layerand $\left(\frac{m}{Q}\right)$ the current productivity, the latter being previously determined for PEDOT[27] (0.875 $mg \cdot C^{-1}$). Although the latter value was obtained in acetonitrile, we studied the kinetics for the oxidation-polymerization of EDOT in aqueous solution to check that it can be rightly applied in the current work. The volume of polymer deposited in the electrode (V_{pol}) was obtained using the values of m_{pol} and the density previously reported for PEDOT (1.665 $g \cdot cm^{-3}$).[44] Accordingly, the thickness of each layer was calculated considering the surface of polymerization (S_{pol}), which is the surface of the electrode (4 cm^2), and V_{pol}.

Structural, morphological and electrical characterization. The structure and distribution of the clay in the PEDOT-MMT nanocomposites were examined using a

Phillips TECNAI 10 transmission electron microscope at an accelerating voltage of 100 kV. For this purpose, small strips of nanocomposite were removed from the electrode with a razor blade and, according to the manufacturer protocol, embedded in a low viscosity modified Spurr epoxy resin and curing at 60ºC for 24 h. Ultra-thin sections (less than 100 nm) of these samples were cut at room temperature using a Sorvall Porter-Blum microtome. Finally, the sections were placed on carbon coated cooper grids. Bright field micrographs were taken with an SIS Mega View II digital camera.

X-ray diffraction (XRD) spectra of PEDOT-MMT films were recorded using a Bruker D8 Advance model to 40 kV and 40 mA (λ= 1.5406 Å). The XRD patterns were taken at ambient laboratory temperature using 10 s / angular step (1 angular step = 0.02º).

Topographic AFM images were obtained with a Molecular Imaging PicoSPM using a NanoScope IV controller in ambient conditions. The averaged RMS roughness (*r*) was determined using the statistical application of the Nanoscope software, which calculates the average considering all the values recorded in the topographic image with exception of the maximum and the minimum. Nanometric measurements were conducted under ambient conditions at ~50% relative humidity and 20-22 ºC. The system was placed on an active vibration isolation table for minimum acoustic disturbance (20 series, TMC, Peabody, MA, USA).

The electrical conductivities (σ_0) were determined using the sheet-resistance method following a previously described procedure.[46]

5.1.3. Results and discussion

Preparation and electrochemical characterization. Figure 1 (solid curve) shows the cyclic voltammogram recorded for the anodic oxidation of EDOT in distilled water with 0.1 M $LiClO_4$. Two anodic peaks, O_1 and O_2, were detected. The anodic potential of the first peak, E_p^a (O_1) = 1.38 V, is lower than that previously obtained under identical experimental conditions with exception of the acetonitrile solvent [E_p^a (O_1) = 1.53 V],[44] while the anodic potential of the second peak O_2 overlaps the oxidation of the medium at a potential higher than 1.60 V. No reduction peak is seen in Figure 1 because the oxidation of EDOT is an irreversible process up to 1.60 V. Uniform, adherent and insoluble PEDOT films grew on the working steel anode when the monomer began to be oxidized from potentials higher than 0.90 V.

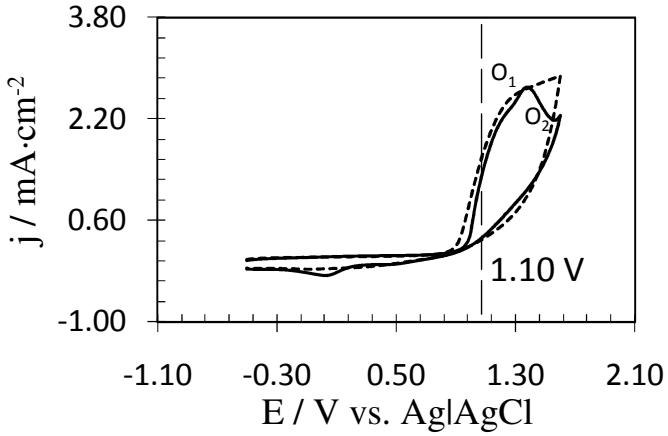

Figure 1. *Control voltammograms for the oxidation of a 10 mM 3,4-ethylenedioxythiophene (EDOT) solution in distilled water with 0.1 M $LiClO_4$. Solid and dashed curves correspond to solutions without MMT and with 5% w/w of MMT, respectively. Voltammograms were recorded using a 4 cm^2 steel electrode. Initial and final potentials: -0.50 V; reversal potential: 1.60 V. Scan rate: 100 $mV \cdot s^{-1}$.*

The cyclic voltammograms of EDOT were used to determine the proper conditions of polymerization in an aqueous solution using $LiClO_4$ as electrolyte. Potentials comprised between 0.90 V and 1.30 V are appropriated for this purpose because the anodic current densities determined from the chronoamperograms recorded at these potentials are relatively high, *i.e.* the molecular diffusion of the monomer is high within this potential range. A potential of 1.10 V, which is just in the middle of such range, was chosen to generate both the PEDOT-MMT nanocomposites and PEDOT homopolymer in this work. Figure 1 (dashed curve) presents the cyclic voltammogram recorded for the EDOT-MMT (5% w/w) solution using the same experimental conditions. As can be seen, 1.10 V is an optimal potential also in this case.

The electrogeneration of PEDOT-MMT and PEDOT films was carried out at a fixed potential of 1.10 V using a polymerization time of 300 s. The resulting films were uniform, adherent, insoluble and homogeneous in all cases. Figure 2 compares the chronoamperograms obtained for the oxidation of a 10 mM EDOT aqueous solution without and with 5% w/w MMT (solid and dashed curves, respectively). The current density stabilizes at 0.43 and 0.57 $mA \cdot cm^{-2}$ for PEDOT homopolymer and PEDOT-MMT (5% w/w) nanocomposite, respectively, indicating that the flow of monomer during the electrogeneration process increases upon the addition of MMT. These values clearly reflect the favourable interaction between the clay and the conducting polymer. On the other hand, it is worth noting that these values are smaller than that previously

reported for PEDOT homopolymer using a constant potential of 1.40 V and acetonitrile as solvent (1.82 $mA \cdot cm^{-2}$),[44] *i.e.* the monomer concentration and the electrolyte were identical to those employed in the current work. Thus, the effect of the polymerization conditions on the diffusion of the monomer seems to be higher than the addition of the exfoliated clay to the monomer solution.

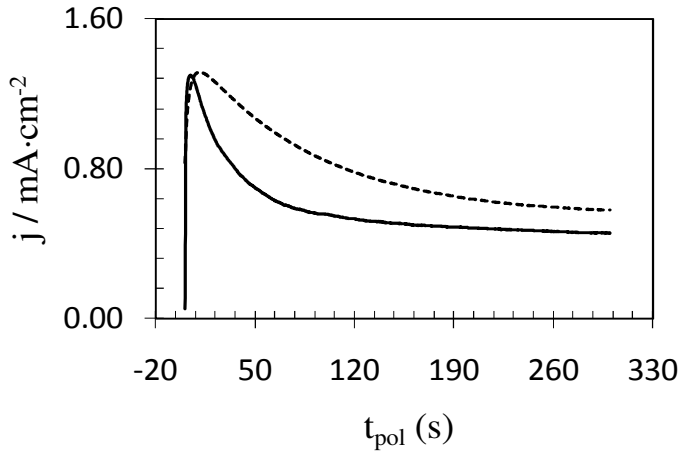

Figure 2. *Chronoamperograms recorded for the oxidation of a 10 mM 3,4-ethylendioxythiophene (EDOT) solution in distilled water with 0.1 M $LiClO_4$ on a steel electrode by applying a constant potential of 1.10 V for a polymerization time of 300 s. Solid and dashed curves correspond to solutions without MMT and with 5% w/w of MMT, respectively.*

Figure 3 compares the control voltammograms of PEDOT and PEDOT-MMT (5% w/w) recorded in the potential range from -0.50 to 1.60 V. As can be seen, the electroactivity of the nanocomposite is higher than that of the homopolymer indicating that the addition of clay enhances the ability to store charge of PEDOT. Similarly, the electroactivity of PEDOT-MMT (1% w/w) and PEDOT-MMT (10% w/w) are higher than that of PEDOT, the difference between the nanocomposite and the homopolymer increasing with the concentration of clay. This effect must be attributed to the favourable interaction between the MMT and the polymeric matrix since both the nanocomposites and the homopolymer were prepared using identical experimental conditions.

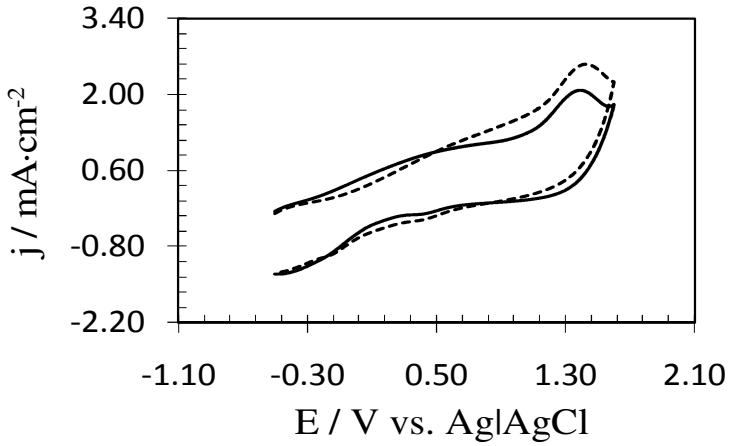

Figure 3. *Control voltammograms for the oxidation of PEDOT homopolymer (solid curve) and PEDOT-MMT (5% w/w) (dashed curve) films on 4 cm^2 steel electrode in distilled water with 0.1 M $LiClO_4$, at 100 $mV \cdot s^{-1}$ and 25 ºC. Initial and final potentials: -0.50 V; reversal potential: 1.60 V.*

However, the electrochemical stability (electrostability) of the PEDOT-MMT nanocomposites is lower than that of PEDOT homopolymer. This feature is illustrated in Figure 4, which shows the control voltammograms from -0.50 V to 1.60 V for 30 consecutive oxidation-reduction cycles of PEDOT and PEDOT-MMT (5% w/w) films. Table 1 compares the performance of the nanocomposites with that of PEDOT homopolymer in terms of electroactivity and electrostability. Specifically, for PEDOT-MMT the cathodic and anodic areas recorded along the 30th cycle indicated a loss of electrostability and electroactivity ranging from 22% to 38% and from 7% to 18%, respectively, while for PEDOT homopolymer the loss of electrostability and electroactivity after 30 cycles were 25% and 3%, respectively.

Table 1. *Loss of electroactivity and electrostability after 30 consecutive oxidation-reduction cycles for PEDOT homopolymer and PEDOT-MMT nanocomposites.*

# Material	***Loss of electroactivity***	***Loss of electrostability***
PEDOT	25%	3%
PEDOT-MMT (1% w/w)	7%	22%
PEDOT-MMT (5% w/w)	11%	34%
PEDOT-MMT (10% w/w)	18%	38%

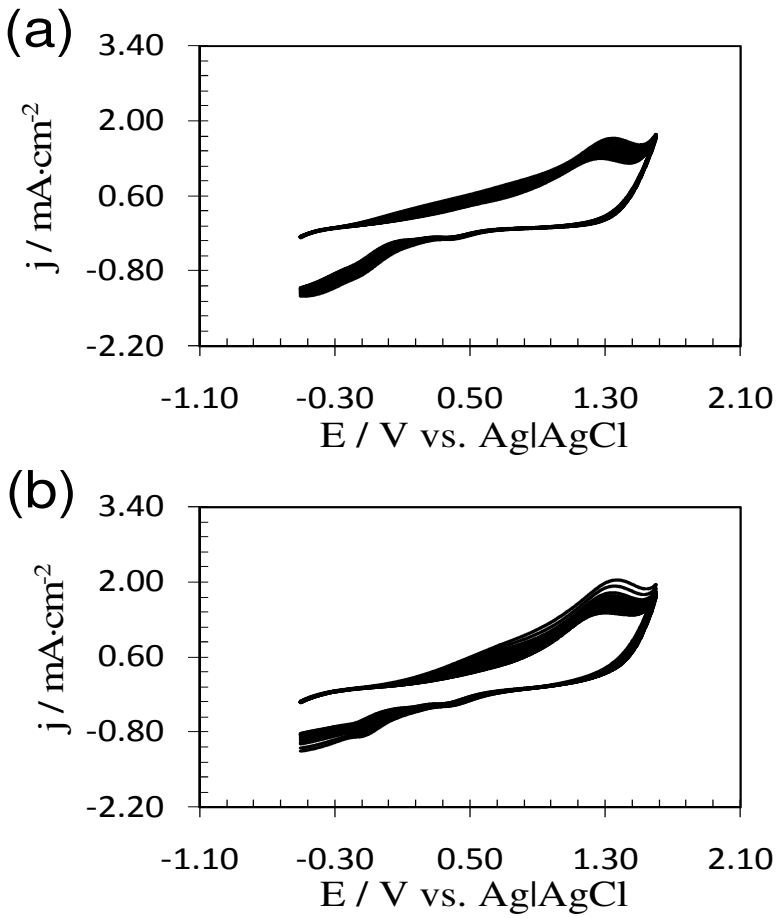

Figure 4. *Control voltammograms for 30 consecutive oxidation-reduction cycles of PEDOT (a) and PEDOT-MMT (5% w/w) (b). The conditions used to record the voltammograms were identical to those described in Fig. 3.*

Distribution of the MMT in the nanocomposites. Transmission electron microscopy (TEM) was used to visualize the exfoliation of the clay in PEDOT-MMT nanocomposites. Thus, preparation of the TEM samples by ultramicrotome allows to cut the nanocomposites perpendicularly to the electrode surfaces and, therefore, to image the distribution of the clay within the polymeric matrix (intercalated or exfoliated). TEM micrographs of PEDOT-MMT nanocomposites reveal that, independently of the clay concentration, MMT is exfoliated into individual platelets within the polymeric matrix. This is illustrated in Figure 5 for the PEDOT-MMT (5% w/w) and PEDOT-MMT (10% w/w) nanocomposites. These results confirm that the strategy used to prepare PEDOT-MMT nanocomposites successfully retains the exfoliated structure of the clay.

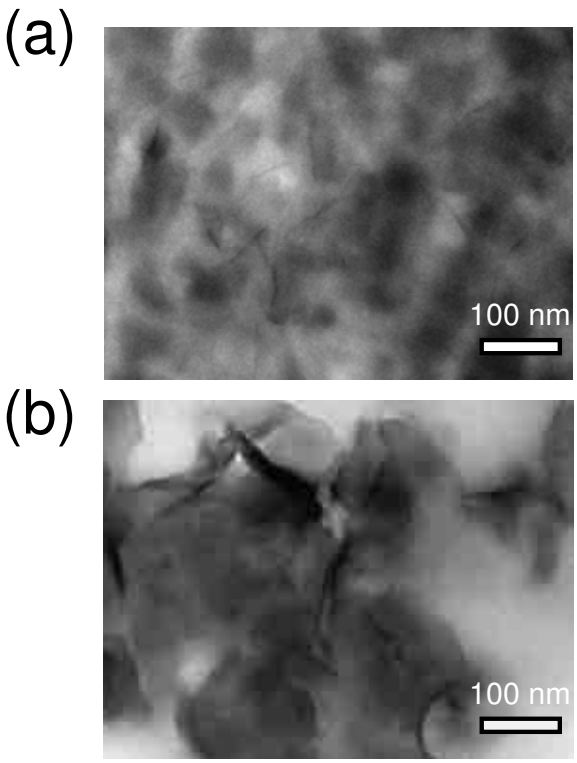

Figure 5. *TEM micrographs of (a) PEDOT-MMT (5% w/w) and (b) PEDOT-MMT (10% w/w).*

XRD patterns provide beneficial information about the *d*-spacing of the MMT, the homopolymer and the nanocomposites by following Bragg's law at peak positions. It can be seen from Figure 6 that the XRD pattern of the MMT is clearly different from those of the nanocomposites at low angles.

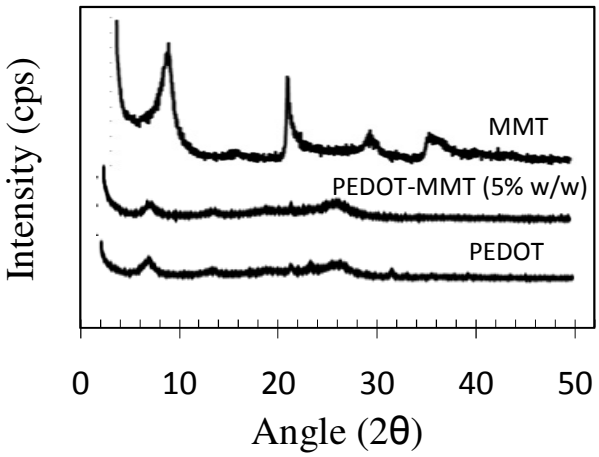

Figure 6. *XRD patterns of MMT, PEDOT and PEDOT-MMT (5% w/w).*

Strong diffraction peaks at $2\theta = 7.04^{\circ}$ (d_{100}) and $2\theta = 19.80^{\circ}$ are displayed for the MMT. These reflections are extinguished in the diffractograms of the nanocomposites. Moreover, the broad peak detected in PEDOT-MMT diffractograms at $2\theta = 6.52^{\circ}$ was also found in the pattern of PEDOT homopolymer (Figure 6). These features confirm the exfoliation of the MMT layers in the polymer matrix of the nanocomposites supporting the images obtained by TEM.

Electrical conductivity. The σ_0 values measured for the three PEDOT-MMT nanocomposites and the PEDOT homopolymer are displayed in Table 2. It is worth noting that the σ_0 obtained in this study for perchlorate-doped PEDOT is similar to that previously reported for the polystyrene sulfonate-doped homopolymer, *i.e.* 1-2 $S \cdot cm^{-1}$.[47] On the other hand, inspection of the σ_0 values determined for the PEDOT-MMT nanocomposites indicate that the incorporation of the clay does not produce significant changes with respect to the homopolymer, being in all cases of the same order of magnitude. Thus, although MMT typically acts as an inhibitor because it is not electronically conductive material, the exfoliated distribution achieved minimizes this effect. Interestingly, the σ_0 values listed in Table 2 for PEDOT-MMT nanocomposites are significantly higher than those recently reported for exfoliated PEDOT-MMT nanocomposites doped with polystyrene sulfonate, *i.e.*σ_0 ranged from $5 \cdot 10^{-7}$ to $8 \cdot 10^{-2}$ $S \cdot cm^{-1}$ depending on the modifications introduced in the clay to facilitate the exfoliation.[31]

Table 2. *Electrical conductivity (σ_0), average thickness (ℓ) and average RMS roughness (r) of PEDOT homopolymer and PEDOT-MMT nanocomposites. In all cases films were generated on a steel substrate by chronoamperometry using a constant potential of 1.10 V and a polymerization time θ= 300 s.*

System	σ_0(S·cm^{1})	ℓ (μm)	*r* (nm)
PEDOT	5.5	0.84	153
PEDOT-MMT (1 % w/w)	3.8	0.92	-
PEDOT-MMT (5 % w/w)	2.7	1.02	112
PEDOT-MMT (10 % w/w)	1.3	1.26	-

Figure 7 represents the temporal evolution of σ_0 for PEDOT homopolymer and PEDOT-MMT (5% w/w). As can be seen, the incorporation of the clay produces a drastic reduction of the electrical stability. Thus, the σ_0 of PEDOT-MMT (5% w/w) becomes practically negligible after 17 days, while that of the homopolymer decreased from 5.6 to 1.4 $S \cdot cm^{-1}$ after 35 days. The behaviour showed by PEDOT-MMT (1% w/w) and PEDOT-MMT (10% w/w) indicates that the loss of electrical stability increases with the concentration of clay.

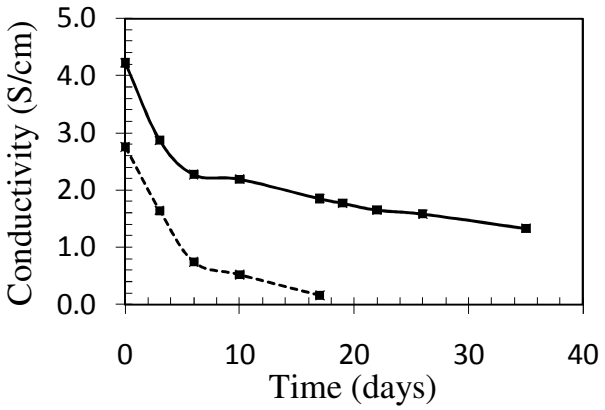

Figure 7. *Temporal evolution of the electrical conductivity (σ_0, in $S \cdot cm^{-1}$) for the PEDOT homopolymer (solid line) and PEDOT-MMT (5% w/w) nanocomposite (dashed line).*

Morphology. The average thickness determined for PEDOT and PEDOT-MMT is included in Table 2. As it was expected, the thickness of the film increases with the concentration of MMT. The morphological analysis has been focused on PEDOT and PEDOT-MMT (5% w/w), the latter being considered as the most representative nanocomposite.

Figure 8a shows an AFM image of the surface of PEDOT homopolymer, which exhibits an irregular, agglomerated and heterogeneous surface. However, the incorporation of MMT (5% w/w) produces a drastic change in this morphology, which is illustrated by the AFM image showed in Figure 8b. Thus, the surface becomes more homogeneous, the irregularities produced by agglomerations being less sharp. This flatten effect, which is also evidenced by a significant reduction of the RMS roughness (Table 2), *i.e. r* decreases from 153 nm to 112 nm upon the incorporation of MMT (5% w/w), has been previously described for other heterocyclic conducting polymers, *e.g.* polypyrrole.[48] Thus, it was proposed that the presence of the clay in the polymerization medium reduces the molecular weight of the polymer.[48]

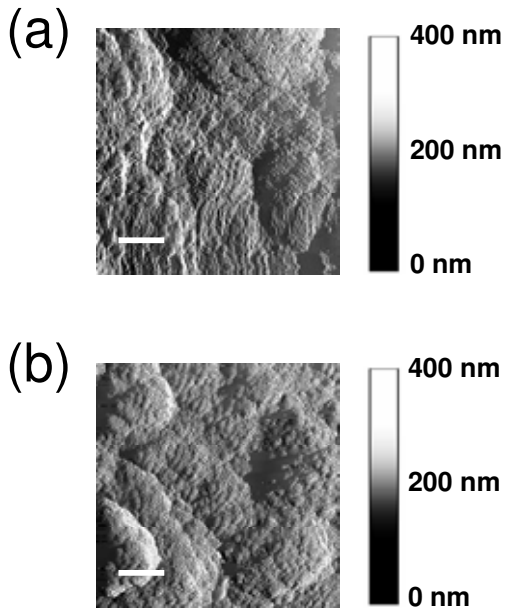

Figure 8. *AFM images of PEDOT homopolymer (a) and PEDOT-MMT (5% w/w) (b) films. Scale bar: 1 μm.*

5.1.4. Conclusions

PEDOT-MMT nanocomposites have been prepared by anodic electropolymerization under a constant potential of 1.10 V into a $LiClO_4$ aqueous solution. Structural characterization using TEM and XRD indicates that the clay is exfoliated in the PEDOT matrix, which represents a significant improvement with respect to the intercalative structure usually found in conducting polymer-clay nanocomposites. Interestingly, the electroactivity of PEDOT-MMT nanocomposites, which increases with the concentration of clay, is higher than that of individual PEDOT, whereas the electrostability is only slightly lower for the former than for the latter. These results indicate that PEDOT-MMT nanocomposites are potential candidates for the fabrication of devices able to store charge. Additionally, the electrical conductivities of the nanocomposites and the homopolymer are very similar. However, the clay reduces significantly the electrical stability of the conducting polymer. The overall of the results evidences that anodic electropolymerization is a suitable procedure for the fabrication of exfoliated conducting PEDOT-clay nanocomposites with reliable properties. Moreover, it should be emphasized that the introduction of special chemical modifications in the MMT, which is usually complicated and expensive, is not required to success with this strategy.

5.1.5. References

[1]. Hasegawa, N.; Okamoto, H.; Kawasumi, M; Kato, M; Tsukigase, A; Usuki, A. *Macromol Mater Eng*. **2000**, *76*, 180.

[2]. Alexandre, M.; Dubois, P. *Mater Sci Eng*. **2000**, *28*, 1.

[3]. Gilman, J. W.; Jackson, C. L.; Morgan, A. B.; Hayyis, Jr. R.; Manias, E.; Giannelis, E. P.; Wuthenow, M.; Hilton, D.; Phillips, S. H. *Chem. Mater.* **2000**, *12*, 1866.

[4]. Biswas, M.; Ray, S. S. *Adv. Polym. Sci.* **2001**, *155*, 167.

[5]. Zheng, Q. H.; Yu, A. B.; Lu, G.Q.; Paul, D.R.J. *Nanosci Nanotech.* **2005**, *5*, 1574.

[6]. Chen, B.; Evans, J. R. G. *Polymer* **2008**, *49*, 5113.

[7]. Paul, D. R.; Robeson, L. M. *Polymer* **2008**, *49*, 3187.

[8]. Skotheim, T. A.; Reynolds, J. R. (Eds). Handbook of Conducting Polymers, 3rd Edition, CRC Press, Boca Raton, 2007.

[9]. Singhal, R.; Datta, M. *J. Appl. Polym. Sci.* **2007**, *103*, 3299.

[10]. Yoshimoto, S.; Ohashi, F.; Kameyama, T. *Macromol. Rapid. Commun.* **2004**, *25*, 1607.

[11]. Kim, B. H.; Jung, J. H.; Hong, S. H.; Kim, J. W.; Choi, H. J.; Joo, J. *Current Appl. Phys.* **2001**, *1*, 112.

[12]. Soundararajah, Q. Y.; Karunaratne, B. S. B.; Rajapakse, R. M. G. *Macromol. Chem. Phys.* **2009**, *113*, 850.

[13]. Yoshimoto, S.; Ohashi, F.; Ohnishi, Y. and Nonami, T. *Synth. Metals* **2004**, *145*, 265.

[14]. Kim, B. H.; Jung, J. H.; Kim, J. W.; Choi, H. J.; Joo, J. *Synth. Metals* **2001**, *117*, 115.

[15]. Aranda, P.; Darder, M.; Fernández-Saavedra, R.;López-Blanco, M.; Ruiz-Hitzky, E. *Thin Solid Films* **2006**, *495*, 104.

[16]. Yeh, J-M.; Chin, C-P.; Chang, S.;*J. Appl. Polym. Sci.* **2003**, *88*, 3264.

[17]. Hong, S. Hm.; Kim, B. H.; Joo, J.; Kim, J. W.; Choi, H. J. *Current Appl. Phys.* **2001**, *1*, 447.

[18]. Kassim, A.; Mahmud, H. N. M. E.; Adzmi, F. *Mater. Sci. Semiconduc. Procc.* **2007**, *10*, 246.

[19]. Boukerma, K.; Piquemal, J-Y.; Chehimi, M. M.; Mravcakova, M.; Omastova, M.; Beaunier, P. *Polymer* **2006**, *47*, 569.

[20]. Kim, J.W.;Lui, F.; Choi, H.J.; Hong, S.H.; Joo, J. *Polymer* **2003**, *44*, 289.

[21]. Pei, Q.; Zuccarello, G.; Ahlskog, M.; Inganas, O. *Polymer* **1994**, *35*, 1347.

[22]. Groenendaal, L.; Jonas, G.; Freitag, D.; Pielartzik, H.; Reynolds, J. R. *Adv. Mater.* **2000**, *12*, 481.

[23]. Alemán, C.; Teixeira-Dias, B.; Zanuy, D.; Estrany, F.; Armelin, E.; del Valle, L. J. *Polymer* **2009**, *50*, 1965.

[24]. Estrany, F.; Aradilla, D.; Oliver, R.; Armelin, E.; Alemán, C. *Eur. Polym. J.* **2008**, *44*, 1323.

[25]. Estrany, F.; Aradilla, D.; Oliver, R.; Alemán, C. *Eur.Polym. J.* **2007**, *43*, 1876.

[26]. Armelin, E.; Meneguzzi, A.; Ferreira, C. A.; Alemán C. *Surf. Coat. Technol.* **2009**, *2003*, 3763.

[27]. Murugan, V. A.; Kwon, C-W.; Campet, G.; Kale, B. B.; Maddanimah, T.; Vijayamohanan, K. *J. Power. Sources* **2002**, *105*, 1.

[28]. Murugan, V. A.; Viswanath, A. K.; Campet, G.; Gopinath, C. S.; Vijayamohanan, K. *Appl. Phys. Lett.* **2005**, *87*, 243511.

[29]. Han, Y.; Lu, Y. *Synth.Met.* **2008**, *158*, 744.

[30]. Letaïef, S.; Aranda, P.; Fernández-Saavedra, M. R.; Detelliera, C.; Ruiz-Hitzky, E. *J. Mater. Chem*. **2008**, *18*, 2227.

[31]. Han, Y.; Lu, Y. *J. Appl. Polym. Sci.* **2009**, *111*, 2400.

[32]. do Nascimento, G. M.; Constantino, V. R.; Landers, R.; Temperini, M. L. A. *Macromolecules* **2004**, *37*, 9373.

[33]. Goddard, Y. A.; Vold, R.L.; Hoatson, G. L. *Macromolecules* **2003**, *36*, 11662.

[34]. Zeng, Q. H.; Wang, D. Z.; Yu, A.B.; Lu, G. Q. *Nanotechnology* **2002**, *13*, 549.

[35]. Hoang, H. V.; Holze, R. *Chem. Mater.* **2006**, *18*, 1976.

[36]. Letaïef, S.; Aranda, P.; Ruiz-Hitzky, E. R. *Appl. Clay Sci.* **2005**, *28*, 123.

[37]. Yoshimoto, S.; Ohasi, F.; Kameyama, T. *Macromol.Rapid.Commun.* **2005**, *26*, 461.

[38]. Mravcakova, M.; Boukerma, K.; Omastova, M.; Chehimi, M. M. *Mater. Sci. Eng.* **2006**, *26*, 306.

[39]. Jui, M. Y.; Shir, J. L.; Chiung, Y. L.; Pei, C. W. *Chem. Mater.* **2001**, *13*, 1131.

[40]. Bae, W. J.; Kim, K. H.; Jo, W. H.; Park, Y. H. *Polymer* **2005**, *46*, 10085.

[41]. Han, Y.; Lu, Y. *J. Appl. Polym. Sci.* **2009**, *111*, 2400.

[42]. Murugan, A. V.; Gopinath, C. S.; Vijayamohanan, K. *Electrochem. Commun.* **2005**, *7*, 213.

[43]. Liu, Y. C. ; Tsai, C. J. *Chem. Mater.* **2003**, *15*, 320.

[44]. Ocampo, C.; Oliver, R.; Armelin, E.; Alemán, C.; Estrany, F. *J. Polym. Res.* **2006**, *13*, 193.

[45]. Schirmeisen, M.; Beck, F.*J. Appl. Electrochem.* **1989**, *19*, 401.

[46]. Brillas, E.; Carrasco, J.; Oliver, R.; Estrany, F.; Vilar, J.; Morlans, J. M. *Electrochim. Acta* **2000**, *45*, 4049.

[47]. Timparano, S.; Kemerink, M.; Touwslager, F. J.;De Kok, M. M.; Schrader, S. *Chem. Phys.Lett.* **2004**, *394*, 339.

[48]. Yeh, J. M.; Chin, C. P.; Chang, S. *J. Appl. Polym. Sci.* **2003**, *88*, 3264.

5.2. Hybrid polythiophene-clay exfoliated nanocomposites for supercapacitor devices

5.2.1. Introduction

Among polythiophene derivatives, poly(3,4-ethylenedioxythiophene) (PEDOT; Scheme 1) has attracted much attention because of its many advantageous properties such as high electrical conductivity (up to 500 S/cm) and transparency in the visible range, excellent thermal and structural stability, suitable morphology and fast doping-undoping mechanism.[1-5] Many of the properties of PEDOT, which was developed at end of the eighties in Germany, are due to the fact that in the monomer, 3,4-ethylenedioxythiophene (EDOT), the dioxane ring fused onto the thiophene ring protects the positions 3 and 4 of the latter. This reduces the possibility of side chain reaction during polymerization, which leads to enhancement in conjugation length of the resulting polymer chain. Furthermore, the oxygen atoms, which are directly attached to the 3- and 4-positions, exert an electrondonating effect reducing the band gap[7-10] and provoking the planarity of the polymer chain.[11] PEDOT has already found useful applications as antistatic film coating,[12-14] electrochromic windows,[15] hole-injection material in organic light emitting diodes (LEDs),[16] supercapacitors,[17-19] and lithium ion batteries.[2,20]

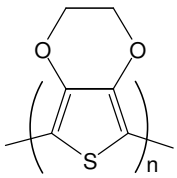

PEDOT

Scheme 1

On the other hand, the development of conducting polymer–clay nanocomposites is receiving increasing interest due to their important technological applications. Specifically, hybrid materials formed by the combination of polyaniline or polypyrrole with clay minerals structured at the nanoscale level, which usually present a unique layered structure, rich intercalation chemistry and availability at low cost, have been used as electrochemical sensors[21,22] and anticorrosive coatings.[23-25] The main benefit induced by the incorporation of the clay was the improvement of the thermal stability,

which was found to be higher for the polyaniline–clay[26-28] and polypyrrole–clay[29,30] nanocomposites than for the pristine conducting polymers.

Some hybrid PEDOT–clay nanocomposites based on montmorillonite (MMT), a smectite group mineral clay that belongs to the general family of 2:1 layered silicates have been reported in the last years.[31-34] Since exfoliated conducting polymer–clay nanocomposites usually have better properties (*e.g.* stiffness, strength and barrier property) than the intercalative ones, it is rationalized that the higher the degree of exfoliation, the greater the enhancement of these properties.[35] Unfortunately, PEDOT–MMT nanocomposites prepared by Leta *et al.*[31] and Rajapakse *et al.*[32] showed an intercalative structure rather than the more desirable exfoliated organization. Han and Lu[33] reported exfoliated PEDOT–MMT nanocomposites that were obtained by *in situ* polymerization in aqueous media using clays organically modified with octadecylammine salt. Although the thermal stability of the nanocomposite was better than that of pristine PEDOT, its electrical conductivity of was very low (10^{-7} – 10^{-2} S/cm).[33] More recently, it was reported an *in situ* electropolymerization procedure to prepare exfoliated PEDOT–MMT nanocomposites using non-modified clays, the electrical conductivities of the produced hybrid materials ranging from 1 to 4 S/cm depending on the clay concentration.[34] Differences in the electrical conductivity of these two PEDOT–MMT nanocomposites should be attributed to both the efficacy of the dopant agent (*i.e.* the oxidant power of lithium perchlorate[34] is higher than that of the organic dopant agents used in reference 33) and the molecular length of PEDOT chains, which is larger when prepared electrochemically. However, in both cases exfoliated composites were prepared using relatively low clay concentrations (≤ 10% w/w).[33,34]

Electrochemical capacitors are charge storage devices of high power and energy density, which exhibit reversibility and long cycle life. If the capacitance in these devices is stored as a build-up of charge in the electrical double-layer in the solution interface, the capacitor is called electric double layer capacitor. However, if the capacitance is stored in the bulk of the electrode material in response to a redox reaction, the capacitor is denoted ultracapacitor or pseudocapacitor. Unlike batteries, electrochemical capacitors store their energy in an electrostatic field rather than in chemical form.[36-38] Electrode materials for ultracapacitors mainly include carbon, transition-metal oxides, and conducting polymers.[39-41] In a recent review Snook *et al.*[41] focused on composites based on conducting polymers that are used for electrochemical capacitor devices. Despite of this, the exploration, improvement and discovery of new

electrode materials to achieve ultracapacitors with better electrochemical properties remains a challenge.

In a recent study the behavior as supercapacitors of electrodes formed by alternated layers of PEDOT and poly(N-methylpyrrole) (ml-PEDOT/PNMPy) was examined.[18] The specific capacitance (SC) for a symmetric assembly of two identical multilayered ml-PEDOT/PNMPy electrodes (SC = 90 $F \cdot g^{-1}$) was found to be significantly higher than that obtained for two PEDOT electrodes (SC = 41 $F \cdot g^{-1}$). However, these values were considerably lower than those reported for supercapacitors fabricated using nanocomposites of PEDOT and inorganic materials (*e.g.* MoO_3, RuO_2, carbon nanotubes, MnO_2, and $NiFe_2O_4$), for which the SC ranged from 153 to 375 $F \cdot g^{-1}$.[42-48] However, there is no investigation about the performance of PEDOT–MMT nanocomposites as ultracapacitors.

Both the inexistence of exfoliated PEDOT–MMT nanocomposites with high concentrations of clay and the lack of information about the performance of these hybrid materials as ultracapacitors motivated the current study. Specifically, this work studies the preparation and characterization of exfoliated PEDOT–MMT nanocomposites obtained using MMT concentrations in the monomer solution that ranged from 5% to 50% w/w (dry weight). After this, the morphology and topography, electrical conductivity, adherence, thermal stability, charge store ability, electrochemical stability, specific capacitance and doping level of the nanocomposites have been investigated and compared with the properties of pristine PEDOT. Next, the performance of PEDOT–MMT nanocomposites to be used as ultracapacitors of both type I (*i.e.* symmetric systems using the same nanocomposite for the two electrodes) and type II (*i.e.* asymmetric based electrodes made of PEDOT and PEDOT–MMT) was examined. Finally, electrochemical impedance spectroscopy (EIS) studies have been performed on selected ultracapacitors to examine the circuit elements that explain their successful behavior as well as to compare the corresponding physical and electrochemical parameters.

5.2.2. Methods

Materials. 3,4-ethylenedioxythiophene (EDOT) monomer and MMT (bentonite) were purchased from Aldrich and used as received. Anhydrous $LiClO_4$, analytical from Aldrich, analytical reagent grade, was stored in an oven at 80 ºC before use in the electrochemical trials.

Synthesis. The synthetic process used to prepare both PEDOT and PEDOT–MMT was identical to that reported in a previous work.[34] The CP and the nanocomposite were produced by chronoamperometry (CA) under a constant potential of 1.10 V using an Ecochimie model VersaStat II potentciostat/galvanostat. Steel AISI 316 sheets of 4 cm^2 were used as electrodes. The generation medium consisted on a 10 mM EDOT solution in distilled water containing 0.1 M $LiClO_4$ as supporting electrolyte. Both micrometric and nanometric films of all the investigated materials were prepared considering polymerization times (τ) of 300 s and 30 s, respectively. The concentration of MMT in the generation medium, which is referred to that of the EDOT monomer, ranged from 5% to 50% w/w (dry weight). Before the addition of MMT to the monomer solution, the clay was exfoliated in deionized water at neutral pH, being sonicated 10 min with an ultrasonic generator. The resulting solution was stirred for 1 day using a magnetic stirrer. Next, the generation medium and the exfoliated MMT solution were mixed and stirred for 20 h in a frozen environment (ice).

FTIR spectroscopy. FTIR spectra were recorded on a FTIR 4100 Jasco spectrophotometer with a resolution of 4 cm^{-1} in the absorbance mode. The samples were placed in an attenuated total reflection accessory with thermal control and a diamond crystal (Golden Gate Heated Single Reflection Diamond ATR).

Thickness. The thickness of the films was determined through gravimetric, electrochemical and structural measurements. Gravimetric estimations were obtained through the mass of polymer deposited in the electrode, which was obtained using a Sartorious ultra-microbalance, the surface of polymerization (*i.e.* the surface of the electrode, 4 cm^2) and the density of the materials that were determined by the flotation method from CCl_4+C_2H_5I mixtures. Electrochemical estimations of the thickness were obtained by determining the current productivity through the mass-charge ratio and, subsequently, the mass of polymer deposited in the electrode. The latter procedure was detailed in previous works.[48,49] Finally, the thickness was also determined by measuring the cross-section of the films by scanning electron microscopy.

Transmission electron microscopy (TEM). The structure and distribution of the clay in nanocomposites was examined using a Phillips TECNAI 10 transmission electron microscope at an accelerating voltage of 100 kV. For this purpose, small trips of nanocomposites were removed from the electrodes with a razor blade and, according the manufacturer protocol, embedded in a low viscosity modified Spurr epoxy resin and curing at 60ºC for 24 h. Ultra-thin sections (less than 100 nm) of these samples were cut

at room temperature using a Sorvall Porter-Blum microtome. Finally, the sections were placed on carbon coated cooper grids. Bright field micrographs were taken with a SIS Mega View II digital camera.

Scanning electron microscopy (SEM) and energy dispersive X-ray (EDX) spectroscopy. EDX spectroscopy and SEM studies were performed to examine the composition of the synthesized nanocomposites and to examine the effect of the clay on the surface morphology, respectively. Dried samples placed in a Focussed Ion Beam Zeiss Neon 40 scanning electron microscope operating at 3 kV, equipped with an EDX spectroscopy system.

Atomic force microscopy (AFM). Topographic AFM images were obtained with a Molecular Imaging PicoSPM using a NanoScope IV controller in ambient conditions. The averaged RMS roughness (*r*) was determined using the statistical application of the Nanoscope software, which calculates the average considering all the values recorded in the topographic image with exception of the maximum and the minimum.

Electrical conductivity and adherence. The electrical conductivity was determined using the sheet resistance method with a previously described procedure.[50]

Adherence measurements were based on the standard sellotape test (TESA-4204 BDF), which consists in cutting the film into small squares, sticking the tape and then stripping it. The ratio between the number of adherent film squares remaining and their total number gives the percentage adherence.

Thermal analyses. The thermal stability was examined by thermogravimetric analysis (TGA) with a PerkinElmer TGA-6 thermobalance at a heating rate of 10ºC/min under a nitrogen atmosphere.

Electrochemistry. The electroactivity, which refers to the charge storage ability, and electrochemical stability (electrostability) were determined by cyclic voltammetry (CV) using a distilled water solution with 0.1 M $LiClO_4$. The initial and final potentials were -0.50 V, while the reversal potential was 1.00 V. The electroactivity increases with the similarity between the anodic and cathodic areas of the first control voltammograms, whereas the electrostability decreases with the oxidation and reduction areas of consecutive control voltammograms. Specifically, the loss of electrostability (LES, in %) was determined as:

$$LES = \frac{\Delta Q}{Q_{II}} 100 \qquad (1)$$

where ΔQ is the difference of voltammetric charges (in C) between the second and the last cycle, and $Q_{II}$is the voltammetric charge corresponding to the second cycle. In this work, measures of LES refer to 100 consecutive oxidation-reduction cycles for both single electrode and two assembled electrodes (supercapacitors) configurations unless a different number of cycles is explicitly specified (*i.e.* selected supercapacitors have been also studied after 500 consecutive oxidation-reduction cycles). Electrochemical estimation of the doping level (dl) was carried using the following Eqn:

$$dl = \frac{2Q_O}{Q_D - Q_O} 100 \quad (2)$$

where Q_D is the total charge used for the nanocomposite deposition and Q_0 is total charge of oxidized species in the nanocomposite films.

The number of electrons consumed to incorporate a monomer into a polymer and to oxidize the resulting chain (n_{ox}) have been determined using a previously procedure.[51,52] For this purpose, the following Eqn has been used:

$$n_{ox} = \frac{M \cdot Q_{pol}}{F \cdot W_{ox}(1 - W_{dop})} \quad (3)$$

where M is the molar mass of PEDOT, Q_{pol} is the polymerization charge consumed in each process (in millicouloms per centimeter square) that was calculated on each chronoamperogram, F is the Faraday constant, W_{ox} is the film weight (in milligram per centimeter square) and W_{dop} is the mass of dopant per polymer unit of mass.

The SC (in $F \cdot g^{-1}$) of PEDOT and the nanocomposites were determined by CV using the following Eqn:

$$SC = \frac{Q}{\Delta V m} \quad (4)$$

where Q is the voltammetric charge, which is determined by integrating either the oxidative or reductive parts of the cyclic voltammetry curve, ΔV is the potential window (in V), and m is the mass of polymer on the surface of the working electrode (in g).

Galvanostatic charge/discharge curves were used to evaluate the power density (P) and the maximum specific energy (E_{max}):

$$P = \Delta V \frac{I}{m} \quad (5)$$

$$E_{max} = \frac{SC \cdot V_{max}^2}{2m} \quad (6)$$

where ΔV is the difference between the potential at the beginning and at the end of the discharge, I is the applied current (1 mA) and m is the mass of active material in the electrodes, and V_{max} is the potential at the beginning of the discharge. Moreover, charge/discharge profiles were also used as alternative method to measure the SC:

$$SC = \frac{i\Delta t}{\Delta V m} \tag{7}$$

where i is the current intensity and Δt is the time interval required for the change in voltage ΔV.

EIS measurements of different ultracapacitor configurations, which were prepared by assembling PEDOT and/or PEDOT–MMT films, were performed in potentiostatic mode at the open circuit potential (OCP) using an AUTOLAB PGSTAT 30/FRA 2 system. The amplitude of the EIS perturbation signal was 50 mV, and the studied frequency ranged from 10 kHz to 10 mHz. All experiments were carried out in a distilled water solution containing 0.1 M $LiClO_4$ at 25°C.

The SC derived from EIS results was derived from the slope of the linear correlation between the imaginary impedance (Z_{im}, in Ω) and the reciprocal of the frequency (f, in Hz) at low frequencies, according to:

$$SC = -\frac{1}{2\pi \cdot f \cdot Z_{im} \cdot m} \tag{8}$$

5.2.3. Results and discussion

Preparation and characterization of PEDOT–MMT nanocomposites. PEDOT–MMT films were prepared by *in situ* anodic polymerization considering 5%, 10%, 20%, 30% and 50% w/w MMT in the generation media and τ = 300 s and 30 s, respectively. In all cases the color of the micrometric (τ = 300 s) and nanometric (τ = 30 s) films was dark blue and blue sky, respectively, no difference being detected with respect to pristine PEDOT prepared using identical experimental conditions. However, the successful incorporation of the clay during the polymerization process was confirmed by FTIR and EDX spectroscopy. The FTIR spectra of all PEDOT–MMT nanocomposites showed the characteristic band of the Si-O stretching mode centered at 1044 cm^{-1} and the absorption bands centered at 524 and 467 cm^{-1}, which correspond to the Si-O-Al and Si-O-Si bending vibrations, respectively.[54] As expected, the spectra of PEDOT–MMT nanocomposites exhibited the characteristic bands of PEDOT in the

range of 1052-837 cm^{-1}. On the other hand, qualitative composition analyses by EDX spectroscopy indicated that the concentration of MMT in the films, which was measured through the peaks of Al, Mg, Si and Na [*i.e.* the latter was the metallic counter-ion of the bentonite used in this work: $Na_x(Al_{4-x}Mg_x)Si_8O_2$], increases with its concentration in the generation medium.

The thickness of all the films was determined through gravimetric, electrochemical and SEM measurements. Table 1 compares the thickness of the films obtained for the different nanocomposites with those obtained for neat PEDOT. The three methods are fully consistent, the thickness obtained for micrometric and nanometric films being ~1 μm and ~200 nm, respectively. Moreover, the thickness increases with the content of clay, even although this effect is more clear for nanometric than for micrometric films.

Table 1. *Thickness of the pure PEDOT and PEDOT–MMT nanocomposite films produced using polymerization times of 300 s and 30 s. The thickness was determined through gravimetric, electrochemical and SEM measurements.*

System	Gravimetric		Electrochemical		SEM	
	300 s	30 s	300 s	30 s	300 s	30 s
PEDOT	0.91 μm	203 nm	1.06 μm	196 nm	0.84 μm	217 nm
PEDOT-MMT 5%	1.07 μm	191 nm	1.16 μm	185 nm	1.19 μm	202 nm
PEDOT-MMT 10%	0.98 μm	208 nm	1.09 μm	204 nm	-	224 nm
PEDOT-MMT 20%	1.27 μm	229 nm	1.48 μm	227 nm	-	243 nm
PEDOT-MMT 50%	1.16 μm	237 nm	1.38 μm	216 nm	1.24 μm	251 nm

The round-like shape morphology of the MMT particles before exfoliation is displayed in Figure 1a. The average diameter of these particles, which shows flake morphology, determined by SEM measurements is 8±1 μm. The exfoliated distribution of the clay in micrometric nanocomposites with MMT 5% w/w and 10% w/w was demonstrated in our previous work.[34] In order to re-investigate this issue, TEM samples were cut perpendicular to the electrode surface. The MMT was found to be exfoliated into individual platelets within the PEDOT matrix in all the nanocomposites, this feature being clearly reflected in Figures 1b and 1c for the nanometric systems with a clay concentration of 5% and 10% w/w, respectively.

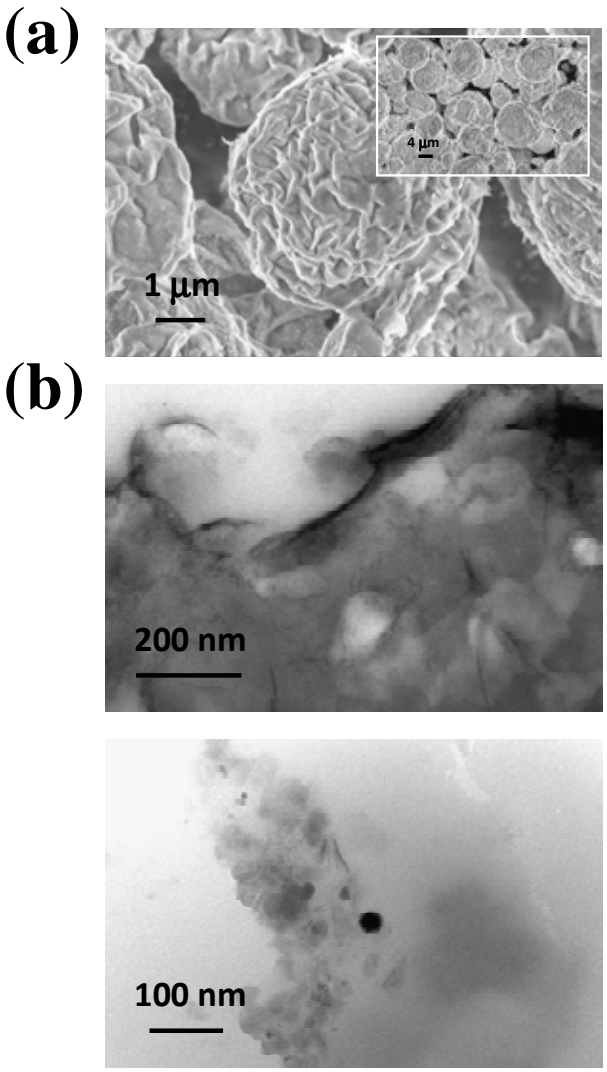

Figure 1. *(a) High- and low-resolution (inset) SEM micrographs of MMT particles before exfoliation. (b) TEM micrographs of nanometric PEDOT–MMT 5% w/w (upper) and PEDOT–MMT 20% w/w (lower).*

Properties of the nanocomposites. Figure 2a and 2b show SEM micrographs of nanometric PEDOT and PEDOT–MMT 5%w/w films, respectively. Although the agglomerates are slightly larger in the latter than in former, low concentrations of clay do not produce appreciable changes in the surface morphology. In spite of this, SEM micrographs of the internal side of the same PEDOT–MMT 5% w/w film shows the presence of granules, which are homogeneously distributed. This feature is also evidenced in the SEM micrograph displayed in Figure 2c, which corresponds to the micrometric PEDOT–MMT 5%w/w film. These results suggest that when the concentration of MMT in the generation medium is very low with respect to that of EDOT monomer, the clay precipitates on the electrode provoking the presence of such

granules. In contrast, large agglomerates appear in the surface of the nanocomposite when the MMT concentration is ≥ 20% w/w.

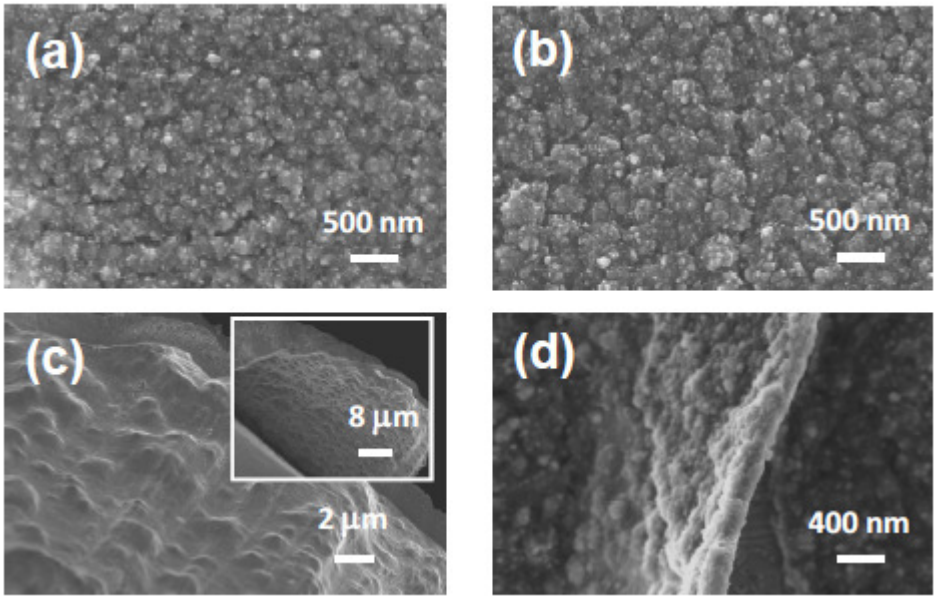

Figure 2. *SEM micrographs of nanometric (a) PEDOT and (b) PEDOT–MMT 5% w/w films. The internal side and the cross section of the latter nanocomposite are displayed in (c) and (d), respectively.*

This is evidenced in Figures 3a and 3b, which compares the SEM micrographs of micrometric PEDOT and PEDOT–MMT 20% w/w films. Moreover, these agglomerates alter the topography of the surface in both micrometric and nanometric films. Figure 4 shows the AFM images of nanometric PEDOT and PEDOT–MMT 20% w/w films. As can be seen, PEDOT presents small clusters of aggregated molecules homogeneously distributed, this topography being consequence of the linear growing of polymer chains (*i.e.* molecules are exclusively formed by α-α linkages because the β-positions of the thiophene ring are occupied by the dioxane ring).[55] This topography becomes much less regular upon the incorporation of MMT 20% w/w, which promotes the formation of larger and higher aggregates. Interestingly, analysis of the internal sides of the films with a MMT concentration > 10% w/w did not show granular structure (as was evidenced in Figure 2c for the films with a lower concentration of MMT) but the presence of thin cracks (Figure 3c).

The latter should be attributed to a swelling effect due to the adsorption of water from the medium. On the other hand, Figures 2d and 3d show the cross section of the nanometric PEDOT–MMT 5% w/w and micrometric PEDOT films, respectively, used to measure the thickness (~200 nm and ~1 µm, respectively).

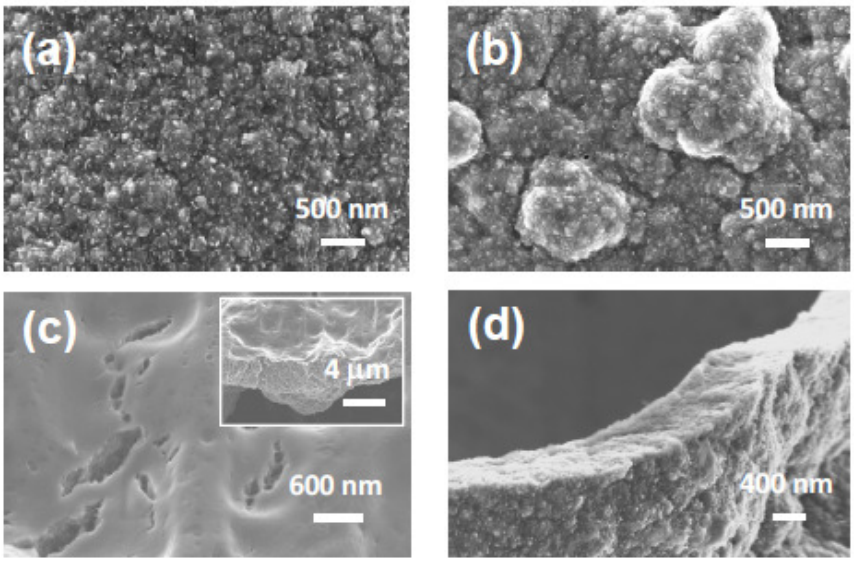

Figure 3. *SEM micrographs of micrometric (a) PEDOT and (b) PEDOT–MMT 20% w/w films. The internal side of the latter nanocomposite is displayed in (c), while (d) shows the cross section of PEDOT.*

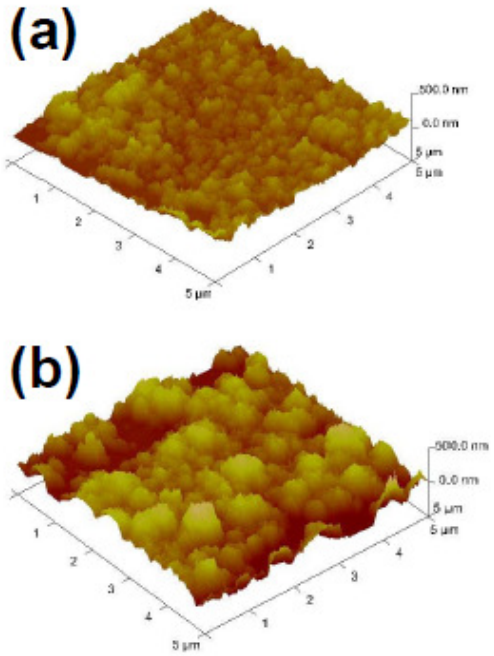

Figure 4. *3D AFM images illustrating the topographical changes induced by the incorporation of MMT ≥ 20% w/w. The images correspond to nanometric films of (a) PEDOT and (b) PEDOT–MMT 20% w/w.*

The electrical conductivities measured at room temperature for micrometric PEDOT and PEDOT–MMT films are compared in Table 2. The effect of the exfoliated clay in the electrical conductivity of PEDOT (5.5 $S \cdot cm^{-1}$) is practically negligible for MMT concentrations ≤ 10 w/w while it drops one order of magnitude when the content of clay is > 10% w/w. These results represent a very remarkable improvement with respect to

those previously reported in the literature. Thus, the conductivity at room temperature reported for intercalated PEDOT–MMT was lower than 10^{-5} S·cm^{-1} in all cases,[31,32] whereas that of the exfoliated nanocomposites prepared using organically modified MMT was around 10^{-8} S·cm^{-1}.[33] In previous studies, the electrical conductivity of PEDOT decreased from 5.6 to 1.4 S·cm^{-1} in 35 days, whereas that of PEDOT–MMT 5% w/w became practically negligible (< 10^{-3} S·cm^{-1}) after 17 days.[34] Analysis of the temporal evolution of the electrical conductivity for PEDOT–MMT 20% w/w indicated a decrease from 0.2 S·cm^{-1} to $9\cdot10^{-4}$ S·cm^{-1} in 15 days, and a subsequent reduction to ~10^{-5} S·cm^{-1} in 40 days, the latter value being retained by more than two months. These features indicate that, although the loss of electrical stability increases with the concentration of clay, this progressive reduction is only moderate. Furthermore, it is worth noting that, in spite of its poor electrical stability, the lower limit of the electrical conductivity reached for these nanocomposites is similar to the value reported for fresh samples of some polythiophene derivatives (~ 10^{-5} – 10^{-7} S·cm^{-1}).[56-58]

The adherence was estimated using a normalized sellotape test, the resulting values relative to PEDOT being displayed in Table 2. The exfoliated clay improves the adherence of micrometric PEDOT films, this effect increasing moderately with the concentration of MMT. Accordingly, the measured adherence gain ranges from 18% (5% w/w) to 32% (50% w/w).

Table 2. *Electrical conductivity (κ; in S·cm^{-1}) and adherence relative to PEDOT (in %) for micrometric films.*

	κ	**Adherence**
PEDOT	5.5	-
PEDOT–MMT 5% w/w	3.5	18
PEDOT–MMT 10% w/w	1.3	22
PEDOT–MMT 20% w/w	0.4	29
PEDOT–MMT 30% w/w	0.2	30
PEDOT–MMT 50% w/w	0.1	32

The thermal stability of clay-containing nanocomposites is typical to be higher than that of pristine polymers.[26-30] TGA curves for PEDOT and PEDOT–MT (both 5% and 20% w/w) are compared in Figure 5. In all cases the thermal decomposition of the

nanocomposites shifts towards higher temperatures than that of pristine PEDOT. Furthermore, the thermal stability increases moderately with the concentration of MMT. The weight loss at temperatures lower than 120º should be attributed to the evaporation of solvent (water). After this, a pronounced fall occurs between 200 ºC and 300 ºC, this process corresponding to the degradation of the polymer. More specifically, the thermal degradation of PEDOT, PEDOT–MMT 5% w/w and PEDOT–MMT 20% w/w occur at 228, 233 and 269 ºC, respectively. The thermal decomposition of $LiClO_4$ occurs between 350 ºC and 390 ºC. Finally, the weight loss detected at temperatures ranging between 430 ºC and 600 ºC corresponds to the thermal degradation of MMT, which undergoes a dehydroxylation process. The TGA curves displayed in Figure 5 clearly shows that the exfoliated MMT acts as a barrier to the heat flow, hindering the different thermal degradation processes.

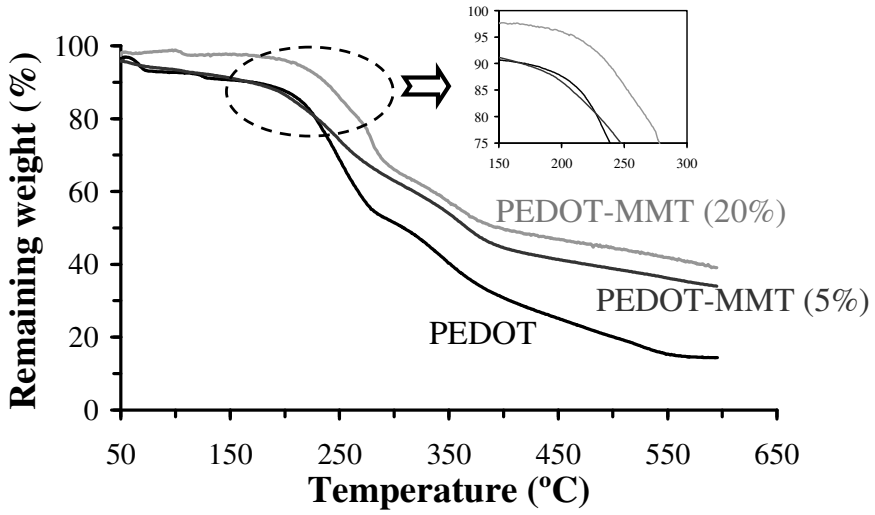

Figure 5. *Thermogravimetric curves of PEDOT, PEDOT–MMT 5% w/w and PEDOT–MMT 20% w/w. Details of the region encircled with a dashed line are provided in the inset.*

Table 3 summarizes the main electrochemical properties of nanometric PEDOT and PEDOT–MMT films. The charge storage decreases slowly but progressively when the concentration of clay increases. Specifically, the reduction in the charge storage of the nanocomposites ranges from 17% (MMT 5% w/w) to 30% (MMT 50% w/w). In contrast, the variation of the electrostability with the concentration of clay is negligible, the LES values of all the nanocomposites and PEDOT being practically identical (~15-16%). Similar behavior has been observed for the charge storage of micrometric films, whereas the electrostability of these systems decreases slightly with the concentration of clay (*e.g.* LES = 24% and 30% for micrometric PEDOT and PEDOT–MMT 20% w/w,

respectively). This small variation was also observed in a previous work for composites with MMT ranging between 1% and 10% w/w.[34]

Table 3. *Electrochemical properties of nanometric PEDOT and PEDOT–MMT films: Charge store ($mC \cdot cm^{-2}$), loss of electrostability (LES, in %; Eqn 1), specific capacitance determined by CV (SC, in $F \cdot g^{-1}$; eq 4), doping level (dl; Eqn 2), n_{ox} and n_{av} (both in electrons; Eqn 3).*

	Charge Storage	**LES**	**SC**	**dl**	$\mathbf{n_{ox}}$	$\mathbf{n_{av}}$
PEDOT	26.1	15	355	0.49	2.05	1.56
PEDOT–MMT (5% w/w)	21.7	15	284	0.37	2.10	1.73
PEDOT–MMT (10% w/w)	20.3	16	265	0.33	2.15	1.82
PEDOT–MMT (20% w/w)	19.7	15	257	0.40	2.19	1.79
PEDOT–MMT (50% w/w)	18.1	16	237	0.37	2.20	1.83

On the other hand, it should be emphasized that the SCs determined by CV (Eqn 4) for all the nanometric films are remarkably high (Table 3). Specifically, the SC of nanometric PEDOT is 355 $F \cdot g^{-1}$, which is one order of magnitude higher than that determined for the micrometric film (SC = 56 $F \cdot g^{-1}$). Moreover, although the SC of nanometric composites undergoes a reduction when the concentration of clay increases, their values are still considerably high, ranging from 284 $F \cdot g^{-1}$ (MMT 5% w/w) to 237 $F \cdot g^{-1}$ (MMT 50% w/w). The SC reported in the literature for micrometric PEDOT-inorganic hybrid nanocomposites involving MoO_3, RuO_2, carbon nanotubes, MnO_2, and $NiFe_2O_4$ varies between 153 and 375 $F \cdot g^{-1}$,[41-47] evidencing the potential interest of nanometric films of both PEDOT and PEDOT–MMT films as electrochemical supercapacitors. In contrast, the SC of micrometric PEDOT–MMT films was lower than 115 $F \cdot g^{-1}$ in all cases (*e.g.* SC = 96 $F \cdot g^{-1}$ for micrometric PEDOT–MMT 20% w/w).

The doping levels (Eqn 2) determined for the PEDOT–MMT clays were found to be slightly lower than those of pure PEDOT. The doping levels measured for the nanometric films (Table 3) were similar to those obtained for the corresponding micrometric films in all cases (*e.g.* dl = 0.54 and 0.49 for micrometric and nanometric PEDOT, respectively). On the other hand, the degree of cross-linking is typically determined by the number of electrons consumed to incorporate a monomer into a polymer and to oxidize the resulting chain (n_{ox}), this information being determined through the electroplymerization kinetics (*i.e.* considering different polymerization

times for the generation of polymer films under a constant potential).[51] After discounting the oxidation charge used to compensate the charge of the dopant ion of n_{ox}, the average number of electrons per monomer (n_{av}, where $n_{av} = n_{ox}$–dl) incorporated into a linear polymer chain obtained from a typical condensation mechanism should be $n_{av} = 2.0$ (*i.e.* two protons and two electrons are involved in the formation of the α-α bond between the terminal monomeric unit of the chain and the incorporated monomer.[56,57] Thus, undesired cross-linking reactions are probed when $n_{av} > 2.0$.

Table 3 includes the values of both n_{ox} and n_{av} for nanometric films of PEDOT and PEDOT–MMT. As it can be seen, n_{av} is lower than 2.0 in all cases. This feature indicates the existence of parallel chemical polymerization reactions based on proton transfer processes during the electrochemical polymerization. Accordingly, as no electron of the external circuit participates in such chemical processes, the resulting n_{av} values are lower than 2.0. However, the most noticeable result is that n_{av} is lower for PEDOT than for PEDOT–MMT, evidencing the protecting role exerted by the clay against parallel chemical processes. All these features, which are independent of the thickness of the film, were also identified in micrometric films.

Fabrication of Type I supercapacitors. Type I supercapacitors consists on symmetric systems which use the same p-dopable conducting polymer for the two electrodes. In this work symmetric PEDOT/PEDOT and PEDOT–MMT/PEDOT–MMT supercapacitors were fabricated (Figure 6a) using nanometric and micrometric films. The SC (Eqn 4) and the LES for 100 consecutive oxidation-reduction cycles (Eqn 1) of nanometric supercapacitors are compared in Table 4. As it can be seen, the SC of the supercapacitor based on the symmetric assembly of two nanometric PEDOT films is 465 $F \cdot g^{-1}$, which represents a significant improvement with respect to the symmetric supercapacitor prepared using micrometric PEDOT films (82 $F \cdot g^{-1}$ in Table 4). Thus, the SC increases one order of magnitude when the thickness of the film is reduced from the micrometric (~ 2μm) to the nanometric (~ 200 nm) scale.

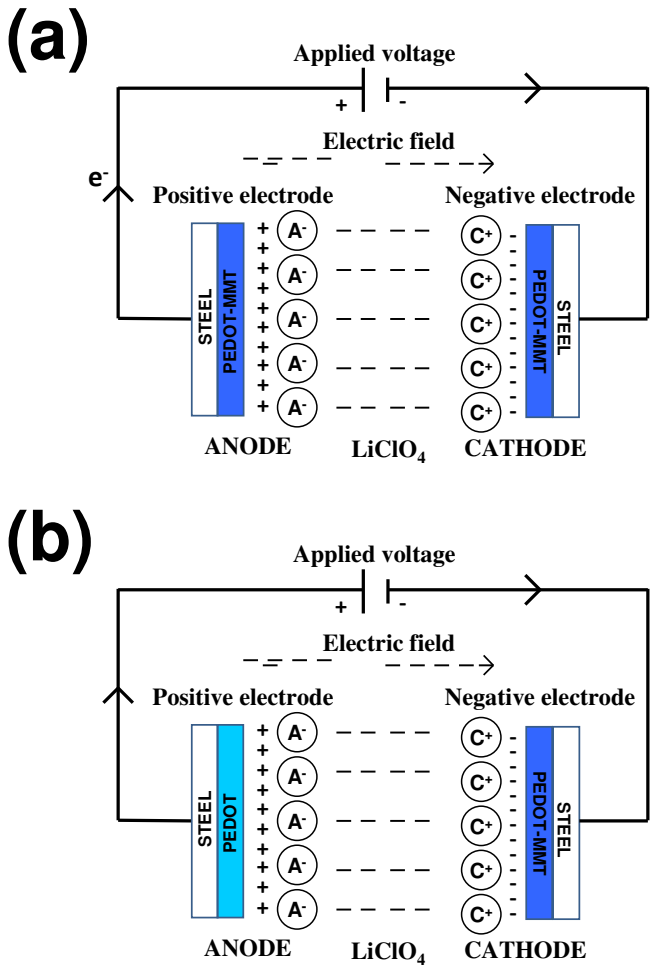

Figure 6. *Scheme of the (a) Type I and (b) Type II ultracapacitors.*

The SC of nanometric PEDOT/PEDOT decreases by about one half when a MMT concentration ≤ 20% w/w is incorporated to the two films. Thus, nanometric PEDOT–MMT/PEDOT–MMT with MMT ≤ 20% w/w assemblies (identical MMT concentration in the two electrodes) show SC values ranging from 207 to 234 $F \cdot g^{-1}$. The drop of the SC is slightly higher for the assembly with MMT = 50% w/w (179 $F \cdot g^{-1}$). The detriment in the SC produced by the incorporation of MMT is fully consistent with the behavior discussed above for single electrode systems (Table 3). On the other hand, the LES values determined for clay-containing supercapacitors are similar to that of the PEDOT/PEDOT one, evidencing that the influence of the MMT in the electrochemical stability is practically negligible at the nanometric scale. The electrostability determined for single electrode systems was higher than obtained for symmetric two electrodes assembled configurations, this feature being independent of the presence and concentration of clay. In spite of this, it should be emphasized that the electrochemical stability of the five symmetric supercapacitors is significantly high, especially

considering that LES values were determined using a large number of consecutive oxidation-reduction cycles.

Table 4. *Performance of PEDOT and PEDOT–MMT electrodes in symmetric and asymmetric supercapacitor configurations (Figure 6). Results obtained for assemblies of both nanometric and micrometric films are displayed.*

Assembly	SC (CV)[a]	LES[b]	SC (EIS)[c]
Nanometric films			
PEDOT/PEDOT	465	35	-
PEDOT–MMT/PEDOT–MMT 5% w/w	217	41	-
PEDOT–MMT/PEDOT–MMT 10% w/w	207	39	-
PEDOT–MMT/PEDOT–MMT 20% w/w	234	40	-
PEDOT–MMT/PEDOT–MMT 50% w/w	179	38	-
PEDOT/PEDOT–MMT 20% w/w	429	37	386
Micrometric films			
PEDOT/PEDOT	82	21	64
PEDOT–MMT/PEDOT–MMT 20% w/w	94	35	75
PEDOT/PEDOT–MMT 20% w/w	116	43	88

[a] *Specific capacitance determined by CV (Eqn 4), in* $F \cdot g^{-1}$. [b] *Loss of electroactivity (Eqn 1), in %.* [c] *Specific capacitance determined by EIS (Eqn 8), in* $F \cdot g^{-1}$.

Table 4 includes the SC and LES values determined by CV for micrometric PEDOT/PEDOT and PEDOT–MMT/PEDOT–MMT 20% w/w configurations, the latter being selected because this clay concentration provided the highest SC in the nanometric supercapacitors. As it can be seen, the SC of the supercapacitor fabricated with the nanocomposite was slightly higher, even though the electrochemical stability of the PEDOT/PEDOT was greater. Moreover, the SC of the supercapacitor fabricated using micrometric PEDOT was slightly than that measured for a single electrode, whereas the opposite tendency is observed for that prepared using the PEDOT–MMT 20% w/w.

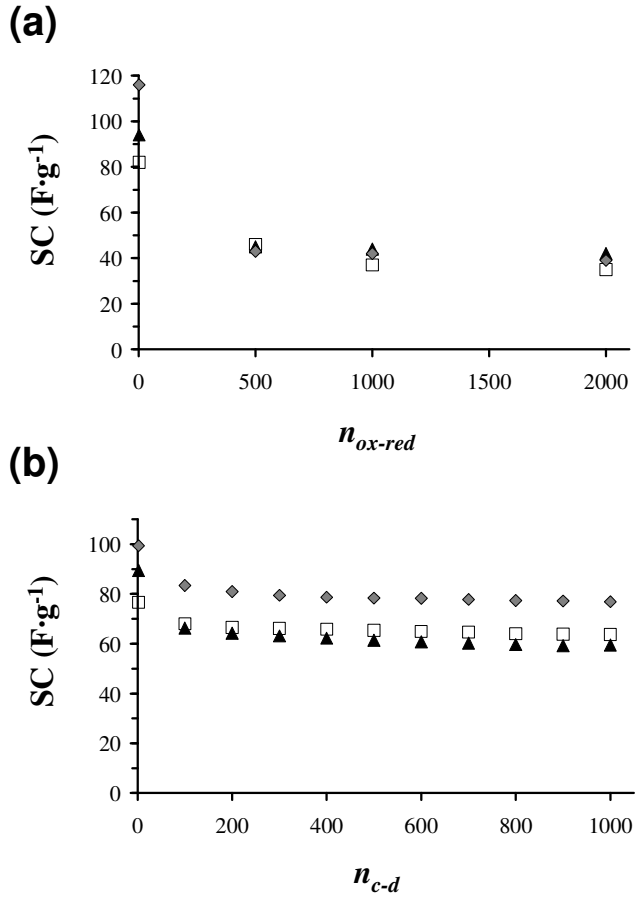

Figure 7. *Variation of the specific capacitance (SC) against (a) the number of consecutive oxidation-reduction cycles ($n_{ox\text{-}red}$) and (b) the number of charge/discharge cycles ($n_{c\text{-}d}$) for PEDOT/PEDOT (empty squares), PEDOT–MMT/PEDOT–MMT 20 % w/w (black triangles) and PEDOT/PEDOT–MMT (grey diamonds).*

The effect of the electrochemical degradation on the ultracapacitor behavior of micrometric PEDOT/PEDOT and PEDOT–MMT/PEDOT–MMT 20% w/w configurations was examined by comparing the SC, LES, P and E_{max} measured for samples as prepared and after 2000 consecutive oxidation-reduction cycles (Table 5). It should be mentioned that the SC determined after 500 and 2000 consecutive oxidation-reduction cycles were similar (Figure 7a), indicating that very small changes are expected for a larger number of cycles. A similar behavior was observed for LES, P and E_{max}. Results suggest that the positive effect of the clay in E_{max} disappears after such amount of oxidation-reduction cycles. In contrast, the power of the clay-containing symmetric ultracapacitor remains significantly higher than that of PEDOT/PEDOT one after 2000 cycles, even though the relative difference between the two systems decreases from 42% to 29%. The relative electrochemical stabilities undergo some changes with the increase in the number of cycles, the PEDOT/PEDOT configuration

being more electrostable than the PEDOT–MMT/PEDOT–MMT one by 14% and 1% after 100 and 2000 cycles, respectively. These features are reflected in Figure 8, which compares the cyclic voltammograms of PEDOT/PEDOT and PEDOT–MMT/PEDOT–MMT 20% w/w recorded after 2, 1000 and 2000 consecutive oxidation-reduction cycles.

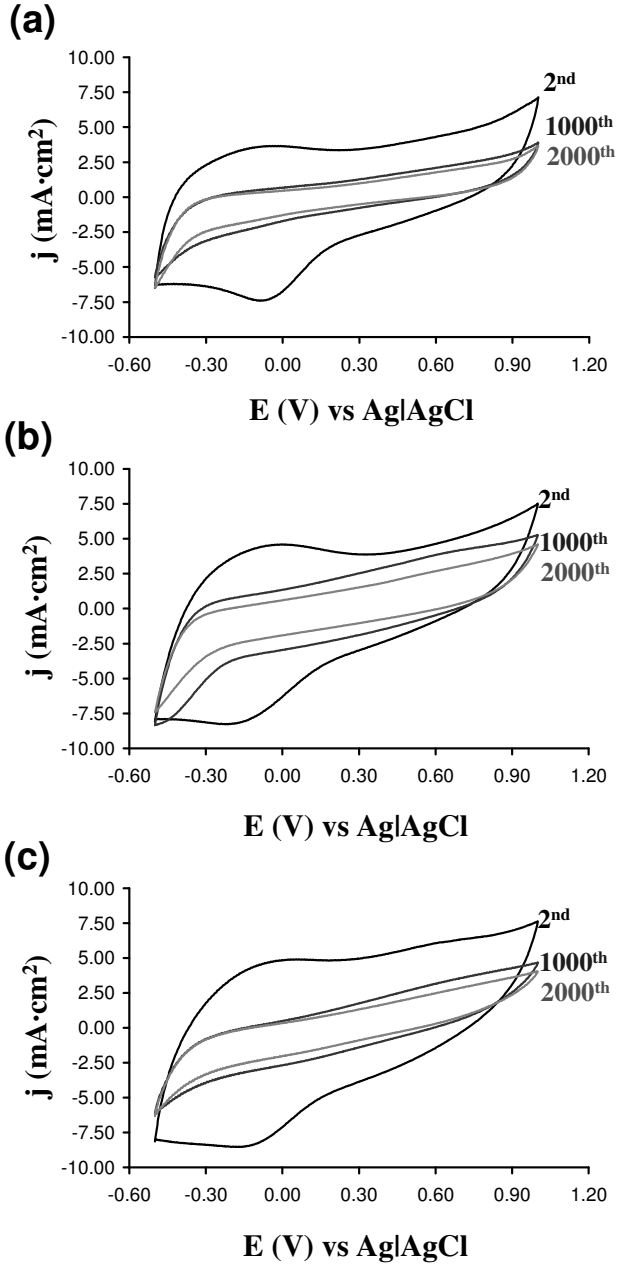

Figure 8. *Control voltammograms for 2, 1000 and 2000 consecutive oxidation-reduction cycles for (a) PEDOT/PEDOT; (b) PEDOT–MMT/PEDOT–MMT 20 % w/w; and (c) PEDOT/PEDOT–MMT 20 % w/w ultracapacitors. Voltammograms were recorded at 100 mV/s. Initial and final potentials: -0.50 V. Reversal potential: 1.00 V.*

Table 5. *Influence of the electrochemical degradation in the specific capacitance, the power density, maximum specific energy and loss of electroactivity of PEDOT and PEDOT–MMT 20% w/w micrometric electrodes in symmetric and asymmetric ultracapacitor configurations.*

	SC[a]	**SC**[b]	**P**[c]	$\mathbf{E_{max}}$[d]	**LES**[e]
PEDOT/PEDOT	82 / 37	77 / 64	1033 / 819	6.6/ 1.8	21/ 44 / 57
PEDOT–MMT/PEDOT–MMT 20% w/w	94 / 44	89 / 69	1465 / 1046	9.7 / 2.9	35 /56 / 58
PEDOT/PEDOT–MMT 20% w/w	116 / 42	99 / 66	1682 / 1285	11.4 / 6.8	43/ 62 / 63

[a] *Specific capacitance determined by CV (Eqn 4) for fresh samples / for samples after 2000 consecutive redox cycles, in* $F \cdot g^{-1}$. [b] *Specific capacitance derived from galvanostatic charge/discharge profiles (Eqn 7) for fresh samples / for samples after 1000 consecutive charge/discharge processes.* [c] *Power density determined from current charge/discharge cycles for fresh samples / for samples after 2000 consecutive redox cycles, (Eqn 5), in* $W \cdot kg^{-1}$. [d] *Maximum specific energy (Eqn 6) determined for fresh samples / for samples after 2000 consecutive redox cycles, in* $W \cdot h \cdot kg^{-1}$. [e] *Loss of electrostability (Eqn 1) after 100 / 500 / 2000 consecutive redox cycles, in %.*

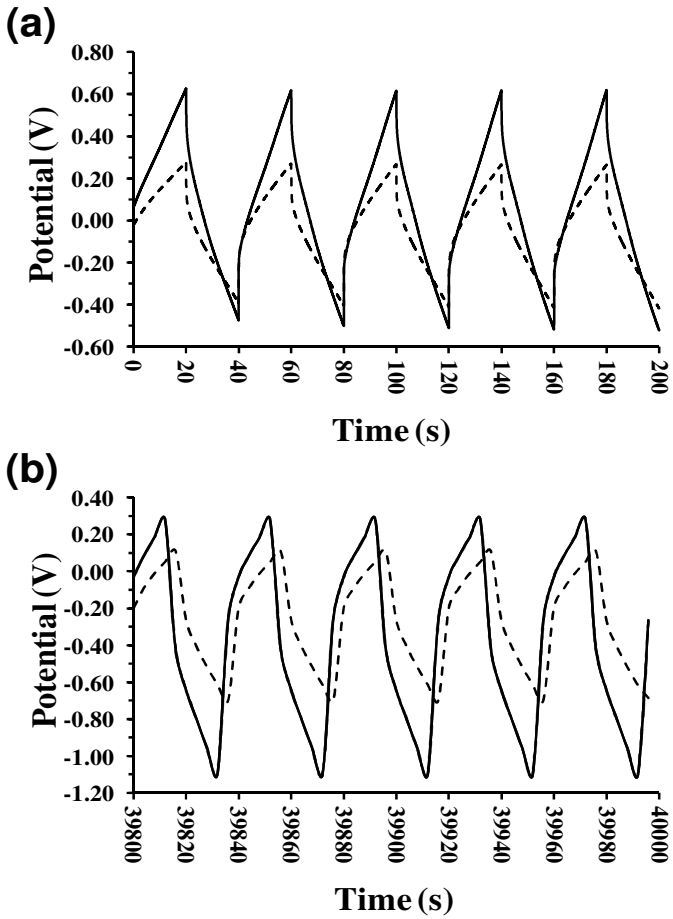

Figure 9. *Galvanostatic charge/discharge curves for PEDOT/PEDOT-MMT (solid line) and PEDOT-MMT/PEDOT-MMT (dashed line) ultracapacitors. Form of total of 1000 charge/discharge cycles the (a) first and (b) last five cycles are displayed.*

The SCs determined by CV (Eqn 4) before and after 2000 consecutive oxidation-reduction cycles show decrease of 55% and 54% for PEDOT/PEDOT and PEDOT–MMT/PEDOT–MMT assemblies. These drastic reductions seem to suggest that the stability of such two capacitors is very low (*i.e.* SCs drop by more than 50%). However, it should be emphasized that application of consecutive oxidation-reduction cycles is the most aggressive electrochemical method to determine the stability of the ultracapacitor behavior. In order to illustrate that the stability of PEDOT/PEDOT and PEDOT–MMT/PEDOT–MMT capacitors is relatively good, a less aggressive electrochemical method has been used. Charge and discharge profiles were linear and relatively symmetric in all cases (Figure 9), which indicated the capacitive behavior of the two systems. The SCs of the two assemblies were re-evaluated using Eqn 7 after apply one and 1000 galvanostatic charge/discharge processes, results being included in Table 5 and Figure 7b. The SCs determined after one charge/discharge process (Eqn 7) are very

similar to those obtained by CV (Eqn 4): the differences between the two procedures amounted to 5%-6% only. However, after application of 1000 charge/discharge processes the SC of PEDOT/PEDOT and PEDOT–MMT/PEDOT–MMT configurations drop 17% and 22% only. Indeed, the SCs remains practically unchanged after 100 cycles only (Figure 7b).

Fabrication of Type II supercapacitors. Type II supercapacitors correspond to asymmetric configurations based on two different CPs with very different electroactivities. In this work, micrometric and nanometric asymmetric systems have been fabricated by combining PEDOT and PEDOT–MMT 20% w/w electrodes in the same supercapacitor (Figure 6b). Results, which are included in Table 4, indicate that the SC and LES of nanometric PEDOT/PEDOT–MMT 20% w/w and PEDOT/PEDOT are very similar. The performance of the former asymmetric assembly is considerably better than that of symmetric PEDOT–MMT/PEDOT–MMT in terms of both capacitance and electrochemical stability. This represents a significant advance since the combination of nanometric thickness with the use of an exfoliated MMT-containing electrode allows the fabrication of thermally stable advanced ultracapacitors. Indeed, the SC measured for nanometric PEDOT/PEDOT–MMT 20% w/w is higher than those determined for conventional nanocomposites of PEDOT and inorganic materials.[42-48] On the other hand, the SC of micrometric PEDOT/PEDOT–MMT 20% w/w is 41% and 23% higher than those of symmetric PEDOT and PEDOT–MMT/PEDOT–MMT 20% w/w, respectively. This feature confirms that the incorporation of the exfoliated clay produces a very significant benefit in asymmetric supercapacitors, independently of the thickness of the films.

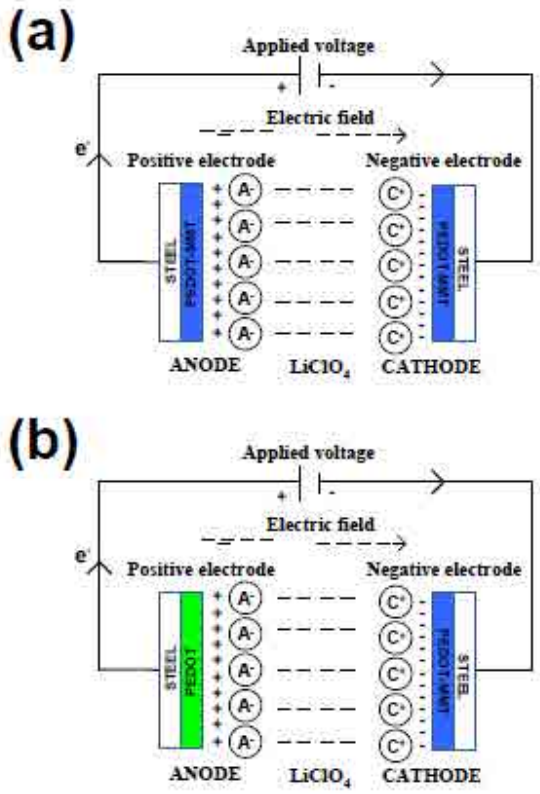

Figure 10. *Scheme of the (a) Type I and (b) Type II supercapacitors.*

The effect of electrochemical degradation on the ultracapacitor behavior of micrometric PEDOT/PEDOT–MMT 20% w/w is included in Table 5 and Figure 7. Results clearly indicate that the impact of 2000 consecutive oxidation-reduction cycles in the SC and LES (Figures 7 and 8) of the type II ultracapacitor is similar to that discussed above for the type I ones. However, reduction of the SC after application of 1000 galvanostatic charge/discharge processes is relatively low (*i.e.* the SC drops 63% and 64% after 500 and 2000 consecutive oxidation-reduction cycles, respectively, and 33% after 1000 consecutive charge/discharge processes). Moreover, as occurred for the type I ultracapacitors, the SC essentially drops during the first 100 charge/discharge cycles, remaining practically unaltered for the next 900 cycles (Figure 7b). Results displayed in Table 5 reflect that the influence of the electrochemical degradation is less important for the asymmetric configuration than for the symmetric one. Thus, the positive effect of the clay in P and E_{max} is retained after such amount of cycles. For example, the power of the type II ultracapacitor is 217 and 239 $W \cdot kg^{-1}$ higher than that of the type I one for the device as prepared and after 2000 cycles, respectively. A very

similar behavior is detected for E_{max}, which is higher for the PEDOT/PEDOT–MMT ultracapacitor than for the PEDOT–MMT/PEDOT–MMT and PEDOT/PEDOT ones.

Electrochemical Impedances Spectroscopy studies of Type I and Type II supercapacitors. Figure 10 shows the EIS spectra of micrometric PEDOT/PEDOT (Figure 10a), PEDOT–MMT/PEDOT–MMT 20% w/w (Figure 10b) and PEDOT/PEDOT–MMT 20% w/w (Figure 10c) ultracapacitors as prepared and after 500 consecutive oxidation-reduction cycles. The spectra were fitted using an equivalent circuit (EC). The aim of the choice of the EC was to obtain a satisfactory fitting of the experimental data, where the circuit elements can be associated with the physical phenomena that are probably taking place at the electrode surface. The EC proposed was $R_s(CPE_1[R_{CT}W])C_{PS}$ (Figure 10d), where Rs represents the electrolyte resistance, CPE_1 the double layer capacitance, R_{CT} the charge-transfer resistance at the polymer film–electrolyte interface, which is in serial connection with the Warburg element (W), and C_{PS} the faradaic pseudo-capacitance corresponding to a practically vertical line at low frequency region of the EIS spectra. The double layer capacitance was replaced by a constant phase element (CPE) that describes a non-ideal capacitor when the phase angle is different from -90º. The CPE impedance has been expressed as:

$$Z_{CPE} = [Q\ (j\omega)^n\ ]^{-1} \qquad (9)$$

The CPE represents a capacitor and a resistor for n= 1 and n= 0, respectively, while it is associated with a diffusion process when n= 0.5. The CPE impedance is attributed to the distributed surface reactivity, surface heterogeneity, and roughness of the current and potential distribution, which in turn are related with the electrode geometry and the electrode porosity.[61] The Warburg impedance was included taking into account the diffusion phenomena.[62] The quality of fitting was evaluated using the error percentage associated to each circuit component, errors smaller than 5% being obtained in all cases.

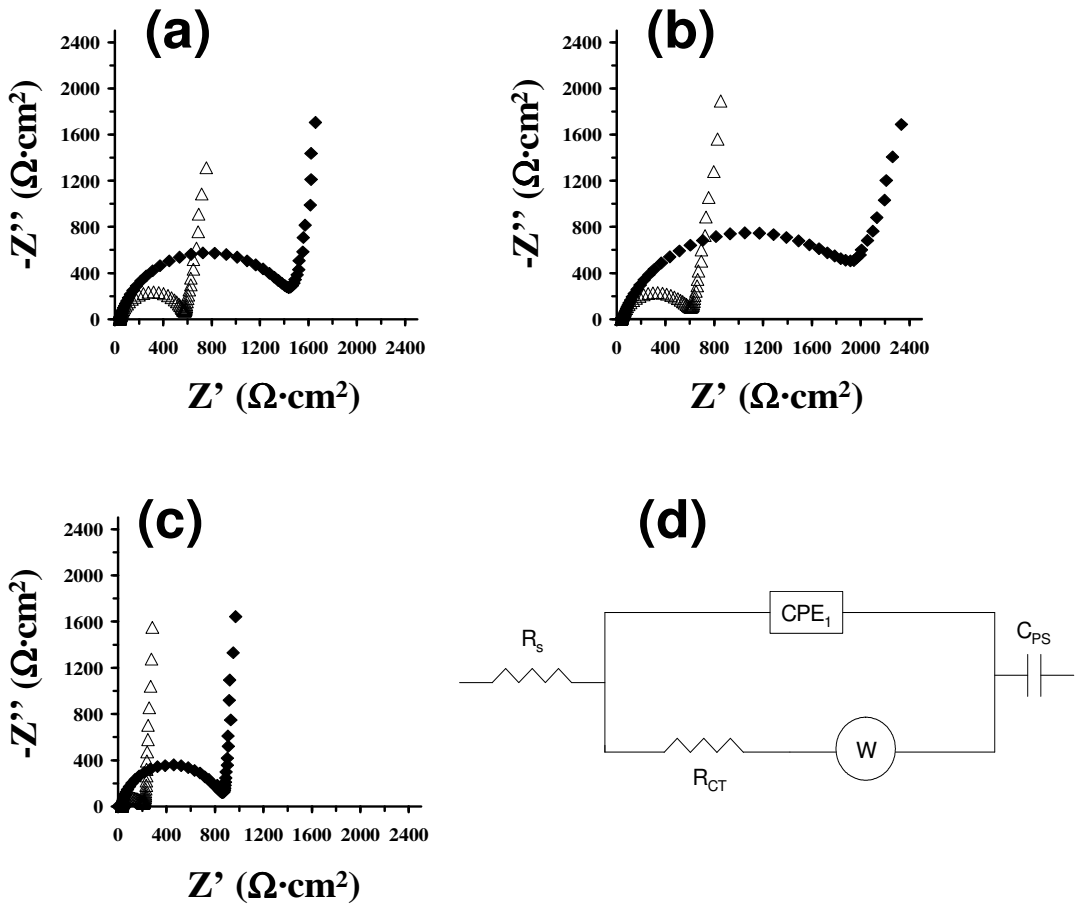

Figure 11. *Nyquist plots showing the evolution of the impedance data of micrometric supercapacitors as prepared (empty triangles) and after 500 consecutive oxidation-reduction cycles (filled diamonds): (a) PEDOT/PEDOT; (b) PEDOT–MMT/PEDOT–MMT 20 % w/w; and (c) PEDOT/PEDOT–MMT 20 % w/w. The experimental data (represented symbols) were fitted to the equivalent circuit model depicted in (d) to produce the parameters listed in Table 6.*

Table 6 lists the parameters derived from the fitting of the EIS plots displayed in Figures 10a-c to the EC previously described. As it can be seen, R_{CT} increases with the number of oxidation-reduction cycles in all cases. The highest R_{CT} value was obtained for the symmetric PEDOT–MMT/PEDOT–MMT configuration, independently of the number of cycles. This has been attributed to a barrier effect induced by the microscopic structure of nanocomposite: the exfoliated clay hinders the entrance of perchlorate ions, which increases the ionic charge-transfer resistance. This behavior is fully consistent with the electrostability of PEDOT–MMT/PEDOT–MMT, which is lower than that of PEDOT/PEDOT (Table 4).

Table 6. *Fitting parameters used to simulate the EIS data obtained for the micrometric supercapacitors studied in this work (Figure 11)*

	Rs^a	$CPE_1{}^b$	$n_1{}^c$	$R_{CT}{}^d$	W^e	$C_{PS}{}^f$
			As prepared			
PEDOT/PEDOT	40.8	49.57	0.88	537.2	10.08	13.22
PEDOT–MMT/PEDOT–MMT	38.6	62.95	0.85	568.8	14.66	9.42
PEDOT/PEDOT–MMT	29.5	9.82	0.87	178.1	25.41	10.95
			After 500 consecutive oxidation-reduction cycles			
PEDOT/PEDOT	36.56	10.85	0.81	1488	2.61	9.75
PEDOT–MMT/PEDOT–MMT	41.44	10.44	0.77	2064	5.02	10.92
PEDOT/PEDOT–MMT	31.01	12.34	0.87	592	13.59	2.92

[a] Electrolyte resistance, in $\Omega \cdot cm^2$. [b] Double layer capacitance, in $\mu F \cdot cm^{-2} \cdot s^{n-1}$. [c] .[d]Charge-transfer resistance at the polymer film–electrolyte interface, in $\Omega \cdot cm^2$. [e] Warburg element, in $\Omega \cdot cm^2$.[f] Faradaic pseudo-capacitance, in $mF \cdot cm^{-2}$.

The CPE impedance is higher for PEDOT–MMT/PEDOT–MMT than for PEDOT/PEDOT, indicating that the effective surface area for interfacial charge transport is highest for the PEDOT–MMT than for PEDOT. This observation suggests that the presence of pores and cavities is higher in the former than in the latter, which is fully consistent with the SEM micrographs displayed in Figures 3a and 3b. On the other hand, Table 6 shows that the Warburg impedance decreases after 500 oxidation-reduction cycles. This feature has been attributed to the fact that the degradation of the polymer increases with the number of cycles. More specifically, electrochemical degradation produces structural changes on the surface of the polymer. Figures 11a and 11b show SEM micrographs of micrometric PEDOT and PEDOT–MMT 20%, respectively, after 500 oxidation-reduction cycles. Comparison with the morphology of fresh samples, which are displayed in Figures 2a and 2b, evidences that electrochemical degradation produce deep cracks on the surface (Figure 11c), which facilitate the diffusion process. This phenomenon has been attributed to the fact that clusters of aggregated molecules tend to collapse when the samples are submitted to a large number of oxidation-reduction cycles.[18] In other words, the homogeneous distribution of small pores and cavities transforms into well localized cracks upon such collapses.

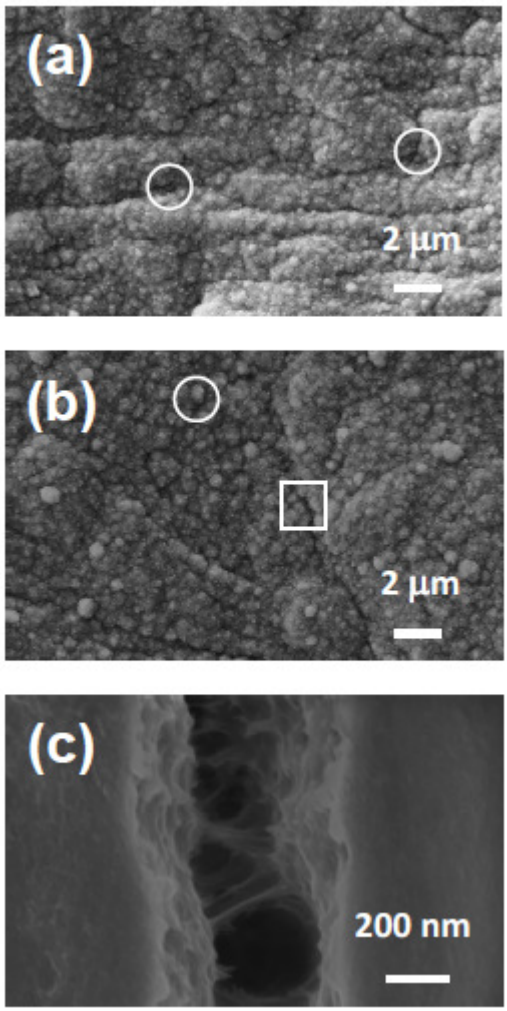

Figure 12. *SEM micrographs of micrometric (a) PEDOT and (b) PEDOT–MMT 20% w/w after 500 consecutive oxidation-reduction cycles. The white circles and the white square illustrate the deep cracks produced by the electrochemical degradation. (c) High resolution SEM micrograph of the crack marked with a white square in (b).*

The asymmetric PEDOT/PEDOT–MMT configuration presents the lowest R_{CT} value, which is consistent with its highest SC, indicating that the diffusion of perchlorate ions is easier than in the two type I supercapacitors. In spite of this, the electrochemical stability of the asymmetric supercapacitor was found to be lower than those of the symmetric ones. Understanding of this apparent contradiction is provided in Table 6. Thus, the low electrostability of the PEDOT/PEDOT–MMT supercapacitor should be attributed to the high Warburg impedance reached after 500 redox cycles.

The nanometric PEDOT/PEDOT–MMT 20% w/w is the only ultracapacitor made of ultrathin films studied in this work. This system has been selected because its SC is two times higher than those determined for all the nanometric symmetric configurations

(Table 4). Figure 12 shows the EIS plots of the nanometric PEDOT/PEDOT–MMT 20% w/w as prepared and after 500 consecutive oxidation-reduction cycles, and Table 7 lists the parameters derived from their fitting to the EC displayed in Figure 10d. This nanometric ultracapacitor follows the same behavior than the corresponding micrometric one, even though the values found for the different elements of the EC were smaller for the former than for the latter. R_{CT} increases with the number of oxidation-reduction cycles, while the Warburg impedance decreases. Moreover, electrochemical degradation of the nanometric films produces deep cracks on the surface similar to those displayed in Figure 11 for micrometric films.

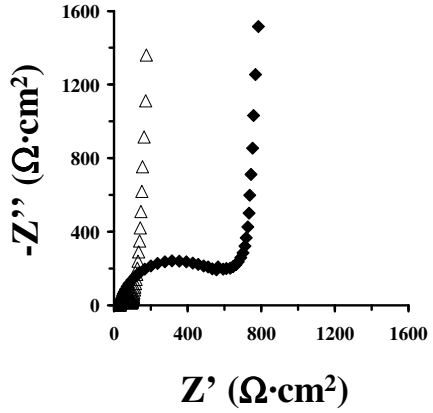

Figure 13. *Nyquist plots showing the evolution of the impedance data of the nanometric PEDOT/PEDOT–MMT 20% w/w supercapacitor as prepared (empty triangles) and after 500 consecutive oxidation-reduction cycles (filled diamonds). The experimental data (represented symbols) were fitted to the equivalent circuit model depicted in Figure 10d to produce the parameters listed in Table 7.*

Table 7. *Fitting parameters used to simulate the EIS data obtained for the nanometric PEDOT/PEDOT–MMT 20% w/w supercapacitor (Figure 13).*

	Rs^a	$CPE_1{}^b$	$n_1{}^c$	$R_{CT}{}^d$	W^e	$C_{PS}{}^f$
As prepared	30.90	8.34	0.86	62.1	59.58	3.08
After 500 consecutive oxidation-reduction cycles	31.01	12.34	0.87	592	13.59	2.92

[a] Electrolyte resistance, in $\Omega \cdot cm^2$. [b] Double layer capacitance, in $\mu F \cdot cm^{-2} \cdot s^{n-1}$. [c] n_1. [d] Charge-transfer resistance at the polymer film–electrolyte interface, in $\Omega \cdot cm^2$. [e] Warburg element, in $\Omega \cdot cm^{-2}$. [f] Faradaic pseudo-capacitance, in $mF \cdot cm^{-2}$.

Finally, the SCs provided by EIS (Eqn 5) for the investigated supercapacitors are included in Table 4. As it can be seen, the resulting values are fully consistent with those derived from CV. For micrometric devices the two methodologies indicate that

the lowest SC corresponds to the PEDOT/PEDOT, whereas the asymmetric PEDOT/PEDOT–MMT 20% w/w shows the highest one. In spite of this, the values determined by EIS are underestimated by 20%-24% with respect those measured using CV. Such overestimation decreases to 10% for the nanometric PEDOT/PEDOT–MMT 20% w/w, the SCs measured by EIS and CV being 386 and 429 $F \cdot g^{-1}$, respectively.

5.2.4. Conclusions

Exfoliated PEDOT–MMT nanocomposites have been prepared by anodic polymerization considering MMT concentrations in the generation medium ranging from 5% w/w to 50% w/w. Nanometric and micrometric films, with a thickness of ~200 nm and ~1 μm, respectively, have been obtained by controlling the polymerization time. SEM and AFM analyses indicate that low concentrations of MMT (≤ 10% w/w) induce changes in the morphology of the internal side of the film only. Specifically, the precipitation of the clay on the electrode provokes a homogeneous distribution of granules in the internal surface. In contrast, MMT concentrations ≥ 20% w/w produce the formation of large aggregates in the surface of the external side of the film and thin cracks in the internal side, the latter being due to the swelling effect promoted by the absorbed water.

The electrical conductivity decreases one order of magnitude upon the incorporation of a concentration of MMT ≥ 20% w/w. The adherence and thermal stability are lower for PEDOT than for the nanocomposites, increasing moderately with the concentration of MMT. In contrast both the charge storage and dl decreases when the concentration of clay increases. The SC and electrostability largely depend on the thickness of the films. Thus, the SCs of nanometric PEDOT and PEDOT–MMT, which range from 355 to 237 $F \cdot g^{-1}$ (PEDOT and PEDOT–MMT 50% w/w, respectively), are one order of magnitude higher than those of the corresponding micrometric films. Similarly, the electrostability of micrometric PEDOT–MMT films is lower than that of nanometric ones.

Nanometric ultracapacitors of types I and II (*i.e.* symmetric and asymmetric configurations of two electrodes) show very high SC values. The larger SC correspond to the symmetric PEDOT/PEDOT and the asymmetric PEDOT/PEDOT–MMT 20% w/w (465 and 429 $F \cdot g^{-1}$, respectively), whereas the SC of PEDOT–MMT/PEDOT–MMT decreases from 217 to 179 $F \cdot g^{-1}$ when concentration of MMT increases from 5% to 50% w/w. In contrast, the clay does not alter the electrostability of these nanometric ultracapacitors, the LES of nanometric ultracapacitors being very similar independently of their symmetric or asymmetric configurations. On the other hand, the SCs of micrometric PEDOT–MMT/PEDOT–MMT 20% w/w and PEDOT/PEDOT–MMT 20% w/w are higher than that of PEDOT/PEDOT, even though the latter shows the highest electrochemical stability. The capabilities and properties of the micrometric

ultracapacitors as well as of the nanometric PEDOT/PEDOT–MMT 20% w/w have been rationalized using EIS assays.

Electrochemical degradation studies using consecutive oxidation-reduction cycles indicate that the favorable effect of the clay on the SC and electrochemical stability of both type I and II ultracapacitors decreases significantly after 500 consecutive oxidation-reduction cycles. This effect is much less pronounced when electrochemical degradation is carried out using charge/discharge cycles. In this case, the reduction of the SC is relatively low and, in addition, the asymmetric configuration retains the favorable effect of the clay on the SC, the power density and the maximum specific energy. On the other hand, EIS and SEM studies indicate that the electrochemical degradation produces deep cracks on the surface of the films, facilitating the diffusion of ions.

5.2.5. References

[1]. Jonas, F.; Schrader, L. *Synth. Met.* **1991**, *41*, 831.

[2]. Dietrich, M.; Heinze, J.; Heywang, G.; Jonas, F. *J. Electroanal. Chem.* **1994**, *369*, 87.

[3]. Heywang, G.; Jonas, F. *Adv. Mater.* **1992**, *4*, 116.

[4]. Groenendaal, L.; Jonas, F.; Freitag, D.; Pielartzik, H.; Reynolds, J. R. *Adv. Mater.* **2000**, *12*, 481.

[5]. Pei, Q.; Zuccarello, G.; Ahlskog, M.; Ingana, O. *Polymer* **1994**, *35*, 1437.

[6]. A.G. Bayer, Euro Patent 339340 (1988).

[7]. Apperloo, J.; Groenendaal, L. B.; Verheyen, H.; Jayakannan, M.; Janssen, R. A.; Dkhissi, A.; Beljonne, D.; Lazzaroni, R.; Brédas, J. L. *Chem. Eur. J.* **2002**, *8*, 2384.

[8]. Yu, J.; Holdcroft, S. *Chem. Mater*. **2002**, *14*, 3705.

[9]. Sankaran, B.; Reynolds, J. R. *Macromolecules* **1997**, *30*, 2582.

[10]. Casanovas, J.; Alemán, C. *J. Phys. Chem. C* **2007**, *111*, 4823.

[11]. Poater, J.; Casanovas, J.; Solà, M.; Alemán, C. *J. Phys. Chem. A* **2010**, *114*, 1023.

[12]. Craft, W.; Jonas, F.; Muys, B.; Qintens, D. (AgfaGevaert), Euro Patent 564911 (1993).

[13]. Soboleva, T; Xie, Z; Shi, Z; Tsang, E; Navessin, T.; Holdcroft, S. *J. Electroanal. Chem.* **2008**, *622*, 145.

[14]. de Leeuw, D. M.; Kraakman, P. A.; Bongaerts, P. F. G.; Mutsaers, C. M. J. *Synth. Metals* **1994**, *66*, 263.

[15]. Heuer, W.H.; Wehrmann, R.; Kirchmayer, S. *Adv. Func. Mater.* **2002**, *12*, 89.

[16]. Cutler, C. A.; Bouguettaya, M.; Reynolds, J. R. *Adv. Mater*. **2002**, *14*, 684.

[17]. Ghosh, S.; Inganas, O. *Adv. Mater.* **1999**, *11*, 1214.

[18]. Aradilla, D.; Estrany, F.; Alemán, C. *J. Phys. Chem. C* **2011**, *115*, 8430.

[19]. Kirchmeyer, S.; Reuter, K. *J. Mater. Chem.* **2005**, *15*, 2077.

[20]. Novak, P.; Muller, K.; Santhanam, K. S. V.; Haas, O. *Chem. Rev.* **1997**, *97*, 207.

[21]. Aranda, P.; Darder, M.; Fernández-Saavedra, R.; López-Blanco, M.; Ruiz-Hitzky, E. *Thin Solid Films* **2006**, *495*, 104.

[22]. Rajesh, Ahuja, T.; Kumar, D. *Sens. Actuators B* **2009**, *136*, 275.

[23]. Yeh, J.-M.; Chang, K.-C. *J. Ind. Engin. Chem.* **2008**, *14*, 275.

[24]. Olad, A.; Rashidzadeh, A. *Prog. Org. Coat.* **2008**, *62*, 293.

[25]. Yeh, J.-M.; Liou, S.-J.; Lai, C.-Y.; Wu, P.-C. *Chem. Mater.* **2001**, *13*, 1131.

[26]. Jia, W.; Segal, E.; Kornemandel, D.; Lamhot, Y.; Narkis, M.; Siegmann, A. *Synth. Met.* **2002**, *128*, 115.

[27]. Kim, B.-H.; Jung, J.-H.; Hong, S.-H.; Joo, J. *Macromolecules* **2002**, *35*, 1419.

[28]. Bae, W. J.; Kim, K.-H.; Jo, W. H.; Park, Y. H. *Macromolecules* **2004**, *37*, 9850.

[29]. Karim, M. R.; Yeum, J. H. *J. Polym. Sci: Part B: Polym. Phys* **2008**, *46*, 2279.

[30]. Suri, K.; Annapoorni, S.; Tandom, R. P.; Mehra, N. C. *Synth. Met.* **2002**, *126*, 137.

[31]. Leta, S.; Aranda, P.; Fernández-Saavedra Margeson, R; Detelliera, C.; Ruiz-Hitzky, E. *J. Mater. Chem.* **2008**, *18*, 2227.

[32]. Rajapakse, R. M. G.; Higgins, S.; Velauthamurthy, K.; Bandara, H. M. N.; Wijeratne, S.; Rajapakse, R. M. M. Y. *J. Compos. Mater.* **2010***, 45*, 597.

[33]. Han, Y.; Lu, Y. *J. Appl. Polym. Sci.* **2009**, *11*, 2400.

[34]. Aradilla, D.; Estrany, D.; Azambuja, D. S.; Casas, M. T.; Puiggalí, J.; Ferreira, C. A.; Alemán, C. *Eur. Polym. J.* **2010**, *46*, 977.

[35]. Bae, W. J.; Kim, K. H.; Park, Y. H.; Jo, W. H. *Macromolecules* **2004**, *37*, 9850.

[36]. Kotz, R.; Carlen, M. *Electrochim. Acta* **2000**, *45*, 2483.

[37]. Frackowiak, E.; Beguin, F. *Carbon* **2002**, *40*, 1775.

[38]. Wang, Y. G.; Zhang, X. G. *Electrochim. Acta* **2004**, *49*, 1957.

[39]. Liu, C.; Li, F.; Ma, L.-P.; Cheng, H.-M. *Adv. Mater.* **2010**, *22*, E28.

[40]. Centi, G.; Perathoner, S. *Eur. J. Inorg. Chem.* **2009**, *26*, 3851.

[41]. Snook, G. A.; Kao, P.; Best, A. *J. Power Sources* **2011**, *196*, 1.

[42]. Chen, L.; Yuan, C.; Dou, H.; Gao, B.; Chen, S.; Zhang, X. *Electrochim. Acta* **2009**, *54*, 2335.

[43]. Murugan, A. V.; Viswanath, A. K.; Gampet, G.; Gopinath, C. S.; Vijayamohanan, K. *Appl. Phys. Lett.* **2005**, *87*, 243511.

[44]. Sharma, R.; Zhai, L. *Electrochim. Acta* **2009**, *54*, 7148.

[45]. Sen, P.M.; De, M. *Electrochim. Acta* **2010**, *55*, 4677.

[46]. Banafsheh, B.; Ivey, D. G. *Electrochim. Acta* **2010**, *55*, 2014.

[47]. Chen, L.; Yuan, C.; Gao, B.; Chen, S.; Zhang, X. *J. Solid State Electrochem.* **2009**, *13*, 1925.

[48]. Murugan, A. V.; Viswanath, A. K.; Gopinath, C. S.; Vijayamohanan, K. *J. Appl. Phys.* **2006**, *100*, 074319.

[49]. Estrany, F.; Aradilla, D.; Oliver, R.; Alemán, C. *Eur. Polym. J.* **2007**, *43*, 1876.

[50]. Estrany, F.; Aradilla, D.; Oliver, R.; Armelin, E. Alemán, C. *Eur. Polym. J.* **2008**, *44*, 1323.

[51]. Carrasco, J.; Brillas, E.; Fernández, V.; Cabot, P. L.; Garrido, J. A.; Centellas, F.; Rodríguez, R. M. *J. Electrochem. Soc.* **2001**, *148*, E19.

[52]. Oliver, R.; Muñoz, A.; Ocampo, C.; Alemán, C.; Armelin, E.; Estrany, F. *Chem. Phys*. **2006**, *328*, 299.

[53]. Ocampo, C.; Oliver, R.; Armelin, E.; Alemán, C.; Estrany, F. *J. Polym. Res.* **2006**, *13*, 193.

[54]. Madejová, J.; Arvaiová, B.; Komadel, P. *Spectrochim. Acta, Part A* **1999**, *55*, 2467.

[55]. Aradilla, D.; Estrany, F.; Armelin, E.; Alemán, C. *Thin Solid Films* **2010**, *518*, 4203.

[56]. Hsieh, K. H.; Ho, K. S.; Wang, Y. Z.; Ko, S. D.; Fu, S. C. *Synth. Met.* **2001**, *123*, 217.

[57]. Bertran, O.; Armelin, E.; Estrany, F.; Gomes, A.; Torras, J.; Alemán, C. *J. Phys. Chem. B* **2010**, *114*, 6281.

[58]. Li, X.-G.; Li, J.; Huang, M.-R. *Chem.-Eur. J.* **2009**, *15*, 6446.

[59]. Geneis, E. M.; Bidan, G.; Diaz, A. F. *J. Electroanal. Chem.* **1983**, *149*, 101.

[60]. Vashanta, V. S.; Phani, K. L. N. *J. Electroanal. Chem.* **2002**, *520*, 79.

[61]. Jorcin, J.-B.; Orazen, M. E.; Pébère, N.; Tribollet, B. *Electrochim. Acta* **2006**, *51*, 1473.

[62]. Walter, G. W. *Corros. Sci.* **1986**, *26*, 681.

5.3. Electrochemical supercapacitors made of multilayered nanocomposites with anti-corrosive applications

5.3.1. Introduction

Over the last decade, nanoscience and nanotechnology have attracted a great attention in academic and industrial sectors since the nanometer-scale plays an important and crucial role in the study and development of nanostructured materials.[1,2] Hybrid nanocomposites formed by inorganic-organic materials are being extensively studied owing to their remarkable properties in terms of thermal stability, gas-barrier, mechanical strength, corrosion inhibitor or in electrochemical and electroanalytical applications.[3-7] Clay minerals are a class of inorganic materials divided in seven main groups: kaolin-serpentine, pyrophyllite-talc, smecticte, vermiculite, mica, chlorite and interstratified clay minerals, respectively.[8] These clay groups have shown interesting applications in the field of sensors (*e.g* biosensors)[9] and in aerospace applications.[10] Precisely, smectite is a clay group which is formed by different species such as saponite, hetorite, sauconite, stevensite, swinefordite or montmorillonite (MMT). Particularly, MMT is a hydrophilic mineral, which belongs to the general family of 2:1 (smectite) phyllosilicates composed of stacked layers of aluminum octahedron and silicon tetrahedrons. This mineral is one of the most commonly used clays in the field of nanocomposites due to its abundance and low-cost.[5] However, clays are also characterized by their cationic exchange properties, particle size and adsorption properties. Particularly, the charged nature of the clays plays an important role on the synthesis of nanocomposites since most of them are generally hydrophilic species and consequently incompatible with organic compounds such as conducting polymers. The modification of the charge through of species as quaternary ammonium cations are frequently used to prepare organoclays, thus, the compatibility of the clay is improved and favors the exfoliation into nanocomposites.[11]

Within context, in the recent years nanocomposites based on clays/conducting polymers have gained significant importance due to their interesting applications.[2,12] Among the large number of conducting polymers (CPs), polypyrrole (PPy), polythiophene (PTh) and polyaniline (PAni) have been extensively studied as nanocomposites in presence of MMT. Accordingly, PAni/MMT nanocomposites have been widely characterized and their applications have been successfully employed as

corrosion inhibitors.[13-20] Other nanocomposites based on PPy/MMT have been also characterized and synthesized using several chemical and electrochemical methods such as polymerization in situ,[21] emulsion polymerization,[22-25] or electro-polymerization,[26,27] with interesting applications as cathode materials for oxygen reduction,[28] or corrosion inhibitors,[29] respectively. Furthermore, nanocomposites based on thiophene derivatives and MMT have been also synthesized employing some procedures based on solvent casting,[30] intercalative polymerization,[31] or electro-polymerization.[32] Specifically, among thiophene derivatives poly(3,4-ethylenedioxythiophene) (PEDOT) is one of the most important conducting polymers due to its excellent electrochemical properties (*e.g.* electroactivity and loss of stability), good environmental stability, high conductivity, fast doping/undoping mechanisms and low band-gap.[33-35] Recently, PEDOT/MMT nanocomposites have been synthesized by using chemical and electrochemical techniques.[32,36-39] Thus, the presence of MMT in PEDOT polymeric matrix was employed as supercapacitor electrodes from a concentration of MMT corresponding to a value of 20% w/w, being this value the optimal concentration for the development of supercapacitor devices.[38] In this way, symmetric supercapacitors made of PEDOT-MMT 20% w/w films exhibited a specific capacitance (SC) value corresponding to 94 F·g, whereas supercapacitors made of PEDOT showed a decrease of the SC to 82 F·g.[38]

In the last years, a new procedure of synthesis of conducting polymers based on the layer by layer (LbL) technique has been widely used. This procedure consists of electrochemical principles, which allows to build thin films. Thus, multilayered systems based on PPy were synthesized by using potentiostatic methods (*e.g.* chronoamperometry) to evaluate its electrochemical properties and ion transport.[40] Within this context, multilayered systems based on PPy and PAni were galvanostatically deposited on steel to evaluate their performance as corrosion inhibitors, or chemical sensors.[41] PPy has been widely employed in the electrochemical layer-by-layer technique, and its use has been evaluated in combination with other conducting such as poly(thiophene) (PTh) or PEDOT in applications as electrochemical actuators.[42,43]

Recently, a great interest has been focused on studying the electrochemical LbL technique employing PTh and Py derivatives. Regarding to this topic, multilayered systems based on two or more conducting polymers were reported in previous works.[44-46] The results evidenced that ml-PEDOT/PNMPy systems present better electrochemical properties, in terms of charge storage, than that of single component PEDOT and

PNMPy films, respectively. [44-46] Consequently, the interface among conducting polymer layers at nanometric and micrometric levels showed the best performance to be employed as supercapacitor materials with excellent results.[47]

The aim of this work is the preparation and characterization of multilayered systems based on PEDOT and PPy films containing MMT particles. The electrochemical properties were evaluated from cyclic voltammetry (CV). The morphological and structural properties of the systems were examined by scanning electron microscopy (SEM), atomic force microscopy (AFM) and transmission electron microscopy (TEM). Finally, the presence of MMT in ml-PEDOT/PPy systems was examined on the corrosion resistance of steel electrodes by using electrochemical impedance spectroscopy (EIS) studies.

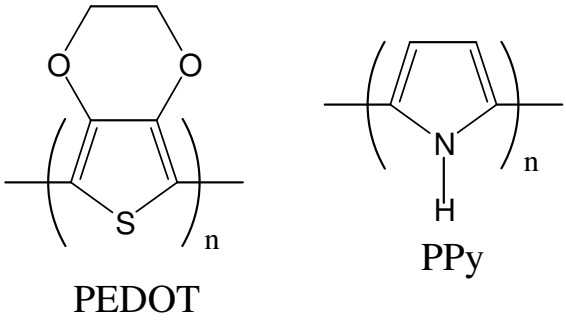

Scheme 1. *Poly(3,4-ethylenedioxythiophene) (PEDOT; left image) and Poly(pyrrole) (PPy; right image)*

5.3.2. Methods

Materials. 3,4-ethylenedioxythiophene (EDOT), pyrrole (Py) monomers, acetonitrile, montmorillonite (MMT), and montmorillonite clay surface modified with 15-35 wt% octadecylamine and 0.5-5 wt% aminopropyltriethoxysilane were purchased from Aldrich and used as received. Anhydrous $LiClO_4$, analytical from Aldrich, analytical reagent grade, was stored in an oven at 80 ºC before use in the electrochemical trials.

Synthesis. The synthetic process used to prepare both PEDOT and PEDOT–MMT was identical to that reported in previous works,[32,38] therefore, a brief summary is discussed. All systems studied in this study were synthesized by chronoamperometry (CA) under a constant potential of 1.40 V using an PGSTAT302N AUTOLAB potenciostat-galvanostat connected to a PC computer controlled through the NOVA 1.6 software, using a three-electrode two-compartment cell under nitrogen atmosphere at 25

ºC. Steel AISI 316 sheets of 4 cm^2 were used as electrodes. After electropolymerization, all coated electrodes were cleaned with acetonitrile and dried with nitrogen. The generation medium consisted on a 10 mM of the corresponding monomer (*e.g.* EDOT or Py) in an acetonitrile/water solution (40:60 v/v) containing 0.1 M $LiClO_4$ as supporting electrolyte.

The electrochemical LbL technique was used to prepare the n-layered PEDOT/PPy films (being *n* the number of layers). For the generation of each layer the working electrode was immersed for a period of 100s in cells filled with 10 mM acetonitrile/water solution of the corresponding monomer with 0.1 M $LiClO_4$. All the investigated materials were prepared considering a polymerization time (τ) of 300s, 500s and 700s (*e.g.* 3-ml, 5-ml and 7-ml were prepared using 100s per layer). Accordingly, the total polymerization time was identical to that of individual PEDOT films. The concentration of MMT in the generation medium, which is referred to that of the EDOT monomer, was estimated a value of 20 % according to a previous work.[38]

Before the addition of MMT to the monomer solution, the clay was exfoliated in deionized water at neutral pH, being sonicated 10 min with an ultrasonic generator. The resulting solution was stirred for 1 day using a magnetic stirrer. Next, the generation medium and the exfoliated MMT solution were mixed and stirred for 20 h in a frozen environment (ice).

Thickness. The thickness of the films (ℓ) was determined through electrochemical measurements. Electrochemical estimations of the thickness were obtained by determining the current productivity through the mass-charge ratio and, subsequently, the mass of polymer deposited in the electrode. The latter procedure was detailed in a previous work.[45]

Transmission electron microscopy. The structure and distribution of the clay in nanocomposites was examined using a Phillips TECNAI 10 transmission electron microscope at an accelerating voltage of 100 kV. For this purpose, small trips of nanocomposites were removed from the electrodes with a razor blade and, according the manufacturer protocol, embedded in a low viscosity modified Spurr epoxy resin and curing at 60ºC for 24 h. Ultra-thin sections (less than 100 nm) of these samples were cut at room temperature using a Sorvall Porter-Blum microtome. Finally, the sections were placed on carbon coated cooper grids. Bright field micrographs were taken with a SIS Mega View II digital camera.

Scanning electron microscopy. EDX spectroscopy and SEM studies were performed to examine the composition of the synthesized nanocomposites and to examine the effect of the clay on the surface morphology, respectively. Dried samples were placed in a Focussed Ion Beam Zeis Neon 40 scanning electron microscope operating at 3 kV, equipped with an EDX spectroscopy system.

Atomic force microscopy. Topographic images were obtained with a Molecular Imaging PicoSPM using a NanoScope IV controller in ambient conditions. The tapping mode AFM was operated at constant deflections (*i.e.* vertical constant force with triangular shaped gold-coated silicon nitride). The row scanning frequency was set to 1 Hz and the physical tip–sample motion speed was 10 $\mu m \cdot s^{-1}$. The root-mean-square (RMS) roughness (*r*) was determined using the statistical application of the Nanoscope software, which calculates the average considering all the values recorded in the topographic image with exception of the maximum and the minimum. The scan window size was 5×5 μm^2 in all cases, a total of 65.536 topographic data being computed in each image. In all images acquired, which are 512×512 $pixel^2$ maps, differences in height are indicated by a color scale: dark is low and white is high.

Electrochemistry. The electroactivity, which refers to the charge storage ability, and electrochemical stability (electrostability) were determined by cyclic voltammetry (CV) using a distilled water solution with 0.1 M $LiClO_4$. The initial and final potentials were -0.50 V, while the reversal potential was 1.00 V. The electroactivity increases with the similarity between the anodic and cathodic areas of the first control voltammograms, whereas the electrostability decreases with the oxidation and reduction areas of consecutive control voltammograms. Specifically, the loss of electrostability (LES, in %) was determined as:

$$LES = \frac{\Delta Q}{Q_{II}} \cdot 100 \qquad (1)$$

where ΔQ is the difference of voltammetric charges (in C) between the second and the last cycle, and Q_{II} is the voltammetric charge corresponding to the second cycle. In this work, measures of LES refer to 100 consecutive oxidation-reduction cycles.

The SC (in $F \cdot g^{-1}$) of the investigated systems were determined by CV using the following Eqn:

$$SC = \frac{Q}{\Delta V m} \qquad (2)$$

where Q is the voltammetric charge, which is determined by integrating either the oxidative or reductive parts of the cyclic voltammetry curve, ΔV is the potential window (in V), and m is the mass of PEDOT polymer on the surface of the working electrode (in g). All electrochemical experiments were carried out in a distilled water solution containing 0.1 M $LiClO_4$ at 25ºC.

Electrochemical Impedance Spectroscopy. EIS measurements films, were performed in potentiostatic mode at the open circuit potential (OCP) using an AUTOLAB PGSTAT 30/FRA 2 system. The amplitude of the EIS perturbation signal was 50 mV, and the studied frequency ranged from 10 kHz to 10 mHz. All the electrochemical experiments were carried out in a distilled water solution containing 0.1 M $LiClO_4$ at 25°C. Corrosion tests were performed using a 3.5% NaCl solution.

Electrical conductivity. The electrical conductivity (σ; $S \cdot cm^{-1}$) of nanocomposite films was measured from using the following relation:

$$\sigma = \frac{l^2 \rho_{pol}}{R m_{pol}} \qquad (3)$$

where l is the length among the two silver terminals of a film, ρ is the density of the polymer, R is the resistance and m_{pol} is the mass of polymer.

X-Ray Diffraction (XRD). X-ray diffraction spectra of MMT and PEDOT-MMT films were recorded using a Bruker D8 Advance model to 40 kV and 40 mA (λ=1.5406 Å). The XRD patterns were taken at ambient laboratory temperature using 10s/angular step (1 angular step = 0.02º).

5.3.3. Results and discussion

Thickness of the films. Figure 1 shows the variation of thickness against the number of layers. As can be observed, a linear behavior is displayed for all systems. Thus, a growing rate of 0.57, 0.49 and 0.46 μm·n was estimated for PEDOT/PPy (20 %), PEDOT/PPy (20 % Mod), and PEDOT/PPy multilayered systems, respectively. The contribution of clay evidences an increase of the thickness in multilayered systems being especially important for ml PEDOT/PPy (20% Mod) systems. The configuration of the multilayered systems containing clay was performed with the first and the third layer corresponding to PEDOT containing the corresponding clay, MMT or modified MMT, respectively.

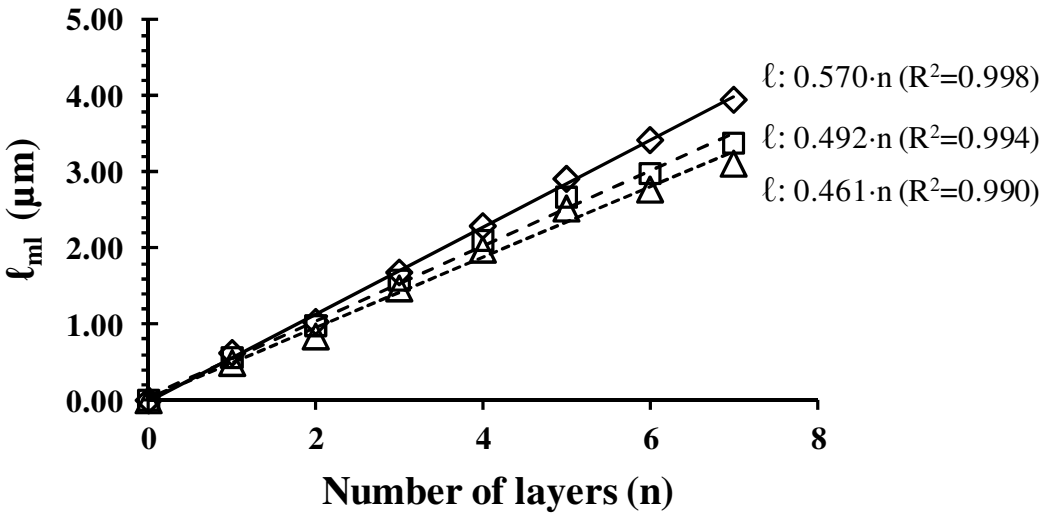

Figure 1. *Variation of the thickness of ml-PEDOT/PPy (20 %) (empty diamonds) ml-PEDOT/PPy (20 % Mod) (empty squares) and ml-PEDOT/PPy (empty triangles) nanocomposites (ℓ_{ml}) against the number of layers. The fittings used to obtain the growing rates are displayed in all cases.*

Distribution of the MMT in the nanoomposites. Figure 2a) displays the morphology of MMT and modified MMT particles, which shows flake morphology. SEM micrographs show that modified MMT has flaky particles arranged into the form of spheres with an average diameter up to 6.5±0.8 µm, whereas MMT particles show an average diameter of 8±1 µm.[38] The exfoliation of the modified MMT particles in the morphology of multilayered systems was demonstrated in Figure 2b. Figure 2b shows the TEM micrograph of the 3-ml PEDOT/PPy (20 % Mod) films. According to the image, the nanocomposite exhibits an exfoliated morphology. The procedure of synthesis of exfoliated nanocomposites by using electrochemical techniques was successfully reported in a previous work.[32] XRD technique was used in order to confirm the exfoliation of clay in the polymeric matrix. Thus, XRD patterns of MMT, modified MMT and PEDOT-MMT (20 % mod MMT) are shown in Figure 2c. Two important peaks are evidenced for modified MMT. The crystalline peak at 2θ=8.04º corresponds to the direction of (100) and 2θ=19.73º, which were found to be similar to MMT according to a previous work.[31] On the other hand, PEDOT-MMT (20 % Mod) diffractogram exhibits a sharp peak at 2θ=11.97º corresponding to the PEDOT polymer. As a consequence, the exfoliation of MMT in the structure of nanocomposites was corroborated by using TEM and XRD techniques.

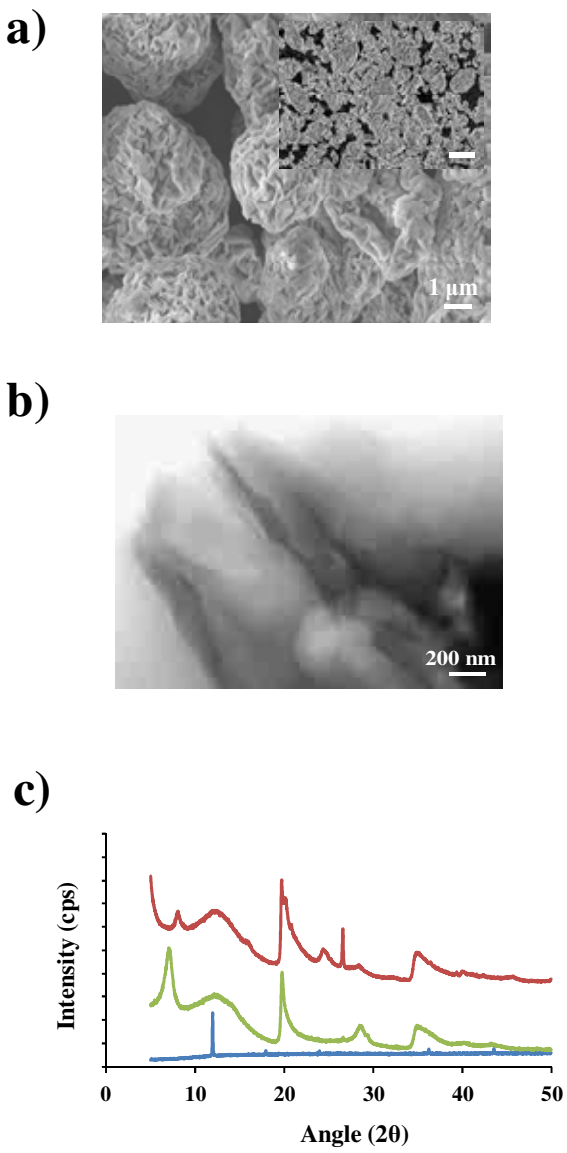

Figure 2. *a) SEM micrograph of MMT. Inset image corresponds to modified MMT (Scale bar: 10 µm). b) TEM micrographs of 3-PEDOT/PPy - modified MMT nanocomposites (20% w/w). c) XRD patterns of modified MMT (red solid line), MMT (green solid line) and PEDOT-MMT (blue solid line).*

Electrochemical properties of nanocomposites. Cyclic voltammetry studies were carried out to evaluate the electrochemical behavior and electrochemical stability of nanocomposites.

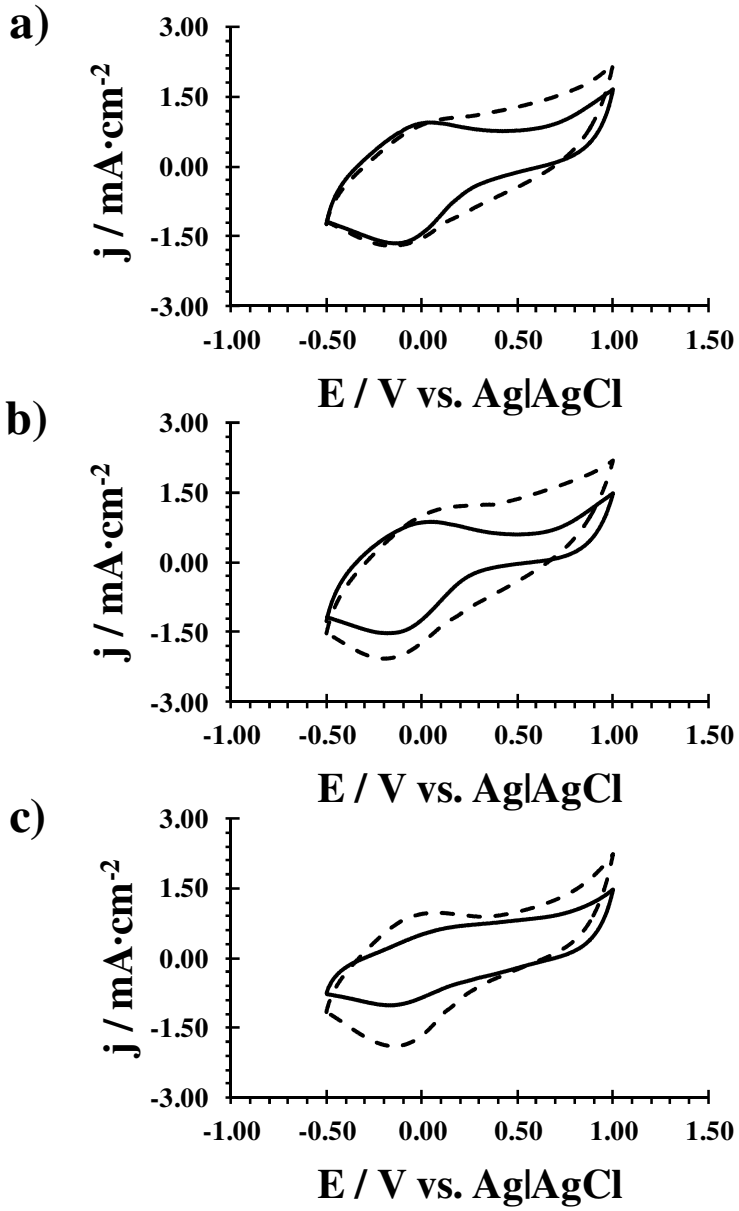

Figure 3. *a) Control voltammogram for PEDOT (solid line) and 3-PEDOT/PPy systems (dashed line). b) Control voltammogram for PEDOT (20% w/w) (solid line) and multilayered 3-PEDOT/PPy (20 %) nanocomposites (dashed line). c) Control voltammogram for PEDOT (20% mod MMT) and multilayered 3-PEDOT/PPy (20 % mod MMT). Voltammogramms were recorded at 100 mV·s^{-1}. Initial and final potentials: -0.50 V. Reversal potential: 1.10 V.*

Fig. 3a) shows the cyclic voltammograms of PEDOT and 3-ml PEDOT/PPy systems. Regarding to the results, it was found that multilayered systems present higher electroactivity and specific capacitance than pure PEDOT systems. According to Table 1, the specific capacitance was evaluated to be 100 F·g for 3-ml PEDOT/PPy systems, whereas PEDOT systems has a specific capacitance value approximately of 87 F·g. The synergistic effect among layers evidences the highest electroactivity for these systems.

This electrochemical behavior was reported in previous works employing PEDOT/PNMPy systems.[47] For multilayered nanocomposites represented in Fig. 3b) and Fig. 3c), the 3-ml PEDOT/PPy nanocomposites exhibited also better electrochemical properties in terms of electroactivity than PEDOT films containing clay. Table 1 displays electrochemical properties of the multilayered nanocomposites. The specific capacitance decreases when the number of layers increases for multilayered systems. On the other hand, the presence of clay improves the ability to charge storage, consequently, multilayered systems containing montmorillonite presented the best performance in terms of specific capacitance. It should be noted that multilayered systems containing modified montmorillonite exhibited the lowest electrochemical stability due to the improvement of the distribution of the clay in the polymeric structure. Nevertheless, the loss of electrochemical stability improves when the number of layers increases in all cases.

Table 1. *Electrochemical and structural properties of the systems studied in this work.*

	Electroactivity[a]	**LES[b]**	**SC[c]**	**ℓ^d**	**σ^e**	**r^f**
3-ML (20 %)	35.08	65.62	117.48	1.68	0.24	60.41
5-ML (20 %)	34.91	51.88	73.10	2.91	$1.71 \cdot 10^{-3}$	--
7-ML (20 %)	27.71	47.68	44.90	3.95	$2.85 \cdot 10^{-4}$	--
3-ML (20 % Mod)	29.52	76.33	103.05	1.58	0.09	78.83
5-ML (20 % Mod)	25.72	59.73	66.77	2.67	$3.65 \cdot 10^{-4}$	--
7-ML (20 % Mod)	18.79	54.60	37.22	3.38	$4.62 \cdot 10^{-5}$	--
3-ML	31.83	63.33	100.05	1.47	2.07	--
5-ML	34.00	59.53	63.18	2.52	--	--
PEDOT	24.43	42.60	86.39	--	--	--

[a] Charge storage in $mC \cdot cm^{-2}$. [b] Loss of electroactivity measured considering 100 consecutive oxidation-reduction cycles. [c] Specific capacitance in $F \cdot g^{-1}$. [d] Thickness in µm. [e] Conductivity in $S \cdot cm^{-1}$. [f] Roughness in nm.

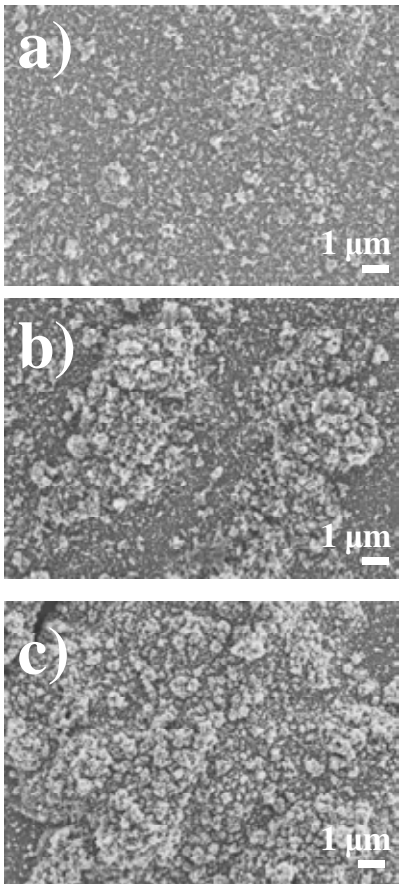

Figure 4. *SEM micrographs of a) PEDOT b) PEDOT (20 %) and c) PEDOT (20 % Mod) systems. All systems were generated using a polymerization time of 300s.*

Morphology of the nanocomposites. SEM micrographs of PEDOT, PEDOT (20 %) and PEDOT (20 % Mod) films are displayed in Fig.4. SEM images showed important differences at morphological level on the surface of the films. PEDOT films show the formation of concentrated agglomerates caused by the incorportation of clay, which are very remarkable in presence of modified montmorillonite. AFM images of the multilayered nanocomposites are shown in Figure 5 and Figure 6. Morphology of the alternated layers of 3-ml PEDOT/PPy (20 %) systems is represented in Fig.5. The first layer corresponds to PEDOT film, which exhibit the formation of agglomerates, which are formed at different heights (r = 69.9 nm). The second layers evidence the formation of globular structures corresponding to PPy films, which tends to create a more planar structure (r = 56.3 nm). Again, the third layer corresponding to PEDOT film shows the formation of larger agglomerates according to the increase of thickness. On the other hand, the morphology detected in 3-PEDOT/PPy (20 % Mod) systems reflected a similar morphology (Fig. 6). The agglomerates in the first and third layer of PEDOT are

more compact and their distribution is more uniform. The second layer is formed by the typical globular surface of PPy.

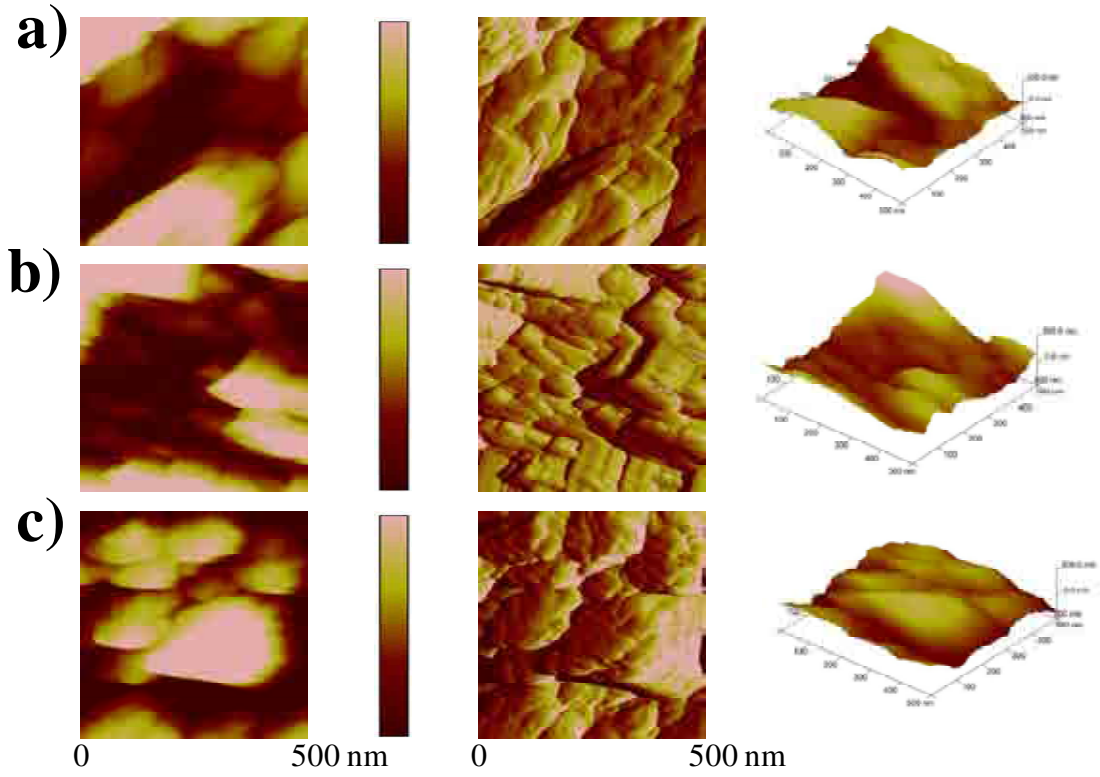

Figure 5. *2D height AFM images showing the topographical changes in the three-layered ml-PEDOT/PPy nanocomposites prepared using τ = 100s per layer: a) 1st layer, PEDOT (20 %), b) 2nd layer, PPy and c) 3rd layer, PEDOT (20 %) (left image) Scale bar: 300 nm. 2D amplitude AFM images corresponding to a), b) and c) (middle image). 3D AFM images corresponding to a), b) and c) (right image).*

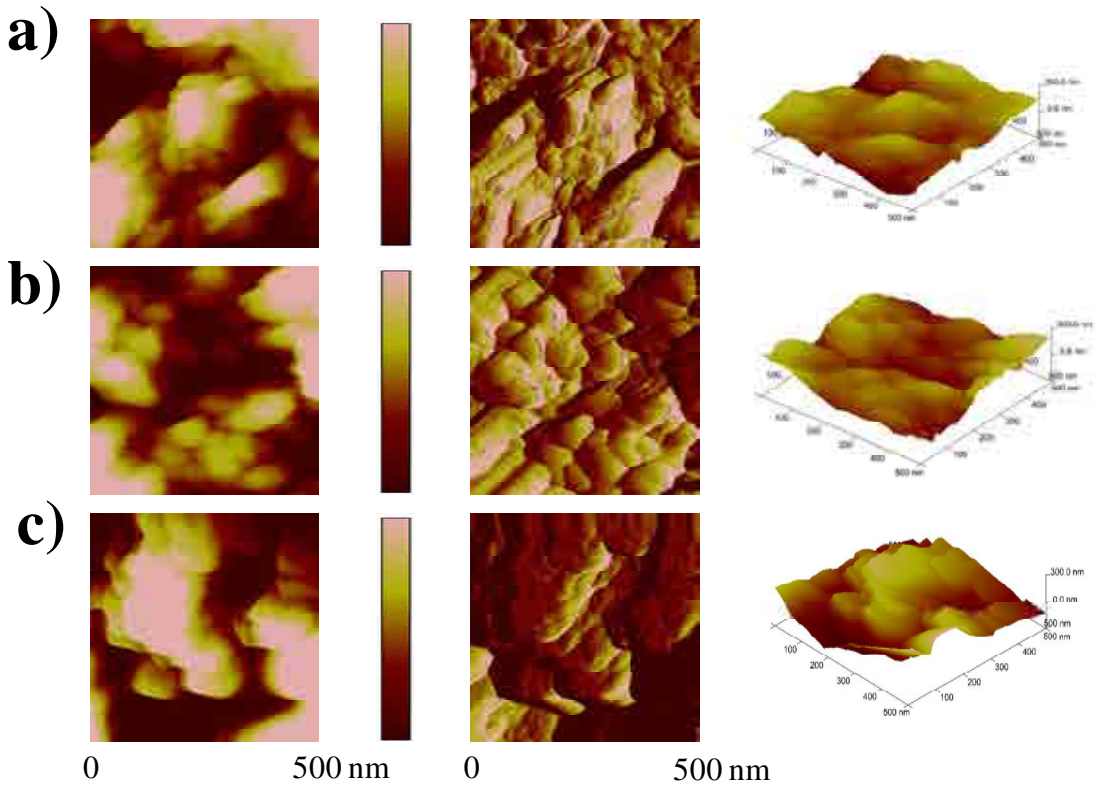

Figure 6. *2D height AFM images showing the topographical changes in the three-layered ml-PEDOT/PPy nanocomposites prepared using τ = 100s per layer: a) 1st layer, PEDOT (20 % Mod), b) 2nd layer, PPy and c) 3rd layer, PEDOT (20 % Mod) (left image) Scale bar: 300 nm. 2D amplitude AFM images corresponding to a), b) and c) (middle image). 3D AFM images corresponding to a), b) and c) (right image).*

Figure 7 illustrates the morphology of the multilayered systems studied in this work. Particularly, Fig 7a) shows the formation of agglomerates with a great presence of protuberances for 3-PEDOT/PPy films. The growth of PEDOT through α – α linkages evidence a linear growth formed by clusters, whereas PPy films tends to form crosslinkings. The third layer of PEDOT grown on the PPy film corroborates this tendency. However, Fig. 7b) evidences the formation of smaller agglomerates in 3-PEDOT/PPy (20 %) systems, which are distributed uniformly on the surface of electrode. This effect can be ascribed to the presence of the clay. Within this context, Fig. 7c) reflects a similar topography observed in Fig 7b), nevertheless, larger clusters were observed compared with 3-PEDOT/PPy (20 %). As conclusion, the inert nature of clay affects the topography and morphology of multilayered systems as it was discussed previously in Fig. 5 and Fig. 6, respectively.

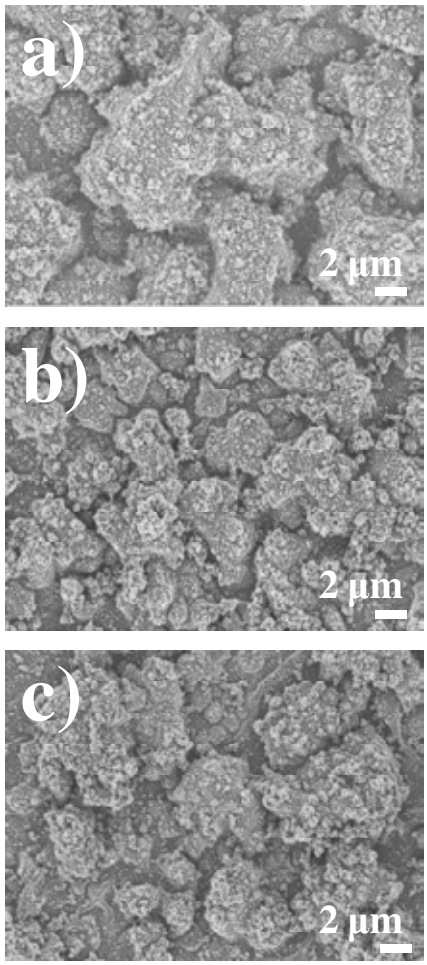

Figure 7*. SEM micrographs of a) 3-PEDOT/PPy, b) 3-PEDOT/PPy (20 %) and c) 3-PEDOT/PPy (20 % Mod) multilayered nanocomposites. All systems were generated using a total polymerization time of 300s (τ = 100s per layer).*

Electrical conductivity. The electrical conductivities (σ) measured for the ml-PEDOT/PPy, ml-PEDOT/PPy MMT (20 %) and ml-PEDOT/PPy MMT (20 % Mod) films are displayed in Table 1. As can be observed, the conductivity decreases in all systems when the number of layers increases. This effect evidences two important features, the first one is associated to the presence of the clay, which precludes and inhibits the electronic movement. The second characteristic is ascribed to the intermediate layer. According to previous works, the conductivity of PPy films was significantly lower than PEDOT, consequently, the presence of PPy films reduces the conductivity in multilayered systems formed by PEDOT and PPy. This behavior was evidenced in previous works for multilayered systems formed by alternated layers of PEDOT and PPy derivatives films.[44,46] The overall of these results conclude that

multilayered systems are influenced by the conductivity of each individual component of lowest σ.

Fig. 8 represents the temporal evolution of conductivity for the studied systems in this report. The results show a clear reduction of the electrical stability in presence of clay. The more drastic reduction is observed for 3-PEDOT/PPy MMT (20% Mod) systems. Moreover, the electrical stability (σ) of the nanocomposites decreased when the number of layers increased.

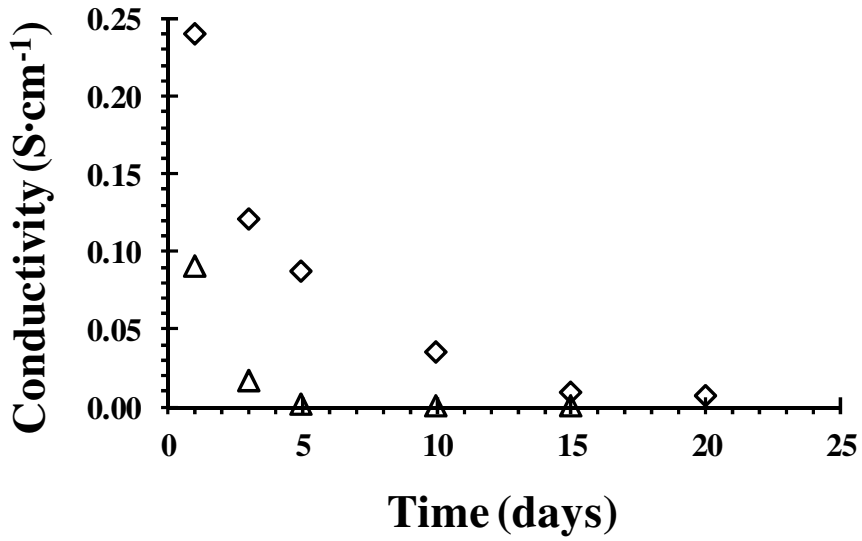

Figure 8. *Conductivity of 3-PEDOT/PPy (20% w/w) (empty diamonds) and 3-PEDOT/PPy (Mod 20 % w/w) (empty triangles) nanocomposites against the number of days.*

Electrochemical impedance spectroscopy studies for multilayered nanocomposites.

The Nyquist plots for the electrochemical impedance spectra recorded 3-PEDOT/PPy (20 %) and 3-PEDOT/PPy (20 % Mod) systems are displayed in Fig.9, Fig. 10 and Fig. 11, respectively. All the curves show a single semicircle in the high-frequency region, intermediate frequency 45º line representing the Warburg diffusion element, and a nearly vertical straight line in the low frequency region, indicating that the electrode process is dominated by charge transfer (*i.e.* electrochemical reaction) in the former region and by charge diffusion (*i.e.* mass transfer) in the latter one.[48] The first intercept of the semicircle with the real axis (Z') at high frequencies is the measure of the solution resistance. The origin of the semicircle at the higher-frequency range is due to the ionic charge-transfer resistance (R_{CT}) at the electrode-solution interface, while it is given by the diameter of the semicircle along the real axis Z'.

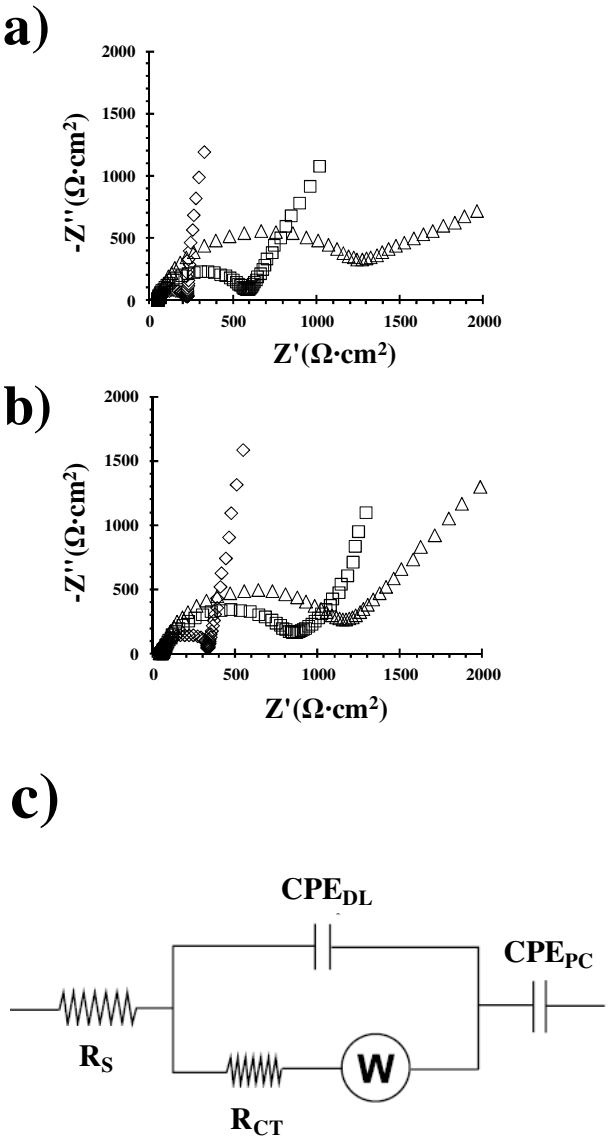

Figure 9. *a) Nyquist plots of ml-PEDOT/PPy nanocomposites as prepared employing a) MMT b) modified MMT. c) Equivalent circuit used to simulate the experimental spectra displayed in a) and b). (3-ml; empty diamonds, 5-ml; empty squares and 7-ml: empty triangles)*

The spectra were fitted using an equivalent circuit (E C). The aim of the choice of the EC was to obtain a satisfactory fitting of the experimental data, where the circuit elements can be associated with the physical phenomena that are probably taking place at the electrode surface. The EC proposed was $R_s(CPE_1[R_{CT}W])C_{PS}$, where Rs represents the electrolyte resistance, CPE_1 the double layer capacitance, R_{CT} the charge-transfer resistance at the polymer film–electrolyte interface, which is in serial connection with the Warburg element (W), and C_{PS} the faradaic pseudo-capacitance corresponding to a practically vertical line at low frequency region of the EIS spectra. The double layer capacitance was replaced by a constant phase element (CPE) that

describes a non-ideal capacitor when the phase angle is different from -90º. The CPE impedance has been expressed as:

$$Z_{CPE} = [Q\ (j\omega)^n\ ]^{-1} \quad (4)$$

The CPE represents a capacitor and a resistor for n= 1 and n= 0, respectively, while it is associated with a diffusion process when n= 0.5. The CPE impedance is attributed to the distributed surface reactivity, surface heterogeneity, and roughness of the current and potential distribution, which in turn are related with the electrode geometry and the electrode porosity.[49] The Warburg impedance was included taking into account the diffusion phenomena.[50] The quality of fitting was evaluated using the error percentage associated to each circuit component, errors smaller than 5% being obtained in all cases.

Table 2 shows the simulated values obtained by fitting the EIS experimental spectra presented in Fig. 9. As can be seen in Table 2, increased R_{CT} values were detected for all tested samples when the number of layers is increased. However, multilayered systems in presence of modified MMT show the highest values, which can be attributed to the presence of the distribution of the nanoclay since modified MMT exhibit better exfoliation than MMT. The presence of the last layer formed by PEDOT in the multilayered systems was found intercalated into the layers of modified MMT, which avoided and blocked the entrance of ions (ClO_4^-) increasing the ionic charge-transfer resistance (R_{CT}). Higher R_{CT} values due to the presence of clays produce also a barrier effect, consequently, the clay incorporated in the polymeric matrix reflects a higher loss of electrochemical properties. According to Table 1, the electroactivity decreases when the number of layers, being the difference more remarkable in the case of ml-PEDOT/PPy-Mod MMT (20%) systems. Another important feature of the EIS analysis concerns to the Warburg element (W). The W element is associated to diffusion phenomena reflecting the same tendency observed for R_{CT}.

Table 2. *Fitting parameters used to simulate the EIS data obtained for the multilayered nanocomposites as prepared studied in this work (Figure 9).*

System	Rs^{a}	$CPE_1{}^{b}$	n_1	$R_{CT}{}^{d}$	W^{e}	$C_{PS}{}^{f}$
20 %						
3-ML	48.04	45.72	0.85	177.61	18.95	212.83
5-ML	43.36	38.12	0.87	520.18	129.65	342.48
7-ML	49.68	38.25	0.88	1197.26	454.90	324.16
20 % Mod						
3-ML	34.68	40.22	0.89	306.43	52.63	167.60
5-ML	53.84	42.92	0.86	794.12	177.62	403.20
7-ML	44.64	38.35	0.88	1061.63	362.97	363.65

[a] Electrolyte resistance, in $\Omega \cdot cm^2$. [b] Double layer capacitance, in $\mu F \cdot cm^{-2} \cdot s^{n-1}$. [d] Charge-transfer resistance at the polymer film–electrolyte interface, in $\Omega \cdot cm^2$. [e] Warburg resistance, in $\Omega \cdot cm^2$. [f] Faradaic pseudo-capacitance, in $mF \cdot cm^{-2}$.

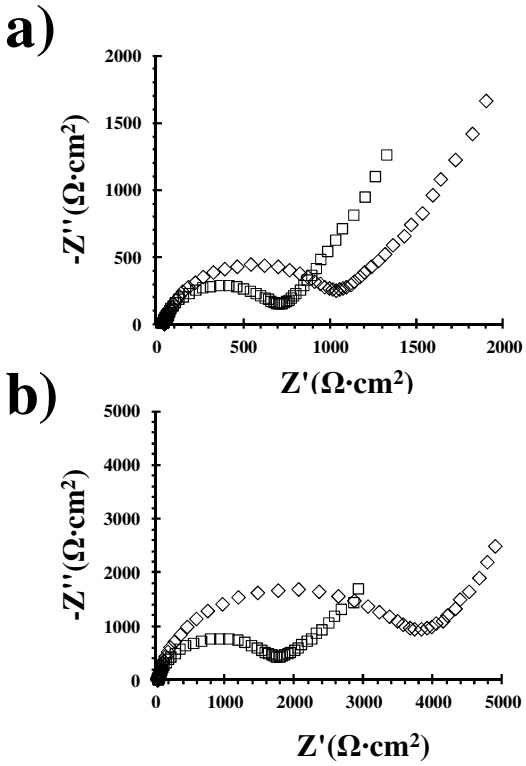

Figure 10. *Nyquist plots of ml-PEDOT/PPy nanocomposites after 1000 consecutive oxidation-reduction cycles employing a) MMT and b) modified MMT. (3-ml; empty diamonds and 5-ml; empty squares). The experimental data (represented symbols) were fitted to the equivalent circuit model depicted in Fig. 9 to produce the parameters listed in Table 3.*

As can be seen Figura 10 after electrochemical degradation all systems evidenced an increase of the charge-transfer resistance (R_{CT}). According to Table 3, the 3-PEDOT/PPy (20% Mod) systems showed the highest value, which can be attributed to its micrometric structure and the better distribution of the clay due to its chemical nature. Thus, the morphology evidenced a more compact structure for 3-PEDOT/PPy (20 % Mod) systems, where the porosity was clearly reduced. The increase of the number of layers showed a decrease of the R_{CT}, whereas the Warburg element remained constant. This effect is associated to the thickness, since it was found to be an important feature on the electrochemical properties. Another important parameter on the EIS analysis is devoted to the CPE element. 3-PEDOT/PPy (20%) systems showed the higher CPE value. This result suggest that the presence of porous and cavities is higher in these electrodes. Consequently, CPE allows to evaluate also the effective surface area for interfacial charge transport, being for the 3-PEDOT/PPy (20%) which showed the highest effective area. Table 3 evidenced that Warburg element increases after electrochemical degradation in all multilayered nanocomposites.

Table 3. *Fitting parameters used to simulate the EIS data obtained for the multilayered nanocomposites studied in this work after electrochemical degradation (Figure 10).*

System	Rs[a]	CPE_1[b]	n_1	R_{CT}[d]	W[e]	C_{PS}[f]
20 %						
3-ML	48.08	56.02	0.88	960.12	303.72	322.46
5-ML	41.88	50.52	0.88	638.46	209.64	379.65
20 % Mod						
3-ML	34	47.27	0.89	3744	418.32	162.42
5-ML	53.36	44.55	0.89	1660	419.59	553.65

[a] *Electrolyte resistance, in* $\Omega \cdot cm^2$. [b] *Double layer capacitance, in* $\mu F \cdot cm^{-2} \cdot s^{n-1}$. [d] *Charge-transfer resistance at the polymer film–electrolyte interface, in* $\Omega \cdot cm^2$. [e] *Warburg resistance, in* $\Omega \cdot cm^2$. [f] *Faradaic pseudo-capacitance, in* $mF \cdot cm^{-2}$.

The anticorrosion performance of the ml-PEDOT/PPy films contanining MMT and modified MMT on the steel substrate was investigated by EIS measurements after 24h in a 3.5 % NaCl solution at OCP (Figure 11a). As can be seen in Table 4, the R_{CT} value increases when the presence of modified montmorillonite in ml-PEDOT/PPy systems, which makes difficult the access of Cl^- anions into the electrode surface. Therefore, modified clay interferes in the penetration of anions into the polymeric backbone increasing the corrosion protection. R_{CT} can be attributed to the electrical resistance against charge transfer by using coating pores, thus it can be employed to evaluate the porosity of the coating. Within this context, R_{CT} values depend on the number of pores or capillary channels perpendicular to the substrate surface, through which the electrolyte reaches the interface.[51] The SEM micrographs displayed in Fig. 11b) and Fig. 11c) show the surface of the multilayered systems after 90 days of immersion in a 3.5 % NaCl solution. The surface reflects that the porosity in 3-PEDOT/PPy (20 %) systems (Fig. 11b) is lower than 3-PEDOT/PPy (20 % Mod) (Fig. 11c). The decrease in the pore provokes the entry of electrolyte into the coating. In Figure 11c) the surface appears more compact blocking the entrance of Cl^- ions. Moreover, the morphology of 3-PEDOT/PPy (20 % Mod) systems tends to form larger agglomerates, which favor the barrier effect. Consequently, the presence of modified montmorillonite into multilayered systems inhibits the entrance of chlorides favoring the anti-corrosive properties of the coating. This tendency was corroborated by the Warburg element, where the diffusion phenomena were precluded in presence of modified montmorillonite. Table 4 shows a Warburg resistance of 57 and 125 Ω for 3-PEDOT/PPy (20 %) and 3-PEDOT/PPy (20 % Mod), respectively.

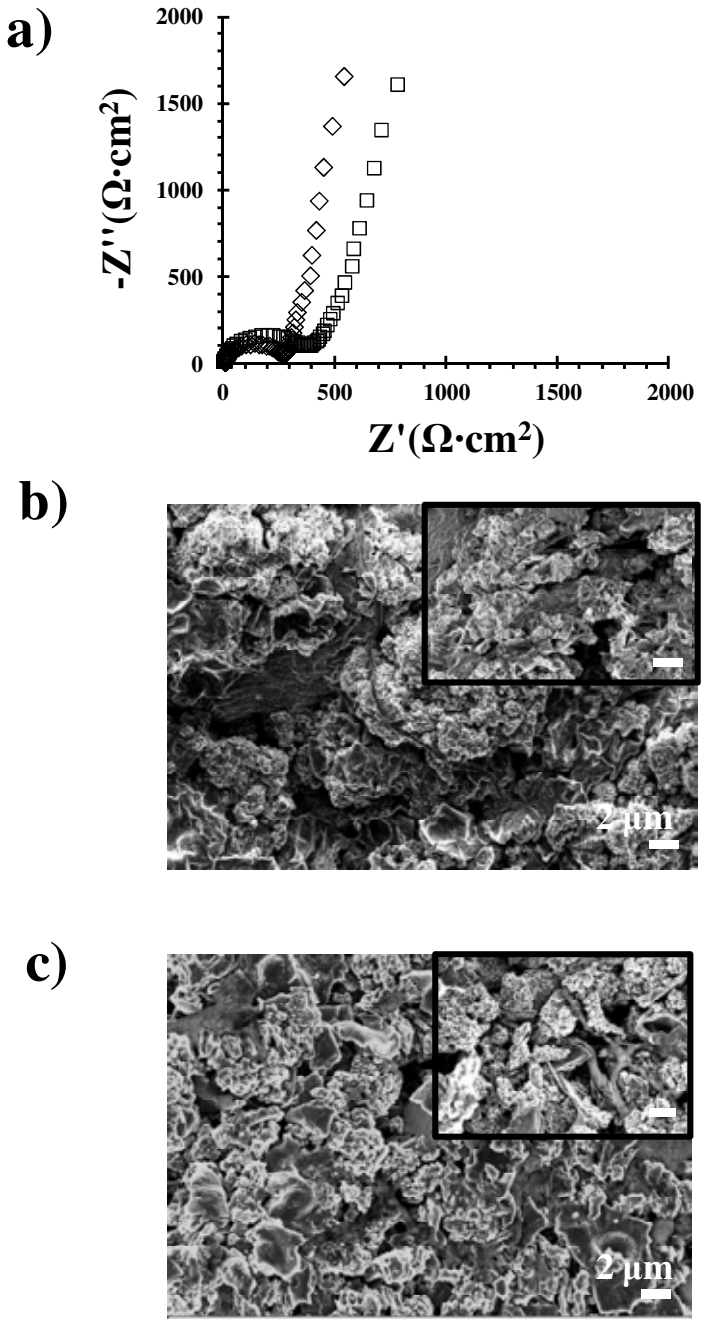

Figure 11. *a) Nyquist plots of 3-PEDOT/PPy nanocomposites using MMT (empty diamonds) and modified MMT (empty squares) after immersion in a 3.5% NaCl solution for 24 h. Films were prepared considering a total polymerization time of 300s. The experimental data (represented symbols) were fitted to the equivalent circuit model depicted in Fig. 9 to produce the parameters listed in Table 4. b) SEM micrographs of 3-PEDOT/PPy-MMT (20 %) and c) 3-PEDOT/PPy-modified MMT (20 %) after 90 days of exposure in NaCl solution. High-resolution images are shown as insets (Scale bar: 500 nm).*

Table 4. *Fitting parameters used to simulate the EIS data obtained for the multilayered nanocomposites studied in this work after corrosion test (Figure 11).*

System	Rs^{a}	$CPE_1{}^{b}$	n_1	$R_{CT}{}^{d}$	W^{e}	$C_{PS}{}^{f}$
3-ML (20%)	12.00	82.10	0.86	262.86	56.68	178.21
3-ML (20% Mod)	11.09	72.72	0.87	364.87	124.41	211.64

[a] Electrolyte resistance, in $\Omega \cdot cm^2$. [b] Double layer capacitance, in $\mu F \cdot cm^{-2} \cdot s^{n-1}$. [d] Charge-transfer resistance at the polymer film–electrolyte interface, in $\Omega \cdot cm^2$. [e] Warburg resistance, in $\Omega \cdot cm^2$. [f] Faradaic pseudo-capacitance, in $mF \cdot cm^{-2}$.

5.3.4. Conclusions

Multilayered nanocomposites have been successfully synthesized by using the electrochemical LbL technique. *In situ* electrochemical polymerization evidenced exfoliated morphologies in all studied systems. The main conclusions of this work are summarized as follows:

a) The highest specific capacitance was performed for 3-PEDOT/PPy (20 %) systems, although this electrochemical parameter decreased when the number of layers increased. This behavior was evidenced for all systems. The overall electrochemical properties in terms of electroactivity and specific capacitance are indicated as follows: 3-PEDOT/PPy (20 %) > 3-PEDOT/PPy (20 % Mod) > 3-PEDOT/PPy. On the other hand, the electrochemical stability is displayed as: 3-PEDOT/PPy > 3-PEDOT/PPy (20 %) > 3-PEDOT/PPy (20 % Mod).

b) The morphology of nanocomposites reflects important differences, which were related with their electrochemical properties. Thus, porosity played a key role on the capacitive properties. The effect of clay influences on the morphology modifying some structural properties such as the arrangement of the polymeric chains.

c) The multilayered nanocomposites showed a clear synergistic effect produced by alternating layers of different chemical nature. The results provided in this work reflected that multilayered nanocomposites exhibit better electrochemical properties than those of single homopolymer films.

d) Higher electrical conductivity values were achieved for the multilayered systems without clay. Again, the electrical conductivity reduced dramatically when the number of layers increased. The electrical stability and electrical conductivity are properties affected mainly by the presence of clay. The 3-PEDOT/PPy (20 % Mod) systems evidenced the lowest conductivity and electrical stability.

e) The results reported in this work demonstrated that 3-PEDOT/PPy (20% Mod) films present the best corrosion protection properties. EIS studies evidenced s a key role on the corrosion field. Consequently, modified montmorillonite induces the formation of compact structures, which precludes the entrance of chloride anions.

5.3.5. References

[1]. Sanchez, C.; Julián, B.; Belleville, P.; Popall, M. *J. Mater. Chem.* **2005**, *15*, 3559.

[2]. Lu, X.; Zhang, W.; Wang, C.; Wen, T-C.; Wei, Y. *Prog. Polym. Sci.* **2011**, *36*, 671.

[3]. Chen, B.; Evans, J. R. G. *Soft Matter* **2009**, *5*, 3572.

[4]. Chan, M.; Lau, K.; Wong, T.; Ho, M.; Hui, D. *Composites Part B* **2011**, *42*, 1708.

[5]. Okada, A.; Usuki, A. *Macromol. Mater. Eng.* **2006**, *291*, 1449.

[6]. Aranda, P.; Darder, M.; Fernandez – Saavedra, R.; López-Blanco, M.; Ruiz-Hitzky, E. *Thin Solid Films* **2006**, *495*, 104.

[7]. Yeh, J-M.; Chang, K-C. *J. Ind. Eng. Chem.* **2008**, *14*, 275.

[8]. Zhang, D.; Zhou, C-H.; Lin, C-X.; Tong, D-S.; Yu, W-H. *App. Clay Sci* **2010**, *50*, 1.

[9]. Mousty, C. *App. Clay Sci.* **2004**, *27*, 159.

[10]. Njuguna, J.; Pielichowski, K. *Adv. Eng. Mater.* **2004**, *6*, 193.

[11]. Bergaya, F.; Theng, B. K. G.; Lagaly, G. *Handbook of clay science. Chapter 10.3: "Clay Mineral – and Organoclay-Polymer Nanocomposites"* **2006**, Ed. Elsevier.

[12]. Gangopadhyay, R.; De, A. *Chem. Mater.* **2000**, *12*, 608.

[13]. Bober, P.; Stejskal, J.; Spirkova, M.; Trchova, M.; Varga, M.; Prokes, J. *Synth. Met.* **2010**, *160*, 2596.

[14]. Olad, A.; Rashidzadeh, A. *Prog. Org. Coat.* **2008**, *62*, 293.

[15]. Yeh, J-M.; Liou, S-J.; Lai, C-Y.; Wu, P-C.; Tsai, T-Y. *Chem. Mater.* **2001**, *13*, 1131.

[16]. Hosseini, M. G.; Jafari, M.; Najjar, R. *Surf. Coat. Technol.* **2011**, *206*, 280.

[17]. Van Hoang, H.; Holze, R. *Chem. Mater.* **2006**, *18*, 1976.

[18]. do Nascimento, G. M.; Constantino, V. R. L.; Temperini, M. L. A. *Macromolecules* **2002**, *35*, 7535.

[19]. Kim, B-H.; Jung, J-H.; Hong, S-H.; Joo, J.; Epstein, A. J.; Mizoguchi, K.; Kim, J. W.; Choi, H. J. *Macromolecules* **2002**, *35*, 1419.

[20]. Narayanan, B. N.; Koodathil, R.; Gangadharan, T.; Yaakob, Z.; Saidu, F. K.; Chandralayam, S. *Mat. Sci. Eng. B* **2010**, *168*, 242.

[21]. Boukerma, K.; Piquemal, J.-Y.; Chehimi, M.; Mravcakova, M.; Omastova, M.; Beaunier, P. *Polymer* **2006**, *47*, 569.

[22]. Hong, S. H.; Kim, B. H.; Joo, J.; Kim, J. W.; Choi, H. J. *Curr. Appl. Phys.* **2001**, *1*, 447.

[23]. Mravcakova, M.; Boukerma, K.; Omastova, M.; Chehimi, M. M. *Mat. Sci. Eng. C* **2006**, *26*, 306.

[24]. Kim, B. H.; Jung, J. H.; Hong, S. H.; Joo, J.; Epstein, A. J.; Mizoguchi, K.; Kim, J. W.; Choi, H. J. *Macromolecules* **2002**, *35*, 1419.

[25]. Kim, J. W.; Liu, F.; Choi, H. J.; Hong, S. H.; Joo, J. *Polymer* **2003**, *44*, 289.

[26]. Liu, Y. C.; Ger, M. D. *Chem. Phys. Lett.* **2002**, *362*, 491.

[27]. Liu, Y. C.; Tsai, C. J. *Chem. Mater.* **2003**, *15*, 320.

[28]. Rajapakse, R. G. M.; Murakami, K.; Bandara, H. M. N.; Rajapakse, R. M. M. Y.; Velauthamurti, K.; Wijeratne, S. *Electrochim. Acta* **2010**, *55*, 2490.

[29]. Hosseini, M. G.; Raghibi – Boroujeni, M.; Ahadzadeh, I.; Najjar, R.; Dorraji, M. S. S. *Prog. Org. Coat.* **2009**, *66*, 321.

[30]. Kuila, B. K.; Nandi, A. K. *Macromolecules* **2004**, *37*, 8577.

[31]. Ballav, N.; Biswas, M. *Synth. Met.* **2004**, *142*, 309.

[32]. Aradilla, D.; Estrany, F.; Azambuja, D. S.; Casas, M. T.; Puiggali, J. Ferreira, C. A.; Alemán, C. *Eur. Polym. J.* **2010**, *46*, 977.

[33]. Groenendaal, L. B.; Jonas, F.; Freitag, D.; Pielartzik, H.; Reynolds, J. R. *Adv. Mater.* **2000**, *12*, 481.

[34]. Kirchmeyer, S.; Reuter, K. *J. Mater. Chem.* **2005**, *15*, 2077.

[35]. Pettersson, L.; Johansson, T.; Carlsson, F.; Arwin, H.; Inganas, O. *Synth. Met.* **1999**, *101*, 198.

[36]. Letaïef, S.; Aranda, P.; Fernández-Saavedra, R.; Margeson, J. C.; Detelliera, C.; Ruiz-Hitzky, E. *J. Mater. Chem.* **2008**, *18*, 2227.

[37]. Rajapakse, R. G. M.; Higgins, S.; Velauthamurty, K.; Bandara, H. M. N.; Wijeratne, S.; Rajapakse, R. M. M. Y. *J. Compos. Mater.* **2010**, *45*, 597.

[38]. Aradilla, D.; Azambuja, D.; Estrany, F.; Casas, M. T.; Ferreira, C. A.; Alemán, C. *J. Mater. Chem.* **2012**, *22*, 13110.

[39]. Sarioglan, S. *Particul. Sci. Technol.* **2012**, *30*, 68.

[40]. Kepas, A.; Grzeszczuk, M. *J. Electroanal. Chem.* **2005**, *582*, 209.

[41]. Tan, C. K.; Blackwood, D. J. *Corros. Sci.* **2003**, *45*, 545

[42]. Han, G.; Shi, G. *Sens. Actuators B* **2004**, *99*, 525

[43]. Zainudeen, U. L.; Careem, M. A.; Skaarup, S. *Sens. Actuators B* **2008**, *134*, 467

[44]. Estrany, F.; Aradilla, D.; Oliver, R.; Alemán, C. *Eur. Polym. J.* **2007***, 43*, 1876.

[45]. Estrany, F.; Aradilla, D.; Oliver, R.; Armelin, E.; Alemán, C. *Eur. Polym. J.* **2008**, *44*, 1323.

[46]. Aradilla, D.; Estrany, F.; Oliver, R.; Alemán, C. *Eur. Polym. J.* **2010**, *46*, 2222.

[47]. Aradilla, D.; Estrany, F.; Alemán, C. *J. Phys. Chem. C* **2011**, *115*, 8430.

[48]. Li, N.; Shan, D.; Xue, H. *Eur. Polym. J.* **2007**, *43*, 2532.

[49]. Jorcin, J.-B.; Orazen, M. E.; Pébère, N.; Tribollet, B. *Electrochim. Acta* **2006**, *51*, 1473.

[50]. Walter, G. W. *Corros. Sci.* **1986**, *26*, 681.

[51]. Amirudin, A. ; Thierry, D. *Prog. Org. Coat.* **1995**, *26*, 1.

Chapter 6. Cyanoalkylpyrroles

6.1. Characterization and properties of poly[N-(2-cyanoethylpyrrole)].[a]

6.1.1. Introduction

6.1.2. Methods

6.1.3. Results and discussion

6.1.4. Conclusions

6.1.5. References

[a]Results presented in this chapter were published in *Macromol. Chem. Phys.* **2010**, *211*, 1663.

6.2. Structural and electronic properties of poly[N-(2-cyanoalkylpyrrole)]s bearing small alkyl groups.[b]

6.2.1. Introduction

6.2.2. Methods

6.2.3. Results and discussion

6.2.4. Conclusions

6.2.5. References

[b]Results presented in this chapter were published in *J. Phys. Chem. B* **2011**, *115*, 2882.

6.3. Understanding of interaction mechanisms in organic solvent vapor sensors based on pyrrole derivatives.

6.3.1. Introduction

6.3.2. Methods

6.3.3. Results and discussion

6.3.4. Conclusions

6.3.5. References

6.1. Characterization and properties of poly[N-(2-cyanoethylpyrrole)]

6.1.1. Introduction

Polypyrrole (PPy), which can be prepared using electrochemical or chemical polymerization methods,[1-4] is among the most extensively used conducting polymers because of its versatile properties: redox activity,[5] ability to form nanowires with room temperature conductivity ranging from 10^{-4} to 10^{-2} $S \cdot cm^{-1}$,[6] ion-exchange and ion discrimination capacities,[7,8] electrochromic effects depending on electrochemical polymerization conditions and charge/discharge processes,[9] strong absorptive properties towards gases,[10] proteins,[11] DNA,[12] catalytic activity,[13-15] ability to protect against corrosion,[16,17] etc. Most of these properties depend on both the synthesis procedure and the properties of the dopant ions. The technological applications of PPy as electrochemical biological sensor, electrically addressable tissue/cell support substrate, ion-to-electron transducers and sensing membranes in solid-state ion-selective electrodes, etc. have been recently reviewed.[18-20]

Among PPy derivatives, a particular interest in poly(N-methylpyrrole) (PNMPy), a well known material with higher oxidation potential than PPy has been studied,[21-24] which has been used to prepare multilayered materials with excellent electrochemical properties.[25,26] Specifically, the electroactivity and electrochemical stability of multilayered films formed by alternated layers of poly(3,4-ethylenedioxythiophene) (PEDOT) and PNMPy, hereafter denoted ml-PEDOT/PNMPy, were found to be significantly higher than those of the pure polymers. Moreover, the electrical conductivity of ml-PEDOT/PNMPy, which were prepared using a layer-by-layer electrodeposition technique, was several orders of magnitude higher than those of copolymers prepared from mixtures of 3,4-ethylenedioxythiophene (EDOT) and N-methylpyrrole (NMPy) with different concentration ratios.[27,28]

On the other hand, the cyano group is a strong electron-withdrawing substituent able to modify the electronic properties of heterocyclic conducting polymers when it is incorporated at the β-position of thiophene and pyrrole repeating units.[29,30] Thus, this substituent perturbs the π-conjugated system of such polymers reducing the barrier for electron injection, increasing the oxidation potential and improving the electron

transport properties. On the other hand, in an early study the cyano functionality was used to improve the abilities of PPy derivatives as selective gas sensors by incorporating it at the N-position of pyrrole repeating units.[31-33] Specifically, poly[N-(2-cyanoethyl)pyrrole] (PNCPy; Scheme 1) films were prepared by electrochemical polymerization and preliminary characterized by cyclic voltammetry and scanning electron microscopy, even though the investigations reported in such studies were mainly focused on the utility of PNCPy to detect organic vapors,[31-33] to develop impedimetric immunosensors[34] and to prepare membranes for ion separation.[35] However, in spite of its potential applicability as selective sensor, the knowledge about the chemical and physical properties of PNCPy is very scarce.

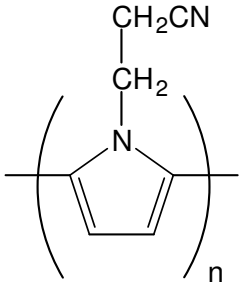

PNCPy

Scheme 1

In this work a comprehensive study of PNCPy providing an exhaustive characterization of the electrochemical, physical, electrical, structural and morphological properties of the oxidized material (doped form) and the reduced material (undoped form) is presented. Furthermore, the electroactivity and electrostability of 3-layered films formed by PNCPy and PEDOT have been explored. Results, which are essential for the fabrication of molecular condensers based on organic conducting polymers have been compared with those recently obtained for ml-PEDOT/PNMPy.[25,26]

6.1.2. Methods

N-(2-cyanoethyl)pyrrole (NCPy) and acetonitrile of analytical reagent grade were purchased from Aldrich and used without further purification. Anhydrouslithium perchlorate, analytical reagent grade, fromAldrich was stored in an oven at 80 ºC before usein the electrochemical trials. Anodic polymerization of NCPy was studied by cyclic

voltammetry (CV), chronopotentiometry (CP) and chronoamperometry (CA) using a VersaStat II potenciostat-galvanostat connected to a computer controlled through a Power Suite Princenton Applied Research program. Electrochemical experiments were conducted in a three-electrode two-compartment cell under nitrogen atmosphere (99.995% in purity) at 25ºC. The anodic compartment was filled with 40 ml of a 10 mM monomer solution in acetonitrile containing 0.1 M $LiClO_4$ as supporting electrolyte. A volume of 10 ml of the same electrolyte solution was placed in the cathodic compartment. Steel AISI 316 sheets of 4 cm^2 area were employed as working and counter electrodes. In order to avoid interferences during the electrochemical analyses, the working and counter electrodes were cleaned with acetone before each trial. The reference electrode was an Ag|AgCl electrode containing a KCl saturated aqueous solution (E^o = 0.222 V at 25 ºC), which was connected to the working compartment through a salt bridge containing the electrolyte solution.

Films of PNCPy doped with ClO_4^-, were electrogenerated by CA considering different polymerization times (t_{pol}). The weight of the insoluble polymer films (W_{ox}) was determined as the difference between the masses of the coated and uncoated electrodes using a COBOS analytical balance with a precision of 10^{-4} g. Samples for analysis were obtained by scratching their deposits from the working steel electrode. The resulting powders were placed in a filter, rinsed with bidistilled water and ethanol, and subsequently dried under vacuum conditions for 24 h.

Composition analyses were carried out with a Carlo Erba NA 1500 CHNO elemental analyzer. The percentage of ClO_4^- in each collected sample was obtained from reduction of approximately 2 mg of polymer with carbon, followed by determination of the amount of chloride ions released by standard ion chromatography. This analysis was performed with a Kontron 600 HPLC liquid chromatograph fitted with a Waters IC-PaK anion column at 30 ºC and equipped with a Wescan conductimeter detector. The density of the polymer was determined by the flotation method from chloroform/1,2-dichloroethane mixtures in which it is insoluble . The electrical conductivity of the polymer was determined using the sheet-resistance method with a previously described procedure.[36]

FTIR spectra were recorded on a FTIR 4100 Jasco spectrophotometer with a resolution of 4 cm^{-1} in the absorbance mode. The samples were placed in an attenuated total reflection accessory with thermal control and a diamond crystal (Golden Gate

Heated Single Reflection Diamond ATR, Specac-Teknokroma). Thermogravimetric analysis (TGA) was carried out with a Perkin-Elmer TGA-6 thermobalance at a heating rate of 15 K/min.

X-ray powder diffraction data were collected using a horizontally mounted cylindrical position-sensitive detector INEL CPS-120 equipped with a INEL CRY950 cryostat (80-500 K). The detector, which was used in Debye-Sherrer geometry, consisted of 4096 channels, the angular step being 0.029º (2q). Scanning electron microscopy (SEM) micrographs of the films surface were carried out with a Focused Ion Beam Zeiss Neon40 scanning electron microscope equipped with an energy dispersive spectroscopy (EDS) system and operating at 3 kV. Tapping-mode AFM measurements were carried out with a Molecular Imaging PicoSPM using a NanoScope IIIa controlled in ambient conditions.

6.1.3. Results and discussion

Synthesis of oxidized PNCPy. The cyclic voltammogram recorded for the anodic oxidation of a 10 mM NCPy solution in acetonitrile with 0.1 M $LiClO_4$ is displayed in Figure 1. An anodic process, O_1, with anodic peak potential E_p^a (O_1) = 1.75 V is detected. PNCPy films grew on the working electrode when the monomer began to be oxidized from potentials higher than 1.25 V. Furthermore, the reduction scan shows a reduction peak, R_1, with cathodic peak potential E_p^c (R_1) = 0.56 V indicating the formation of electroactive polarons in the range of potentials investigated, *i.e.* from -0.50 to 1.80 V.

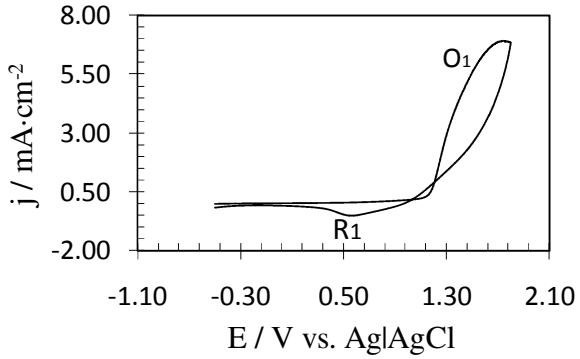

Figure 1. *Cyclic voltammogram for the oxidation of a 10^{-2} M NCPysolution in acetonitrile with 0.1M LiClO4 on a 4 cm^2 steel electrode.Initial and final potentials: -0.50 V; reversalpotential: 1.80 V. Scan rate: 100 mV s^{-1}. Temperature: 25 ºC.*

Potentials comprised between 1.30 and 1.60 V are suitable for the anodic electrogeneration of PNCPy because of the following two reasons: (i) the anodic current density in this potential range varies from 3.0 $mA \cdot cm^{-2}$ (1.30 V) to 6.5 $mA \cdot cm^{-2}$ (1.60 V) ensuring a fast polymerization process; and (ii) the potentials comprised in this interval are lower than $E_p^a(O_1)$, which is essential to avoid the overoxidation of the generated material. A constant potential of 1.40 V was selected for the generation of PNCPy by CA, this value being identical to that previously used for the electropolymerization of PNMPy[27] and PEDOT.[37] Figure 2 displays the chronoamperogram obtained for the oxidation of a 10 mM NCPy solution in acetonitrile with 0.1 M $LiClO_4$. The current density stabilizes at 0.75 $mA \cdot cm^{-2}$. Although this value is lower than those obtained for PNMPy[27]and PEDOT[37] using identical experimental conditions (2.28 and 1.82 $mA \cdot cm^{-2}$, respectively), it indicates that the flow of diffused monomer is considerably high. Uniform, adherent, insoluble and dark-green polymer films grew on the working electrodes.

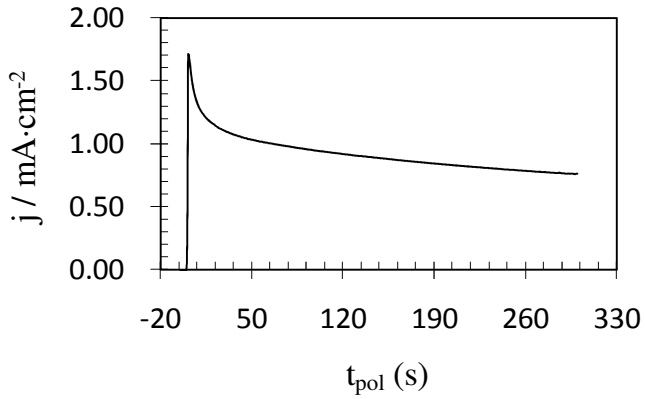

Figure 2. *Chronoamperogram recorded for the oxidation of a 10^{-2} M NCPy solution in acetonitrile with 0.1 M $LiClO_4$ on a 4 cm^2 steel electrode by applying a constant potential of 1.40 V. Temperature: 25 ^oC.*

Electrochemical characterization of PNCPy. Films of PNCPy generated using the experimental conditions determined in the previous section and t_{pol} = 300 s were rinsed several times with acetonitrile, dried in a nitrogen flow and immersed in the electrolyte solution of the control cell for CV analysis. Figure 3 shows the control voltammogram of PNCPy recorded in the potential range from -0.50 to 1.60 V. An oxidation peak, O_1', is detected, $E_p^a(O_1')$ overlapping the oxidation potential of the medium. The cathodic scan shows two reduction peak, $R_1'$and R_2', with $E_p^c(R_1')$ = 0.07 V and $E_p^c(R_2')$ =

0.83 V. These two reduction peaks evidence the existence of another peak, $O_2^{'}$, which is also overlapping the oxidation potential of the medium. On the other hand, the control voltammogram indicates that the current density through the electrode is negligible for potentials lower than 1.10 V growing very rapidly after such value, *i.e.* the current density is 0.62 mA·cm^{-2} for a potential of 1.60 V. This variation suggests that PNCPy may be appropriated for technological applications based on the control of the current flow, *e.g.* electric circuit components to block the current flow below a potential of 1.10 V.

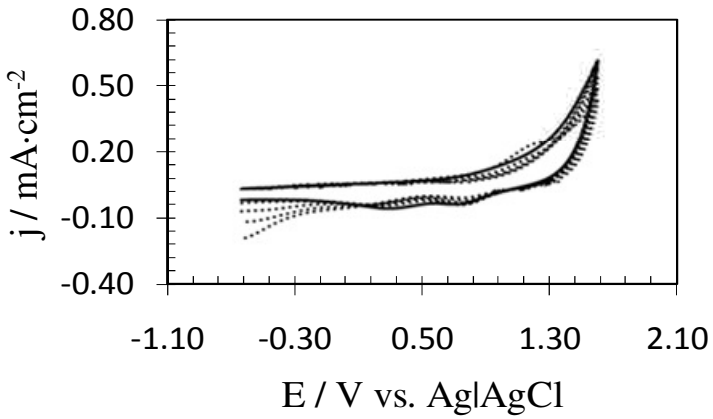

Figure 3. *Thick solid line: control voltammogram for the oxidation of a PNCPy film on 4 cm^2 steel electrode in acetonitrile with 0.1 M $LiClO_4$ at 100 mV·s^{-1} and 25 ºC. Thin dashed lines: control voltammograms for additional 24 consecutive oxidation-reduction cycles. Initial and final potentials: -0.50 V; reversal potential: 1.60 V. The film was generated for 300 s under the conditions given in Figure 2.*

The electrochemical stability of PNCPy was determined by recording the control voltammograms from -0.50 V to 1.60 V for 25 consecutive oxidation-reduction cycles (Figure 3). PNCPy shows a loss of electroactivity, the cathodic and anodic areas recorded along the 25th cycle being ~15% smaller than those recorded in the first cycle. These results indicate that the electrochemical stability of PNCPy is similar to that for PNMPy films prepared under identical experimental conditions[27] and lower than that of PEDOT.[37] On the other hand, it is should be remarked that the sharp variation detected in current density for potentials higher than 1.10 V is not altered by consecutive oxidation-reduction cycles. This repetitive behaviour is relevant for the design of potential technological applications based on the control of the current flow.

Polymerization kinetics and doping level. The kinetics for the anodic polymerization of PNCPy was investigated by generating films under a constant

potential of 1.40 V and considering different t_{pol} values, *i.e.* 300, 500, 700, 900, 1100, 1300 and 1500 s. Reproducible film weights, W_{ox} (in $mg \cdot cm^{-2}$), were always obtained until a t_{pol} of 700 s. The polymerization charge, Q_{pol} (in $mC \cdot cm^{-2}$), consumed in each process was directly calculated on each chronoamperogram. The variation of W_{ox} against Q_{pol} is represented in Figure 4 providing a linear correlation with an excellent regression coefficient ($R^2 = 0.99$). This is consistent with a faradic process. The slope of this plot corresponds to the current productivity, which is expressed as mg of PNCPy electrogenerated per Coulomb of charge consumed during the anodic polymerization process. Thus, the resulting productivity, 0.531 $mg \cdot C^{-1}$, is completely independent of the electrode area. It should be noted that this value is slightly smaller than those reported for PNMPy (0.619 $mg \cdot C^{-1}$) and, specially, PEDOT (0.875 $mg \cdot C^{-1}$) using identical experimental conditions.[36]

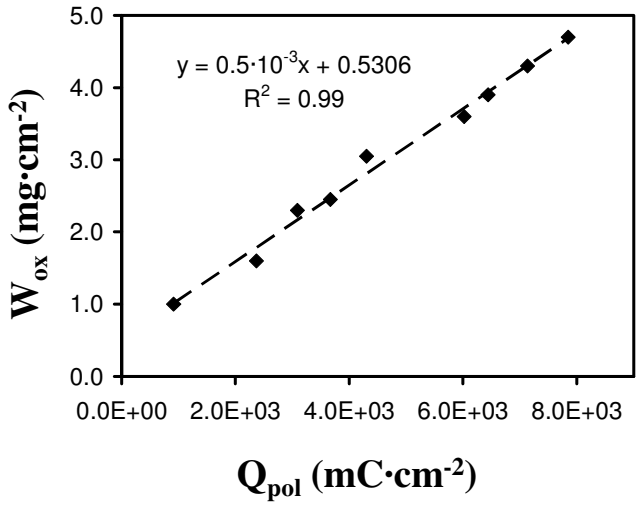

Figure 4. *Variation of the weight by area unit of PNCPy deposited on steel from a 10^{-2} M NCPy solution in acetonitrile with 0.1 M $LiClO_4$ at a constant potential of 1.40 V with polymerization charge consumed. Temperature: 25 ºC*

Elemental analysis of the electrogenerated material revealed that oxidized PNCPy contains 43.2% in weight of ClO_4^- counterions, indicating a salt structure. This feature reflects that each repeating unit contains 0.912 ClO_4^- ions, the formula of the oxidized PNCPy being $[(NCPy^{0.912+})_n(ClO_4^-)_{0.912n}]_{solid}$. Accordingly, as suggested above the doping level of PNCPy is larger than that determined for PNMPy (0.716 ClO_4^- ions) following the same procedure.[27]

Preparation of the reduced polymer: undoping process. PNCPy films generated by anodic polymerization under a constant potential of 1.40 V were reduced by CP

applying a cathodic current density -0.25 mA·cm^{-2}, *i.e.* a constant intensity of -1.0 mA on the film of 4 cm^2 area during 190 s. The color of the films changed from dark-green to yellow upon reduction. Elemental analysis of the reduced material, hereafter denoted undoped PNCPy, indicated that the weight of ClO_4^- counterions is 31.8%, which is consistent with the following formula: $[(NCPy^{0.558+})_n(ClO_4^-)_{0.558n}]_{solid}$. Thus, reduction of the electrochemically generated PNCPy led to drop the doping level in 0.354 ClO_4^- ions per repeating unit.

Figure 5 compares the control voltammograms recorded for oxidized and reduced films of PNCPy. The behavior of the two species is similar allowing the flow of anodic intensity after a potential of ~ 0.9 V. However, the potential reached by the undoped material is about 2.5 times higher than that achieved using the oxidized one. These results suggest that the potential applications in electronics of the undoped material are very promising.

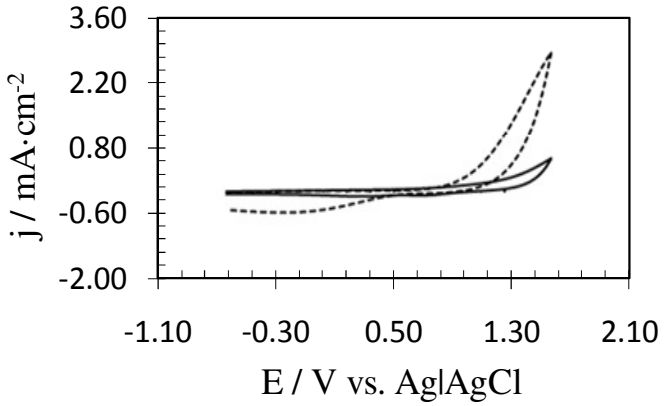

Figure 5. *Control voltammograms for one oxidation-reduction cycle of as-electrogenerated (1) and reduced (2) PNCPy films on 4 cm^2 steel electrode in acetonitrile with 0.1 M $LiClO_4$ at 100 mV·s^{-1} and 25 ºC. Initial and final potentials: -0.50 V; reversal potential: 1.60 V. The films of PNCPy were generated for 300 s under the conditions given in Figure 2. The reduced film was obtained by applying a cathodic current density of -0.25 mA·cm^{-2}*

Physical, electrical and structural properties. Solubility tests in a wide variety of organic and polar solvents showed that both oxidized and the undoped PNCPy are insoluble, which should be attributed to the formation of long molecular chains during the electrogeneration process. On the other hand, the density of oxidized PNCPy is 1.432 g·cm^{-3}, which is smaller than those obtained for PNMPy (1.595 g·cm^{-3}) and

PEDOT (1.66 $g \cdot cm^{-3}$).[27] As expected, the undoping process led to decrease the density, which was determined to be 1.404 $g \cdot cm^{-3}$ for undoped PNCPy.

The electrical conductivity (σ_o) measured for doped samples of PNCPy was $5.5 \cdot 10^{-3}$ $S \cdot cm^{-1}$. This value is practically identical to that obtained for PNMPy[28] and significantly smaller than that determined for PEDOT (σ_o = 210 $S \cdot cm^{-1}$).[37] Thus, the electrical conductivity of N-substituted PPy derivatives is five orders of magnitude smaller than that of PEDOT. Obviously, the σ_o of PNCPy decreased significantly upon reduction, *i.e.* $\sigma_o \approx 10^{-7}$ $S \cdot cm^{-1}$, which is consistent with the dropping of the doping level.

Figure 6 compares the FTIR spectra of NCPy, oxidized PNCPy and undoped PNCPy. The FTIR spectrum of the monomer (Figure 6a) shows a sharp and medium intensity absorption band at 2246 cm^{-1}, which corresponds to the C≡N stretching. Other characteristic bands of NCPy are: 1694, 1551 and 1497 cm^{-1} (pyrrole ring vibrations); 1439 cm^{-1} (CH_2); 1363 and 1082 cm^{-1} (C-H in plane vibrations in the pyrrole ring); 1286 cm^{-1} (N-C stretching); and 968 cm^{-1} (C=C out of plane deformation). Finally, the absorptions at 891 and 730 cm^{-1} correspond to the C^{β}-H and C^{α}-H out of plane bending modes, respectively, the latter sharp and strong band being used to follow the polymerization process.

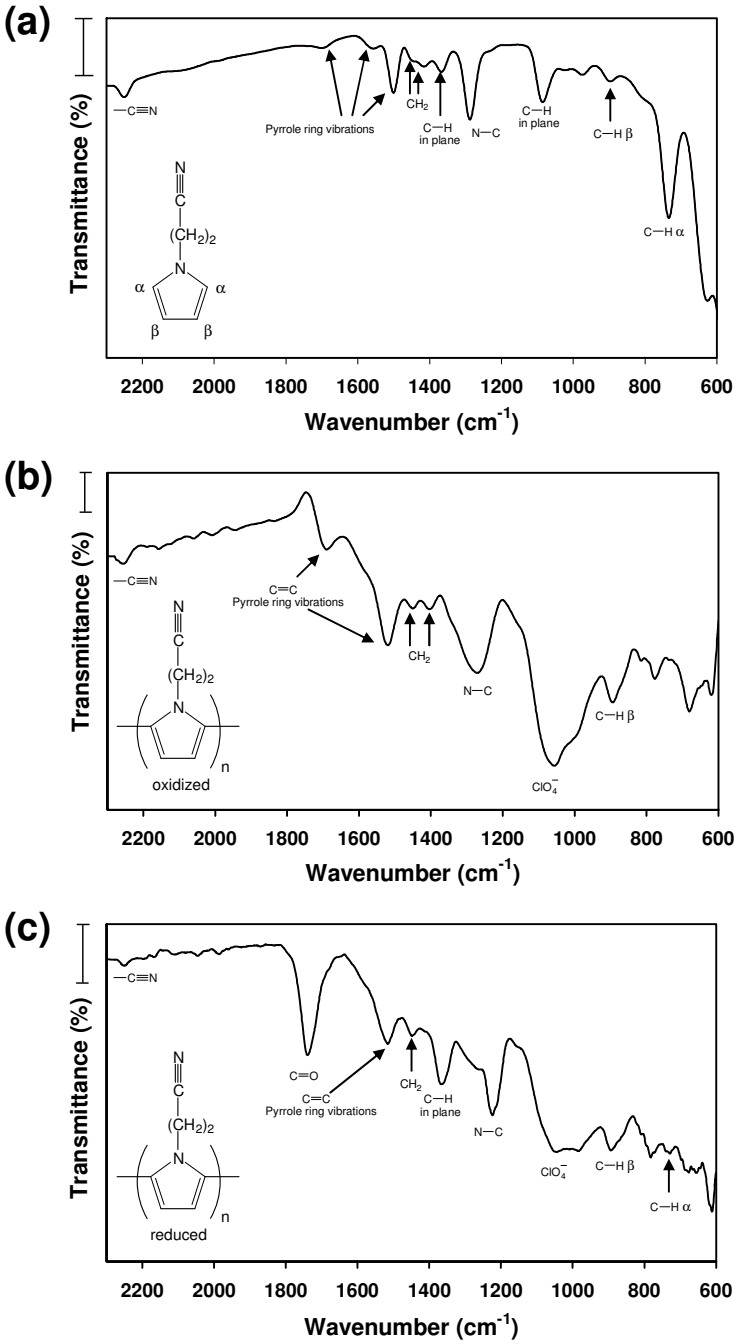

Figure 6. *FTIR spectra of the (a) NCPy monomer, (b) oxidized PCNPy and (c) reduced PNCPy. Scale bars for transmittance: 10% (a), 1% (b) and 5% (c).*

The spectrum of the oxidized PNCPy (Figure 6b) presents pyrrole ring vibrations at 1684 and 1516 cm^{-1}. These bands, which are typically found in conjugated polyenes, are very strong and well defined, as it is expected for a quinoid-like structure. The broad band at 1267 cm^{-1} may be assigned for N-C stretching band, while the peak observed at 890 cm^{-1} corresponds to the C^{β}-H out of plane vibration. The absence of signal for the C^{α}-H out of plane bending mode in the 730 cm^{-1} region confirms the polymerization of

the NCPy. On the other hand, the absorption band of the C≡N stretching appears at 2245 cm^{-1} indicating that this functional group does not undergo any oxidative process or secondary reaction during the electropolymerization. Both the significant band detected at 1050 cm^{-1}, which corresponds to the ClO_4^-, and the disappearance of the C-H in plane deformation that was identified at 1363 cm^{-1} for the monomer, reflect that the doping level is very high. This is in excellent agreement with the weight of dopant determined above for the oxidized polymer, *i.e.* elemental analysis revealed 0.912 ClO_4^- per repeating unit. Moreover, the significant weight inorganic material is responsible of the reduction in the intensity of the bands, *i.e.* the transmittance, with respect to that observed for the monomer (Figure 6a).

The FTIR spectrum of the reduced material (Figure 6c) shows an intense band at 1042 cm^{-1} evidencing that a high content of ClO_4^- remains in the polymeric matrix. However, the absorption of the C-H in plane deformation mode at 1360 cm^{-1}, which is not detected in Figure 6b, indicates that the doping level is lower than in the oxidized polymer. These results are fully consistent with the elemental analysis discussed in the previous subsection. However, the most remarkable feature of Figure 6c is the strong and sharp band at 1740 cm^{-1}, which corresponds to the stretching vibration of carbonyl groups. The origin of these CO groups is the oxidative process undergone by some five-membered rings during the preparation of the undoped PNCPy samples (Scheme 2). Although the carbonyl group typically absorbs at 1700 cm^{-1}, the conjugation with the unsaturated groups produces a shift towards a higher wavenumber. On the other hand, the low intensity band at 730 cm^{-1}, which corresponds to the C^{α}-H out of plane bending mode, indicates that the undoping also induces degradation processes in the molecular chains.

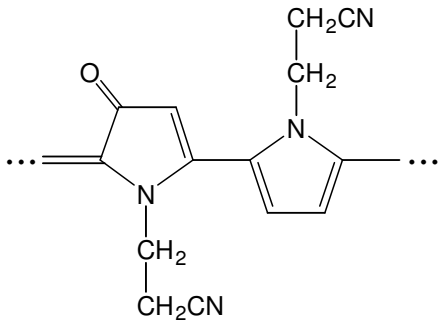

Scheme 2

The cristallinity of oxidized PNCPy was examined by X-ray diffraction (XRD). Unfortunately, processing of the samples to enhance molecular order was not possible because of their insolubility and the lack of the disability to melt (see below). The recorded XRD spectrum, which is displayed in Figure 7, indicated that the polymer doped with ClO_4^- presents some degree of structural order. More specifically, the peaks detected at $2\theta \approx 8^\circ$ and 20º, which correspond to a spacing of ~1.1 and ~0.4 nm, respectively, reflect a preferential periodic arrangement of the molecules.

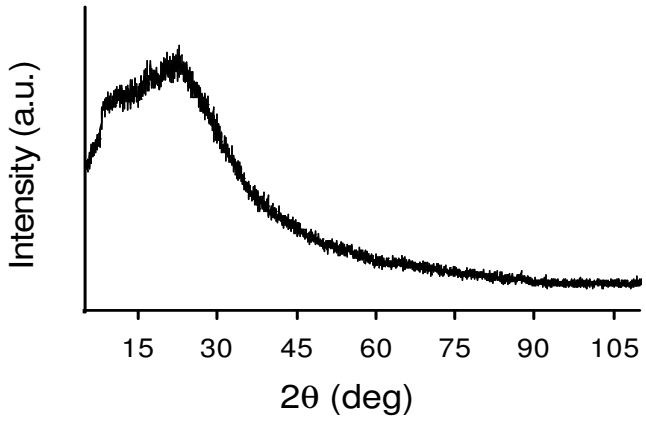

Figure 7. *X-ray spectra of the doped PNCPy film.*

Thermal stability. The TGA analysis of the oxidized PNCPy, which is displayed in Figure 8, shows three decomposition steps. The weight loss (~10%) associated with the first step corresponds to the evaporation of the acetonitrile solvent molecules trapped in the polymeric matrix, this process occurring at around 85 ºC. After this a degradation process, which corresponds to the decomposition of linear segments of polymer chains, begins at 207 ºC. Finally, at 390ºC starts a degradation process that should be attributed to the decomposition of ClO_4^-, *i.e.* the decomposition of $LiClO_4$ starts at *ca.* 400 ºC and the remanent weight at 390 ºC (45%) is very close to the weight of ClO_4^- counterions determined by elemental analysis. Thus, previous studies indicated that the electrogeneration of PPy and its N-substituted derivatives produces a significant number of chemical couplings involving the β and β' positions of the repeating units.[38] The decomposition temperature is higher for such crosslinked segments than for the linear ones.

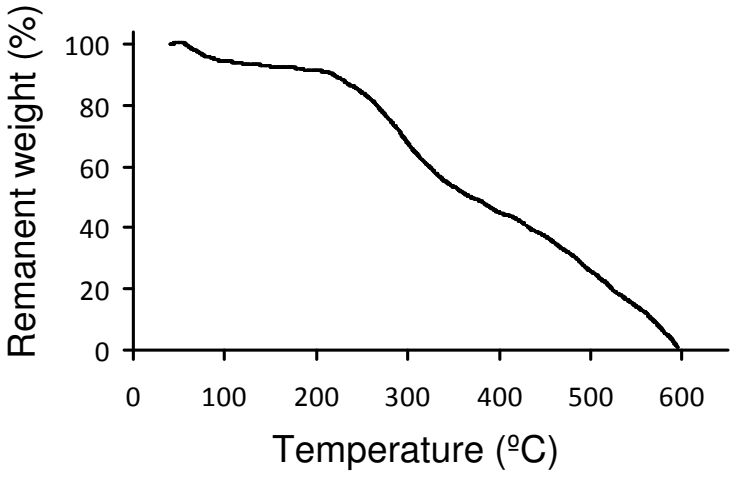

Figure 8. *Thermogravimetry of electrogenerated PNCPy.*

Morphology. Scanning electron micrographs of the oxidized PNCPy (Figure 9) indicate a heterogeneous compact structure with elliptical lumps homogeneously distributed in the surface. The regular shape of these protuberances on the surface is evidenced in the inset of Figure 9a. Moreover, a new PNCPy was prepared using the same experimental conditions but enlarging the polymerization time to t_{pol}=1500 s. The side-view of such film, which is displayed in Figure 9b, clearly shows the lumpy aspect of the surface. The thickness of this film (*l*), which pointed out by an arrow in Figure 9b, was estimated to be $l \approx 4.0$ μm.

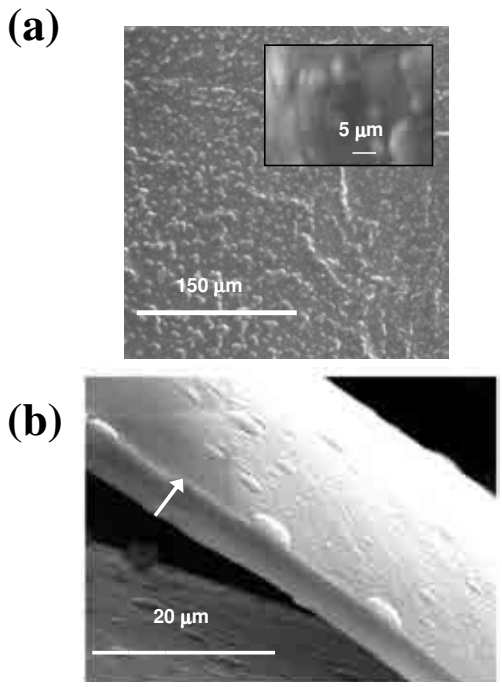

Figure 9*. SEM micrographs of PNCPy: (a) powder and (b) cross-section of a film.*

A quantitative characterization was performed by applying AFM (Figure 10a), which evidenced that the average RMS roughness (r) for the doped material is $r \approx 210$ nm. The thickness of the film (l), which was generated using t_{pol} = 300 s, was determined using a direct relationship between the mass of polymer deposited in the electrode and the polymerization charge[26] providing a value of $l \approx 1.0$ μm. This value is fully consistent with the estimation derived from SEM micrographs for films generated using t_{pol} = 1500 s.

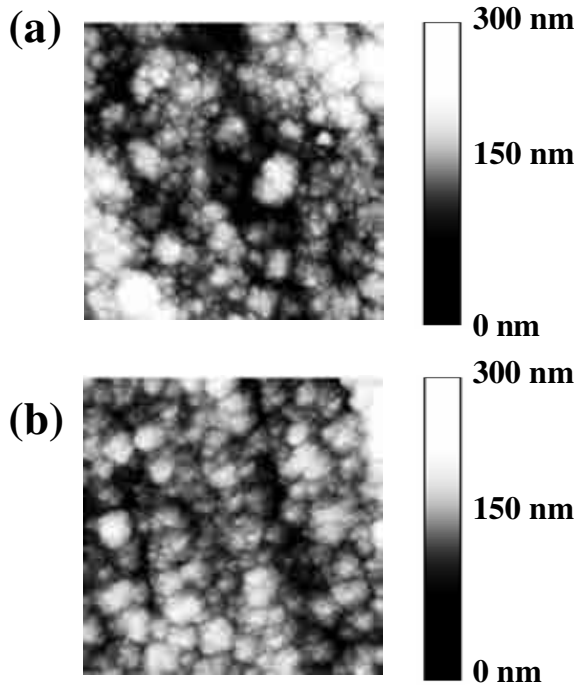

Figure 10. *AFM images of electrogenerated (a) and reduced (b) PNCPy. Scan size: 5 μm.*

Accordingly, the l / r ratio found for PNCPy films obtained using t_{pol} = 300 s, ~5, is about a half smaller than that found for PEDOT (~13) generated using identical experimental conditions ($l \approx 2.8$ μm and $r \approx 214$ nm).[26] The high l value found for PEDOT indicates the formation of linear polymer molecules growing perpendicularly to the surface of the electrode,[26] *i.e.* PEDOT molecules are exclusively formed by α,α-linkages since the dioxane ring fused onto the thiophene ring occupies the β-positions of the latter. In contrast, the l value measured for oxidized PNCPy suggests a multidirectional growing of the polymer chains due to the formation of chemical crosslinks. The lack of directional preferences along such non-regular growing process, in which polymer chains form multidirectional branches, leads to a significant reduction of the film thickness, even although the two systems show similar roughness. A recent study of PNMPy and PPy using both theoretical calculations and CV experiments

evidenced the intrinsic tendency of these materials to form chemical couplings in the β and β' positions of their repeating units,[38] which is in concordance with the results obtained for PNCPy.

On the other hand, Figure 10b displays the AFM image recorded for the undoped film of PNCPy. It is worth noting that the peaks become significantly smoother after the undoping process, even although in general terms the morphology is similar to that found for the doped material, *i.e.* consistent with a multidirectional growing. On the other hand, the escape of the dopant anions produces a drastic reduction of the average RMS roughness ($r \approx 31$ nm), which becomes one order of magnitude smaller than identified for the oxidized PNCPy.

Multilayered systems. As was mentioned in the introduction, one of current research aims consists on the development of multilayered systems formed by alternated layers of two different conducting polymers,[25,26] which were found to present higher electroactivity and electrostability than the corresponding individual materials. Multilayered systems have been shown to be useful for different technological applications, *e.g.* ml-PEDOT/PNMPy is more effective as anticorrosive additive of conventional organic coatings than pure PEDOT and PNMPy[39] and biological assays demonstrated that this material is a potential candidate to replace some electronic components of orthopedic devices.[40] In this section, the benefits of multilayered systems formed by PNCPy and PEDOT with respect not only to the pure polymers but also to ml-PEDOT/PNMPy have been examined.

3-Layered systems formed by PNCPy and PEDOT were generated at 25º C under a constant potential of 1.4 V using a layer-by-layer electrodeposition procedure, which was previously detailed.[25] Two 3-layered systems were prepared: PEDOT/PNCPy/PEDOT and PNCPy/PEDOT/PNCPy, where the first polymer is in contact with the electrode. The polymerization time was t_{pol}= 100 s per layer, results being compared with those obtained for PEDOT and PNCPy generated using t_{pol}= 300 s, and with those reported for 3-layered PEDOT/PNMPy/PEDOT (t_{pol}= 100 s per layer). [25] The adherence between PEDOT and PNCPy layers was excellent, no separation between layers being detected when the 3-layered films were scrapped to take off them from the electrodes. It should be mentioned that the formation of multilayered films constituted by PEDOT and PNMPy was recently investigated in detail using AFM.[41] In this work the formation of the each layer in PEDOT/PNCPy/PEDOT and

PEDOT/PNMPy/PEDOT has been evidenced by the following procedures: (a) visual inspection of the color, *i.e.* PEDOT, PNCPy and PNMPy layers are blue, dark green and black, respectively; and (b) energy dispersive X-ray analysis, which was performed in conjunction with SEM analysis, to identify the elemental composition.

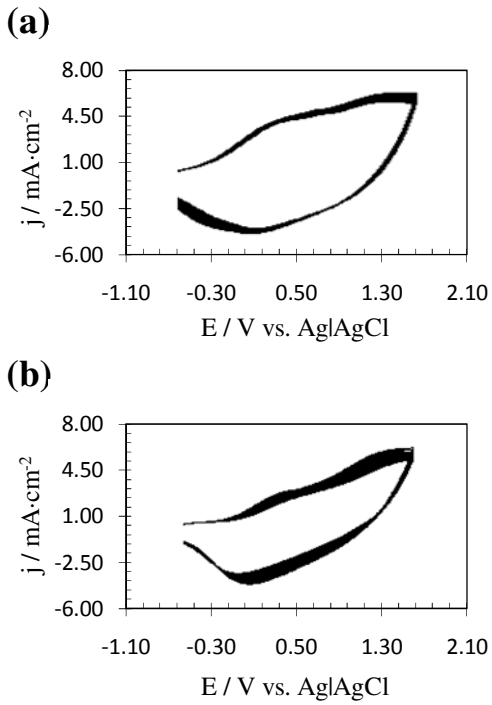

Figure 11. *Control voltammograms for 25 consecutive oxidation-reduction cycles of (a) PEDOT/PNCPy/PEDOT and (b) PNCPy/PEDOT/PNCPy 3-layered systems. Voltammograms were recorded using a 4 cm^2 steel electrode in acetonitrile with 0.1 M $LiClO_4$ at 100 $mV \cdot s^{-1}$ and 25 ºC. Initial and final potentials: -0.50 V; reversal potential: 1.60 V.*

Figure 11 shows 25 consecutive oxidation-reduction cycles recorded in the potential range from -0.5 to 1.6 V for PEDOT/PNCPy/PEDOT and PNCPy/PEDOT/PECPy films. The electroactivity of the two 3-layered systems is higher than that of pure PEDOT[37] and PNCPy (Figure 3), the improvement with respect to the latter being particularly significant. Furthermore, the electrochemical stability of the two 3-layered films, and especially of the PEDOT/PNCPy/PEDOT one, is very high. Thus, about 89% and 72% of the initial cathodic and anodic areas are retained after 25 consecutive oxidation-reduction cycles for PEDOT/PNCPy/PEDOT and PNCPy/PEDOT/PNCPy films, respectively. The electroactivity and the electrostability of PEDOT/PNCPy/PEDOT are slightly higher than that obtained for PEDOT/PNMPy/PEDOT.[25] Accordingly, PNCPy is a potential candidate to replace PNMPy in the fabrication of molecular devices with a

high ability to store charge, *i.e.* molecular organic condensers, based on multilayered conducting polymers.

6.1.4. Conclusions

PNCPy was prepared by anodic polymerization using a constant potential of 1.40 V and $LiClO_4$ as polyelectrolite. CV assays evidence the existence of two oxidation peaks, which overlap the oxidation potential of the medium, and two reduction peaks with $E_p^c(R_1')$= 0.07 V and $E_p^c(R_2')$= 0.83 V. The electrochemical stability and the electrical conductivity of PNCPy are similar to those reported for PNMPy electrogenerated using identical experimental conditions, while the current productivity and the doping level are lower for the former material.[27] Furthermore, the oxidized PNCPy was reduced to prepare the undoped material, which was also electrochemically and electrically characterized. Interestingly, both the oxidized and the undoped PNCPy showed a negligible flow of current density through the electrode for potentials lower than 1.10 V, while this flow increases rapidly and significantly after such potential. This particular electrochemical characteristic suggests that PNCPy is suitable for some specific applications in electronics.

TGA evidenced that the thermal degradation of PNCPy begins at 207 ºC. The *l* / *r* ratio found for PNCPy, which is significantly smaller than that reported for linear PEDOT using identical experimental conditions. Moreover, AFM images showed that PNCPy chains grow without any preferred direction indicating that chemical crosslinks induce the formation of multidirectional branches. XRD evidenced that PNCPy presentssome degree of structural order and SEM micrographs reflected a compact structure with elliptical protuberances homogeneously distributed in the surface.

Finally, the electroactivity and electrostability of PEDOT/PNCPy/PEDOT and PNCPy/PEDOT/PNCPy 3-layered systems, which were significantly higher than those recorded for films with similar thickness of pure PEDOT and pure PNCPy, suggest that PNCPy can be used to prepare molecular condensers based on multilayered films made of two conducting polymers replacing PNMPy.

6.1.5. References

[1]. Henry, M.C.; Hsueh, C. C.; Timko, B. P.; Freunda, M. S. *J. Electrochem. Soc.* **2001**, *148*, 155.

[2]. Pringle, J.; Efthimiadis, J.; Howlett, P.; Efthimiadis, J.; MacFarlane, D.; Chaplin, A.; Hall, B.; Officer, D.; Wallace, G.; Forsyth, M. *Polymer* **2004**, *45*, 1447.

[3]. Bazzaoui, M.; Martins, J. I.; Reis, T. C.; Bazzaoui, E. A.; Nunes, M. C.; Martins, L. *Thin Solid Films* **2005**, *485*, 155.

[4]. Schuhmann, W.; Lammert, R.; Uhe, B.; Schmidt, H. L. *Sens. Actuators B* **1990**, *1*, 537.

[5]. Han, D. H.; Lee, H. J.; Park, S. M. *Electrochim. Acta* **2005**, *50*, 3085.

[6]. Khomenko, V.; Frackowiak, E.; Béguin, F. *Electrochim. Acta* **2005**, *50*, 2499.

[7]. Johanson, U.; Marandi, A.; Tamm, T.; Tamm, J. *Electrochim. Acta* **2005**, *50*, 1523.

[8]. Weidlich, C.; Mangold, K. M.; Juttner, K. *Electrochim. Acta* **2005**, *50*, 1547.

[9]. Krivan, E.; Peintler, G.; Visy, C. *Electrochim. Acta* **2005**, *50*, 1529.

[10]. Chehimi, M. M.; Abel, M. L.; Perruchot, C.; Delamar, M.; Lascelles, S. F.; Armes, S. P.*Synth. Met.* **1995**, *104*, 51.

[11]. Azioune, A.; Siroti, F.; Tanguy, J.; Jouini, M.; Chehimi, M. M.; Miksa, B.; Slomkowski, S. *Electrochim.Acta* **2005**, *50*, 1661.

[12]. Saoudi, B.; Despas, C.; Chehimi, M. M.; Jammul, N.; Delamar, M.; Bessiere, J.; Walcarius, A. *Sens. Actuators B* **2000**, *62*, 35.

[13]. Raoof, J. B.; Ojani, R.; Rashid-Nadimi, S. *Electrochim. Acta* **2004**, *49*, 271.

[14]. Khomenko, V. G.; Barsukov, V. Z.; Katashinskii, A. S. *Electrochim. Acta* **2005**, *50*, 1675.

[15]. Ramanavicius, A.; Malinauskas, A.; Ramanaviciene, A. *Advanced Biomaterials for Medical Applications*, Kluwer Academic Publishers, Netherlands 2004, p. 93.

[16]. Hien, N. T. L.; Garcia, B.; Pailleret, A.; Deslouis, C. *Electrochim. Acta* **2005**, *50*, 1747.

[17]. Krstajic, N. V.; Grgur, B. N.; Jovanovic, S. M.; Vijnovic, M. W. *Electrochim. Acta* **1997**, *42*, 1685.

[18]. Ramanavicius, A.; Ramanaviciene, A.; Malinauskas, A.*Electrochim. Acta* **2006**, *51*, 6025.

[19]. Ateh, D. D.; Navsaria, H. A.; Vadgama, P. *J. R. Soc. Interface* **2006**, *3*, 741.

[20]. Bobacka, J. *Electroanalysis* **2006**, *18*, 7.

[21]. Redondo, M. I.; Sánchez de la Blanca, E.; García, M. V.; Raso, M. A.; Tortajada, J.; González-Tejera, M. J.*Synth. Met.* **2001**, *122*, 431.

[22]. Sánchez de la Blanca, E.; Redondo, M. I.; García, M. V.; Raso, M. A.; Tortajada, J.; González-Tejera, M. J. *Synth. Met.* **2003**, *139*, 145.

[23]. Cambra, A.; Redondo, M. I.; González-Tejera, M. J. *Synth. Met.* **2004**, *142*, 93.

[24]. González-Tejera, M. J.; Sánchez de la Blanca, E.; Carrillo, I.; Redondo, M. I.; Raso, M. A.; Tortajada, J.; García, M. V. *Synth. Met.* **2005**, *151*, 100.

[25]. Estrany, F.; Aradilla, D.; Oliver, R.; Alemán, C. *Eur. Polym. J.***2007**, *43*,1876.

[26]. Estrany, F.; Aradilla, D.; Oliver, R.; Armelin, E.; Alemán, C. *Eur. Polym. J.* **2008**, *44*, 1323.

[27]. Oliver, R.; Muñoz, A.; Ocampo, C.; Alemán, C.; Armelin, E.; Estrany, F. *Chem. Phys.* **2006**, *328*, 299.

[28]. Ocampo, C.; Alemán, C.; Arnedillo, M. L.; Ruíz, O.; Estrany, F. *Polym. Int.* **2007**, *56*, 803.

[29]. Gordon, K. C.; MacArthur, S.; David, G.; Clarke, T. M.; Officer, D. L.; Wagner, P.; Hall, S. B. *Synth. Met.* **2005**, *153*, 225.

[30]. Xu, J. M.; Nq, S. C.; Chan, H. S. O. *Macromolecules* **2001**, *34*, 4314.

[31]. Deng, Z.; Stone, D. C.; Thompson, M. *Can. J. Chem.* **1995**, *73*, 1427.

[32]. Deng, Z.; Stone, D. C.; Thompson, M. *Analyst* **1997**, *122*, 1129.

[33]. Deng, Z.; Stone, D. C.; Thompson, M. *Analyst* **1996**, *121*, 1341.

[34]. Ouerghi, O.; Senillou, A.; Jaffrezic-Renault, N.; Martelet, C.; Ben Ouada, H.; Cosnier, S. J. *Electroanal. Chem.* **2001**, *501*, 62.

[35]. Naji, A.; Marzin, C.; Tarrago, G.; Cretin, M.; Innocent, C.; Perzin, M.; Sarrazin, J. *J. Appl. Electrochem.* **2001**, *31*, 547.

[36]. Carrasco, J.; Brillas, E.; Fernández, V.; Cabot, P. L.; Garrido, J. A.; Centellas, F.; Rodríguez, R. M. *J. Electrochem. Soc.* **2001**, *148*, E19.

[37]. Ocampo, C.; Oliver, R.; Armelin, E.; Alemán, C.; Estrany, F. *J. Polym. Res.* **2006**, *13*, 193.

[38]. Alemán, C.; Casanovas, J.; Torras, J.; Bertran, O.; Armelin, E.; Oliver, R.; Estrany, F. *Polymer* **2008**, *49*, 1066.

[39]. Aradilla, D.; Ocampo, C.; Armelin, E.; Oliver, R.; Estrany, F.; Alemán, C. *Mater. Corr.* **2007**, *58*, 867.

[40]. del Valle, L.; Estrany, F.; Armelin, E.; Oliver, R.; Alemán. C. *Macromol. Biosci.* **2008**, *8*, 1144.

[41]. Aradilla, D.; Estrany, F.; Armelin, E.; Alemán, C. *Thin Solid Films* **2010**, *518*, 4203.

6.2. Structural and electronic properties of poly[N-(2-cyanoalkylpyrrole)]s bearing small alkyl groups

6.2.1. Introduction

Among organic conducting polymers (CPs), polypyrrole (PPy) is the most extensively applied due to its interesting properties: redox activity,[1] the ability to form supercapacitors in combination with multiwalled carbon nanotubes,[2] ion-exchange and ion discrimination capacities,[3,4] strong absorptive properties towards gases,[5] proteins,[6] DNA,[7] catalytic activity,[8,9] ability to protect against corrosion,[10,11] etc. Besides such large spectrum of applications, PPy is easy to prepare using either by electrochemical or chemical polymerization techniques.[12-15]

PPy derivates can be obtained by incorporating the substituent at the nitrogen or the carbon (3-position) atoms.[16,17] The polymers produced by polymerizing N-substituted pyrrole (Py) monomers usually present a regular structure because of the molecular symmetry, while irregular polymeric structures are typically derived from 3-substituted Py monomers. In addition, the substitution at the nitrogen atom is also more versatile because of the characteristics of the synthetic process.[17] Specifically, among N-substituted PPy derivatives, poly(N-hydroxypropylpyrrole) and poly(N-methylpyrrole) (abbreviated PNMPy) has been prepared as DNA sensors[18] (*i.e.* systems able to recognize specific DNA sequences) and micro/nano-condensers formed by alternated layers of two different conducting polymers,[19,20] respectively.

On the other hand, the incorporation of a strong electro-withdrawing substituent, such as the cyano group, at the 3-position of the thiophene or Py ring induces interesting changes in properties of the corresponding CP.[21,22] Thus, this substituent perturbs the π-conjugated system of the polyheterocycle reducing the barrier for electron injection, increasing the oxidation potential and improving the electron transport properties. Interestingly, an early study devoted to examine the ability of different PPy derivatives to detect vapor gases showed that the incorporation of the cyano group at the N-position of the Py repeating units improves the capabilities of these materials as selective gas sensors.[23-25] Specifically, poly[N-(2-cyanoethyl)pyrrole] (PNCEPy; Scheme 1) was found to be an excellent detector of molecules in the vapor phase.[23-25] More recently, PNCEPy has been used to develop impedimetric immunosensors,[26] ion-selective membranes,[27] and electrochemical nanocoatings of metallic medical devices.[28]

In spite of these potential applications, the knowledge about the chemical and physical properties of PNCEPy is, unfortunately, very scarce. Recently, a comprehensive experimental study of PNCEPy was studied,[29] which provided an exhaustive characterization of the electrochemical, physical, electrical, structural and morphological properties of the material in both the oxidized and the reduced states. Additionally, three-layered films formed by poly(3,4-ethylenedioxythiophene), abbreviated PEDOT (first and last layers), and PNCPy (middle layer) were prepared, their ability to act as microcondenser being compared with that observed for multilayered films of PEDOT and PNMPy.[18,19]

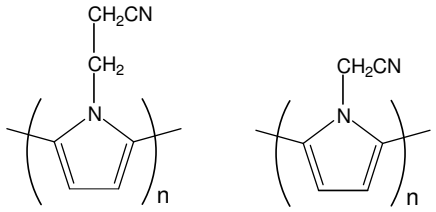

PNCEPy **PNCMPy**

Scheme 1

In this work quantum mechanical calculations was employed to propose an atomistic model for poly[N-(2-cyanoalkyl)pyrrole]s bearing short alkyl groups. Results have allowed provide not only a detailed structural model but also to determine the electronic properties of these materials, *i.e.* π-π* lowest transition energy (ε_g), ionization potential (IP), and electron affinity (EA), which remained totally unknown. Calculations have been performed considering model oligomers of poly[N-(2-cyanomethyl)pyrrole], abbreviated PNCMPy (Scheme 1), containing *n* chemical repeating units with *n* ranging from 2 to 15. Previous studies on oligomers of poly(N-hydroxyalkylpyrrole)s with alkyl = methyl, ethyl and propyl evidenced that the length of the alkyl group has a negligible effect on the structural and electronic properties.[30] This characteristic is expected to be also valid for poly[N-(2-cyanoalkyl)pyrrole]s bearing short alkyl groups. On the other hand, the electronic properties, calculated for PNCMPy have been compared with those experimentally determined for PNCEPy using UV-vis spectroscopy and cyclic voltammetry (CV).

6.2.2. Methods

Experimental Methods. N-(2-cyanoethyl)pyrrole (NCEPy) and acetonitrile of analytical reagent grade were purchased from Aldrich and used without further purifications. Anhydrous lithium perchlorate, analytical reagent grade, from Aldrich was stored in an oven at 80 ºC before use in the electrochemical trials. PNCEPy films were prepared by chronoamperometry (CA) using a polymerization time of 300 s and, subsequently, studied by cyclic voltammetry (CV) using a VersaStat II potenciostat-galvanostat connected to a PC computer controlled through a Power Suite Princeton Applied Research Program. All electrochemical experiments were conducted in a three-electrode two-compartment cell under nitrogen atmosphere (99.995% in purity) at 25 ºC. The anodic and cathodic compartments were filled with 40 and 10 mL of a 0.1 M monomer solution in acetonitrile containing 0.1 M $LiClO_4$ as supporting electrolyte, respectively. Steel AISI 316 sheets of 4 cm^2 area were employed as working and counter electrodes. In order to avoid interferences during the electrochemical analyses, the working and counter electrodes were cleaned with acetone before each trial. The reference electrode of Ag|AgCl|sat-KCl was connected to the working compartment through a salt bridge containing a KCl saturated aqueous solution (E^0=0.222 V *vs.* standard hydrogen electrode at 25 ºC).

The recorded cyclic voltammograms were used to estimate the electrochemical IP and EA through the empirical relationship previously proposed by Brédas *et al.*:[31]

$$IP = \Phi_{ox} + 4.4\ eV \quad (1)$$

$$EA = \Phi_{red} + 4.4\ eV \quad (2)$$

where Φ_{ox} and Φ_{red} are the onset potentials for oxidation and reduction, respectively, relative to Ag|AgCl electrode. The electrochemical ε_g was determined as difference between the electrochemical IP and EA.

The optical ε_g was derived from the UV-vis spectra of reduced material. For this purpose, PNCEPy was generated by anodic polymerization under a constant potential of 1.40 V using indium-tin-oxide (ITO) electrodes rather steel electrodes. The resulting films were de-doped by CA applying a cathodic current density of -0.25 $mA \cdot cm^{-2}$, *i.e.* a constant intensity of -1.0 mA on the film of 4 cm^2 area, during 190 s.[29] Absorption spectra were recorded on a UV-3600 (Shimadzu) UV-vis-NIR spectrophotometer

controlled by the UVProbe 2.31 software at room temperature, in the 200-900 nm range, with a bandwidth of 2 mm and a scan speed of 600 $nm \cdot min^{-1}$. The film was deposited on indium-tin-oxide (ITO) electrode by electrochemical polymerization of NCEPy (10 mM) in the 0.1 M $LiClO_4$/acetonitrile under a constant potential of 1.40 V.

Theoretical methods. The molecular model of poly[N-(2-cyanoalkyl)pyrrole] bearing short alkyl groups was derived from a conformational study on small oligomers formed by *n* N-(2-cyanomethyl)pyrrole units (*n*-NCMPy). Complete geometry optimizations in gas phase of 2-NCMPy and 3-NCMPy were performed using the density functional theory (DFT) method. All DFT calculations were carried out using the Becke's three parameter hybrid functional (B3)[32] with the Lee, Yang, and Parr (LYP)[33] expression for the nonlocal correlation, combined with the 6-31G(d) basis set (B3LYP/6-31G(d)).[34] Previous studies indicated that this methodology is able to provide a very satisfactory description of the molecular geometry and relative energy for the minimum energy conformations of heterocyclic oligomers.[35]

The most stable conformation obtained from calculations on the dimer and the trimer was used as starting point for the modeling of larger oligomers. Specifically, the molecular geometries of *n*-NCMPy with *n* ranging from 6 to 15 were fully optimized using two different methods: (i) the B3LYP/6-31G(d); and (ii) the B3 functional with the Perdew and Wang's 1991[36,37] expression for the gradient-corrected correlation functional, combined with the 6-31+G(d,p)[38,39] basis set (B3PW91/6-31G+(d,p). In addition, the molecular geometries of the positively charged oligomers, n-$NCMPy^+$, were fully optimized using the unrestricted formalism of these two methods, *i.e.* UB3LYP/6-31G(d) and UB3PW91/6-31G+(d,p).

The IP of each calculated system was determined using two different methodologies. The first one was the Koopmans' theorem,[40] according to which the IPs were taken as the negative of the highest occupied molecular orbital (HOMO) energy (*i.e.* $IP^{KT} = -\varepsilon_{HOMO}$). More accurate values were obtained by calculating the IPs as the energy difference between optimized structures of the oxidized and neutral species ($IP^{\Delta SCF} = E_{oxidized} - E_{neutral}$). This approach takes into account the relaxation energy of the ionization state, which can be calculated as the difference between the IP^{KT} and $IP^{\Delta SCF}$. The EAs were calculated using the Koopman's theorem: $EA = -\varepsilon_{LUMO}$, where ε_{LUMO} refers to the energy of the lowest unoccupied molecular orbital (LUMO). Although Koopman's theorem does not apply to DFT and the energies of Kohn–Sham orbitals do not involve any physical meaning, the Janak's theorem[41] was used by Perdew[42] to show

the connection between these electronic properies (*i.e.* IPs and EAs) and the energies of the frontier orbitals (*i.e.* ε_{HOMO} and ε_{LUMO}). The ε_g was estimated using two different strategies. In the first, ε_g was approximated as the difference between the energies of the frontier orbitals: $\varepsilon_g = \varepsilon_{LUMO} - \varepsilon_{HOMO}$. In an early work, Levy and Nagy showed that in DFT calculations ε_g can be correctly estimated using this procedure.[43] The second estimation of ε_g was derived from the excitation energies calculated with time-dependent density functional theory (TD-DFT). This method, which is widely applied to study the UV-vis spectra of conjugated organic compounds, provides a robust and efficient description of the low-lying molecular states.[44-46] Electronic excitations were evaluated with the B3P86[32,47] functional combined with the 6-31G(d) basis set.[34]

All the quantum mechanical calculations were performed with the Gaussian 03 computer program.[48]

6.2.3. Results and discussion

Electrochemical estimation of the electronic properties. PNCEPy films were generated by CA under a constant potential of 1.40 V using the experimental conditions determined in a previous work[29] and considering a polymerization time of 300 s. Films were rinsed several times with acetonitrile, dried in a nitrogen flow and immersed in the electrolyte solution of the control cell for CV analysis. Figure 1a shows the cyclic voltammogram recorded in the potential range from -1.20 to 1.60 V, which was used to determine the onset potential Φ_{ox}. Using the procedure reported for other π-conjugated polymers,[49,50] taking the energy corresponding to the oxidation onset, Φ_{ox}= 0.9±0.1 eV, and making the conversion from the reference electrode to the vacuum level,[31] we estimate the IP of PNCEPy as (0.9±0.1)+4.4 = 5.3±0.1 eV. On the other hand, Figure 1b shows the voltammegram recorded in the reduction potential range from -2.40 to 1.60 V, the resulting onset potential Φ_{red} being -1.5±0.1 eV. The yields an EA value of (-1.5±0.1)+4.4 = 2.9±0.1 eV. Finally, the electrochemical ε_g, 2.4±0.1 eV, was derive from the Koopman's theorem as the difference between the IP and EA.

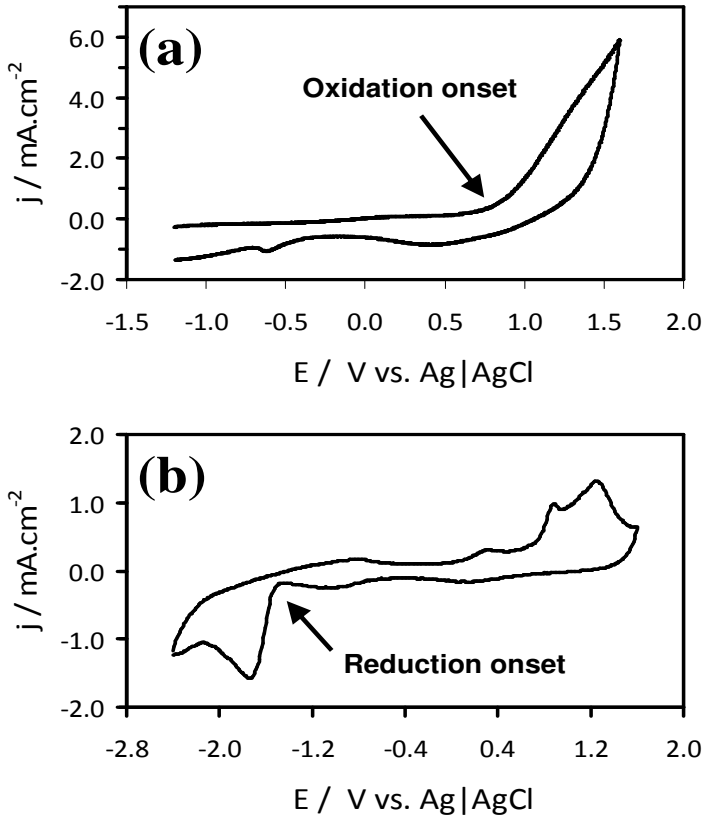

Figure 1*.Cyclic voltammograms recorded at a scan rate of 100 mV·s^{-1} for PNCEPy thin films deposited on steel electrodes. The onsets of (a) oxidation and (b) reduction were derived from the voltammogram recorded in the potential range from -1.20 to 1.60 V and from -2.40 to 1.60 V, respectively.*

Spectroscopical estimation of the electronic properties. PNCEPy was electrochemically deposited on an ITO substrate using the same experimental conditions that in our previous work.[29] After reduction of the film by CA, the UV-vis absorption spectrum was recorded (Figure 2a). As it can be seen, a strong absorption, which corresponds to the π-π* transition, is detected at 372 nm. From analysis of the absorption edge and assuming direct transition, the optical ε_g was calculated with help of the $(h\nu\times\alpha)^2$ versus $h\nu$ plot (where α is the absorption coefficient, h is Plack's constant and ν the frequency)[51,52] as presented in Figure 2b. The optical ε_g of PNCEPy was estimated to be 2.5 eV, which is in excellent agreement with the electrochemical value.

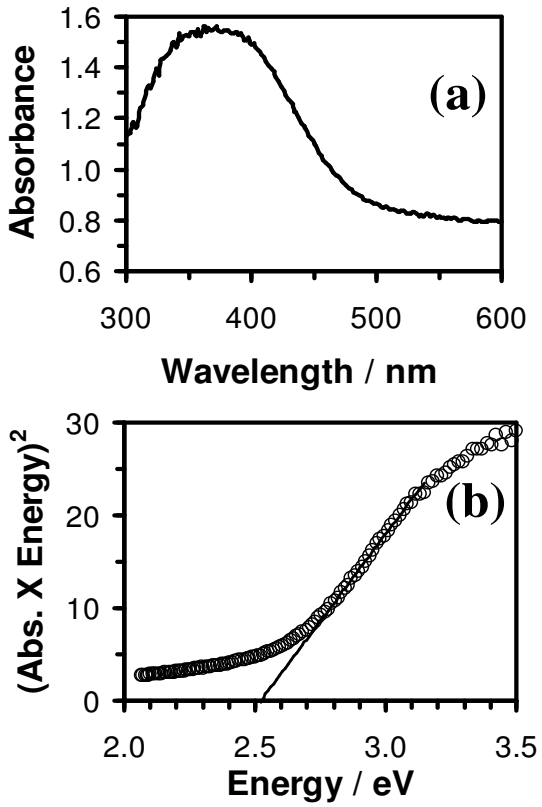

Figure 2. *(a) UV-vis absorption spectrum of a PNCEPy thin film deposited on a ITO working electrode. (b) Absorption edge analysis to extract the band gap.*

Conformational analysis**.** Previous studies considering small oligomers of poly(N-hydroxyalkylpyrrole)s with methyl, ethyl and propyl groups evidenced that the alkyl group exerts a small influence on the conformational and electronic properties.[30] Furthermore, such difference decreases when the number of repeating units increases. According to this observation, the conformational properties of poly[N-(2-cyanoalkyl)pyrrole]s were investigated considering model oligomers of the polymer with the smallest alkyl group, PNCMPy (Scheme 1).

Table 1. *Structural and electronic properties of selected minimum energy conformations of 2-NCMPy and 3-NCMPy calculated at B3LYP/6-31G(d) level. Minima have been labeled considering a roman number following by n, where n refers to the number of repeating units. Dihedral angles (θ, χ)[a] in degrees; relative energy (ΔE) in kcal/mol, ionization potential (IP) and π-π* lowest transition energy (ε_g) in eV.*

#	θ_1	θ_2	χ_1	χ_2	χ_3	ΔE	IP	ε_g
				2-NCMPy				
I-2	-114.9		80.1	-86.8		0.0	5.79	5.52
II-2	-131.6		-96.3	-96.3		0.1	5.59	5.16
III-2	122.7		-114.3	-114.3		1.3	5.77	5.55
				3-NCMPy				
I-3	-92.7	-132.7	-129.2	-99.1	85.0	0.0	5.82	5.07
II-3	-96.1	-107.2	128.8	-97.2	-90.6	0.0	6.10	5.63
III-3	-104.4	-121.1	76.2	94.7	-52.2	1.6	5.80	5.35

[a]*The dihedral angle θ_i refers to the inter-ring dihedral angle formed by repeating units i and i+1. The dihedral angle χ_i refers to the substituent of the repeating unit i.*

DFT calculations were performed to ascertain the conformational preferences of *n*-NCMPy oligomers, which have been expressed through the dihedral angles θ and χ (Scheme 2). These indicate the relative arrangement of two adjacent Py rings and the disposition of the N-cyanoalkyl substituents, respectively. Initially, all the possible initial conformations were constructed for 2-NCMPy and 3-NCMPy (*i.e.* those without steric clashes) and subsequently submitted to complete geometry optimization at the B3LYP/6-31G(d) level. Three different minimum energy conformations, which are described in Table 1, were identified for each compound. As it can be seen, the three minimum energy conformations of 2-NCMPy are within a relative energy interval of 1.3 kcal/mol and adopt an *anti-gauche* conformation. Interestingly, the side groups of the two conformations of lower energy (**I-2** and **II-2**), which are practically isoenergectic, are almost perpendicular to the Py rings (*i.e.*$\chi \approx -90^{o}$). These features are illustrated in Figure 3a, which depicts the lowest energy conformation. Inspections of the IP and ε_g values listed in Table 1 reveals relative variations lower than 0.2 and 0.4 eV, respectively, which should be essentially attributed to the differences in θ.

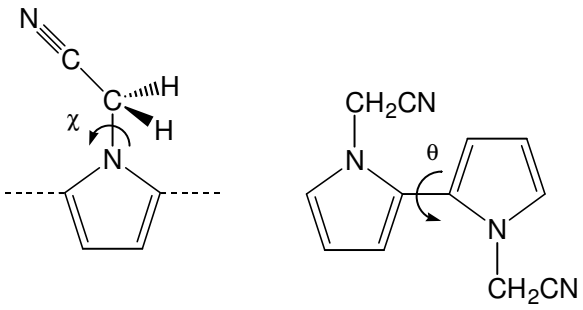

Scheme 2

In order to get more information about the stability of the *anti-gauche* conformation predicted for 2-NCMPy, the potential energy curve associated to the rotation of the inter-ring dihedral angle θ was calculated using a flexible rotor approximation (*i.e.* molecular geometry optimizations were performed at the B3LYP/6-31G(d) level considering fixed values of θ). In addition, the transition states at θ = 0º (*syn*) and 180º (*anti*) were obtained using the synchronous transit-guided Quasi-Newton (STQN) algorithm.[53] The N-substituents were arranged perpendicularly to the Py rings, as is displayed in Figure 3a. The resulting energy profile, which was obtained by scanning θ in steps of 20º, is displayed in Figure 4. As it can be seen, the *syn-gauche* conformation is not an energy minimum, which must attributed to the steric interactions between the hydrogen atoms of the adjacent substituents. These repulsive interactions are maximum in the planar *syn* conformation (θ = 0º), which is destabilized by 11.5 kcal/mol with respect to the lowest energy minimum. The steric interactions induced by the substituents are less repulsive in the *anti* conformation, which is unfavored by 7.1 kcal/mol.

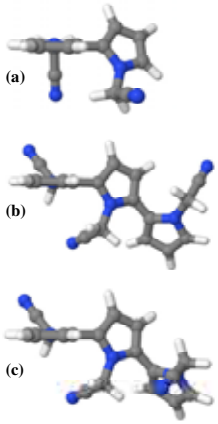

Figure 3. *Selected energy minima calculated for 2-NCMPy and 3-NCMPy at B3LYP/6-31G(d) level: (a)* ***I-2****; (b)* ***I-3****; and (c)* ***II-3****.*

The results obtained for 3-NCMPy are included in Table 1. As it can be seen, the value of θ_1 (*i.e.* the inter-ring dihedral angle formed by the first two repeating units) for **I-3** and **II-3** (Figures 3b and 3c, respectively), which are isoenergetic, is very similar to that obtained for **I-2** and **II-2**, respectively. Moreover, the dispositions of the substituents for the first two repeating units of the trimer were also similar to those of the dimer. Thus, the two minima of lowest energy obtained for the 3-NCMPy differ from those of the 2-NCMPy in the third repeating unit, which adopts a *gauche-gauche* conformation. Comparison between **III-3** and **III-2** reveals the same features. These results evidence that, in order to reduce the repulsive steric interactions induced by the third repeating unit of the trimer, the inter-ring dihedral angle defined by the second and third units (θ_2) evolves from the *anti-gauche* to the *gauche-gauche*. However, the torsional profile displayed in Figure 4 shows that the *gauche-gauche* arrangement is within the low-energy region.

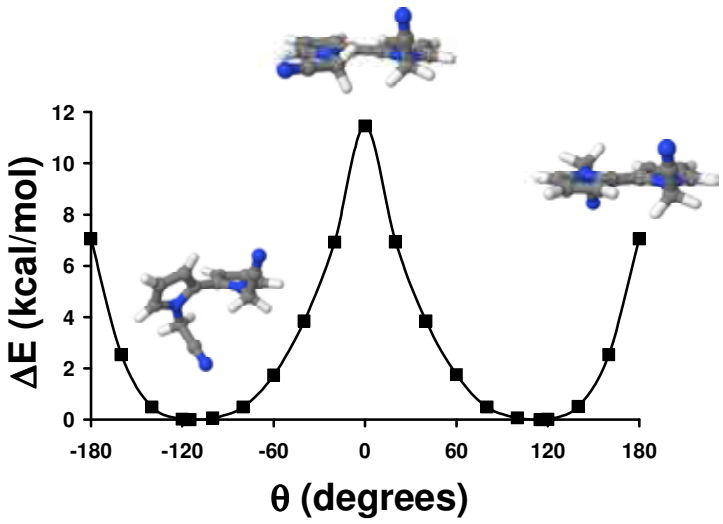

Figure 4*. Potential energy curve for the internal rotation of 2-NCMPy as a function of the inter-ring dihedral angle θ using B3LYP/6-31G(d) geometry optimizations. Energies are relative to the global minimum.*

Calculation of the electronic properties. *n*-NCMPy oligomers with *n* = 3, 6, 9, 12, and 15 were constructed using the most stable conformation of 2-NCMPy (*i.e.***I-2** in Table 1). These structures were optimized at the B3LYP/6-31G(d) level considering two different situations: (i) optimizations were performed without any restriction; and (ii) optimizations were performed fixing all the inter-ring dihedral angles at 180º (*i.e.* the *anti-gauche* found in **II-2** was changed to *anti*, even though the arrangement of the N-substituent was preserved). Previous studies on different polythiophene derivatives

and PPy indicated that the all-*anti* planar conformation allows obtain good estimations of the electronic properties for infinite polymer chains.[54-56] Although the *anti* conformation has been identified as a maximum of energy in the torsional profile of 2-NCMPy (Figure 4), the comparison between the idealized *all-anti* and the *anti-gauche* is expected to explain the influence of the geometrical distortions induced by the N-substituents on the electronic properties of poly[N-(2-cyanoalkyl)pyrrole]s.

Table 2 compares the ε_g, IP and EA values predicted at the B3LYP/6-31G(d), B3PW91/6-31+G(d,p) and TD-DFT-B3P86/6-31G(d) levels for an infinite chain of PNCMPy, which were estimated by extrapolating the linear variation of such electronic properties against $1/n$,[54-56] with those determined experimentally for PNCEPy. Inspection of the regression coefficients (R^2 in Table 2) indicates that the behavior followed by the properties calculated for the *anti-gauche* is not linear in some cases. Specifically, the R^2 calculated for the IP^{KT} and EA ranges from 0.28 to 0.84 depending on the method. Furthermore, the ε_g derived from TD-DFT calculations also shows a low R^2 (0.73). On the other hand, although the ε_g and $IP^{\Delta SCF}$ calculated at the B3LYP/6-31G(d) and B3PW91/6-31+G(d,p) levels follows a linear behavior, the values extrapolated for an infinite polymer chain are considerably overestimated with respect to the experimental ones (*i.e.*~2 and ~1 eV, respectively). These features should be attributed to the steric interactions produced by the N-cyanomethyl groups, which induced significant conformational distortions during the geometry optimization process (*i.e.* the initial *anti-gauche* arrangement evolved towards the *gauche-gauche* one in some cases). These structural changes not only disturbed the expected linear behavior but also reduced the π-π conjugation effects. Similar findings were reported in a previous study devoted to examine the electronic properties of poly(N-hydroxymethylpyrrole).[54] Calculations on N-hydroxymethylpyrrole-containing oligomers (*n*-MeOHPy) showed that some dihedral angles changed from the initial *anti-gauche* conformation towards a *gauche-gauche* one, producing both the loss of the linear behavior and the overestimation of the ε_g. In order to overcome such limitations, the *n*-MeOHPy oligomers were re-optimized considering all the inter-ring dihedral angles fixed at 180º.[54]

Table 2. *Electronic properties (ε_g, IP^{KT}, $IP^{\Delta SCF}$ and EA; all in eV) predicted by different theoretical methods for an infinite chain of PNCMPy arranged in anti and anti-gauche. The coefficients R^2 derived from the linear regression analyses used to extrapolate the properties obtained for n-NCMPy oligomers towards an infinite polymer chain (i.e. calculated property against 1/n) are displayed in parenthesis. Experimental values measured for PNCEPy are included for comparison.*

	anti-gauche				***anti***			
	ε_g	IP^{KT}	$IP^{\Delta SCF}$	EA	ε_g	IP^{KT}	$IP^{\Delta SCF}$	EA
B3LYP/6-31G(d)	4.5	5.8	6.1	1.3	2.2	4.7	5.1	2.5
	(0.92)	(0.28)	(0.96)	(0.84)	(1.00)	(0.97)	(0.99)	(1.00)
B3PW91/6-31+G(d,p)	4.4	6.1	6.5	1.6	2.2	5.0	5.6	2.8
	(0.90)	(0.49)	(0.97)	(0.76)	(1.00)	(0.97)	(0.99)	(0.99)
TD-DFT-B3P86/6-31G(d)	4.3	-	-	-	1.8	-	-	-
	(0.73)				(1.00)			

	ε_g	IP	EA
Electrochemical measures	2.4	5.3	2.9
Optical measures	2.5	-	-

The electronic properties predicted for the all-*anti* conformation of PNCMPy are included in Table 2. Inspection of the R^2 values reveals a perfect linear behavior in all cases. Moreover, the calculated values are in excellent agreement with the experimental values determined in this work. Specifically, the ε_g, IP^{KT}, $IP^{\Delta SCF}$, and EA values predicted at the B3PW91/6-31+G(d,p) level differ from electrochemical measures by less than 0.3 eV only. On the other hand, the ε_g calculated at the TD-DFT level for an idealized planar chain is 0.7 eV lower than the experimental value, which represents a reduction of 2.5 eV with respect to the value predicted with the same methodology for the *anti-gauche* conformation. The TD-DFT methodology typically provides an accurate description of the experimental ε_g values, results displayed in Table 2 suggesting that the calculated oligomers do not represent satisfactorily the chemical and/or conformational characteristics of PNCEPy.

As can be seen in the torsional profile displayed in Figure 4, there is a maximum of energy at $\theta = 180º$, which makes the *anti* conformation ~7 kcal/mol less stable than the *anti-gauche* one. Moreover, an early crystallographic study on N,N-dimethyl-2,2'-bypyrrole (*i.e.* the dimer formed by two repeating units of N-methylpyrrole) evidenced that this dimer adopts a *gauche-gauche* conformation also in the solid state.[57] The loss of planarity produced by the N-methyl substitution allowed to explain the higher oxidation peak potential measured for the dimer of N-methylpyrrole as compared to the dimer of pyrrole and the smaller conductivity of PNMPy as compared to PPy.[57,58] Obviously, these findings are against the assumption that PNCMPy chains adopt a planar *anti* conformation, as seems to suggest the very good agreement between experimental and calculated electronic properties. In opposition, recent studies on PNCEPy, PNMPy and PPy evidenced that polymer chains made of N-substituted repeating units grow following a multidirectional mechanism, which should be attributed to their tendency to form of chemical crosslinks.[29,59] Specifically, PPy was found to form linear chains with some irregularities,[59] while branched molecules with many irregularities are the most stable for PNMPy[59] and PNCEPy[29] because of the steric repulsions induced by the N-substituents. The formation of α-β and/or β-β linkages should favor the planarity in small tracts of PNCMPy. In addition to these observations, there is a chemical oxidative process, which was found to be characteristic of poly[N-(2-cyanoalkyl)pyrrole]s,[29] that is expected to affect the electronic properties

of PNCEPy. Therefore, explicit analysis of this specific process is presented in the next subsection.

Effects of the oxidative process on the electronic properties. Our previous experimental study evidenced the presence of a strong and shard band at 1740 cm^{-1} in the FTIR spectrum of PNCEPy, which was assigned to the stretching vibration of carbonyl groups.[29] The origin of these C=O groups corresponds to the oxidative process undergone by some five membered rings, as is illustrated in Scheme 3. Thus, although the carbonyl group typically absorbs at 1700 cm^{-1}, the conjugation with the unsaturated groups of the polymer backbone produced a shift towards a higher wavenumber. Obviously, the presence of carbonyl groups interacting with the π-conjugated system is expected to induce significant changes in both the structural and optical properties of PNCEPy. In order to provide a careful study of these changes, calculations have been performed on oligomers containing *n* repeating units of NCMPy and *x* carbonyl groups, hereafter denoted *n*-NCMPy$(CO)_x$. The carbonyl groups were located at the β-position of selected pyrrole rings, as is displayed in Scheme 3. The molecular geometries of all the generated oligomers, which were initially arranged considering an *anti-gauche* conformation, were re-optimized at the Hartree-Fock (HF) level using the 6-31G(d) basis set. The resulting geometries were used for single point calculations at both the B3LYP/6-31G(d) and the TD-DFT-B3P86/6-31G(d) levels. The carbonyl groups were distributed on the oligomers with *n* ranging from 3 to 12 considering two different situations: (i) each oligomer contains a single carbonyl group, which is located in the first repeating unit, *i.e.n*-NCMPy$(CO)_x$with $x = 1$; and (ii) one of every three repeating units, starting from the first one, contains a carbonyl group. *i.e.n*-NCMPy$(CO)_x$with $x \approx n/3$. It is worth nothing that *n*-NCMPy$(CO)_1$ oligomers allow examine the extension of the influence of the carbonyl group, while *n*-NCMPy$(CO)_{\sim n/3}$ oligomers show the effect of the concentration of carbonyl groups.

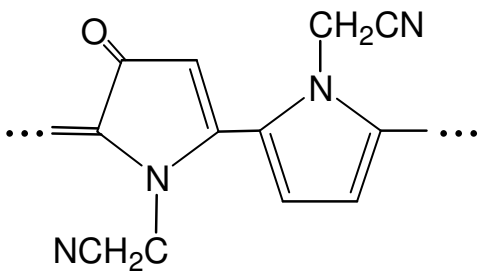

Scheme 3

The bond length alternation pattern calculated for the conjugated π-system of 9-NCMPy, 9-NCMPy(CO)$_1$, and 10-NCMPy(CO)$_4$ are represented in Figure 5. As it can be seen, the C–C bond lengths found for *n*-NCMPy corresponds to a typical benzenoid structure, in which the inter-ring bond lengths are larger than the intra-ring ones. This regular pattern is altered for the two oligomers containing carbonyl groups. Specifically, the presence of a single carbonyl group located at the first unit produces a relatively homogeneous distribution of intra-ring C–C lengths and a shortening of the inter-ring bond length with respect to 9-NCMPy. These effects decrease progressively and are completely erased after the fifth repeating unit, which shows the benzenoid pattern found for 9-NCMPy. On the other hand, 10-NCMPy(CO)$_4$ presents a quinoid-like structure, in which the inter-ring bond length corresponds to that of a double bond. Moreover, this structure is reinforced at every unit with a carbonyl group (indicated by arrows in Figure 5).

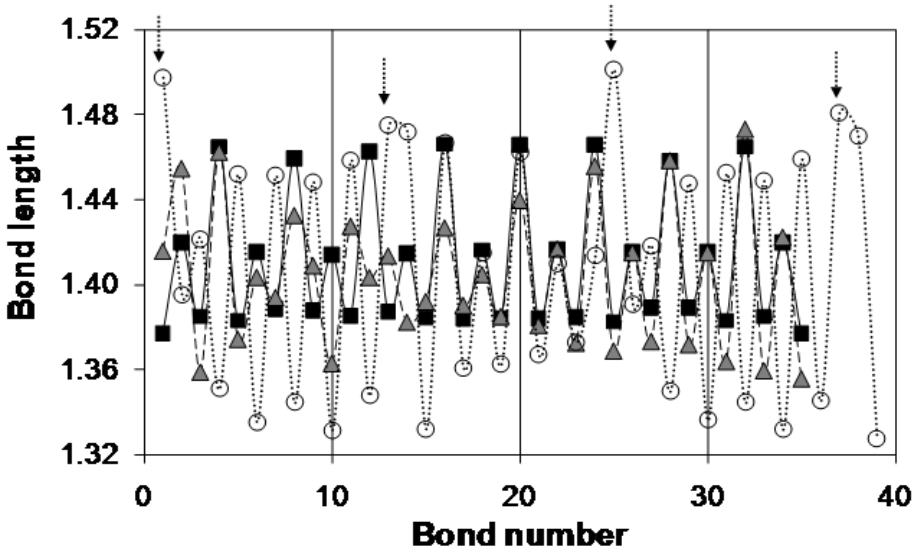

***Figure 5**. Bond length alternation pattern along the conjugated π-system of 9-NCMPy (■; solid line), 9-NCMPy(CO)$_1$ (▲; dashed line) and 10-NCMPy(CO)$_4$ (○; dotted line). The position of carbonyl groups is marked with arrows.*

Table 3 lists the electronic properties extrapolated for infinite chains using the results calculated for *n*-NCMPy(CO)$_x$ oligomers with x= 1 and $x \approx n/3$. It is worth noting that in all cases a good linear behavior ($R^2 \geq 0.84$) was obtained for the variation of the computed electronic properties with the inverse of the chain length ($1/n$). Interestingly, the ε_g value derived from single point calculations at the TD-DFT-B3P86/6-31G(d) level on *n*-NCMPy(CO)$_1$ oligomers is in excellent agreement with the experimental

measure. In contrast, the ε_g estimated using B3LYP/6-31G(d) calculations is significantly overestimated, which should be attributed to a drastic underestimation of the EA. On the other hand, the ε_g values obtained at both the TD-DFT and DFT levels for a *n*-NCMPy(CO)$_{\sim n/3}$ chain with $n \rightarrow \infty$ are underestimated with respect to the experimental ones. Indeed, DFT calculations evidence a significant overestimation of the EA when the number of units that undergone the oxidative process is one of every three. The overall of these results suggest that the ratio between the number of N-substituted pyrrole units with and without carbonyl groups, which seems to be comprised between 1/11 and 1/2, looks closer to the former than to latter value.

Table 3. *Electronic properties (ε_g, IP^{KT} and EA; all in eV) predicted by different theoretical methods for an infinite chain of PNCMPy considering oxidative processes on selected repeating units. Specifically, calculations have been performed considering n-NCMPy(CO)$_1$ and n-NCMPy(CO)$_{\sim n/3}$ oligomers with n ranging from 3 to 12 (see text). The coefficients R^2 derived from the linear regression analyses used to extrapolate the properties obtained for oligomers towards an infinite polymer chain (i.e. calculated property against 1/n) are displayed in parenthesis.*

	n-NCMPy(CO)$_1$			***n-NCMPy(CO)$_{\sim n/3}$***		
	ε_g	IP^{KT}	EA	ε_g	IP^{KT}	EA
B3LYP/6-31G(d)	5.0	6.0	1.0	1.3	4.9	3.7
	(0.94)	(0.88)	(0.84)	(0.97)	(0.88)	(0.96)
TD-DFT-B3P86/6-31G(d)	2.6	-	-	1.0	-	-
	(1.0)			(0.84)		

Figure 6 shows the evolution of the ε_g calculated at the TD-DFT-B3P86/6-31G(d) level against 1/*n* for *n*-NCMPy(CO)$_1$. As it can be seen, ε_g behaves linearly for *n*= 3, 6 and 9 up with values pretty close to the experimental measures. In opposition to what it is usually observed, the band gap grows with *n* showing a negative slope. Furthermore, 12-NCMPy(CO)$_1$ shows a drastic increment of ε_g indicating that the properties of this oligomer are not dominated by the carbonyl group. Thus, the carbonyl group plays a crucial role in oligomers made up to nine repeating units but its influence vanishes for larger molecules. These results combined with the experimental evidences of the multidireccional growing of PNCEPy[29] and the hypotheses that oxidative processes in pyrrole electropolymerization correspond to termination steps,[60,61] allow propose an idealized model for poly[N-(2-cyanoalkyl)pyrrole]s bearing short alkyl groups. This

consists on a highly crosslinked structure made of very small branches (*i.e.* tracts of nine or even less repeating units) with carbonyl group in the last repeating unit of each one.

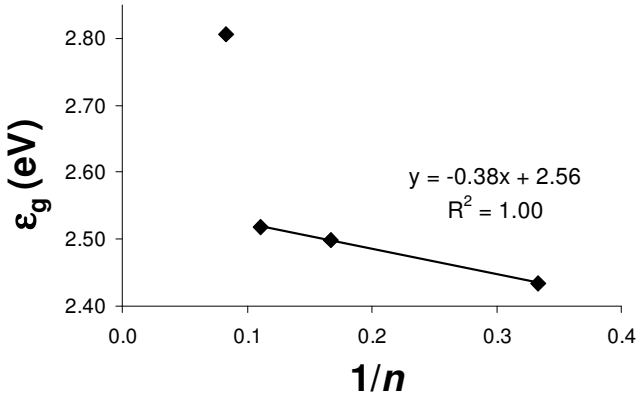

***Figure 6**. Evolution of the ε_g calculated at the TD-DFT-B3P86/6-31G(d) level for n-NCMPy(CO)$_1$ against 1/n.*

6.2.4. Conclusions

The electronic properties of PNCEPy have been determined experimentally and compared with those predicted theoretically for PNCMPy. Films of PNCEPy were prepared by anodic polymerization using a constant potential of 1.40 V. Cyclic voltammograms were recorded to estimate the IP (5.3 eV), EA (2.9 eV) and ε_g (2.4 eV). The ε_g value was also measured using the UV-vis absorption spectrum, which showed the π-π^*transition peak at 372 nm (*i.e.* 2.5 eV) in excellent agreement with the electrochemical estimation.

A systematic conformational analysis considering all the possible arrangements of 2-NCMPy and 3-NCMPyas starting points for geometry optimizations allow us to propose a model, which presents minimum repulsive interactions between consecutive repeating units, for idealized chains of poly[N-(2-cyanoalkyl)pyrrole]s bearing short alkyl groups. This is defined by the inter-ring dihedral angles, which adopt alternatively the *anti-gauche* and *gauche-gauche*conformations, and the side groups arranged perpendicularly to the Py rings.

DFT and TD-DFT calculations indicated that the electronic properties of poly[N-(2-cyanoalkyl)pyrrole]s bearing short alkyl groups are not only influenced by the effect of the conformation on the conjugation of the π-system but also on the existence of carbonyl groups attached to the pyrrole ring of selected repeating units. Thus, previously detected secondary oxidative processes produce significant changes, which extend up to around nine repeating units, in both the optical and geometrical molecular properties. A systematic study on *n*-NCMPy$(CO)_x$ oligomers with $x = 1$ and $x \approx n/3$ allow us to conclude that poly[N-(2-cyanoalkyl)pyrrole]s present a crosslinked structure formed by small branches, the last repeating unit of each one bearing a carbonyl group.

6.2.5. References

[1]. Han, D.-H.; Lee, H. J.; Park, S.-M. *Electrochim. Acta* **2005**, *50*, 3085.

[2]. Khomenko, V.; Frackowiak, E.; Béguin, F. *Electrochim. Acta* **2005**, *50*, 2499.

[3]. Johanson, U.; Marandi, M.; Tamm, T.; Tamm, J. *Electrochim. Acta* **2005***, 50*, 1523.

[4]. Weidlich, C.; Mangold, K. M.; Jüttner, K. *Electrochim. Acta* **2005**, *50*, 1547.

[5]. Chehimi, M. M.; Abel, M.-L.; Perruchot, C.; Delamar, M.; Lascelles, S. F.; Armes, S. P. *Synth. Met.* **1999**, *104*, 51.

[6]. Azioune, A.; Siroti, F.; Tanguy, J.; Jouini, M.; Chehimi, M. M.; Miksa, B.; Slomkowski, S. *Electrochim. Acta* **2005**, *50*, 1661.

[7]. Saoudi, B.; Despas, C.; Chehimi, M. M.; Jammul, N.; Delamar, M.; Bessière, J.; Walcarius, A. *Sens. Actuat B* **2000**, *62*, 35.

[8]. Raoof, J.-B.; Ojani, R.; Rashid-Nadimi, S. *Electrochim. Acta* **2004**, *49*, 271.

[9]. Khomenko, V. G.; Barsukov, V. Z.; Katashinskii, A. S. *Electrochim. Acta* **2005**, *50*, 1675.

[10]. Hien, N. T. L.; Garcia, B.; Pailleret, A.; Deslouis, C. *Electrochim. Acta* **2005**, *50*, 1747.

[11]. Krstajic, N. V.; Grgur, B. N.; Jovanovic, S. M.; Vojnovic, M. V. *Electrochim. Acta* **1997**, *42*, 1685.

[12]. Henry, M. C.; Hsueh, C.-C.; Timko, B. P.; Freund, M. S. *J. Electrochem. Soc.* **2001**, *148*, D155.

[13]. Pringle, J. M.; Efthimiadis, J.; Howlett, P. C.; Efthimiadis, J.; MacFarlane, D. R.; Chaplin, A. B.; Hall, S. B.; Officer, D. L.; Wallace, G. G.; Forsyth, M. *Polymer* **2004**, *45*, 1447.

[14]. Bazzaoui, M.; Martins, J. I.; Reis, T. C.; Bazzaoui, E. A.; Nunes, M. C.; Martins, L. *Thin Solid Films* **2005**, *485*, 155.

[15]. Schuhmann, W.; Lammert, R.; Uhe, B.; Schmidt, H. L. *Sens. Actuat B* **1990**, *1*, 537.

[16]. Sigmund, W. M.; Weerasekera, G.; Marestin, C.; Styron, S.; Zhou, H.; Elsabee, M. Z.; Rühe, J.; Wegner, G.; Duran, R. S. *Langmuir* **1999**, *15*, 6423.

[17]. Chen, Y.; Harrison, W. T. A.; Imrie, C. T.; Ryder, K. S. *J. Mater. Chem.* **2002**, *12*, 579.

[18]. Pfeiffer, P.; Armelin, E.; Estrany, F.; del Valle, L. J.; Cho, L. Y.; Alemán, C. *J. Polym. Res.* **2008**, *15*, 225.

[19]. Estrany, F.; Aradilla, D.; Oliver, R.; Alemán, C. *Eur. Polym. J.* **2007**, *43*, 1876.

[20]. Estrany, F.; Aradilla, D.; Oliver, R.; Armelin, E.; Alemán, C. *Eur. Polym. J.* **2008**, *44*, 1323.

[21]. Xu, J. M.; Ng, S. C.; Chan, H. S. O. *Macromolecules* **2001**, *34*, 4314.

[22]. Gordon, K. C.; MacArthur, S.; David, G.; Clarke, T. M.; Officer, D. L.; Wagner, P.; Hall, S. B. *Synth. Met.* **2005**, *153*, 225.

[23]. Deng, Z.; Stone, D. C.; Thompson, M. *Can. J. Chem.* **1995**, *73*, 1427.

[24]. Deng, Z.; Stone, D. C. *Analyst* **1997**, *122*, 1129.

[25]. Deng, Z.; Stone, D. C.; Thompson, M. *Analyst* **1996**, *121*, 1341.

[26]. Ouerghi, O.; Senillou, A.; Jaffrezic-Renault, N.; Martelet, C.; Ben Ouada, H.; Cosnier, S. *J. Electroanal. Chem.* **2001**, *501*, 62.

[27]. Kaden, H.; Jahn, H.; Berthold, M.; Jüttner, K.; Mangold, K. M.; Schäfer, S. *Chem. Eng. Technol.* **2001**, *24*, 1120.

[28]. Weiss, Z.; Mandler, D.; Shustak, G.; Domb, A. *J. Polym. Sci., Part A: Polym. Chem.* **2004**, *42*, 1658.

[29]. Aradilla, D.; Estrany, F.; Armelin, E.; Oliver, R.; Iribarren, J. I.; Alemán, C. *Macromol. Chem. Phys.* **2010**, *211*, 1663.

[30]. Casanovas, J.; Cho, L. Y.; Ocampo, C.; Alemán, C. *Synth. Met.* **2005**, *151*, 239.

[31]. Brédas, J. L.; Silbey, R.; Boudreaux, D. S.; Chance, R. R. *J. Am. Chem. Soc.* **1983**, *105*, 6555.

[32]. Becke, A. D. *J. Chem. Phys.* **1993**, *98*, 1372.

[33]. Lee, C.; Yang, W.; Parr, R. G. *Phys. Rev. B* **1988,** *37*, 785.

[34]. Hariharan, P. C.; Pople, J. A. *Chem. Phys. Lett.* **1972**, *16*, 217.

[35]. Torras, J.; Bertran, O.; Alemán, C. *J. Phys. Chem. B* **2009**, *113*, 15196.

[36]. Perdew, J. P. In *Electronic structure of solids '91;* Ziesche, P.; Eschrig, H. Eds.; Akademie Verlag: Berlin, **1991**, p 11-20.

[37]. Burke, K.; Perdew, J. P.; Wang, Y. In *Electronic Density Functional Theory: Recent Progress and New Directions;* Dobson, J. F.; Vignale, G.; Das, M. P.; Eds.; Plenum Press: New York, **1998**, p 81-111.

[38]. Hariharan, P. C.; Pople, J. A. *Theor. Chim. Acta* **1973**, *28*, 213.

[39]. McLean, A. D.; Chandler, G. S. *J. Chem. Phys.* **1980**, *72*, 5639.

[40]. Koopmans, T. *Physica* **1934**, *1*, 104.

[41]. Janak, J. F. *Phys. Rev. B* **1978**, *18*, 7165.

[42]. Perdew, J. P. In *Density Functional Methods in Physics;* Dreizler, R. M.; Providenca, J., Eds.; Plenum Press: New York and London, 1985.

[43]. Levy, M.; Nagy, A. *Phys. Rev. A* **1999**, *59*, 1687.

[44]. Casida, M. E. In *ACS Symp. Ser.*; Hoffmann, M. R.; Dyall, K. G. Eds. Washington DC, **2002**, *828*, p. 199-220.

[45]. Baerends, E. J.; Ricciardi, G.; Rosa, A.; van Gisbergen, S. J. A. *Coord. Chem. Rev.* **2002**, *230*, 5.

[46]. Jamorski-Jöpdicke, C.; Lüthi, H. P. *J. Am. Chem. Soc.* **2002**, *125*, 252.

[47]. Perdew, J. P. *Phys. Rev. B* **1986**, *33*, 8822.

[48]. Gaussian 03, Revision B.02, Frisch, M. J.; Trucks, G. W.; Schlegel, H. B.; Scuseria, G. E.; Robb, M. A.; Cheeseman, J. R.; Montgomery, J. A.; Vreven Jr T.; Kudin, K. N.; Burant, J. C.; Millam, J. M.; Iyengar, S. S.; Tomasi, J.; Barone, V.; Mennucci, B.; Cossi, M.; Scalmani, G.; Rega, N.; Petersson, G. A.; Nakatsuji, H.; Hada, M.; Ehara, M.; Toyota, K.; Fukuda, R.; Hasegawa, J.; Ishida, M.; Nakajima, T.; Honda, Y.; Kitao, O.; Nakai, H.; Klene, M.; Li, X.; Knox, J. E.; Hratchian, H. P.; Cross, J. B.; Adamo, C.; Jaramillo, J.; Gomperts, R.; Stratmann, R. E.; Yazyev, O.; Austin, A. J.; Cammi, R.; Pomelli, C.; Ochterski, J. W.; Ayala, P. Y.; Morokuma, K.; Voth, G. A.; Salvador, P.; Dannenberg, J. J.; Zakrzewski, V. G.; Dapprich, S.; Daniels, A. D.; Strain, M.; Farkas, O.; Malick, D. K.; Rabuck, A. D.; Raghavachari, K.; Foresman, J. B.; Ortiz, J. V.; Cui, Q.; Baboul, A. G.; Clifford, S.; Cioslowski, J.; Stefanov, B. B.; Liu, G.; Liashenko, A.; Piskorz, P.; Komaromi, I.; Martin, R. L.; Fox, D. J.; Keith, T.; Al-Laham, M. A.; Peng, C. Y.; Nanayakkara, A.; Challacombe, M.; Gill, P. M. W.; Johnson, B.; Chen, W.; Wong, M. W.; Gonzalez, C.; Pople, J. A. Gaussian, Inc., Pittsburgh PA, 2003.

[49]. Janietz, S.; Bradley, D. D. C.; Grell, M.; Giebeler, C.; Inbasekaran, M.; Woo, E. P. *Appl. Phys. Lett.* **1998**, *73*, 2453.

[50]. Micaroni, L.; Nart, F.; Hümmelgen, I. J. *Solid State Electrochem.* **2002**, *7*, 55.

[51]. Morita, S.; Akashi, T.; Fujii, A.; Yoshida, M.; Ohmori, Y.; Yoshimoto, K.; Kawai, T.; Zakhidov, A. A.; Lee, S. B.; Yoshino, K. *Synth. Met.* **1995**, *69*, 433.

[52]. Mello, R.; Serbena, J.; Benvenho, A.; Hümmelgen, I. *J. Solid State Electrochem.* **2003**, *7*, 463.

[53]. Peng, C.; Schlegel, H. B. *Isr. J. Chem.* **1993**, *33*, 233.

[54]. Ocampo, C.; Casanovas, J.; Liesa, F.; Alemán, C. *Polymer* **2006**, *47*, 3257.

[55]. Bertran, O.; Pfeiffer, P.; Torras, J.; Armelin, E.; Estrany, F.; Alemán, C. *Polymer* **2007**, *48*, 6955.

[56]. Casanovas, J.; Alemán, C. *J. Phys. Chem. C* **2007**, *111*, 4823.

[57]. Gatti, C.; Frigerio, G.; Benincori, T.; Brenna, E.; Sannicolò, F.; Zotti, G.; Zechhin, S.; Schiavon, G. *Chem. Mater.* **2000**, *12*, 1490.

[58]. Benincori, T.; Brenna, E.; Sannicolò, F.; Zotti, G.; Zecchin, S.; Schiavon, G.; Gatti, C.; Frigerio, G. *Chem. Mater.* **2000**, *12*, 1480.

[59]. Alemán, C.; Casanovas, J.; Torras, J.; Bertrán, O.; Armelin, E.; Oliver, R.; Estrany, F. *Polymer* **2008**, *49*, 1066.

[60]. Genies, E. M.; Bidan, G.; Diaz, A. F. *J. Electroanal. Chem.* **1983**, *149*, 101.

[61]. Sadki, S.; Schottland, P.; Brodie, N.; Sabouraud, G. *Chem. Soc. Rev.* **2000**, *29*, 283.

6.3. Understanding of interaction mechanisms in organic solvent vapor sensors based on pyrrole derivatives.

6.3.1. Introduction

Since the discovery of polyacetylene in the late of 1970s, many investigations have been carried out to understand the chemical and physical properties of conducting polymers (CPs).[1,2] They have aroused a great attention due to their interesting applications in different technological areas such as electronic devices,[3] solar cells,[4] sensors,[5-7] electrochromic displays,[8] biomedicine,[9] or as corrosion inhibitors.[10] Precisely, sensors based on polythiophene (PTh),[11-13] polyaniline (PAni),[14,15] and polypyrrole (PPy)[16-18] have been widely developed during the last years. Among heterocyclic-based electroactive polymers, PPy is one of the most important because of its ionic exchange properties, conductivity, biocompatibility, electroactivity or high yield redox process.[19,20] Within this context, PPy is considered an excellent candidate in supercapacitors,[21,22] batteries,[23] bioactive platforms,[24] and biomedicine.[25,26]

As it was discussed previously, recently, pyrrole and its derivatives have emerged as promising materials in the field of chemical sensors. These CPs have shown good electrical and optical properties, which can be employed as transducers in different type of sensors.[27] In this way, biological sensors based on polypyrrole (PPy) have attracted a great interest due to the ultra-sensitive detection of biological species such as DNA,[28-32] dopamine,[33-36] glucose,[37-40] galactose,[41] cholesterol,[42,43] urea,[44] or proteins.[45,46] Among chemical sensors exist a wide range of possibilities, thus, new sensors based on the response to organic vapors and gas molecules (*e.g.* ammonia or NO_2) have been employed using PPy.[47-54] The chemical sensor is formed by an electrode coated with a polymeric film, which is capable of detecting changes influenced by the environment effect (*e.g.* pH, ionic strength or analyte). Consequently, the electrical response of the system varies acting as sensor.

In spite of PPy is a good candidate to be used as solvent-gas sensor, some works have been published to improve its performance as sensor using copolymers or substituents in the monomer.[55] Within this context, 3-alkyl and 3-carboxy substituted pyrroles have been synthesized chemically providing better results in terms of sensitivity and efficiency.[56] Thus, in the last years, several works have been focused on

studying the electronic, structural and morphological properties of a new PPy derivative known as poly[N-(2,cyanoethylpyrrole)] (PNCEPy; Scheme 1).[57-59] Besides, several works have been also devoted to study the electronic and electrochemical properties of this polymer at theoretical level.[60-62] According to its properties, this conducting polymer has been employed in different applications, specifically, as solvent-gas sensor,[63-65] and immunosensor.[66] Precisely, the cyano group (CN) is a strong electron-withdrawing group, which has been incorporated to modify some properties on conducting polymers such as the increase in the oxidation potential or improvement of electron transporting along the polymer backbone.[67] Thus, in previous works, PNCEPy showed excellent abilities to detect biological units such as dopamine.[33,34,68] Furthermore, its good electrochemical properties suggested a potential candidate for the fabrication of electric circuit components.[57] Although PNCEPy has been widely employed as biological and solvent-gas sensor, to the best of knowledge scarce works have been reported in order to study its interactions with molecules in vapor-phase.[64] *Thompson et al* published some works devoted to study some PPy derivatives as chemical sensors in the detection of solvent molecules. Specifically, PNCEPy was one of the most studied.[63-65] An exhaustive experimental study was carried out to study the differences between PPy and PNCEPy films as chemical sensors.[64] In that work, neutral PPy and PNCEPy films were synthesized electrochemically through potentiodynamic methods, where PNCEPy exhibited better properties in terms of sensitivity and affinity than PPy films in presence of some solvents (*e.g.* acetonitrile).

The aim of this work is to examine and to study the properties of PNCEPy and PPy as solvent-gas sensor through their specific interactions with some polar solvents (*e.g.* water, methanol, acetonitrile and chloroform respectively). For this purpose an exhaustive theoretical study has been carried out using quantum mechanical calculations based on model oligomers in its neutral, cationic and dicationic (both singlet and triplet) states. Calculations have been performed using model oligomers of [N-(2-cyanomethyl)pyrrole], abbreviated NCMPy and Py containing up to 4 units. In this work NCMPy oligomers were considered since in previous studies the length of the alkyl group had a negligible effect on the structural and electronic properties of poly(N-hydroxyalkylpyrrole)s and poly[N-(2-cyanoalkyl)pyrrole)s.[69,60] Results have shown that the presence of cyano group in NCMPy improves its capacity to be employed as gas-solvent sensor. Additionally, experimental results evidenced the best performance of PNCEPy as chemical sensor through a chemiresistive device.

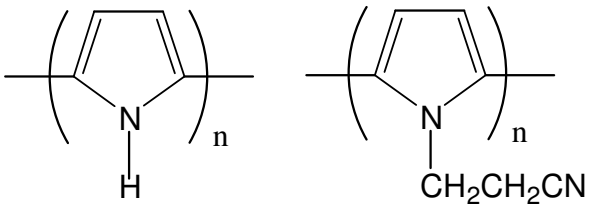

Scheme 1. *Polypyrrole (PPy) (left) and poly[N-(2,cyanoethylpyrrole)] (PNCEPy) (right)*

6.3.2. Methods

Experimental methods. N-(2-cyanoethyl)pyrrole (NCEPy), pyrrole (Py) and acetonitrile of analytical reagent grade were purchased from Aldrich and used without further purifications. Anhydrous lithium perchlorate, analytical reagent grade, from Aldrich was stored in an oven at 80ºC before use in the electrochemical trials. PNCEPy and PPy films were prepared by potentiodynamic methods in the potential range from 0 to 1.40 V after 30 cyclic voltammograms recorded at a scan rate of 50 $mV \cdot s^{-1}$. The anodic potential 1.40 V was estimated an optimal potential for the electropolymerization of PPy and PNCEPy films.[57,70] Electrochemical experiments were conducted on a VersaStat II potenciostat-galvanostat connected to a computer controlled through a Power Suite Princenton Applied Research program using a three-electrode two-compartment cell under nitrogen atmosphere at 25 ºC. The working compartment was filled with 40 mL of a 10 mM monomer solution in acetonitrile with 0.1 M $LiClO_4$, while the cathodic compartment was filled with 10 mL of the same electrolyte solution. Steel AISI 316 sheets with an area of 6 cm^2 were employed as working and counter electrodes. The reference electrode was an Ag|AgCl electrode containing KCl saturated aqueous solution (E^0= 0.222 V at 25ºC), which was connected to the working compartment through a salt bridge containing the electrolyte solution. After electropolymerization, the coated electrodes were cleaned with acetonitrile and dried with nitrogen. In all cases, the solution was purged with nitrogen for 5 minutes prior electrochemical synthesis.

Preparation of the sensor. The neutral polymeric films electrodeposited onto steel substrates were removed carefully and deposited on an insulating tape, which was fixed over a glass substrate.

Testing the sensor. The sensor's response was evaluated by exposing the polymeric films in a closed vessel to saturated air with an organic vapour (acetonitrile) during 5

min, followed by 2 min of exposition to clean dry air. The measurement of resistance was performed through the contact pairs. The sensor's response (S) was estimated by using the following equation:

$$SR(\%) = \left(\frac{R_a - R_g}{R_g} \right) \cdot 100 \qquad (1)$$

$$S = \frac{R_a}{R_g} \qquad (2)$$

where R_a represents the resistance measured in air and R_g corresponds to the absolute resistance measured immediately after the exposure to the organic vapour.

Theoretical methods. The most stable conformation obtained from calculations on the dimer and the trimer was used as starting point for the modeling of the complexes based on $(NCMPy)_n$, where n refers to the number of monomers.[60] Complete geometry optimizations of both neutral and oxidized $(Py)_n$ oligomers were carried out considering the anti-planar conformation as the starting geometry; *e.g.* all the inter-ring dihedral angles N-C-C-N were initially set at 180º. This tendency was reported to be the most stable conformation of the Py.[71] Calculations for both systems NCMPy and Py oligomers, were performed using the Becke's three parameter hybrid functional (B3)[72] with the Lee, Yang, and Parr (LYP)[73] expression for the nonlocal correlation, combined with the 6-31G(d) basis set, (B3LYP/6-31G(d)).[74] The structures of the complexes were determined by full geometry optimization from gas-phase using two different methods: (i) B3LYP/6-31G(d) and (ii) the MP2 level[75] with the 6-31G+(d,p)[76,77] basis set (MP2/6-31+G(d,p)). Frequency calculations were performed to obtain the zero-point vibrational energy and both the thermal and entropic corrections. Calculations were carried out considering the neutral, monocationic and dicationic ionization states for Py and NCMPy oligomers, the singlet (two paired electrons) and triplet (two unpaired electrons) electronic states being considered for the dication. The restricted formalism was considered for complexes involving neutral oligomers (closed-shell systems), while for monocationic and dicationic oligomers the unrestricted formalism of the MP2 and B3LYP method (UMP2 or UB3LYP) was used.

Calculated model complexes involved Py and NCMPy-oligomers, hereafter denoted $n\text{Py}^m$ or $n\text{NCMPy}^m$ (where *n* refers to the number of oligomeric units and *m* indicates

the charge and electronic state, being m= 0, +1, +2S and +2T for the neutral state, monocationic state, singlet dicationic state and triplet dicationic state, respectively).

Interaction energies (ΔE^{int}), which were obtained by correcting the basis set superposition error (BSSE) with counterpoise (CP) method,[78] were estimated as the difference between the total energy of the optimized complex and the energies of the isolated monomers with the geometries obtained from the optimization of the complex.

The effect of the solvent on the strength of the binding was estimated following the polarizable continuum model (PCM) developed by Tomasi and co-workers.[79,80] This self-consistent reaction field (SCRF) method involves the generation of a solvent cavity from spheres centered at each atom in the molecules and the calculation of virtual point charges on the cavity surface representing the polarization of the solvent. The magnitude of these charges is proportional to the derivative of the solute electrostatic potential at each point calculated from the molecular wavefunction. Then, the point charges are included in the one-electron Hamiltonian inducing polarization of the solute. An iterative calculation is carried out until the wavefunction and the surface charges are self-consistent.

PCM calculations were performed in the framework of the ab initio (U)MP2/6-31+G(d,p) and (U)B3LYP/6-31G(d) level using the standard protocol and considering the dielectric constant of chloroform (ε = 4.9), water (ε = 78.4), acetonitrile (ε = 35.7) and methanol (ε = 32.7). Calculations were performed considering the gas-phase optimized geometries. Thus, solvent-induced changes in bond lengths and angles were found to have little influence on the free energy of solvation (ΔG_{sol}),[81-83] that is, solute geometry relaxations in solution and single point calculations on the gas-phase optimized geometries provided almost identical values of ΔG_{sol}. The interaction energy of the complexes in solution (ΔE_{sol}^{int}) was estimated from:

$$\Delta E_{sol}^{int} = \Delta E^{int} + \Delta\Delta G_{sol} \qquad (3)$$

where $\Delta\Delta G_{sol}$ is the difference between the free energy of solvation of the complex and the separated monomers.

The benzoid and quinoid structures of the optimized complexes were examined using two parameters: δ_{inter} and δ_{ring}. These bond alternation parameters were calculated according to:

$$\delta_{inter} = \frac{r_{\alpha,\alpha} - r_{\alpha,\beta}}{(r_{\alpha,\alpha} + r_{\alpha,\beta})/2} \qquad (4)$$

$$\delta_{ring} = \frac{r_{\beta,\beta} - r_{\alpha,\beta}}{(r_{\beta,\beta} + r_{\alpha,\beta})/2} \quad (5)$$

where $r_{\alpha\text{-}\alpha}$ denotes the inter-ring bond length, and $r_{\alpha\text{-}\beta}$ and $r_{\beta\text{-}\beta}$ are the intra-ring bond lengths as labeled in Scheme 2.

The IP of each calculated complex was determined using two different methodologies. The first one was the Koopman's theorem (KT),[84] according to which the IPs were taken as the negative of the highest occupied molecular orbital (HOMO) energy (*e.g.* $IP^{KT} = -\varepsilon_{HOMO}$). According to the Janak's theorem can be applied to density functional theory (DFT) calculations.[85] The second methodology was calculated as the energy difference between the optimized structures of the cation radical and neutral complexes (first adiabatic ionization potential; IP^{1a}). To evaluate the influence of the solvent media in IP^{1a}, calculations in solvent solutions were performed for the oxidized and neutral states of complexes.

The π-π^* lowest electron transition energy (ε_g) was estimated using two different strategies. In the first, ε_g was approximated as the difference between the highest occupied molecular orbital (HOMO) and the lowest unoccupied molecular orbital (LUMO), ($\varepsilon_g = \varepsilon_{HOMO} - \varepsilon_{LUMO}$). Thus, Levy and Nagy evidenced that ε_g can be rightly estimated by this procedure using DFT calculations.[86] The second estimation of ε_g was derived from the excitation energies calculated with time-dependent density functional theory (TD-DFT). This methodology provides an accurate description of the experimental ε_g values. Electronic excitations were evaluated with the B3P86[71,87] functional combined with the 6-31G(d) basis set.[74]

All calculations were performed using the Gaussian 03 computer program.[88]

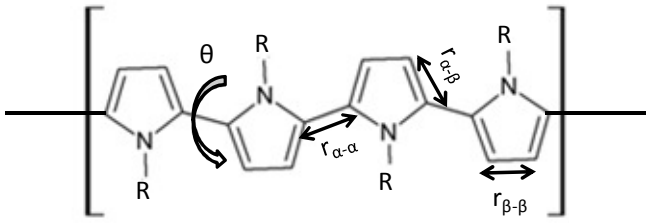

n - Py: R=H

n - NCMPy: R= CH_2CN

***Scheme 2**. Theoretical systems studied in this work.*

6.3.3. Results and discussion

Solvent effects on the geometric properties of Py and NCMPy complexes. Table 1 shows the average of the most relevant geometric parameters calculated for the neutral, cationic, dicationic (singlet), dicationic (triplet) 4Py and 4NCMPy complexes in presence of the solvents studied in this work. Geometry optimizations of the $4Py^{0}$ complex shows an average inter-ring dihedral angle (N-C-C-N) of 154.20º, 156.72º, 159.36º and 155.12º for water, methanol, acetonitrile and chloroform, respectively. Thus, an anti-gauche average conformation (θ=156.35º) was evidenced for the $4Py^{0}$ complex at B3LYP/6-31G(d) level. This trend was corroborated at MP2/6-31+G(d,p) level, being the average inter-ring dihedral angle of 136.77º. On the other hand, $4Py^{+1}$, $4Py^{+2S}$ and $4Py^{+2T}$ complexes showed an average inter-ring dihedral angle of approximately 180º corresponding to an anti-conformation. In contrast, as can be observed in Table 2, 4NCMPy complexes present a gauche-gauche conformation. This conformation was corroborated in a previous work employing 2 and 3 oligomers of NCMPy.[60] These conformation changes between 4Py and 4NCMPy complexes are related with the effect of cyano group, which induce significant conformation distortions.

The bond length alternation pattern for the conjugated π-system of 4Py and 4NCMPy oligomers is represented in Figure 1. As can be seen, the C-C bond lengths for $4Py^{0}$ and $4NCMPy^{0}$ complexes correspond to a benzenoid structure, in which the inter-ring bond lengths are larger than the intra-ring ones (Table 1). The bond alternation is more marked for $4NCMPy^{0}$ than $4PPy^{0}$ complex, respectively. On the other hand, the benzenoid structure is lost when the oxidized state is increased in the complexes, therefore, $4Py^{+1}$ and $4NCMPy^{+1}$ complexes evidence a quinoid-like structure. The $4Py^{+2S}$ and $4Py^{+2T}$ complexes present an intering dihedral angle of ~180º, and quinoid structure was confirmed according to Figure 1. It should be noted that $4Py^{+2S}$ and $4Py^{+2T}$ complexes presents the maximal quinoid effect centered on their backbones, whereas the minimum was observed at the end of oligomers. This tendency was also confirmed for $4NCMPy^{+2S}$ and $4NCMPy^{+2T}$ complexes, being more marked for the latter. Consequently, the presence of cyano group plays an important role on the structural changes observed between Py and NCMPy complexes. This tendency should be attributed to the unfavourable steric interaction produced by the strong electron-withdrawing effect induced by cyano group. As can be observed in Table 1, CN group

affects significantly the geometric parameters, specifically, the inter-ring bond distances are larger for 4NCMPy complexes than 4Py complexes. Thus, an increase of 0.016 Å, 0.014 Å, 0.008 Å and 0.015 Å was evidenced for 4NCMPy complexes in the neutral, cationic, dication (singlet) and dicationic (triplet) states, respectively. Within this context, the geometric parameters assigned as the average inter-ring bond alternation and average intra-ring alternation according to Eqn 3 and Eqn 4 were also larger for 4NCMPy complexes. Thus, the effect of δ_{inter} parameter resulted in an increase of 0.014 Å, 0.014 Å, 0.006 Å and 0.012 Å for 4NCMPy complexes, whereas the δ_{ring} parameter evidence a slight increase of approximately 0.01 Å. These results highlighted that the cyano group perturbs the $\pi - \pi$ conjugation effects. Consequently, these changes are directly related with the electronic properties, which will be discussed in the later section.

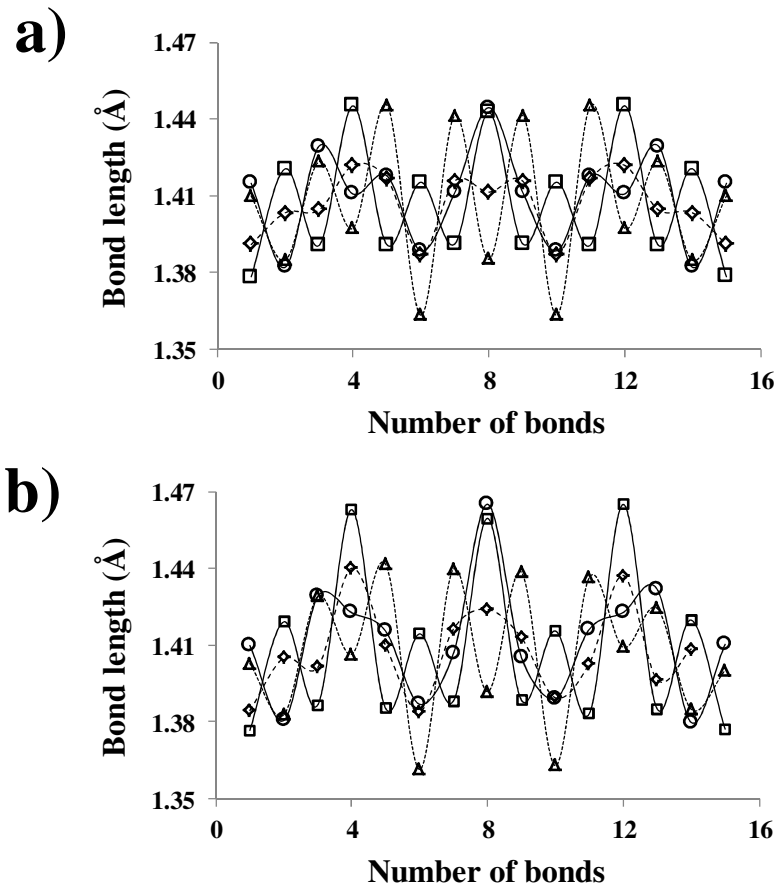

Figure 1. *a) C – C bond length alternation pattern for $4Py^{0}$ (empty squares), $4Py^{+1}$ (empty diamonds), $4Py^{+2S}$ (empty triangles) and $4Py^{+2T}$ (empty cercles). b) C-C bond length alternation pattern for $4NCMPy^{0}$ (empty squares), $4NCMPy^{+1}$ (empty diamonds), $4NCMPy^{+2S}$ (empty triangles) and $4NCMPy^{+2T}$ (empty cercles).*

Table 1. *Optimized geometries for Py and NCMPy complexes considering the neutral, cationic, dicationic (singlet) and dicationic (triplet) states at (U)B3LYP/6-31G(d) level. Calculations performed at (U)MP2/6-31+G(d,p) level were expressed in parentheses for comparison. The results correspond to average values considering water, methanol, acetonitrile and chloroform solvents, respectively.*

Species[a]	$r_{\alpha-\alpha}$[b]	δ_{inter}[c]	δ_{ring}[d]	$\theta^{e,f}$
$4Py^{0}\cdots$Solvents	1.446 (1.450)	0.041 (0.037)	0.022 (0.014)	156.35 (136.77)
$4Py^{+1}\cdots$Solvents	1.419 (1.434)	0.009 (0.029)	-0.008 (0.004)	~180 (141.11)
$4Py^{+2S}\cdots$Solvents	1.394 (1.401)	-0.024 (-0.018)	-0.039 (-0.028)	~180 (~180)
$4Py^{+2T}\cdots$Solvents	1.421 (1.420)	0.002 (0.004)	-0.023 (-0.026)	~180 (~180)
$4NCMPy^{0}\cdots$Solvents	1.462 (1.456)	0.055 (0.047)	0.024 (0.019)	--
$4NCMPy^{+1}\cdots$Solvents	1.433	0.023	-0.003	--
$4NCMPy^{+2S}\cdots$Solvents	1.402	-0.016	-0.038	--
$4NCMPy^{+2T}\cdots$Solvents	1.436	0.014	-0.022	--

[a] *All complexes are relative to the most stable of each class according to the zero-point vibrational energies (ZPVE) and the thermal and the entropic corrections.*
[b] $r_{\alpha-\alpha}$ *is the average inter-ring bond distance (in Å)*
[c] δ_{inter} *is the average inter-ring bond alternation parameter (in Å). See Eqn. (4)*
[d] δ_{ring} *is the average intra-ring bond alternation parameter (in Å). See Eqn. (5)*
[e] θ *is the average dihedral angle (in º)*
[f] *Dihedral angles for 4NCMPy oligomers are displayed for clarity in Table 2.*

Table 2. *Optimized geometries for NCMPy complexes considering the neutral, cationic, dicationic (singlet) and dicationic (triplet) states at (U)B3LYP/6-31G(d) level.*

Species[a]	θ_A	θ_B	θ_C	Species	θ_A	θ_B	θ_C
4NCMPy^{0}--Water	-106.05	-130.57	-93.43	**4NCMPy^{0}--Methanol**	-103.45	-131.21	-92.98
4NCMPy^{+1}--Water	-47.29	-154.20	-137.85	**4NCMPy^{+1}--Methanol**	-46.73	-153.94	-137.76
4NCMPy^{+2S}--Water	-28.30	-164.10	160.37	**4NCMPy^{+2S}--Methanol**	-28.63	-164.19	160.12
4NCMPy^{+2T}--Water	-150.08	-132.56	-148.07	**4NCMPy^{+2T}--Methanol**	-149.11	-136.04	-151.86

Species[a]	θ_A	θ_B	θ_C	Species	θ_A	θ_B	θ_C
4NCMPy^{0}--Acetonitrile	-115.85	-131.12	-92.57	**4NCMPy^{0}--Chloroform**	-94.44	-131.24	-94.72
4NCMPy^{+1}--Acetonitrile	-47.22	-153.17	-137.22	**4NCMPy^{+1}--Chloroform**	-47.27	-154.65	-140.09
4NCMPy^{+2S}--Acetonitrile	-34.69	-165.60	161.31	**4NCMPy^{+2S}--Chloroform**	-30.15	-164.28	160.68
4NCMPy^{+2T}--Acetonitrile	-151.15	-132.69	-119.62	**4NCMPy^{+2T}--Chloroform**	-147.27	-131.98	-152.07

[a]*All complexes are relative to the most stable of each class according to the zero-point vibrational energies (ZPVE) and the thermal and the entropic corrections.*

Solvent effects on the electronic properties of Py and NCMPy complexes. Table 3 shows the electronic properties of Py and NCMPy complexes using water, methanol, acetonitrile and chloroform as solvents. Complexes based on Py exhibit IP values similar for all solvents, being 4.29, 4.29, 4.20 and 4.23 eV for water, methanol, acetonitrile and chloroform, respectively. Within context, it should be noted that IP^{1a} values obtained are lower than IP values, being ranged from 3.71 to 3.91 eV. This similarity of IP values among different solvents (*e.g.* acetonitrile and water) was also observed and examined in thiophene and its derivatives, specifically in polythiophene (PTh), poly(3,4-ethylenedioxythiophene) (PEDOT) and poly(3,4-phenylenedioxythiophene) (PhEDOT) using the PCM method.[89] On the hand, the π-π^* lowest transition energy (ε_g) was determined 4.04, 4.00, 3.93 and 3.09 eV for 4Py complexes, respectively. This electronic property exhibited the same tendency observed for the IP electronic property in presence of solvents. In the literature some works have been devoted to study the influence of solvents in Py oligomers.[90] Specifically, electronic properties of Py oligomers containing 4 rings were evaluated in acetonitrile and dichloromethane from UV-vis technique. The experimental results showed a ε_g value of 3.54 and 3.87 eV, respectively.[91,92] *Zotti et al* studied also the influence of the solvent on the electronic properties of *n*PPy oligomers (being, n=1,2,3,5 and 7 respectively) from spectroscopy techniques in acetonitrile solution.[93] The results allowed us to predict the ε_g value by extrapolating the linear variation of this property against 1/n. Calculation on 4Py oligomer exhibited a ε_g value of 3.60 eV. In this way, a comparative study of electronic properties was carried out for cationic complexes, thus, experimental values estimated a ε_g value of 2.30 and 2.48 eV in presence of acetonitrile and chloroform, respectively. These values are in good agreement with those predicted theoretically (2.87 and 2.81 eV, respectively) in this work. The electronic properties estimated using experimental techniques can be corroborated with theoretical values using PCM/TD-DFT methodology according to Table 3.

From Table 3 a comparative study of electronic properties considering 4NCMPy and 4Py complexes was carried out. NCMPy complexes showed IP values higher than Py complexes, being 5.59, 5.63, 5.50 and 5.76 eV for the solvents described previously. The nature of electron-withdrawing strong substituents such as cyano group (-CN) decreases HOMO energies compared with un-substituted analogues (*e.g.* Py). NCMPy complexes exhibited IP^{1a} values lower than IP values, ranging from 4.97 to 5.42 eV.

Table 3. *Electronic properties (ε_g, IP^{KT}, IP^{1a}; all in eV) predicted for neutral Py and NCMPy complexes at (U)B3LYP/6-31G(d) level using the PCM method. TD-DFT methodology was performed at (U)B3P86/6-31G(d) level for neutral (N) and cationic (C) complexes. Complete geometry optimizations were carried out at (U)B3LYP/6-31G(d) level. Experimental values for the neutral and monocationic complexes, which were obtained using spectroscopy and electrochemical techniques have been included by comparison (in parentheses).*

	4Py---H_2O	**4Py--CH_3OH**	**4Py--CH_3CN**	**4Py--$CHCl_3$**
IP^{KT}	4.29	4.29	4.20	4.23
IP^{1a}	3.71	3.72	3.88	3.91
ε_g^{KT}	4.04	4.00	3.93	4.09
$\varepsilon_g^{(N)TDDFT}$	3.70	3.64	3.62 (3.54[a]/3.60[b])	3.79 (3.87)[c]
$\varepsilon_g^{(C)TDDFT}$	2.88	2.87	2.87 (2.30)[a]	2.81 (2.48)[c]

	4NCMPY---H_2O	**4NCMPy--CH_3OH**	**4NCMPy--CH_3CN**	**4NCMPy--$CHCl_3$**
IP^{KT}	5.59	5.63	5.50	5.76
IP^{1a}	4.97	4.92	5.08 (5.30)[d]	5.42
ε_g	4.94	4.95	4.81	4.61
ε_g^{TDDFT}	4.38	4.40	4.26 (2.50)[d]	4.60

[a]Data from Ref 90. [b]Data from Ref 93. [c]Data from Ref 91. [d]Data from Ref 60 considering PNCEPy polymer

According to previous works, the IP of NCMPy polymer was evaluated from electrochemical techniques in an acetonitrile solution. Thus, an IP value of 5.30 eV was estimated, which is in excellent agreement with the theoretical results obtained in Table 3 (5.08 eV). Furthermore, the ε_g was also estimated from experimental techniques based on electrochemical and spectroscopic techniques for PNCEPy. Both techniques exhibited similar values, the result showed ε_g values of approximately 2.5 eV. These results were found to be in excellent agreement with theoretical studies considering an anti-conformation for NCMPy ($\theta = 180°$).[60] In spite of this good correlation between the experimental and theoretical level, the most stable conformation of NCMPy oligomers was considered the anti-gauche conformation.[60] This structural change can be ascribed to the steric interaction produced by the cyano group, which is corroborated according to Table 2. As we cited previously, the IP value was found in excellent agreement with the experimental results in both anti and anti-gauche conformation. However, the ε_g

value estimated from TD-DFT methodology was 4.38, 4.40, 4.26 and 4.60 for water, methanol, acetonitrile and chloroform solution, respectively. These values are not in agreement with the experimental results according to Table 3. This feature can be explained from the chemical structure of PPy derivatives.

It is well known that PPy derivatives have shown to be oxidized easily during the synthesis process. Therefore, a carbonyl group (C=O) is formed in the rings of PPy derivatives, causing the overoxidation of the pyrrole ring.[94,95] This characteristic was identified in the electrochemical synthesis of PNCEPy from the fourier-transform infrared technique (FTIR). The result showed a strong band at 1740 cm^{-1}, which corresponds to the stretching vibration of carbonyl groups.[57,58] This feature has been shown to affect dramatically the electronic properties (*e.g* IP and ε_g) of PNCEPy.[60] This characteristic was identified in the electrochemical synthesis of PNCEPy from the fourier-transform infrared technique (FTIR). The result showed a strong band at 1740 cm^{-1}, which corresponds to the stretching vibration of carbonyl groups.[57,58] This feature has been shown to affect dramatically the electronic properties (*e.g* IP and ε_g) of PNCEPy.[60] Accordingly, although carbonyl groups (C=O) influences the electronic properties in Py derivatives, the theoretical model based on complexes has been considered without presence of carbonyl groups in pyrrole rings.

The models described in this work have demonstrated an excellent agreement between theoretical and experimental levels in the field of electronic properties, thus, the influence of solvent on the electronic properties depends on the chemical nature and conformation of the oligomers.

Theoretical calculations on complexes formed by solvents containing -OH groups and Py and NCMPy oligomers. In this section specific interactions between 4Py$\cdots H_2O$ and 4PPy$\cdots CH_3OH$ complexes have been studied. Figure 2 shows the most favorable molecular geometries of 4Py$\cdots H_2O$ and 4NCMPy$\cdots H_2O$ complexes for the neutral and oxidized states, respectively. All complexes are stabilized by H-O$\cdots$H hydrogen bonds. Specifically, neutral $4Py^0\cdots H_2O$ complexes present intermolecular parameters for these interactions, being $d_{O\cdots H}$ = 1.929 Å and $<$ N-H$\cdot\cdot$O = 159.98º, respectively. On the other hand, neutral $4NCMPy^0\cdots H_2O$ complexes present hydrogen bonds larger ($d_{O\cdots H}$ = 2.132 Å) than $4Py^0\cdots H_2O$. The strength of this interaction was evaluated through of binding energy in gas-phase (ΔE_{int}) and in solution (ΔE^{int}_{sol}). The values of ΔE_{int} for 4Py$\cdots H_2O$ and 4NCMPy$\cdots CH_3OH$ complexes were estimated to be similar (-6.73 and -6.80

kcal/mol, respectively). However, in solution, the neutral 4NCMPy^{0}···H_2O complex evidenced a ΔE_{sol}^{int} value of -1.46 kcal/mol, whereas 4Py^{0}···H_2O complex was calculated 0.02 kcal/mol (Table 4). The results reflect that the affinity of NCMPy oligomers with watery solutions is higher than that of Py oligomers.

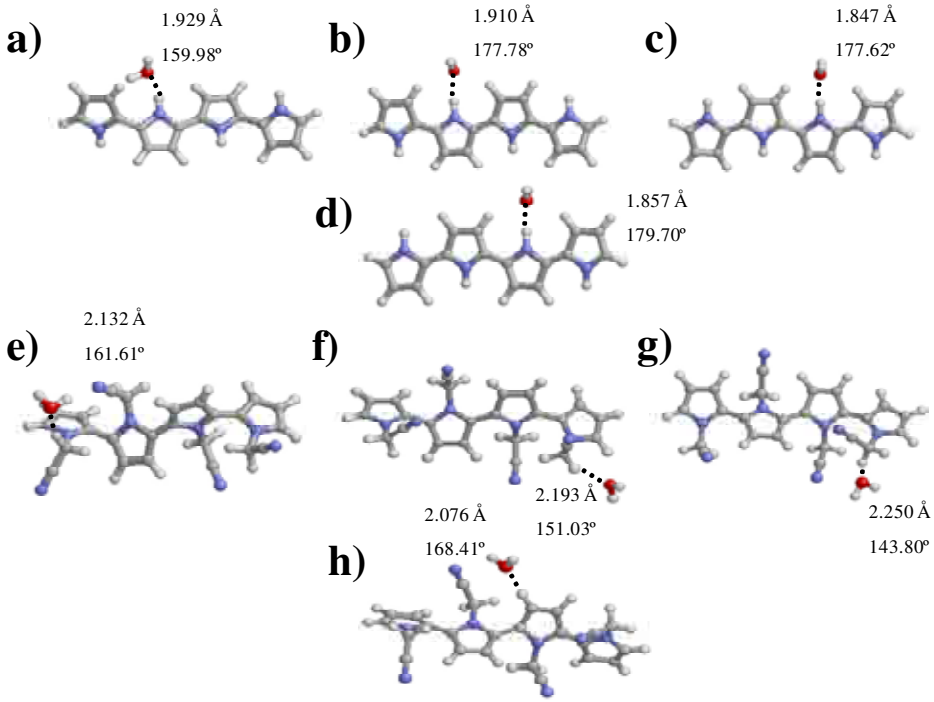

Figure 2. *Geometry of the most favored a) 4Py^{0}····H_2O, b) 4Py^{+1}····H_2O, c) 4Py^{+2S}···H_2O, d) 4Py^{2T}···H_2O, e) 4NCMPy^{0}····H_2O, f) 4NCMPy^{+1}····H_2O, g) 4NCMPy^{+2S}···H_2O, h) 4NCMPy^{+2T}···H_2O complexes calculated at the (U)B3LYP/6-31G(d). H-O···H interactions are displayed using black dashed lines. Hydrogen bonding parameters (distances and angles) are displayed.*

In spite of the excellent interactions between neutral NCMPy oligomers with water, this tendency is changed when the oxidized state is increased. Thus, the results for cationic, dicationic (singlet) and dicationic (triplet) 4Py···H_2O complexes exhibited ΔE_{int} values of -12.38, -18.68 and -18.12 kcal/mol, respectively. In contrast, 4NCMPy···H_2O complexes presented lower ΔE_{int} values (-8.91, -12.57 and -11.43 kcal/mol, respectively). In solution, monocationic and dicationic 4Py complexes presented more favourable interactions than monocationic and dicationic 4NCMPy complexes, respectively. Therefore, the oxidation degree plays an important role on the specific interactions of NCMPy and Py oligomers in presence of water. Moreover, the effect of cyano group favours the interaction between neutral NCMPy oligomers with water solvent. In summary, in the neutral state, NCMPy complexes showed the best

affinity with water, whereas oxidized Py complexes presented the best behavior in watery solution.

Table 4. *Interaction energies in the gas-phase and in solution (water and methanol) (ΔE_{int} and ΔE_{sol}^{int} respectively, in kcal·mol^{-1}) obtained at the (U)B3LYP/6-31G(d) level for the complexes. Calculations performed at (U)MP2/6-31+G(d,p) level were expressed in parentheses for comparison. Complete geometry optimizations were carried out at (U)B3LYP/6-31G(d) and (U)MP2/6-31+G(d,p) level, respectively.*

Complex[a]	ΔE_{int}[b]	ΔE_{sol}^{int}	Complex	ΔE_{int}[b]	ΔE_{sol}^{int}
4Py^{0}--Water	-6.73 (-7.27)	0.02 (2.29)	**4Py^{0}--Methanol**	-6.59 (-7.82)	2.96 (2.48)
4Py^{+1}--Water	-12.38 (-11.20)	-2.96 (1.64)	**4Py^{+1}--Methanol**	-11.92 (-14.44)	-1.42 (-1.01)
4Py^{+2S}--Water	-18.68 (-17.02)	-3.44 (1.48)	**4Py^{+2S} --Methanol**	-19.10 (-19.84)	-2.13 (0.22)
4Py^{+2T}--Water	-18.12 (-16.94)	-3.60 (-0.47)	**4Py^{+2T} --Methanol**	-18.46 (-19.73)	-2.26 (-2.02)

Complex[a]	ΔE_{int}[b]	ΔE_{sol}^{int}	Complex	ΔE_{int}[b]	ΔE_{sol}^{int}
4NCMPy^{0}--Water	-6.80 (-7.46)	-1.46 (-2.11)	**4NCMPy^{0}--Methanol**	-6.52 (-7.57)	0.47 (0.24)
4NCMPy^{+1}--Water	-8.91	-2.28	**4NCMPy^{+1}--Methanol**	-8.35	-0.86
4NCMPy^{+2S}--Water	-12.57	-3.12	**4NCMPy^{+2S} --Methanol**	-14.30	-2.17
4NCMPy^{+2T}--Water	-11.43	-1.60	**4NCMPy^{+2T} --Methanol**	-13.11	-0.29

[a]All complexes are relative to the most stable of each class according to the zero-point vibrational energies (ZPVE) and the thermal and the entropic corrections.[b]Binding energies were computed using the counterpoise correction method.

Inspection of Py and NCMPy complexes with methanol were studied as can be seen in Figure 3. Again, the complexes were stabilized through H-O···H hydrogen bonds. The geometric parameters of the interaction were determined $d_{O\cdots H}$ = 1.914 Å and $<$N-H··O = 160.24º for $4Py^0\cdots CH_3OH$ complexes. These values are slightly lower than $Py^0\cdots H_2O$ complexes. The $4Py^0\cdots CH_3OH$ complex presented similar values of interaction energy compared with $4Py^0\cdots H_2O$ and $4NCMPy^0\cdots CH_3OH$ complexes (-6.59 and -6.52 kcal/mol) in gas-phase. However, neutral NCMPy complexes in methanol solution evidenced an interaction energy more favoured than neutral Py complexes (0.47 and 2.96 kcal/mol, respectively). As we discussed previously, neutral NCMPy complexes present better interaction with methanol solvent than Py complexes. Nevertheless, interactions between monocationic and dicationic Py complexes are more favoured than monocationic and dicationic NCMPy complexes. This tendency was also observed for water molecules according to Table 4. Calculations performed at MP2/6-31+G(d,p) level exhibited similar values compared with B3LYP/6-31G(d).

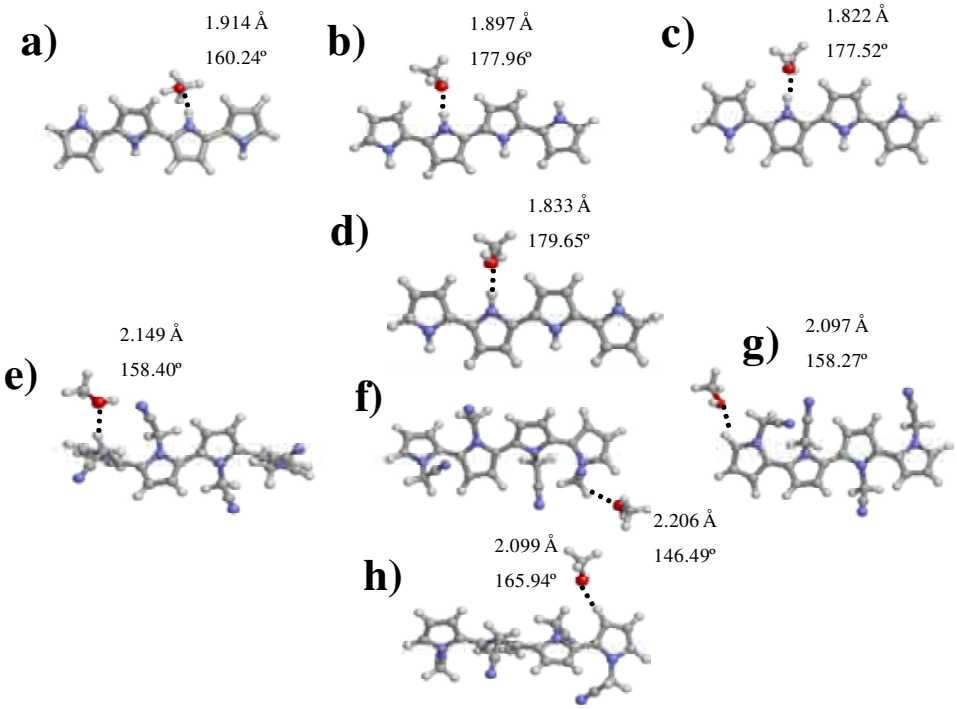

Figure 3. *Geometry of the most favored a) $4Py^0\cdots CH_3OH$, b) $4Py^{+1}\cdots CH_3OH$, c) $4Py^{+2S}\cdots CH_3OH$, d) $4Py^{2T}\cdots CH_3OH$, e) $4NCMPy^0\cdots CH_3OH$, f) $4NCMPy^{+1}\cdots CH_3OH$, g) $4NCMPy^{+2S}\cdots CH_3OH$, h) $4NCMPy^{+2T}\cdots CH_3OH$ complexes calculated at the (U)B3LYP/6-31G(d) level. H-O···H interactions are displayed using black dashed lines. Hydrogen bonding parameters (distances and angles) are displayed.*

The study of 4NCMPy complexes performed at MP2/6-31+G(d,p) showed similar values for the interaction energy in gas-phase (ΔE_{int}) and in solution (ΔE_{sol}^{int}) for both 4Py and 4NCMPy complexes in presence of water and methanol respectively.

Theoretical calculations on complexes formed by Py and NCMPy oligomers in presence of acetonitrile and chloroform. Figure 4 shows the optimized molecular geometries of 4Py···CH_3CN and 4NCMPy···CH_3CN complexes. All complexes are stabilized by (C-N···H) hydrogen bonds. The intermolecular parameters for these interactions are displayed in Figure 4. As can be seen, the interaction distances decreases when the oxidized state of the polymer increases. This tendency was observed for both 4Py and 4NCMPy complexes, although 4Py···CH_3CN presents interaction distances shorter than 4NCMPy···CH_3CN complexes. This result can be ascribed to the steric effects of the cyano group in the conformational properties of NCMPy. This tendency was also observed for water and methanol solvents. Thus, planar conformations exhibited by Py oligomers evidenced shorter interaction distances.

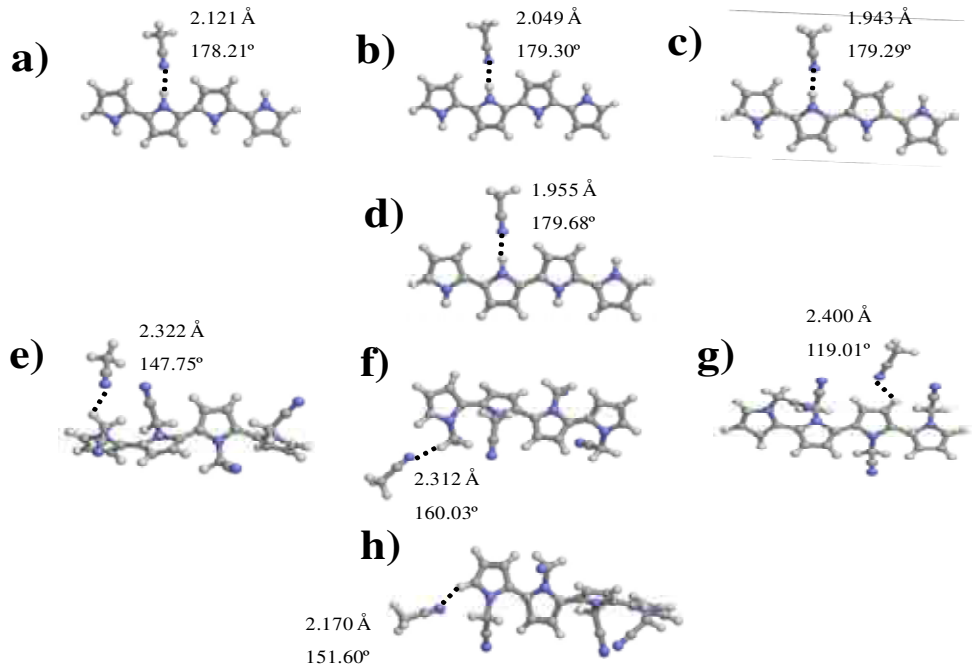

Figure 4. *Geometry of the most favored a) $4Py^{0}$····CH_3CN, b) $4Py^{+1}$····CH_3CN, c) $4Py^{+2S}$···CH_3CN, d) $4Py^{2T}$···CH_3CN, e) $4NCMPy^{0}$····CH_3CN, f) $4NCMPy^{+1}$····CH_3CN, g) $4NCMPy^{+2S}$···CH_3CN, h) $4NCMPy^{+2T}$···CH_3CN complexes calculated at the (U)B3LYP/6-31G(d) level. C-N···H interactions are displayed using black dashed lines. Hydrogen bonding parameters (distances and angles) are displayed.*

Table 5. *Interaction energies in the gas-phase and in solution (acetonitrile and chloroform) (ΔE_{int} and ΔE_{sol}^{int}, respectively, in kcal·mol^{-1}) obtained at the (U)B3LYP/6-31G(d) level for the complexes. Calculations performed at (U)MP2/6-31+G(d,p) level were expressed in parentheses for comparison. Complete geometry optimizations were carried out at (U)B3LYP/6-31G(d) and (U)MP2/6-31+G(d,p) level, respectively.*

Complex[a]	ΔE_{int}[b]	ΔE_{sol}^{int}	Complex	ΔE_{int}[b]	ΔE_{sol}^{int}
4Py^{0}--Acetonitrile	-4.12 (-6.21)	2.08 (1.86)	**4Py^{0}--Chloroform**	-0.23 (-4.16)	2.51 (0.34)
4Py^{+1}--Acetonitrile	-12.76 (-13.46)	2.01 (2.79)	**4Py^{+1}--Chloroform**	-3.11 (-4.08)	5.37 (1.06)
4Py^{+2S}--Acetonitrile	-22.10 (-23.91)	2.08 (2.39)	**4Py^{+2S} --Chloroform**	-6.84 (-7.32)	6.76 (7.45)
4Py^{+2T}--Acetonitrile	-21.39 (-22.94)	1.69 (1.24)	**4Py^{+2T} --Chloroform**	-6.88 (-7.56)	5.85 (6.13)

Complex[a]	ΔE_{int}[b]	ΔE_{sol}^{int}	Complex	ΔE_{int}[b]	ΔE_{sol}^{int}
4NCMPy^{0}--Acetonitrile	-3.14 (-4.27)	3.57 (4.77)	**4NCMPy^{0}--Chloroform**	-3.38 (-4.60)	2.56 (0.54)
4NCMPy^{+1}--Acetonitrile	-9.42	1.69	**4NCMPy^{+1}--Chloroform**	-2.74	3.55
4NCMPy^{+2S}--Acetonitrile	-12.66	3.28	**4NCMPy^{+2S} --Chloroform**	-4.38	5.06
4NCMPy^{+2T}--Acetonitrile	-16.89	0.01	**4NCMPy^{+2T} --Chloroform**	-5.26	4.34

[a]All complexes are relative to the most stable of each class according to the zero-point vibrational energies (ZPVE) and the thermal and the entropic corrections.[b]Binding energies were computed using the counterpoise correction method.

According to the Table 5, the complexes involving 4Py showed a higher interaction than 4NCMPy in gas phase. Indeed, the difference between the two systems increases with the oxidation degree of the oligomer. The interaction energy increases with the charge for both 4NCMPy and 4Py oligomers in presence of acetonitrile. Again, the interaction energies showed at MP2/6-31G(d) level showed an energy difference of approximately 2 kcal/mol.

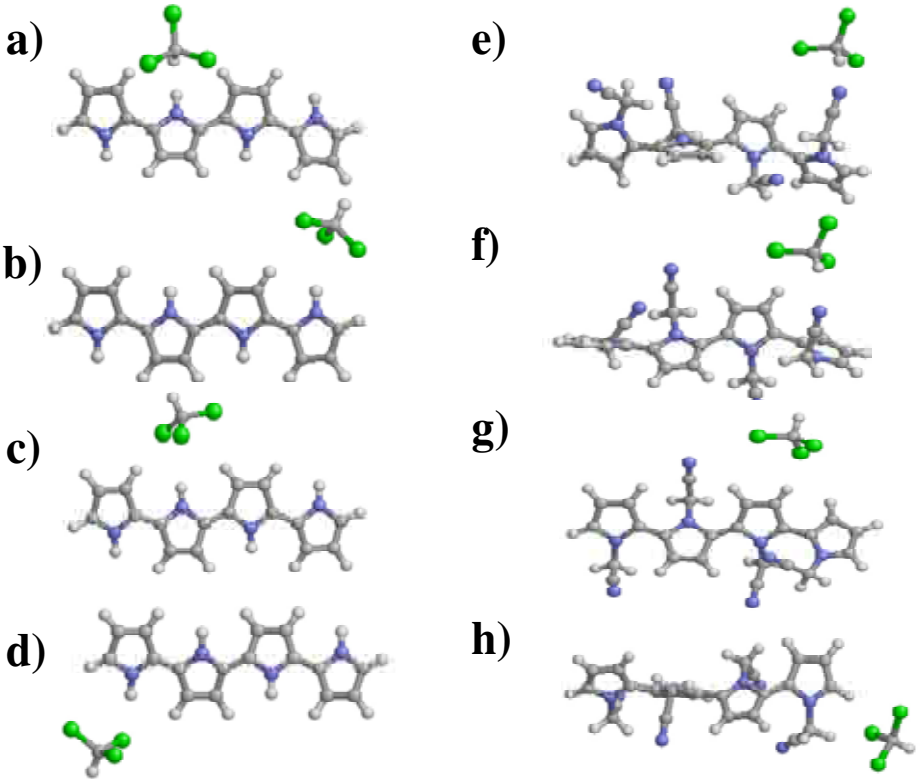

Figure 5. *Geometry of the most favored a) $4Py^{0}\cdots CHCl_3$, b) $4Py^{+1}\cdots CHCl_3$, c) $4Py^{+2S}\cdots CHCl_3$, d) $4Py^{2T}\cdots CHCl_3$, e) $4NCMPy^{0}\cdots CHCl_3$, f) $4NCMPy^{+1}\cdots CHCl_3$, g) $4NCMPy^{+2S}\cdots CHCl_3$, h) $4NCMPy^{+2T}\cdots CHCl_3$ complexes calculated at the (U)B3LYP/6-31G(d) level.*

Figure 5 shows the most stable conformation of 4Py and 4NCMPy complexes in presence of chloroform at (U)B3LYP/6-31G(d) level. 4Py oligomers evidenced no specific interaction with chloroform, thus, this tendency was corroborated at neutral, oxidized, cationic and dicationic states, respectively. Recently, some works concluded that Py films shows strong response to diisopropyl methylphosphonate (DIMP), ethanol, methanol and no response to chloroform, toluene and hexane vapors.[96] When gas molecules are adsorbed into the polymeric film, the gas interact with the film to generate a repulsive force between the polymeric chains, which cause internal changes in the volume of the film (*e.g.* swelling).[97,98] Consequently, the refractive index and reflectance, which is generated by the swelling effect, are easily detected as a

consequence of the interaction of small molecular volume and large polarity of organic compounds, such as methanol, ethanol or water vapors.[99]

However, several works evidenced the ability of Py to be employed as chemical sensor depending on the use of the dopant agent[100,101] and concentration of chloroform (*e.g.* detection limit, 3 mg).[49] According to the aforementioned characteristics, the theoretical results show similar tendencies to NCMPy oligomers, it should be noted that the interaction energies in solution are clearly favoured in presence of 4NCMPy···$CHCl_3$ complexes. The results displayed in Table 5 concluded these results in all charged states.

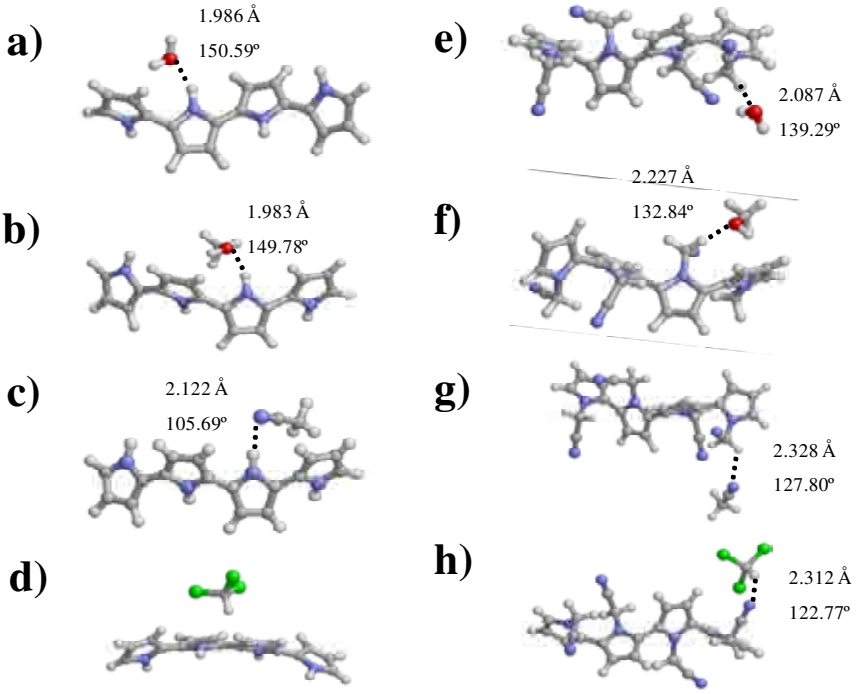

Figure 6. *Geometry of the most favoured a) $4Py^0$····H_2O, b) $4Py^0$···CH_3OH, c) $4Py^0$···CH_3CN, d) $4Py^0$···$CHCl_3$, e) $4Py^0$···$C_6H_5CH_3$, f) $4NCMPy^0$····H_2O, g) $4NCMPy^0$···CH_3OH, h) $4NCMPy^0$···CH_3CN, i) $4NCMPy^0$···$CHCl_3$ and j) $4NCMPy^0$···$C_6H_5CH_3$ complexes calculated at the MP2/6-31+G(d,p) level. H-O···H, C-N···H interactions are displayed using black dashed lines. Hydrogen bonding parameters (distances and angles) are displayed.*

According to Figure 6 specific interactions of NCMPy and Py complexes with polar solvent molecules have been performed at MP2/6-31+G(d,p) level considering the neutral state. The results show that NCMPy and Py complexes are stabilized through hydrogen bonding in presence of water, methanol, and acetonitrile, being the geometric parameters displayed in Figure 6. As can be seen, 4NCMPy complexes present intermolecular distances larger than 4Py complexes. The binding strength estimated at MP2/6-31+G(d,p) level was similar to B3LYP/6-31G(d) level for both complexes in

gas-phase. The results showed that the interaction energies ΔE_{int} were practically equal in water and methanol solution for both 4Py and 4NCMPy complexes in gas-phase (Table 4). This tendency was corroborated for the acetonitrile and chloroform solvents (Table 5). It is worth noting that 4NCMPy···$CHCl_3$ complexes showed a specific interaction through bonding hydrogen at MP2/6-31+G(d,p), whereas 4Py···$CHCl_3$ evidenced no interaction between the polymer and the solvent.

As we cited previously, *Thompson et al* reported an exhaustive experimental work where the influences of neutral PPy and PNCEPy systems to be employed as chemical sensor were discussed.[64] The theoretical results obtained in Figure 7 show that neutral NCMPy complexes shows better affinity and sensitivity than neutral Py complexes in presence of water, methanol, and chloroform solution. This effect is clearly dominated by the presence of the cyano group, which induces a polarizable effect. In contrast, Py complexes presented the best performance in acetonitrile solution. These results are in good concordance with Thompson's works. On the other hand, Py complexes showed better affinity and response as chemical sensor than NCMPy complexes at different oxidation states of the polymers (cationic and dicationic) in water, methanol and chloroform.

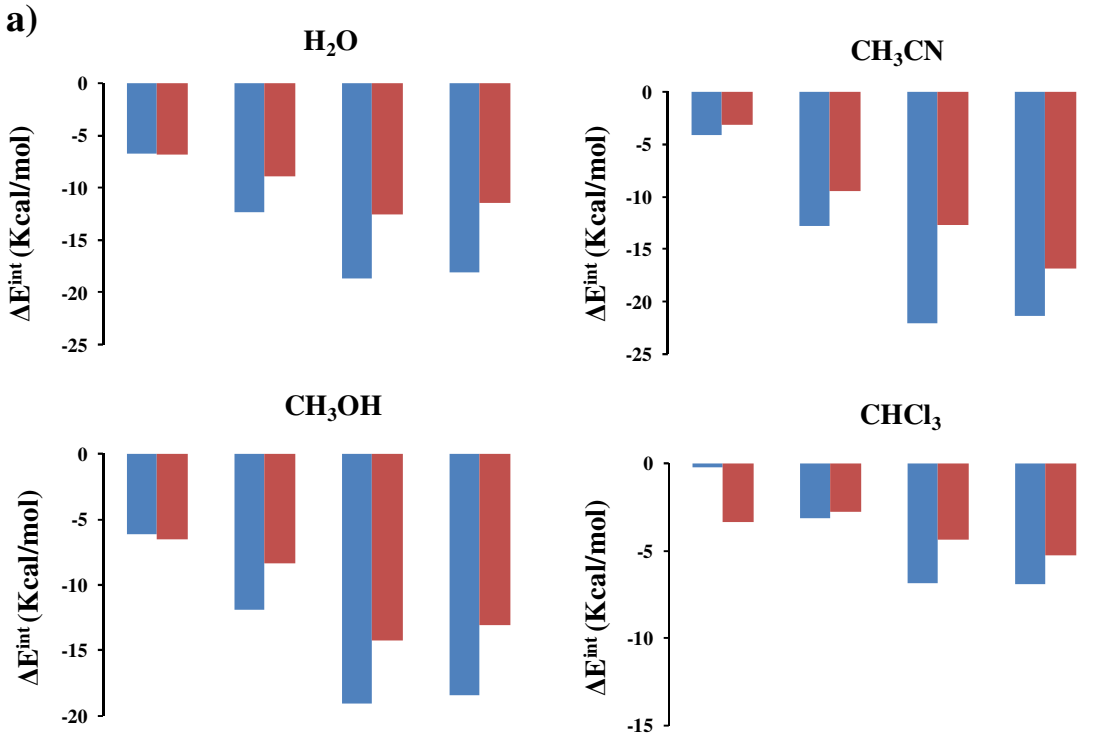

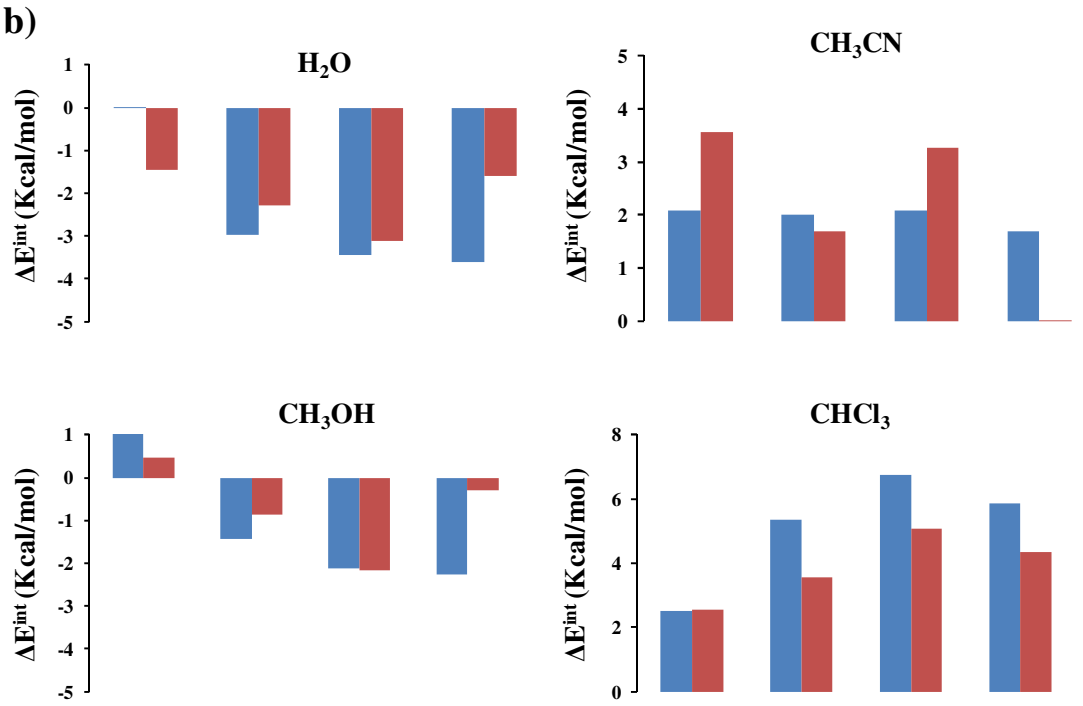

Figure 7. *a) Binding energies in gas-phase obtained at the (U)B3LYP/6-31G(d) level for the 4PPy and 4NCMPy oligomers in presence of solvents (H_2O, CH_3OH, CH_3CN, $CHCl_3$, respectively). b) Binding energies in solution obtained at the (U)B3LYP/6-31G(d) level for the 4Py and 4NCMPy oligomers in presence of solvents (H_2O, CH_3OH, CH_3CN, $CHCl_3$, respectively). Red and blue bar corresponds to Py NCMPy complexes. N, C, DS, and DT corresponds to neutral, cationic, dicationic (singlet) and dicationic (triplet) states, respectively.*

Application of PPy and PNCEPy as solvent vapors sensors. A chemical sensor known as chemiresistor was built from PPy and PNCEPy films fixed on an insulating substrate. The sensor was exposed in contact with a vapor solvent (analyte) at a fix concentration, while simultaneously measures of the electrical resistances were carried out. The vapor chosen was acetonitrile since theoretical results showed an inverse tendency according to Thompson's works. Fig. 8a shows the sensitivity of the sensor against the exposure time. In this case, PNCEPy exhibited a better sensitivity than PPy films during all the experiment. On the other hand, the sensor's response displayed in Fig. 8b reflects that PNCEPy films present an excellent behavior as chemical sensor (17 %) due to the presence of the cyano group, whereas the sensor's response for PPy films is approximately 5 %. These results conclude that PNCEPy films are sensitive to vapors and the chemical nature of this polymer plays a role key in the detection for organic compound vapors.

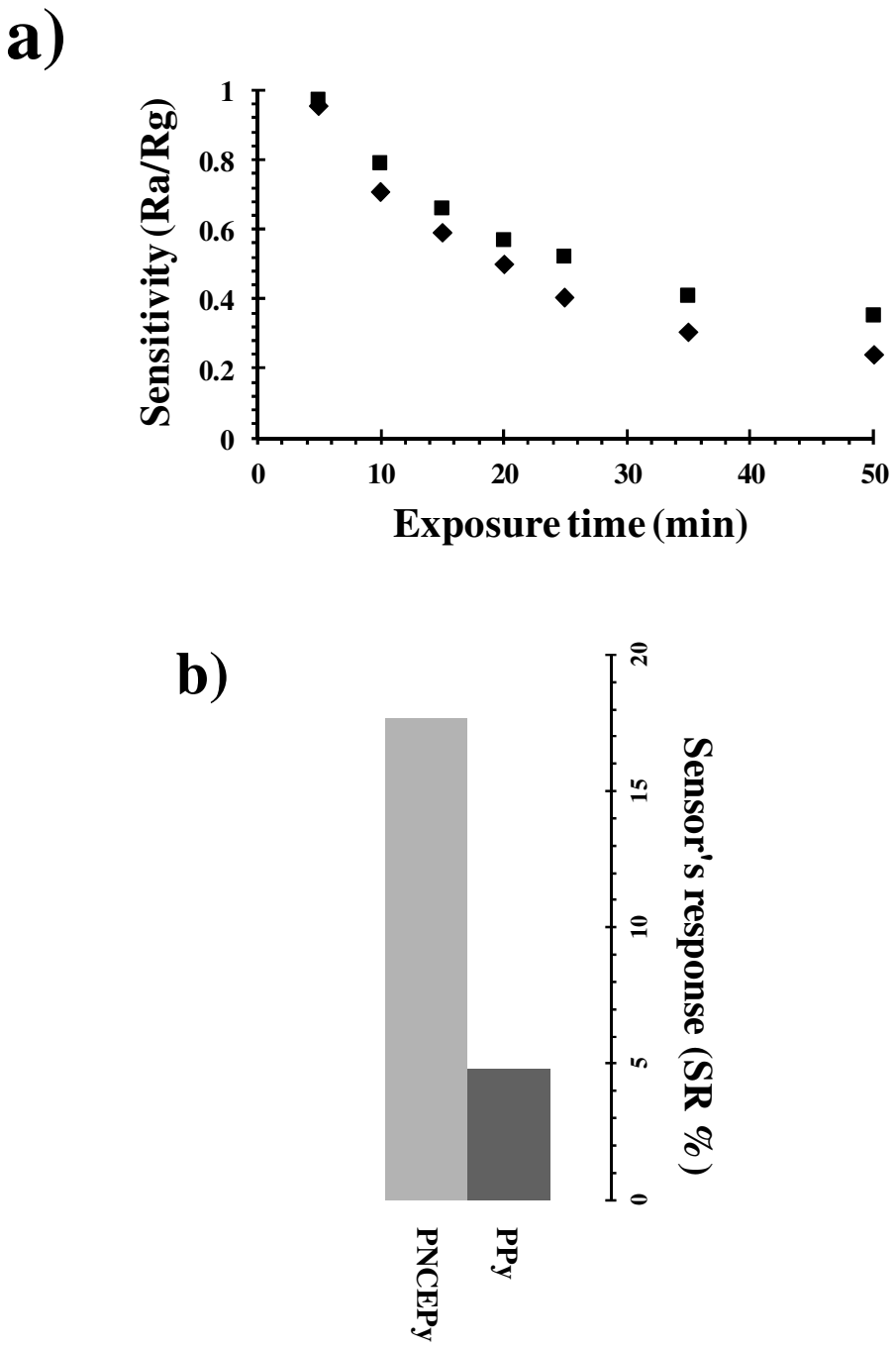

Figure 8. *a) Change of sensitivity against exposure time in presence of acetonitrile vapour for chemiresistors based on PNCPEy (black squares) and PPy (black diamonds). b) Sensor's response for neutral PPy (black bar) and PNCEPy (grey bar) films in presence of acetonitrile vapour.*

6.3.4. Conclusions

Quantum mechanical calculations on model complexes based on 4Py and 4NCMPy oligomers with solvent molecules have been employed to study and to understand the electronic properties, conformation changes and specific interactions. The results exhibited in this work have shown the affinity of Py derivatives with polar solvents. Moreover, the model complexes considered in this work have shown an excellent consistency with experimental observations employed in chemical sensors. Next, we discussed the most important conclusions obtained in this work.

The electronic properties of the complexes reported in this work (ε_g and IP) have been calculated in solution and compared with experimental results. Among solvents employed in this work, acetonitrile and chloroform have been reported in the literature to study their influences on the electronic properties of Py oligomers. Thus, experimental calculations based on spectroscopy techniques estimated a ε_g values of 3.60 and 3.87 eV in presence of acetonitrile and chloroform solutions. These values are fully consistent with those predicted theoretically (3.62 and 3.79 eV, respectively). On the other hand, oxidized Py complexes were also evaluated at both theoretical and experimental level with an excellent agreement. The electronic properties estimated for the other solvents estimated similar values (*e.g.* < 0.1 eV of difference respect acetonitrile and chloroform solvents) for Py complexes. Therefore, the complex model based on complexes presented in this work allowed to understand the solvent effects on the electronic properties of neutral and cationic Py oligomers, respectively. Furthermore, the different chemical nature of the solvents presented a negligible effect on the electronic properties of Py complexes. In contrast, the electronic properties of NCMPy complexes showed an IP and ε_g values higher than Py complexes because of the presence of cyano group. This substituent has a strong electron-withdrawing effect, which distorts the conformation structural of NCMPy oligomers modifying the electronic properties. Thus, whereas Py oligomers exhibited an anti-gauche conformation (neutral state) and anti-planar conformation (excited states), NCMPy presented a gauche-gauche conformation in all its states.

The Py and NCMPy complexes studied in this work presented similar specific interactions in presence of water, methanol, and acetonitrile solvents. Thus, complexes were stabilized through hydrogen bonding (H-O···H and C-N···H) for all their electronic states (neutral, cationic and dicationic). The strength of this interaction in gas-

phase for neutral Py complexes grows in the following order: $4Py^0\cdots H_2O$ > $4Py^0\cdots CH_3OH$ > $4Py^0\cdots CH_3CN$ > $4Py^0\cdots CHCl_3$, whereas for NCMPy complexes the order is showed as follow: $4NCMPy^0\cdots H_2O$ > $4NCMPy^0\cdots CH_3OH$ > $4NCMPy^0\cdots CHCl_3$ > $4NCMPy^0\cdots CH_3CN$. The strength of the interaction energy in gas phase increases with the charge of the complexes. It should be noted that the charge distribution, chemical nature and polarity of the solvent plays an important role on the formation of the complexes. Thus, neutral NCMPy complexes presented a better affinity in water, methanol and chloroform solvents than neutral Py complexes according to the interaction energies in solution. These tendencies are fully consistent with experimental observations.

In conclusion, the model NCMPy and Py complexes reported in this work can be successfully applied to understand the interactions among Py derivatives oligomers (solute) and solvent. Particularly, NCMPy complexes have been demonstrated to present better interaction with polar solvents than Py complexes. Therefore, NCMPy can be applied as a highly sensitive detector various organic solvents in vapor-phase.

6.3.5. References

[1]. MacDiarmid, A. G. *Angew. Chem. Int. Ed.* **2001**, *40*, 2581.

[2]. Heeger, A. J. *Angew. Chem. Int. Ed.* **2001**, *40*, 2591.

[3]. Gurunathan, K.; Murugan, A. V.; Marimuthu, R.; Mulik, U. P.; Amalnerkar, D. P. *Mater. Chem. Phys.* **1999**, *61*, 173.

[4]. Krebs, F. C. *Sol. Energ. Mat. Sol. C.* **2009**, *93*, 394.

[5]. McQuade, D. T.; Pullen, A. E.; Swager, T. M. *Chem. Rev.* **2000**, *100*, 2537.

[6]. Ates, M.; Sarac, A. S. *Progr. Org. Coat.* **2009**, *66*, 337.

[7]. Janata, J.; Josowicz, M. *Nat. Mater.* **2002**, *2*, 19.

[8]. Argun, A. A.; Aubert, P. H.; Thompson, B. C.; Schwendeman, I.; Gaupp, C. L.; Hwang, J.; Pinto, N. J.; Tanner, D. B.; MacDiarmid, A. G.; Reynolds, J. R. *Chem. Mater.* **2004**, *16*, 4401.

[9]. Smela, E. *Adv. Mater.* **2003**, *15*, 481.

[10]. Bierwagen, G. P.; Twite, R. L. *Progr. Org. Coat.* **1998**, *33*, 91.

[11]. Khot, L. R.; Panigrahi, S.; Lin, D. *Sens. Actuators B* **2011**, *153*, 10.

[12]. Abasiyanik, M. F.; Senel, M. *J. Elecroanalyt. Chem.* **2010**, *639*, 21.

[13]. Atta, N. F.; El-Kady, M. F. *Sens. Actuators B* **2010**, *145*, 299.

[14]. Brugnollo, E. D.; Paterno, L. G.; Leite, F. L.; Fonseca, F. J.; Constantino, C. J. L.; Antunes, P. A.; Mattoso, L. H. C. *Thin Solid Films* **2008**, *516*, 3274.

[15]. Wang, P.; Li, S.; Kan, J. *Sens. Actuators B* **2009**, *137*, 662.

[16]. Kim, D.; Yoo, B. *Electrochim. Acta* **2011**, *160*, 1168.

[17]. Jeon, S. S.; An, H. H.; Yoon, C. S.; Im, S. S. *Polymer* **2011**, *52*, 652.

[18]. Maksymiuk, K. *Electroanal.* **2006**, *18*, 1537.

[19]. Wang, L. X.; Li, X. G.; Yang, Y. L. *React. Funct. Polym.* **2001**, *47*, 125.

[20]. Ateh, D. D.; Navsaria, H. A.; Vadgama, P. *J. R. Soc. Interface* **2006**, *3*, 741.

[21]. Zhang, J.; Kong, L. B.; Li, H.; Luo, Y.; Kang, L. *J. Mater. Sci.* **2010**, *45*, 1947.

[22]. Zang, J.; Li, X. *J. Mater. Chem.* **2011**, *21*, 10965.

[23]. Guo, Z. P.; Wang, J. Z., Liu, H. K.; Dou, S. X. *J. Power Sources* **2005**, *146*, 448.

[24]. Lee, J. W.; Serna, F.; Nickels, J.; Schmidt, C. E. *Biomacromolecules* **2006**, *7*, 1962.

[25]. Lee, J. Y.; Bashur, C. A.; Goldstein, A. S.; Schmidt, C. E. *Biomaterials* **2009**, *30*, 4325.

[26]. Wuang, S. C.; Neoh, K. G.; Kang, E. T.; Pack, D. W.; Leckband, D. E. *J. Mater. Chem.* **2007**, *17*, 3354.

[27]. Ramanavicius, A.; Ramanaviciene, A.; Malinauskas, A. *Electrochim. Acta* **2006**, *51*, 6025.

[28]. Travas-Sejdic, J.; Peng, H.; Kilmartin, P. A.; Cannell, M. B.; Bowmaker, G. A.; Cooney, R. P.; Soeller, C. *Synth. Met.* **2005**, *152*, 37.

[29]. Peng, H.; Soeller, C.; Travas-Sejdic, J. *Macromolecules* **2007**, *40*, 909.

[30]. Peng, H.; Zhang, L.; Soeller, C.; Travas-Sejdic, J. *Biomaterials* **2009**, *30*, 2132.

[31]. Travas-Sejdic, J.; Peng, H.; Cooney, R.P.; Bowmaker, G. A.; Cannell, M. B.; Soeller C. *Curr. Appl. Phys.* **2006**, *6*, 562.

[32]. Komarova, E.; Aldissi, M.; Bogomolova, A. *Biosens. Bioelectron.* **2005**, *21*, 182.

[33]. Fabregat, G.; Córdova-Mateo, E.; Armelin, E.; Bertrán, O.; Alemán, C. *J. Phys. Chem. C* **2011**, *115*, 14933.

[34]. Martí, M.; Fabregat, G.; Estrany, F.; Alemán, C.; Armelin, E. *J. Mater. Chem.* **2010**, *20*, 10652.

[35]. Kan, X.; Zhou, H.; Li, C.; Zhu, A.; Xing, Z.; Zhao, Z. *Electrochim. Acta* **2012**, *63*, 69.

[36]. Zhuang, Z.; Li, J.; Xu, R.; Xiao, D. *Int. J. Electrochem. Sci.* **2011**, *6*, 2149.

[37]. Genies, E. M.; Marchesiello, M. *Synth. Met.* **1993**, *57*, 3677.

[38]. Callegari, A.; Cosnier, S.; Marcaccio, M.; Paolucci, D.; Paolucci, F.; Georgakilas, V.; Tagmatarchis, N.; Vazquez, E.; Prato, M. *J. Mater. Chem.* **2004**, *14*, 807.

[39]. Singh, M.; Kathuroju, P. V.; Jampana, N. *Sens. Actuators B* **2009**, *143*, 430.

[40]. Sung, W. J.; Bae, Y. H. *Biosens. Bioelectron.* **2003**, *18*, 1231.

[41]. Senel, M.; Bozgeyik, I.; Cevik, E.; Abasiyanik, M. F. *Synth. Met.* **2011**, *161*, 440.

[42]. Arya, S. K.; Datta, M.; Malhotra, B. D. *Biosens. Bioelectron.* **2008**, *23*, 1083.

[43]. Yildirmoglu, F.; Arslan, F.; Cete, S.; Yasar, A. *Sens.* **2009**, *9*, 6435.

[44]. Bourigua, S.; Errachid, A.; Dzyadevych, S.; Maaref, A.; Renault, N. J. *Sens. Lett.* **2011**, *9*, 2232.

[45]. Hu, W.; Li, C. M.; Cui, X.; Dong, H.; Zhou, Q. *Langmuir* **2007**, *23*, 2761.

[46]. O'Grady, M. L.; Parker, K. K. *Langmuir* **2008**, *24*, 316.

[47]. Jiang, L.; Jun, H. K.; Hoh, Y. S.; Lim, J. O.; Lee, D. D.; Huh, J. S. *Sens. Actuators B* **2005**, *105*, 132.

[48]. Kincal, D.; Kumar, A.; Child, A. D.; Reynolds, J. R. *Synth. Met.* **1998**, *92*, 53.

[49]. Pirsa, S.; Alizadeh, N. *Sens. Actuators B* **2012**, *168*, 303.

[50]. Hosono, K.; Matsubara, I.; Murayama, N.; Woosuck, S.; Izu, N. *Chem. Mater.* **2005**, *17*, 349.

[51]. Kan, X.; Zhou, H.; Li, C.; Zhu, A.; Xing, Z.; Zhao, Z. *Electrochim. Acta* **2012**, *63*, 69.

[52]. Carquigny, S.; Sanchez, J. B.; Berger, F.; Lakard, B.; Lallemand, F. *Talanta* **2009**, *78*, 199.

[53]. Brie, M.; Turcu, R.; Neamtu, C.; Pruneanu, S. *Sens. Actuators B* **1996**, *37*, 119.

[54]. Joshi, A.; Gangal, S. A.; Gupta, S. K. *Sens. Actuators B* **2011**, *156*, 938

[55]. Dong, H.; Cao, X.; Li, C. M. *App. Mat. Interf.* **2009**, *7*, 1599.

[56]. Lacy Costello, B. J. P.; Evans, P.; Guernion, N.; Ratcliffe, N.M.; Sivanand, P.S.; Teare, G. C. *Synth. Met.* **2000**, *114*, 181.

[57]. Aradilla, D.; Estrany, F.; Armelin, E.; Oliver, R.; Iribarren, J. I.; Alemán, C. *Macromol. Chem. Phys.* **2010**, *211*, 1663.

[58]. Fabregat, G.; Alemán, C.; Casas, M. T.; Armelin, E. *J. Phys. Chem. B* **2012**, *116*, 5064.

[59]. Yamauchi, T.; Kojima, K.; Tanaka, K.; Unuma, T.; Shimomura, M.; Miyauchi, S. *Polymer* **1996**, *37*, 1289.

[60]. Aradilla, D.; Torras, J.; Alemán, C. *J. Phys. Chem. B* **2011**, *115*, 2882.

[61]. Tuzun, N. S.; Bayata, F.; Sarac, A. S. *J. Mol. Struct.* **2008**, *857*, 95.

[62]. Rimarcik, J.; Lukes, V.; Klein, E.; Griesser, M.; Kelterer, A. M. *Chem. Phys.* **2008**, *353*, 177.

[63]. Deng, Z.; Stone, D. C.; Thompson, M. *Analyst* **1997**, *122*, 1129.

[64]. Deng, Z.; Stone, D. C.; Thompson, M. *Can. J. Chem.* **1995**, *73*, 1427.

[65]. Deng, Z.; Stone, D. C.; Thompson, M. *Analyst* **1996**, *121*, 1341.

[66]. Ouerghi, O.; Senillou, A.; Jaffrezic-Renault, N.; Martelet, C.; Ouada, H. B.; Cosnier, S. *J. Electroanal. Chem.* **2001**, *501*, 62.

[67]. Gambhir, S.; Wagner, K.; Officer, D. L. *Synth. Met.* **2005**, *154*, 117.

[68]. Arrigan, D. W. M. *Anal. Commun.* **1997**, *34*, 241.

[69]. Casanovas, J.; Cho, L. Y.; Ocampo, C.; Alemán, C. *Synth. Met.* **2005**, *151*, 239.

[70]. Aradilla, D.; Estrany, F.; Oliver, R.; Alemán, C. *Eur. Polym. J.* **2010**, *46*, 2222.

[71]. Alemán, C.; Casanovas, J.; Torras, J.; Bertrán, O.; Armelin, E.; Oliver, R.; Estrany, F. *Polymer* **2008**, *49*, 1066.

[72]. Becke, A. D.; *J. Chem. Phys.* **1993**, *98*, 1372.

[73]. Lee, C.; Yang, W.; Parr, R. G. *Phys. Rev. B* **1988**, *37*, 785.

[74]. Hariharan, P. C.; Pople, J. A. *Chem. Phys. Lett.* **1972**, *16*, 217.

[75]. Møller, C.; Plesset, M. *Phys. Rev.* **1934**, *46*, 618.

[76]. Hariharan, P. C.; Pople, J. A. *Theor. Chim. Acta* **1973**, *28*, 213.

[77]. McLean, A. D.; Chandler, G. S. *J. Chem. Phys.* **1980**, *72*, 5639.

[78]. Boys, S. F.; Bernardi, F. *Mol. Phys.* **1970**, *19*, 553.

[79]. Miertus, M.; Scrocco, E.; Tomasi, J. *Chem. Phys.* **1981**, *55*, 117.

[80]. Miertus, S.; Tomasi, J. *Chem. Phys.* **1982**, *65*, 239.

[81]. Hawkins, G. D.; Cramer, C. J.; Truhlar, D. G. *J. Phys. Chem. B* **1998**, *102*, 3257.

[82]. Jang, Y. H.; Goddard III, W. A.; Noyes, K. T.; Sowers, L. C.; Hwang, S.; Chung, D. S. *J. Phys. Chem. B* **2003**, *107*, 344.

[83]. Iribarren, J. I.; Casanovas, J.; Zanuy, D.; Alemán, C. *Chem. Phys.* **2004**, *302*, 77.

[84]. Koopmans, T. *Physica* **1934**, *1*, 104.

[85]. Janak, J. F. *Phys. Rev. B* **1978**, *18*, 7165.

[86]. Levy, M.; Nagy, A. *Phys. Rev. A* **1999**, *59*, 1687.

[87]. Perdew, J. P. *Phys. Rev. B* **1986**, *33*, 8822.

[88]. Frisch, M. J.; Trucks, G. W.; Schlegel, H. B.; Scuseria, G. E.; Robb, M. A.; Cheeseman, J. R.; Montgomery, J. A.; Vreven Jr. T.; Kudin, K. N.; Burant, J. C.; Millam, J. M.; Iyengar, S. S.; Tomasi, J.; Barone, V.; Mennucci, B.; Cossi, M.; Scalmani, G.; Rega, N.; Petersson, G. A.; Nakatsuji, H.; Hada, M.; Ehara, M.; Toyota, K.; Fukuda, R.; Hasegawa, J.; Ishida, M.; Nakajima, T.; Honda, Y.; Kitao, O.; Nakai, H.; Klene, M.; Li, X.; Knox, J. E.; Hratchian, H. P.; Cross, J. B.; Adamo, C.; Jaramillo, J.; Gomperts, R.; Stratmann, R. E.; Yazyev, O.; Austin, A. J.; Cammi, R.; Pomelli, C.; Ochterski, J. W.; Ayala, P. Y.; Morokuma, K.; Voth, G. A.; Salvador, P.; Dannenberg, J. J.; Zakrzewski, V. G.; Dapprich, S.; Daniels, A. D.; Strain, M.; Farkas, O.; Malick, D. K.; Rabuck, A. D.; Raghavachari, K.; Foresman, J. B.; Ortiz, J. V.; Cui, Q.; Baboul, A. G.; Clifford, S.; Cioslowski, J.; Stefanov, B. B.; Liu, G.; Liashenko, A.; Piskorz, P.; Komaromi, I.; Martin, R. L.; Fox, D. J.; Keith, T.; Al-Laham, M. A.; Peng, C. Y.; Nanayakkara, A.; Challacombe, M.; Gill, P. M. W.; Johnson, B.; Chen, W.; Wong, M. W.; Gonzalez, C.; Pople, J. A. *Gaussian 03, revision B.02;* Gaussian, Inc.: Wallingford, CT, 2004

[89]. Alemán, C.; Torras, J.; Casanovas, J. *Chem. Phys. Lett.* **2011**, *511*, 283.

[90]. Okur, S.; Salzner, U. *J. Phys. Chem. A* **2008**, *112*, 11842.

[91]. Guyard, L.; Hapiot, P.; Neta, P. *J. Phys. Chem. B* **1997**, *101*, 5698.

[92]. E. W.; Ohkubo, K.; Sanchez-Garcia, D.; Zhang, M.; Sessler, J. L.; Fukuzumi, S.; Kadish, K. M. *J. Phys. Chem. B* **2007**, *111*, 4320.

[93]. Zotti, G.; Martina, S.; Wegner, G.; Schlüter, A. D. *Adv. Mater.* **1992**, *4*, 798.

[94]. Lallemand, F.; Auguste, D.; Amato, C.; Hevesi, L.; Delhalle, J.; Mekhalif, Z. *Electrochim. Acta* **2007**, *52*, 4334.

[95]. Ghosh, S.; Bowmaker, G. A.; Cooney, R. P.; Seakins, J. M. *Synth. Met.* **1998**, *95*, 63.

[96]. Im, J.; Sengupta, S.; Baruch, M. F.; Granz, C. D.; Ammu, S.; Manohar, S. K.; Whitten, J. E. S. *Sens. Actuators B* **2011**, *156*, 715.

[97]. Singh, A.; Mukherjee, M. *Macromolecules* **2003**, *36*, 8728.

[98]. Yang, J.; Lee, S.; Lee, E.; Hong, S. *Desalination* **2009**, *247*, 148.

[99]. Qin, H.; Kulkarni, A.; Zhang, H.; Kim, H.; Jiang, D.; Kim, T. *Sens. Actuators B* **2011**, *158*, 223.

[100]. Kukla, A. L.; Pavluchenko, A. S.; Shirshov, Y. M.; Konoshchuk, N. V.; Posudievsky, O. Y. *Sens. Actuators B* **2009**, *135*, 541.

[101]. Posudievsky, O. Y.; Konoshchuk, N. V.; Kukla, A. L.; Pavluchenko, A. S.; Shirshov, Y. M.; Pokhodenko, V. D. *Sens. Actuators B* **2011**, *151*, 351.

Chapter 7. Halidethiophenes

7.1. New insights on the characterization of poly(3-chlorothiophene) for electrochromic devices.[a,c]

7.1.1. Introduction

7.1.2. Methods

7.1.3. Results and discussion

7.1.4. Conclusions

7.1.5. References

[a]Results presented in this chapter were published in *Polym. Chem.* **2012**, *3*, 436.

7.2. Properties of poly(3-halidethiophene)s.[b,c]

7.2.1. Introduction

7.2.2. Methods

7.2.3. Results and discussion

7.2.4. Conclusions

7.2.5. References

[b]Results presented in this chapter were published in *Phys. Chem. Chem. Phys.* **2012**, *14*, 10050

[c]*In this chapter theoretical calculations were performed by Dr. Jordi Poater and Prof. Miquel Solà from the University of Girona, and Prof. Jordi Casanovas from the University of Lleida.*

7.1. New insights on the characterization of poly(3-chlorothiophene) for electrochromic devices

7.1.1. Introduction

In recent years electrically conducting polymers (CPs) have been widely studied due to their remarkable applications (*e.g.* supercapacitors, photovoltaic cells, diodes and electrochromic devices).[1-3] Among CPs, polythiophene (PTh) derivatives have attracted considerable interest as electrochromic materials (*i.e.* materials that change color reversibly by an electrochemical reaction) since, in addition to their high electrochromic contrast, they exhibit good thermal, electrochemical and environmental stability, high conductivity, low oxidation potentials, and ease of doping-undoping process.[1-9]

An electrochromic device (ECD) is essentially an electrochemical cell in which the electrochromic electrode is separated by a suitable electrolyte from the charge-balancing counter electrode, and color changes occur by charging and discharging the battery with applied potentials.[10] Poly(3,4-ethylenedioxythiophene), abbreviated as PEDOT, is one of the most representative electrochromic PTh derivative, exhibiting high contrast color changes from transmissive sky-blue in the oxidized state, to opaque deep-blue in the reduced state.[6,10-14] Poly(3-methylthiophene)s, a CP with non-degenerated ground state symmetry, is considered another promising electrochromic material with a response time of a few milliseconds and high cyclability.[15-18] In this way, ECDs based on CPs are of great interest in emerging technologies as large-area smart windows capable of varying the radiant energy under the action of a voltage pulse, display panels, variable reflectance mirrors and camouflage materials.

Poly(3-halidethiophene)s are another interesting class of PTh derivatives bearing a small substituent at the 3-position of the thiophene ring. Thus, the electron-withdrawing halogen atoms, which are directly attached to the polyconjugated main chain, are expected to reduce the electronic density of the thiophene rings affecting the optical properties of PTh, including electrochromism. In spite of this, the literature on poly(3-halidethiophene)s, including the most known poly(3-chlorothiophene),[19-23] hereafter denoted PClTh (Scheme 1), is very scarce. PClTh has been electrochemically synthesized in ionic liquids (*i.e.* boron trifluoride diethyl etherate and 1-butyl-3-methylimidazolium hexafluorophosphate, abbreviated BFEE and [BMIM]PF_6, respectively) using platinum and nanoporous TiO_2 as substrates, their electrochemical

and optical properties being characterized using cyclic voltammetry (CV), spectroelectrochemistry and UV-vis spectroscopy.[19-23] Furthermore, the influence of the concentration of electrolyte in the generation medium and the thickness of the films on the doping level of PClTh was examined using Raman spectroscopy.[20,21]

The π-π^* lowest electron transition energy (ε_g) of PClTh was found to range from 1.61 to 1.80 eV, these values being lower than those determined for unsubstituted PTh (1.9-2.3 eV)[24-27] but higher than those found for PEDOT (1.5-1.7 eV).[28-34] Moreover, the ε_g values reported for PClTh were lower than those measured for PThs bearing oxygen-containing electron-withdrawing groups attached at the 3-position of thiophene ring (*e.g.* the ε_g of PThs bearing acrylic acid and malonic acid substituents ranged from 2.25 to 2.75 eV).[35-38]A preliminary inspection of the electrochromic properties of PClTh was reported by Jin and co-workers,[22,23] which described color changes between deep red and deep blue for the polymer produced by galvanostaticmethods using [BMIM]PF_6 as both generation medium and supporting electrolyte.

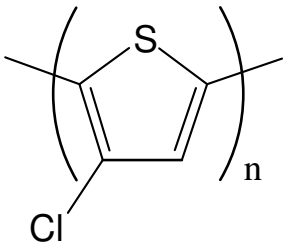

PClTh

Scheme 1. *Poly(3-chlorothiophene)*

In this work the fabrication of a new ECD using both PEDOT and PClTh is carried out. PEDOT was obtained by potentiostatic electropolymerization at 1.40 V from a 0.01 M monomer solution in acetonitrile with 0.1 M $LiClO_4$ as supporting electrolyte. Details about the synthesis[39] and complete characterization of the properties[39-42] of PEDOT produced using such procedure were discussed in previous studies. On the other hand, PClTh has been obtained by anodic polymerization of 3-chlorothiophene in BFEE solution at a constant potential. In order to optimize the experimental conditions, a complete characterization of the physical, electrochemical, morphological, electronic, and electrochromic properties of PClTh samples prepared using potentials ranging from 1.60 to 1.90 V was carried out. These properties have been compared with those reported for PEDOT. Finally, the PEDOT/PClTh ECDs fabricated with the PClTh

electrode produced using the optimum experimental conditions have proved to present very high cycling stability.

7.1.2. Methods

Materials. 3-chlorothiophene and 3,4-ethylenedioxythiophene monomers, BFEE and acetonitrile analytical reagent grade were purchased from Aldrich and used without further purification. Lithium perchlorate ($LiClO_4$) and anhydrous tetrabutylammonium tetrafluoroborate [$(Bu)_4NBF_4$], analytical reagent grade, from Aldrich were stored in an oven at 80 ºC before use in the electrochemical trials.

Synthesis of PClTh films. The anodic polymerization of 3-chlorothiophene ClTh was studied by CV and chronoamperometry (CA) using an Autolab PGSTAT302N equipped with the ECD module to measure very low current densities (100 mA–100 pA). All electrochemical experiments were performed in a standard three-electrode cell containing 50 mL of a 0.01 M monomer solution in BFEE containing 0.1 M$(Bu)_4NBF_4$ at room temperature. Steel AISI 316 sheets of 4 cm^2 area were employed as working and counter electrodes. The reference electrode was an Ag|AgCl electrode containing a KCl saturated aqueous solution (E^o = 0.222 V at 25ºC), which was connected to the working compartment through a salt bridge containing the electrolyte solution. In order to avoid interferences during the electrochemical analyses, the working and counter electrodes were cleaned with acetone and dried with an air flow before each trial. After electropolymerization, the coated electrodes were cleaned with acetonitrile and dried with nitrogen. In all cases, the solution was purged with nitrogen for 5 min. prior electrochemical synthesis.

Thickness of the films. The thickness (ℓ) of the films was estimated using the following relation:

$$\ell = \frac{m_{pol}}{S_{pol} \cdot \rho} \qquad (1)$$

where m_{pol} is the mass of polymer deposited in the electrode that was determined using a Sartorius ultra-microbalance, S_{pol} is the surface of polymerization (*i.e.* the surface of the electrode, 4 cm^2) and ρ is the density (see below).

Physical properties. FTIR spectra were recorded on a FTIR 4100 Jasco spectrophotometer with a resolution of 4 cm^{-1} in the absorbance mode. Samples were

placed in an attenuated total reflection accessory with thermal control and a diamond crystal (Golden Gate Heated Single Reflection Diamond ATR).

The average degree of polymerization (ADP) of PClTh samples was evaluated using the procedure proposed by Furakawa and Saujavol:[43]

$$ADP = 2\left(\frac{R_0}{R} + 2\right) \qquad (2)$$

where R is the integrated intensity ratio of the IR bands at 703 and 813 cm^{-1}, and R_0 is the value of R determined for α-sexithiophene, 1.07.

The density of PClTh samples obtained using different experimental conditions was determined by the flotation method from 1,2-dichloroethane and chlorobenzene mixtures, in which this polymer is insoluble.

The electrical conductivity was determined using the sheet resistance method with a previously described procedure.[44]

Electrochemical properties. The electroactivity, which refers to the charge storage ability, was determined by CV using an acetonitrile solution with 0.1 $M(Bu)_4NBF_4$. The initial and final potentials were -0.20 V, while the reversal potential was 1.60 V. The electroactivity increases with the similarity between the anodic and cathodic areas of the control voltammograms, which were registered at a scan rate of 100 $mV \cdot s^{-1}$.

The doping level (dl) of the electrochemically produced PClTh was carried using the following Eqn:

$$dl = \left(\frac{2Q_0}{Q_D - Q_0}\right)100 \qquad (3)$$

where Q_D is the total charge used for the polymer deposition and Q_0 is total charge of oxidized species in the polymer films.

The specific capacitance (SC, in $F \cdot g^{-1}$) of PClTh was determined by CV using the following Eqn:

$$SC = \frac{Q}{\Delta V m_{pol}} \qquad (4)$$

where Q is the voltammetric charge, which is determined by integrating either the oxidative or reductive parts of the cyclic voltammogram, ΔV is the potential window (in V), and m_{pol} is expressed in g.

The loss of electroactivity (LES, in %), which decreases with the oxidation and reduction areas of consecutive control voltammograms, was determined as:

$$LES = \frac{\Delta Q}{Q_{II}} \cdot 100 \qquad (5)$$

where ΔQ is the difference of voltammetric charges (in C) between the second and the last cycle, and Q_{II} is the voltammetric charge corresponding to the second cycle. In this work, measures of LES refer to 100 consecutive oxidation-reduction cycles in all cases.

The current efficiency of polymerization (η, in %), which indicates the charge consumed by the growth of the polymer film relative to the total charge passed through the cell, was measured as follows:

$$\eta = \left[\frac{\left(n_{ox} \cdot F \cdot m_{pol} \Big/ M \right)}{Q_{pol}} \right] 100 \qquad (6)$$

where F is the Faraday constant (96487 C mol^{-1}), Q_{pol} is the charge passed through the cell during the polymer film growth (*i.e.* the polymerization charge consumed in the process, in millicoulombs per centimeter square) that was calculated on each chronoamperogram, M is the molar mass of the monomer (118.58 gr mol^{-1}), and n_{ox} corresponds to the number of electrons consumed to incorporate a monomer into a polymer and to oxidize the resulting chain. The following equation has been used to evaluate n_{ox}:

$$n_{ox} = \frac{M \cdot Q_{pol}}{F \cdot m_{pol} (1 - m_{dop})} \qquad (7)$$

where m_{dop} is the mass of dopant per polymer unit of mass.

Electrochemical impedance spectroscopy (EIS). EIS measurements were performed using an AUTOLAB PGSTAT 30/FRA 2 system in potenciostatic mode at the open circuit potential (OCP). The amplitude of the EIS perturbation signal was 50 mV, and the studied frequency ranged from 10^3 to 10^{-3} Hz. All experiments were carried out in a BFEE solution containing 0.1 $M(Bu)_4NBF_4$ at 25 ºC.

Electronic properties. Cyclic voltammograms recorded in acetonitrile containing 0.1 $M(Bu)_4NBF_4$ at room temperature were used to estimate the electrochemical ionization potential (IP) through the empirical relationship previously proposed by Brédas *et al.*:[45]

$$IP = \varepsilon^{ox} + 4.4 \;\; eV \qquad (8)$$

where ε^{ox} is the onset potential for oxidation relative to an Ag|AgCl electrode.

The optical ε_g was derived from the UV-vis spectra of the reduced materials using the following relation:

$$\varepsilon_g = \frac{1240}{\lambda^{onset(abs)}} \qquad (9)$$

Absorption spectra were obtained with a Shimadzu 3600 spectrophotometer equipped with a tungsten halogen visible source, a deuterium arc UV source, a photomultiplier tube UV-vis detector, and a InGaAs photodiode and cooled PbS photocell NIR detectors. Spectra were recorded in the absorbance mode using the integrating sphere accessory (model ISR-3100), the wavelength range being 200-900 nm. The interior of the integrating sphere is coated with a highly diffuse BaO reflectance standard. Single-scan spectra were obtained at a scan speed of 60 $nm \cdot min^{-1}$ with a bandwidth of 2 nm using the UVProbe 2.31 software.

Morphology. Morphological studies were performed using scanning electron microscopy (SEM) and tapping-mode atomic force microscopy (AFM). Topographic AFM images were obtained with a Molecular Imaging PicoSPM using a NanoScope IV controller in ambient conditions. The averaged RMS roughness (*r*) was determined using the statistical application of the Nanoscope software, which calculates the average considering all the values recorded in the topographic image with exception of the maximum and the minimum.

SEM studies were carried out using a Focussed Ion Beam Zeiss Neon 40 scanning electron microscopy operating at 3 kV and equipped with an energy dispersive X-ray (EDX) spectroscopy system, which was used for the elemental analyses of the prepared materials.

Quantum mechanical calculations. All calculations were performed using the Gaussian 03 computerprogram.[46] The internal rotations of the model compounds formed by two 3-chlorothiophene units (*i.e.* 2-ClTh) were studied by scanning the inter-ring

dihedral angle S-C-C-S (θ) in steps of 30º between θ = 0º and 360º. A flexible rotor approximation was used, each point of the path being obtained from geometry optimization of the molecule at a fixed value of θ. Furthermore, minimum energy conformations were determined from complete geometry optimization using a gradient method. The rotational profiles and the geometry of the minimum energyconformations were calculated using the B3LYP[47,48] method combined with the 6-31+G(d,p) basis set.[49] Similarly, molecular geometries of *n*-ClTh oligomers, where *n* refers to the number of chemical repeating units and ranged from 3 to 16, were fully optimized at the B3LYP/6-31+G(d,p) level. Starting geometries of 3-ClTh were constructed considering head-to-head, tail-to-tail and head-to-tail linkages, whereas the latter was the only used for oligomers with $n > 3$.

The first ionization potential (IP) and the electron affinity (EA) were estimated using the Koopmans' theorem.[50] Accordingly, IPs and EAs were taken as the negative of the highest occupied molecular orbital (HOMO) energy and the lowest unoccupied molecular orbital (LUMO) energy, respectively, *i.e.* IP = $-\varepsilon_{HOMO}$ and EA = $-\varepsilon_{LUMO}$. The IP indicates if a given acceptor (p-type dopant) is capable of ionizing, at least partially, the molecules of the compound, while the EA refers to the ionization through a given donor (n-type dopant). The ε_g was approximated as the difference between the HOMO and LUMO energies, *i.e.* $\varepsilon_g = \varepsilon_{LUMO} - \varepsilon_{HOMO}$. All the electronic properties presented in this work were estimated at the B3LYP/6-31+G(d,p) level. It is worth noting that according to the Janak´s theorem,[51] the approximation mentioned above for the calculation of the IP can be applied to DFT calculations, while Levy and Nagy evidenced that ε_g can be rightly approximated as the difference between ε_{LUMO} and ε_{HOMO} in DFT calculations.[52]

With respect to the analysis of the aromaticity of the thiophene rings in 3-chlorothiophene and EDOT, criteria based on different physical properties have been calculated. First, the magnetic-based nucleus independent chemical shifts[53,54] (NICS) calculations were performed to determine the aromaticity of the rings under analysis. The GIAO method[55] was used to perform calculations of NICS at ring centers (NICS(0)) determined by the non-weighted mean of the heavy atoms coordinates and at 1.0 Å above the ring taken into study (NICS(1)).[56] Finally, as a geometry-based aromaticity measure, the HOMA index[57], which is based on C-C and C-S bond length alternation pattern along the π-system, was evaluated as:

$$HOMA = 1 - \frac{\alpha}{l}\sum_{i=1}^{l}(R_{opt} - R_i)^2 \qquad (10)$$

where l is the number of bonds, α is an empirical constant (α = 257.7 and 94.09 for C-C and C-S bonds, respectively), R_i is the bond length and R_{opt} is the optimal bond length (R_{opt}= 1.388 and 1.677 Å for C-C and C-S bonds, respectively). It is worth noting that HOMA is equal to zero for a Kekulé structure formed by a typical aromatic system with single and double bonds arranged alternatively, and is equal to 1 for a system with all bonds equal to the optimal value (R_i=R_{opt}). All the aromaticity parameters were calculated at the B3LYP/6-31+G(d,p) level.

7.1.3. Results and discussion

Polymerization. Figure 1a presents the cyclic voltammogram of 0.01 M 3-chlorothiophene in BFEE with 0.1 $M(Bu)_4NBF_4$ on a steel electrode, which was registered at a scan rate of 10 $mV \cdot s^{-1}$ in the potential range from -0.60 to 2.20 V. Onset of polymerization occurs at 1.55 V. This potential, which corresponds to the oxidation of the monomer, is higher than that reported for 0.1 M 3-chlorothiophene in pure BFEE using a scan rate of 100 $mV \cdot s^{-1}$ (1.31 V).[19] The second peak, with $E_p^a(O_2)$ = 1.87 V, refers to the oxidation of the polymer. In addition, a reduction peak with $E_p^c(R_1)$ = 0.78 V is detected in the cathodic scanning, indicating the reduction of the polymer.

The effect of repeating oxidation-reduction cycling in the potentiodynamic synthesis of PClTh in BFEE with 0.1 $M(Bu)_4NBF_4$ is displayed in Figure 1b. As it can be seen, repeating cycling resulted in an increase of both the current response of the monomer oxidation peak and the redox response of the polymer deposited in the steel electrode surface. Moreover, repeated cycling resulted in a gradual reduction in the onset of the oxidation potential, which decreases from 1.55 to 0.57 V and from 0.78 to 0.62 V, respectively, after 25 oxidation-reduction scans. These characteristics are similar to those reported for 3-bromothiophene solutions in pure BFEE.[58] On the other hand, the colour of the solution close to the working electrode changed slightly from colourless to blue upon cycling, indicating that part of the 3-chlorothiophene monomer was oxidized into oligomers. Simultaneously, PClTh was deposited on the steel electrode surface, its colour changing from light blue to deep blue with the thickness of the films. Figure 1c compares the redox behaviour of the generated PClTh at various scan rates ranging between 20 and 400 $mV \cdot s^{-1}$. The current density of the anodic and cathodic peaks is

proportional to the scan rate, indicating a redox couple fixing on the electrode. Furthermore, the linear response between the scan rate and the current response (R^2> 0.98) indicates that the associated redox processes are surface bound and non-diffusion limited for scan rates up to 400 $mV \cdot s^{-1}$.

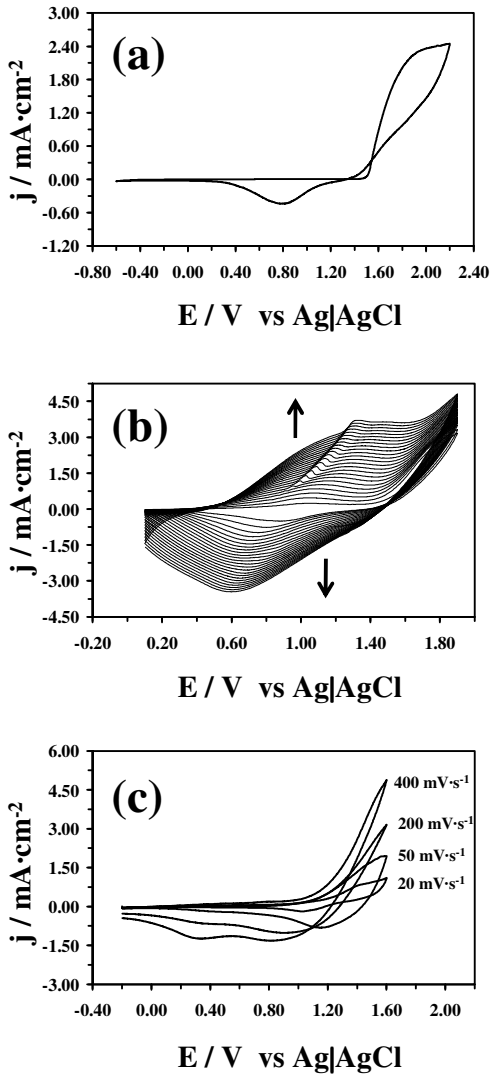

Figure 1. *(a) Cyclic voltammogram of 0.01 M 3-chlorothiophene in BFEE with 0.1 M$(Bu)_4NBF_4$ on a steel electrode. Initial and final potentials: -0.60 V; reversal potential: 2.20 V. Scan rate: 10 $mV \cdot s^{-1}$. (b) Successive cyclic voltammograms (25 scans) of 0.01 M 3-chlorothiophene in BFEE with 0.1 M$(Bu)_4NBF_4$ on a steel electrode. Initial and final potentials: 0.10 V; reversal potential: 1.90 V. Scan rate: 50 $mV \cdot s^{-1}$. Arrows indicate the increasing number of cycles. (c) Cyclic voltammograms of PClTh films in BFEE with 0.1 M$(Bu)_4NBF_4$ at scan rates of 20, 50, 200 and 400 $mV \cdot s^{-1}$*

Physical properties of PClTh. Table 1 compares the physical properties of PClTh films prepared by anodic polymerization in BFEE with 0.1 M $(Bu)_4NBF_4$ applying a constant potential of 1.60, 1.70, 1.80 and 1.90 V, the polymerization time being 150 s in all cases. As it can be seen, both the thickness and roughness of the films increase

significantly with the applied potential, suggesting morphological variations in the surface and, therefore, in the electrochemical properties (see below). Thus, the absolute (and relative) increments of the thickness and the roughness when the potential increases from 1.60 to 1.90 V are $\Delta\ell$ = 1.06 μm (97 %) and Δr = 145 nm (403 %), respectively.

On the other hand, the density increases very slightly (~5%) with the applied potential, whereas the average degree of polymerization undergoes a drastic reduction (~35%) when the potential increases from 1.60 to 1.90 V. The average degree of polymerization estimated for PClTh generated using BFEE with 0.1 M $(Bu)_4NBF_4$ varies between 17 (1.60 V) and 11 (1.90 V). This interval is lower than those obtained using BFEE containing 10-15% of trifluoroacetic acid[20] (ADP ≈ 24-32) or sulfuric acid[19] (ADP ≈ 18-21). The variation of the electrical conductivity applied potential was measured to be very small, ranging from 0.16 (1.90 V) to 0.96 $S \cdot cm^{-1}$ (1.70 V). Finally, the current efficiency of polymerization decreases from 82% to 57% when the applied potential increases from 1.60 to 1.90 V. In spite of this reduction, it should be noted that these current efficiencies are considerably larger that these current efficiencies are considerably larger than those determined in BFEE containing 10-15% of trifluoroacetic acid ($\eta \approx$ 32-36%).[20]

Table 1. *Physical properties of PClTh films produced by CA in BFEE with 0.1 M$(Bu)_4NBF_4$ applying a constant potential, which is comprised between 1.60 and 1.90 V, and using a polymerization time of 150 s.*

Potential (V)	ℓ (μm)[a]	r (nm)[b]	ρ ($g \cdot cm^{-3}$)[c]	σ ($S \cdot cm^{-1}$)[d]	ADP[e]	η (%)[f]
1.60	1.09	36	1.10	0.67	17	82
1.70	1.24	45	1.12	0.96	15[a]	88
1.80	1.56	138	1.13	0.48	13	70
1.90	2.15	181	1.16	0.16	11	57

[a] Thickness. [b] Roughness. [c] Density. [d] Electrical conductivity. [e] Average degree of polymerization. [f] Current efficiency of polymerization

Comparison of the electrical conductivity of PClTh with that determined for PEDOT reflects the high performance of the latter CP. Thus, the electrical conductivity of

PEDOT produced at 1.40 V in acetonitrile with $LiClO_4$ as supporting electrolyte is 315 $S \cdot cm^{-1}$.[39]

Electrochemical properties of PClTh. Table 2 provides the electroactivity and LES of PClTh films prepared applying different potentials while Fig. 2 compares the control voltammograms of the 1st and the 100th oxidation-reduction cycles. As it can be seen, the higher electroactivity was obtained for 1.60 and 1.70 V, the ability to store charge undergoing a drastic reduction for films generated at higher potentials. On the other hand, the LES upon 100 consecutive oxidation-reduction cycles ranges from 24% to 38% for samples electrogenerated by applying potentials lower than 1.90 V while it increase to 52% for films produced using the latter potential.

Table 2. *Electrochemical properties of poly(3-chlorothiophene) films produced by CA in BFEE with 0.1 $M(Bu)_4NBF_4$ applying different potentials and using a polymerization time of 150 s.*

Potential (V)	Electroactivity /mC·cm^{-2}	LES (%)[a]	f (%)[b]	SC (F·g^{-1})[c]
1.60	41	38	0.42	26
1.70	40	29	0.42	29
1.80	27	24	0.33	19
1.90	21	52	0.23	14

[a]Loss of electroactivity measured considering 100 consecutive oxidation-reduction cycles. [b] Doping level.[c]Specific capacitance.

The variation of the doping level and the SC against the generation potential follows a behaviour similar to that described for the electroactivity. Thus, the doping level and the SC are very similarfor the PClTh obtained using 1.60 and 1.70 V, while they decrease considerably at higher potentials. It should be noted that the SC of PClTh, which ranges from 14 to 29 F g^{-1} depending on the potential, is comparable to those of PEDOT (35 F·g^{-1}) and PNMPy (16 F·g^{-1}), respectively.[42] However, these values are considerably lower than those reported for CP-based nanocomposites. For example, the combination of PEDOT with inorganic materials (*e.g.* MoO_3, RuO_2, carbon nanotubes, MnO_2, and $NiFe_2O_4$) allows reach SC ranging from 153 to 375 F·g^{-1}.[59-65]

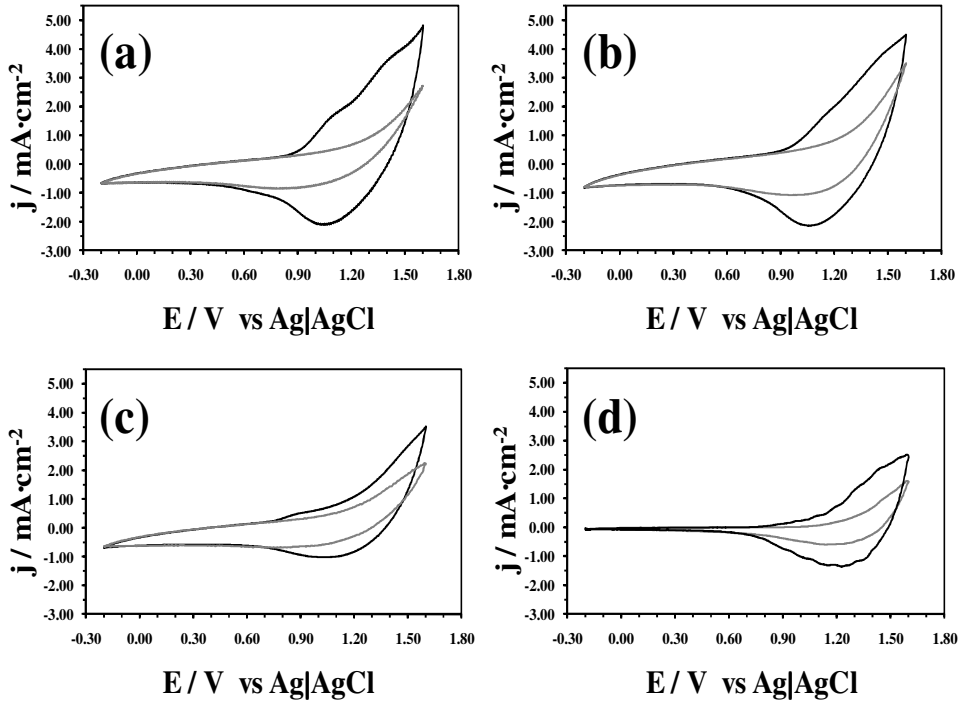

Figure 2. *Control voltammograms for the PClTh films prepared in BFEE with 0.1 M(Bu)$_4$NBF$_4$ applying the following potential: (a) 1.60 V; (b) 1.70 V; (c) 1.80 V; and (d) 1.90 V. In all cases voltammograms after the 1st (black) and 100th (grey) oxidation-reduction cycles are displayed. Initial and final potentials: -0.20 V; reversal potential: 1.60 V. Scan rate: 100 mV·s^{-1}. Temperature 25ºC.*

Morphology and topography of PClTh. High- and low-resolution SEM scanning micrographs of PClTh prepared using 1.60 and 1.90 V are displayed in Figure 3. High resolution micrographs clearly indicate that the porosity of the surface decreases significantly when the applied potential increases. The morphology of PClTh films generated at 1.60 V consists on the aggregation of interconnected nanosticks with a nanofiber-like morphology, which allows the formation of narrow and tortuous pores. This nanoporous morphology, which is not appreciable in the low-resolution micrograph, plays a crucial role in the electroactivity and electrostability (Figure 2) of the material.

Nanopores facilitate the mobility of dopant ions in oxidation (*i.e.* access of ions into the polymer matrix) and reduction (*i.e.* escape of ions from the polymer matrix) processes, enhancing the electroactivity and electrostability with respect to materials with more compact morphologies. This is case of PClTh prepared at 1.90 V, which shows a globular compact structure as is reflected in the high-resolution micrograph. This type of morphology is typically related with a homogeneous distribution of molecules that arises from a multidirectional growing of cross-linked polymer chains.

These features indicates that the tendency to form chemical couplings at the β'-position of chemical repeating units increases with the potential. Thus, the poor electrochemical properties observed for the CP generated at 1.90 V (Figure 2) are due to the compact structure produced by the lack of directional preferences in the polymerization process, which makes difficult the mobility of the ions during the faradaic processes.

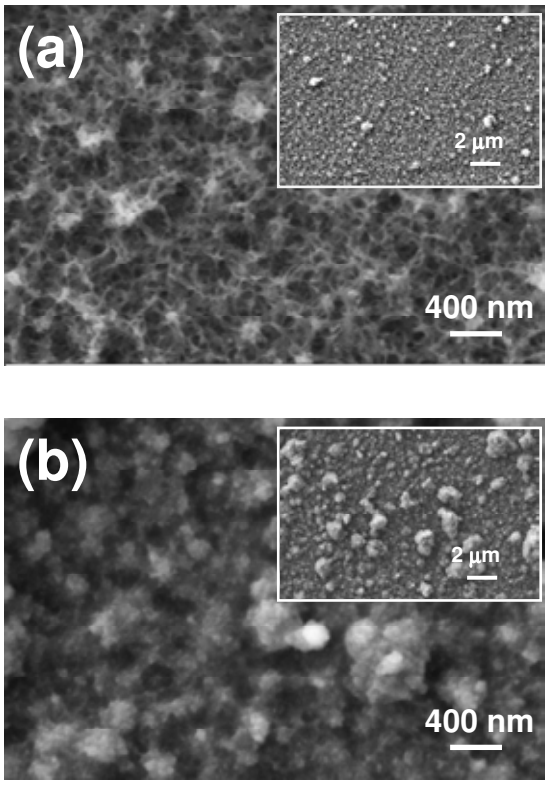

Figure 3. *High and low (inset) resolutionSEM micrographs of PClTh films generated at (a) 1.60 V and (b) 1.90 V in BFEE 0.1 M(Bu)$_4$NBF$_4$ using a polymerization time of 150 s. Films were deposited on a stainless steel electrode.*

Figure 4 compares AFM images of PClTh samples generated at a constant potential of 1.60, 1.70, 1.80 and 1.90 V. As can be seen, films electrogenerated using 1.60 and 1.70 V show similar surface topology. This consists on relatively dense distributions of sharp peaks that are grouped forming small and well-defined clusters that resemble mountain ranges. This topography suggests that PClTh are molecules mainly formed by α-α linkages (*i.e.* linear molecules), which group in small compact molecular aggregates probably stabilized by the incorporated dopant anions. It is worth noting that such aggregates of linear molecules are also fully consistent the sticks with a nanofiber-like morphology displayed in Figure 3a. The roughness of the films produced at 1.60 and 1.70 V is r = 45 and 37 nm, respectively. Moreover, the roughness and, especially,

topography of these films resembles those reported for ultra-thin films of PEDOT films,[40] which is exclusively formed by linear molecules since the dioxane ring fused onto the thiophene ring occupies the β-positions of the latter.

The AFM images of the PClTh films generated using potentials of 1.80 and 1.90 shows compact blocks of aggregated molecules that form plateau regions and large clusters located at very different levels. Accordingly, the growing of PClTh chains generated at potentials higher than 1.70 V seems to be accompanied by the formation of chemical α-β linkages. This cross-linking phenomenon, which is also fully consistent with the SEM micrographs displayed in Figure 3b, increases with the potential and induces the formation of multidirectional branches. This particular topography produces significant increases in the roughness (r = 138 and 181 nm for films produced at 1.80 and 1.90 V, respectively) with respect to those of films obtained at 1.60 and 1.70 V.

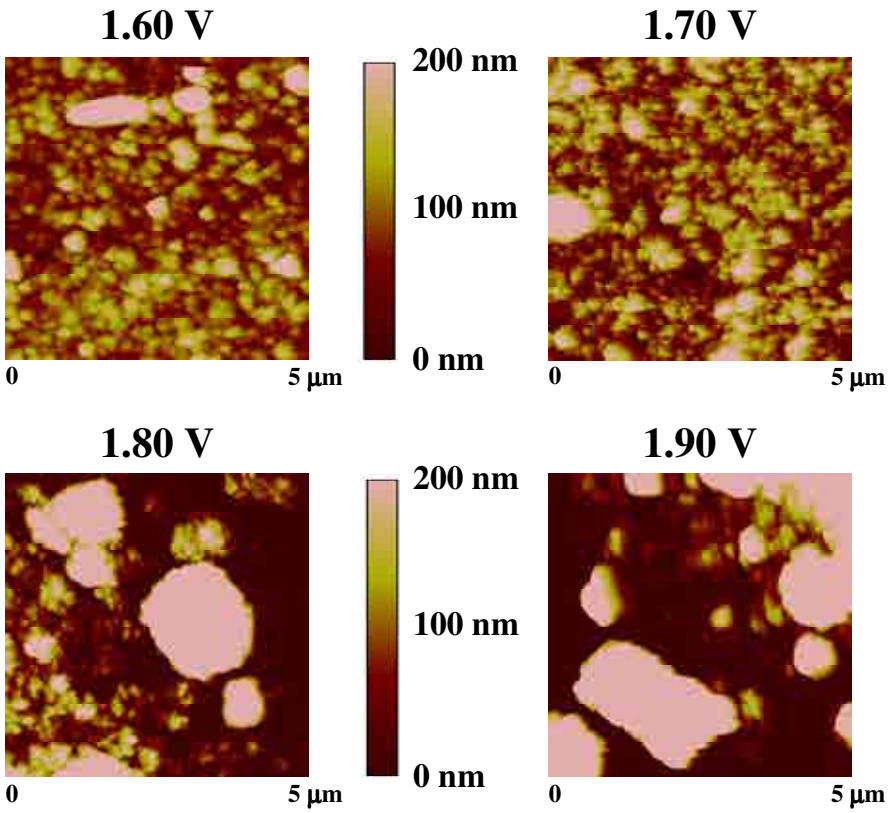

Figure 4. *2D AFM height images of PClTh films generated in BFEE with 0.1 M$(Bu)_4NBF_4$at 1.60, 1.70, 1.80 and 1.90 V. The polymerization time was 150 s in all cases.*

Impedance studies. The morphology and porosity of multilayered films made of PEDOT and poly(N-methylpyrrole) were recently correlated with their electrochemical impedance spectra.[42] Similarly, in this work EIS studies of PClTh films obtained using

different potentials have been carried out in BFEE with 0.1 $M(Bu)_4NBF_4$ at 25 ºC, results being compared with the morphological properties described in the previous subsection. Typical Nyquist diagrams for the PClTh films prepared using 1.70 and 1.90 V are displayed in Figure 5. The two impedance curves show a depressed semicircle over the high frequency range and a nearly straight line in the low frequency range, which indicate that the electrode process is dominated by a faradaic reaction (*i.e.* charge transfer) and by charge diffusion (*i.e.* mass transfer) in the former and latter region, respectively.

EIS diagrams were analyzed using the equivalent circuit (EC) depicted in Figure 5c. The proposed EC is given by $R_s(CPE_1[R_{CT}W])C_{PS}$, where: R_s is the internal resistance and corresponds to the intercept of the semicircle with the real axis (Z') at high frequencies; R_{CT} is the charge-transfer at the PClTh film, which depends on the area of the surface and the size of the pores, and is in serial connection with the Warburg diffusion element W typically attributed to the ion diffusion into the structure of the electrode; $C_{PS}$is the pseudocapacitance, which is used to account for the faradaic reaction; and CPE is the constant phase element at low frequencies that depends on the distributed surface reactivity, surface heterogeneity and roughness of the current and potential distribution, which in turn are related with the electrode geometry and the electrode porosity.When a CPE, which describes a non-ideal capacitor when the phase angle is different from -90º, is placed parallel to a resistor, a depressed semicircle is produced. CPE was expresses as $Z_{CPE} = [Q(jw)^n]^{-1}$ where *Q* is a frequency-independent constant, *w* is the angular frequency and *n* values are the correlation coefficients for the CPE.The fitting with experimental data provided errors percentage smaller than 5% for each circuit component indicating a satisfactory behavior.

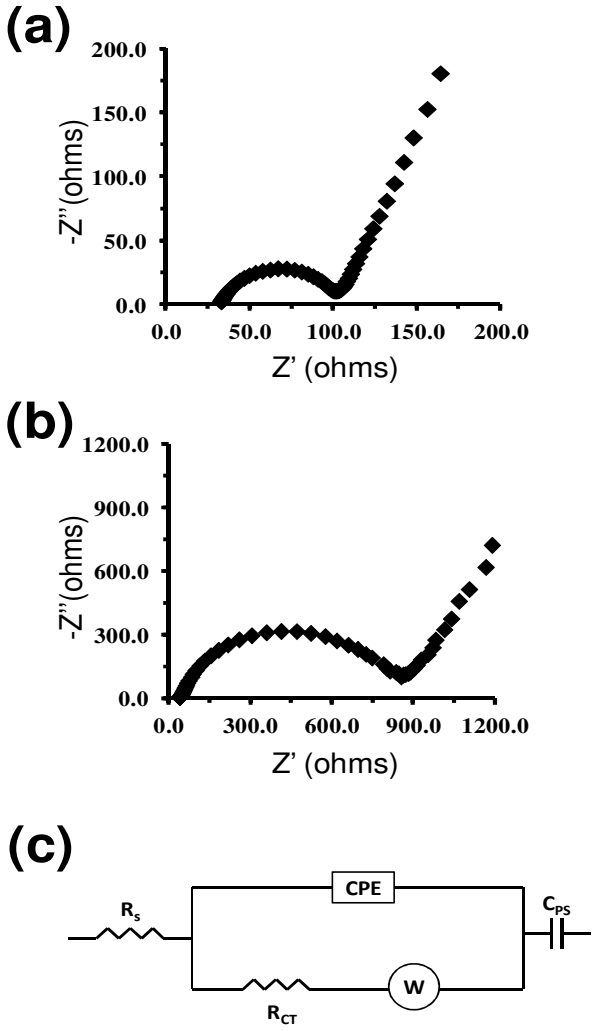

Figure 5. *Nyquist diagrams of PClTh films obtained using fixed potentials of (a) 1.70 V and (b) 1.90 V. The equivalent circuit used for modeling the experimental data is displayed in (c).*

The most important feature of the circuit is the element $R_{CT,}$ which is influenced by the number of pores or capillary channels perpendicular to the substrate surface, through which the electrolyte reaches the interface. The R_{CT} element can be used to evaluate the resistance associated with the transport within the porous structure of the material. Table 3 shows the R_s, R_{CT}, W, C_{PS} and CPE values derived from the fitting of the EIS plots (Figures 5a and 5b) to the EC (Figure 5c). As can be seen, the R_{CT} value for films produced using 1.70 V is considerably lower than that of films prepared using 1.90 V. This effect has been attributed to the influence of the generation potential on the porosity of the PClTh films. The variation in the porosity with respect to the film obtained using a potential of 1.60 V has been quantified through the changes in the thickness:[42,66]

$$\Delta = \frac{\ell_0 - \ell_{200}}{\ell_0} \times 100 \qquad (11)$$

where ℓ_o refers to the thickness of the film generated using a given potential and $\ell_{200}$is the thickness of the same film after 200 consecutive oxidation-reduction cycles (*i.e.* when the film reaches the maximum compactness). Thus, the growth of the R_{CT} with the generation potential is consistent with a reduction of both the diffusion rate of ions towards the electrode and the electrostability. Similarly, the CPE and W values derived from the proposed EC indicate that the presence of pores and cavities is higher for the material obtained using the lower potential. These features are fully consistent with SEM micrographs and AFM images (Figure 3 and 4, respectively) discussed above.

Table 3. *EIS results for PClTh films obtained using fixed potentials of 1.70 and 1.90 V derived from the fitting of the spectra (Figures 5a and 5b) to the equivalent circuit displayed in Figure 5c.*

PClTh	Rs (Ω)	CPE_1 (μF s^{n-1})	n_1	R_{CT} (Ω)	W (Ω)	C_{PS} (mF)
1.70 V	33.21	47.19	0.88	63.27	55.38	22.45
1.90 V	38.46	38.93	0.84	785.12	174.21	18.69

Electronic properties of PClTh. The IP (in eV) for PClTh samples generated using different potentials was estimated using Eqn 8, which eliminates the environmental effects from the oxidation onset. As can be seen in Table 4, the IP decreases from 5.57 to 5.20 eV when the potential used for the electrochemical polymerization increases from 1.60 to 1.90 V. These values are significantly higher than that derived by the same procedure for PEDOT generated in acetonitrile with 0.1M $LiClO_4$ at a fixed potential of 1.40 V (*i.e.* 4.28 eV).[66] Moreover, the latter value was higher than previous estimations for PEDOT prepared using very different experimental conditions (*i.e.* 4.1 eV).[67] These results clearly indicate that, independently of the potential used for the generation, the ability to be p-doped by an acceptor is significantly lower for PClTh than for PEDOT.

Table 4 includes the ε_g values measured by UV-vis spectroscopy for the different PClTh samples. The lowest ε_g (1.50 eV) was obtained for the CP generated at 1.90 V, even though influence of the applied constant potential was relatively small (*i.e.* the ε_g of PClTh obtained at 1.60 V was 1.61 eV). These values are smaller than those measured by spectroelectrochemistry[22,23] (1.74 and 1.80 eV) and UV-vis spectroscopy[68]

(2.14 eV) when the polymer is prepared using different procedures and experimental conditions. Interestingly, the ε_g values determined for PEDOT by spectroscopic methods ranged from 1.60 to 1.70 eV,[6] indicating that the energy gaps associated to the lowest π-π^* transition are relatively similar for PClTh and PEDOT.

Table 4. *Electronic and electrochromic properties of PClTh films films produced by CA in BFEE with 0.1 M* $(Bu)_4NBF_4$ *applying different potentials.*

Potential (V)	λ_{max} (nm)[a]	ε_g (eV)[a]	IP (eV)[b]	Color [ox][c]	Color [red][c]
1.60	490	1.61	5.57		
1.70	450	1.58	5.38		
1.80	440	1.52	5.28		
1.90	432	1.50	5.20		

[a] *From UV-vis absorption spectra.* [b] *From control voltammograms.* [c] *[ox] and [red] corresponds to the oxidized and reduced states, respectively.*

Quantum mechanical calculations. Calculations on dimers of 3-chlorothiophene were carried out considering three isomeric derivatives, which differ in the relative position of the substituents (Scheme 2). These isomers, which have been labeled as 2-ClTh(4,4'), 2-ClTh(3,3') and 2-ClTh(3,4') must be considered as model compounds of the tail-to-tail, head-to-head and head-to-tail polymer linkages, respectively.

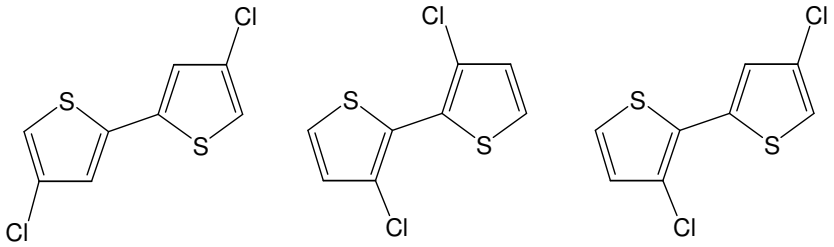

2-ClTh(4,4') 2-ClTh(3,3') 2-ClTh(3,4')

Scheme 2

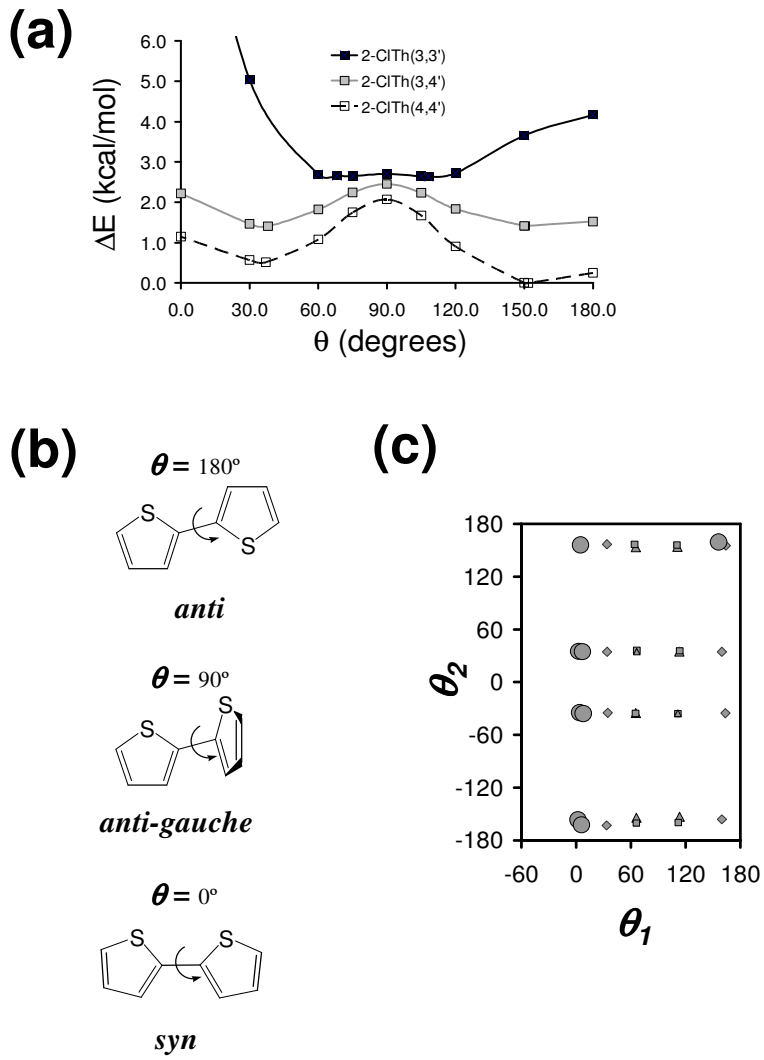

Figure 6. *(a) Potential energy curves for the internal rotation of dimers formed by two 3-chlorothiophene units (see Scheme 2) against the inter-ring dihedral angle (θ) using B3LYP/6-31+G(d,p) optimizations: 2-ClTh(3,3'), 2-ClTh(3,4') and 2-ClTh(4,4'). Energies are relative to the global minimum of 2-ClTh(4,4'). (b) Schematic representation of the most important conformations found for thiophene derivatives. The inter-ring dihedral angle, θ, is provided is each case. (c) θ_1-θ_2 maps (θ_1 and θ_2 refer to the inter-ring dihedral angles; in degrees), indicating the location of the minimum energy conformations found for 3-ClTh(3,3'-3,4') (squares), 3-ClTh(3,3'-4,4') (triangles), 3-ClTh(3,4'-3,4') (diamonds) and 3-ClTh(4,4'-3,4') (circles), as is indicated in Scheme 2. The minima of the four isomers has been categorized in three groups: (i) minima with relative energies lower than 1.0 kcal/mol (largest size symbols); (ii) minima with relative energies comprised between 1.0 and 2.0 kcal/mol (medium size symbols); and (iii) minima with relative energies larger than 2.0 kcal/mol (smallest size symbols). The relative energies have been computed with respect to the lowest energy minimum of the most stable isomer.*

Figure 6a represents the energy profiles of the three 2-ClTh isomers calculated at the B3LYP/6-31+G(d,p) level, which are relative to the global minimum of the most favored isomer. Figure 6b provides a schematic representation of the most characteristic

conformations of the systems under study. The more relevant features extracted from the calculated profiles can be summarized as follows: (i) the lowest energy conformation of 2-ClTh(4,4') corresponds to the *anti-gauche* arrangement; (ii) the most favored conformation of 2-ClTh(3,3') is relatively close to the conventional *gauche-gauche* arrangement (θ = 108.2º); (iii) the *anti-gauche* and *syn-gauche* minima of 2-ClTh(3,4') (θ = 38.0º and 150.3º, respectively) are isoenergetic; (iv) all isomers show a *syn-gauche* local minimum (θ ranging from 37.1º to 68.2º), whose relative stability depends on the position of the halogen atoms; and (v) both the relative energy of the minima and the height of the barriers, especially the planar *syn*, are significantly higher for the 2-ClTh(3,3') isomer than for the 2-ClTh(4,4') and 2-ClTh(3,4') ones.

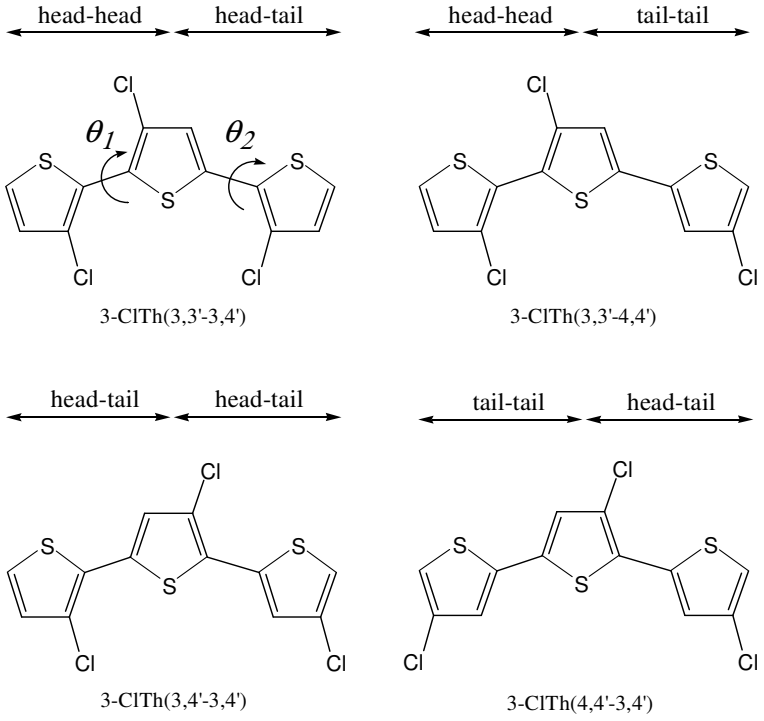

Scheme 3

The inter-ring dihedral angles of both the global and local minima found for the different isomers of 2-ClTh were combined and used to construct starting geometries for trimers, hereafter denoted 3-ClTh. The structures constructed for all these trimers, which are explicitly depicted in Scheme 3, were submitted to geometry optimizations at the B3LYP/6-31+G(d,p) level. It should be emphasized that trimers are expected to provide a more accurate representation of the homopolymer derived from 3-chlorothiophene than dimers. Specifically, 3-ClTh(3,3'-3,4') combines the

characteristics of 2-ClTh(3,3') and 2-ClTh(3,4'), defining the linkage between the head-to-head and head-to-tail units. The same procedure has been used to construct 3-ClTh(3,3'-4,4'), 3-ClTh(3,4'-3,4') and 3-ClTh(4,4'-3,4') (see Scheme 2), which involve head-to-head/tail-to-tail, head-to-tail/head-to-tail and tail-to-tail/head-to-tail linkages, respectively.

Geometry optimizations on 3-ClTh led to 24 minima within a relative energy interval of 2.9 kcal/mol. Inspection of the θ_1-θ_2 map (Figure 6c) reveals that the conformations obtained for the 3-ClTh(4,4'-3,4') isomer were the only with relative energies lower than 1.0 kcal/mol, indicating that steric interactions induced by the halogen substituents play an important role. Larger *n*-ClTh oligomers, with *n* ranging from 5 to 16, were constructed using a repetitive sequence of head-to-tail linkages. which has been found to be the most consistent with the results obtained for compounds with $n = 2$ and 3. Thus, repetition of the most favored isomer of 3-ClTh, which is the 4,4'-3,4' one, produces a high concentration of tail-to-tail linkages that are the least favored, as was evidenced in Figure 6a. However, the next isomer in terms of relative energies corresponds to the 3-ClTh(3,4'-3,4'), which is formed by two adjacent head-to-tail linkages. It should be mentioned that the high stability of the head-to-tail sequence in large oligomers ($n > 3$) was corroborated in previous theoretical studies involving other 3-substituted thiophene units.[35-38] On the other hand, it should be mentioned that molecular geometries were similar for the four isomers.

n-ClTh oligomers with $n = 5$, 7, 9, 11, 13, 15 and 16 were constructed according to these principles and considering all the inter-ring dihedral angles initially arranged at 180.0º. These structures were used as starting points for complete geometry optimizations at the B3LYP/6-31+G(d,p) level. The optimized oligomers were employed for the theoretical prediction of the electronic properties of PClTh.

Figure 7a represents the linear variation of the IP and ε_g against $1/n$ for *n*-ClTh oligomers. Linear regression analyses, which are included in Figure 7a, allowed extrapolation of the IP, and ε_g values for infinite chains of PClTh, the resulting values being 5.18 and 1.83 eV, respectively. The IP predicted for PClTh, 5.18 eV, is in excellent agreement with the electrochemical estimation, which ranges from 5.20 to 5.57 eV depending on the potential used in the anodic polymerization. The ε_g derived from DFT calculations, 1.83 eV, is overestimated by 0.22-0.33 eV with respect the determined experimentally UV-vis spectroscopy (Table 4). However, the ε_g measured

using spectroelectrochemical methods, 1.74 and 1.80 eV,[22,23] is in excellent agreement with this theoretical prediction. The ε_g predicted for PClTh is significantly smaller than those calculated for PThs with electron-withdrawing carboxylic acid groups in the 3-position of the thiophene ring using a similar theoretical level, *e.g.* poly(3-thiophene-3-yl acrylic acid methyl ester) (2.28 eV),[35] poly(3-thiophene-3-yl acrylic acid) (2.12 eV),[36] poly(2-thiophene-3-yl-malonic acid dimethyl ester) (2.38 eV),[37] and poly(2-thiophen-3-yl-malonic acid) (2.39 eV).[38] This should be attributed to the size of the bulky carboxylic acid groups that produce drastic geometrical distortions, leading to a detriment of the optical properties.

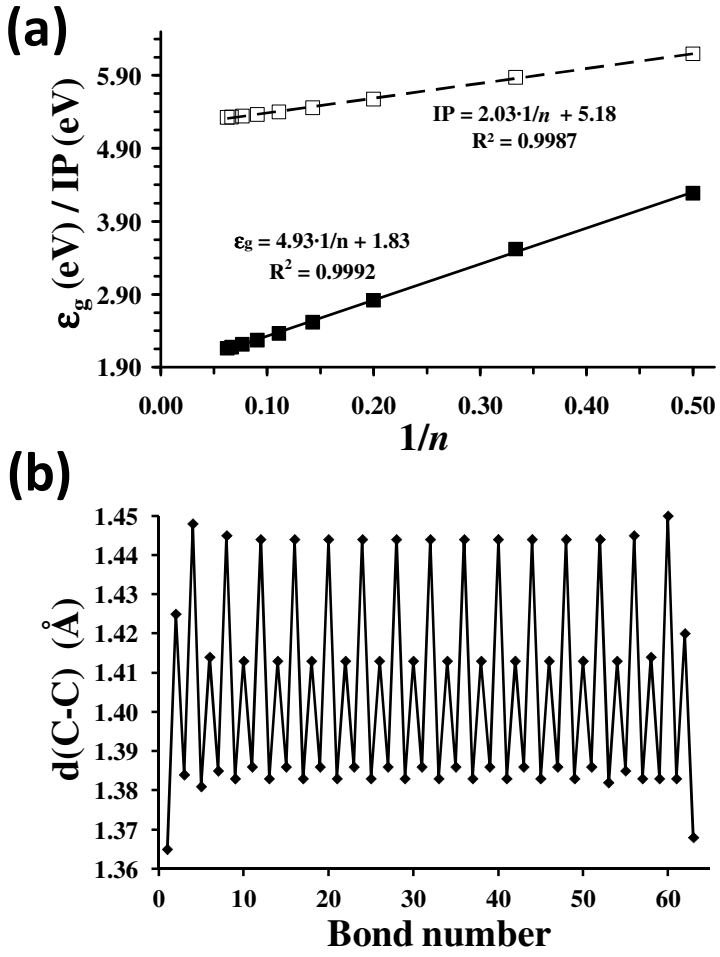

Figure 7. *(a)Variation of the IP and ε_g against 1/n, where n is the number of repeat units in n-ClTh oligomers. The solid and dashed lines correspond to the linear regressions used to extrapolate these electronic properties towards infinite polymer systems. (b) C-C bond distance along the conjugated π-system of 16-ClTh.*

The C-C bond lengths in the π-system of 16-ClTh are depicted in Fig. 7b. As it can be seen, the oligomer shows a clear benzenoid character similar to those reported for other oligothiophenes bearing electron-withdrawing groups.[69] Comparison with the bond length alternation pattern reported for the unsubstituted oligothiophene[69] indicates that the chloride atoms induce a reduction in the resonance character of the thiophene ring.

Table 5 compares the aromaticity parameters predicted for the 3-chlorothiophene units with those calculated for both the unsubstituted thiophene ring and the 3,4-ethylenedioxythiophene monomer. Most of the aromaticity measures indicate that the substituents cause a decrease in the aromaticity of the thiophene ring. Thus, the unsubstituted thiophene ring presents the highest aromaticity followed by the 3-chlorothiophene and, finally, the 3,4-ethylenedioxythiophene. This result is fully consistent with the bond length alternation pattern displayed in Fig. 7b for 16-ClTh.

Table 5. *Aromaticity parameters (see text) calculated for unsubstituted thiophene, 3-chlorothiophenes and 3,4-ethylenedioxythiophene.*[a]

	NICS(0)[a]	**NICS(1)**[a]	**HOMA**
unsubstituted thiophene	-12.7	-10.1	0.870
3-chlorothiophene	-13.0	-9.5	0.743
3,4-ethylenedioxythiophene	-15.2	-9.2	0.684

[a]*NICS in ppm*

Electrochromic properties of PClTh. PClTh films generated at potentials ranging from 1.60 to 1.90 V were reduced by applying a potential of -1.00 V during 50 s. Table 4 shows the colors of the films as prepared (oxidized species) and after reduction (reduced species). Colors were found to be similar in shape (*i.e.* blue and Bordeaux red for oxidized and reduced species, respectively), but the intensity of the colors was found to depend on the generation potential. More specifically, the oxidized CP changes from a relatively transmissive sky-blue color to deep-blue when the generation potential increases from 1.60 to 1.90 V. Similar changes were detected in the intensity of the Bordeaux red color found for the reduced form. This behavior is consistent with the ε_g values displayed in Table 4 (*i.e.* ε_g decreases when the generation potential increases).

Figure 8a compares the electrochemical and electrochromic properties of PEDOT and PClTh films in acetonitrile with 0.1 M $(Bu)_4NBF_4$, the former being generated in acetonitrile containing 0.1 M $LiClO_4$ at 1.40 Vwhile PClTh was obtained in BFEE at a constant potential of 1.70 V. Although the color of oxidized PEDOT is relatively similar to that of oxidized PClTh, the color of two CPs differs significantly in the reduced form. Thus, the light sky-blue color of oxidized PEDOT transforms into deep-blue upon reduction.

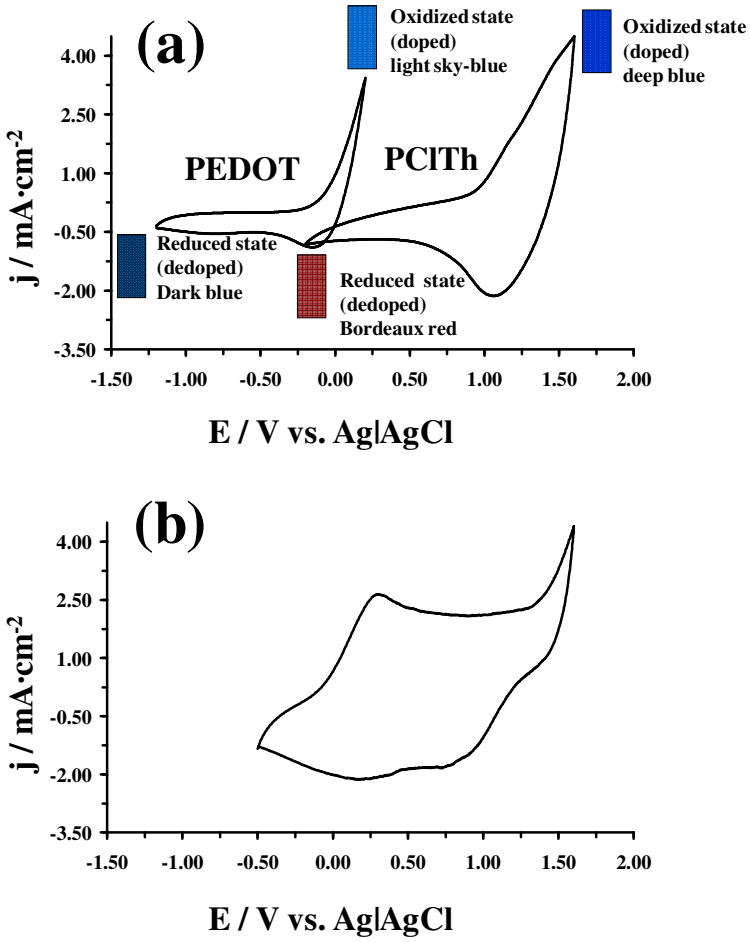

Figure 8. *(a) Control voltammograms and electrochromism of PEDOT and PClTh films (initial and final potentials: -1.20 and -0.20V for PEDOT and PClTh, respectively; reversal potential: 0.20 and 1.60 V for PEDOT and PClTh, respectively).(b) Control voltammogram of the PEDOT/PClTh ECD (initial and final potentials:-0.50V; reversal potential: 1.60 V) in acetonitrile with 0.1 M $(Bu)_4NBF_4$. ThePEDOT film was generated in acetonititrile with 0.1 M $LiClO_4$ at a constant potential of 1.40 V. The PClTh was obtained in BFEE with 0.1 M $(Bu)_4NBF_4$ at a constant potential of 1.70V and subsequently dedoped in acetonitrile with 0.1 M $(Bu)_4NBF_4$ applying a potential of -1.00 V for 50s. Scan rate: 100 $mV{\cdot}s^{-1}$. Temperature 25ºC.*

Influence of oxidation and reduction processes on the morphology of PClTh. The electrochromic device fabricated in this work (see next section) is based on oxidation (doping) and reduction (dedoping) processes of PClTh and PEDOT in acetonitrile with 0.1 M $(Bu)_4NBF_4$. Although the influence of oxidation and reduction on the morphology of PEDOT was reported in a very recent study,[42] no information about the influence of such processes on PClTh has been reported yet. Figure 9 compares the morphology of PClTh as prepared by CA in BFEE with 0.1 M $(Bu)_4NBF_4$ using a constant potential of 1.70 V with that obtained after subsequent doping and dedoping processes in acetonitrile with 0.1 M $(Bu)_4NBF_4$ applying a potential of ±1.00 V for 50 s.

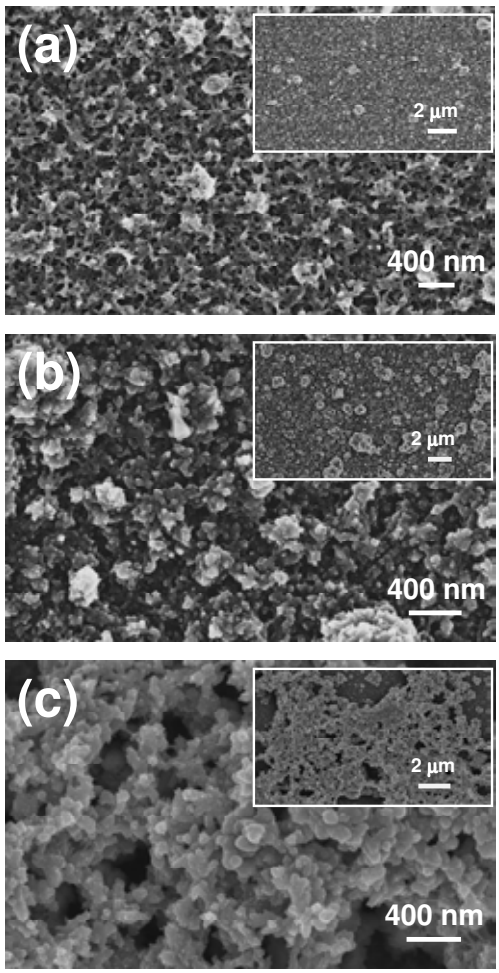

Figure 9. *High and low (inset) resolution SEM micrograhs of: (a) PClTh film generated at 1.70 V in BFEE 0.1 M$(Bu)_4NBF_4$ using a polymerization time of 150 s; (b) PClTh film generated as in (a) and subsequently doped in acetonitrile with 0.1 M $(Bu)_4NBF_4$ applying a potential of 1.00 V during 50 s; (c) PClTh film generated as in (a) and subsequently dedoped in acetonitrile with 0.1 M $(Bu)_4NBF_4$ applying a potential of (-1.00) V during 50 s.*

As it can be seen, the aggregates of nanosticks (see previous sections) displayed in Figure 9a grow significantly after electrochemical doping. This morphological change,

which is due to the incorporation of dopant ions, is accompanied by both a reduction in the number of pores and an enlargement of the remaining ones (Figure 9b). Consequently, the surface of the film becomes more porous after doping, even though the pores are still homogeneously distributed. Dedoping of electrochemically doped films also produces drastic morphological changes. Specifically, the escape of the dopant ions induces the compaction of the aggregates, which tend to collapse (Figure 9c). This phenomenon gives place to the appearance of large pores, even micrometric holes, at the surface of the film, even though a very compact material is appreciated just below such holes. The morphological behavior of the PClTh films generated using a constant potential of 1.70 V upon consecutive electrochemical doping-dedoping processes suggests that the stability of this material as electrochromic device will be very high.

PEDOT/PClTh electrochromic device. Before assembling, a PClTh electrode was prepared in BFEE with 0.1 M $(Bu)_4NBF_4$ at a constant potential of 1.70 V and subsequently dedoped in acetonitrile with 0.1 M $(Bu)_4NBF_4$, while a PEDOT electrode was generated in acetonitrile with 0.1 M $LiClO_4$ at a constant potential of 1.40 V. The PEDOT/PClTh ECD was successfully assembled by sandwiching the dedoped PClTh electrode and the doped PEDOT electrode, separated by a 8 mm spacer and an acetonitrile with 0.1 M $(Bu)_4NBF_4$-based liquid electrolyte. This ECD can be switched electrochemically between Bordeaux red and blue. The control voltammogram in the potential range between -0.50 and 1.60 V is displayed in Figure 8b. It shows that no other side reaction occurred during cycling and that the operating potential window is safe for the ECD.

Redox stability is an important requirement for production of reliable ECDs with long lifetimes. To test the stability of the fabricated PEDOT/PClTh ECD, potentials between -0.50 V and +1.60 V at a scan rate swept repeatedly with a scan rate of 100 $mV \cdot s^{-1}$. Fig. 10 represents the variation of the oxidation and reduction charge capacities (Q_{ox} and Q_{red}, respectively) as a function of the consecutive oxidation - reduction cycles. The variation of Q_{ox} and Q_{red}, which measures the change in the electroactivity, indicates that the ECD has good environmental and redox stabilities. Thus, the electroactivity of PEDOT/PClTh ECD decreases to 35% of the initial value after 390 cycles, this value being retained after 500 cycles (*i.e.* after the completion of the first 390 cycles, the system remains very stable). On the other hand, the Coulombic

efficiency, which is defined as ($\delta Q = Q_{ox}/Q_{red}$), becomes 1.0 after only 50 cycles (Fig. 10) remaining at such value after the 500 cycles.

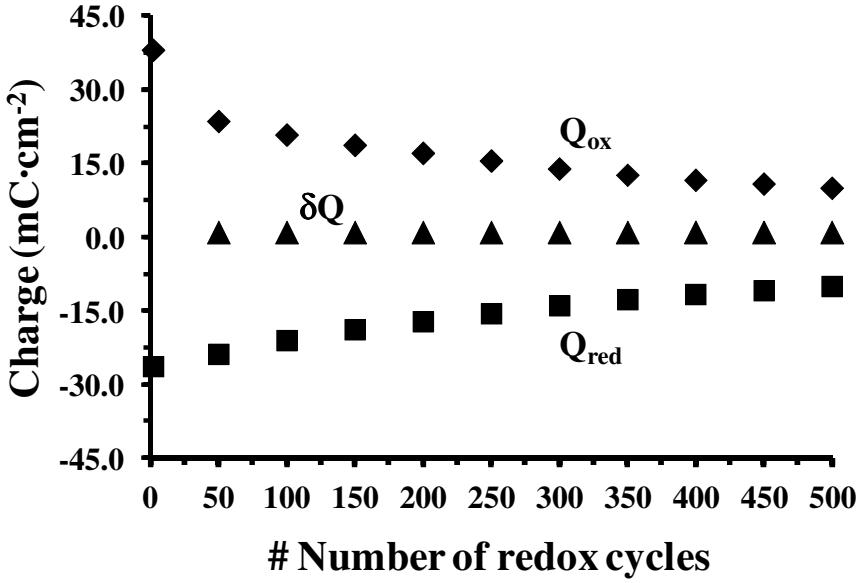

Figure 10. *Variations of the oxidation charge capacity, (Q_{ox}; diamonds) and reduction charge capacity (Q_{red}; squares), and redox efficiency ($\delta Q = Q_{ox}/Q_{red}$; triangles) of the PEDOT/PClTh ECD as a function of the number of consecutive oxidation-reduction cycles. Charge capacities were evaluated using an acetonitrile solution containing 0.1 M$(Bu)_4NBF_4$ scanned from -0.50 V to 1.60 V at a scan rate of 100 $mV \cdot s^{-1}$.*

7.1.4. Conclusions

3-Chlorothiophene has been electrochemically polymerized in BFEE with 0.1 $M(Bu)_4NBF_4$ using steel electrodes. Analyses of PClTh films obtained by CA using different potentials, which range from 1.60 to 1.90 V, indicate that the thickness and the roughness increase with the applied potential while the average degree of the polymerization, the current efficiency, the electroactivity, the SC and the doping level decrease when the potential increase. The electrical conductivity of PClTh, which is practically independent of the applied potential, is three orders of magnitude smaller than that of PEDOT. On the other hand, SEM and AFM studies indicate that samples obtained using a constant potential of 1.60 or 1.70 present a porous morphology and a topology compatible with linear molecules mainly formed by α-α linkages, whereas samples obtained at higher potentials are consistent with a multidirectional growing of cross-linked polymer chains. These features explain the variation of the electrochemical properties of PClTh with the potential used for its generation. Thus, the access and escape of dopant ions in oxidation and reduction, respectively, is easier in samples with a porous structure than in those with a compact one. Moreover, the presence of pores and cavities in PClTh samples obtained using the 1.70 V has been corroborated by EIS studies. Thus, the resistance associated with the transport of ions within the porous structure of the material, R_{CT}, has been found to increase drastically with the potential used to generate the polymer.

On the other hand, the IP and ε_g of PClTh has been measured by cyclic voltammentry and UV-vis spectroscopy, respectively. Results indicate that the electrochemical is ~1 eV higher for PClTh than for PEDOT, which indicates that p-doping of the latter material is easier. In contrast the optical energy gaps associated to the lowest π-π^* transition are relatively similar for PClTh and PEDOT. Quantum mechanical calculations on oligomers of up to 16 repeating units have been used to reproduce satisfactorily these electronic properties. Calculations were carried out using a repetitive sequence of head-to-tail linkages, as was found to be most stable arrangement between adjacent repeating units by a systematic conformational study on dimers and trimers. Study of the electrochromic properties indicates that the oxidized and reduced forms of PClTh adopt blue and the Bordeaux red colors, respectively, the intensity of such two colors depending on the potential used during the generation of the films. Moreover, the electrochromism observed after doping and dedoping processes is

accompanied by drastic morphological changes, which suggests that this polymer is a very suitable to fabricate stable electrochromic devices.

Finally, an all thiophene ECD made of PEDOT and PThCl with acetonitrile with 0.1 M $(Bu)_4NBF_4$-based liquid electrolyte has been successfully fabricated. The operating potential interval of this device ranges from -0.5 V to 1.60 V, no side electrochemical process being detected in this window. The device shows very large redox stability, the electroactivity after 500 cycles is 35% of the initial value and the Coulombic efficiency becomes 1 after 50 cycles only, remaining constant at such a value for an additional 450 cycles.

7.1.5. References

[1]. Wallace G.G, Spinks G. M, Kane-Maguire LAP, Teasdale PR. in "Conductive Electroactive Polymers", CRC Press, Boca Raton, 2009.

[2]. Freund MS, Deore B. in "Self-Doped Conducting Polymers", John Wiley & Sons Ltd, West Sussex, England, 2007.

[3]. Skotheim T. A, Reynolds J. R. in "Conjugated Polymers", CRC Press, Boca Raton, 2007.

[4]. Roncali, J. *Chem. Rev.* **1992**, *92*, 711.

[5]. Roncali J. *Chem. Rev*. **1997**, *97*, 173.

[6]. Groenendaal, L.; Jonas, F.; Freitag, V.; Pielartzik, H.; Reynolds, J. R. *Adv. Mater.* **2000**, *12*, 481.

[7]. Granstrom, M. *Polym. Adv. Technol.* **1997**, *8*, 424.

[8]. Perepichka, I. F.; Perepichka, D. F.; Meng, H.; Wudl, F. *Adv. Mater.* **2005**, *17*, 2281.

[9]. Leclerc, M.; Faïd, K. *Adv. Mater.* **1997**, *9*, 1087.

[10]. Somani, P. R.; Radhakrishnan, S. *Mater. Chem. Phys.* **2002**, *77*, 117.

[11]. Sapp, S. A.; Sotzing, G. A.; Reynolds, J. R. *Chem. Mater.* **1998**, *10*, 2101.

[12]. Grunathan, K.; Murugan, A. V.; Marimuthu, R.; Mulik, U. P.; Amenerkar, D. P. *Mater. Chem. Phys.* **1999**, *61*, 173.

[13]. Kumar, A.; Welsh, D.; Morvant, M. C.; Piroux, F.; Abboud, K. A.; Reynolds, J. R. *Chem. Mater.* **1998**, *10*, 986.

[14]. Roncali, J.; Horges, A.; Jubault, M. *Chem. Mater.* **1993**, *5*, 1456.

[15]. Corradini, A.; Marinangeli, A. M.; Mastragostino, M. *Electrochim. Acta* **1990**, *30*, 1757.

[16]. Arbizzani, C.; Mastragostino, M.; Passerini, S.; Pileggi, R.; Scrosati, B. *Electrochim. Acta* **1991**, *36*, 837.

[17]. Garnier, F.; Tourillon, G. *J. Electroanal. Chem.* **1983**, *148*, 299.

[18]. Huang, S.-W.; Ho, K.-C. *Solar Energy Mater. Solar Cells* **2006**, *90*, 491.

[19]. Xu, J.; Shi, G.; Chen, F.; Wang, F.; Zhang, J.; Hong, X. *J. Appl. Polym. Sci.* **2003**, *87*, 502.

[20]. Xu, J.; Shi, G.; Xu, Z.; Chen, F.; Hong, X. *J. Electrochem. Chem.* **2001**, *514*, 16.

[21]. Shi, G.; Xu, J.; Fu, M. *J. Phys. Chem. B* **2002**, *106*, 288.

[22]. Pang, Y.; Xu, H.; Li, X.; Ding, H.; Cheng, Y.; Shi, G.; Jin, L. *Electrochem. Commun*. **2006**, *8*, 1757

[23]. Pang, Y.; Li, X.; Shi, G.; Jin, L. *Thin Solid Films* **2008**, 516, 6512.

[24]. Kobayashi, M.; Chen, J.; Chung, T. C.; Moraes, F.; Heeger, A. J.; Wudl, F. *Synth. Met*. **1984**, *9*, 77.

[25]. Chung, T. C.; Kaufman, J. H.; Heeger, A. J.; Wudl, F. *Phys. Rev. B* **1984**, *30*, 702.

[26]. Hernández, V.; López, J. T.; Marcos, J. L. *Synth. Met.* **1991**, *41*, 789.

[27]. Xu, Z.; Horowitz, G.; Garnier, F. *J. Electroanal. Chem.* **1988**, *246*, 467.

[28]. Sankaran, B.; Reynolds, J. R. *Macromolecules* **1997**, *30*, 2582.

[29]. Huang, H.; Pickup, P. G. *Chem. Mater.* **1998**, *10*, 2212.

[30]. Ahonen, H.; Lukkari, J.; Kankare, J. *Macromolecules* **2000**, *33*, 6787.

[31]. Fu, Y.; Cheng, H.; Elsenbaumer, R. L. *Chem. Mater.* **1997**, *9*, 1720.

[32]. Sotzing, G. A.; Reynolds, J. R.; Steel, P. J. *Chem. Mater.* **1996**, *8*, 882.

[33]. Roncali, J.; Akoudad, S. *Synth. Met.* **1998**, *93*, 111.

[34]. Kumar, A.; Reynolds, J. R. *Macromolecules* **1996**, *29*, 7629.

[35]. Bertran, O.; Pfeiffer, P.; Torras, J.; Armelin, E.; Estrany, F.; Alemán, C. *Polymer* **2007**, *48*, 6955.

[36]. Bertran, O.; Armelin, E.; Torras, J.; Estrany, F.; Codina, M.; Alemán, C. *Polymer* **2008**, *49*, 1972.

[37]. Armelin, E.; Bertran, O.; Estrany, F.; Salvatella, R.; Alemán, C. *Eur. Polym. J.* **2009**, *45*, 2211.

[38]. Bertran, O.; Armelin, E. A.; Estrany, F.; Gomes, A.; Torras, J.; Alemán, C. *J. Phys. Chem. B* **2010**, *114*, 6281.

[39]. Ocampo, C.; Oliver, R.; Armelin, E.; Alemán, C.; Estrany, F. *J. Polym. Res.* **2006**, *13*, 193.

[40]. Aradilla, D.; Estrany, F.; Armelin, E.; Alemán, C. *Thin Solid Films* **2010**, *518*, 4203.

[41]. Estrany, F.; Aradilla, D.; Oliver, R.; Alemán, C. *Eur. Polym. J.* **2007**, *43*, 1876.

[42]. Aradilla, D.; Estrany, F.; Alemán, C. *J. Phys. Chem. C* **2011**, *115*, 8430.

[43]. Sauvajol, J. L.; Chenouini, D.; Lere-Porte, J. P.; Chorro, C.; Moukala, B.; Petrissans, J. *Synth. Met.* **1990**, *38*, 1.

[44]. Carrasco, E. B.; Fernández, V.; Cabot, P. L.; Garrido, J. A.; Centellas, F.; Rodriguez, R. M. *J. Electrochem. Soc.* **2001**, *148*, E19.

[45]. Brédas, J. L.; Silbey, R.; Boudreaux, D. S.; Chance, R. R. *J. Am. Chem. Soc*. **1983**, *105*, 6555.

[46]. Gaussian 03, Revision B.02, Frisch, M. J.; Trucks, G. W.; Schlegel, H. B.; Scuseria, G. E.; Robb, M. A.; Cheeseman, J. R.; Montgomery, J. A.; Vreven Jr T.; Kudin, K. N.; Burant, J. C.; Millam, J. M.; Iyengar, S. S.; Tomasi, J.; Barone, V.; Mennucci, B.; Cossi, M.; Scalmani, G.; Rega, N.; Petersson, G. A.; Nakatsuji, H.; Hada, M.; Ehara, M.; Toyota, K.; Fukuda, R.; Hasegawa, J.; Ishida, M.; Nakajima, T.; Honda, Y.; Kitao, O.; Nakai, H.; Klene, M.; Li, X.; Knox, J. E.; Hratchian, H. P.; Cross, J. B.; Adamo, C.; Jaramillo, J.; Gomperts, R.; Stratmann, R. E.; Yazyev, O.; Austin, A. J.; Cammi, R.; Pomelli, C.; Ochterski, J. W.; Ayala, P. Y.; Morokuma, K.; Voth, G. A.; Salvador, P.; Dannenberg, J. J.; Zakrzewski, V. G.; Dapprich, S.; Daniels, A. D.; Strain, M.; Farkas, O.; Malick, D. K.; Rabuck, A. D.; Raghavachari, K.; Foresman, J. B.; Ortiz, J. V.; Cui, Q.; Baboul, A. G.; Clifford, S.; Cioslowski, J.; Stefanov, B. B.; Liu, G.; Liashenko, A.; Piskorz, P.; Komaromi, I.; Martin, R. L.; Fox, D. J.; Keith, T.; Al-Laham, M. A.; Peng, C. Y.; Nanayakkara, A.; Challacombe, M.; Gill, P. M. W.; Johnson, B.; Chen, W.; Wong, M. W.; Gonzalez, C.; Pople, J. A. Gaussian, Inc., Pittsburgh PA, 2003.

[47]. Becke, A. D. *J. Chem. Phys.* **1993**, *98*, 5648.

[48]. Lee, C.; Yang, W.; Parr, R. G. *Phys. Rev. B* **1988**, *37*, 785.

[49]. Frisch, M. J.; Pople, J. A.; Binkley, J. S. *J. Chem.Phys.* **1984**, *80*, 3265.

[50]. Koopmans, T. *Physica* **1934**, *1*, 104.

[51]. Janak, J. F. *Phys. Rev. B* **1978**, *18*, 7165.

[52]. Levy, M.; Nagy, A. *Phys. Rev. A* **1999**, *59*, 1687.

[53]. Schleyer, P. v. R.; Jiao, H. *Pure Appl. Chem.* **1996**, *68*, 209.

[54]. Schleyer, P. v. R.; Maerker, C.; Dransfeld, A.; Jiao, H.; van Eikema Hommes, N. J. R. *J. Am. Chem. Soc.* **1996**, *118*, 6317.

[55]. Wolinski, K.; Hilton, J. F.; Pulay, P. *J. Am. Chem. Soc.* **1990**, *112*, 8251.

[56]. Fallah-Bagher-Shaidaei, H.; Wannere, C. S.; Corminboeuf, C.;Puchta, R.; Schleyer, P. v. R. *Org. Lett.* **2006**, *8*, 863.

[57]. Krygowski, T. M. *J. Chem. Inf. Comput. Sci.* **1993**, *33*, 70.

[58]. Alkan, S.; Cutler, C. A.; Reynolds, J. R. *Adv. Funct. Mater.* **2003**, *13*, 331.

[59]. Chen, L.; Yuan, C.; Dou, H.; Gao, B.; Chen, S.; Zhang, X. *Electrochim. Acta* **2009**, *54*, 2335.

[60]. Murugan, A. V.; Viswanath, A. K.; Gampet, G.; Gopinath, C. S.; Vijayamohanan, K. *Appl. Phys. Lett.* **2005**, *87*, 243511.

[61]. Sharma, R.; Zhai, L. *Electrochim. Acta* **2009**, *54*, 7148.

[62]. Sen, P. M.; De, M. *Electrochim. Acta* **2010**, *55*, 4677.

[63]. Banafsheh, B.; Ivey, D. G. *Electrochim. Acta* **2010**, *55*, 2014.

[64]. Chen, L.; Yuan, C.; Gao, B.; Chen, S.; Zhang, X. *J. Solid State Electrochem.* **2009**, *13*, 1925.

[65]. Murugan, A. V.; Viswananth, A. K.; Gopinath, C. S.; Vijayamohanan, C. K. *J. Appl. Phys.* **2006**, *100*, 074319.

[66]. Aradilla, D.; Estrany, F.; Alemán, C. *J. Appl. Polym. Sci.* **2011**, *121*, 1982.

[67]. Grenier, C. R. G.; Pisula, W.; Joncheray, T. J.; Müllen, K.; Reynolds, J. R. *Angew. Chem. Int. Ed.* **2007***, 46*, 714.

[68]. Alakhras, F.; Holze, R. *J.SolidState Electrochem.* **2008**, *12*, 81.

[69]. Casanovas, J.; Alemán, C. *J. Phys. Chem C* **2007**, *111*, 4823.

7.2. Properties of poly(3-halidethiophene)s

7.2.1. Introduction

Polythiophenes (PThs) are one of the most important classes of conducting polymers (CPs). These materials, which can be prepared by chemical or electrochemical methods, exhibit good electrical and optical properties, environmental and thermal stabilities in conducting (doped) form, rapid response time, and easy functionalization. These unique advantages result in a tremendous interest for their application as conducting films, electrochromic and nonlinear optical devices, field-effect transistors, organic condensers, light-emitting diodes, sensors, etc.[1-12]

In recent years, a particular interest in the development of PThs with electron-withdrawing groups in the 3-position of the thiophene ring, efforts being essentially focused in the incorporation of carboxylic acid groups (*e.g.* acetic acid, acrylic acid and malonic acid hydrophilic substituents) have been reported.[13-18] Poly(3-halidethiophene)s is another interesting family of PThs substituted with electron-withdrawing groups (Scheme 1). In these materials halogen atoms are directly attached to the polyconjugated main chain, which may produce a reduction in the electronic density of the thiophene rings. In spite of characterization of poly(3-halidethiophene)s (where the halogen is fluorine, chlorine or bromine) is crucial for a complete understanding of the effects produced by such electron-withdrawing groups in the PTh backbone, only few works have been reported in the literature.

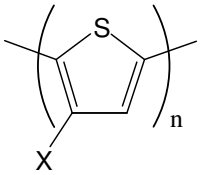

X= F	poly(3-fluorothiophene)	PFTh
X= Cl	poly(3-chlorothiophene)	PClTh
X= Br	poly(3-bromothiophene)	PBrTh

Scheme 1

Poly(3-chlorothiophene), hereafter denoted PClTh, is the most known of the three poly(3-halidethiophene)s. This material has been electrochemically synthesized in ionic liquids (*i.e.* boron trifluoride diethyl etherate and 1-butyl-3-methylimidazolium

hexafluorophosphate, abbreviated BFEE and [BMIM]PF_6, respectively) using platinum and nanoporous TiO_2 as substrates, their electrochemical, electrochromic and optical properties being characterized using cyclic voltammetry (CV), spectroelectrochemistry and UV-vis spectroscopy.[19-22] Moreover, the influence of the concentration of electrolyte in the generation medium and the thickness of the films on the doping level of PClTh was examined using Raman spectroscopy.[23,24] In a very recent work a very complete characterization of the physical, electrochemical, morphological, electronic and electrochromic properties of PClTh, which was prepared by anodic polymerization of 3-chlorothiophene in BFEE solution at a constant potential was reported.[25] In addition, an all-thiophene electrochromic device made of poly(3,4-ethylenedioxythiophene), abbreviated PEDOT, and PClTh was successfully fabricated and tested.[25]

Poly(3-bromothiophene), abbreviated PBrTh, has been prepared in BFEE using platinum, indium tin oxide and nanoporous TiO_2 substrates,[26-28] its properties being in general much less known that those of PClTh. Amazingly, the π-π^* lowest transition energy (ε_g) values determined for PBrTh by UV-vis spectroscopy[27,28] (2.55 eV) and spectroelectrochemistry[26] (1.90 eV) were significantly high compared with those reported for PClTh (*i.e.* 1.50-1.61 and 1.74-1.80 eV by UV-vis[25] and spectroelectrochemistry,[20,22] respectively). Finally, a single work about the electrochemical synthesis and properties of poly(3-fluorothiophene), denoted PFTh, has been reported.[29] Such study reflected the difficulties in the synthesis of PFTh, which were attributed to the high oxidation potential of 3-fluorothiophene, (*i.e.* the oxidation potential of the 3-halidethiophene monomers decrease with the electronegativity of halogen atom reflecting the control of the inductive electron-withdrawing effects on the polymerization). In spite of this limitation, it was found that PFTh exhibits higher electrical conductivity compared to PClTh and PBrTh.

In this work a combination of both experimental methods and quantum mechanical calculations to provide new insights into the characterization of PBrTh and a comprehensive comparison of the three poly(3-halidethiophene)s at the molecular level has been carried out. More specifically, PBrTh has been obtained by anodic polymerization of 3-bromothiophene in BFEE at a constant potential, such potential being optimized by examining the properties of materials prepared using a potential comprised within the 1.60-1.90 V interval. The electrochemical, electric, morphological and electronic properties of the material obtained using the optimum experimental

conditions have been examined and compared with those recently reported for PClTh.[25] Furthermore, the conformational preferences and electronic properties of PFTh, PClTh and PBrTh have been determined using Density Functional Theory (DFT) calculations on model oligomers containing *n* repeating units, where *n* ranged from 2 to 16. Finally, the strength and nature of sulfur···halide non-covalent intramolecular interactions have been analyzed using electronic calculations.

7.2.2. Methods

Materials. 3-Bromothiophene and acetonitrile analytical reagent grade were purchased from Aldrich and used without further purification. Anhydrous tetrabutylammonium tetrafluoroborate, $(Bu)_4NBF_4$, analytical reagent grade from Aldrich was stored in an oven at 80 ºC before use in the electrochemical trials.

Synthesis. The anodic polymerization of 3-bromothiophene was studied by cyclic voltammetry (CV) and chronoamperometry (CA) using an Autolab PGSTAT302N equipped with the ECD module to measure very low current densities (100 mA–100 pA). Electrochemical experiments were conducted in a three-electrode two-compartment cell under nitrogen atmosphere (99.995% in purity) at 25ºC. The anodic compartment was filled with 40mL of a 0.01M monomer solution in BFEE containing 0.1 M $(Bu)_4NBF_4$, as supporting electrode. A volume of 10 mL of the same electrolyte solution was placed in the cathodic compartment. Steel AISI 316 sheets of 4 cm^2 area were employed as working and counter electrodes. In order to avoid interferences during the electrochemical analyses, the working and counter electrodes were cleaned with acetone and, subsequently, dried with an air flow before each trial. The reference electrode was an Ag|AgCl electrode containing KCl saturated aqueous solution (E^0= 0.222 V at 25ºC), which was connected to the working compartment through a salt bridge containing the electrolyte solution. After electropolymerization, the coated electrodes were cleaned with acetonitrile and dried with nitrogen. In all cases, the solution was purged with nitrogen for 5 minutes prior electrochemical synthesis.

Electrochemical and electrical properties. The electroactivity, which refers to the charge storage ability, was determined by CV using an acetonitrile solution with 0.1 M $(Bu)_4NBF_4$. The initial and final potentials were -0.20 V, while the reversal potential was 1.60 V. The electroactivity increases with the similarity between the anodic and cathodic areas of the control voltammograms, which were registered at a scan rate of 100 $mV \cdot s^{-1}$.

The specific capacitance (SC, in $F \cdot g^{-1}$) was determined by CV using:

$$SC = \frac{Q}{\Delta V m_{pol}} \tag{1}$$

where Q is the voltammetric charge that was obtained by integrating either the oxidative or reductive parts of the cyclic voltammogram, ΔV is the potential window (in V), and m_{pol} is the mass of polymer deposited in the electrode (in g) that was determined using a Sartorius ultra-microbalance.

The doping level (dl) of the electrochemically produced PBrTh was carried out using the following Eqn:

$$dl = \frac{2Q_O}{Q_O - Q_D} 100 \tag{2}$$

where Q_D is the total charge used for the polymer deposition and Q_0 is total charge of oxidized species in the polymer films.

The electrical conductivity was determined using the sheet resistance method with a previously described procedure.[30]

The current efficiency of polymerization (η, in %), which indicates the charge consumed by the growth of the polymer film relative to the total charge passed through the cell, was measured as follows:

$$\eta = \left[\frac{\left(n_{ox} \cdot F \cdot m_{pol} \Big/ M \right)}{Q_{pol}} \right] 100 \tag{3}$$

where F is the Faraday constant (96487 C mol^{-1}), Q_{pol} is the charge passed through the cell during the polymer film growth (*i.e.* the polymerization charge consumed in the process, in Coulombs that was calculated on the chronoamperogram, M is the molar mass of the monomer, and n_{ox} corresponds to the number of electrons consumed to incorporate a monomer into a polymer and to oxidize the resulting chain. The following Eqn has been used to evaluate n_{ox}:

$$n_{ox} = \frac{M \cdot Q_{pol}}{F \cdot m_{pol} (1 - m_{dop})} \tag{4}$$

where m_{dop} is the mass of dopant per polymer unit of mass.

The loss of electroactivity (LES, in %), which decreases with the oxidation and reduction areas of consecutive control voltammograms, was determined as:

$$LES = \frac{\Delta Q}{Q_{II}} 100 \quad (5)$$

where ΔQ is the difference between voltammetric charges (in C) of the second and the last cycle, and $Q_{II}$is the voltammetric charge of the second cycle. In this work, measures of LES refer to 100 consecutive oxidation-reduction cycles.

The reduction in the porosity (Δp) was evaluated as follows:

$$\Delta p = \frac{l_0 - l_{200}}{l_0} 100 \quad (6)$$

where the l_0 refers to the thickness of the film as generated, which shows the maximal porosity, and l_{200} refers to the thickness of the film after 200 consecutive oxidation-reduction cycles. The thickness was determined using the procedure reported in a previous work.[25]

Morphology. Morphological studies were performed using scanning electron microscopy (SEM) and tapping-mode atomic force microscopy (AFM). Topographic AFM images were obtained with a Molecular Imaging Pico SPM using a NanoScope IV controller under ambient conditions. The averaged RMS roughness (*r*) was determined using the statistical application of the Nanoscope software, which calculates the average considering all the values recorded in the topographic image with exception of the maximum and the minimum. SEM studies were carried out using a Focussed Ion Beam ZeissNeon 40 scanning electron microscope operating at 3 kV and equipped with an energy dispersive X-ray (EDX) spectroscopy system.

Absorption spectroscopy. Absorption spectra were obtained with a Shimadzu 3600 spectrophotometer equipped with a tungsten halogen visible source, a deuterium arc UV source, a photomultiplier tube UV-vis detector, and a InGaAs photodiode and cooled PbS photocell NIR detectors.Spectra were recorded in the absorbance mode using the integrating sphere accessory (model ISR-3100), the wavelength range being 200-800 nm. The interior of the integrating sphere is coated with a highly diffuse BaO reflectance standard. Single-scan spectra were obtained at a scan speed of 60 nm·min^{-1} with a bandwidth of 2 nm using the UVProbe 2.31 software. The optical ε_g was derived from the UV-vis spectra of the reduced materials on ITO electrodes using a procedure previously described.[31]

Theoretical methods. All quantum mechanical calculations were performed using the Gaussian 03 computerprogram.[32] The internal rotations of the model compounds

formed by two 3-halidethiophene units (*i.e.* 2-XTh with X= F, Cl and Br, respectively) were studied by scanning the inter-ring dihedral angle S-C-C-S (θ) in steps of 30º between θ = 0º and 360º. A flexible rotor approximation was used, each point of the path being obtained from geometry optimization of the molecule at a fixed value of θ. Furthermore, minimum energy conformations were determined from complete geometry optimization using a gradient method. The rotational profiles and the geometry of the minimum energy conformations were calculated using the B3LYP[33,34] method combined with the 6-31+G(d,p) basis set.[35]

Similarly, molecular geometries of *n*-XTh (with X= F, Cl and Br) oligomers, where *n* refers to the number of chemical repeating units and ranged from 3 to 16, were fully optimized at the B3LYP/6-31+G(d,p) level. Starting geometries of 3-XTh were constructed considering head-to-head, tail-to-tail and head-to-tail linkages (see next section), whereas the latter was the only used for oligomers with $n > 3$.

The first ionization potential (IP) and the electron affinity (EA) were estimated using the Koopmans' theorem.[36] Accordingly, IPs and EAs were taken as the negative of the highest occupied molecular orbital (HOMO) energy and the lowest unoccupied molecular orbital (LUMO) energy, respectively, *i.e.* IP= $-\varepsilon_{HOMO}$ and EA= $-\varepsilon_{LUMO}$. The IP indicates if a given acceptor (p-type dopant) is capable of ionizing, at least partially, the molecules of the compound, while the EA refers to the ionization through a given donor (n-type dopant). It is worth noting that according to the Janak´s theorem,[37] the approximation mentioned above for the calculation of the IP can be applied to DFT calculations. All the IPs and EAs estimated in this work were calculated at the B3LYP/6-31+G(d,p) level.

The π-π^* lowest transition energy (ε_g) was estimated using two different strategies. In the first, ε_g was approximated as the difference between the HOMO and LUMO energies, *i.e.* $\varepsilon_g = \varepsilon_{LUMO} - \varepsilon_{HOMO}$, obtained at the B3LYP/6-31+G(d,p) level. Recent studies showed that the ε_g values predicted for conducting polymers using the B3LYP hybrid functional are in excellent agreement with experimental values.[38-41] The second estimation of ε_g was derived from the excitation energies calculated with time dependent DFT (TD-DFT) calculations. This method, which is widely applied to study the spectroscopic properties of conjugated organic compounds, provides a robust and efficient description of the low-lying molecular states.[42,43] Electronic excitations were evaluated with the PBE0[44] functional combined with the 6-31+G(d,p) basis set using the

geometries previously optimized at the B3LYP/6-31+G(d,p) level. In all cases the ε_g was extracted from the first low-lying transition with a large oscillator strength.

With respect to the analysis of the aromaticity of the thiophene rings in 2-XTh dimers, criteria based on different physical properties have been used. First, the magnetic-based nucleus independent chemical shifts[45-47] (NICS) calculations were performed to determine the aromaticity of the rings under analysis. The GIAO method[48] was used to perform calculations of NICS at ring centers (NICS(0)) determined by the non-weighted mean of the heavy atoms coordinates and at 1.0 Å above the ring taken into study (NICS(1)), with this latter being considered a better measure of π aromaticity due to the reduced effect of the in-plane components to the isotropic shielding.[49,50]

After, the electronic-based multicenter index (MCI) was applied.[51,52] MCI is a particular extension of the I_{ring} index[53]defined as:

$$I_{ring}(\mathcal{A}) = \sum_{i_1,i_2,\cdots,i_N} n_{i_1} \cdots n_{i_N} S_{i_1 i_2}(A_1) S_{i_2 i_3}(A_2) \cdots S_{i_N i_1}(A_N) \qquad (7)$$

n_i being the occupancy of the molecular orbital i and $\mathcal{A} = \{ A_1, A_2, ..., A_N\}$ a string containing the set of N atoms forming the ring structure. Summing up all I_{ring} values resulting from the permutations of indices A_1, A_2, ...,A_N the mentioned MCI index[44] is obtained from the expression:

$$MCI(\mathcal{A}) = \frac{1}{2N} \sum_{P(\mathcal{A})} I_{ring}(\mathcal{A}) \qquad (8)$$

where $P(\mathcal{A})$ stands for a permutation operator which interchanges the atomic labels A_1, A_2, ..., A_N to generate the N! permutations of the elements in the string $\mathcal{A}$.[49,54] MCI and I_{ring} give an idea of the electron sharing between all atoms in the ring. The more positive the MCI values, the more aromatic the rings. The analysis of the delocalization in the ring by MCI has been complemented with the calculation of the fluctuation index of aromaticity (FLU),[55] which measures the amount of electron sharing between contiguous atoms. It is defined as:

$$FLU(\mathrm{A}) = \frac{1}{N} \sum_{i=1}^{N} \left[\left(\frac{V(A_i)}{V(A_{i-1})} \right)^{\alpha} \left(\frac{\delta(A_i, A_{i-1}) - \delta_{ref}(A_i, A_{i-1})}{\delta_{ref}(A_i, A_{i-1})} \right) \right]^2 \qquad (9)$$

where $A_0 \equiv A_N$ and V(A) is the atomic valence given by:

$$V(A_i) = \sum_{A_j \neq A_i} \delta(A_i, A_j) \tag{10}$$

And α is a simple function to make sure that the first term in eqn (9) is always greater or equal to 1, so it takes the values:

$$\alpha = \begin{cases} 1 & V(A_i) > V(A_{i-1}) \\ -1 & V(A_i) \leq V(A_{i-1}) \end{cases} \quad . \tag{11}$$

The δ_{ref}(C,C) = 1.389 e and δ_{ref}(C,S) = 1.270 e, calculated from benzene at the B3LYP/6-311++G(d,p) level, was used in the calculations. FLU is close to 0 in aromatic species, and differs from it in non-aromatic ones. Calculation of atomic overlap matrices (AOM) and computation of MCI and FLU have been performed with the AIMPAC[56] and ESI-3D[57] collection of programs.

Finally, as a geometry-based aromaticity measure, the HOMA index,[58] which is based on C–C and C–S bond length alternation pattern along the π-system, was evaluated as:

$$HOMA = 1 - \frac{\alpha}{l} \sum_{i=1}^{l} (R_{opt} - R_i)^2 \quad . \tag{12}$$

where l is the number of bonds, α is an empirical constant (α = 257.7 and 94.09 for C–C and C–S bonds, respectively), R_i is the bond length and R_{opt} is the optimal bond length (R_{opt} = 1.388 and 1.677 Å for C–C and C–S bonds, respectively). It is worth noting that HOMA is equal to zero for a Kekulé structure formed by a typical aromatic system with single and double bonds arranged alternatively, and is equal to 1 for a system with all bonds equal to the optimal value ($R_i = R_{opt}$).

For the indices used, the more negative the NICS, the lower the FLU index, and the higher the HOMA and MCI values, the more aromatic the rings are.

7.2.3. Results and discussion

Synthesis, electrochemical and electrical properties. Figure 1a displays the cyclic voltammogram of 0.01 M 3-bromothiophene in BFEE with 0.1 M $(Bu)_4NBF_4$ on a steel electrode in the potential range from -0.50 to 2.20 V. The onset of polymerization occurs at 1.58 V, whereas the anodic peak at 2.01 V and the cathodic peak at 0.84 V

correspond to oxidation and reduction of the polymer, respectively. In the oxidation process (*i.e.* from 1.58 to 2.01 V) a blue film was deposited on the steel electrode, its colour changing to red upon reduction. Figure 1b evidences that the current response of the monomer oxidation peak and the redox response of the polymer deposited on the electrode change upon successive cycling. Specifically, the current density increases with the number of scans, indicating that this potentiodynamic procedure gives place to the formation of polymer. Furthermore, after 50 oxidation-reduction scans from 0.10 to 1.90 V, the onset of polymerization, the oxidation of the polymer and the corresponding reduction decrease to 0.67, 1.36 and 0.46 V, respectively. These variations should be attributed to the fact that the mass of polymer deposited in the steel electrode increases after each cycle, making more difficult the access and escape of dopant ions upon repeated cycling. This electrochemical behavior is similar to that previously observed for PClTh using the same experimental conditions.[25]

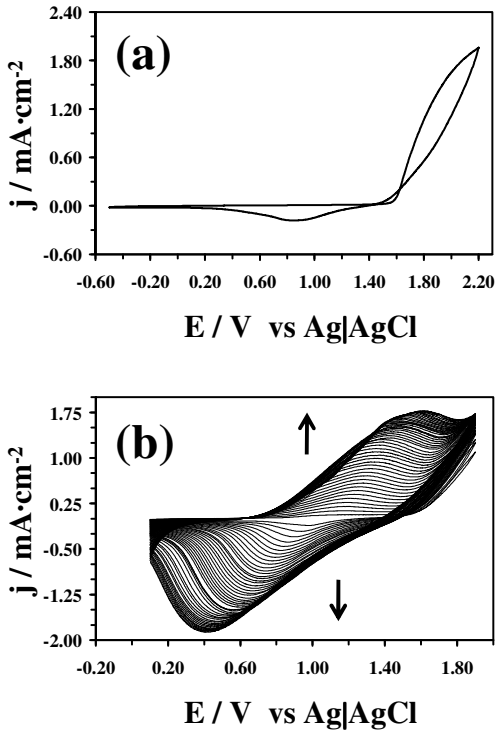

Figure 1. *(a) Cyclic voltammogram of 0.01 M 3-bromothiophene in BFEE with 0.1 M $(Bu)_4NBF_4$ on a steel electrode. Initial and final potentials: -0.50 V; reversal potential: 2.20 V. Scan rate: 20 $mV \cdot s^{-1}$. (b) Successive cyclic voltammograms (50 scans) of 0.01 M 3-bromothiophene in BFEE with 0.1 M $(Bu)_4NBF_4$ on a steel electrode. Initial and final potentials: 0.10 V; reversal potential: 1.90 V. Scan rate: 50 $mV \cdot s^{-1}$. Arrows indicate the increasing number of cycles.*

Table 1 compares the electroactivity and specific capacitance of PBrTh films produced using a constant potential of 1.60, 1.70, 1.80 and 1.90 V. As it can the been,

these properties are very similar for the materials produced at 1.60 and 1.70 V, whereas the values determined for the polymers obtained using 1.80 and 1.90 V are significantly lower. According to these results, the optimum potential for the generation of PBrTh by CA has been selected to be 1.70 V. Comparison with the properties measured for PClTh produced under identical experimental conditions, which have been included in Table 1, indicates that the electrochemical performance of PBrTh is considerably worse than that of PClTh, independently of the potential used in the anodic polymerization process.

Table 1. *Comparison of the electroactivity (i.e. ability to store charge) and specific capacitance (SC, Eqn 1) of PBrTh and PClTh, respectively, produced by CA in BFEE with 0.1 M $(Bu)_4NBF_4$ applying different potentials and using a polymerization time of 150 s. Properties for the material produced using potentiodynamic methods[a] (0.1-1.9 V) are also displayed for comparison. Data for PClTh were taken from reference 25.*

	Electroactivity ($mC \cdot cm^{-2}$)		**SC ($F \cdot g^{-1}$)**	
Potential (V)	**PBrTh**	**PClTh**	**PBrTh**	**PClTh**
1.60	17.4	40.6	15	26
1.70	17.5	40.0	17	29
1.80	14.8	27.4	10	19
1.90	11.0	20.9	6	14
0.1-1.90 V[a]	12.4	23.7	8	17

[a] *Films were generated from 25 consecutive oxidation-reduction cycles in a solution containing monomer in BFEE with 0.1 M $(Bu)_4NBF_4$ at 50 mV/s.*

On the other hand, Table 2 compares the doping level, the current efficiency of polymerization, loss of electroactivity and electrical conductivity of PBrTh and PClTh generated by CA at 1.70 V using identical experimental conditions. With exception of the loss of electroactivity, which reveals that the electrochemical stability of PBrTh is significantly lower than that of PClTh, all the other properties are very similar for the two poly(3-halidethiophene)s. These features combined with the differences found in both the electroactivity and the specific capacitance indicates that the electrochemical behavior of PBrTh is worse than that of PClTh.

Table 2. *Current efficiency of polymerization (η; Eqn 3), doping level (dl; Eqn 2), loss of electroactivity (LES; Eqn 5) and electrical conductivity of PBrTh and PClTh films produced by CA in BFEE with 0.1 M $(Bu)_4NBF_4$ applying a constant potential of 1.70 V and using a polymerization time of 150 s.*

Polymer	η (in %)	dl	LES (in %)[a]	σ ($S \cdot cm^{-1}$)
PBrTh	88	0.42	47	0.96
PClTh[b]	85	0.41	29	0.59

[a] *Determined by considering 100 consecutive oxidation-reduction cycles.* [b] *From reference 25.*

Morphology. Figure 2a shows SEM and AFM high resolution images of PBrTh films as prepared by CA in BFEE with 0.1 M $(Bu)_4NBF_4$ using a constant potential of 1.70 V. As it can be seen, the material can be described as a compact distribution of nanoaggregates, the porosity of the films being very low. Comparison with the porous morphology of PClTh, which was generated using identical experimental conditions,[25] allows us to understand the different electrochemical behavior of the two materials. Thus, the access and escape of dopant ions in oxidation and reduction processes, respectively, are easier in materials with a porous structure than in those with a compact one. The nanopores found in PClTh facilitate the mobility of dopant ions in redox processes, enhancing the electrochemical properties with respect to the compact morphology of PBrTh. The low porosity of PBrTh with respect to PClTh has been quantified through the parameter Δp, which was determined though the variation of the thickness of polymer after 200 consecutive oxidation-reduction cycles (Eqn 6). The value of Δp obtained for PBrTh and PClTh is 27% and 36%, respectively.

Figure 2b, which displays microscopy images of PBrTh films after reduction in acetonitrile with 0.1 M $(Bu)_4NBF_4$ applying a constant potential of -1.00 V for 50 s, reveals significant morphological changes upon dedoping. Specifically, the dimensions of the aggregates located at the surface increase significantly, which is accompanied by a notable reduction in the roughness. Specifically, the average RMS roughness decreases from r = 229 nm in the oxidized material to r = 72 nm in the reduced one. This re-organization, which is due to the escape of the dopant ions induced by the electrochemical reduction, is not accompanied by an apparent increase of the porosity. Again, this behavior is drastically different from that reported for PClTh.[25] Thus, dedoping of PClTh films produced a compaction of the nanoaggregates at the surface, giving place to the appearance of micrometric pores. Accordingly, the morphologies of

both doped and dedoped PBrTh films are not suitable to favor the mobility of the molecular ions, whereas those of PClTh favor electrochemical oxidation and reduction process allowing the transport of dopant ions through the pores.

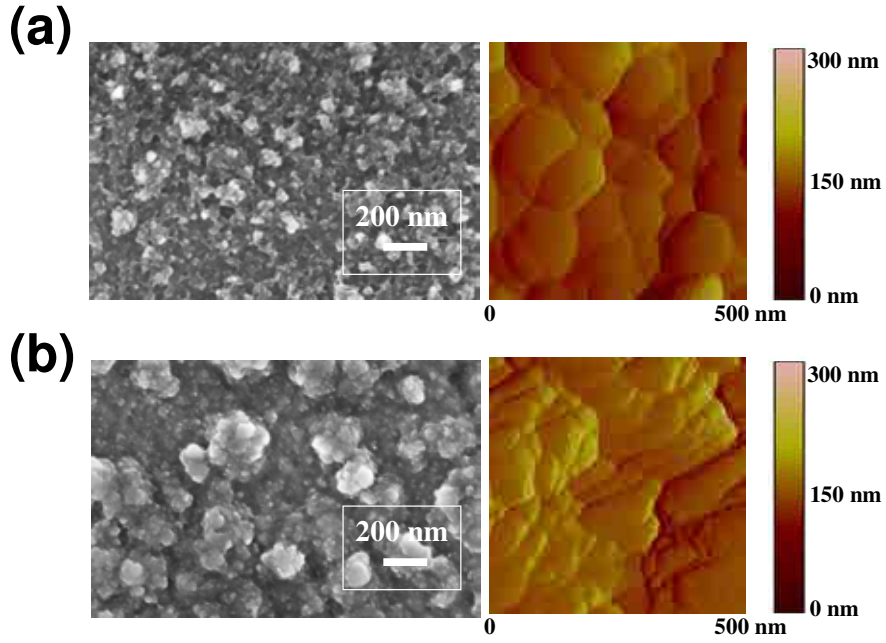

Figure 2. *SEM (left) and AFM (right) high resolution images of: (a) PBrTh films generated by CA at 1.70 V in BFEE with 0.1 M $(Bu)_4NBF_4$ using a polymerization time of 150 s; and (b) PBrTh films generated as in (a) and subsequently dedoped in acetonitrile with 0.1 M $(Bu)_4NBF_4$ applying a potential of -1.00 V during 50 s.*

Experimental determination of the electronic properties. Cyclic voltammograms have been used to derive the IP of PBrTh. According to Brédas and co-workers,[59] the IP (in eV) can be estimated using the following equation: IP = E_{ox} + 4.4, which eliminates the environmental effects from the oxidation (E_{ox}) onset (versus Ag|AgCl). The value of E_{ox} (Figure 3a) obtained for PBrTh is 1.03 and 1.22 for samples prepared by potentiostatic and potentiodynamic methods, respectively, the resulting IP values being 5.43 and 5.62 eV. The latter estimations are similar to that found for PClTh using the same electrochemical procedure (*i.e.* 5.38 eV).[25]

The ε_g determined for PBrTh by UV-vis spectroscopy, which is defined as the onset energy for the π-π^* transition (Figure 3b), is 1.93 eV and 1.97 eV for samples prepared by potentiostatic and potentiodynamic methods, respectively. These values are in excellent agreement with that determined by spectroelectrochemistry[26] (1.90 eV) but smaller than those determined by UV-vis spectroscopy[27,28] (~2.0 and 2.55 eV) for the

same polymer prepared using other experimental conditions. On the other hand, the ε_g values reported for PClTh are 1.58 eV (UV-vis spectroscopy),[25] ~1.8 eV (spectroelectrochemistry)[20,22] and 2.14 eV (UV-vis spectroscopy).[21] Finally, it should be mentioned that reduced PBrTh presents a Bordeaux red colour (λ^{max} = 420 nm) similar to that reported for reduced PClTh (λ^{max} = 450 nm).[25]

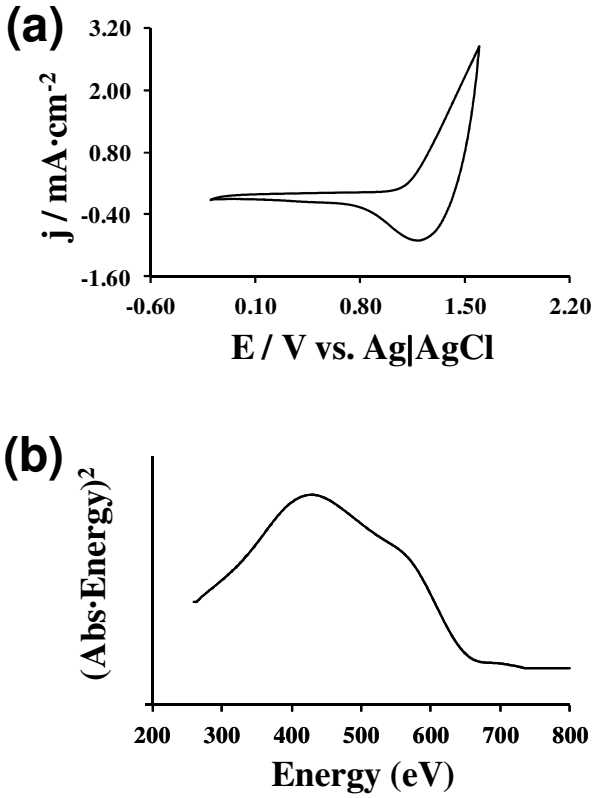

Figure 3. *(a) Control voltammogram for PBrTh film prepared by CA at 1.70 V in BFEE with 0.1 M $(Bu)_4NBF_4$ using a polymerization time of 150 s. Initial and final potentials: -0.20 V; reversal potential: 1.60 V. Scan rate: 100 mV·s^{-1}. (b) Absorbance squared versus the photon energy (hυ) extrapolated to zero absorption of PBrTh prepared by CA at 1.70 V in BFEE with 0.1 M $(Bu)_4NBF_4$.*

Conformational analysis: Influence of the halogen on the molecular conformation. Calculations on dimers of 3-halidethiophene were carried out considering three isomeric derivatives, which differ in the relative position of the substituents (Scheme 2). These isomers, which have been labeled as 2-XTh(4,4'), 2-XTh(3,3') and 2-XTh(3,4') (with X=F, Cl and Br), must be considered as model compounds of the tail-to-tail, head-to-head and head-to-tail polymer linkages, respectively.

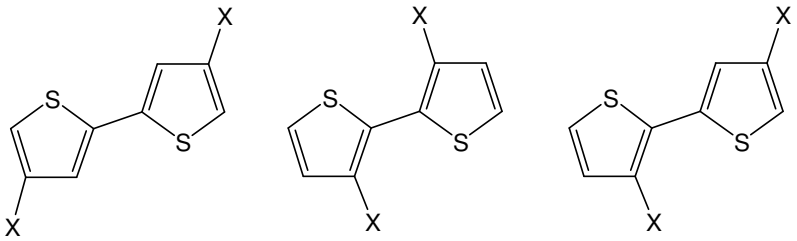

Scheme 2

Figure 4 represents the energy profiles of the three series of dimers calculated at the B3LYP/6-31+G(d,p) level, which are relative to the most stable conformation of each series (*i.e.* the global minimum of the most favored of the three isomers involving the same halogen atom).

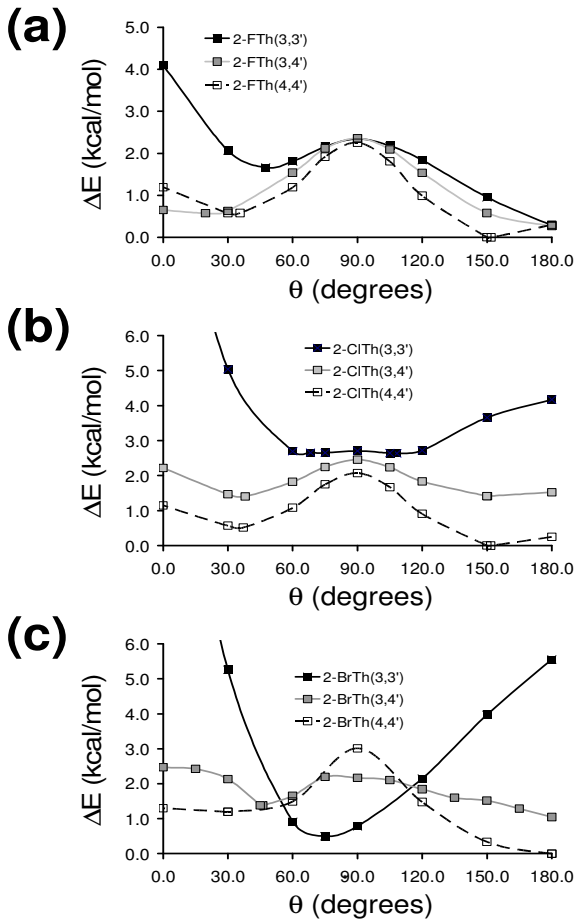

Figure 4. *Potential energy curves for the internal rotation of dimers formed by two 3-halidethiophene units (see Scheme 2) against the inter-ring dihedral angle (θ) using B3LYP/6-31+G(d,p) optimizations: (a) 2-FTh(3,3'), 2-FTh(3,4') and 2-FTh(4,4'); (b) 2-ClTh(3,3'), 2-ClTh(3,4') and 2-ClTh(4,4'); and (c) 2-BrTh(3,3'), 2-BrTh(3,4') and 2-BrTh(4,4'). Energies are relative to the global minimum of (a) 2-FTh(4,4'), (b) 2-ClTh(4,4') and (c) 2-BrTh(4,4').*

Figure 5 provides a schematic representation of the most characteristic conformations of the systems under study. Even though the isomer with the substituents attached at the 4,4'-positions was the most favored in all cases, results reflect a significant dependence on the halogen atom.

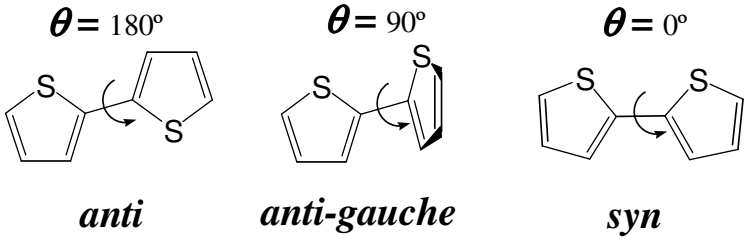

Figure 5. *Schematic representation of the most important conformations found for thiophene derivatives. The inter-ring dihedral angle, θ, is provided is each case.*

Table 3. *Energies (in kcal/mol) and inter-ring dihedral angles (θ) for the minimum energy conformations (plain numbers) of the 2-XTh dimers under study. The barriers (in kcal/mol) are also indicated (italic numbers).*

	***syn* (θ= 0º)**	***syn-gauche***	***gauche-gauche*** (θ= 90º)	***anti-gauche***	***anti*** (θ= 180º)
2-FTh(3,3')[a]	*4.1*	1.7 (θ = 47.5º)	*2.3*	-	0.3
2-FTh(3,4')[a]	*0.6*	0.6 (θ = 19.6º)	*2.4*	-	0.3
2-FTh(4,4')[a]	*1.2*	0.6 (θ = 35.7º)	*2.3*	0.0 (θ 152.0º)	0.3
2-ClTh(3,3')[b]	*12.0*	2.7 (θ = 68.2º)	*2.7*	2.6 (θ 108.2º)	4.2
2-ClTh(3,4')[b]	*2.2*	1.4 (θ = 38.0º)	*2.4*	1.4 (θ 150.3º)	1.5
2-ClTh(4,4')[b]	*2.1*	0.5 (θ = 37.1º)	*2.1*	0.0 (θ 151.7º)	0.2
2-BrTh(3,3')[c]	*14.3*	0.5 (θ = 75.5º)	-	-	5.5
2-BrTh(3,4')[c]	*2.5*	1.4 (θ = 46.1º)	*2.2*	-	1.0
2-BrTh(4,4')[c]	*1.3*	1.2 (θ = 30.1º)	*3.0*	-	0.0

[a] Energies of the minima (plain numbers) and barriers (italic numbers) are relative to the global minimum (anti-gauche) of 2-FTh(4,4'). [b] Energies of the minima (plain numbers) and barriers (italic numbers) are relative to the global minimum (anti-gauche) of 2-ClTh(4,4'). [c] Energies of the minima (plain numbers) and barriers (italic numbers) are relative to the global minimum (anti) of 2-BrTh(4,4')

Differences among the different groups of isomers are detailed in Table 3 and can be summarized as follows: (i) the lowest energy conformation of both 2-FTh(4,4') and 2-ClTh(4,4') corresponds to the *anti-gauche* arrangement ($\theta \approx 152º$), whereas 2-BrTh(4,4') prefers the planar *anti* arrangement ($\theta = 180.0º$); (ii) the most favored conformation of 2-ClTh(3,3') and 2-BrTh(3,3') are relatively close to the conventional *gauche-gauche* arrangement ($\theta = 108.2º$ and 75.5º, respectively), whereas 2-FTh(3,3') shows a planar

conformation; (iii) all compounds show a *syn-gauche* local minimum (θ ranging from 19.6º to 75.5º), whose relative stability depends on the halogen atoms; and (iv) both the relative energy of the minima and the height of the barriers, especially the planar *syn*, are higher for the compounds with chloride and bromine substituents than for those with fluorine.

The inter-ring dihedral angles of both the global and local minima found for the different isomers of 2-XTh with X= F, Cl and Br were combined and used to construct starting geometries for trimers, hereafter denoted 3-XTh. The structures constructed for all these trimers, which are explicitly depicted in Scheme 3, were submitted to geometry optimizations at the B3LYP/6-31+G(d,p) level. It should be emphasized that trimers are expected to provide a more accurate representation of the homopolymers derived from 3-halidethiophene than dimers. Specifically, 3-XTh(3,3'-3,4') combines the characteristics of 2-XTh(3,3') and 2-XTh(3,4'), defining the linkage between the head-to-head and head-to-tail units. The same procedure has been used to construct 3-XTh(3,3'-4,4'), 3-XTh(3,4'-3,4') and 3-XTh(4,4'-3,4') (see Scheme 3), which involve head-to-head/tail-to-tail, head-to-tail/head-to-tail and tail-to-tail/head-to-tail linkages, respectively.

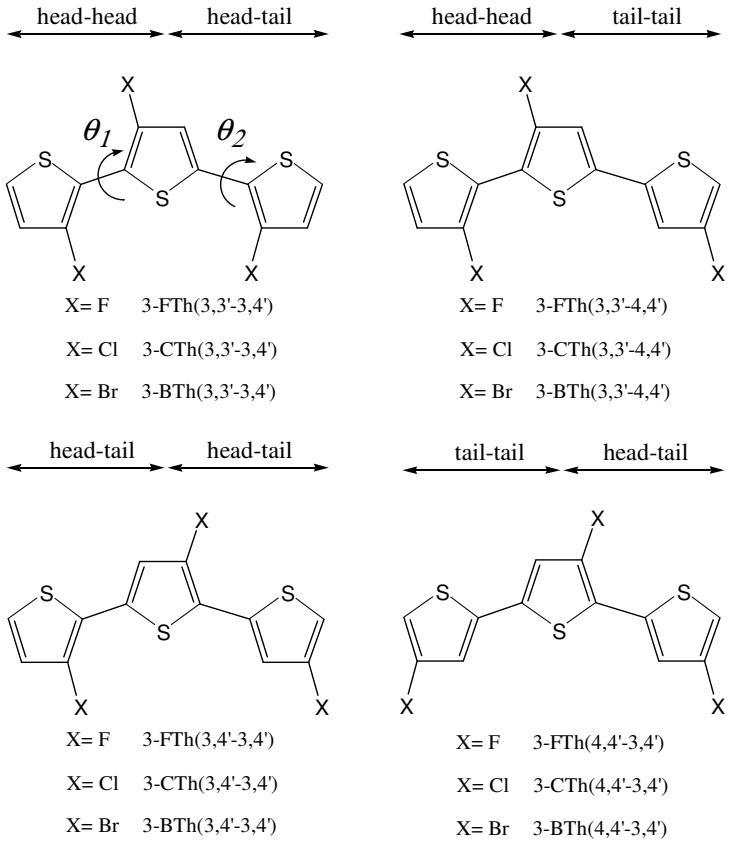

Scheme 3

A total of 22 minimum energy conformations separated by less than 2.3 kcal/mol were obtained for 3-FTh with the following distribution: 5, 6, 5 and 6 minima for 3-FTh(3,3'-3,4'), 3-FTh(3,3'-4,4'), 3-FTh(3,4'-3,4') and 3-FTh(4,4'-3,4'), respectively. The lowest energy conformation corresponds to the isomer 3-FTh(3,3'-4,4'), even though the number of minima with a relative energy lower than 1 kcal/mol amounts to 12. Figure 6 plots the position of the different minima in the θ_1-θ_2 map, where θ_1 and θ_2 refer to the two inter-ring dihedral angles, their relative energies being expressed through the size of the symbols. As it can be seen, 3-FTh is a very flexible compound independently of the kind of linkages between the units. Furthermore, analysis of the inter-ring dihedral angles obtained for the four isomers indicates that they are slightly more planar than those typically observed for unsubstituted thiophene-containing oligomers. Thus, the dihedral angles predicted for the *anti-gauche* and *syn*-gauche conformations unsubstituted thiophene oligomers were 147.9º and 42.2º,[53,54] respectively, whereas the average values found for 3-FTh are 174.1º±14.4º and 23.5º±12.7º, independently of the position of the ring (*i.e.* considering both θ_1 and θ_2 in the average).

Geometry optimizations on 3-ClTh led to 24 minima within a relative energy interval of 2.9 kcal/mol. Inspection of the θ_1-θ_2 map (Figure 6) reveals significant differences with respect to 3-FTh. Thus, the conformations obtained for the 2-ClTh(4,4'-3,4') isomers were the only with relative energies lower than 1.0 kcal/mol, indicating that steric interactions induced by the halogen substituents play an important role. Furthermore, the inter-ring dihedral angles found for the different isomers of 3-ClTh are, in general, closer to the *anti-gauche* and *syn-gauche* of the unsubstituted thiophene derivative (*i.e.* average values for 3-ClTh: 163.1º±27.9º and 41.3º±13.9º, independently of the position of the ring) than those of 3-FTh, even though standard deviations with respect to the average values are larger in the 3-ClTh than in 3-FTh. Regarding to 3-BrTh, two isomers, 3-BrTh(3,3'-4,4') and 3-BrTh(4,4'-3',4'), show minima within a relative energy interval of 1.0 kcal/mol. However, the most remarkable feature is the tendency of some minima to adopt a folded conformation close to the perpendicular one (Figure 6), even though the planar *anti* is also identified as minimum. These features are reflected by the averaged values of the dihedral angles for arrangements around the *anti* (176.2º±6.3º) and *syn-gauche* (47.7º±17.2º) conformations.

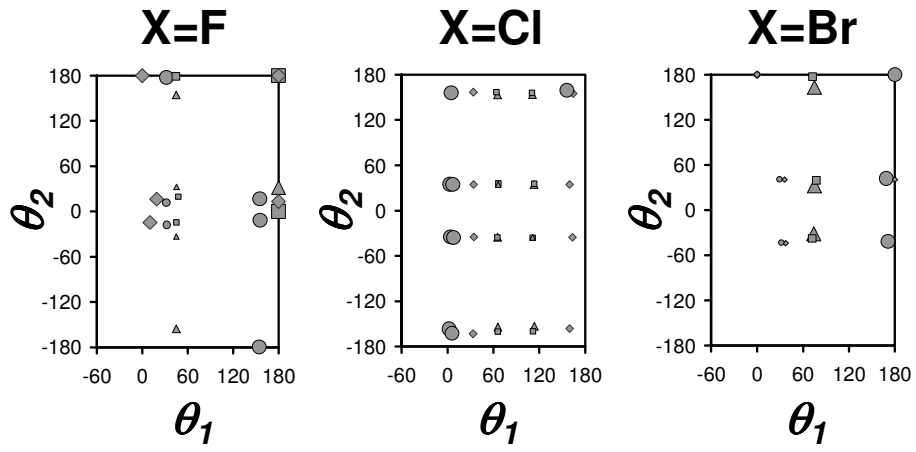

Figure 6. *θ_1-θ_2 maps (θ_1 and θ_2 refer to the inter-ring dihedral angles; in degrees), indicating the location of the minimum energy conformations found for 3-XTh(3,3'-3,4') (squares), 3-XTh(3,3'-4,4') (triangles), 3-XTh(3,4'-3,4') (diamonds) and 3-XTh(4,4'-3,4') (circles) where X= F, Cl and Br, as is indicated in Scheme 3. For each compound the minima of the four isomers has been categorized in three groups: (i) minima with relative energies lower than 1.0 kcal/mol (largest size symbols); (ii) minima with relative energies comprised between 1.0 and 2.0 kcal/mol (medium size symbols); and (iii) minima with relative energies larger than 2.0 kcal/mol (smallest size symbols). For each compound, the relative energies have been computed with respect to the lowest energy minimum of the most stable isomer.*

Larger *n*-XTh (X = F, Cl and Br) oligomers, with *n* ranging from 5 to 16, were constructed using a repetitive sequence of head-to-tail linkages. It should be emphasized that consideration of a regular chemical structure, which in addition should be identical for the three families of oligomers, is essential to compare the influence of the different halogen atoms on the electronic properties of the polymers without interference of undesirable substitutional effects. Thus, a repetition of head-to-tail linkages has been found to be the most consistent with the results obtained for compounds with $n = 2$ and 3, independently of the halogen. Specifically, although the energies of 3-FTh(3,3'-4,4') and 3-FTh(3,4'-3,4') differ by less than 0.1 kcal/mol, the 2-FTh(3,4') isomer is clearly favored with respect to the 2-FTh(3,3') one. On the other hand, repetition of the most favored isomer of 3-ClTh, which is the 4,4'-3,4' one, produces a high concentration of tail-to-tail linkages that are the least favored, as was evidenced in Figure 4b. However, the next isomer in terms of relative energies corresponds to the 3-ClTh(3,4'-3,4'), which is formed by two adjacent head-to-tail linkages. Finally, the 3,4'-3,4' is the 3-BrTh isomer that upon repetition produces the lowest concentration of tail-to-tail linkages and maintains that inter-ring dihedral angles close to the *anti* conformation. It should be mentioned that the high stability of the head-to-tail sequence in large oligomers ($n > 3$)

was corroborated in previous theoretical studies involving other 3-substituted thiophene units.[13-16]

n-XTh (X = F, Cl and Br) oligomers with *n* = 5, 7, 9, 11, 13, 15 and 16 were constructed according to these principles and considering all the inter-ring dihedral angles initially arranged at 180.0º. These structures were used as starting points for complete geometry optimizations at the B3LYP/6-31+G(d,p) level. The optimized oligomers were employed for the analyses of the electronic properties of PFTh, PClTh and PBrTh, which will be discussed in next sections.

Prediction of the electronic properties. Figure 7 represents the linear variation of the IP, and EA against 1/*n* for *n*-XTh (X= F, Cl and Br) oligomers. Linear regression analyses, which are included in Figure 7, allowed extrapolation of the IP, EA values for infinite chains of PFTh, PClTh and PBrTh (Table 4).

As it can be seen, the IP values predicted for PClTh and PBrTh are practically identical (~ 5.2 eV) and are in excellent agreement with the electrochemical measures for PClTh and PBrTh prepared by CA using a fixed potential of 1.70 V (5.38 and 5.43 eV for PClTh[25] and PBrTh, respectively). On the other hand, the electronegative fluorine substituents induce a slight reduction (~ 0.2 eV) in the IP calculated for PFTh. DFT calculations predict an EA of ~ 3.3 eV for the three polymers.

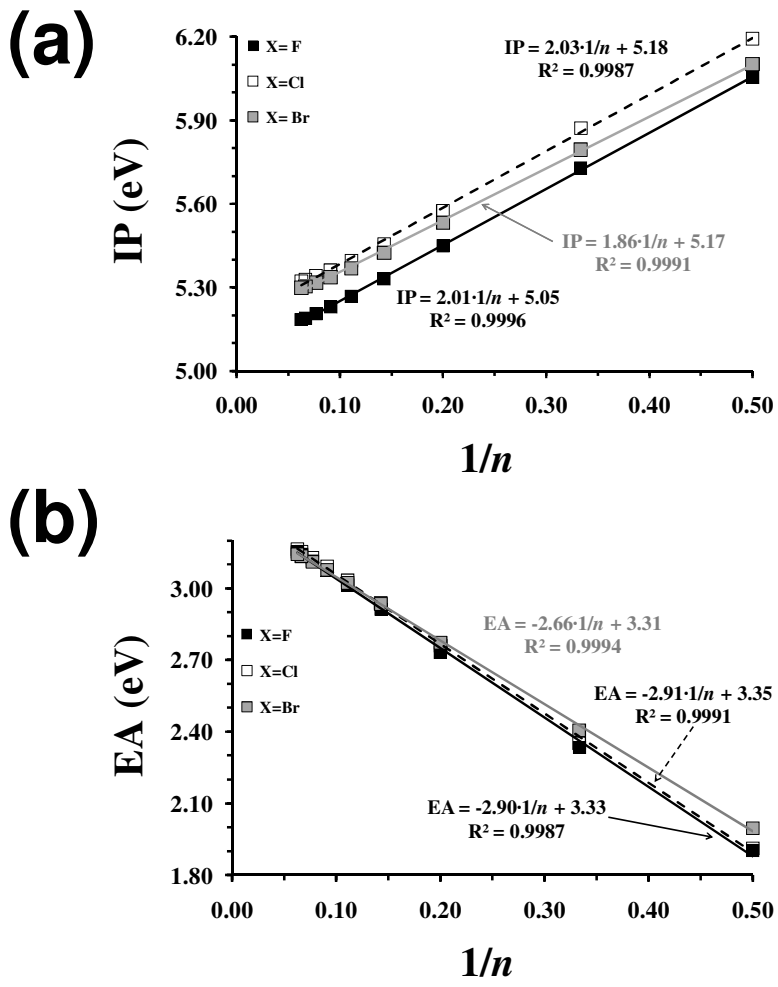

Figure 7. *Variation of the (a) IP and (b) EA against 1/n, where n is the number of repeat units in n-XTH oligomers with X = F, Cl and Br (data for X = Cl taken from ref. 25). The solid lines correspond to the linear regressions used to extrapolate these electronic properties towards infinite polymer systems.*

As was mentioned in the previous section, in this work the IPs and EAs have been estimated using the DFT extension of the Koopmans' theorem,[36] or more precisely of the Janak´s theorem.[37] However, this procedure may be affected by the so-called self-interaction (SI) error, which has been identified when some early DFT approaches are applied to some compounds.[62-65] The SI arises from the interaction of an electron with itself, and it is related to the Coulomb energy of the Kohn-Sham Hamiltonian, which is not totally cancelled by the exchange contribution. Previous studies reported that the DFT HOMO energy is too small with respect to experimental values, which was attributed to the SI. However, the good concordance between the calculated and the experimental IP values for the compounds studied in this work suggests that the SI error is small for this family of compounds, probably because of a fortuitous cancellation of errors.

The variation of the ε_g values calculated using DFT and TD-DFT calculations against $1/n$ for *n*-XTh (X = F, Cl and Br) oligomers are displayed in Figure 8, values extrapolated for infinite polymer chains being included in Table 4. As it can be seen, the DFT value is overestimated with respect to the TD-DFT one by 0.11, 0.16 and 0.18 eV for PFTh, PClTh and PBrTh, respectively. The relative order predicted by the two strategies for the ε_g is PFTh < PClTh ≈ PBrTh, even though the difference between the three CPs predicted by DFT and TD-DFT calculations is lower than 0.15 and 0.08 eV, respectively. This is consistent with the increase of the π-donor character of the halogen substituent in the order F > Cl ≈ Br.[66] The discrepancy between the ε_g determined experimentally using UV-vis spectroscopy and those predicted by DFT calculations is 0.25 and 0.07 eV for PClTh and PBrTh, respectively, the difference with respect to the TD-DFT values being 0.08 and 0.25 eV for PClTh and PBrTh, respectively. Interestingly, the UV-vis estimation for PClTh and PBrTh is closest to the DFT and TD-DFT value, respectively. In contrast, the ε_g values measured using spectroelectrochemical methods are in excellent agreement with the DFT predictions, the experimental/theoretical values obtained for PClTh and PBrTh being 1.74-1.80[20,22]/1.83 and 1.90[27]/1.86 eV, respectively. Considering that samples measured using UV-vis spectroscopy and spectroelectrochemistry were prepared using very similar experimental conditions, the overall of these results suggests that the environment affects the ε_g values provided by UV-vis spectroscopy.

Table 4. *Ionization potential (IP), electron affinity (EA) and band gap (ε_g) reported in the literature and determined in this work for PFTh, PClTh and PBrTh.*

	IP (eV)	EA (eV)	ε_g (eV)	Ref.	Description
PFTh	5.05	3.33	1.72	This work	DFT calculations
	-	-	1.61	This work	TD-DFT calculations
PClTh	5.38[a]/5.29[b]	-	-	25	Electrochemical (CV)
	-	-	1.58	25	UV-vis spectroscopy
	-	-	1.74	20	Spectroelectrochemistry
	-	-	1.80	21	Spectroelectrochemistry
	-	-	2.14	22	UV-vis spectroscopy
	5.18	3.35	1.83	This work	DFT calculations
	-	-	1.67	This work	TD-DFT calculations
PBrTh	5.43[a]/5.62[b]	-	-	This work	Electrochemical (CV)
	-	-	1.93[a]/1.97[b]	This work	UV-vis spectroscopy
	-	-	1.90	26	Spectroelectrochemistry
	-	-	2.55	27	UV-vis spectroscopy
	-	-	~2.0[c]	28	UV-vis spectroscopy
	5.17	3.31	1.86	This work	DFT calculations
	-	-	1.68	This work	TD-DFT calculations

[a] Samples prepared by potentiostatic methods (CA). [b] Samples prepared by potentiodynamic methods (CV). [c] Extrapolated from $E_g = (1240/\lambda^{onset})$.

On the other hand, the ε_g predicted for PClTh and PBrTh are significantly smaller than those calculated for PThs with electron-withdrawing π-acceptor carboxylic acid groups in the 3-position of the thiophene ring using a similar DFT level, *e.g.* poly(3-thiophene-3-yl acrylic acid methyl ester) (2.28 eV),[13] poly(3-thiophene-3-yl acrylic acid) (2.12 eV),[14] poly(2-thiophene-3-yl-malonic acid dimethyl ester) (2.38 eV),[15] and poly(2-thiophen-3-yl-malonic acid) (2.39 eV).[16] This should be attributed to the size of the bulky carboxylic acid groups that produce drastic geometrical distortions, leading to a detriment of the optical properties.

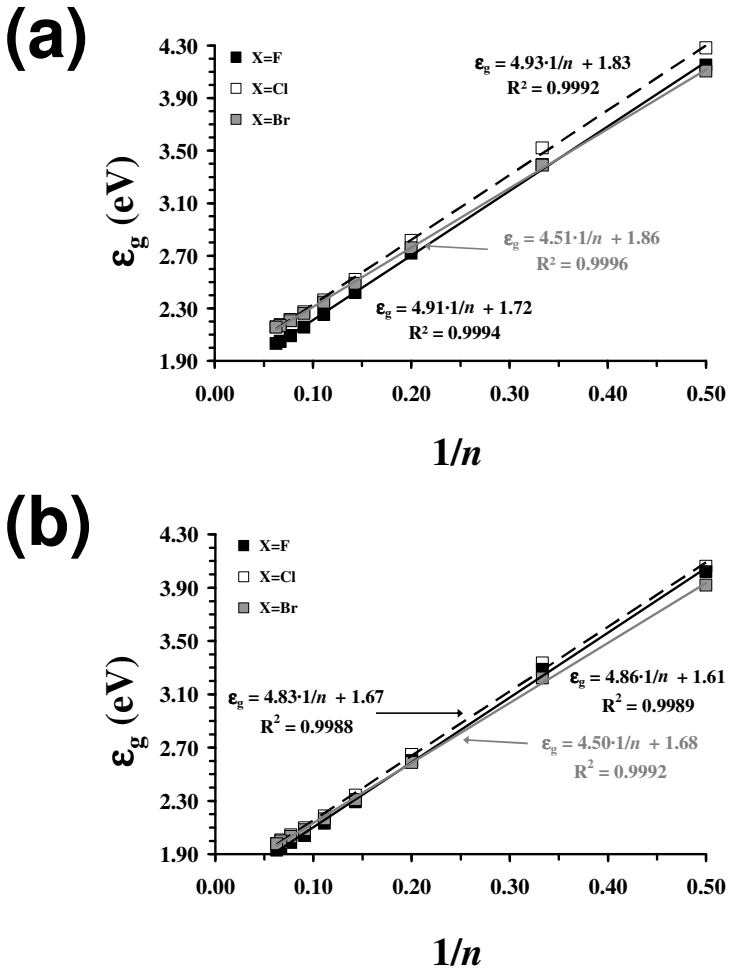

Figure 8. *Variation of the ε_g derived from (a) DFT and (b) TD-DFT calculations against 1/n, where n is the number of repeat units in n-XTh oligomers with X = F, Cl and Br (data for X = Cl taken from reference 25). The solid lines correspond to the linear regressions used to extrapolate these electronic properties towards infinite polymer systems.*

S-H interactions and effect of aromaticity in conformational equilibria. Early studies on the 3,4-ethylenedioxythiophene dimer, denoted 2-EDOT (Scheme 4), showed that in the crystallographic structure the non-bonded distances between the sulfur and oxygen atoms belonging to different units (2.92 Å) are shorter than the sum of the van der Waals radii of sulfur and oxygen (3.25 Å).[67,68] This feature was also observed in the X-ray structure of the tricyclic system based on thieno[3,4-*c*]-pyrazine.[69] These short distances led to postulate the existence of strong S···O intramolecular non-covalent interactions (dashed lines in Scheme 4), which promote the fully planar *anti* conformation in the π-conjugated structure. This phenomenon was denoted *self-rigidification* and was assumed to be responsible, in addition to the electron donor effect, for the optimization of the (opto)electronic properties of various classes of molecular functional π-conjugated systems.[70,71] Nevertheless, this assumption was not in

agreement with results reported in a very recent quantum mechanical study, in which the weight of the different intramolecular interactions for the planarity (and by extension for the rigidification) observed in 2-EDOT and PEDOT was examined.[72] Specifically, the relative influence of electron-donating effects, π-conjugation, geometric restrictions induced by the fused dioxane ring and S···O non-covalent interactions were carefully examined by considering a wide number of 2-EDOT derivatives. Results evidenced that S···O interactions between sulfur and oxygen atoms belonging to neighboring units (dashed lines in Scheme 4) are slightly repulsive destabilizing the planar *anti* conformation,[72] in opposition to the assumption postulated on the basis of non-bonded distances. In contrast, the latter conformation was found to be favored by the π-conjugation produced by both geometric restrictions imposed by the cyclic substituent and the electron-donating effects provided by the oxygen atoms attached to positions three and four of each thiophene ring. Therefore, these factors produce gain in aromaticity and favorable electrostatic interactions when the planarity is reached, compensating the Pauli repulsions between the shared electron pairs of the sulfur and oxygen atoms.

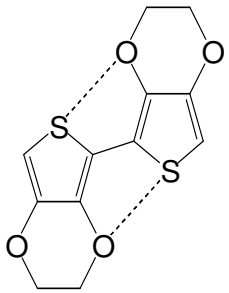

2-EDOT

Scheme 4

In a recent study, Roncali and co-workers proposed that the presence of a bromine atom at the 3-position of the thiophene ring leads to the development of non-covalent intramolecular S···Br interactions in BrTh-EDOT and poly(3-bromo-4-methoxythiophene).[73] Thus, these authors postulated that S···Br interactions contribute to strengthening the self-rigidification of these conjugated compounds. In addition, it has been reported that S···F interactions contribute to rigidify oligomers in which the thiophene ring is associated with 3,4-difluorothiophene[74,75] or fluorophenylene units.[74,76,77] The repulsive nature found for the S···O interactions, which were also previously postulated as attractive,[67,68] has motivated a detailed analysis of the S···X (where X= F, Cl and Br) interactions in 2-XTh. Aromaticity analyses have been carried

out on the 3-halidethiophene monomeric units and the 2-XTh(3,3') dimers. The minimum energy conformations listed in Table 3 were used for calculations on the dimers. For each compound the following aromaticity indices have been calculated for the thiophene rings: electronic based FLU and MCI, magnetic based NICS(0) and NICS(1) and geometric-based HOMA aromaticity descriptors.

The aromaticity parameters predicted for the three 3-halidethiophene units are compared in Table 5 with those calculated for the unsubstituted thiophene ring. Most of the aromaticity measures indicate that the substituents cause a slight decrease in the aromaticity of the thiophene ring. Thus, the aromaticity of the unsubstituted thiophene is slightly higher than that of the 3-halidethiophenes. Table 5 also lists the aromaticity parameters obtained for the minimum energy conformations of the 2-XTh(3,3') series of dimers, as well as the unsubstituted bithiophene (2-Th). The values indicate that the effect of introducing a substituent to 2-Th, or the replacement of F by Cl or Br is almost unnoticeable. Therefore, at difference with the previous series of 2-EDOT and PEDOT, in this case the preference for a given conformation is not determined by changes in aromaticity since it keeps almost constant for all substituents and conformations. As to assign an attractive or repulsive character to the S···X bond, the relative energies in Table 3 may help in such purpose. First, it must be pointed out that the *anti* conformation of the 2-XTh(3,3') system presents two S···X interactions, whereas that of the 2-XTh(3,4') isomer presents one, and that of the 2-XTh(4,4') species does not present any S···X interaction. In all cases the (4,4') isomers are the most stable *anti* conformations, those with no S···X interaction, especially compared to (3,3') ones. On the other hand, the energy difference between (3,3') and (4,4') increases from F to Cl and to Br. If they would be attractive, the S···X interactions they should be stronger for Br and energy differences between (3,3') and (4,4') smaller or even in favor of the (3,3') isomer. Thus, energy values reveal that S···Br interactions are the most repulsive. Moreover, for the 2-XTh(3,3') isomer, the *anti* conformation is the most stable only for X = F. In this case the repulsive character of the S···F interaction is compensated by the favorable conjugation along the two thiophene rings in this planar conformer. This does not occur for X = Cl and Br due to the larger repulsive character of the S···X interactions. All these observations point out to the repulsive character of the S···X interactions for these systems (lone pair Pauli repulsion). Thus, not unexpectedly, the most stable isomers are in all cases the 2-XTh(4,4') either in the *anti* conformation (X = Br) or in the *anti-gauche* one (X = F and Cl).

Table 5. *Aromaticity parameters (see text) calculated for the minimum energy conformations of 2-XTh(3,3') with X = F, Cl and Br, as well as the corresponding monomeric units. For each compound the minimum energy conformations are identified by the inter-ring dihedral angle (θ).*[a,b]

	FLU	MCI	NICS(0)	NICS(1)	HOMA
2-Th (θ = 155.9º)	0.0088	0.0346	-10.8	-8.5	0.727
2-Th (θ = 32.6º)	0.0061	0.0355	-11.2	-8.8	0.730
unsubstituted thiophene	0.0079	0.0415	-12.7	-10.1	0.870
2-FTh(3,3') (θ = 180.0º)	0.0078	0.0315	-12.9	-8.3	0.741
2-FTh(3,3') (θ = 47.5º)	0.0087	0.0310	-12.9	-8.6	0.732
3-fluorothiophene	0.0086	0.0367	-13.9	-9.4	0.752
2-ClTh(3,3') (θ =108.2º)	0.0079	0.0365	-11.9	-8.5	0.729
2-ClTh(3,3') (θ = 68.2º)	0.0080	0.0353	-11.9	-8.4	0.722
3-chlorothiophene	0.0081	0.0398	-13.0	-9.5	0.743
2-BrTh(3,3') (θ =180.0º)	0.0076	0.0338	-11.6	-8.5	0.695
2-BrTh(3,3') (θ =75.5º)	0.0079	0.0363	-11.5	-8.6	0.726
3-bromothiophene	0.0082	0.0405	-12.6	-9.5	0.743

[a] *MCI in atomic units, NICS in ppm.* [b] *For comparison, the values for benzene: FLU=0.0001, MCI=0.0732, NICS(0)=-8.2, NICS(1)=-10.2 and HOMA=0.972; and for bi-phenylene: 6-membered-ring: FLU=0.0055, MCI=0.0567, NICS(0)=-2.7, NICS(1)=-4.7 and HOMA=0.827, 4-membered-ring: FLU=0.0470, MCI=0.0210, NICS(0)=20.5, NICS(1)=10.0 and HOMA=-1.074.*

7.2.4. Conclusions

The doping level and electrical conductivity of PBrTh and PClTh films prepared using identical conditions have been found to be very similar. In spite of this, the electrochemical stability of PBrTh is significantly smaller than that of PClTh, which has been attributed to the lower porosity of the former with respect to the latter. Thus, the access and escape of dopant ions in oxidation and reduction processes, respectively, are easier in the material with the most porous structure than in that with the most compact one.

Quantum mechanical calculations indicate that the halogen atom has a significant impact on the conformational preferences of 2-XTh and 3-XTh oligomers. Thus, the conformational freedom of oligomers with X = Br is restricted by strong steric repulsive interactions, especially when repeating units are associated by head-to-head linkages, while oligomers with X = F show a significant conformational flexibility. Compounds with X = Cl present an intermediate behavior. The ε_g order predicted for poly(3-halidethiophene)s by DFT calculations is: PFTh < PClTh ≤ PBrTh. For the latter two polymers, this relative order is fully consistent with the ε_g values determined in this work using UV-vis spectroscopy and spectroelectrochemistry. On the other hand, the IPs estimated by CV are in very good agreement with theoretical predictions.

The aromaticity slightly varies from unsubstituted 2-Th to 2-XTh(3,3'), independently of the halogen atom. Moreover, within each series the effect of the halogen atom is very small. The repulsive character of the S···X interaction explains the higher stability of 2-XTh(4,4') isomer compared to 2-XTh(3,3') in the *anti* conformation. Finally, at variance with previously analyzed 2-EDOT and PEDOT systems, in this case aromaticity and favorable conjugation along the two thiophene rings in planar conformers do not play a key role in determining the conformational preferences.

7.2.5. References

[1]. Wallace, G. G.; Spinks, G. M.; Kane-Maguire, L. A. P.; Teasdale, P. R. in "Conductive Electroactive Polymers", CRC Press, Boca Raton, 2009.

[2]. Freund, M. S.; Deore, B. in "Self-Doped Conducting Polymers", John Wiley & Sons Ltd, West Sussex, England, 2007.

[3]. Skotheim, T. A.; Reynolds, J. R. in "Conjugated Polymers", CRC Press, Boca Raton, 2007.

[4]. Roncali, J. *Chem. Rev.* **1992**, *92*, 711.

[5]. Roncali, J. *Chem. Rev.* **1997**, *97*, 173.

[6]. Groenendaal, L.; Jonas, F.; Freitag, V.; Pielartzik, H.; Reynolds, J. R. *Adv. Mater.* **2000**, *12*, 481.

[7]. Aradilla, D.; Estrany, F.; Alemán, C. *J. Phys. Chem. C* **2011**, *115*, 8430.

[8]. Granstrom, M. *Polym. Adv. Technol.* **1997**, *8*, 424.

[9]. Perepichka, I. F.; Perepichka, D. F.; Meng, H.; Wudl, F. *Adv. Mater.* **2005**, *17*, 2281.

[10]. Fabregat, G.; Córdova-Mateo, E.; Armelin, E. A.; Bertran, O.; Alemán, C. *J. Phys. Chem. C* **2011**, *115*, 14933.

[11]. Martí, M.; Fabregat, G.; Estrany, F.; Alemán, C.; Armelin, E.*J. Mater. Chem.* **2010**, *20*, 10652.

[12]. Leclerc, M.; Faïd, F. *Adv. Mater.* **1997**, *9*, 1087.

[13]. Bertran, O.; Pfeiffer, P.; Torras, J.; Armelin, E.; Estrany, F.; Alemán, C. *Polymer* **2007**, *48*, 6955.

[14]. Bertran, O.; Armelin, E.; Torras, J.; Estrany, F.; Codina, M.; Alemán, C. *Polymer* **2008**, *49*, 1972.

[15]. Armelin, E.; Bertran, O.; Estrany, F.; Salvatella, R.; Alemán, C. *Eur. Polym. J.* **2009**, *45*, 2211.

[16]. Bertran, O.; Armelin, E. A.; Estrany, F.; Gomes, A.; Torras, J.; Alemán, C. *J. Phys. Chem. B* **2010**, *114*, 6281.

[17]. Armelin, E.; Gomes, A. L.; Pérez-Madrigal, M. M.; Puiggalí, J.; Franco, L.; Del Valle, L. J.; Rodríguez-Galán, A.; de Campos, J. S.; Ferrer-Anglada, N.; Alemán, C. *J. Mat. Chem.* **2012**, *22*, 585.

[18]. Gomes, A. L.; Casanovas, J.; Bertran, O.; de Campos, J. S.; Armelin, E.; Alemán, C. *J. Polym. Res.* **2011**, *18*, 1509.

[19]. Xu, J.;Shi, G.; Chen, F.; Wang, F.; Zhang, J.; Hong, X. *J. Appl. Polym. Sci.* **2003**, *87*, 502.

[20]. Pang, Y.; Xu, H.; Li, X.; Ding, H.; Cheng, Y.; Shi, G.; Jin, L. *Electrochem. Commun.* **2006**, *8*, 1757.

[21]. Alakhras, F.; Holze, R. *J. Solid State Electrochem.* **2008**, *12*, 81.

[22]. Pang, Y.; Li, X.; Shi, G.; Jin, L. *Thin Solid Films* **2008**, *516*, 6512.

[23]. Shi, G.; Xu, J.; Fu, M. *J. Phys. Chem.***2002**, *106*. 288.

[24]. Xu, J.; Shi, G.; Xu, Z.; Chen, F.; Hong, X. *J. Electrochem. Chem.* **2001**, *514*, 16.

[25]. Aradilla, D.; Casanovas, J.; Estrany, F.; Iribarren, J. I.; Alemán, C. *Polym. Chem.* **2012**, *3*, 436.

[26]. Alkan, S.; Cutler, C. A.; Reynolds, J. R. *Adv. Funct. Mater.* **2003**, *13*, 331.

[27]. He, X.; Zeng, L.-P.; Xing, S.-J.; Xian, Y.-Z.; Shi, G.-Y.; Jin, L.-T. *Chin. J. Chem.* **2008**, *26*, 1991.

[28]. Zhou, L.; Xue, G. *Synth. Met.* **1997**, *87*, 193.

[29]. El Kassmi, A.; Fache, F.; Lemaire, M. *J. Electroanal. Chem.* **1994**, *373*, 241.

[30]. Carrasco, E. B.; Fernández, V.; Cabot, P.L.; Garrido, J. A.; Centellas, F.; Rodriguez, R.M. *J. Electrochem. Soc.* **2001**, *148,* E19.

[31]. Seguy, I.; Solinat, P.; Destruel, P.; Farence, J.; Many, R.; Buck, H.; Ip, J.; Nguyen, T. P. *J. Appl. Phys.* **2001**, *89*, 5442.

[32]. Gaussian 03, Revision B.02, Frisch, M. J.; Trucks, G. W.; Schlegel, H. B.; Scuseria, G. E.; Robb, M. A.; Cheeseman, J. R.; Montgomery, J. A.; Vreven, Jr., T.; Kudin, K. N.; Burant, J. C.; Millam, J. M.; Iyengar, S. S.; Tomasi, J.; Barone, V.; Mennucci, B.; Cossi, M.; Scalmani, G.; Rega, N.; Petersson, G. A.; Nakatsuji, H.; Hada, M.; Ehara, M.; Toyota, K.; Fukuda, R.; Hasegawa, J.; Ishida, M.; Nakajima, T.; Honda, Y.; Kitao, O.; Nakai, H.; Klene, M.; Li, X.; Knox, J. E.; Hratchian, H. P.; Cross, J. B.; Adamo, C.; Jaramillo, J.; Gomperts, R.; Stratmann, R. E.; Yazyev, O.; Austin, A. J.; Cammi, R.; Pomelli, C.; Ochterski, J. W.; Ayala, P. Y.; Morokuma, K.; Voth, G. A.; Salvador, P.; Dannenberg, J. J.; Zakrzewski, V. G.; Dapprich, S.; Daniels, A. D.; C. Strain, M.; Farkas, O.; Malick, D. K.; Rabuck, A. D.; Raghavachari, K.; Foresman, J. B.; Ortiz, J. V.; Cui, Q.; Baboul, A. G.; Clifford, S.; Cioslowski, J.; Stefanov, B. B.; Liu, G.; Liashenko, A.; Piskorz, P.; Komaromi, I.; Martin, R. L.; Fox, D. J.; Keith, T.; Al-Laham, M. A.; Peng, C. Y.; Nanayakkara, A.; Challacombe, M.; Gill, P. M. W.; Johnson, B.; Chen, W.; Wong, M. W.; Gonzalez, C.; Pople, J. A. Gaussian, Inc., Pittsburgh PA, 2003.

[33]. Becke, A. D. *J. Chem. Phys.* **1993**, *98*, 5648.

[34]. Lee, C.; Yang, W.; Parr, R. G. *Phys. Rev. B* **1988**, *37*, 785.

[35]. Frisch, M. J.; Pople, J. A.; Binkley, J. S. *J. Chem.Phys.* **1984**, *80*, 3265.

[36]. Koopmans, T. *Physica* **1934**, *1*, 104.

[37]. Janak, J. F. *Phys. Rev. B* **1978**, *18*, 7165.

[38]. Pino, R.; Scuseria, G. E. *J. Chem. Phys.* **2004**, *121*, 8113.

[39]. Cao, H.; Ma, J.; Zhang, G.; Jiang, Y. *Macromolecules* **2005**, *38*, 1123.

[40]. Kertesz, M.; Choi, C. H.; Yang, S. *Chem. Rev.* **2005**, *105*, 3448.

[41]. Zade, S. S.; Bendikov, M. *Org. Lett.* **2006**, *8*, 5243.

[42]. Jacquemin, D.; Preat, J.; Perpète, E.; Adamo, C. *Int. J. Quantum Chem.* **2010**, *110*, 2121.

[43]. Preat, J. ; Jacquemin, D. ; Perpète, E. *Int. J. Quantum Chem.* **2010**, *110*, 2147.

[44]. Adamo, C. ; Barone, V. *J. Chem. Phys.* **1999**, *110*, 6158.

[45]. Schleyer, P. v. R.; Jiao, H. *Pure Appl. Chem.* **1996**, *68*, 209.

[46]. Schleyer, P. v. R.; Maerker, C.; Dransfeld, A.; Jiao, H.; van Eikema Hommes, N. J. R. *J. Am. Chem. Soc.* **1996**, *118*, 6317.

[47]. Wolinski, K.; Hilton, J. F.; Pulay, P. *J. Am. Chem. Soc.* **1990**, *112*, 8251.

[48]. Fallah-Bagher-Shaidaei, H.; Wannere, C. S.; Corminboeuf, C.; Puchta, R.; Schleyer, P. v. R. *Org. Lett.* **2006**, *8*, 863.

[49]. Schleyer, P. v. R.; Manoharan, M.; Wang, Z.; Kiran, X. B.; Jiao, H.; Puchta, R.; Hommes, N. J. *Org. Lett.* **2001**, *3*, 2465.

[50]. Bultinck, P.; Ponec, R.; Van Damme, S. *J. Phys. Org. Chem.***2005**, *18*, 706.

[51]. Bultinck, P.; Rafat, M.; Ponec, R,; van Gheluwe, B.; Carbó-Dorca, R.; Popelier, P. *J. Phys. Chem. A* **2006**, *110*, 7642.

[52]. Giambiagi, M; de Giambiagi, M. S.; dos Santos, C. D.; de Figueiredo, A. P. *Phys. Chem. Chem. Phys.* **2000**, *2*, 3381.

[53]. Cioslowski, J; Matito, E; Solà, M. *J. Phys. Chem. A* **2007**, *111*, 6521.

[54]. Matito, E.; Duran, M.; Solà, M. *J. Chem. Phys.* **2005**, *122*, 014109.

[55]. Biegler-König, F. W.; Bader, R. F. W.; Tang, T.-H. *J. Comput. Chem.***1982**, *3*, 317.

[56]. http://www.chemistry.mcmaster.ca/aimpac/

[57]. Matito, E.; ESI-3D: Electron Sharing Indexes Program for 3D Molecular Space Partitioning. http://iqc.udg.es/~eduard/ESI, Institute of Computational Chemistry: Girona, 2006.

[58]. Krygowski, T. M. *J. Chem. Inf. Comput. Sci.* **1993**, *33*, 70.

[59]. Brédas, J. L.; Silbey, R.; Boudreaux, D. S.; Chance, R. R. *J. Am. Chem. Soc.* **1983**, *105*, 6555.

[60]. Alemán, C.; Juliá. L. *J. Phys. Chem.* **1996**, *100*, 1524.

[61]. Alemán, C.; Domingo, V. M.; Fajarí, Ll.; Juliá, L.; Karpfen, A. *J. Org. Chem.* **1998**, *63*, 1041.

[62]. Garza, J. ; Nichols, J. A. ; Dixon, D. A. *J. Phys. Chem. A* **2000**, *112*, 7880.

[63]. Patchkowski, S. ; Autschbach, J. ; Ziegler, T. *J. Chem. Phys.* **2001**, *115*, 26.

[64]. Patchkowski, S. ; Ziegler, T. *J. Phys. Chem. A* **2002**, *106*, 1088.

[65]. Proynov, E. ; Chermette, H. ; Salahub, D. R. *J. Chem. Phys.* **2000**, *113*, 10013.

[66]. Hansch, C. ; Leo, A. ; Taft, R. W. *Chem. Rev.* **1991**, *91*, 165.

[67]. Brédas, J. L. ; Silbey, R. ; Boudreaux, D. S. ; Chance, R. R. *J. Am. Chem. Soc.* **1983**, *105*, 6555.

[68]. Raimundo, J.-M. ; Blanchard, P. ; Frère, P. ; Mercier, N. ; Ledoux-Rak, I. ; Hierle, R. ; Roncali, J. *Tetrahedron Lett.* **2001**, *42*, 1507.

[69]. Akouda, S. ; Roncali, J. *Synth. Met.* **1998**, *93*, 114.

[70]. Roncali, J. ; Blanchard, P. ; Frère, P. *J. Mater. Chem.* **2005**, *15*, 1589.

[71]. Raimundo, J.-M. ; Blanchard, P. ; Gallego-Planas, N. ; Mercier, N. ; Ledoux-Rak, I. ; Hierle, R. ; Roncali, J. *J. Org. Chem.* **2002**, *67*, 205.

[72]. Poater, J.; Casanovas, J.; Solà, M.; Alemán, C. *J. Phys. Chem. A* **2010**, *114*, 1023.

[73]. Hergué, N.; Leriche, P.; Blanchard, P.; Allain, M.; Gallego-Planas, N.; Frère, P.; Roncali, J. *New J. Chem.* **2008**, *32*, 932.

[74]. Facchetti, A.; Yoon, M. H.; Stern, C. L.; Katz, H. E.; Marks, T. J. *Angew. Chem., Int. Ed.* **2003**, *42*, 3900.

[75]. Sakamoto, Y.; Komatsu, S.; Suzuki, T. *Synth. Met.* **2003**, *133*, 361.

[76]. Crouch, D. J.; Skabara, P. J.; Heeney, M.; McCulloch, I.; Coles, S. J.; Hursthouse, M. B. *Chem. Commun.* **2005**, 1465.

[77]. Crouch, D. J.; Skabara, P. J.; Lohr, J. E.; McDouall, J. J. W.; Heeney, M.; McCulloch, I.; Sparrowe, D.; Shkunov, M.; Coles, S. J.; Horton, P. N.; Hursthouse, M. B. *Chem. Mater* .**2005**, *17*, 6567.

Chapter 8. Photoelectronic properties in conducting polymers

8.1. Synergy of the I^-/I_3^- redox pair in the capacitive properties of nanometric poly(3,4-ethylenedioxythiophene).[a]

8.1.1. Introduction

8.1.2. Methods

8.1.3. Results and discussion

8.1.4. Conclusions

8.1.5. References

[a]Results presented in this chapter were published in *Org. Electron.* **2012**.

8.2. All conducting-polymer rechargeable batteries based on poly(3,4-ethylenedioxythiophene).[b]

8.2.1. Introduction

8.2.2. Methods

8.2.3. Results and discussion

8.2.4. Conclusions

8.2.5. References

[b]Results presented in this chapter were submitted.

8.3. New insight on the optoelectronic properties of nanocomposites based on poly(3,4-ethylenedioxythiophene)-montmorillonite films.

8.3.1. Introduction

8.3.2. Methods

8.3.3. Results and discussion

8.3.4. Conclusions

8.3.5. References

8.1. Synergy of the I^-/I_3^- redox pair in the capacitive properties of nanometric poly(3,4-ethylenedioxythiophene)

8.1.1. Introduction

Poly(3,4-ethylenedioxythiophene), hereafter abbreviated PEDOT, is not only the most important poly(thiophene) derivative but also one of the more important conducting polymers (CPs). PEDOT (Scheme 1) has been widely studied due to its impressive properties, such as high electrical conductivity (up to 500 $S \cdot cm^{-1}$), moderate band-gap, low oxidation potential and good thermal and environmental stability.[1,2] Consequently, PEDOT has been recently employed in different technological applications devoted to bioelectrochemistry (*e.g.* electrochemical biological sensors),[3-5] corrosion inhibitors,[6-8] and electronic and optoelectronic devices.[9,10] Among the latter, the characteristic electro-optical properties of PEDOT have allowed the design and construction of light-emitting diodes,[11] electrochromic and electroluminescent devices,[12,13] photovoltaic devices,[14] and dye-sensitized solar cells (DSSCs).[15] DSSCs are currently receiving particular attention since they are considered one type of photoelectric conversion devices, which present high theoretical conversion efficiency, and, in addition, they are obtained using a simple fabrication process at a relatively low cost. [16]

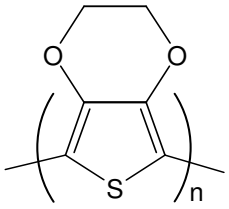

PEDOT

Scheme 1

The major drawback of PEDOT is the insolubility, which has been overcome by using polyelectrolytes, such as poly(styrene-sulfonate) (PSS), whose stability is improved by some of them (*e.g.* ionic liquid electrolytes).[17,18] Moreover, electrolytes containing a redox couple are a key component for DSSCs because they can fill the gap between the electrodes. Among these, electrolytes formed by the iodide (I^-)/tri-iodide (I_3^-) redox pair have been studied and successfully employed in DSSCs.[19] Thus, during

the last decade, systems based on PEDOT and I^-/I_3^- redox electrolytes have been widely used in DSSCs.[20-24] Within this conext, it should be mentioned that the effect of other dopant ions different from I^-/I_3^- in the construction of DSSCs based on PEDOT has been investigated,[25-29] results indicating that some of them also enhance the efficiency of DSSCs (*e.g* trifluoromethanesulfonylimide and perchlorate).[28,29] Moreover, nanocomposites from multi-walled carbon nanotubes,[30] TiO_2, ZnO/ZnS or CoS particles,[31-34] and graphene[35,36] have been also used to to improve the efficiency of DSSCs.

Recently, some investigations have been devoted to study the influence of electrochemical processes associated to the I^-/I_3^- redox pair in the properties and applications of CPs.[37-40] For example, PEDOT was used to fabricate an arsenite sensor in presence of KI.[40] Although the effect of I^-/I_3^- in solar cells based on PEDOT has been investigated previously,[20-23] to the best of our knowledge the influence of this redox pair on the capacitive properties of CPs has not been studied yet. Accordingly, this work has been focused on the evaluation of the capacitive properties of nanometric and micrometric PEDOT films in presence of I^-/I_3^- redox electrolyte. For this purpose, exhaustive electrochemical, morphological and topological studies have been carried out. Results allow us to state that ultracapacitor electrodes fabricated using nanometric PEDOT films show excellent capacitive properties in I^-/I_3^--containing solutions.

8.1.2. Methods

Materials. 3,4-ethylenedioxythiophene (EDOT) monomer, acetonitrile, potassium iodide (KI) and iodide (I_2) were purchased from Aldrich and used as received. Anhydrous $LiClO_4$, analytical reagent grade, from Aldrich was stored in an oven at 80 ºC before use in the electrochemical trials.

Synthesis. PEDOT films were obtained potentiostatically on stainless steel electrodes applying a previously determined optimal oxidation potential (1.40 V)[41] to the generation medium. An Autolab PGSTAT302N equipped with the ECD module to measure very low current densities (100 mA–100 pA) was used for the electrochemical experiments, including the anodic polymerizations. The polymerization charge (Q_{pol}) was controlled using the chronocoulometry technique (CC). The generation of PEDOT films was carried out using a standard three-electrode cell filled with 50 mL of a 0.01 M

monomer solution in acetonitrile containing 0.1 M $LiClO_4$ at room temperature. Steel AISI 316 sheets of 2×2 cm^2 area were employed as working and counter electrodes. The reference electrode was an Ag|AgCl electrode containing a KCl saturated aqueous solution (E° = 0.222 V at 25ºC), which was connected to the working compartment through a salt bridge containing the electrolyte solution. In order to avoid interferences during electrochemical analyses, the working and counter electrodes were cleaned with acetone and dried with an air flow before each trial. After electropolymerization, the coated electrodes were cleaned with acetonitrile and dried with nitrogen. In all cases, the solution was purged with nitrogen for 5 min. prior electrochemical synthesis.

Thickness. The thickness of the films (ℓ) was determined using both electrochemical and structural measurements. Electrochemical estimations of the thickness were obtained by determining the current productivity through the mass-charge ratio and the mass of polymer deposited in the electrode at nanometric[42] and micrometric[41] levels. The thickness was also determined by measuring the cross-section of the films by scanning electron microscopy (SEM).

Electrochemistry. The electroactivity, which refers to the charge storage ability, and electrochemical stability (electrostability) were determined by cyclic voltammetry (CV) using an acetonitrile/distilled water (4% v/v) solution with 0.1 M $LiClO_4$, 10 mM KI and 1 mM I_2. The initial and final potentials were -0.20 V, while the reversal potential was 1.20 V. Specifically, the loss of electrostability (*LES*; in %) was determined as:

$$LES = \frac{\Delta Q}{Q_{II}} 100 \qquad (1)$$

where ΔQ is the difference of voltammetric charges (in C) between the second and the last cycle, and Q_{II} is the voltammetric charge corresponding to the second cycle. In this work, measures of *LES* refer to 250 consecutive oxidation-reduction cycles. A scan rate of 20 $mV \cdot s^{-1}$ was used in all cases.

Electrochemical estimation of the doping level (*f*) was carried using the following equation:

$$f = \frac{2Q_o}{Q_d - Q_o} 100 \qquad (2)$$

where Q_D is the total charge used for PEDOT deposition and Q_0 is the total charge of oxidized species in the PEDOT films. The doping level was estimated using an

acetonitrile solution with 0.1 M $LiClO_4$. The initial and final potentials were -0.50 V, while the reversal potential was 1.60 V.

Galvanostatic charge/discharge curves were used to evaluate the specific capacitance (SC; in $F \cdot g^{-1}$) of PEDOT films according to:

$$SC = \frac{\int I \cdot \Delta t}{\Delta V \cdot m} \tag{3}$$

where I is the applied current (1 mA), Δt is the time of discharge (in s), ΔV is the difference between the potential at the beginning and at the end of the discharge (in V) and m is the mass of PEDOT (in g).

The energy density (E_d; in $W \cdot h \cdot kg^{-1}$) and power density (P_d; in $kW \cdot kg^{-1}$) at a constant current were determined using Eqns (3) and (4):

$$E_d = \frac{I \int \Delta V \cdot t}{m} \tag{4}$$

$$P_d = \frac{E_d}{t_d} \tag{5}$$

where t_d is the discharge time.

Electrochemical Impedance Spectroscopy (EIS). EIS measurements of micrometric and nanometric PEDOT films were performed in potentiostatic mode at the open circuit potential (OCP) using an AUTOLAB PGSTAT 30/FRA 2 system. The amplitude of the EIS perturbation signal was 50 mV, and the studied frequency ranged from 10 kHz to 10 mHz. All experiments were carried out in an acetonitrile/distilled water (4% v/v) solution with 0.1 M $LiClO_4$, 10 mM KI and 1 mM I_2.

Electrochemical properties of the I^-/I_3^- redox pair. The diffusion coefficient (D) of I^-/I_3^- species was calculated by CV using the Randles-Sevick equation:[43]

$$i_p = K \cdot n^{3/2} \cdot A \cdot D^{1/2} \cdot c \cdot v^{1/2} \tag{6}$$

where i_p is the peak current (in A), K is a constant which has a value of $2.69 \cdot 10^5$ (in $C \cdot mol^{-1} \cdot V^{-1/2}$), n is the number of electrons transferred in the redox process, A is the electrode area (in cm^2), D is the diffusion coefficient (in $cm^2 \cdot s^{-1}$), c is the concentration of the electroactive species (in $mol \cdot cm^{-3}$) and v is the scan rate (in $V \cdot s^{-1}$).

Some important electrochemical parameters for electroactive species, such as the electron transfer rate constant (k_p; in $cm \cdot s^{-1}$) and the charge transfer coefficient (β) were obtained from the Kochi and Klinger equation:

$$k_p = 2.18\left(\frac{\beta DnFv}{RT}\right)^{1/2} e^{\left[\frac{-\beta^2 nF}{RT}\left(E_p^a - E_p^c\right)\right]} \quad (7)$$

where F is the Faraday's constant (~96500 $C \cdot mol^{-1}$), R is the gas constant (8.314 $J \cdot K^{-1} \cdot mol^{-1}$), T is the thermodynamic temperature (in K), and E_p^a and E_p^c are the anodic and cathodic peak potentials (both in V), respectively. The element β corresponds to the slope of the straight line obtained by representing the variation of ln$v$ as a function of the potential separation ΔE, where $\Delta E = E_p^a - E_p^c$. On the other hand, the intercept of such plot with the y-axis allows to calculate the k element.

Morphological characterization. SEM micrographs were carried out using a Focussed Ion Beam Zeiss Neon 40 scanning electron microscope operating at 3kV. Topographic images were derived from tapping-mode atomic force microscopy (AFM) measurements using a Molecular Imaging PicoSPM using a NanoScope IV controller in ambient conditions. The tapping mode AFM was operated at constant deflections (*i.e.* vertical constant force with triangular shaped gold-coated silicon nitride). The row scanning frequency was set to 1 Hz and the physical tip-sample motion speed was 10 $\mu m \cdot s^{-1}$. The scan window size was 5×5 μm^2, a total of 65536 topographic data points being recorded for each image. Finally, optical microscopy observations were performed using an Olympus BX51 microscope.

Electrical conductivity and optical properties. The electrical conductivity (σ; $S \cdot cm^{-1}$) was determined by the two- and four-probes procedures.

Absorption spectra were obtained with a Shimadzu 3600 spectrophotometer equipped with a tungsten halogen visible source, a deuterium arc UV source, a photomultiplier tube UV-vis detector, and a InGaAs photodiode and cooled PbS photocell NIR detectors. Spectra were recorded in the absorbance mode using the integrating sphere accessory (model ISR-3100), the wavelength range being 300-800 nm. The interior of the integrating sphere is coated with a highly diffuse BaO reflectance standard. Single-scan spectra were obtained at a scan speed of 60 $nm \cdot min^{-1}$ with a bandwidth of 2 nm using the UVProbe 2.31 software. The optical ε_g was derived from the UV-vis spectra using a previously described procedure.[44]

8.1.3. Results and Discussion

Preparation of PEDOT films. Figure 1a shows the influence of the charge density on the thickness, ℓ, of PEDOT films. As it can be seen, charge densities lower than 225 $mC \cdot cm^{-2}$ (*i.e.* Q_{pol} values lower than 0.9 C) result in nanometric and sub-micrometric PEDOT films (*i.e.* those with $\ell < 1$ µm), higher charge densities being necessary to produce micrometric PEDOT films.

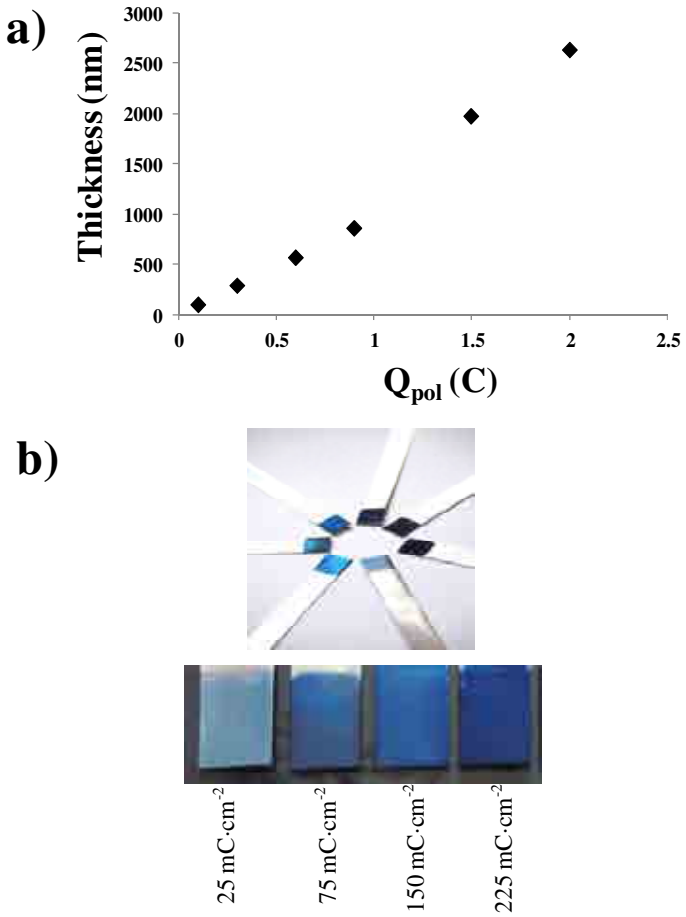

Figure 1. *(a) Variation of the thickness (ℓ) against the charge density for PEDOT films produced by chronocoulometry. (b) Digital camera images showing the influence of Q_{pol} on the color of PEDOT films prepared under a constant potential of 1.40 V.*

Potentiostatic synthesis of PEDOT films controlling the charge density through the chronocoulometry technique allowed to get information about the important relationship between the color of the films and the charge density. Thus, films produced using low charge densities exhibited a transparent blue color, this color changing gradually to deep blue when the charge density increased. This phenomenon, which is displayed in Figure 1b, has been ascribed to the thickness and roughness of the films.

Figure 2 displays optical and AFM images of nanometric films deposited using a charge density of 75 $mC \cdot cm^{-2}$. Images reveal the existence of small agglomerates (*i.e.* aggrupations of pronounced clusters) at the surface. On the other hand, the cross section of the same film, which was used to measure the thickness, is illustrated in Figure 2d. It should be mentioned that the agreement between the thickness determined by electrochemical and structural methods was excellent in all cases (*e.g.* 284 and 312 nm, respectively, for PEDOT films produced using 75 $mC \cdot cm^{-2}$).

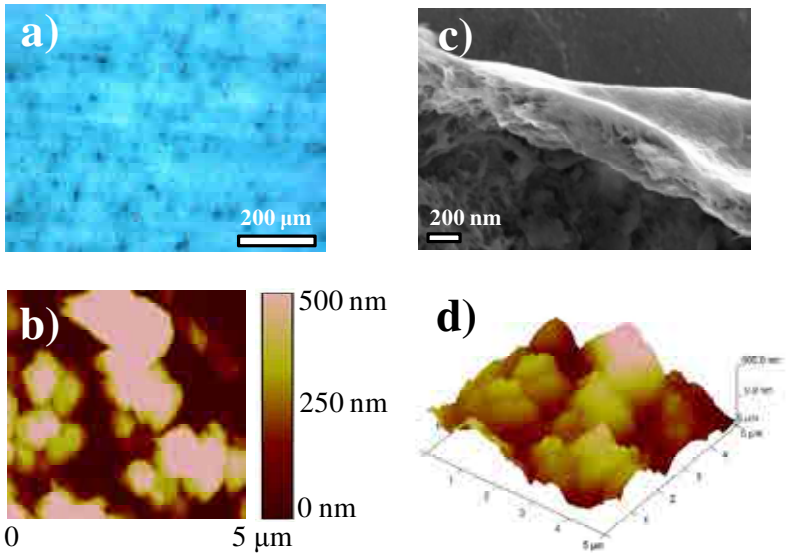

Figure 2. *Morphology of nanometric PEDOT films obtained using 75 $mC \cdot cm^{-2}$: (a) optical image; (b) and (c) 2D and 3D AFM images, respectively; and (d) cross-sectional scanning electron micrograph.*

Electrochemical and electrocatalytic activity of I^-/I_3^- *on PEDOT films.* Figure 3a shows the two anodic and cathodic peaks of nanometric PEDOT films (75 $mC \cdot cm^{-2}$). In the anodic scan, iodide is oxidized sequentially to triiodide (Eqn 8) and then to iodine (Eqn 9):[45]

$$3I^- \rightarrow I_3^- + 2e^- \qquad (8)$$

$$2I_3^- \rightarrow 3I_2 + 2e^- \qquad (9)$$

The linear relationship between both the anodic and cathodic peaks and the square root of the scan rate is shown in Figure 3b, indicating that the redox reactions of the I^-/I_3^- species are under diffusion control. The diffusion coefficient (D) for these electroactive species (Eqn 6) was estimated to be $1.39 \cdot 10^{-6}$ $cm^2 \cdot s^{-1}$, this value being

similar to that of PEDOT:PSS for DSSCs ($D = 5.12 \cdot 10^{-6}$ cm$^2 \cdot$s^{-1}).[34] Results reported in Figure 3a were used to evaluate the charge transfer coefficient and the rate constant (Eqn 7) of the I^-/I_3^- redox pair, which were 0.21 and $9.85 \cdot 10^{-4}$ cm$\cdot$s^{-1}, respectively. These values indicate that a relative fast charge transfer rate occurs on the interface of the PEDOT: ClO_4^-/electrolyte.

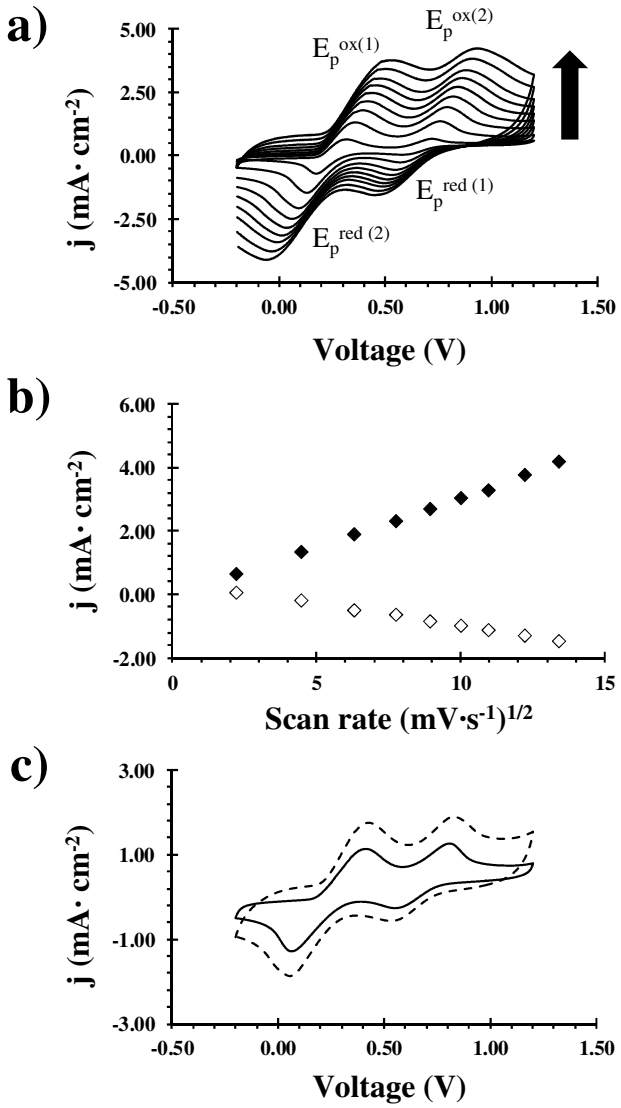

Figure 3. *(a) Cyclic voltammograms of nanometric PEDOT films in an acetonitrile/distilled water (4% v/v) solution containing 0.1 M $LiClO_4$, 10 mM KI and 1 mM I_2 at different scan rates (5, 20, 40, 60, 80, 100, 120, 150 and 180 mV·s^{-1}). The arrow indicates the increase of the scan rate. Initial and final potentials: -0.20 V. Reversal potential: 1.20 V. (b) Relationship between the anodic and cathodic peaks against the square root of the scan rate. (c) Control voltammogram of electrogenerated PEDOT films at 75 mC·cm^{-2} (nanometric thickness, solid line) and 375 mC·cm^{-2} (micrometric thickness, dashed line).*

Figure 3c displays the control voltammogram for micrometric and nanometric PEDOT films in an acetonitrile/distilled water (4% v/v) solution containing 0.1 M

$LiClO_4$, 10 mM KI and 1 mM I_2. The electrochemical behavior represented in Figure 3c highlights the importance of the thickness on PEDOT films, consequently, the micrometric film showing higher charge storage ability (electroactivity) and oxidation current density than the nanometric one. Table 1 illustrates the increase of the electroactivity when the thickness increases.

Table 1. *Electrochemical and structural parameters for micrometric and nanometric PEDOT films in an acetonitrile/(distilled) water solution (4% v/v) containing 0.1 M $LiClO_4$, 10 mM KI and 1 mM I_2.*

Q_{pol} [(a)] ($mC \cdot cm^{-2}$)	Q^{ox} [(b)] ($mC \cdot cm^{-2}$)	Q^{red} [(c)] ($mC \cdot cm^{-2}$)	Q^{tot} [(d)] ($mC \cdot cm^{-2}$)	ℓ [(e)] (nm)	Porosity[(f)] (Δ in %)
25	51.0	24.0	75.0	95	-
75	51.9	24.6	76.5	284	41
150	67.3	30.8	98.1	567	-
225	72.7	33.3	106.0	851	-
375	82.1	42.8	125.0	1976	-
500	85.8	47.2	133.0	2636	52

[(a)] Polymerization charge. [(b)] Oxidation charge. [(c)] Reduction charge. [(d)] Total charge, which is defined as the sum of the oxidation and reduction charges. [(e)] Thickness. [(f)] Porosity values were obtained from the Eqn 9.

Influence of the I^-/I_3^- ***redox pair on the thickness.*** Thickness plays an important role in the electrochemical properties of CPs since it is intimately related with the superficial morphology (morphology will be discussed in the next subsection). Figures 4a and 4b, which compares the evolution of the control voltammograms during 250 consecutive oxidation-reduction cycles for nanometric (prepared using a charge density of 75 $mC \cdot cm^{-2}$) and micrometric (prepared using a charge density of 500 $mC \cdot cm^{-2}$) films, respectively, evidence the importance of the thickness in electrochemical degradation. Moreover, Figures 4c and 4d show the variation of the electroactivity and the *LES* (Eqn 1), respectively, for such films against the number of consecutive oxidation-reduction cycles.

Results indicate that the electrochemical stability of nanometric PEDOT films is higher than that of the micrometric ones. Thus, nanometric films retain ~83% of its initial electroactivity, evidencing an excellent electrochemical behavior. On the other hand, the electroactivity of micrometric films decrease to ~73 % of their initial value after 250 cycles. Despite of such difference, it should be emphasized that the two

systems present remarkable redox stability. Thus, although the resistance to degradation has been proved very high for nanometric systems, the electrostability of micrometric films is still remarkable. Moreover, the electroactivity of the micrometric films is, in terms of absolute values, higher than that of the nanometric ones (*i.e.* 133.03 and 76.50 $mC \cdot cm^{-2}$, respectively).

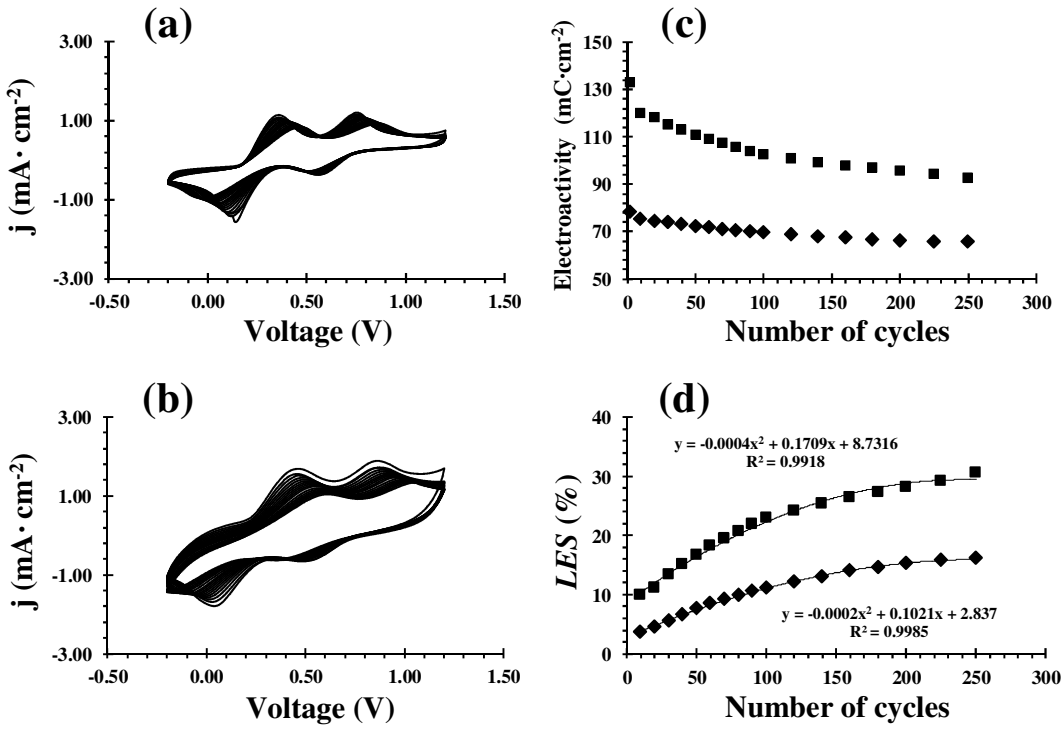

Figure 4. *Control voltammograms for 250 consecutive oxidation-reduction cycles for PEDOT films generated at (a) 75 $mC \cdot cm^{-2}$ (nanometric thickness) and (b) 500 $mC \cdot cm^{-2}$ (micrometric thickness). Variation of (c) the electroactivity and (d) the loss of electroestability (LES) against the number of consecutive oxidation-reduction cycles for nanometric and micrometric PEDOT films (diamonds and squares, respectively). All the electrochemical performances were evaluated in an acetonitrile/distilled water (4% v/v) solution containing 0.1 M $LiClO_4$, 10 mM KI and 1 mM I_2. Voltammogramms were recorded at 20 $mV \cdot s^{-1}$. Initial and final potentials: -0.20 V. Reversal potential: 1.20 V*

Comparison with previous studies on PEDOT indicate that the I^- / I_3^- redox pair has an important benefit in the electrochemical stability. For example, the LES of ultracapacitors made of two identical nanometric PEDOT films deposited on steel (or ITO) substrates was found to increase to 46% (or 34%) after 200 consecutive oxidation-reduction cycles in acetonitrile with 0.1 M $LiClO_4$.[42] On the other hand, the *LES* of micrometric PEDOT films was found to be 45% after 200 consecutive oxidation-reduction cycles in acetonitrile with 0.1 M $LiClO_4$.[9] In contrast, the *LES* of such films

was 30% after only 30 consecutive oxidation-reduction cycles in water with 0.1 M $LiClO_4$, evidencing the importance of the electrochemical medium in the electrostability.[46] The iodine-induced benefit should be attributed to formation of charge transfer complexes with the polymer molecules. Indeed, early studies demonstrated the ability of PEDOT to form charge transfer complexes with iodine,[36,47] which in addition affected to the surface morphology of the polymer.

Morphological characterization. The electrochemical properties of CPs can be rationalized in terms of topology and morphology. Figure 5 displays the morphology of the surface of PEDOT films deposited at 25, 75, 150 and 500 $mC \cdot cm^{-2}$. As it can be seen, the morphology changes drastically with the polymerization charge, the important differences among the different micrographs being essentially related with the variation of the thickness (*i.e.* the thickness increases with the polymerization charges, as was reflected in Figure 1a). The films obtained using the lower charge densities (*i.e.* 25 and 75 $mC \cdot cm^{-2}$) present a fiber-like morphology structure, which produce heterogeneous and porous surfaces. In contrast, films generated using a charge densiy of 150 $mC \cdot cm^{-2}$ show small agglomerates (clusters) in the surface, which are interconnected through fiber-like structures. Finally, the film obtained using 500 $mC \cdot cm^{-2}$ presents globular morphology formed by the aggregation of clusters. In addition of the morphological changes displayed in Figure 5, the variation of the polymerization charge also affects to the porosity. The porosity was quantified through the parameter Δp calculated as follows[48]:

$$\Delta p = \frac{\ell_0 - \ell_{200}}{\ell_0} 100 \qquad (10)$$

where ℓ_0 and ℓ_{200} refer to thickness before applying any redox cycles and after 200 consecutive oxidation-reduction cycles. The value of Δ obtained for the film prepared using 500 $mC \cdot cm^{-2}$ is 11% higher than that of the film producing using 75 $mC \cdot cm^{-2}$ (Table 1).

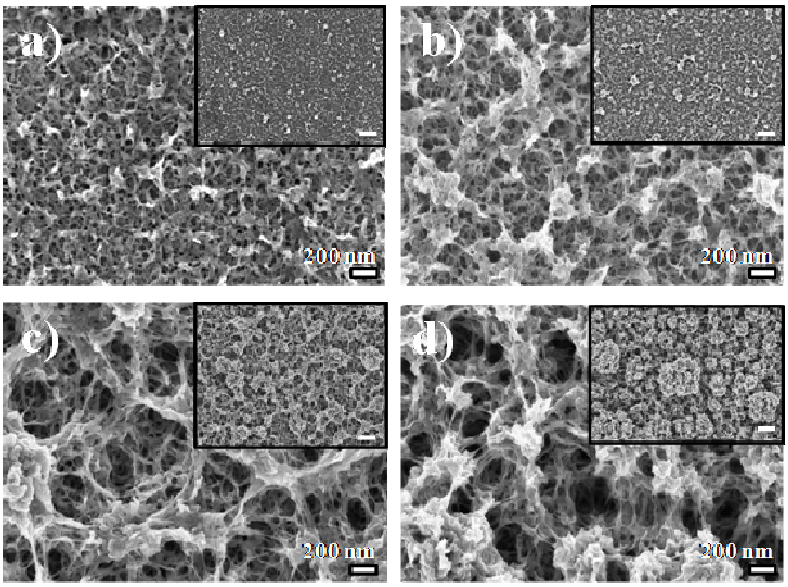

Figure 5. *SEM micrographs of PEDOT films deposited on steel electrodes using different polymerization charges: (a) 25 mC·cm^{-2}; (b) 75 mC·cm^{-2}; (c) 150 mC·cm^{-2}; and (d) 500 mC·cm^{-2}. Low resolution images (scale bar: 1μm) are shown as insets.*

Electrochemical results discussed above (Figure 4) are consistent with the micrographs displayed in Figure 5. In particular, the porosity plays an important role in the electroactivity and electrostability of CPs since it is related with the transport of ions through of the polymeric matrix. As it can be seen, the porosity is very high in both cases (*i.e.* Δp 45% and 49%, respectively, in Table 1), which is related with the significant electroactivity of these system (*i.e.* porosity facilitates the access and escape of dopant ions).

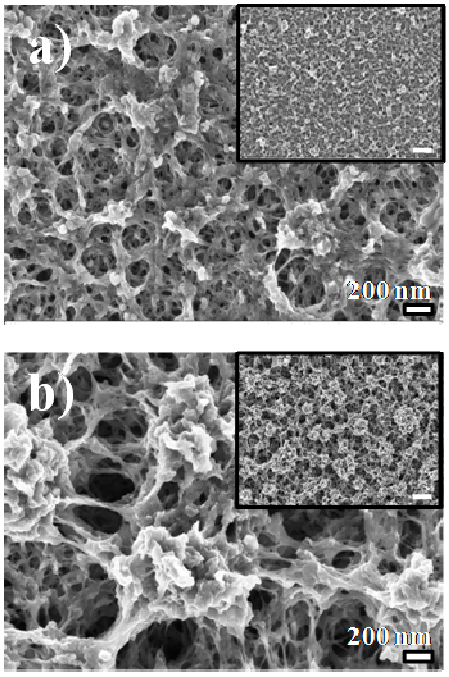

Figure 6. *SEM micrographs of PEDOT films prepared using (a) 75 mC·cm^{-2} (nanometric thickness) and (b) 500 mC·cm^{-2} (micrometric thickness) after 250 consecutive oxidation-reductions cycles at a scan rate of 20 mV·s^{-1}. Low resolution images (scale bar: 1μm) are shown as insets.*

Figure 6 shows the morphology of films produced using charge densities of 75 and 500 mC·cm^{-2} after 250 consecutive oxidation-reduction cycles in an acetonitrile/distilled water (4% v/v) solution with 0.1 M $LiClO_4$, 10 mM KI and 1 mM I_2. Amazingly, the resulting morphologies are similar to those displayed in Figure 5, especially for the nanometric film. Thus, the remarkable porosity of the as prepared films is partially retained after the electrochemical treatment in presence of I^-/I_3^-, explaining their stability. Thus, the I^-/I_3^- plays a protecting role that allows preserve the morphology of the film, this behavior being completely different from that observed in absence of the redox pair.[9] More specifically, PEDOT films were found to undergo significant structural changes after 200 consecutive oxidation-reduction cycles in acetonitrile with 0.1 M $LiClO_4$. The thin fiber-like elements tended to collapse, forming thicker organizations and reducing the distance between the cluster and, consequently, the porosity.[9] The preservation of the initial morphology and porosity after electrochemical degradation in presence of I^-/I_3^- species indicate that nanometric PEDOT films combined with this redox pair are excellent materials to be employed as supercapacitors.

Electrochemical impedance spectroscopy studies for nanometric and micrometric PEDOT films. Nyquist diagrams of micrometric and nanometric films as prepared (*i.e.* without introduce any effect related with the I^-/I_3^- redox pair and after 250 consecutive oxidation-reduction cycles in an acetonitrile/distilled water (4% v/v) solution with 0.1 M $LiClO_4$, 10 mM KI and 1 mM I_2 are displayed in Figure 7. These EIS spectra were fitted to an equivalent circuit (EC) with two time constants, which is represented in Figure 7c. The proposed EC is $R_s\{CPE_1[R_{pore}(CPE_2R_{CT})]\}$, where R_s represents the electrolyte resistance, CPE_1 is ascribed to the capacitance of the film, R_{pore} is the pore resistance, and CPE_2 corresponds to the double layer capacitance, which is in parallel with the charge transfer resistance element (R_{CT}). The capacitance was replaced by a constant phase element (CPE) that describes a non-ideal capacitor when the phase angle is different from -90º. The CPE impedance is attributed to the distributed surface reactivity, surface heterogeneity, and roughness of the current and potential distribution, which in turn are related with the electrode geometry and the electrode porosity. The CPE impedance has been expressed as $Z_{CPE} = \left[Q(j\cdot w)^n\right]^{-1}$, where Q is a frequency-independent constant and w is the angular frequency. The CPE represents a capacitor and a resistor for $n = 1$ and $n = 0$, respectively, while it is associated with a diffusion process when $n = 0.5$. The quality of fitting was evaluated using the error percentage associated to each circuit component, errors smaller than 5% being obtained in all cases.

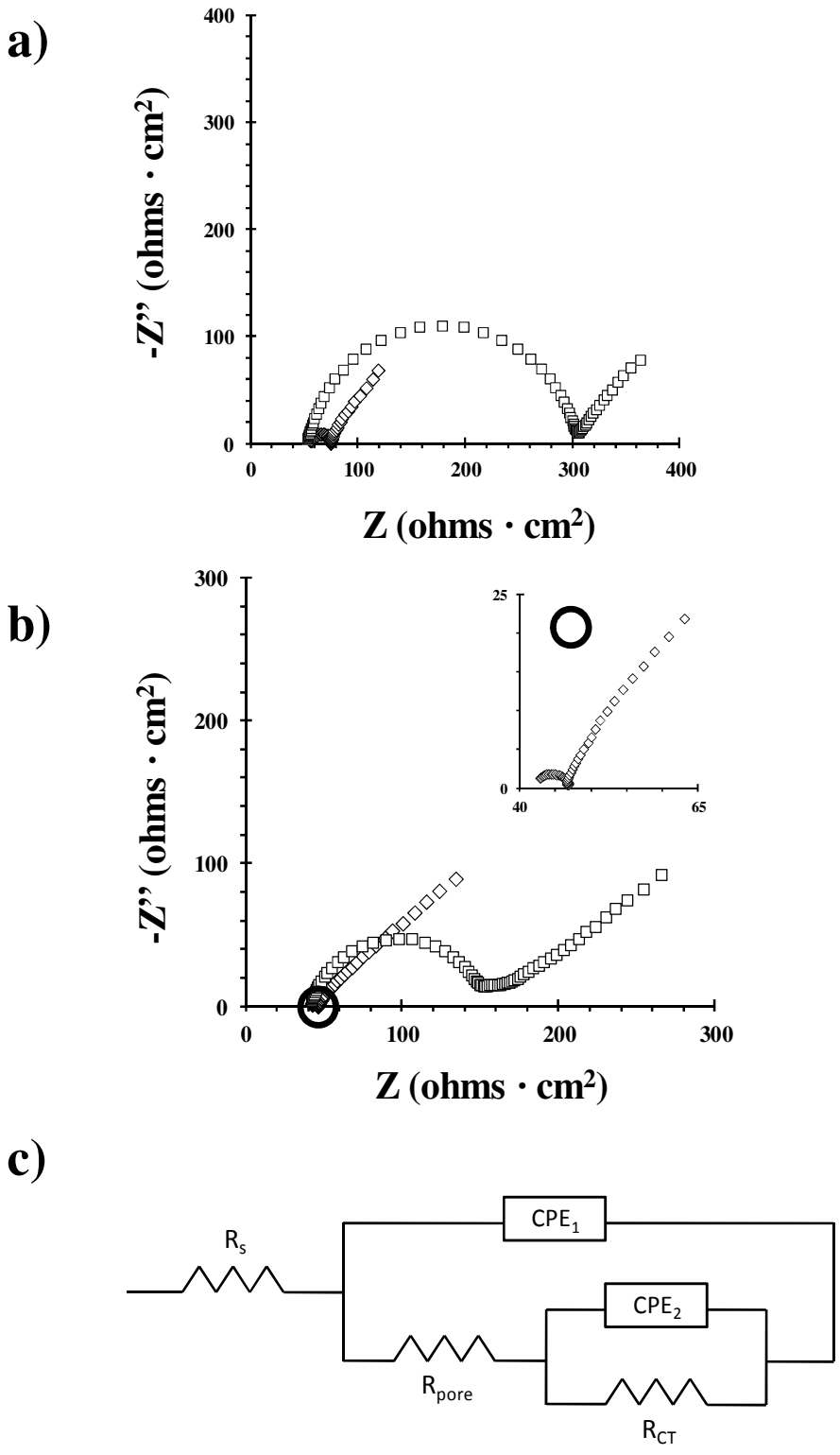

Figure 7. *Nyquist diagrams of (a) micrometric and (b) nanometric PEDOT films (charge density of 500 and 75 mC·cm^{-2}, respectively) as prepared (empty diamonds) and after 250 consecutive oxidation-reduction cycles (empty squares). (c) Equivalent circuit used to simulate the experimental spectra displayed in (a) and (b). The inset in (b) was provided to clarify the experimental data for the as prepared sample.*

Table 2 lists the impedance parameters obtained from fitting the experimental spectra with the EC (Figure 7c). As it can be seen, the R_{pore} of micrometric/nanometric films increased from 18.8/3.7 to 250.8/104.9 $\Omega \cdot cm^2$ after 250 consecutive oxidation-reduction cycles. Accordingly, the resistance of the pore is smaller for the nanometric films than for micrometric ones, independently of the electrochemical degradation, indicating that the facility of I^-/I_3^- species to penetrate into the polymeric matrix is higher for the former than for the latter. This observation is fully consistent not only with the *LES* values reported in Figure 4 but also with the size and distribution of the pores (Figures 5 and 6). Thus, the number and size of the pores is higher and smaller, respectively, for nanometric films than for micrometric ones. Another important parameter is the R_{CT} element, which decreases when the thickness increases. This effect, which occurs before and after electrochemical degradation, has been attributed to the higher porosity measured for micrometric films (Table 1).

Table 2. *Fitting parameters used to simulate the EIS data obtained for the nanometric and micrometric PEDOT films (Figure 7).*

	R_s [a]	CPE_1 [b]	n_1	R_{pore} [c]	CPE_2 [d]	n_2	R_{CT} [e]
Micrometric films (500 mC·cm^{-2})							
Sample as prepared	56.40	$2.24 \cdot 10^{-5}$	0.93	18.82	$9.72 \cdot 10^{-2}$	0.79	266.41
Sample after 250 redox cycles	54.16	$2.01 \cdot 10^{-5}$	0.90	250.83	$6.31 \cdot 10^{-2}$	0.70	440.47
Nanometric films (75 mC·cm^{-2})							
Sample as prepared	42.48	$1.27 \cdot 10^{-4}$	0.89	3.74	$3.85 \cdot 10^{-2}$	0.63	434.82
Sample after 250 redox cycles	42.68	$2.29 \cdot 10^{-5}$	0.89	104.92	$2.17 \cdot 10^{-2}$	0.58	867.21

[a] *Electrolyte resistance, in $\Omega \cdot cm^2$.* [b] *Film pseudo-capacitance, in $F \cdot cm^{-2} \cdot s^{n-1}$.* [c] *Pore resistance, in $\Omega \cdot cm^2$.* [d] *Double layer capacitance, in $F \cdot cm^{-2} \cdot s^{n-1}$.* [e] *Charge transfer resistance, in $\Omega \cdot cm^2$.*

Electrical and optical properties. In previous sections we evidenced that PEDOT prepared using $LiClO_4$ as electrolyte interacts favorably with the I^-/I_3^- redox pair. Moreover, here we show that the electrical conductivity of PEDOT as prepared in this work is two orders of magnitude higher than that reported for PEDOT doped with PSS (σ = 2 S·cm^{-1}).[31,49] Specifically, the electrical conductivity determined for micrometric PEDOT films prepared using $Q_{pol} > 225$ mC·cm^{-2} (*i.e.* the thickness of the films used in the measures was required to be large enough to separate them from the electrode

without breaking) was 210 and 176 $S \cdot cm^{-1}$, respectively. Thus, as the resistance of the CP was significantly higher than that of the contact, the two methods led to very similar results This value decreased to 125 $S \cdot cm^{-1}$ after 20 days and remained practically constant during 40 additional days. This result clearly indicates that the electrical conductivity of PEDOT: ClO_4^- is higher also in terms of temporal stability than that of PEDOT:PSS systems.[30] Moreover, the high electrical conductivity measured in this work is fully consistent with the doping level, which was estimated using an acetonitrile solution with 0.1 M $LiClO_4$. The doping level (Eqn 2) of PEDOT films prepared using a charge density of 75 and 500 $mC \cdot cm^{-2}$ was 0.24 and 0.37, respectively, evidencig that the doping level increases with the thickness of the film. Recent studies reported that the conductiviy of CPs increases with the doping level for small dopants with relatively high mobility[50], which was attributed to the dominating role played by the Coulombic interactions between charges of opposite site in the electrical conductivity.

Figure 8 shows the color of PEDOT for different oxidation and reduction states reached in presence of the I^-/I_3^- redox pair. The color changes from pale blue to deep blue when the oxidation state increases (Figure 8a), whereas the color varies to greenish–blue when the material is reduced (Figure 8b). These results indicate that the presence of I^-/I_3^- species affect the electrochromic effect of PEDOT. On the other hand, Figure 8c, which shows the UV-vis absorption spectrum of nanometric PEDOT after 2000 charge-discharge cycle in acetonitrile/distilled water (4 % v/v) solution containing 0.1 M $LiClO_4$, 10 mM KI and 1 mM I_2, reflects that the λ^{max} value for the π–π^* transition is 616 nm (greenish - blue color in Figure 8b). Accordingly, the electronic band-gap energy (ε_g), which is defined as the onset energy for the π–π^* transition, obtained using the Tauc's relation[44] was estimated to be 1.57 eV. This value is very similar to other measures of as prepared samples obtained using UV-vis spectroscopy (1.6-1.7 eV)[2] and slightly lower than the estimation derived from electrochemical methods (1.98 eV).[51] Moreover, the experimental estimation obtained in this work is even lower than that predicted by quantum mechanical calculations for an idealized polymer chain (1.73 eV).[51] These results indicate the the I^-/I_3^- redox pair exerts a protecting effect, precluding the increase of the ε_g after electrochemical treatment through charge-discharge cycles.

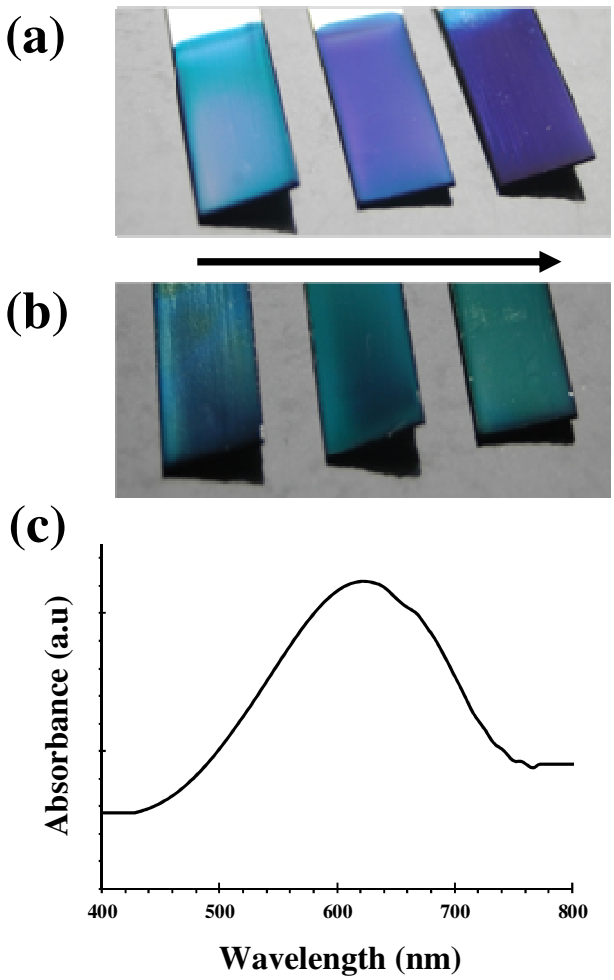

Figure 8. *Color of nanometric PEDOT films (Q_{pol} = 75 mC·cm^{-2}) after apply (a) 0.25 and (b) -0.25 mA·cm^{-2} during 25s, 50s and 75s. The arrow indicates the variation of colour against the time for oxidized and reduced films, respectively. (c) UV-vis absorption spectrum of a nanometric PEDOT film after 2000 charge-discharge cycles in acetonitrile/distilled water (4 % v/v) solution containing 0.1 M $LiClO_4$, 10 mM KI and 1 mM I_2.*

Nanometric PEDOT films in contact with the I^-/I_3^- ***species as supercapacitor electrodes.*** Figure 9a shows typical charge-discharge cycles in presence of the I^-/I_3^- redox pair of nanometric PEDOT recorded at a current density of 0.25 mA·cm^{-2}. Results provide a specific capacitance of 185 F·g^{-1} at the beginning of the cycling process, this value decreasing by only ~ 6 % after 2000 cycles. The discharge specific capacitance as a function of the number of cycles is represented in Figure 9b. It is worth noting that these specific capacitances are one order of magnitude higher than those reported for PEDOT supercapacitors in absence of I^-/I_3^-: micrometric (41 F·g^{-1})[9] and nanometric films (45-67 F·g^{-1}, depending on the thickness)[42] prepared using similar conditions (*i.e.* films generated using an acetonitrile solution with 0.1 M $LiClO_4$ and steel electrodes).

Indeed, the values found in this work are similar to those reported for supercapacitors fabricated using nanocomposites of PEDOT and inorganic materials (*e.g.* MnO_2, MoO_3, carbon nanotubes, V_2O_5 and $NiFe_2O_4$), for which the specific capacitance ranged from 153 to 375 $F \cdot g^{-1}$.[52-57]

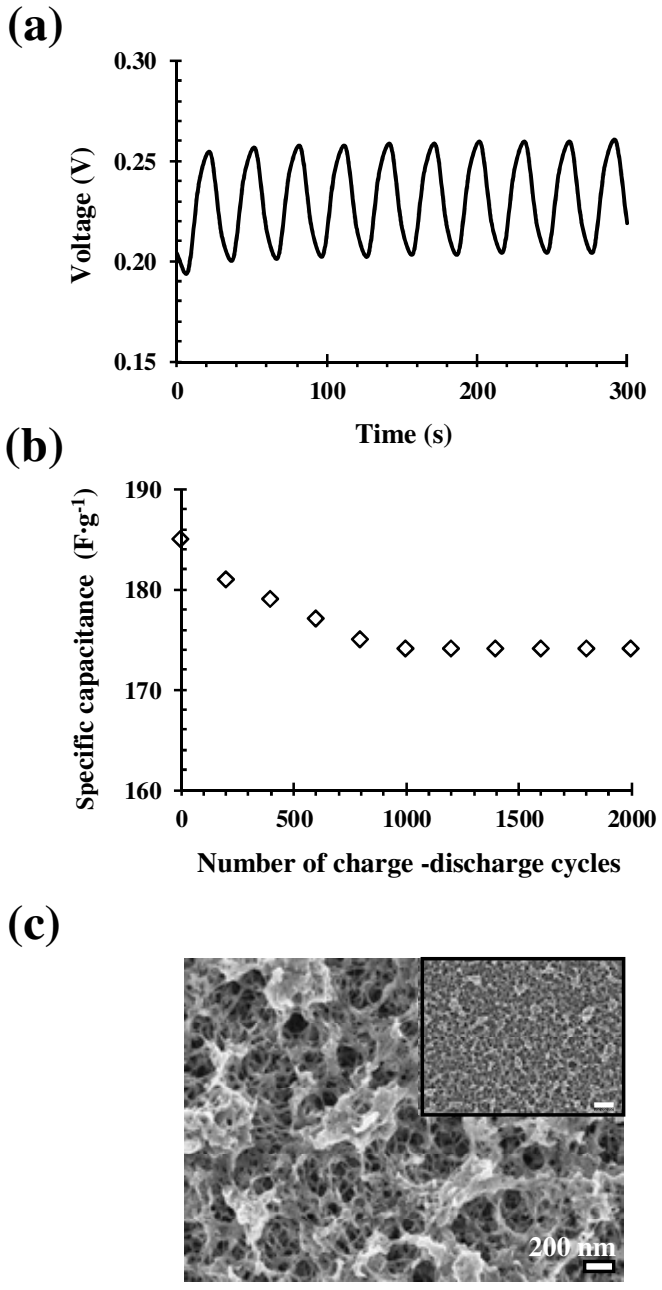

Figure 9. *(a) Galvanostatic (current density: 0.25 $mA \cdot cm^{-2}$) charge-discharge cycles in an acetonitrile/distilled water (4 % v/v) solution containing 0.1 M $LiClO_4$, 10 mM KI and 1 mM I_2 of a nanometric PEDOT film prepared using 75 $mC \cdot cm^{-2}$. (b) Variation of the specific capacitance against the number of charge-discharge cycles using the conditions indicated in (a). (c) SEM micrographs of a nanometric PEDOT film after 2000 charging-discharging cycles (~17 h). Low resolution images are shown as insets in the high resolution images (scale bar: 1μm).*

The coulombic efficiency was found to be very high (~99 %) during the whole experiment, while other capacitive properties such as the energy density and the power density were found to be E_d = 1.2 W·h·kg^{-1} and P_d = 0.3 kW·kg^{-1}, respectively. The excellent behavior as supercapacitor of nanometric PEDOT in presence of I^-/I_3^- has been again attributed to the porosity of the film after 2000 consecutive charge-discharge cycles, as is evidenced in Figure 9c. The power density reported for PEDOT:PSS with poly(ethylene oxide) in presence of I^-/I_3^- was P_d = 0.1 kW·kg^{-1},[58] while Ghosh and Inganäs described P_d values ranging from 0.1 to 1.0 kW·kg^{-1} and E_d = 1.0 W·h·kg^{-1} for their synthesized PEDOT:PSS.[59] The overall of these results indicate that, although PEDOT:ClO_4^- cannot replace PEDOT:PSS in DSSCs because of its insolubility, it represents a good alternative for the fabrication of supercapacitor electrodes.

8.1.4. Conclusions

The electrochemical and capacitive properties of PEDOT films in presence of the I^-/I_3^- redox pair have been investigated. Although the electrocatalytic activity of I^-/I_3^- species improved the properties of both nanometric and micrometric PEDOT films, benefits were more important in the former than in the latter. The loss of electroactivity of nanometric films was of only ~17% after 250 consecutive oxidation-reduction cycles, reflecting exceptional electrochemical stability. Moreover, the specific capacitance was ~ 185 $F \cdot g^{-1}$, this value decreasing by only 6% after 2000 charge-discharge cycles. Morphological characterization has evidenced that the porosity plays a crucial role on the electrochemical and capacitive properties of PEDOT. In conclusion, the synergy between I^-/I_3^- species and nanometric PEDOT films allows to propose the use of this combination as a reliable supercapacitor material.

8.1.5. References

[1]. Kirchmeyer, S.; Reuter, K. *J. Mater. Chem.* **2005**, *15*, 2077.

[2]. Groenendaal, L.; Jonas, F.; Freitag, V.; Pielartzik, H.; Reynolds, J. R. R. *Adv. Mater.* **2000**, *12*, 481.

[3]. Lin, K. C.; Tsai, T. H.; Chen, S. M. *Biosens. Bioelectron.* **2010**, *26*, 608.

[4]. Liu, J.; Agarwal, M.; Varahramyan, K. *Sens. Actuators B* **2008**, *135*, 195.

[5]. Krishnamoorthy, K.; Gokhale, R. S.; Contractor, A. Q.; Kumar, A. *Chem. Commun.* **2004**, 820.

[6]. Prabakar, S. J. R.; Pyo, M. *Corros. Sci.* **2012**, *57*, 42

[7]. Armelin, E.; Meneguzzi, A.; Ferreira, C. A.; Alemán, C. *Surf. Coat. Technol.* **2009**, *203*, 3763

[8]. Aradilla, D.; Azambuja, D.; Estrany, F.; Iribarren, J. I.; Ferreira, C. A.; Alemán, C. *Polym. Chem.* **2011**, *2*, 2548.

[9]. Aradilla, D.; Estrany, F.; Alemán, C. *J. Phys. Chem. C* **2011**, *115*, 8430.

[10]. Ouyang, J.; Chu, C. W.; Chen, F. C.; Xu, Q.; Yang, Y. *Adv. Funct. Mater.* **2005**, *15*, 203.

[11]. Kim, W. H.; Mäkinen, A. J.; Nikolov, N.; Shashidhar, R.; Kim, H.; Kafafi, Z. H. *Appl. Phys. Lett.* **2002**, *80*, 3844.

[12]. DeLongchamp, D.; Hammond, P. T. *Adv. Mater.* **2001**, *13*, 1455.

[13]. Neuer, H. W.; Wehrmann, R.; Kirchmeyer, S. *Adv. Funct. Mater.* **2002**, *12*, 89.

[14]. Song, M. Y.; Kim, K. J.; Kim, D. Y. *Sol. Energ. Mat. Sol. Cell.* **2005**, *85*, 31.

[15]. Saito, Y.; Fukuri, N.; Senadeera, R.; Kitamura, T.; Wada, Y.; Yanagida, S. *Electrochem. Comm.* **2004**, *6*, 71.

[16]. Dennler, G.; Scharber, M. C.; Brabec, C. J. *Adv. Mater.* **2009**, *21*, 1323.

[17]. Ahmad, S.; Yum, J. H.; Xianxi, Z.; Grätzel, M.; Butt, H. J.; Nazeerduddin, M. K. *J. Mater. Chem.* **2010**, *20*, 1654.

[18]. Saito, Y.; Kitamura, T.; Wada, Y.; Yanagida, S. *Synth. Metals* **2002**, *131*, 185.

[19]. Boschloo, G.; Hagfeldt, A. *Acc. Chem. Res.* **2009**, *42*, 1819.

[20]. Saito, Y.; Kubo, W.; Kitamura, T.; Wada, Y.; Yanagida, S. *J. Photochem. Photobiol. A: Chem.* **2004**, *164*, 153.

[21]. Pringle, J. M.; Armel, V.; MacFarlane, D. R. *Chem. Commun.* **2010**, *46*, 5367.

[22]. Tsai, T. H.; Chiou, S. C.; Chen, S. M.; Lin, K. C. *Int. J. Electrochem. Sci.* **2011**, *6*, 3938.

[23]. Fukuri, N.; Masaki, N.; Kitamura, T.; Wada, Y.; Yanagida, S. *J. Phys. Chem B* **2006**, *110*, 25251.

[24]. Tamburri, E.; Gugielmotti, V. V.; Orlanducci, S.; Terranova, M. L. *Inorg. Chim. Acta* **2011**, *377*, 170.

[25]. Xia, J.; Masaki, N.; Jiang, K.; Yanagida, S. *J. Mater. Chem.* **2007**, *17*, 2845.

[26]. Yanagida, S.; Yu, Y.; Manseki, K. *Acc. Chem. Res.* **2009**, *42*, 1827.

[27]. Kim, Y.; Sung, Y. E.; Xia, J. B.; Cantu, M. L.; Masaki, N.; Yanagida, S. *J. Photochem. Photobiol. A: Chem.* **2008**, *193*, 77.

[28]. Xia, J.; Masaki, N.; Cantu, M. L.; Kim, Y.; Jiang, K.; Yanagida, S. *J. Am. Chem. Soc.* **2008**, *130*, 1258.

[29]. Sakurai, S.; Jiang, H. Q.; Takahashi, M.; Kobayashi, K. *Electrochim. Acta* **2009**, *54*, 5463.

[30]. Lee, K. M.; Chiu, W. H.; Wei, H. Y.; Hu, C. W.; Suryanarayanan, V.; Hsieh, W. F.; Ho, K. C. *Thin Solid Films* **2010**, *518*, 1716.

[31]. Chen, J. G.; Wei, H. Y.; Ho, K. C. *Sol. Energ. Mat. Sol. Cell.* **2007**, *91*, 1472.

[32]. Liao, J. Y.; Ho, K. C. *Sol. Energ. Mat. Sol. Cell.* **2005**, *86*, 229.

[33]. Mozer, A. J.; Wada, Y.; Jiang, K. J.; Masaki, N.; Yanagida, S.; Mori, S. N. *Appl. Phys. Lett.* **2006**, *89*, 043509.

[34]. Sudhagar, P.; Nagarajan, S.; Lee, Y. G.; Song, D.; Son, T.; Cho, W.; Heo, M.; Lee, K.; Won, J.; Kang, Y. S. *ACS Appl. Mater. Interfaces* **2011**, *3*, 1838.

[35]. Roy-Mayhew, J. D.; Bozym, D. J.; Punckt, C.; Aksay, I. A. *ACS Nano* **2010**, *4*, 6203.

[36]. Velten, J.; Mozer, A. J.; Li, D.; Officer, D.; Wallace, G.; Baughman, R.; Zakhidov, A. *Nanotechnology* **2012**, *23*, 085201.

[37]. Biallozor, S.; Kupniewska, A. *Electrochem. Comm.* **2000**, *2*, 480.

[38]. Li, Q.; Wu, J.; Tang, Q.; Lan, Z.; Li, P.; Lin, J.; Fan, L. *Electrochem. Comm.* **2008**, *10*, 1299.

[39]. Wu, J.; Li, Q.; Fan, L.; Lan, Z.; Li, P.; Lin, J.; Hao, S. *J. Pow. Sourc.* **2008**, *181*, 172.

[40]. Chen, T. W.; Tsai, T. H.; Chen, S. M.; Lin, K. C. *Int. J. Electrochem. Sci.* **2011**, *6*, 2043.

[41]. Ocampo, C.; Oliver, R.; Armelin, E.; Alemán, C.; Estrany, F. *J. Polym. Research* **2006**, *13*, 93.

[42]. Aradilla, D.; Estrany, F.; Armelin, E.; Alemán, C. *Thin Solid Films* **2012**, *520*, 4402.

[43]. Bard, A. J.; Faulkner, L. R. *Electrochemical Methods: Fundamentals & Applications* Eds.; John Wiley & Sons: New York, 1980, p 218.

[44]. Tauc, J.; Grigorovici, R.; Vancu, A. *Phys. Status Solidi* **1966**, *15*, 627.

[45]. Yoon, C. H.; Vittal, R.; Lee, J.; Chae, W. S.; Kim, K. J. *Electrochim. Acta* **2008**, *53*, 2890.

[46]. Teixeira-Dias, B.; del Valle, L. J.; Estrany, F.; Mano, J.; Reis, R. L.; Alemán, C. *Macromol. Mater. Engin.* **2012**, *297*, 359.

[47]. Kanciurzewska, A.; Dobruchowska, E.; Baranzahi, A.; Carlegrim, E.; Fahlman, M.; Girtu, M. A. *J. Optoelec. Adv. Mater.* **2007**, *9*, 1052.

[48]. Pal, E.; Hornok, V.; Sebo, D.; Majzik, A.; Dekay, I. *Colloids Surf. B* **2010**, *79*, 276.

[49]. Tamburri, E.; Sarti, S.; Orlanduccia, S.; Terranova, M. L.; Rossi, M. *Macromol. Chem. Phys.* **2011**, *125*, 397.

[50]. Posudievsky, O. Y.; Konoschuk, N. V.; Kukla, A. L.; Pavluchenko, A. S.; Shirshov, Y. M.; Pokhodenko, V. D. *Sens. Actuators B* **2011**, *151*, 351.

[51]. Aradilla, D.; Estrany, F.; Alemán, C. *J. Appl. Polym. Sci.* **2011**, *121*, 1982.

[52]. Banafsheh, B.; Ivey, D. G. *Electrochim. Acta* **2010**, *55*, 2014.

[53]. Chen, L.; Yuan, C.; Gao, B.; Chen, S.; Zhang, X. *J. Solid State Electrochem.* **2009**, *13*, 1925.

[54]. Murugan, A. V.; Viswanath, A. K.; Gopinath, C. S.; Vijayamohanan, K. *J. Appl. Phys.* **2006**, *100*, 074319.

[55]. Fusalba, F.; Ho, H. A.; Breau, L.; Belanger, D. *Chem. Mater.* **2000**, *12*, 2581.

[56]. Peng, C.; Snook, G. A.; Fray, D. J.; Shaffer, M. P.; Chen, G. Z. *Chem. Commun.* **2006**, *44*, 4629.

[57]. Peng, C.; Jin, J.; Chen, G. Z. *Electrochim. Acta* **2007**, *53*, 525.

[58]. Snook, G. A.; Kao, P.; Best, A. S. *J. Power. Sourc.* **2011**, *196*, 1.

[59]. Ghosh, S.; Inganäs, O. *Adv. Mater.* **1999**, *11*, 1214.

8.2. All conducting-polymer rechargeable batteries based on poly(3,4-ethylenedioxythiophene)

8.2.1. Introduction

Conducting polymers (CPs) are employed as charge storage materials for rechargeable batteries.[1-5] Works in this field are typically based on designs to use the CP as a positive electrode material in combination with a negative electrode such as Li, Mg and Zn, since CPs are not only electronic but also ionic conductors.[1] From a practical point of view, the application of CPs as electrodes in batteries relies on their electrochemical redox processes (*i.e.* doping/dedoping processes), which permit the access and escape of the electrolyte into the polymer mass. Polyaniline (PAni),[6-14] polypyrrole (PPy),[12,15-20] and polythiophene (PTh)[21-28] derivatives are among the most used CPs, which can be employed alone[6-9,15-17,21-24] or forming composites with metallic oxides (*e.g.* TiO_2,[10] V_2O_5,[11,12] SnO_2,[18] MnO_2,[24-25] $LiMn_2O_4$[26] and $LiCoO_2$[27]), metallic phosphates (*e.g.* $LiFePO_4$[19]), carbon (*e.g.* vitreous carbon,[13] graphite[14] and multi-walled carbon nanotubes[20,28]), etc.

Polymer batteries play a crucial role in research towards developing high energy density batteries because of the advantages provided by their certain unique properties: easy thin film formation, light weight, elasticity, etc. This motivated the research in all-CPs based batteries just at the beginning of the new century.[29-32] Unfortunately, all-CPs based batteries, in which the oxidation level of the two electrodes must differ as much as possible, were found to present poor performance. This was attributed to the low electrical conductivity in the electrode with the material in the undoped state and also to the low environmental stability of CPs.[29-31] However, in a very recent study Crispin and coworkers reported the properties of an air battery where the anode and cathode are based on poly(3,4-ethylenedioxythiophene),[32] a PTh derivative with excellent electrochemical and electrical properties and high environmental stability.[33,34] Specifically, polyethyleneimine (PEI) was combined with the low oxidized form of PEDOT (undoped) at the anode (PEI/PEDOT), while PEDOT in the oxidized state (doped) was used at the cathode. The difference between the oxidation levels at the electrodes produced an open circuit voltage of 0.5 V.[32]

In recent studies we reported the high electroactivity (*i.e.* ability to store charge) and specific capacitance of PEDOT films doped with ClO_4^- anions.[35,36] Moreover, these properties were found to be significantly enhanced in other ClO_4^--doped systems, like multilayered composites made of alternated layers of PEDOT and poly(N-methylpyrrole) (PNMPy),[36-38] abbreviated ml-PEDOT/PNMPy, and hybrid PEDOT/clay exfoliated nanocomposites.[39,40] Thus, the capability of oxidation and reduction processes, which is generally controlled by the diffusion of the dopant anions through the CP structure, greatly depends upon the nature (size and charge density) of the dopant anions and the morphology (*i.e.* porosity of the CPs and characteristics of the interfaces in the composites). In this work we present the fabrication of all-CP batteries using ClO_4^- as dopant agent. Specifically, batteries in which both the anode and cathode are made of individual PEDOT, ml-PEDOT/PNMPy or PEDOT/clay composites, hereafter denoted all-PEDOT, all-PEDOT/PNMPy and all-PEDOT/clay batteries, respectively, have been constructed and characterized. As a proof of concept, these all-CP batteries have been used to power LED bulbs demonstrating that their practical application is a reality.

8.2.2. Methods

***Materials*.** The two monomers, 3,4-ethylenedioxythiophene (EDOT) and N-methylpyrrole (NMPy), the montmorillonite (bentonite) and acetonitrile were purchased from Aldrich and used as received. Anhydrous $LiClO_4$ analytical from Aldrich, analytical reagent grade, was stored in an oven at 80 ºC before use in the electrochemical trials.

Synthesis. Electrochemical experiments were conducted on a PGSTAT302N AUTOLAB potenciostat-galvanostat connected to a PC computer controlled through the NOVA 1.6 software, using a three-electrode two-compartment cell under nitrogen atmosphere at 25 ºC. Steel AISI 316 sheets of 6 cm^2 were used as working and counter electrodes while the reference electrode was a Ag|AgCl electrode containing a KCl saturated aqueous solution (E^0= 0.222 V at 25 ºC). Lithium perchlorate ($LiClO_4$) dissolved in acetonitrile (PEDOT and multilayered films) or water/acetonitrile (PEDOT/clay films) was used as the electrolytic solution. Specifically, the working compartment was filled with 40 mL of a 10 mM monomer solution with 0.1 M $LiClO_4$, while the cathodic compartment was filled with 10 mL of the same electrolyte solution.

Chronocoulometry was used to synthesize the polymer films since this technique allows to determine the charge quantity brought to the electrode. Films were obtained by applying an oxidation potential fixed at 1.40 V to the generation medium and controlling the charge density at 500 $mC \cdot cm^{-2}$. In the case of 3-layered PEDOT/PNMPy/PEDOT films, which were prepared using the electrochemical layer-by-layer technique described in previous works,[36,38,41] the charge density for each layer was 167 $mC \cdot cm^{-2}$.

The amount of montmorillonite in the solution used to prepare PEDOT/clay films was 20% w/w. This concentration value, which is referred to that of the EDOT monomer, was found to provide the optimum electrochemical properties.[39] The montmorillonite was exfoliated in a water:acetonitrile (60:40 v/v) mixture at neutral pH, being sonicated for 10 minutes with an ultrasonic generator. After this, a 10 mM monomer solution in water:acetonitrile (60:40 v/v) with 0.1 M $LiClO_4$ was added to the above exfoliated clay solution, and stirred for 20 h in a frozen environment (ice). The potential and charge density used in the chronocoulometry were the same that for PEDOT.

***Preparation of the organic electrodes*.** Electrodes were prepared by imposing doping and dedoping processes to the synthesized films. Oxidized PEDOT, 3-layered and PEDOT/clay films were generated by applying a current of +1.0 mA during 280, 260 and 135 s, respectively, whereas reduced films were obtained by applying a current of -1.0 mA during 190, 125 and 88 s, respectively. The difference in the oxidation level between the oxidized and reduced electrodes obtained using these times produced an open circuit voltage of 1.1 V. All chronopotentiometric assays were carried out in an acetonitrile solution containing 0.2 M $LiClO_4$ at 25ºC.

***Scanning electron microscopy* (SEM).** SEM studies were performed to examine the influence of the oxidation and reduction processes on the surface morphology of the generated films. Dried samples were placed in a Focussed Ion Beam Zeiss Neon 40 scanning electron microscope operating at 3 kV, equipped with an EDX spectroscopy system.

Capacitive behaviour. Galvanostatic charge/discharge curves were used to evaluate the specific capacitance (SC, in F/g), the power density (P, in W/Kg) and the Coulomb efficiency (η, in %):

$$SC = \frac{I\Delta t}{\Delta V m} \qquad (1)$$

$$P = \Delta V \frac{I}{m} \quad (2)$$

$$\eta = \frac{t_d}{t_c} 100 \quad (3)$$

where ΔV is the difference between the potential at the beginning and at the end of the discharge, I is the current intensity (1 mA), Δt is the time interval required for the change in voltage ΔV (30 s), m is the mass of active material in the electrode (PEDOT, in g), and t_d/t_c refers to the ratio between the discharge and charge times. All experiments were carried out in an acetonitrile solution containing 0.2 M $LiClO_4$ at 25ºC.

8.2.3. Results and Discussion

In Figure 1a, which compares scanning electron microscopy (SEM) micrographs of as prepared, oxidized and reduced PEDOT films. As it can be seen, the three specimens show a sponge-like morphology, which can be described as a homogeneous distribution of clusters connected by sticks with a fiber-like morphology forming relatively narrow and tortuous pores. The thickness of the sticks is ~50 nm, this threshold value increasing with the level of aggregation, clusters being formed when such level is maximal. However, the surface porosity of both the anode and cathode is higher than that of the as prepared films, which is reflected by the increment in the number of pores as well as of their size. Thus, oxidation and reduction processes enhanced the aggregation level increasing the size of the clusters, which results in an enhancement of the porosity. This is expected to facilitate the access and escape of the perchlorate dopant ions into the polymer matrix during electrochemical redox processes.

Similar features are reflected in Figure 1b for the 3-layered system, even though a significant morphological difference is detected with respect to individual PEDOT. The porosity of the upper PEDOT layer, which grows above the intermediate PNMPy layer, is significantly more porous than that of individual PEDOT (Figure 1a). This is fully consistent with previous observations,[35,36] which showed that PEDOT directly electrodeposited on steel is less porous than PEDOT deposited on top of another CP. Moreover, this remark can be extended from the as prepared films to the oxidized and reduced ones. On the other hand, the incorporation of a significant amount of exfoliated clay (20% w/w) into the polymeric matrix results in a drastic morphological change, as is evidenced in Figure 1c. Thus, large agglomerates of granules appear in the compact

surface of PEDOT/clay films. Moreover, oxidation and reduction of the as prepared films to fabricate the anode and cathode, respectively, does not produce significant structural alterations at the surface.

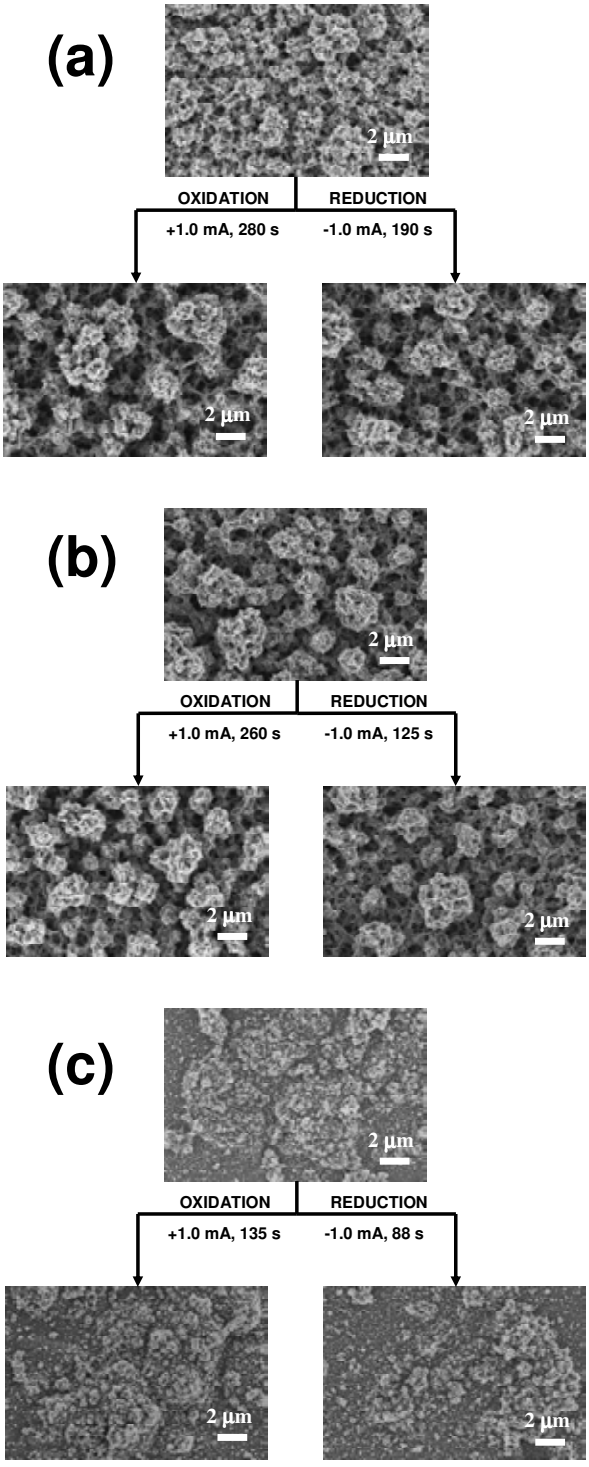

Figure 1. *Scanning electron micrographs of (a) PEDOT, (b) PEDOT/PNMPy/PEDOT 3-layered and (c) PEDOT/clay films as prepared by anodic polymerization using the chronocoulometry technique (top), and after subsequent oxidation (bottom, left) and reduction (bottom, right).*

The electrochemical performance of the films deposited on steel substrates was initially examined by considering two galvanostatic experiments. The first one consisted in the following three steps: (1) 5 galvanostatic charge/discharge cycles of 30 s were consecutively conducted at currents that increased from 1 to 7 mA in steps of 2 mA (*i.e.* 5 cycles at each current); (2) after the last charge/discharge cycle at 7 mA, another 5 cycles at a current of 1 mA were applied; and finally (3) 10 consecutive oxidation-reduction cycles were applied between -0.20 and +1.20 V at 50 mV/s. The same three steps were applied in the second experiment, even though the order was changed with respect to the first one. Thus, the system was initially degraded by 10 consecutive oxidation reduction cycles (step 3), the galvanostatic charge/discharge cycles at increasing current densities (step 1) and at 1 mA (step 2) being subsequently applied. Figure 2a compares the control voltammograms of PEDOT and 3-layered films recorded after the application of such two electrochemical treatments. The two materials show an excellent electrochemical stability, even though the retention of the ability to store charge is slightly higher when the galvanostatic cycles are applied before than the oxidation-reduction cycles (*i.e.* first experiment). On the other hand, the supercapacitor behavior of PEDOT is better than that of the 3-layered system, as reveals the symmetrical and rectangular voltammetric curves found for the former. In opposition, the anodic and cathodic areas of 3-layered films are higher than those of PEDOT, reflecting that the former material is more electroactive than the latter one. Finally, the electrochemical stability of the PEDOT/clay films was worse than those of PEDOT and 3-layered films, independently of the galvanostatic experiment. Although the electroactivity of PEDOT/clay film was found to be higher than that of PEDOT,[39] the electrochemically inert nature of the clay affects to the stability of the nanocomposite.

The specific capacitances (SCs) were determined for PEDOT, 3-layered and PEDOT/clay considering the same systems later used to construct batteries (*i.e.* combining oxidized and reduced films as explained below), the resulting values being 46, 60 and 38 F/g, respectively. Although these SC values are one order of magnitude lower than those reported for symmetric ultracapacitors of identical chemical nature but nanometric thickness, the capacitive response of micrometric films against electrochemical degradation is known to be significantly better.[35,36,39] The latter feature is evidenced in Figure 2b, which represents the variation of the SC against the number of 1 mA charge-discharge cycles for PEDOT and 3-layered films. The stability of PEDOT/clay was not investigated because its SC was the smallest. As it can be seen,

after 1000 cycles the SC of PEDOT and 3-layered films decreases by only 13.0% and 8.5%, respectively. On the other hand, the Coulomb efficiency (η) / power density (P) of the PEDOT and 3-layered materials are η = 94% / P = 54 W/Kg and η = 97% / P =76 W/Kg, respectively. Figure 2c reflects the linearity and symmetry of charge-discharge profiles for PEDOT and 3-layered films, corroborating the capacitive behavior of the investigated materials.

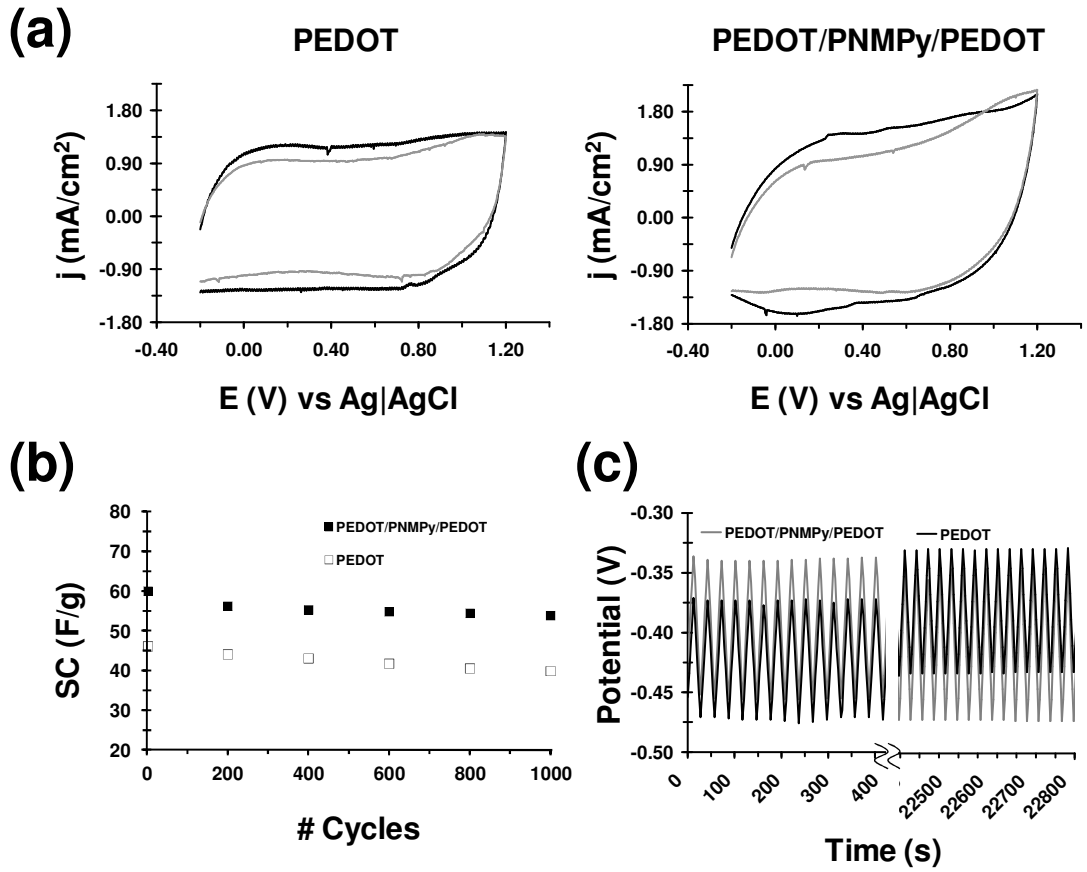

Figure 2. *(a) Control voltammograms of PEDOT (left) and 3-layered (right) films recorded after the application of the two electrochemical treatments described in the text: (i) charge-discharge cycles at different current intensities + oxidation-reduction cycles using cyclic voltammetry (black profile); and (ii) oxidation-reduction cycles using cyclic voltammetry + charge-discharge cycles at different current intensities (grey profile). Control voltammograms were recorded at 50 mV/s. Initial and final potentials: -0.20 V. Reversal potential: 1.20 V. (b) Variation of the specific capacitance (SC) against the number of charge-discharge cycles (current: 1 mA; time: 30 s per cycle) for PEDOT and 3-layered films films. (c) Galvanostatic charge-discharge curves for PEDOT and 3-layered films. From a total of 1000 charge-discharge cycles the first cycles (time < 400 s) and cycles relatively close to the end (time < 22000 s) are displayed. All electrochemical measures were carried out considering battery systems, which were constructed combining the oxidized with reduced electrodes (i.e. the anode with cathode).*

Batteries were fabricated by combining oxidized electrodes (anodes) with reduced electrodes (cathodes) of the same nature. In this way, PEDOT, PEDOT/PNMPy/PEDOT and PEDOT/clay electrodes were used to construct all-PEDOT, all-PEDOT/PNMPy and all-PEDOT/clay batteries, respectively. The scheme of a cell all-PEDOT battery is illustrated in Figure 3a, the half-reactions upon discharge being:

Anode: $\text{PEDOT}\ (\text{ClO}_4^-)_x + xe^- \rightarrow \text{PEDOT}^0 + xClO_4^-$

Cathode: $\text{PEDOT}^0 + xClO_4^- \rightarrow \text{PEDOT}\ (\text{ClO}_4^-)_x + xe^-$

As the voltage required to power a red LED bulb is ~1.5 V, two battery cells were connected in series with the LED bulb to get an open circuit voltage of ~2.2 V (Figure 3b).

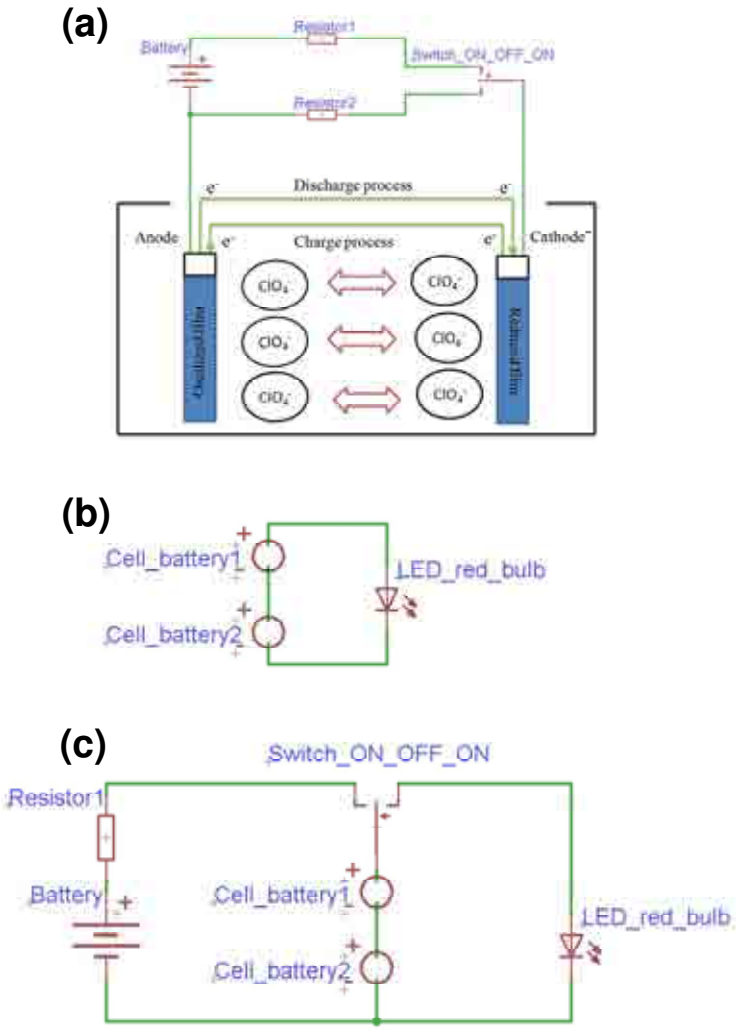

Figure 3. *Schematic diagram of (a) the configuration of all-PEDOT battery, (b) the circuit used to power the LED bulb using the all-CP batteries, and (c) the circuit used for the recharging of the all-CP batteries.*

Figure 4 shows photographs of the PEDOT electrodes (Figure 4a) used in the construction of the all-CP battery (Figure 4b) to power the LED bulb (Figure 4c). All-PEDOT, all-PEDOT/PNMPy and all-PEDOT/clay batteries fabricated using this simple concept allowed us to maintain the power of the LED bulb during intervals of time of 150, 135 and 60 s, respectively, a discharge cut-off potential of 1.5 V being reached after such time. As mentioned above, the lowest performance of the all-PEDOT/clay battery must be attributed to the inert nature of the clay, whereas the all-PEDOT and all-PEDOT/PNMPy batteries were exclusively made of electroactive polymers. Recharging of the batteries was carried out by coupling a power supply of 12 V and a resistance of 10 kΩ (Figure 3c). Such two elements were retired after complete the recharge, which took ~65 s, the LED bulb being powered again during very similar intervals of time. These recharge-power processes were repeated by more than 10 times without detriment in the performance of the batteries.

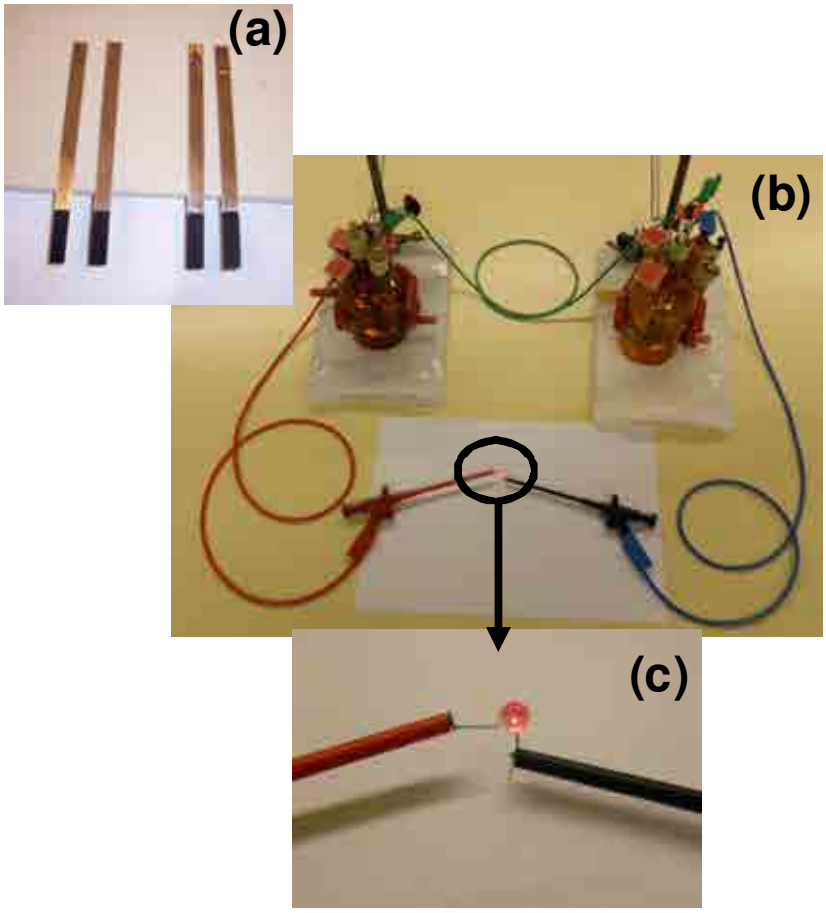

Figure 4. *Experimental dispositive used to power the LED bulb: (a) electrodes of the all-PEDOT battery; (b) circuit with the two cell batteries connected in series; and (c) amplification image of the powered LED bulb.*

The discharge curves of the all-PEDOT, all-PEDOT/PNMPy and all-PEDOT/clay batteries are provided in Figure 5a, which represents the voltage dropping from 1.20 V (initial charge) to 0.20 V against the discharge time. A resistance of 1 kΩ was used for the discharge process, measures being performed every 5 s. The values displayed in Figure 5a correspond to the average of three independent experiments for each battery. The voltage of all-PEDOT, all-PEDOT/PNMPy and all-PEDOT/clay batteries drops 1.00 V after 165, 195 and 45 s, respectively. Figure 5b shows the curve for a typical charge-discharge cycle after 50 days, the LED bulb remaining powered during the charging process as is reflected in the circuit displayed in Figure 3c. As it can be seen, for both all-PEDOT/PNMPy and all-PEDOT batteries the charge and discharge times were ~50 and ~135 s, respectively, whereas all-PEDOT/clay batteries exhibited times of 70 and 30s. Moreover, although the time required for the discharge of the two batteries was observed to decrease when the number of cycles increases, such reduction was relatively low evidencing the high stability of the batteries. For the all-PEDOT/clay battery, the time required to store 1.2 V (~70 s) is three and a half times higher than that used in the discharge (~20 s), evidencing a drastic reduction in the stability in comparison with the other two batteries. Figure 5c represents the variation of the stability, which was calculated as the reduction of the total time used for the charge-discharge process relative to that of the first cycle, against the time (in days). Several charge-discharge cycles distributed in a period of 65 days were performed to examine the stability of the batteries from a quantitative point of view. The behavior of the all-PEDOT/PNMPy and all-PEDOT/clay batteries was similar for first 10 days, the stability of the all-PEDOT system being higher than that of the all-PEDOT/PNMPy after this time. After 65 days the stability of all-PEDOT, all-PEDOT/PNMPy and all-PEDOT/clay batteries decreased by 20%, 30% and 48%, respectively.

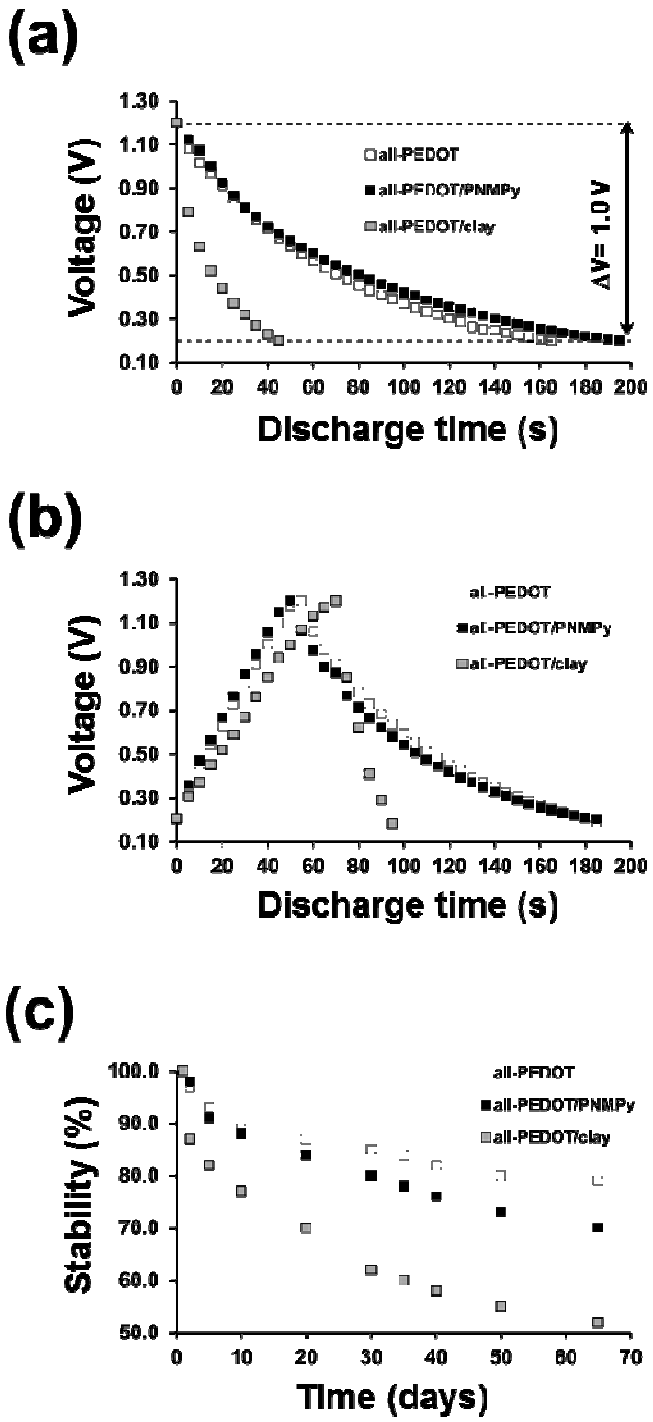

Figure 5. *For the all-PEDOT, all-PEDOT/PNMPy and all-PEDOT/clay batteries: (a) discharge curves, the LED was powered at time t = 0 s; (b) Charge-discharge cycle after 50 days according to the circuit displayed in Figure 3c; and (c) stability expressed as the variation of the time required for the charge-discharge process relative to that of the first cycle (in %) against time.*

8.2.4. Conclusions

In summary, all-PEDOT, all-PEDOT/PNMPy and all-PEDOT/clay batteries have been successfully fabricated. Although the three materials show a very high ability to store charge, the performance of batteries fabricated with PEDOT/clay electrodes is considerably lower than that of the batteries prepared using PEDOT and, specially, 3-layered electrodes. This has been attributed to the inert nature of the clay, which does not promote good electrical contacts to aid the penetration of the electrolyte in the material, which results in a poor stability. All-PEDOT and all-PEDOT/PNMPy batteries are easily rechargeable and exhibit excellent cyclability and environmental stability. The all-CP batteries prepared in this work have been successfully used to power a LED light, suggesting that they are promising in future applications as, for example, power source for devices with low-power consumption requirements. Moreover, these results combined with those previously reported[36] indicate that 3-layered films show a dual behavior, being useful for the fabrication of all-CP capacitors and batteries. Our future research is oriented towards the improvement of the electrical contacts in 3-layered electrodes to improve the performance of all-PEDOT/PNMPy batteries.

8.2.5. References

[1]. Novak, P.; Muler, K.; Santhanan, K. S. V.; Hass, O. *Chem. Rev.* **1997**, *97*, 207.

[2]. Scrosati, B. *Advances in Lithium-Ion Batteries*, (Eds: W. A. Van Schalkwijk, B. Scrosati), Kluwer, Academic/Plenum Publishers, London **2002**, 251.

[3]. Baumgarten, M.; Muellen, K. *Top. Curr. Chem.* **1994**, *169*, 1.

[4]. Levi, M. D.; Gofer, Y.; Aurbach, D. *Polym. Adv. Technol.* **2002**, *13*, 697.

[5]. Malunauskas, A.; Malinauskiené, J.; Ramanavicius, A. *Nanotechnology* **2005**, *16*, R51.

[6]. Ryu, K. S.; Kim, K. M.; Kang, S.-G.; Lee, J.; Joo, J.; Chang, S. H. *Synth. Met.* **2010**, *110*, 213.

[7]. Ryu, K. S.; Jeong, S. K,; Joo, J.; Kim, K. M. *J. Phys. Chem. B* **2007**, *111*, 731.

[8]. Cheng, F.; Tang, W.; Li, C.; Chen, J.; Liu, H.; Shen, P.; Dou, S. *Chem. Eur. J.* **2006**, *12*, 3082.

[9]. Liu, J.; Zhou, M.; Fan, L.-Z.; Li, P.; Qu, X. *Electrochim. Acta* **2010**, *55*, 5819.

[10]. Gurunathan, K.; Amalnerkar, D. P.; Trivedi, D. C. *Mater. Lett.* **2003**, *57*, 1642.

[11]. Lira-Cantú, M.; Gómez-Romero, P. *J. Electrochem. Soc.* **1999**, *146*, 2029.

[12]. Huguenin, F.; Torresi, R. M. *J. Phys. Chem. C* **2008,** *112*, 2202.

[13]. Mirmohseni, A.; Solhjo, R. *Eur. Polym. J.* **2003**, *39*, 219.

[14]. Ghanbari, K.; Mousavi, M.-F.; Shamsipur, M.; Karami, H. *J. Power Sources* **2007**, *170*, 513.

[15]. Park, K.-S.; Schougaard, S. B.; Goodenough, J. B. *Adv. Mater.* **2007**, *19*, 848.

[16]. Moon, D.-K.; Padias, A. B.; Hall, H. K. Jr.; Huntton, T.; Calvert, P. D. *Macromolecules* **1995**, *28*, 6205.

[17]. Song, H.-K.; Palmore, G. T. *Adv. Mater.* **2006**, *18*, 1764.

[18]. Yuan, L.; Wang, J.; Chew, S. Y.; Chen, J.; Guo, Z. P.; Zhao, L.; Konstantino, K.; Liu, H. K. *J. Power Sources* **2007**, *174*, 1183.

[19]. Huang, Y. H.; Goodenough, J. B. *Chem. Mater.* **2008,** *20*, 7237.

[20]. Shao, Q.-G.; Chen, W.-M.; Wang, Z.-H.; Qie, L.; Yaun, L.-X.; Zhang, W.-X.; Hu, X.-L.; Huang, Y.-H. *Electrochem. Commun.* **2011**, *13*, 1431.

[21]. Ryu, K. S.; Lee, Y.; Han, K.-S.; Kim, M. G. *Mat. Chem. Phys.* **2004**, *84*, 380.

[22]. Tang, J.; Kong, L.; Zhang, J.; Zhan, L.; Zhan, H.; Zhou, Y.; Zhan, C. *React. Funct. Mater.* **2008**, *68*, 1408.

[23]. Chang, C. C.; Her, L.-J.; Hong, J.-L. *Electrochim. Acta* **2005**, *50*, 4461.

[24]. Bahloul, A.; Nessark, B.; Chelali, N.-E.; Groult, H.; Mauger, A.; Julien, C. M. *Solid State Phys.* **2011**, *204-205*, 53.

[25]. Xiao, W.; Chen, J. S.; Lu, Q.; Lou, X. W. *J. Phys. Chem. C* **2010,** *114*, 12048.

[26]. Arbizzani, C.; Balducci, A.; Mastragostino, M.; Rossi, M.; Soavi, F. *J. Electroanal. Chem.* **2003**, *553*, 125.

[27]. Chang, C.-C.; Her, L.-J.; Hong, J.-L.; Ho, W.-L.; Liu, S.-J. *J. New Mat. Electrochem. Systems* **2008**, *11*, 49.

[28]. Sivakkumar, S. R.; Howlett, P. C.; Winther-Jensen, B.; Forsyth, M.; MacFarlane, D. R. *Electrochim. Acta* **2009**, *54*, 6844.

[29]. Murata, K.; Izuchi, S.; Yshihisa, Y. *Electrochim. Acta* **2000**, *45*, 1501.

[30]. Song, J. Y.; Wang, Y. Y.; Wan, C. C. *J. Power Sources* **1999**, *77*, 183.

[31]. Cai, Z.; Geng, M. M.; Tang, Z. *J. Mater. Sci.* **2004**, *39*, 4001.

[32]. Xuan, Y.; Sandberg, M.; Berggren, M.; Crispin, X. *Org. Electron.* **2012**, *13*, 632.

[33]. Kirchmeyer, S.; Reuter, K. *J. Mater. Chem.*, **2005**, *15*, 2077.

[34]. Groenendaal, L.; Jonas, F.; Freitag, V.; Pielartzik, H.; Reynolds, J. R. R. *Adv. Mater.* **2000**, *12*, 481.

[35]. Aradilla, D.; Estrany, F.; Armelin, E. A.; Alemán, C. *Thin Solid Films* **2012**, *520*, 4402.

[36]. Aradilla, D.; Estrany, F.; Alemán, C. *J. Phys. Chem. C* **2011**, *115*, 8430.

[37]. Aradilla, D.; Estrany, F.; Oliver, R.; Alemán, C. *Eur. Polym. J.* **2010**, *46*, 2222.

[38]. Estrany, F.; Aradilla, D.; Oliver, R.; Alemán, C. *Eur. Polym. J.* **2007**, *43*, 1876.

[39]. Aradilla, D.; Azambuja, D.; Estrany, F.; Casas, M. T.; Ferreira, C. A.; Alemán, C. *J. Mater. Chem.* **2012**, *22*, 13110.

[40]. Aradilla, D.; Estrany, F.; Azambuja, D. S.; Casas, M. T.; Puiggali, J.; Ferreira, C. A.; Alemán, C. *Eur. Polym. J.* **2010**, *46*, 977.

[41]. Aradilla, D.; Estrany, F.; Armelin, E.; Alemán, C. *Thin Solid Films* **2010**, *518*, 4203.

8.3. New insight on the optoelectronic properties of nanocomposites based on poly(3,4-ethylenedioxythiophene)-montmorillonite films.

8.3.1. Methods

The discovery of a new class of organic material known as conducting polymer (CP) in the late of 1970 opened up a new era in the field of polymer science.[1] The structure and chemical nature of CPs shows interesting electrical, electrochemical, optical and magnetic properties.[2] Specifically, optical properties associated to photoluminescence, photoelectrochemistry, electrochromism, or organic photovoltaic have been widely studied in π-organic systems.[3-5] According to their interesting optoelectronic properties, CPs have been employed to build and to design electronic devices such as organic light-emitting diodes (OLEDs),[6] organic field-effect transistors (OFETs),[7,8] solar cells,[9,10] electrochromic devices,[11,12] or electroluminiscent devices.[13] Particularly, thiophene derivatives have been performed as promising materials for optoelectronic devices. Thus, the excellent performances of poly(3-hexylthiophene) and poly(3,4-ethylenedioxythiophene (PEDOT) were reported in this field.[14-20] Within this context, the influence of optoelectronic properties in poly(3-alkylthiophenes) was examined to build flexible solar cells.[21] Furthermore, other multidisciplinary applications based on optical sensors were also built using photovoltaic properties of conducting polymers. Particularly, poly(2-methoxy-5-(20-ethylhexyloxy)-1,4-phenylenevinylene) (MEH-PPV) was successfully reported in the literature.[22] This polymer has been widely investigated and characterized[23] to enhance optoelectronic properties in terms of electroluminescence,[24] photoluminiscence[25-27] or in solar cells.[28-31] Another interesting technological application related with optoelectronic properties of CPs is devoted to the biotechnological field, which has attracted a great attention in the synthesis of nanobiocomposites. Thus, nanobiocomposites made from PAni and RNA evidenced excellent results in terms of optoelectronic properties (*e.g.* electrical dc-conductivity).[32]

Photoconductivity is the net increase of electrical conductivity of a material under irradiation.[33] This property has attracted a special attention in the field of conducting polymers due to its interesting applications. CPs such as poly(3-alkylthiophenes)[34,35] or

polyaniline (PAni) films have evidenced a persistent photoconductivity under illumination.[36-38] During the last years, investigations to improve the photoconductive response in conducting polymers by using nanotechnology have been reported.[39] Within this context, photoconductivity of CPs experimented a significant improvement in presence of fullerenes,[40] viologen,[41] nanoparticles (*e.g.* TiO_2,[42-44] ZnO[45,46]), quantum dots (*e.g.* CdS),[26,47,48] nanotubes[49] or transition-metal complexes.[50] Precisely, the field of nanotechnology has allowed to design optoelectronic devices as optical detectors, specifically, nanocomposite thin films of PAni/TiO_2 showed very strong photoresponse when exposed to UV radiation.[51] Other CPs such as PPV derivatives in presence of CdSe nanoparticles exhibited also excellent photovoltaic properties.[52] Recently, a new class of inorganic nanostructured materials designated as mineral clays have aroused a great interest since they can be employed as reinforcement in polymers. The nanocomposites based on clay exhibit interesting results in terms of mechanical properties (*e.g.* impact strength and tensile elongation at break).[53] Moreover, their properties have been employed as sensors[54] and in aerospace applications.[55] As a consequence, hybrid organic-inorganic nanocomposites have allowed to design, and to synthesize new nanocomposites with interesting technological applications.[56]

As it was discussed previously, thiophene derivatives are excellent candidates due to their excellent optoelectronic properties. The use of nanotechnology allowed to improve their photovoltaic and photoresponsive performances through CdS and CdSe single crystal nanorods,[57-59] and transition metal nanoparticles (*e.g.* TiO_2, ZnO, NiO, WoO_3).[60,61] Among thiophene derivatives, PEDOT has received a great deal of attention due to its interesting properties such as low band gap, high conductivity (up to 550 $S \cdot cm^{-1}$) and good environmental stability.[62-64] Precisely, one of its interesting properties is focused on the electronic band gap (*e.g.* the π-π^* lowest transition) due to its low value (1.6 – 1.7 eV), which provides a bluish tonality.[65] According to its properties, PEDOT has been employed in electrochromic devices,[66] fuel cells,[67] field emitter,[68] dye-sensitized solar cells DSSCs,[69] biosensor,[70] or as biomaterial.[71,72]

Lately, some works have been focused on the study of the photoconductivity for PEDOT:PSS films.[73] In this way, *Kažukauskas et al* reported several works on the photoconductivity of functionalized DNA:PEDOT-PSS films.[74-77] The investigations showed that the presence of organic bioentities such as DNA influences on the photoelectrical properties of PEDOT:PSS films under controlled conditions of temperature and light excitation.

In this study, an investigation of the electrical properties and photoconductivity of PEDOT and PEDOT-Montmorillonite (MMT) nanocomposite films is carried out. Moreover, a new insight of the conductivity mechanism and charge carrier phenomena has been discussed. Both systems were synthesized by using electrochemical methods evidencing excellent optoelectronic properties. The results revealed that the presence of MMT affects considerably the photoelectonic properties of nanocomposites, thus, a new alternative to common inorganic nanostructured materials was evidenced. The ability to tune the optoelectonic properties in CPs by using MMT allows to design photoresponsive electronic devices such as optical sensors.

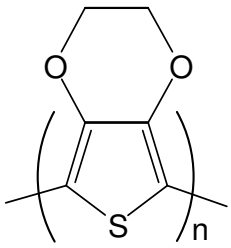

Scheme 1. *Structure of poly(3,4-ethylenedioxythiophene) (PEDOT)*

8.3.2. Methods

Materials. 3,4-ethylenedioxythiophene (EDOT), acetonitrile, and montmorillonite clay surface modified with 15-35 wt% octadecylamine and 0.5-5 wt% aminopropyltriethoxysilane were purchased from Aldrich and used as received. Anhydrous $LiClO_4$, analytical from Aldrich, analytical reagent grade, was stored in an oven at 80 ºC before use in the electrochemical trials.

Synthesis. The synthetic process used to prepare both PEDOT and PEDOT–MMT was identical to that reported in previous works,[78,79] therefore, here a brief summary is provided. All systems studied in this work were synthesized by chronocoulometry (CC) under a constant potential of 1.40 V using an PGSTAT302N AUTOLAB potentiostat-galvanostat connected to a PC computer controlled through the NOVA 1.6 software, using a three-electrode two-compartment cell under nitrogen atmosphere at 25 ºC. Steel AISI 316 sheets of 6 cm^2 were used as electrodes. After electropolymerization, all coated electrodes were cleaned with acetonitrile and dried with nitrogen. The generation medium consisted on a 10 mM of the corresponding monomer in an acetonitrile/water

solution (40:60 v/v) containing 0.1 M $LiClO_4$ as supporting electrolyte. The thickness of the films measured in this work were approximately 5µm.

The concentration of MMT in the generation medium, which is referred to that of the EDOT monomer, was estimated a value of 20 % according to our previous work.[40] Before the addition of MMT to the monomer solution, the clay was exfoliated in deionized water at neutral pH, being sonicated 10 min with an ultrasonic generator. The resulting solution was stirred for 1 day using a magnetic stirrer. Next, the generation medium and the exfoliated MMT solution were mixed and stirred for 20 h in a frozen environment (ice).

Scanning electron microscopy. SEM studies were performed to examine the surface morphology of PEDOT and PEDOT-MMT 20% w/w films after thermal degradation. Dried samples were placed in a Focussed Ion Beam Zeis Neon 40 scanning electron microscope operating at 3 kV, equipped with an EDX spectroscopy system.

Electrochemical Impedance Spectroscopy. EIS measurements were performed in potentiostatic mode at the open circuit potential (OCP) using an AUTOLAB PGSTAT 30/FRA 2 system. The amplitude of the EIS perturbation signal was 50 mV, and the studied frequency ranged from 10 kHz to 10 mHz. All the electrochemical experiments were carried out in a distilled water solution containing 0.1 M $LiClO_4$ at 25°C.

Conductivity measurements. Four-point probe measurements were performed upon films made of PEDOT and PEDOT-MMT 20% w/w films.

Photoconductivity measurements. Samples were illuminated by using a halogen lamp whose illumination intensity was monitored at 7000 lux by using a TES 1330 light meter.

8.3.3. Results and discussion

Conductivity – Temperature. Figure 1 displays the variation of conductivity with temperature. The results showed in Figure 1a) evidence that conductivity decreases exponentially with temperature, being this tendency more remarkable for PEDOT-MMT. This effect can be ascribed to the inert nature of the clay. However, Figure 1b) reflects an inverse tendency, the thermal degradation occurred at 353K during more than 40h evidenced that PEDOT-MMT films present higher conductivity than PEDOT systems. The temperature affects the chemical structure of polymers provoking a degradation process of the polymeric chains. The presence of clay inhibits the

degradation of polymers when the temperature is applied continuously, thus, the conductivity is higher in PEDOT-MMT films than PEDOT systems.

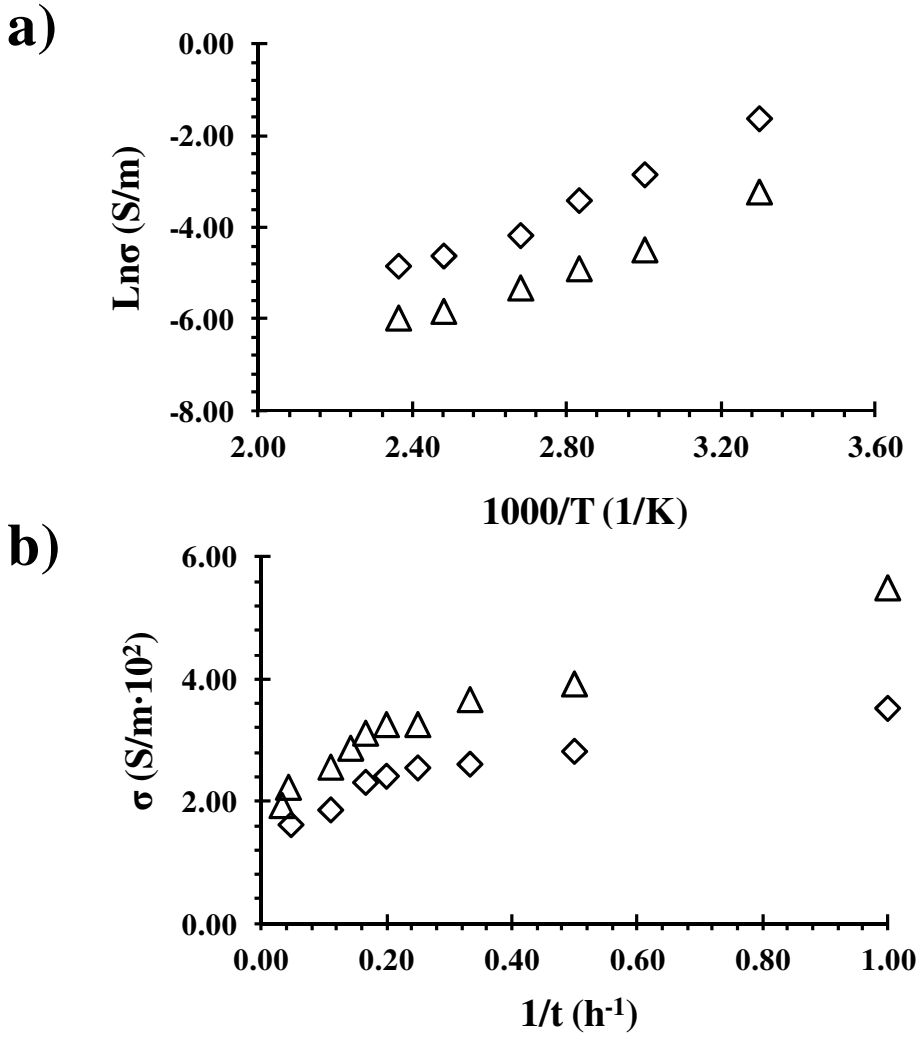

Figure 1. *a) Variation of the conductivity with inverse temperature b) Variation of the conductivity versus inverse time at 353 K. PEDOT (empty diamonds) and PEDOT –MMT 20% w/w films (empty triangles).*

The temperature dependence with electrical conductivity can be evaluated as follows according to Figure 1a):

$$\sigma = \sigma_O \exp\left(\frac{-E_\sigma}{k_B T}\right) \qquad (1)$$

where σ_o is the pre-exponential factor, E_σ is the activation energy of carriers, k_B is the Boltzmann's constant, and T is the temperature.

Conducting polymers according to their band-gap values can be considered as organic semiconductors. It has been reported that conductivity of organic semiconductor changes exponentially with inverse temperature and data fit the hopping mechanism.[80] Thus, the relation between the conductivity and temperature of conducting polymer films can provide information about the phenomena associated to the charge transport in these systems. Within this context, the variable range hopping (VRH) mechanism proposed by Mott[81] explains the transport mechanisms associated in the process of conductivity, being this mechanism predominant at low temperatures.[82] According to Mott's, Variable Range Hopping mechanism of charge transport is described as follows:

$$\sigma = \sigma_O \exp\left(\frac{-T_O}{T}\right)^{\frac{1}{1+n}} \qquad (2)$$

where σ_o T_o are the pre-exponential factor, and *n* is the hopping space dimensionality. The *n* value can be n = 1 (1-D), n = 2 (2-D) and n = 3 (3-D) VRH charge transport mechanism respectively. On the other hand, the value of *n* can be estimated from the temperature dependence with activation energy. The activation energy (E_a) is represented as follows:

$$E_a = \frac{d(\log\sigma)}{d\left(\frac{1}{k_B T}\right)} \qquad (3)$$

The combination of the equations 2 and 3 results a new equation described as follows:

$$E_a = \gamma k_B T_O \left(\frac{T_O}{T}\right)^{\gamma-1} \qquad (4)$$

where $\gamma = \frac{1}{1+n}$. By plotting Log (Ea) versus T a straight line of slope $\{-(\gamma\text{-}1)\}$ is obtained, where n corresponds approximately 3. This indicates that the 3-D variable range hopping dominates the mechanism of charge transport in PEDOT and PEDOT-MMT nanocomposites. According to this value, the equation 2 can be ascribed as:

$$\sigma = \sigma_O \exp\left(\frac{-T_O}{T}\right)^{\frac{1}{4}} \quad (5)$$

Figure 2 illustrates a linear relation between the Lnσ against temperature ($T^{-1/4}$). This tendency corroborates the conductivity mechanism associated to the variable range hopping. Thus, a 3-D variable range hopping was observed for both PEDOT and PEDOT-MMT films.

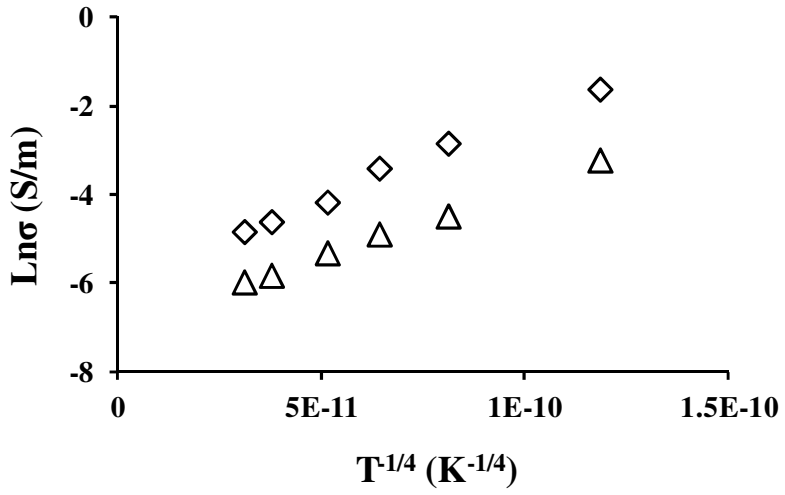

Figure 2. *Ln σ – $T^{-1/4}$ variations of PEDOT (empty diamonds) and PEDOT-MMT 20 w/w films (empty triangles).*

From Figure 2 and according to Eqn 5 some parameters associated to the conductivity mechanism can be calculated. Thus, the pre-exponential factors can be expressed as:

$$\sigma_O = e^2 L^2 \upsilon_{ph} N(E_F) \quad (6)$$

$$T_O = \frac{\lambda \alpha^3}{k_B N(E_F)} \quad (7)$$

where *e* is the electron charge, *L* is the variable hopping distance (value estimated from literature),[83] υ_{ph} is the phonon frecuency (10^{13} s^{-1}), $N(E_F)$ is the density of states about Fermi energy level, λ is a dimensionless constant (18.1), and α is the coefficient of exponential decay of the localized states involved in the hopping process.

The other two hopping parameters involved in the hopping mechanism are the hopping distance, *R*, and the average hopping energy *W*.

$$R = \left[\frac{9}{8}\pi\alpha k_B T N(E_F)\right] \quad (8)$$

$$W = \left[\frac{3}{4}\pi R^3 N(E_F)\right] \quad (9)$$

Table 1 reflects the parameters obtained in the previous equations. As can be observed density of states was found to be decreased with the incorportation of MMT in PEDOT systems. This tendency was corroborated for hopping energy and hopping distance. All results reflect that clay effect predominates and influence on the parameters associated to charge transport mechanisms.

Table 1. *Calculated Mott parameters for the PEDOT and PEDOT-MMT 20% w/w films.*

System	α[a]	$N(E_F)$[b]	R[c]	W[d]	E_σ[e]
PEDOT	$5.52\cdot10^{12}$	$8.87\cdot10^{32}$	$1.45\cdot10^{-11}$	6.37	0.13
PEDOT-MMT 20% w/w	$3.63\cdot10^{12}$	$3.35\cdot10^{32}$	$1.02\cdot10^{-11}$	0.83	0.10

[a] coefficient of exponential decay of the localized states involved in the hopping process, in cm^{-1}. [b] density of states about Fermi energy level, in $cm^{-3}eV^{-1}$. [c] average hopping distance, in cm. [d] hopping energy, in eV. [e] activation energy of carriers, in eV

Morphology. As could be observed in the previous section, the conductivity is affected considerably by temperature effect. According to Fig. 3, the temperature affects the morphology of PEDOT and PEDOT-MMT films. Fig 3a) shows the formation of agglomerated clusters forming a compact layer with high protuberances after 8h at 353K, next, when the time increases the clusters evidence thermal degradation and the structure loses its compactness and the clusters are smaller (Fig. 3b). On the other hand, Fig 3c) shows the morphology of PEDOT after 8h. The micrograph illustrates the formation of dispersed clusters which evidenced a strong degradation when the time increases up tp 20h. (Fig 3d).

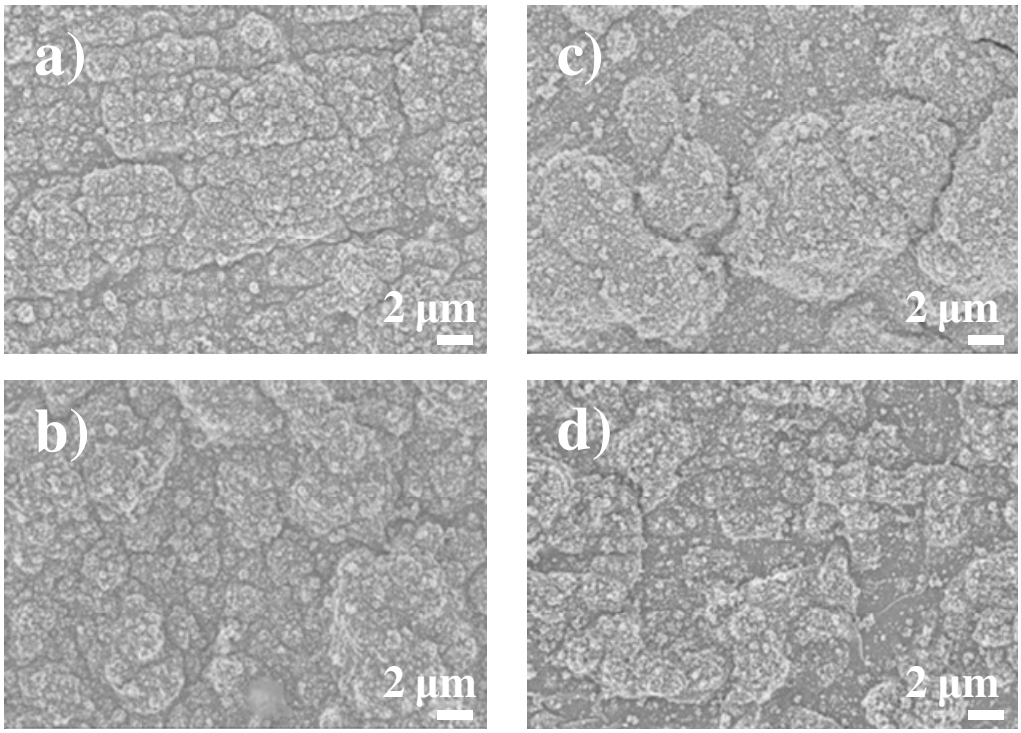

Figure 3. *SEM micrographs of a) PEDOT-MMT and b) PEDOT 20% w/w films after 8h of thermal degradation at 353 K. c) PEDOT- MMT 20% w/w and d) PEDOT films after 20h at the same temperature.*

Electrochemical Impedance Spectroscopy studies. The Nyquist plots for the electrochemical impedance spectra recorded PEDOT and PEDOT-MMT systems are displayed in Fig.4. All the curves show a single semicircle in the high-frequency region, intermediate frequency 45º line representing the Warburg diffusion element, and a nearly vertical straight line in the low frequency region, indicating that the electrode process is dominated by charge transfer (*i.e.* electrochemical reaction) in the former region and by charge diffusion (*i.e.* mass transfer) in the latter one.[84] The first intercept of the semicircle with the real axis (Z') at high frequencies is the measure of the solution

resistance. The origin of the semicircle at the higher-frequency range is due to the ionic charge-transfer resistance (R_{CT}) at the electrode-solution interface, while it is given by the diameter of the semicircle along the real axis Z'.

The spectra were fitted using an equivalent circuit (EC). The aim of the choice of the EC was to obtain a satisfactory fitting of the experimental data, where the circuit elements can be associated with the physical phenomena that are probably taking place at the electrode surface. The EC proposed was $R_s(CPE_1[R_{CT}W])C_{PS}$, where Rs represents the electrolyte resistance, CPE_1 the double layer capacitance, R_{CT} the charge-transfer resistance at the polymer film–electrolyte interface, which is in serial connection with the Warburg element (W), and C_{PS} the faradaic pseudo-capacitance corresponding to a practically vertical line at low frequency region of the EIS spectra. The double layer capacitance was replaced by a constant phase element (CPE) that describes a non-ideal capacitor when the phase angle is different from -90º. The CPE impedance has been expressed as:

$$Z_{CPE} = [Q\ (j\omega)^n\ ]^{-1} \qquad (10)$$

The CPE represents a capacitor and a resistor for n = 1 and n = 0, respectively, while it is associated with a diffusion process when n = 0.5. The CPE impedance is attributed to the distributed surface reactivity, surface heterogeneity, and roughness of the current and potential distribution, which in turn are related with the electrode geometry and the electrode porosity.[85] The Warburg impedance was included taking into account the diffusion phenomena.[86] The quality of fitting was evaluated using the error percentage associated to each circuit component, errors smaller than 5% being obtained in all cases.

Table 2 shows the simulated values obtained by fitting the EIS experimental spectra presented in Fig. 4. As can be seen in Table 2, increased R_{CT} values were detected for nanocomposite systems, which can be ascribed to the effect of the clay into the polymeric matrix. The presence of clay avoids and blocks the entrance of ions (ClO_4^-) increasing the ionic charge-transfer resistance (R_{CT}). Another important feature of the EIS analysis concerns to the Warburg element (W). The W element is associated to diffusion phenomena reflecting the same tendency observed for R_{CT}.

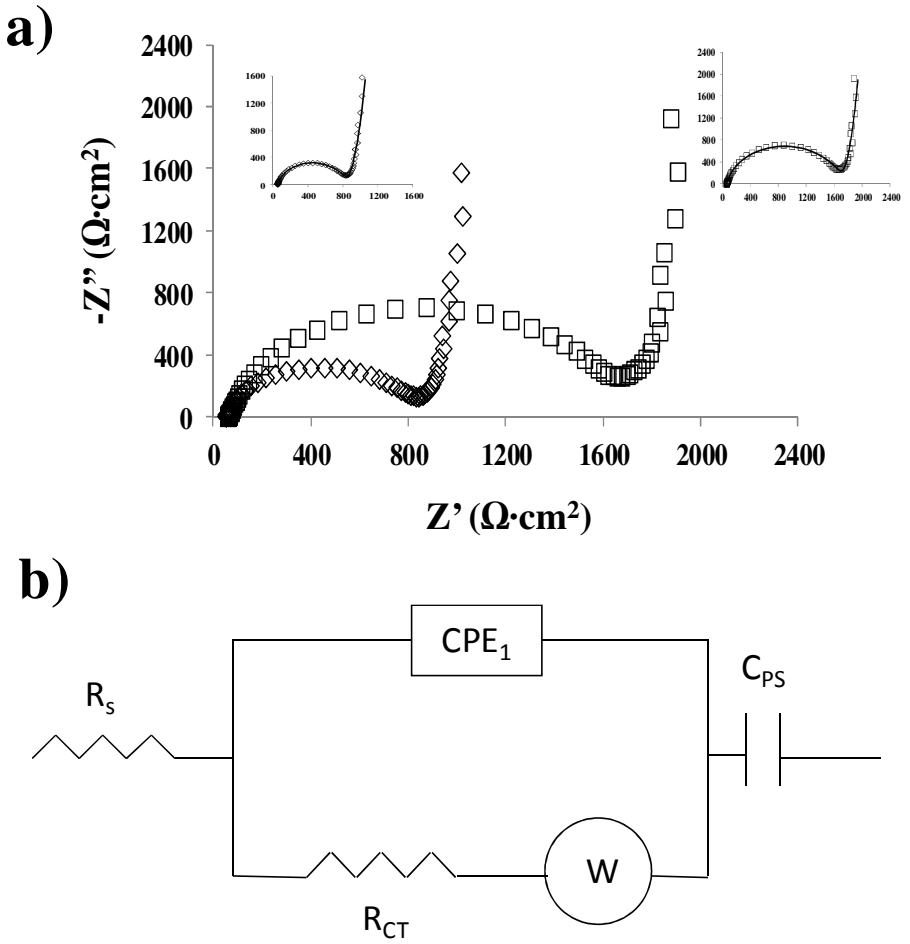

Figure 4. *a) Nyquist diagrams of PEDOT (empty diamonds) and PEDOT-MMT 20% w/w (empty squares) films as prepared at room temperature. b) Equivalent circuit used to simulate the experimental spectra displayed in a). The insets in a) provide the fitting according to the equivalent circuit model depicted in b) to produce the parameter listed in Table 2.*

Table 2. *Fitting parameters used to simulate the EIS data obtained for the systems studied in this work (Figure 4).*

System	R_s[a]	CPE_1[b]	n_1	R_{CT}[d]	W[e]	C_{PS}[f]
PEDOT	54.20	42.60	0.86	776.82	97.29	208.42
PEDOT-MMT 20% w/w	61.40	49.14	0.87	1624.13	135.67	188.67

[a] Electrolyte resistance, in $\Omega \cdot cm^2$. [b] Double layer capacitance, in $\mu F \cdot cm^{-2} \cdot s^{n-1}$. [d] Charge-transfer resistance at the polymer film–electrolyte interface, in $\Omega \cdot cm^2$. [e] Warburg resistance, in $\Omega \cdot cm^2$. [f] Faradaic pseudo-capacitance, in $mF \cdot cm^{-2}$.

Photoconductivity. Conductivity against radiation was evaluated using two different conditions according to Figure 5. The first one was studied using dark conditions. In this case, PEDOT and PEDOT-MMT films showed similar tendencies, where the conductivity decreases with time. In this way, PEDOT films showed the highest conductivity values as can be observed in Fig. 5a). However, under illumination (*e.g.* 7000 lux), the conductivity showed a decrease with time in all cases, but the conductivity for PEDOT-MMT systems increases considerably, thus, a initial conductivity value of approximately 60 $S/m \cdot 10^2$ was measured. This result evidences that the effect clay favors the conductivity in presence of light radiation. Moreover, the stability of the conductivity was improved in all cases, being more stable for PEDOT films.

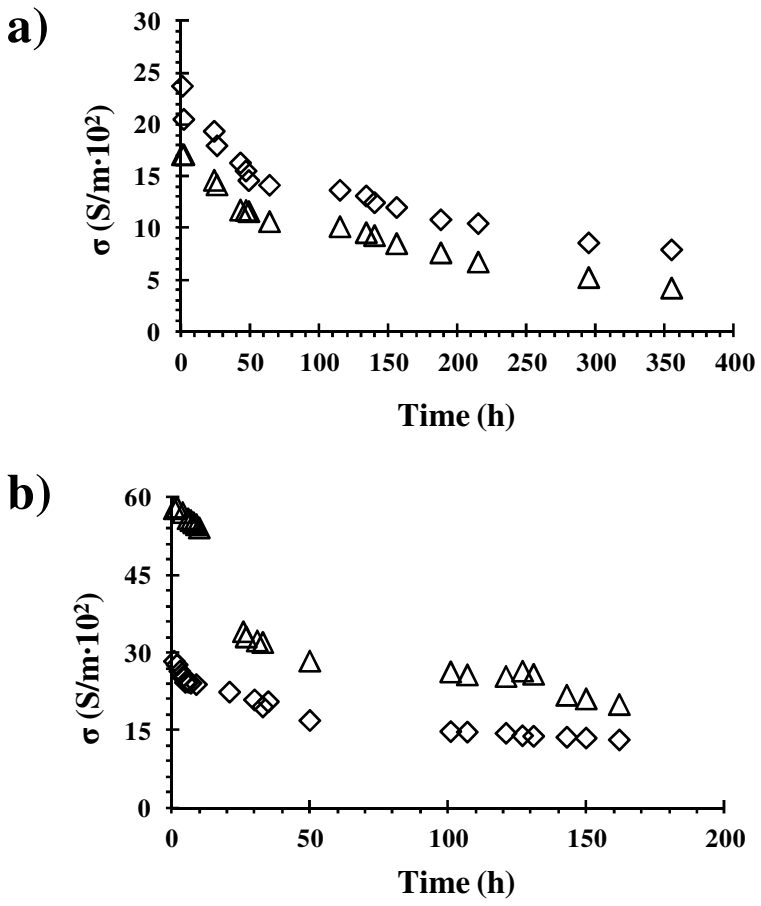

Figure 5. *a) Variation of the conductivity versus time at dark illumination. b) Variation of the conductivity versus time at intensity illumination (7000 lux). PEDOT (empty diamonds) and PEDOT – MMT 20% w/w films (empty triangles).*

The photoconductivity can be defined as:

$$\sigma = e\left[\left(n_h \mu_h \tau_h\right) + \left(n_e \mu_e \tau_e\right)\right] \tag{11}$$

where n is the number of either electrons or holes, μ is the carrier mobility and τ is the carrier lifetime.

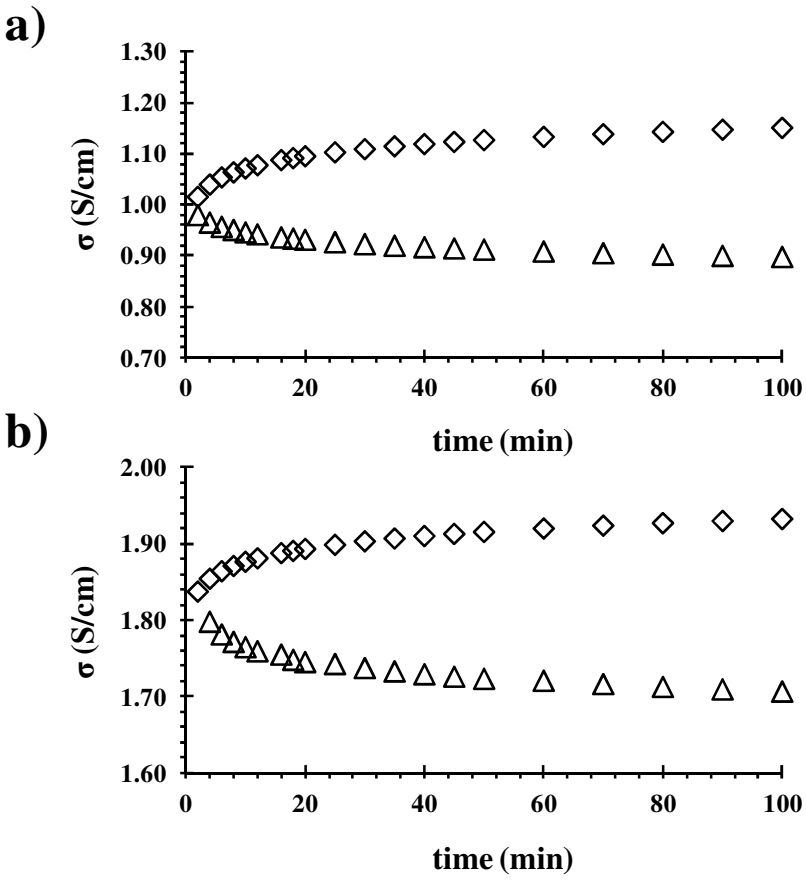

Figure 6. *a) Photoconductive response for PEDOT films and b) PEDOT-MMT 20% w/w films at room temperature. Illumination is indicated as empty diamonds whereas darkness is indicated as empty triangles.*

Figure 6 shows the photoconductive response for PEDOT and PEDOT-MMT films. As can be evidenced, conductivity increases with the illumination, whereas conductivity decreases in dark illumination. This effect is known as photoconductivity. In specific terms, photoconductivity is the net increase of electrical conductivity of a material under irradiation.[33] The photosensitive reponses of the systems displayed in Figure 6 were fitted by using the following relation:

$$R_{(t)} = R_{\infty} + \left(R_O - R_{\infty}\right) e^{-\left(\frac{t}{\tau}\right)} \tag{12}$$

where R_∞ is the saturation resistance, R_o is the initial resistance, and τ is the characteristic time.

The photoconductivity mechanism observed in PEDOT and PEDOT-MMT films could be fitted to first order linear systems according to their relatively slow response, thus, the τ was estimated 14.79 and 15.95 min for PEDOT and PEDOT-MMT systems, respectively. The result reflect that hybrid nanocomposites present a similar characteristic compared with PEDOT films, consequently, conducting polymers and hybrid nanocomposites can be employed as photoresponsive detectors.

8.3.4. Conclusions

PEDOT and PEDOT-MMT hybrid nanocomposites were successfully obtained by *in-situ* electropolymerization in a water/acetonitrile (40:60 v/v) solution. The results showed that the presence of clay affects the conductivity of nanocomposites. Due to the inert and insulating layers of MMT, the conductivity decreased for PEDOT-MMT nanocomposites at room temperature. On the other hand, the conductivity was affected by temperature. Thus, conductivity values for both PEDOT and PEDOT-MMT systems decreased with temperature, being the highest values for PEDOT films. Precisely, the study of conductivity against temperature allowed to evaluate and to explore the charge transport mechanisms in CPs. In this context, a three-dimensional (3-D) VRH model was confirmed by fitting the $Ln\sigma$ vs $T^{-1/4}$ for both PEDOT and PEDOT-MMT systems.

The effect of temperature on the morphology was studied by scanning electron microscopy. SEM images revealed that the thermal degradation affects considerably the morphology, as a consequence, a reduction of the clusters size was evidenced in PEDOT films. The clay precludes the thermal degradation acting as barrier effect. EIS studies concluded that the presence of clay avoids and blocks the entrance of ions (ClO_4^-) increasing the ionic charge-transfer resistance (R_{CT}).

Finally, the effect of radiation on the structures of PEDOT and PEDOT-MMT films showed photoconductive responses, consequently, these materials can be employed as photoreceptor devices.

8.3.5. References

[1]. Shirakawa, H.; Louis, E. J.; MacDiarmid, A. G.; Chiang, C. K.; Heeger, A. J. *Chem. Soc. Chem. Commun.* **1977**, 578.

[2]. MacDiarmid, A. G. *Angew. Chem. Int. Ed.* **2001**, *40*, 2581.

[3]. Xu, Y.; Zhang, F.; Feng, X. *Small* **2011**, *7*, 1338.

[4]. Moliton, A.; Hiorns, R. *Polym. Int.* **2004**, *53*, 1397.

[5]. Spanggaard, H.; Krebs, *Sol. Energ. Mat. Sol. C.* **2004**, *83*, 125.

[6]. Gurunathan, K.; Murugan, A. V.; Marimuthu, R.; Mulik, U. P.; Amalnerkar, D. P. *Mater. Chem. Phys.* **1999**, *61*, 173.

[7]. Fraboni, B.; DiPietro, R.; Cavallini, A.; Cosseddu, P.; Bonfiglio, A.; Vogel, J. O. *Appl. Phys. A* **2009**, *95*, 37.

[8]. Virkar, A. A.; Mannsfeld, S.; Bao, Z.; Stingelin, N. *Adv. Mater.* **2010**, *22*, 3857.

[9]. Cravino, A.; Sariciftci, N. S. *J. Mater. Chem.* **2002**, *12*, 1931.

[10]. Kippelen, B.; Brédas, J.-L. *Energy Environ. Sci.* **2009**, *2*, 251.

[11]. Camurlu, P.; Bicil, Z.; Gultekin, C.; Karagoren, N. *Electrochim. Acta* **2012**, *63*, 245.

[12]. Atak, S.; Içli-Özkut, M.; Önal, A. M.; Cihaner, A. *J. Polym. Sci. Pol. Chem.* **2011**, *49*, 4398.

[13]. Yin, H.-E.; Wu, C.-H.; Kuo, K.-S.; Chiu, W.-Y.; Lee, C.-F.; Li, N.-T.; Chen, P.-J. *Synth. Met.* **2011**, *161*, 1878.

[14]. Jang, K.-S.; Kim, D. O.; Hee, J.-H.; Hong, S.-C.; Lee, T.-W.; Lee, Y.; Nam, J.-D. *Org. Electron.* **2010**, *11*, 1868.

[15]. Jang, K.-S.; Eom, Y.-S.; Lee, T.-W.; Kim, D. O.; Oh, Y. S.; Jung, H.-C.; Nam, J. D. *ACS Appl. Mater. Inter.* **2009**, *1*, 1567.

[16]. Dayal, S.; Reese, M. O.; Ferguson, A. J.; Ginley, D. S.; Rumbles, G.; Kopidakis, N. *Adv. Funct. Mater.* **2010**, *20*, 2629.

[17]. Yun, M. H.; Lee, J.; Cho, S.; Yang, C.; Kim, J. Y. *Curr. Appl. Phys.* **2012**, *12*, 531.

[18]. Tada, K. *Sol. Energ. Mat. Sol. C.* **2013**, *108*, 82.

[19]. Tada, K.; Onoda, M. *Sol. Energ. Mat. Sol. C.* **2012**, *100*, 246.

[20]. Nardes, A. M.; Ferguson, A. J.; Whitaker, J. B.; Larson, B. W.; Larsen, R. E.; Maturová, K.; Graf, P. A.; Boltalina, O. V.; Strauss, S. H.; Kopikadis, N. *Adv. Funct. Mater.* **2012**, *22*, 4115.

[21]. Al-Ibrahim, M.; Roth, H.-K.; Schroedner, M.; Konkin, A.; Zhokhavets, U.; Gobsch, G.; Scharff, P.; Sensfuss, S. *Org. Electron.* **2005**, *6*, 65.

[22]. Yakuphanoglu, F. *Sensor Actuat. A* **2008**, *141*, 383.

[23]. Nguyen, T.-Q.; Martini, I. B.; Liu, J.; Schwartz, B. J. *J. Phys. Chem. B* **2000**, *104*, 237.

[24]. Wu, C.-S.; Yang, Y.-J.; Fang, S.-W.; Chen, Y. *J. Polym. Sci. Pol. Chem.* **2012**, *50*, 3875.

[25]. Deng, D.; Shi, M.; Chen, F.; Chen, L.; Jiang, X.; Che, H. *Sol. Energ.* **2010**, *84*, 771.

[26]. Petrella, A.; Tamborra, M.; Cosma, P.; Curri, M. L.; Striccoli, M.; Comparelli, R.; Agostiano, A. *Thin Solid Films* **2008**, *516*, 5010.

[27]. Tada, K.; Onoda, M. *Sol. Energ. Mat. Sol. C.* **2011**, *95*, 688.

[28]. Ravirajan, P.; Haque, S. A.; Durrant, J. R.; Bradley, D. D. C.; Nelson, J. *Adv. Funct. Mater.* **2005**, *15*, 609.

[29]. Ayllon, J. A.; Lira-Cantu, M. *Appl. Phys. A* **2009**, *95*, 249.

[30]. Onoda, M.; Tada, K. *Thin Solid Films* **2001**, *393*, 284.

[31]. Lira-Cantu, M.; Krebs, F. C. *Sol. Energ. Mat. Sol. C.* **2006**, *90*, 2076.

[32]. Mukherjee, P.; Nandi, S.; Nandi, A. K. *Synth. Met.* **2012**, *162*, 904.

[33]. Bube, R. H. *"Photoconductivity of Solids"* **1967**, Ed. John Wiley & Sons, New York.

[34]. Micaroni, L.; Dini, D.; Decker, F.; De Paoli, M. A. *Electrochim. Acta* **1998**, *44*, 753.

[35]. Komolov, A.; Schaumburg, K.; Monakhov, V. *Synth. Met.* **1999**, *105*, 29.

[36]. Bubb, D. M.; O'Malley, S. M.; Antonacci, C.; Belmont, R.; McGill, R. A.; Crimi, C. *Appl. Phys. A* **2005**, *81*, 119.

[37]. Sankir, N. D.; Sankir, M.; Parlak, M. *Appl. Phys. A* **2009**, *95*, 589.

[38]. Bondarenko, V. E.; Zhuravleva, T. S.; Efimov, O. N.; Nikolaeva, G. V. *Synth. Met.* **1997**, *84*, 793.

[39]. Kim, F. S.; Ren, G.; Jenekhe, S. A. *Chem. Mater.* **2011**, *23*, 682.

[40]. Peet, J.; Soci, C.; Coffin, R. C.; Nguyen, T. Q.; Mikhailovsky, A.; Moses, D.; Bazan, G. C. *Appl. Phys. Lett.* **2006**, *89*, 252105.

[41]. Park, J. Y.; Lee, S. B.; Park, Y. S.; Park, Y. W.; Lee, C. H.; Lee, J. I.; Shim, H. K. *Appl. Phys. Lett.* **1998**, *72*, 2871.

[42]. Däubler, T. K.; Glowacki, I.; Scherf, U.; Ulanski, J.; Hörhold, H.-H.; Neher, D. *J. Appl. Phys.* **1999**, *86*, 6915.

[43]. Sharma, G. D. S.; Roy, M. S. *J. Mater. Sci. – Mater. Electron.* **2004**, *15*, 69.

[44]. Han, Y.-G.; Wu, L. L. *J. Electron. Mater.* **2011**, *40*, 2147.

[45]. Mridha, S.; Basak, D. *Appl. Phys. Lett.* **2008**, *92*, 142111.

[46]. Venkataprasad, S.; Govindaraj, A.; Rao, C. N. R. *Sol. Energ. Mat. Sol. C.* **2011**, *95*, 2318.

[47]. Madani, A.; Nessark, B.; Boukherroub, R.; Chehimi, M. M. *J. Electroanal. Chem.* **2011**, *650*, 176.

[48]. Bera, D.; Qian, L.; Tseng, T.-K.; Holloway, P. H. *Mater.* **2010**, *3*, 2260.

[49]. Kim, K.; Kim, B. H.; Joo, S.-H.; Park, J. S.; Joo, J.; Jin, J.-I. *Adv. Mater.* **2005**, *17*, 464.

[50]. Liu, S.-J.; Chen, Y.; Xu, W.-J.; Zhao, Q.; Huang, W. *Macromol. Rapid Commun.* **2012**, *33*, 461.

[51]. Sharma, S.; Pal, A. R.; Chutia, J.; Bailung, H.; Sarma, N. S.; Dass, N. N.; Patil, D. *Appl. Surf. Sci.* **2012**, *258*, 7897.

[52]. Liang, Z.; Dzienis, K. L.; Xu, J.; Wang, Q. *Adv. Funct. Mater.* **2006**, *16*, 542.

[53]. Chen, B.; Evans, J. R. G. *Soft Matter* **2009**, *5*, 3572.

[54]. Mousty, C. *App. Clay Sci.* **2004**, *27*, 159.

[55]. Njuguna, J.; Pielichowski, K. *Adv. Eng. Mater.* **2004**, *6*, 193.

[56]. Sanchez, C.; Julian, B.; Belleville, P.; Popall, M. *J. Mater. Chem.* **2005**, *15*, 3559.

[57]. Liao, H.-C.; Chen, S.-Y.; Liu, D.-M. *Macromolecules* **2009**, *42*, 6558.

[58]. Schierhorn, M.; Boettcher, S. W.; Peet, J. H.; Matioli, E.; Bazan, G. C.; Stucky, G. D.; Moskovits, M. *ACS Nano* **2010**, *4*, 6132.

[59]. Zotti, G.; Vercelli, B.; Berlin, A.; Pasini, M.; Nelson, T. L.; McCullough, R. D.; Virgili, T. *Chem. Mater.* **2010**, *22*, 1521.

[60]. Nogueira, A. F.; Micaroni, L.; Gazotti, W. A.; De Paoli, M.-A. *Electrochem. Commun.* **1999**, *1*, 262.

[61]. Chen, S.; Manders, J. R.; Tsang, S.-W.; So, F. *J. Mater. Chem.* **2012,** DOI: 10.1039/c2jm33838f.

[62]. Groenendaal, L. B.; Jonas, F.; Freitag, D.; Pielartzik, H.; Reynolds, J. R. *Adv. Mater.* **2000**, *12*, 481.

[63]. Kirchmeyer, S.; Reuter, K. *J. Mater. Chem.* **2005**, *15*, 2077.

[64]. Pettersson, L.; Johansson, T.; Carlsson, F.; Arwin, H.; Inganas, O. *Synth. Met.* **1999**, *101*, 198.

[65]. Dietrich, M.; Heinze, J.; Heywang, G.; Jonas, F. *J. Electroanal. Chem.* **1994**, *369*, 87.

[66]. Kumar, A.; Welsh, D. M.; Morvant, M. C.; Piroux, F.; Abboud, K. A.; Reynolds, J. R. *Chem. Mater.* **1998**, *10*, 896.

[67]. Winther-Jensen, B.; Winther-Jensen, O.; Forsyth, M.; MacFarlane, D. R. *Science* **2008**, *321*, 671.

[68]. Joo, J.; Park, S.-H.; Seo, D.-S.; Lee, S.-J.; Kim, H.-S.; Ryu, K.-W.; Lee, T.-J.; Seo, S.-H.; Lee, C.-L. *Adv. Funct. Mater.* **2005**, *15*, 1465.

[69]. Koh, J. K.; Kim, J.; Kim, B.; Kim, J. H.; Kim, E. *Adv. Mater.* **2011**, *23*, 1641.

[70]. Santhosh, P.; Manesh, K. M.; Uthayakumar, S.; Komathi, S.; Gopalan, A. I.; Pee, K.-P. *Bioelectrochemistry* **2009**, *75*, 61.

[71]. Richardson-Burns, S. M.; Hendricks, J. L.; Foster, B.; Povlich, L. K.; Kim, D-H.; Martin, D. C. *Biomaterials* **2007**, *28*, 1539.

[72]. Collazos-Castro, J. E.; Polo, J. L.; Hernández-Labrado, G. R.; Padial-Cañete, V.; García-Rama, C. *Biomaterials* **2010**, *31*, 9244.

[73]. Lilly, G. D.; Whalley, A. C.; Grunder, S.; Valente, C.; Frederick, M. T.; Stoddart, J. F.; Weiss, E. A. *J. Mater. Chem.* **2011**, *21*, 11492.

[74]. Kažukauskas, V.; Pranaitis, M.; Sakavičius, A.; Krupka, O.; Kajzar, F.; Sahraoui, B. *Mol. Cryst. Liq. Cryst.* **2012**, *554*, 83.

[75]. Kažukauskas, V.; Arlauskas, A.; Pranaitis, M.; Krupka, O.; Kajzar, F.; Essaidi, Z.; Sahraoui, B. *Mol. Cryst. Liq. Cryst.* **2010**, *522*, 203.

[76]. Kažukauskas, V.; Pranaitis, M.; Arlauskas, A.; Krupka, O.; Kajzar, F.; Essaidi, Z.; Sahraoui, B. *Opt. Mater.* **2010**, *32*, 1629.

[77]. Kažukauskas, V.; Pranaitis, M.; Krupka, O.; Sahraoui, B. *Acta Phys. Pol. A* **2011**, *119*, 151.

[78]. Aradilla, D.; Estrany, F.; Azambuja, D. S.; Casas, M. T.; Puiggali, J. Ferreira, C. A.; Alemán, C. *Eur. Polym. J.* **2010**, *46*, 977.

[79]. Aradilla, D.; Azambuja, D.; Estrany, F.; Casas, M. T.; Ferreira, C. A.; Alemán, C. *J. Mater. Chem.* **2012**, *22*, 13110.

[80]. Yoon, C. O.; Reghu, M.; Moses, D.; Heeger, A. J.; Cao, Y.; Chen, T.-A.; Wu, X.; Rieke, R. D. *Synth. Met.* **1995**, *75*, 229.

[81]. Mott, N. F. *Philos. Mag.* **1969**, *19*, 835.

[82]. Moreau, C.; Antony, R.; Moliton, A.; François, B. *Adv. Mat. Opt. Electron.* **1997**, *7*, 281.

[83]. Nardes, A. M.; Janssen, R. A. J.; Kemerink, M. *Adv. Funct. Mater.* **2008**, *18*, 865.

[84]. Li, N.; Shan, D.; Xue, H. *Eur. Polym. J.* **2007**, *43*, 2532.

[85]. Jorcin, J.-B.; Orazen, M. E.; Pébère, N.; Tribollet, B. *Electrochim. Acta* **2006**, *51*, 1473.

[86]. Walter, G. W. *Corros. Sci.* **1986**, *26*, 681.

Chapter 9. Summary and discussion of the results

The synthesis, characterization, application and development of novel organic conducting polymers were the main objectives of this thesis. The results have been divided into five groups as follows:

- Multilayered systems based on conducting polymers
- Influence of substrate on the properties of conjugated polymers
- Nanotechnology in the field of π-conjugated systems
- Functionalized conducting polymers
- Optoelectronic properties in conducting polymers

Multilayered systems based on conducting polymers and influence of substrate on the properties of conjugated polymers

Several strategies based on the layer-by-layer technique through electrochemical methods were investigated to build multilayered systems. This procedure showed that multilayered systems exhibit excellent electrochemical properties in terms of specific capacitance, storage charge and loss of electrostability, respectively. The results evidenced a clear synergistic effect among layers, which provides them a potential application as supercapacitors. Thus, the performance of multilayered systems based on thiophene and pyrrole derivatives was better than pure homopolymers and copolymers, showing that the interface plays a key role on the design of supercapacitors. However, comparison between multilayered systems made of two and three conducting polymers indicates that the third component introduces heterogeneity in the interfaces between consecutive layers, reducing the ability to storage charge. Other structural factors such as the porosity influences on the capacitive properties of multilayered systems, since it favors the access and exit of anions into polymeric backbone. Analyses of the morphology, topography and roughness of the surfaces indicate clearly the direct relation between specific capacitance and structure of the components. Consequently, after hundreds of consecutive oxidation-reduction processes, the porosity in multilayered systems remained relatively high, whereas it was moderate or even null in the homopolymers, this difference being crucial to understanding the very different electrochemical degradation of the specific capacitance observed for these materials. Within this context, multilayered systems were used to fabricate a supercapacitor in the type I configuration, which was found to present a very high specific capacitance compared with pure homopolymers. According to this data, some procedures were

carried out to improve the performance of supercapacitors based on multilayered systems. In this way, symmetric ultracapacitors were fabricated considering nanometric 3-layered films made of alternated layers of poly(3,4-ethylenedioxythiophene) (external and internal layers) and polypyrrole (intermediate layer) deposited on steel uncoated and coated with octanethiol self-assembled monolayers. The highest electrochemical and capacitance parameters (*i.e.* electroactivity, doping level, stored charge, specific capacitance, Coulomb efficiency, energy density and power density) correspond to the ultracapacitor derived from the assembly of 3-layered films deposited on pre-treated steel. Thus, the interface separating the octanethiol monolayer and the most internal layer of the 3-layered film produces a very favorable interaction, which promotes important electrochemical benefits similar to those found for the interfaces in conventional multilayered films.

Modification of substrates employing self-assembled monolayers of octanethiol provided interesting results in the field of energy storage as it was discussed previously. Within this context, the influence of the alkanethiol monolayers onto stainless steel substrates provided also an important influence on the process of electrodeposition, porosity, morphology, topology, and roughness of ultra-thin PEDOT films. Such changes depend on both the length of the alkyl chain in the alkanethiol and the incubation period used for the preparation of self-assembled monolayers. The modification of substrates employing alkanethiols monolayers evidenced that PEDOT films deposited on treated substrates exhibited higher protection against corrosion than PEDOT films deposited on bare stainless steel substrates. Although steel substrates has been widely employed in this thesis, other substrates such as ITO were also studied. ITO substrates showed a peculiar characteristic since this substrate affected considerably the growing process of some conducting polymers, and consequently their structural and morphological properties. Thus, during the process of electropolymerization an ultraporous three-dimensional network involving ultrathin sticks with a fiber-morphology was evidenced for PEDOT films. This characteristic growth allowed to design asymmetric and symmetric supercapacitors by assembling electrodes of PEDOT deposited on ITO and steel. The excellent performance as supercapacitor was obtained in the ITO/Steel configuration.

Nanotechnology in the field of π-conjugated systems

The innovation of new hybrid nanocomposites was an important goal in this thesis. The synthesis of new nanocomposites from electrochemical techniques highlighted the validity of these methods. One of the most important challenges in the field of nanotechnology consists of obtaining exfoliated nanostructures, which were evaluated in this work by means of microscopic, morphological, spectroscopic and structural techniques. Thus, exfoliated nanocomposites of poly(3,4-ethylenedioxythiophene) and montmorillonite were synthesized and characterized using concentrations of clay ranging from 1% w/w to 50% w/w. The electrochemical properties revealed that the electroactivity of the nanocomposites is higher than that of the individual homopolymer, while the electrical conductivity is lower in the case of hybrid nanocomposites. The excellent capacitive properties exhibited in PEDOT-MMT nanocomposites allowed to develop ultracapacitors, specifically, Type I and II ultracapacitors were fabricated using nanometric and micrometric films of PEDOT and PEDOT-MMT. The highest specific capacitance value was obtained employing a concentration of clay of 20 % using nanometric and micrometric type II ultracapacitors. Again, the structural scale played a crucial role on the properties of nanocomposites. The development of new hybrid nanocomposites was also carried out using modified organic- montmorillonite, since it favours the exfoliation and compatibility with organic systems. Thus, multilayered nanocomposites of poly(3,4-ethylenedioxythiophene) and poly(pyrrole) in presence of unmodified and modified montmorillonite were synthesized by the electrochemical layer-by-layer technique. Multilayered nanocomposites evidenced excellent electrochemical properties in terms of electroactivity, charge storage and electrochemical stability for both types of clay. On the other hand, the electrical conductivity of multilayered nanocomposites was evidenced to be affected by the influence of layers, the type of clay and the chemical nature of the polymers. Besides, electrochemical impedance spectroscopy studies revealed that nanocomposites in presence of modified montmorillonite showed the best protection against corrosion.

Functionalized conducting polymers

Throughout this thesis some studies based on the functionality of conducting polymers were carried out. In basis of the results, investigations of electron-withdrawing sustituents showed to affect the electronic and structural properties of

conducting polymers. The first group concerns to halide atoms, which were studied in the family of 3-halidethiophenes. Thus, poly(3-halidethiophene)s were synthesized by anodic polymerization in boron trifluoride diethyletherate in presence of tetrabutylammonium tetrafluoroborate in the interval ranging from 1.60 to 1.90 V. The potential applied for the generation of the polymers was found to affect considerably both physical and electrochemical properties, whereas the density and the electrical conductivity remain practically unaltered in the range of potential (1.60 – 1.90 V). Halide atoms, which evidence a strong electronegativity according to their electronic structure, reflected a clear change on the optical, electrochemical, electrical, electronic and morphological properties of 3-halidethiophenes. Thus, the electrochemical stability and porosity are smaller for poly(3-bromothiophene) than for poly(3-chlorothiophene) while the π-π^* lowest transition energy is higher for the former than for the latter. The ionization potential and the ε_g were predicted to increase when the π-donor character of the halogen atom decreases. Precisely, the optical properties of some poly(3-halidethiophenes), specifically, poly(3-chlorothiophene) showed important colour differences corresponding to its oxidized and reduced states. Regarding to this data, oxidized and reduced poly(3-chlorothiophene) films were found to be blue and Bordeaux red, respectively. This peculiar characteristic indicated that this polymer is a potential candidate for the fabrication of very stable electrochromic devices. Accordingly, an all-thiophene electrochromic device made of poly(3,4-ethylenedioxythiophene) and poly(3-chlorothiophene) was successfully fabricated with very remarkable redox stability. At theoretical level, quantum chemical calculations on model oligomers evidenced that the conformational properties of poly(3-halidethiophenes) are dominated by steric interactions and, therefore, are significantly influenced by the size of the halogen atoms. Moreover, the electronic properties predicted by using quantum mechanics calculations evidenced an excellent agreement with experimental results.

The second group of strong electron-withdrawing sustituents evaluated in this thesis corresponds to cyano group, which was examined in the family of poly[N-(2-cyanoalkyl)pyrrole]s. In this way, PNCPy was studied and characterized by means of electrochemical, morphological and structural techniques at both oxidized and reduced states. The results showed that cyano group induces changes in the structural and electronic properties of pyrrole, which favour its application for the fabrication of electrical circuit components. Within this context, theoretical calculations indicated that

the electronic properties of poly[N-(2-cyanoalkylpyrroles)] are not only influenced by effect of the conformation in the conjugation of the π-system but also by the existence of secondary oxidative processes on the pyrrole ring. The combination of experimental information and quantum mechanical calculations proved to be essential to propose a structural model, which consists of a cross-linked structure formed by small branches of around nine repeating units in each one, with a carbonyl group at the last repeating unit of each branch.

In this thesis, a technological application based on chemical sensors was carried out using PNCPy and Py films. Thus, a theoretical study based on quantum mechanical calculations was carried out to evaluate the interactions of these polymers with polar solvent molecules (e.g. water, methanol, acetonitrile and chloroform). The complex model was used to study the specific interactions and to evaluate their conformations at different oxidized states (neutral, cationic, and dicationic states, respectively) employing B3LYP/6-31G(d) and MP2/6-31+G(d,p) calculations. Accordingly, conformational changes induced by the presence of cyano group and solvent molecules have been shown to play an important role on the electronic properties, which were found to be in excellent agreement with experimental values. On the other hand, the results have demonstrated that the specific interactions formed between Py and Py derivatives oligomers with such solvent molecules, are based mainly on hydrogen bonding. This interaction resulted to be crucial to understand the working and principle of some chemical sensors, specifically solvent vapor sensors. The different chemical responses found between Py and NCMPy complexes are influenced mainly by the chemical nature, oxidation state of the polymer and polarity of the solvent, respectively. Particularly, neutral NCMPy complexes have shown the best response in terms of affinity in presence of water, methanol, and chloroform solvents. According to this data, the presence of cyano group (CN) indicates the importance of this substituent in chemical sensors. The theoretical results obtained in this work were corroborated with experimental analyses based on detecting solvent molecules in vapor-phase through a chemiresistive device.

Optoelectronic properties in conducting polymers

The last chapter of this thesis is devoted to the study of optoelectronic properties in conducting polymers. In the first work of this chapter the effect of the I^-/I_3^- redox pair electrolyte in conducting polymers was investigated since it has been widely used in DSSCs. Thus, a new insight of the effect on the structural, electrochemical and capacitive properties of micrometric and nanometric PEDOT films was studied. The results evidenced that the thickness of the films plays a key role on the capacitive properties, outstanding electrochemical properties being achieved at the nanometric scale. Electrochemical and capacitive properties were extensively investigated using cyclic voltammetry, recurrent galvanostatic pulse, chronopotentiometry and electrochemical impedance spectroscopy techniques. Results showed that nanometric PEDOT films exhibit very high electrochemical stabilities and excellent specific capacitances (~185 $F \cdot g^{-1}$), the latter being preserved in ~94 % after 2000 cycles in a I^-/I_3^--containing solution. Morphological studies revealed that the electrochemical and capacitive properties of PEDOT films are significantly influenced by their porosity, this property being relatively unaffected by the I^-/I_3^- redox pair. Consequently, nanometric PEDOT films in presence of I^-/I_3^- were estimated excellent candidates to be employed as supercapacitors.

The second part of this chapter was devoted in terms of application, thus, all-conducting polymer batteries, in which both the anode and cathode consist of films made of perchlorate-doped pure poly(3,4-ethylenedioxythiophene) (PEDOT), alternated layers of PEDOT and poly(N-methylpyrrole) or PEDOT/clay nanocomposites, were fabricated. Batteries, which were used as power source for a LED bulb, are rechargeable and exhibit excellent charge/discharge cyclability and stability. Therefore, the organic devices prepared using PEDOT and multilayered films have been found to be promising platforms to achieve metal-free power sources. In particular the multilayered films showed a dual behavior being useful for the fabrication of both capacitors and batteries.

Finally, the optoelectronic properties of conducting polymers were investigated in PEDOT and hybrid nanocomposites films. The results showed that the conductivity is clearly affected in presence of factors such as temperature and illumination. Again, the effect of clay modifies the conductive properties of conducting polymers, thus, the lowest conductivity values were exhibited by hybrid nanocomposites. This tendency

was also corroborated in presence of temperature. However, the conductivity evaluated by influence of temperature during hours revealed an inverse tendency, being the conductivity values higher for PEDOT-MMT films. Within this context, the charge transport mechanisms were explained by using the VRH theory. On the other hand, the illumination radiated on the surface of PEDOT and PEDOT-MMT films verified the photoconductive response of both systems, showing similar response in all cases. Consequently, PEDOT and hybrid nanocomposites based on modified montmorillonite showed an excellent behaviour to be employed as photoreceptor devices.

Chapter 10. Conclusions

(1) AFM images showed that PEDOT films tend to form compact aggregates, which are stabilized by the perchlorate dopant anions. This growing is ascribed to the linearity of the polymer through α – α linkages, which enhance the electroactive properties of PEDOT. On the other hand, PNMPy films show a linear growth during the first stages of electropolymerization (θ < 30s). However, this tendency changes when the θ ≥ 30s. At higher polymerization times, the growth of PNMPy films is dominated by formation of chemical crosslinks and branches. The electrochemical properties of PNMPy verified the high and low electrochemical stabilites of the PNMPy films using θ < 30s and θ ≥ 30s. In terms of properties, nanometric PEDOT films exhibit higher charge storage than nanometric PNMPy films. Multilayered nanometric systems formed by alternated layers of PEDOT and PNMPy exhibit higher electroactivity than PEDOT and PNMPy films, although the electrochemical stability is lower than PEDOT. Electrical properties were evaluated by using C-AFM, which verified that the conductivity of multilayered films is similar to those of PEDOT homopolymer.

(2) Multilayered films formed by three CPs (ml-PEDOT/PPy/PNCPy) employing different polymerization times in order to control the thickness (nanometric and micrometric structure) evidenced important differences in terms of properties. Thus, at electrochemical level, PEDOT/PPy/PNCPy films reach an increment of the electroactivity until a threshold thickness (~ 2 μm), whereas a negligible difference was observed for thicker films. On the other hand, the loss of electroactivity upon consecutive oxidation-reduction cycles is significantly important for the nanometric films, while the electrostability increases when a threshold thickness (≥ 4 μm). The multilayered systems formed by PEDOT/PPy/PNCPy films exhibit a reduction of electroactivity and electrostability compared with those formed by two CPs only (ml-PEDOT/PPy and ml-PEDOT/PNCPy).

(3) The synergistic effect produced among layers of PEDOT and PNMPy favors the specific capacitance, being considerably higher than the pure homopolymers.Thus, the specific capacitance values grow in the following order: PNMPy < PEDOT < ml-PEDOT/PNMPy. The higher porosity and structural changes observed in the multilayered system have proved to be fundamental on the application of supercapacitors. Consequently, symmetric supercapacitors (Type I) were fabricated by assembling three-layered ml-PEDOT/PNMPy system.

The results showed a specific capacitance value of 90 F·g, being the highest value compared with PEDOT and PNMPy systems, respectively. In this context, multilayered systems formed by alternated layers of PEDOT/PPy onto self-assembled monolayers of octanethiol were also proved as supercapacitors. The effect of the SAMs has been found to be particularly relevant in the specific capacitance, capacity to store charge and power density. Thus, the 3-layered/C_8-SH shows the highest specific capacitance, capacity to store charge, Coulomb efficiency, energy density and power density (*i.e.* the *SC* after 2000 consecutive cycles is 80 $F \cdot g^{-1}$) in a symmetric ultracapacitor.

(4) Self-assembled monolayers (SAMs) of octanethiol and dodecanethiol onto stainless steel electrodes modify the electrochemical deposition of PEDOT. SAMs promote both the electroactivity and the adherence of micrometric PEDOT films, such enhancements increasing with the length of alkyl chain of the alkanethiol. The influence of SAMs on the topology, morphology and electrochemical properties is clearly evidenced at nanometric level employing a polymerization time of 10s. The electroactivity and electrostability of PEDOT films produced on the modified substrates are significantly higher than those of the material electropolymerized on untreated-steel. At morphological level, the results show that SAMs promote the formation of compact molecular aggregates in the first stages of the electropolymerization of PEDOT films. This effect, which produces a reduction of the porosity in the internal side of the films, together with the intrinsic barrier properties of alkanethiols SAMs is responsible for the significant improvement of the abilities of PEDOT to inhibit corrosion.

(5) The morphology of PEDOT deposited on ITO electrodes can be described as an ultraporous three-dimensional network of ultrathin sticks. This particular fiber-like morphology is fully consistent with the significant enhancement of electroactivity observed for the material deposited on ITO with respect to that obtained using steel electrodes. On the other hand, PEDOT grown on steel shows a compact and relatively dense packing of agglomerated connected by sticks. The influence of the substrate affects the roughness, topography, morphology and porosity of the material. Precisely, porosity plays a key role on the design of supercapacitor. Asymmetric supercapacitors made of electrodes consisting on PEDOT deposited on ITO and steel substrates were found to present very high specific capacitance, electrochemical stability and coulombic efficiency.

(6) PEDOT-MMT nanocomposites have been synthesized successfully by using electrochemical methods *(i.e.* anodic electropolymerization under a constant potential of 1.10 V) employing a concentration of clay corresponding to 1, 5 and 10, 20 and 50 % w/w. At electrochemical level, the electroactivity of PEDOT-MMT nanocomposites increases with the concentration of clay, being higher than that of individual PEDOT. The SC and electrostability largely depend on the thickness of the films. Thus, the SCs of nanometric PEDOT and PEDOT–MMT films, which range from 355 to 237 $F \cdot g^{-1}$ (PEDOT and PEDOT–MMT 50% w/w, respectively), are one order of magnitude higher than those of the corresponding micrometric films. Similarly, the electrostability of micrometric PEDOT–MMT films is lower than that of nanometric ones. On the other hand, the electrostability is higher for PEDOT systems than PEDOT-MMT nanocomposites, although the electrical conductivity decreases one order of magnitude upon the incorporation of a concentration of MMT ≥ 20% w/w. The adherence and thermal stability are lower for PEDOT than for the nanocomposites, increasing moderately with the concentration of MMT.

(7) Nanometric ultracapacitors of types I and II show very high SC values for exfoliated PEDOT-MMT nanocomposites. The larger SC correspond to the symmetric PEDOT/PEDOT and the asymmetric PEDOT/PEDOT–MMT 20% w/w (465 and 429 $F \cdot g^{-1}$, respectively), whereas the SC of PEDOT–MMT/PEDOT–MMT decreases from 217 to 179 $F \cdot g^{-1}$ when concentration of MMT increases from 5% to 50% w/w. In contrast, the clay does not alter the electrostability of these nanometric ultracapacitors, the LES of nanometric ultracapacitors being very similar independently of their symmetric or asymmetric configurations. On the other hand, the SCs of micrometric PEDOT–MMT/PEDOT–MMT 20% w/w and PEDOT/PEDOT–MMT 20% w/w are higher than that of PEDOT/PEDOT, even though the latter shows the highest electrochemical stability.

(8) Electrochemical degradation studies using consecutive oxidation-reduction cycles indicate that the favorable effect of the clay on the SC and electrochemical stability of both type I and II ultracapacitors decreases significantly after 500 consecutive oxidation-reduction cycles. This effect is much less pronounced when electrochemical degradation is carried out using charge/discharge cycles. In this case, the reduction of the SC is relatively low and, in addition, the

asymmetric configuration retains the favorable effect of the clay on the SC, the power density and the maximum specific energy. On the other hand, EIS studies and SEM micrographs evidenced that the electrochemical degradation produces deep cracks on the surface of the films, facilitating the diffusion of ions.

(9) Multilayered electrochemical nanocomposites evidenced that the highest specific capacitance was performed for 3-PEDOT/PPy (20 %) systems, although this electrochemical parameter decreased when the number of layers increased. The overall electrochemical properties in terms of electroactivity and specific capacitance are indicated as follows: 3-PEDOT/PPy (20 %) > 3-PEDOT/PPy (20 % Mod) > 3-PEDOT/PPy. On the other hand, electrochemical stability is indicated as: 3-PEDOT/PPy > 3-PEDOT/PPy (20 %) > 3-PEDOT/PPy (20 % Mod). The results reflected that multilayered nanocomposites exhibit better electrochemical properties than those of single homopolymer films. Moreover, 3-PEDOT/PPy (20 % Mod) films presented the best corrosion protection properties since the clay effect induces the formation of compact structures, thus, multilayered electrochemical nanocomposites based on modified montmorillonite preclude the entrance of chloride anions.

(10) The novel pyrrole derivative known as poly[N-(2-cyanoethylpyrrole)] was synthesized through electrochemical methods from an optimal oxidation potential of 1.40 V. Both the doped and undoped PNCPy showed a negligible flow of current density through the electrode for potentials lower than 1.10 V, while this flow increases rapidly after such potential. The morphological characterization of PNCPy evidenced a growing without any preferred direction indicating that chemical crosslinks induce the formation of multidirectional branches. Moreover, XRD evidenced that PNCPy presents some degree of structural order and SEM micrographs reflected a compact structure with elliptical protuberances homogeneously distributed in the surface.

(11) Cyclic voltammograms were recorded to estimate the IP (5.3 eV), EA (2.9 eV) and ε_g (2.4 eV) of PNCPy. The ε_g value measured using the UV-vis absorption spectrum, which showed the π-π^* transition peak at 372 nm, was found to be in excellent agreement with the electrochemical estimation. DFT and TD-DFT calculations corroborated the experimental values taking into account a model based on the existence of carbonyl groups attached to the pyrrole ring of selected repeating units. The theoretical study concluded the possible structure, which is

definied as a cross-linked structure formed by small branches, the last repeating unit of each one bearing a carbonyl group.

(12) The Py and NCMPy complexes studied in this thesis presented similar specific interactions in presence of water, methanol, and acetonitrile solvents. Thus, complexes were stabilized through hydrogen bonding (H-O···H and C-N···H) for all their electronic states (neutral, cationic and dicationic). The strength of this interaction in gas-phase for neutral Py complexes grows in the following order: $4Py^0\cdots H_2O$ > $4Py^0\cdots CH_3OH$ > $4Py^0\cdots CH_3CN$ > $4Py^0\cdots CHCl_3$, whereas for NCMPy complexes the order is showed as follow: $4NCMPy^0\cdots H_2O$ > $4NCMPy^0\cdots CH_3OH$ > $4NCMPy^0\cdots CHCl_3$ > $4NCMPy^0\cdots CH_3CN$. The strength of the interaction energy in gas phase increases with the charge of the complexes. The charge distribution, chemical nature and polarity of the solvent plays an important role on the formation of the complexes. Thus, neutral NCMPy complexes presented a better affinity in water, methanol and chloroform solvents than neutral Py complexes according to the interaction energies in solution. These tendencies are fully consistent with experimental observations. Thus, NCMPy can be applied as a highly sensitive detector of solvents in vapour-phase.

(13) The electronic properties of NCMPy complexes showed an IP and ε_g values higher than Py complexes because of the presence of cyano group. This substituent has a strong electron-withdrawing effect, which distorts the conformation structural of NCMPy oligomers modifying the electronic properties. In this way, Py oligomers exhibited an anti-gauche conformation (neutral state) and anti-planar conformation (excited states), whereas NCMPy presented a gauche-gauche conformation in all its electronic states. The electronic properties of NCMPy complexes in presence of solvents were estimated from theoretical calculations, which showed an excellent agreement with experimental observations.

(14) The synthesis of novel 3-halidethiophenes was successfully carried out by using electrochemical techniques in a BFEE solution containing $(Bu)_4NBF_4$. Potentiostatic methods estimated an optimal oxidation potential at 1.70 V for both PClTh and PBrTh. Morphological studies evidence a favorable growth through α-α linkages on 3-halidethiophenes. The presence of strong sustituents such as halide atoms influences the electronic and electrochemical properties of thiophene, thus the ε_g and IP values were corroborated at theoretical and experimental level as

follows PFTh < PClTh < PBrTh. The electrochemical properties of PClTh in terms of electroactivity and electrostability are better than PBrTh according to its higher porosity induced by its chemical structure. Quantum mechanical calculations indicate that the halogen atom has a significant impact on the conformational preferences of 2-XTh and 3-XTh oligomers. Thus, the conformational freedom of oligomers with X = Br is restricted by strong steric repulsive interactions, especially when repeating units are associated by head-to-head linkages, while oligomers with X = F show a significant conformational flexibility. Compounds with X = Cl present an intermediate behavior. On the other hand, the aromaticity slightly varies from unsubstituted 2-Th to 2-XTh(3,3'), independently of the halogen atom. Moreover, within each series the effect of the halogen atom is very small. The repulsive character of the S···X interaction explains the higher stability of 2-XTh(4,4') isomer compared to 2-XTh(3,3') in the *anti* conformation.

(15) The electrocatalytic activity of I^-/I_3^- species improved the properties of both nanometric and micrometric PEDOT films, benefits were more important in the former than in the latter. The loss of electroactivity of nanometric films was of only ~17% after 250 consecutive oxidation-reduction cycles, reflecting exceptional electrochemical stability. Moreover, the specific capacitance was ~ 185 $F.^{g-1}$, this value decreasing by only 6% after 2000 charge-discharge cycles.

(16) The performance of batteries fabricated with PEDOT/clay electrodes is considerably lower than that of the batteries prepared using PEDOT and, specially, 3-layered electrodes. This has been attributed to the inert nature of the clay, which does not promote good electrical contacts to aid the penetration of the electrolyte in the material, which results in a poor stability. All-PEDOT and all-PEDOT/PNMPy batteries are easily rechargeable and exhibit excellent cyclability and environmental stability. The all-CP batteries prepared in this work have been successfully used to power a LED light, suggesting that they are promising in future applications as, for example, power source for devices with low-power consumption requirements.

(17) The conductivity is clearly affected by temperature and radiation in conducting polymers. Regarding to this topic, conductivity values for both PEDOT and PEDOT-MMT systems decreased with temperature. The relation between temperature and conductivity allowed to confirm a three-dimensional (3-D) VRH

model by fitting the Lnσ vs $T^{-1/4}$ for both PEDOT and PEDOT-MMT systems. SEM images revealed that the thermal degradation affects considerably the morphology, as a consequence, a reduction of the clusters size was evidenced in PEDOT films. In this context, hybrid nanocomposite films showed better thermal degradation than PEDOT films, thus, the clay precludes the thermal degradation acting as barrier effect. EIS studies concluded that the presence of clay avoids and blocks the entrance of ions (ClO_{4-}) increasing the ionic charge-transfer resistance ($R_{CT)}$. On the other hand, the radiation effect induced by illumination evidenced an increase of the conductivity compared with dark conditions for both PEDOT and PEDOT-MMT films, respectively. This phenomena evidenced that the light radiation on the structures of PEDOT and PEDOT-MMT films shows interesting photoconductive responses, consequently, these materials can be employed as photoreceptor devices.